

# **MekIT'19**

Tenth national conference on

# **Computational Mechanics**

Trondheim 3-4 June 2019

Editors: Bjørn Skallerud and Helge I. Andersson

**International Center for Numerical  
Methods in Engineering (CIMNE)**  
Gran Capitán s/n, 08034 Barcelona, Spain  
[www.cimne.com](http://www.cimne.com)



Printed by: Artes Gráficas Torres S.L., Huelva 9, 08940 Cornellà de Llobregat, Spain

Deposito legal: B-21132-2018

ISBN: 978-84-949194-9-7



## Preface

The present volume contains 24 papers based on the 33 contributions presented at the 10<sup>th</sup> *National Conference on Computational Mechanics -MekIT'19* held at The Norwegian University of Science and Technology (NTNU) in Trondheim (Norway) June 3<sup>rd</sup> and June 4<sup>th</sup>, 2019.

The series of national conferences on Computational Mechanics dates back to *MekIT'01*, which was arranged at NTNU in Trondheim early May 2001. The motivation of the first MekIT-conference was to bring together those involved in Computational Mechanics in Norway, both in industry and academia, to share their experiences and report on their research in an informal and friendly setting. At that time, an arena where those involved with rather different applications of Computational Mechanics, as well as scientists developing new computational methods of more generic nature, could meet was non-existing in Norway.

The conferences have from the very beginning aimed to cover all sub-areas of Computational Mechanics and not only computational solid mechanics and computational fluid dynamics. In spite of distinctions in approach and methodology the difficulties faced by the researchers are often of similar nature and problems can perhaps be remedied in the same way irrespective of the actual application. It has all the time been our hope that the conference series will demonstrate that Computational Mechanics is a viable research tool by which both human curiosity and industrial needs can be satisfied by scrutinizing the laws of classical mechanics, provided that adequate numerical methods are implemented in reliable software, and efficient computers are available.

A particular mission has been to offer a stimulating environment in which doctoral students and other young researchers can present results of their own project work, perhaps for the first time, and at the same time get an impression of the multifaceted research which takes place in other research groups and at other institutions in Norway.

In addition to the contributed talks, keynote lectures are delivered by carefully selected scientists, normally recruited from the other Scandinavian countries, to give an impression of state-of-the art in Computational Mechanics. This year, however, we were delighted that Professor Robert M. McMeeking (Department of Mechanical Engineering & Materials Department, University of California at Santa Barbara, USA) and Professor Eric Lamballais (Institut P', CNRS -Université de Poitiers, France) shared their vast expertise with us in fascinating lectures on computational biomechanics and large-eddy simulations, respectively.

The regular contributions have primarily been written by PhD students and other young researchers together with their supervisor(s) or project leader(s) and always in English. The manuscripts were submitted before the start of the conference. Each manuscript has been subjected to reviewing by at least one member of the Scientific Committee and in some cases also by a peer outside of the Scientific Committee. The authors were thereafter asked to revise their manuscripts in accordance with the comments and suggestions made by the reviewers. The majority of the authors accepted our invitation to prepare a carefully revised version of their manuscript, which now is included in the printed conference proceedings. Following the contributions by the two invited lecturers, the 22 contributed papers appear alphabetically according to the family name of the first author and are listed in the Table of Contents. The names of all authors and co-authors of the contributed papers are included in the Author Index.

Earlier proceedings have been published by Tapir Academic Press and Akademika Publishing just prior to the conference. For the first time in 2015 the conference proceedings were published by CIMNE and not until a couple of months after the conference. This new scheme enables a more thorough reviewing process and contributes to the quality of this collection of 2+22 papers.

We, as the organizers of the series of ten MekIT-conferences, could instead have arranged separate conferences in computational fluid dynamics (CFD) and computational solid mechanics (CSM). But we realized that there are a number of common challenges in CFD and CSM, although there are also differences like fractures/cracks and shocks.

In common, however, CFD and CSM are based on *Newtonian mechanics* and *continuum theory*, although different material models are used. Water, for example, is an isotropic and Newtonian

fluid, but sediments or polymer additives will i) change the viscosity and ii) induce anisotropy. The material model (the rheological model) is an essential issue both in CFD and CSM.

Also in common is the fact that the fundamental equations are partial differential equations (PDEs) which depend on the material or fluid properties. The PDEs are often *non-linear* and have to be solved by means of *numerical methods*: finite-element, finite-difference, finite-volume, spectral element methods etc.

Also in common is that the governing PDEs have to be *discretized* into grid cells or finite or spectral elements. The solutions will therefore be discrete rather than continuous and resolution refinement is required to handle cracks in CSM and shocks in CFD.

Also in common is that *initial conditions* are needed at the beginning of the simulation and *boundary conditions* are required in space. Like in weather forecasting, for instance, the solution may depend crucially on the initial conditions.

After a simulation has been performed, quality assessment is required both in CFD and CMS. This includes *validation*, namely to justify that the right equations are solved, and *verification*, namely to assure that the equations are solved right. The latter includes *grid independency* testing.

The majority of problems in CFD and CSM are *non-linear*. Therefore, although a problem is perfectly symmetric, an *asymmetric solution* may develop as a result of a bifurcation that sets in above a certain parameter value which makes the symmetric solution asymmetric due to a competition between two stable but asymmetric solutions. Such bifurcations are sensitive to the choice of initial conditions as well as to proper discretization and resolution.

Also after the simulation is ready and the quality has been assessed, *post-processing* (to get out the data your sponsor asked for) and 3D *visualizations* (to convince your sponsor and politicians what you talk about) are required and represent an integral part of Computational Mechanic.

During the years of MekIT, we as the organizers have observed a couple of trends since the start-up back in 2001:

- A move from mostly steady problems to time-dependent problems.
- A move from mostly 2D to 3D problems, which implies much larger computations.
- A move from linear to non-linear problems, which implies more challenging computations.
- A move from simple physics towards multi-physics and coupled problems.
- A move from mono-scale to multi-scale problems.
- An improving quality of the oral presentations at the conference and the written contributions to the proceedings.

The latest conference, *MekIT'19*, was hosted by NTNU's Faculty of Engineering and arranged jointly by Department of Energy and Process Engineering and Department of Structural Engineering. The Editors appreciate the willingness of the authors to stick to the time schedule for paper submission and revision. We are particularly thankful to the members of the Scientific Committee and their peers for reviewing the submitted papers and thereby assure the quality of these Proceedings. Administrative assistance from Department of Energy and Process Engineering and financial support from Faculty of Engineering are gratefully acknowledged.

We, as the organizers of the ten MekIT-conferences and editors of the ten MekIT-proceedings, appreciate the long-lasting interest in this biennial event and the willingness of present and former PhD-students and colleagues to contribute parts of their research work to the MekIT conferences.

September 2019

Helge Andersson

Bjørn Skallerud

Chairmen: Professor Bjørn Skallerud – Department of Structural Engineering (NTNU) Professor Helge I. Andersson – Department of Energy and Process Engineering (NTNU)

Scientific Committee: Helge I. Andersson (NTNU) Hans Bihs (NTNU) John Grue (University of Oslo) Trond Kvamsdal (NTNU/SINTEF) Mikael Mortensen (University of Oslo) Muk Chen . (University of Stavanger) Bjørnar Pettersen (NTNU) Bjørn Skallerud (NTNU) Geir Skeie (DNV GL, Oslo) Magnus Svärd (University of Bergen)

Sponsors: NTNU's Department of Energy and Process Engineering (EPT) and Faculty of Engineering (IV)

Front cover graphics:

The Editors would like to express their gratitude to Hans Martin Aguilera and Victorien Prot for the front cover graphics.



# Table of Contents

E. Lamballais and R. Vicente Cruz <i>From Explicit to Implicit Subgrid-Scale and Wall Modelling in Large-Eddy Simulation</i> .....	1
Robert M. McMeeking, Mattia Bacca and Omar A. Saleh <i>Contraction of polymer gels due to the activity of molecular motors</i> .....	25
Hans Martin Dahl Aguilera, Victorien Prot, Bjørn Skallerud and Stig Urheim <i>Finite Element Analysis of a Barlow Mitral Valve: Patient Specific Geometry and Comparison With Three-Dimensional Echocardiographic Data</i> .....	27
Jan Christian Anker <i>Pipe Fsi in Generalized Coordinates</i> .....	51
Mads Aursand, Bjørn Skallerud <i>Numerical Simulation of Fatigue Crack Growth in Offshore Mooring Chains</i> .....	61
Cai Tian, Fengjian Jiang, Bjørnar Pettersen and Helge I. Andersson <i>The Long Periodicity of Vortex Dislocations in the Wake Behind a Step Cylinder</i> .....	81
C. Pakozdi, W. Wang, A. Kamath and H. Bihs <i>Definition of the Vertical Spacing of a Sigma Grid Based on the Constant Truncation Error</i> .....	101
Hannibal E. Fossum, Andreas N. Osnes and Tor E. Kristensen <i>Evaluation of Safety Distances for Storage of Explosive Materials Using a Combination of Thermochemical Computations and CFD</i> .....	115
Knut Erik Teigen Giljarhus and Steinar Evje <i>Use of the Finite Volume Framework Openfoam for Simulation of Tumor Growth</i> .....	139
Henrik Granum, David Morin, Tore Brvik and Odd Sture Hopperstad <i>Simulation of Blast-Loaded Aluminium Plates With Crack-Like Defects</i> .....	149
Tore Holmas and Ingar Fossan <i>Accidental Load Assessment of Process Pipe Systems</i> .....	165
Marek Jan Janocha and Muk Chen Ong <i>Flow-Induced Vibration of Tandem Cylinders in the Vicinity of a Horizontal Plane Wall</i> ..	181
Rohith Jayaram, Jurriaan J.J. Gillissen, Lihao Zhao and Helge I. Andersson <i>Numerical Solution of Poisson Equation Using Sherman-Morrison Algorithm in Taylor-Green Vortex Flow</i> .....	197
Frederik Kristoffersen and Bernhard Müller <i>Adaptive Mesh Refinement on Unstructured Cartesian Grids for the Euler Equations</i> .....	211
Trond Kvamsdal, Knut M. Okstad, Mukesh Kumar, Arne M. Kvarving and Kjell M. Mathisen <i>Adaptive Isogeometric Methods for Thin Plates</i> .....	237

Xuyan Liu, Bjørn H. Skallerud, Victorien E. Prot and Gerhard A. Holzapfel <i>An Anisotropic Growth Model For Fibrous Tissues: Continuum Formulation and Computational Aspects</i> .....	249
Adina Moraru, Oddbjørn Bruland, Andrew Perkis and Nils Rüther <i>Visualizing Hydrodynamic Fluid Simulations Within an Immersive Experience as a Scientific Dissemination Strategy</i> .....	265
Andreas N. Osnes, Magnus Vartdal, Marianne G. Omang and Bjørn A. P. Reif <i>Numerical Investigation of Shock Wave Particle Cloud Interaction in Cylindrical Geometries</i> .....	285
Sen Qu, Shengnan Liu and Muk Chen Ong <i>Application of Different Rans Turbulence Models for Breaking Waves Past a Vertical Circular Cylinder</i> .....	311
Mandar V. Tabib, Adil Rasheed and Trond Kvamsdal <i>High-Resolution Cfd Modelling and Prediction of Terrain-Induced Wind Shear and Turbulence for Aviation Safety</i> .....	323
Laurel Ohm, Benjamin K. Tapley, Helge I. Andersson, Elena Celledoni and Brynjulf Owren <i>A Slender Body Model for Thin Rigid Fibers: Validation and Comparisons</i> .....	343
W. Wang, C. Pakozdi, A. Kamath, H. Bihs <i>High Performance Phase-Resolved Wave Modelling for Irregular Coastal Topography</i> ...	367
Guang Yin and Muk Chen Ong <i>Numerical Investigation of Scour Beneath a Submarine Piggyback Pipeline</i> .....	381
Yucheng Jie, Helge I. Andersson and Lihao Zhao <i>A Power Law of Particle Enstrophy in a Turbulent Channel Flow at a Medium Reynolds Number</i> .....	395
Zhaoyu Shi, Fengjian Jiang, Helge I. Andersson and Hakon Strandenes <i>On Simulation of Particle-Laden Wake Flow</i> .....	407
AUTHOR INDEX .....	419

# FROM EXPLICIT TO IMPLICIT SUBGRID-SCALE AND WALL MODELLING IN LARGE-EDDY SIMULATION

ERIC LAMBALLAIS AND RODRIGO VICENTE CRUZ

Incompressible Turbulence and Control Group, Pprime Institute, CNRS - University of Poitiers - ISAE/ENSMA, France

**Key words:** Turbulence, Large-Eddy Simulation, Subgrid-Scale Modelling, Wall-layer Modelling, Implicit Modelling.

**Abstract.** In this paper, the concept of implicit modelling via the numerical error is exemplified in the context of large-eddy simulation. It is shown how the control of numerical errors at small scales can be an ersatz of subgrid-scale modelling while playing even the role of wall-layer model in functional terms. Despite the lack of rigorous formalism, implicit large-eddy simulation is found to be more accurate than conventional large-eddy simulation based on explicit subgrid-scale modelling. To illustrate these features, two academic turbulent flows are investigated by direct and large-eddy simulation: (i) the Taylor-Green vortex problem; (ii) the pipe flow. It is shown that the crucial quality of implicit subgrid-scale modelling lies in its ability to damp the smallest scales allowed by the computational mesh. This feature is beneficial for the two flow configurations investigated, with a remarkable improvement of the near-wall turbulent statistics for the pipe. On the contrary, the very popular Smagorinsky model is found to be unable to control this type of spurious oscillations with a structural difficulty to ensure numerical convergence in the Taylor-Green vortex problem. Even if implicit large-eddy simulation is always found more accurate than conventional large-eddy simulation for this flow, a limitation of the approach is clearly exhibited for a challenging computational configuration where the mesh is very coarse by comparison with direct numerical simulation. In this situation, the fundamental assumption that very large scales are not subjected to subgrid-scale effects is shown to be erroneous. Because this assumption is inherent to implicit large-eddy simulation, it is suggested that a specific explicit modelling should be developed to correctly model the influence of subgrid-scales on very large scales.

## 1 INTRODUCTION

In large-eddy simulation (LES), the purpose is to compute a reduced solution less demanding in terms of number of degrees of freedom in order to save computational resources. Naturally, this reduction has to preserve the most important features of the

“full” solution to enable reliable predictions. In this work, the full solution is assumed to satisfy the incompressible Navier-Stokes equations while being assimilated to its highly-accurate numerical approximation obtained by direct numerical simulation (DNS). The reliability of the prediction is then connected to the ability of LES to provide mean velocity and basic turbulent statistics with accuracy close to DNS.

The strategy of conventional LES is to derive the governing equations of the reduced solution through the definition of the reduction procedure. Typically, a low-pass filter is invoked to establish the governing equations without specifying the exact form of the filter but referring to a separation scale  $\Delta$  to split the solution into its large-scale (LS) and subgrid-scale (SGS) components. Non-linearities of Navier-Stokes equations introduce new unknowns leading to a closure problem. The most popular way to close the equations is to use a constitutive relation of Boussinesq-type by defining a SGS eddy viscosity with in particular the well-known Smagorinsky model which is a physical closure designed to match the expected SGS dissipation. Unfortunately, the formalism to establish the governing equations suffers from severe shortcomings with in particular the commutation error between the filter and the spatial differentiation [15, 14, 13, 30]. Another important weakness is the sensitivity of the equations to numerical errors. To ensure numerical convergence, a discretization clearly finer than the separation scale  $\Delta$  should be employed. This requirement is fully recognized (see for instance [5, 29, 1, 26, 27, 28]) but almost never fulfilled by LES users who normally use a computational mesh with a cell size simply adjusted on the separation scale  $\Delta$ , a practice which is clearly against the numerical accuracy. Naturally, it has to be recognized that the requirement of mesh refinement makes LES less computationally attractive by comparison to DNS, especially if the slow numerical convergence of the solution is considered, as shown by [9] for the Smagorinsky model.

A more pragmatic approach of LES is to renounce to well defined governing equations by discretizing the Navier-Stokes equations on a coarser mesh than in DNS and without any explicit modelling terms. In this strategy, a regularization effect is expected from numerics in order to automatically provide the reduced/filtered solution. This idea started with the development of the MILES approach [2]. Here, following the more recent terminology, we refer to implicit LES when the regularization provided by the numerical error is used as a substitute of subgrid-scale (SGS) modelling, irrespective of the techniques used to apply the resulting artificial dissipation. In this paper, we investigate the concept of implicit LES using a generic solver of Navier-Stokes equations in which the numerical dissipation can be expressed as an implicit spectral vanishing viscosity (SVV) which can be easily controlled while ensuring high-order accuracy. To have an overview of the diversity of approaches in implicit LES, the reader is referred to the collective book [16] where connections with explicit SGS modelling are also discussed. Note that the distinction between conventional and implicit LES is not so clear because some techniques can be based on a mixed strategy. For instance, a controlled regularization can be obtained by making scale selective an explicit model (Variational Multiscale Model, see [17, 3]).



The aim of the present contribution is to explain why and to what extent implicit LES can be successful despite the lack of clear formalism. This investigation is based on a particular technique of regularization but the main conclusions of the present study can be related to any implicit SGS modelling provided that it is highly accurate (in terms of numerical convergence) and scale selective (concentration of numerical dissipation at small scales). Two academic flow configurations are considered with the Taylor-Green vortex problem and the turbulent pipe flow. The former is a prototype of flow in transition up to fully developed turbulence whereas the latter is a generic flow with wall turbulence. Both flow configurations are analysed by DNS and LES at high Reynolds number.

Thanks to the new generation of massively parallel computers, it has become possible to generate DNS database at typical Reynolds numbers of LES applications. This is a major advantage for the development of SGS modelling which can be based on reliable data at realistic turbulent regimes and with a representative reduction of degrees of freedom associated with the LES filtering. This is particularly true for the Taylor-Green vortex problem considered here at the Reynolds number  $Re = 40000$ . To the best of the authors' knowledge, a DNS at this high value has never been documented. It is an unprecedented opportunity to assess very challenging LES while investigating rigorously the LS-SGS interactions as it was done by [9, 23] at lower Reynolds number. For the pipe flow, a DNS of reference at the same Reynolds number as considered here has already been reported in the literature [18]. The originality of present results lies in the use of very coarse mesh in the near-wall region and in the development of a robust method to estimate filtered turbulent statistics from DNS data obtained at marginal resolution. The possibility to compare with relevance turbulent statistics from implicit LES and DNS will enable us to rigorously confirm trends reported in [8] at lower Reynolds number.

The paper is organized as follows. First, the whole methodology is presented in section 2. Then, results from DNS/LES of the Taylor-Green vortex problem are discussed in section 3 through a posteriori and a priori analyses of the SGS modelling. The turbulent pipe flow is investigated in section 4 by DNS and LES to exhibit an unexpected feature of implicit wall-layer modelling. The main conclusions of the study are reported in section 5 while discussing prospects for further developments.

## 2 METHODOLOGY

### 2.1 Governing equations

For a fluid of constant density  $\rho$  and kinematic molecular viscosity  $\nu$ , the governing equations

$$\frac{\partial u_i}{\partial t} + \frac{1}{2} \left( u_j \frac{\partial u_i}{\partial x_j} + \frac{\partial u_i u_j}{\partial x_j} \right) = -\frac{1}{\rho} \frac{\partial p}{\partial x_i} + \nu \frac{\partial^2 u_i}{\partial x_j \partial x_j} - \frac{\partial \tau_{ij}}{\partial x_j} \quad (1)$$

$$\frac{\partial u_i}{\partial x_i} = 0 \quad (2)$$

correspond to the Navier-Stokes equations with an extra-term  $\tau_{ij}$  designed to model the influence of subgrid-scale (SGS) stresses. In DNS mode, pressure  $p(x_j, t)$  and velocity fields  $u_i(x_j, t)$  are assumed to be captured up to their smallest significant scales enabling to assume  $\tau_{ij} = 0$ . In LES mode,  $p(x_j, t)$  and  $u_i(x_j, t)$  are interpreted as only the LS component of pressure and velocity respectively by reference to a separation scale  $\Delta$  which is the lower bound of LS and the upper bound of SGS. In implicit LES, no explicit SGS modelling is used with  $\tau_{ij} = 0$ . In conventional LES, a constitutive relation is used to express  $\tau_{ij}$  as a function of  $p(x_j, t)$  and  $u_i(x_j, t)$ .

For the present study, only the very popular Smagorinsky model [31] is used with

$$\tau_{ij} = -2 (C_s \Delta)^2 |S| S_{ij} \quad (3)$$

where

$$S_{ij} = \frac{1}{2} \left( \frac{\partial u_i}{\partial x_j} + \frac{\partial u_j}{\partial x_i} \right) \quad (4)$$

is the strain rate tensor and  $|S|$  its magnitude with  $|S| = \sqrt{2S_{ij}S_{ij}}$ . This SGS model is considered in its simplest version where the constant  $C_s = 0.1$  is actually a constant without any attempt to adjust it through a dynamic procedure as originally proposed in [12, 11]. For comparison between standard and dynamic Smagorinsky models in the context of section 3, the reader is referred to [9], where it is shown that these two versions have similar drawbacks for the type of analysis carried out here.

An obvious but important remark is that the governing equations of LES based on the Smagorinsky model are continuous, as well as for DNS, without any need to refer to the spatial discretization. The single extra parameter is the separation scale  $\Delta$  which is only present in the constitutive relation (3). On the contrary, since implicit LES is based on artificial dissipation coming from numerical errors, discretization has to be introduced in this alternative technique.

## 2.2 Numerical methods

To solve equations (1,2), the massively parallel code Incompact3d is used. This solver has a spatial differentiation entirely based on centered compact finite difference schemes of sixth-order accuracy when free-slip or periodic boundary conditions are used as in the present study. Its mesh is Cartesian with  $n_x \times n_y \times n_z$  nodes regularly distributed in the computational domain  $L_x \times L_y \times L_z$ <sup>1</sup>. For a detailed presentation of this code, see [20, 21, 22].

In Incompact3d, the spatial differentiation of the convective term is kinetic energy conserving up to the time integration error. This crucial feature is ensured thanks to the use of the skew-symmetric form in equation (1). The only sources of dissipation are the viscous and the explicit SGS modelling terms. As a consequence, in the inviscid case free from any SGS modelling with periodic or free-slip boundary conditions, the kinetic

---

<sup>1</sup>The mesh refinement in one direction, enabled by Incompact3d, is not used here.

energy is trapped inside the computational domain at any mesh resolution. This property, observed in practice (as illustrated in section 3), is particularly convenient for the separate analysis of viscous/artificial and SGS dissipations.

Finally, it must be mentioned that a customised immersed boundary method has been developed in Incompact3d to enable the treatment of complex geometry despite the use of a Cartesian mesh [10]. This feature is used in section 4 to consider a cylindrical geometry.

### 2.3 Implicit SGS modelling

In Incompact3d, as a technique to perform implicit LES, a targeted numerical dissipation can be introduced by artificially boosting at small scales the computation of second derivatives in the viscous term while keeping the sixth-order accuracy. This particular technique makes hyperviscous the corresponding numerical errors with a scale-selectivity which leaves LS virtually free from any artificial dissipation. It can be shown that this approach is the discrete counterpart of SVV<sup>2</sup> leading to the concept of implicit SVV. The vanishing feature refers to the lack of any significant effect at LS. For instance, in the wavenumber range  $k \in [0, k_c]$  with  $k_c = \pi/\Delta x$  where  $\Delta x$  is the cell size, the artificial dissipation is only active in the range  $k \in [k_c/2, k_c]$  while being highly concentrated near the cutoff wavenumber  $k \lesssim k_c$ . For more details about this way to introduce numerical dissipation, the reader is referred to [24, 7, 9].

The advantage of the present technique is its flexibility through an easy control of numerical dissipation in terms of intensity and scale selectivity. In particular, the value of the implicit SVV at the cutoff wavenumber can be imposed through the free choice of the numerical viscosity defined as  $\nu_0 = \nu_s(k_c)$ . To make this choice consistently with the implicit LES methodology, [9] have proposed a very simple spectral closure of the Lin equation which provides a Pao-like solution as a prediction of the influence of the numerical dissipation on the kinetic energy spectrum in the context of homogeneous and isotropic turbulence. In this tool, the input is the ratio of LES and DNS cell sizes  $\Delta x_{LES}/\Delta x_{DNS}$  and the output is value of  $\nu_0$  that should ensure satisfactory numerical convergence of the LES solution through an efficient damping of the kinetic energy at small scales. In section 3, only two values of this ratio are considered with  $\Delta x_{LES}/\Delta x_{DNS} = (10, 25)$  leading to  $\nu_0 = (89, 351)$  respectively as predicted by the Pao-like closure.

## 3 LES OF THE TAYLOR-GREEN VORTEX PROBLEM

### 3.1 Flow configuration and DNS of reference

The solution of the Taylor-Green vortex problem is periodic in the three directions of space in a cubic domain  $(2\pi)^3$ . The initial condition has only one harmonic in every

---

<sup>2</sup>Spectral meaning as a function of the wavenumber  $k$  with  $\nu_s(k)$ .

direction and one zero velocity component with

$$\begin{aligned} u(x_i, 0) &= \sin(x) \cos(y) \cos(z) \\ v(x_i, 0) &= -\cos(x) \sin(y) \cos(z) \\ w(x_i, 0) &= 0. \end{aligned} \tag{5}$$

This generates a flow subjected to a strong turbulent breakdown up to a fully developed state close to turbulence at equilibrium. It is a free evolving flow where the kinetic energy

$$E_k = \frac{1}{(2\pi)^3} \int_{(2\pi)^3} \frac{u_i u_i}{2} d\mathbf{x}^3 \tag{6}$$

can only decrease through the effect of molecular dissipation

$$\varepsilon = \frac{1}{(2\pi)^3} \int_{(2\pi)^3} \nu \frac{\partial u_i}{\partial x_j} \frac{\partial u_i}{\partial x_j} d\mathbf{x}^3 \tag{7}$$

with the simple equation

$$\frac{dE_k}{dt} = -\varepsilon. \tag{8}$$

In this paper, only one Reynolds number  $Re = 1/\nu$  is reported with  $Re = 40000$ . This high value has required a mesh of  $5400^3$  nodes to reach the DNS accuracy. Using some symmetries of the problem, the number of degrees of freedom actually considered has been reduced by a factor 8 by limiting the calculation to the impermeable sub-box  $\pi^3$ . The flow has been simulated from  $t = 0$  to  $t = 20$  while generating a database composed of instantaneous fields and turbulent statistics. The state of the flow at two characteristic times is illustrated in figure 1 by visualization of the  $Q$ -criterion.

### 3.2 A posteriori analysis

To assess the various LES performed for this study, two mesh resolutions have been addressed. The High Resolution (HR) and Low Resolution (LR) terms refer to the use of  $540^3$  and  $216^3$  mesh nodes respectively. This corresponds to ratios  $\Delta x_{LES}/\Delta x_{DNS} = (10, 25)$  which are associated to a reduction of the computational cost by  $10^4$  (0.01%) and  $25^4$  (0.000256%) respectively. In view of these drastic computational savings, both cases can be seen as very challenging while enabling LES to potentially capture more than 97% (HR) and 92% (LR) of the kinetic energy throughout the simulation. The time evolution of the unfiltered/filtered kinetic energy and their associated dissipation are presented in figure 2. Filtered data are obtained using the prediction of the Pao-like solver as explained in [23].

In order to assess that kinetic energy conservation is ensured by the convective term discretization, two preliminary calculations have been performed by removing the viscous term at high and low resolution (HR-LR). These type of calculations can be designated as

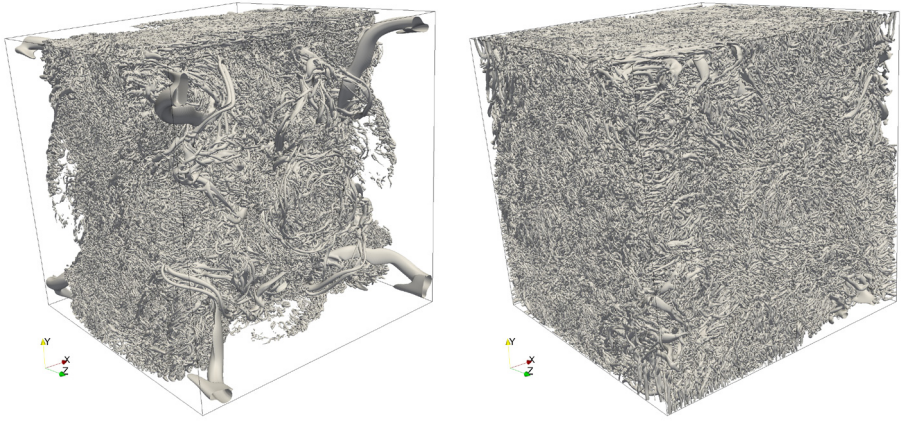


**Figure 1:** Isosurface of  $Q$ -criterion at  $t = 10$  (left) and  $t = 15$  (right). DNS data in the sub-box  $\pi^3$  with  $Q = 4$ .

solving the truncated Euler equations. For the time sequence  $0 \leq t \leq 20$  considered while choosing a timestep  $\Delta t$  close to the CFL limit at LR, the deviation from  $E_k = 0.125$  is less than 1%. Additionally, it has been checked that the loss of kinetic energy approximately scales on  $\Delta t^3$  as expected for the third-order time advancement scheme used here. The analysis of kinetic energy spectra  $\bar{E}(k)$  clearly shows that the flow progressively evolves as a white noise with  $\bar{E}(k) \sim k^2$  corresponding to fully thermalized state [6]. This behaviour is illustrated in figure 3.

Two additional preliminary calculations have been carried out by solving the Navier-Stokes equations at HR/LR but without any attempt to model SGS effects, neither explicitly nor implicitly. The kinetic energy spectra obtained for these “no-model LES” are presented in figure 4. At LR, a thermalization can be observed on more than 80% of wavenumbers with a spectacular pile-up of  $\bar{E}(k)$  near the cutoff wavenumber  $k_c$  as soon as  $t = 5$ . As expected, the extension of this pile-up is more limited at HR thanks to the molecular dissipation which prevents the establishment of a wide thermalized zone in the wavenumber range considered. However, the examination of instantaneous fields clearly shows that the solution is subjected to spurious numerical oscillations in the whole computational domain similarly to the LR case (see figure 7 for an illustration based on the  $Q$ -criterion). The lack of physical realism of this type of no-model solutions can be confirmed by comparing the time evolution of the resulting total dissipation  $\bar{\varepsilon} = -d\bar{E}_k/dt$  with its filtered DNS counterpart. This comparison is presented in figure 5. It can clearly be observed that the lack of any SGS modelling leads to completely wrong prediction with a dramatic overestimation of the dissipation during the turbulence breakdown due to the partial thermalization which magnifies the viscous friction phenomena. This paradoxical

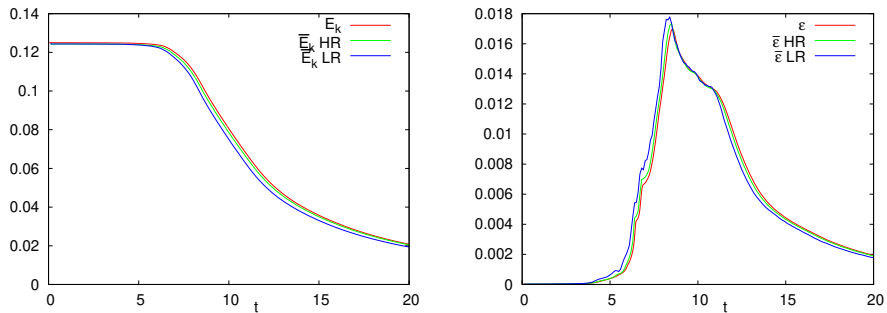


**Figure 2:** Time evolution of the unfiltered and filtered kinetic energy and its associated dissipation.

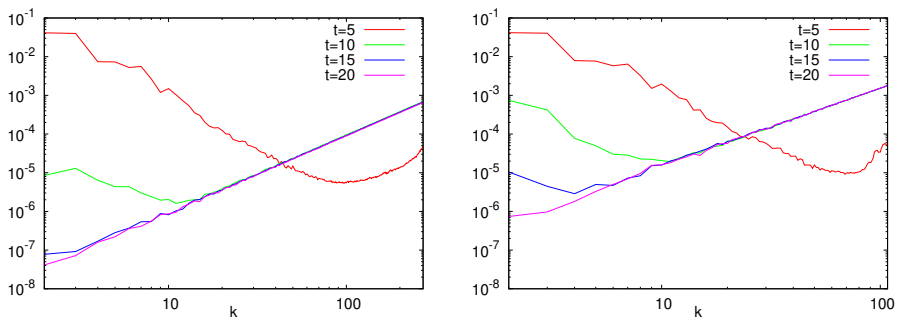


**Figure 3:** Energy spectra  $\bar{E}(k, t)$  at  $t = 5, 10, 15, 20$  when solving the truncated Euler equations. Left: HR case. Right: LR case.

cal situation, in which a subdissipative operator leads eventually to an overdissipative behaviour, has already been reported by [9]. These two no-model LES lead to two important conclusions. First, when free from numerical dissipation, the discretization itself has no implicit filtering effect on any scale captured by the LES mesh. This implicit filtering effect of the mesh, sometimes claimed in the LES community, is not at all recovered here due to the feature of kinetic energy conservation. The second conclusion is that a relevant SGS modelling is required to expect realistic results.

Figure 5 compares the time evolution of the dissipation  $\bar{\varepsilon}$  for the Smagorinsky model and for the present technique of implicit SVV at HR and LR. For the Smagorinsky model at HR, two options are tested: (i) standard condition where the separation scale is adjusted on the cell size  $\Delta = \Delta x$ ; (ii) improved condition where this adjustment is designed to better ensure the numerical convergence  $\Delta = 2.5\Delta x$ . Although it is fully recognized that only the improved condition is numerically meaningful (see for instance [13]), it is

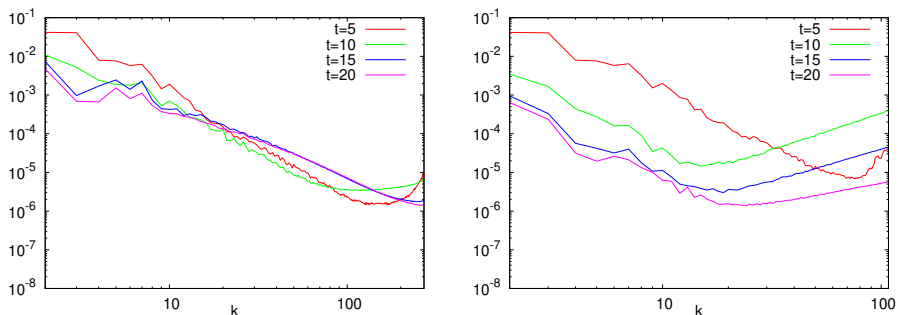


**Figure 4:** Energy spectra  $\bar{E}(k, t)$  at  $t = 5, 10, 15, 20$  obtained by no-model LES. Left: HR case. Right: LR case.

almost never used by the LES community. The effect of using a cell size  $\Delta x$  smaller than the separation scale  $\Delta$  has been investigated by [9] by considering the Taylor-Green vortex problem at lower Reynolds number  $Re = 5000$ . It was shown that the standard condition  $\Delta = \Delta x$  leads to a solution that is far from numerical convergence while being subjected to spurious oscillations. The increase of the ratio  $\Delta/\Delta x$  was found to restore the numerical convergence but only slowly (see [9] for more details). Here, this type of sensitivity is examined at significantly higher Reynolds number.

The quality of the present LES predictions can be evaluated through their deviation from the ideal curve obtained by filtering the DNS data. At HR (see figure 5-left), by reference to the no-model LES, the improvement provided by the Smagorinsky model is significant but the best prediction is obtained by the implicit LES. For the latter, the dissipation curve is found to match closely its DNS reference with only a slight overestimation of the peak. Once the turbulence breakdown completed (at  $t \gtrsim 11$ ), a very good agreement with filtered DNS is recovered. Interestingly, it can be observed that the improved condition  $\Delta = 2.5\Delta x$  makes the Smagorinsky model clearly more accurate. However, it cannot outperform the implicit SVV while requiring an extra computational cost connected to the calculation of the divergence of (3) in the governing equation (1). At LR (see figure 5-right), the results given by the Smagorinsky model becomes completely unrealistic with a marginal improvement by comparison to the no-model case. This very poor prediction can be again interpreted as the consequence of the use of the standard condition  $\Delta = \Delta x$  for which no numerical accuracy should be expected. The use of HR mesh with  $\Delta x = \Delta/2.5$  while keeping constant  $\Delta$  clearly confirms the complete inadequacy of the standard condition  $\Delta = \Delta x$  for which the solution is far from numerical convergence, especially for the present high Reynolds number.

By comparison to HR, implicit SVV is less efficient at LR with a significant loss of accuracy. From the early transition  $t \gtrsim 6$ , this implicit SGS model is found underdissipative while missing the dissipation peak and with also the erroneous prediction of a

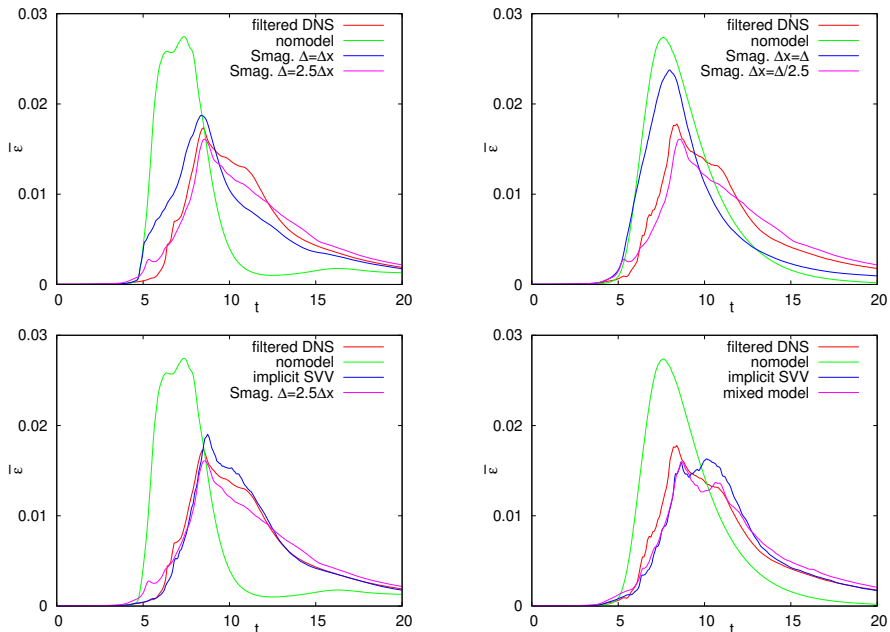


**Figure 5:** Time evolution of the total dissipation  $\bar{\varepsilon}$  predicted by LES. Left: HR cases. Right: LR cases. (except Smag.  $\Delta x = \Delta/2.5$ ). The cases Smag.  $\Delta = 2.5\Delta x$  (left-top) and Smag.  $\Delta x = \Delta/2.5$  (right-top) correspond to the same calculation.

secondary peak at  $t \approx 10$ . The overall agreement with filtered DNS is clearly better than for the Smagorinsky model, but it cannot be considered as fully satisfactory, especially during the transition. The fundamental reason of this discrepancy is the main subject of subsection 3.3.

Before going further in this analysis, it is worth comparing the spectra obtained using the Smagorinsky model with their counterparts using the implicit SVV as presented in figure 6. It can be observed that the Smagorinsky model in standard condition  $\Delta = \Delta x$  is unable to control the pile-up of kinetic energy near the cutoff wavenumber  $k_c$ . As for the no-model LES, this partial thermalization corresponds to the development of small-scale spurious oscillations everywhere in the computational domain. This pile-up is less pronounced than for the no-model LES (see figure 4 for comparison), especially at HR for which the improvement provided by the Smagorinsky model is significant. On the contrary, the use of implicit SVV is found to remarkably damp  $\bar{E}(k)$  in the wavenumber range  $k_c/2 \lesssim k \lesssim k_c$  for both HR and LR. This ability to prevent any thermalization is interpreted as the most important condition of present implicit LES to enable the



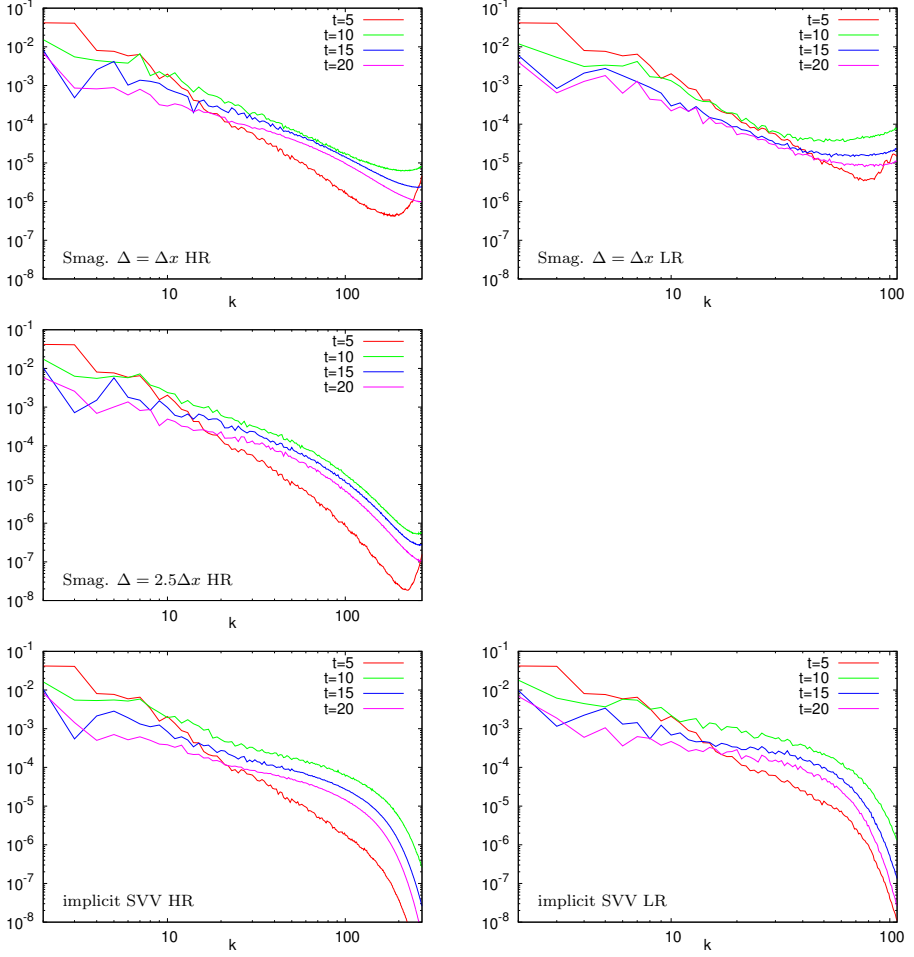


**Figure 6:** Energy spectra  $\bar{E}(k, t)$  at  $t = 5, 10, 15, 20$ . Left: HR cases. Right: LR cases.

production of realistic and accurate results. Even the improved condition  $\Delta = 2.5\Delta x$  with the Smagorinsky model cannot remove correctly the thermalization, especially at the early transition  $t = 5$  where a clear pile-up of kinetic energy can be observed in figure 6. This is the confirmation of the poor filtering effect of the Smagorinsky model which is against the numerical accuracy as already observed by [9] at lower Reynolds number.

The loss of physical realism of the vortical structures in presence of spurious oscillations can also be clearly exhibited by instantaneous visualization based on  $Q$ -criterion as shown in figure 7 for  $t = 10$ . Numerical noise completely hides the large-scale organisation of the flow for the no-model case at LR. For the Smagorinsky model with  $\Delta = \Delta x$ , unrealistic small-scale oscillations can be seen at LR and also at HR to a lesser extent. The use of  $\Delta = 2.5\Delta x$  at HR with this model seems to fix this problem but it must be mentioned that spurious oscillations are visible at the start of the turbulence breakdown (not shown). For the LES based on implicit SVV, vortical structures are not polluted by numerical noise. Their characteristic scale is consistent to what can be expected from a filtered solution with a smoothing that is logically more pronounced at LR by comparison to HR.

### 3.3 A priori analysis

The DNS database can be more extensively used to understand why implicit LES is found to be underdissipative at LR. Because implicit SVV can fully prevent partial thermalization for both HR and LR, the reason of its underdissipative behaviour at LR must be found elsewhere. As explained in subsection 2.2, a filter consistent with the implicit SVV can be obtained by solving the Lin equation using a simplified Pao-like spectral closure [9]. The application of this filter in every spatial direction on the DNS solution enables a consistent definition of the targeted LES solution that can be used as reference as it was done in section 3.2 to provide the “filtered DNS” data. This methodology can be extended to compute various LS and SGS contributions. The resulting decomposition is illustrated in figure 8 where the total dissipation  $\bar{\varepsilon}$  associated with the filtered kinetic energy  $\bar{E}_k$  is compared with the dissipation  $\varepsilon$ , the LS dissipation  $\varepsilon_{LS}$  and the SGS dissipation  $\varepsilon_{SGS}$  with  $\bar{\varepsilon} = \varepsilon_{LS} + \varepsilon_{SGS}$ . It can be observed that the main contribution to the dissipation comes from SGS with a ratio  $\varepsilon_{SGS}/\bar{\varepsilon}$  up to 77% at HR and 93% at LR. These ratios clearly emphasize the major role that must be played by the SGS modelling for this high Reynolds number case.

Although the expected dissipation  $\varepsilon_{SGS}$  is already a precious information, the knowledge of its distribution through scales is essential to determine the scale selectivity of an ideal SGS modelling. As shown by [23], this scale by scale analysis can be based on the LS Lin equation written in the following form

$$\left(\frac{\partial}{\partial t} + 2\nu k^2\right) \bar{E}(k, t) = \bar{T}(k, t) + T_{SGS}(k, t) \quad (9)$$

where  $\bar{E}(k, t)$  is the kinetic energy spectrum of the filtered solution,  $\bar{T}(k, t)$  the transfer term involving only the filtered solution and  $T_{SGS}(k, t)$  the remaining term that describes

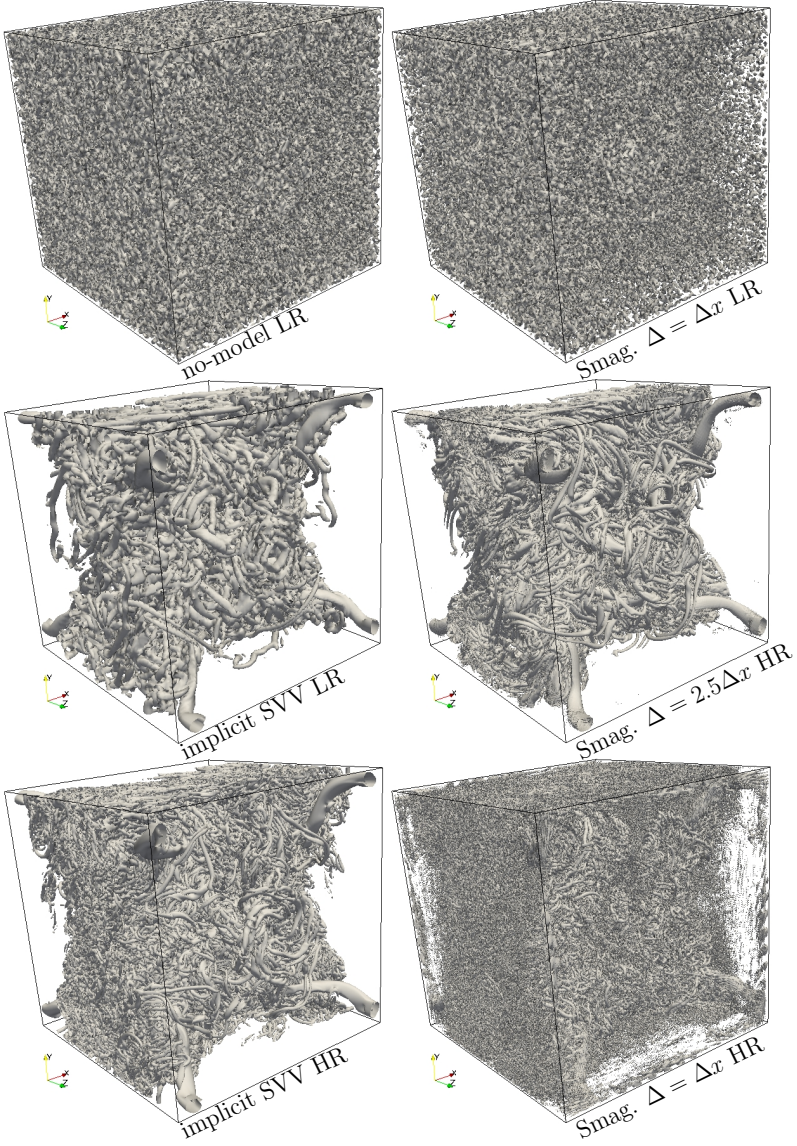


**Figure 7:** Isosurface of  $Q$ -criterion at  $t = 10$ . LES data in the sub-box  $\pi^3$  with  $Q = 4$ .

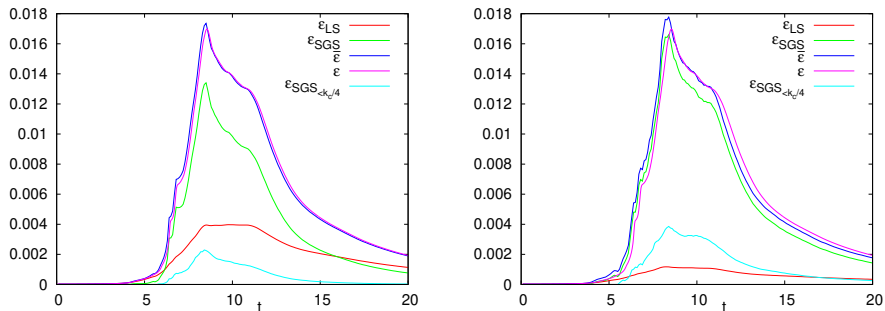


**Figure 8:** Time evolution of the viscous LS, SGS, SGS for  $k < k_c/4$ , filtered DNS and full DNS dissipations ( $\varepsilon_{LS}$ ,  $\varepsilon_{SGS}$ ,  $\varepsilon_{SGS, < k_c/4}$ ,  $\bar{\varepsilon}$ ,  $\varepsilon$ ). Left: HR case. Right: LR case.

transfers between the supergrid and subgrid scales.  $T_{SGS}(k, t)$  corresponds, in absolute value, to the spectral density of  $\varepsilon_{SGS}$  with

$$\varepsilon_{SGS} = - \int_0^{k_c} T_{SGS}(k, t) dk. \quad (10)$$

Equivalently, it is common to introduce the spectral eddy viscosity

$$\nu_t(k, t) = - \frac{T_{SGS}(k, t)}{2k^2 \bar{E}(k, t)} \quad (11)$$

that makes easier comparison with molecular and eddy viscosity, even if the latter is based on Boussinesq’s hypothesis whereas the definition of  $\nu_t(k, t)$  is exact in the framework of Fourier analysis.

Using the present DNS database, the spectral eddy viscosity associated with the implicit SVV filtering at HR and LR is presented in figure 9 at four characteristic times  $t = 5, 10, 15$  and  $20$  and using a normalization with the molecular viscosity  $\nu$ . At HR as well as at LR,  $\nu_t(k, t)/\nu$  is maximum at the cutoff wave number  $k_c$  with a  $k$ -dependency corresponding qualitatively to a hyperviscous behaviour. This “cusp” behaviour, predicted by two-point closure theories at high Reynolds number [19, 4, 25] and with a sharp scale separation in the Fourier space, is recovered here despite the use of a more progressive decomposition between LS and SGS. It is the signature of triad interactions between the subgrid and the smallest supergrid scales. An important remark is that after the early transition, the levels of  $\nu_t(k_c, t)/\nu$  are about one order of magnitude lower than the predicted values of  $\nu_0$  for the considered ratios  $\Delta x_{LES}/\Delta x_{DNS} = (10, 25)$  associated with HR and LR. Another difference with the implicit SVV is that  $\nu_t(k_c, t)/\nu$  is actually non-vanishing at small wavenumbers. Time evolving “plateau” values, to use the terminology employed by [19, 4, 25], can be clearly observed in figure 9, with spectral

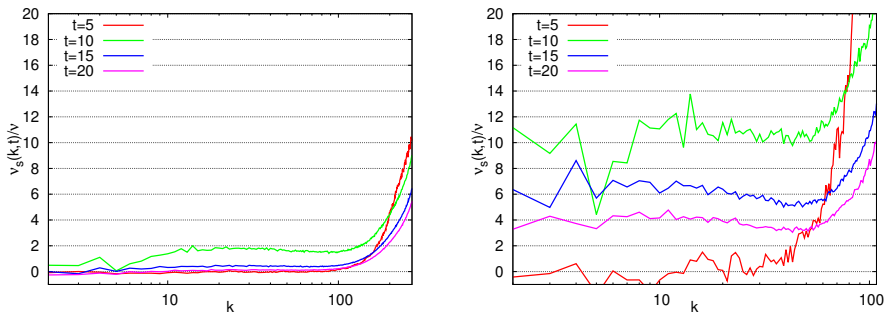


**Figure 9:** Spectral eddy viscosity  $\nu_t(k, t)$  at  $t = 5, 10, 15$  and  $20$ . Left: HR case. Right: LR case.

eddy viscosity more than 10 times the molecular viscosity at  $t = 10$  (when the turbulence breakdown is maximum) for the LR case. For the HR case, a similar plateau in the range  $10 < k < 100$  can be observed but with a spectral eddy viscosity only about twice the molecular viscosity. Considering this drastic change of  $\nu_t(k, t)$  levels depending on the ratio  $\Delta x_{LES}/\Delta x_{DNS}$ , it can be understood why implicit SVV is found to be underdissipative at LR. The lack of any SGS dissipation at very LS, as a fundamental assumption in implicit LES, is not compatible with the major role of distant triad interactions.

The fraction of SGS dissipation at very LS

$$\varepsilon_{SGS < k_c/4} = - \int_0^{k_c/4} T_{SGS}(k, t) dk \quad (12)$$

is presented in figure 8. It can be more than 14%-24% of  $\varepsilon_{SGS}$  for the HR-LR cases respectively, during the turbulence breakdown, with a strong decrease thereafter for the HR case (about 1.5% at  $t = 20$ ) but a non-negligible contribution until the end of the calculation for the LR case (about 15% at  $t = 20$ ). This is the clear indication that the assumption of zero SGS influence at very LS can be accepted for moderate ratios  $\Delta x_{LES}/\Delta x_{DNS}$  (i.e. highly resolved LES) while being unrealistic for more challenging situation where the LES is performed using a very coarse mesh by comparison to DNS.

Implicit SGS modelling is essentially inactive at very LS while concentrating its influence on the smallest scales potentially captured by the LES. This scale selectivity is an attractive feature through the ability to efficiently damp spurious oscillations at small scale as a way to control numerical errors. However, it is known that a too selective dissipative operator has the potential to interfere with the turbulent cascade through a too strong interruption of the kinetic energy flux from large to small scales. In that case, a pile-up of energy is observed at the smallest scales free from extra dissipation. This phenomenon, refereed to as "bottleneck effect", can be observed in figure 10 through the presence of bumps on the present implicit LES spectra. The extension of these bumps is

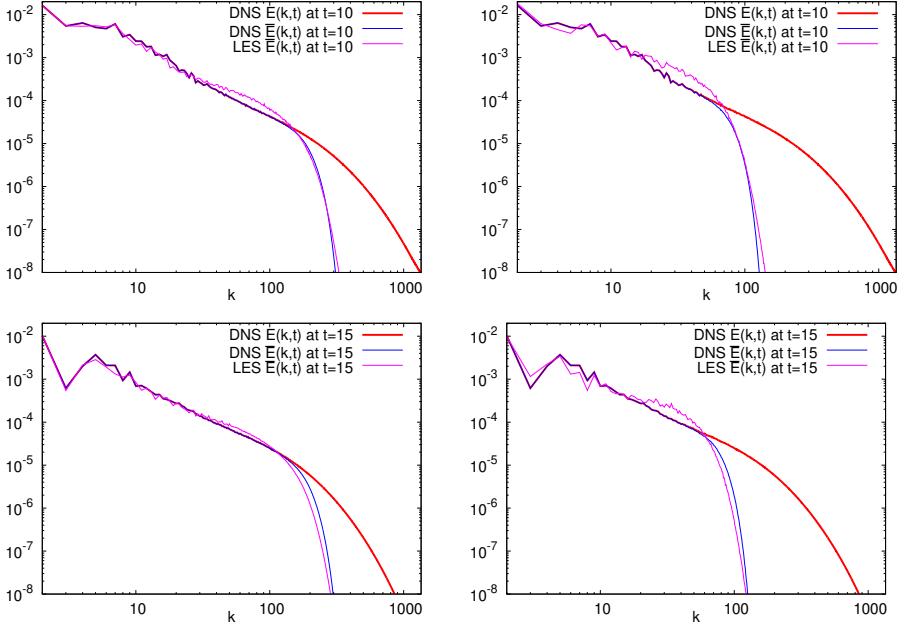


**Figure 10:** Energy spectra  $\bar{E}(k, t)$  at  $t = 10$  and  $15$ . Left: HR case. Right: LR case.

within the wavenumber range  $k_c/6 < k < k_c/2$  while being more marked at LR. At HR, once the turbulent breakdown completed, it is worth noting that the bump is damped (see figure 10-left/bottom) with only a very slight bottleneck effect. These observations confirm that the framework of implicit LES should be restricted to situations where the computational mesh is not too coarse by comparison to DNS.

It could be thought that the combination of the Smagorinsky model with the implicit SVV is a way to both prevent the development of spurious oscillations at small scale while applying an explicit SGS at very LS. This mixed explicit/implicit SGS modelling has been tried but was unsuccessful. The resulting time evolution of the total dissipation  $\bar{\varepsilon}$  is shown in figure 5. Schematically, it can be considered that the dominant influence comes from the implicit SVV component without any ability of the Smagorinsky model component to increase  $\bar{\varepsilon}$  during the transition. The only significant difference with the purely implicit LES is that the spurious secondary peak is removed. Even if this change moves in the direction of improving the agreement with filtered DNS data, it is difficult to identify the origin of this phenomenon which could be only an artefact free from any physical meaning.

## 4 LES OF PIPE FLOW

### 4.1 Flow configuration and DNS of reference

To consider the pipe geometry, as already mentioned in section 2.2, an immersed boundary technique is used to ensure the no-slip boundary condition at the wall while using a regular Cartesian mesh. This approach avoids the need for near-wall mesh refinement while providing an irregular mesh node distribution in terms of wall distance. A similar computational configuration has already been used by [8] and accurate basic statistics have been obtained despite the use of a coarse mesh in terms of wall units in the transverse directions:  $\Delta x^+ = \Delta y^+ = 5.5$ . These unexpected results, against the usual recommendation of near-wall refinement to capture small-scale structures close to the wall, were obtained at the global Reynolds number  $Re_D = 19000$ , where  $D$  is the pipe diameter.

Here, the goal is to similarly investigate a higher Reynolds number case  $Re_D = 37700$  for which  $Re_\tau = 1000$  is the nominal value of the Reynolds number based on the friction velocity  $u_\tau$  and the radius  $R = D/2$ . For this particular flow configuration, accurate DNS results are documented in [18]. As a first step, a quasi-DNS has been performed with a mesh of  $n_x \times n_y \times n_z = 768 \times 768 \times 1920$  nodes, in a computational domain of  $L_x \times L_y \times L_z = 1.12D \times 1.12D \times 12.5D$ , with periodic boundary conditions for the three directions of space. The pipe length  $L_z = 12.5D$  is the same as in [18] and the computational domain is slightly oversized in the  $(x, y)$  directions for improved accuracy of the immersed boundary technique. The resulting mesh resolution in the transverse directions  $\Delta x^+ = \Delta y^+ \approx 2.9$  is finer in wall units than in [8] but remains beyond the typical recommendation for DNS/LES that suggests a cell size  $\Delta x$  for which the minimal scale computed with accuracy  $L_{min} = 4\Delta x$  may capture the thickness of the viscous sublayer, i.e.,  $L_{min}^+ \lesssim 5$ . For the present resolution, we have instead  $L_{min}^+ = 11.6$ . Despite the resulting bypass of the viscous sublayer, it can be seen in figure 11 that a remarkable agreement with the reference DNS results of [18] is obtained for the mean velocity and Reynolds stress profiles. We refer here to quasi-DNS because this agreement is achieved by using a slight amount of numerical dissipation highly concentrated at small scales. As far as these basic statistics are concerned, it can be concluded that the ability of the computational mesh to capture the viscous sublayer is not mandatory. Thanks to this, it is estimated that the computational cost of the present quasi-DNS is reduced by about two orders of magnitude by comparison to the DNS of [18].

The main purpose of this quasi-DNS was the generation of an easy-to-handle database, in which results can be freely post-processed and filtered DNS data can be easily estimated consistently with the implicit SVV. Thanks to the use of periodic conditions, together with the solution reconstruction provided by the immersed boundary as explained in [10, 8], the same filtering technique as in section 3 is employed here to enable rigorous comparison between implicit LES and filtered-DNS results for the present pipe flow configuration. This comparison is the subject of the next section.

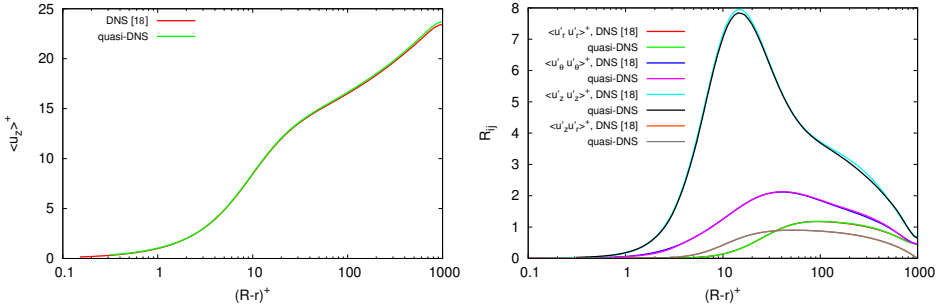


**Figure 11:** Mean velocity (left) and Reynolds stress (right) profiles. Comparison of the present quasi-DNS data with the reference DNS data of [18].

## 4.2 Results

The present LES results have been obtained using a mesh of  $n_x \times n_y \times n_z = 320 \times 320 \times 960$  nodes in a computational domain of  $L_x \times L_y \times L_z = 1.44D \times 1.44D \times 12.5D^3$ , corresponding to ratios of  $\Delta x_{LES}/\Delta x_{qDNS} \approx 3.1$  and  $\Delta z_{LES}/\Delta z_{qDNS} = 2$ . In terms of cost, these ratios represent a least computational saving when compared to the Taylor-Green vortex cases in section 3. Such a limitation is inherent to LES of wall turbulence given the near-wall scaling of statistics in wall units. However, it is interesting to highlight that, by comparison to a conventional DNS based on a distorted mesh with near-wall refinement, the actual computational cost is about 0.03%.

The near-wall mesh resolution of the present LES is particularly coarse:  $\Delta x^+ = \Delta y^+ \approx 9$  corresponding to  $L_{min}^+ \approx 36$ . With such a cell size in the wall-normal direction, for which not only the viscous sublayer but even the turbulent production region is bypassed in terms of scale, it is highly questionable to refer to an explicit calculation of near-wall turbulence. This critical point is confirmed by the no-model LES for which the obtained turbulent statistics are completely unrealistic as shown in figure 12. Note that for the sake of simplicity, only the turbulent kinetic energy profiles are presented to assess the quality of the velocity fluctuations. The corresponding friction velocity  $u_\tau$  is overestimated by 15%, as a clear indication that the predicted turbulent dynamics in the near-wall region is unphysical. This point can be confirmed by the instantaneous axial velocity view in figure 13 where spurious phenomena at small scales can be identified for the no-model LES, especially in the neighbourhood of the wall. This numerical noise seems to distort the large-scale dynamics of the near-wall structures. For the present pipe flow and similarly to the Taylor-Green vortex problem, it can be concluded that without any SGS modelling, a spurious partial thermalization artificially magnifies the friction phenomena without any link to physics.

<sup>3</sup>The use of a slightly extended domain in  $(x, y)$  is for improving the reconstruction of the solution inside the immersed boundary as explained in [8].



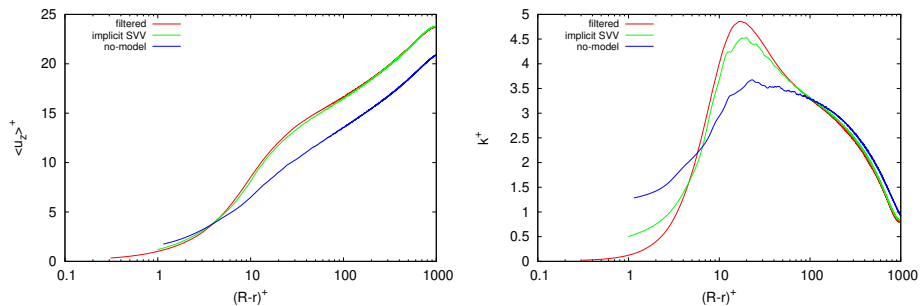


**Figure 12:** Mean velocity (left) and turbulent kinetic energy (right) profiles. Comparison between no-model and implicit LES.

The use of implicit SVV leads to a remarkable improvement of the LES results. First, the friction velocity  $u_\tau$  is estimated with an accuracy of about 1%. However, it must be recognized that this prediction of  $u_\tau$  is somewhat sensitive to the choice of  $\nu_0$  and the scale selectivity of the implicit modelling. Here, we have used the value predicted by the Pao-like solver for  $\Delta z_{qDNS}/\Delta z_{LES} = 2$  while concentrating the numerical dissipation near the cutoff wave number in order to reduce the influence of implicit SVV at LS. Naturally, the prediction from the Pao-like solver, based on the assumption of homogeneous isotropic turbulence, should be considered as only indicative for the present pipe flow, especially in the near-wall zone. Despite this rough approximation, convincing statistics can be obtained as shown in figure 12. By comparison to the no-model case, the improvement achieved with the implicit SVV is spectacular. Since the computational grid is strictly identical for the no-model and implicit LES, and keeping in mind that  $L_{min}^+ \approx 36$  is the minimal scale captured with accuracy in this context, it can be stated that the implicit SVV behaves as a wall-layer model.

The fundamental reason of this unexpected wall-layer modelling feature remains to be clarified. Similarly to the Taylor-Green vortex problem, the ability of numerical dissipation to control the development of numerical noise seems to be a necessary condition for a successful prediction of basic statistics. This ability is illustrated in figure 13 where it can be seen that the smoothness of the longitudinal velocity fluctuations is restored by the implicit SVV in agreement with the patterns obtained by quasi-DNS. Because no vortical structure smaller than the thickness of the turbulent production zone can be captured by the present LES mesh, it cannot be referred to any explicit calculation of near-wall turbulence. Since the only source of modelling comes from the extra numerical dissipation, an interpretation in terms of implicit wall-layer modelling seems to be reasonable.

Before proceeding to the conclusion, it should be mentioned that the value of the kinetic energy in the very near-wall region is estimated from the mesh nodes very close to the wall through the data projection from the Cartesian to the cylindrical coordinate

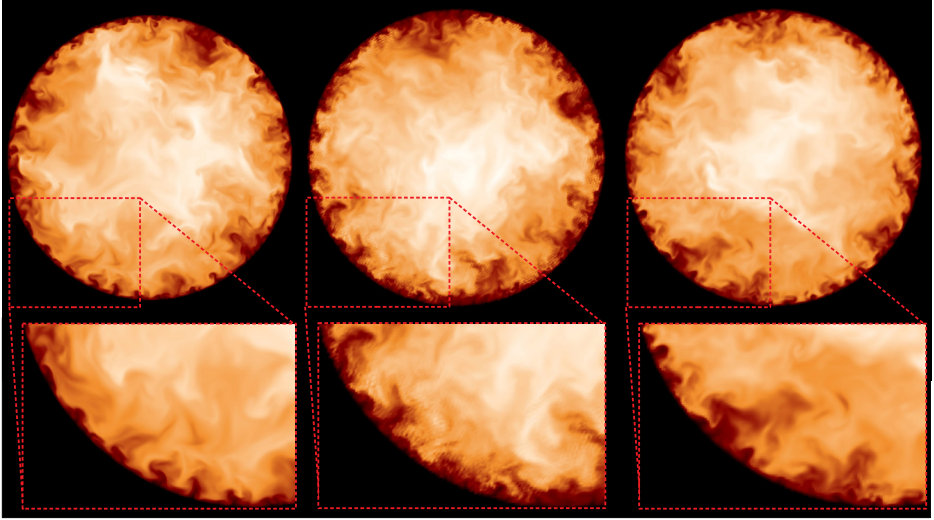


**Figure 13:** Visualisation of the instantaneous axial velocity. Left: quasi-DNS. Centre: no-model LES. Right: implicit LES.

systems (see [8] for more explanations). A careful examination of each node contribution shows that the resulting azimuthal average associated with this projection contains error compensations that are related to the azimuthal location of the nodes and are caused by the immersed boundary method. An improvement of this technique is under progress to reduce the phenomenon and hopefully achieve more accurate turbulent statistics.

## 5 CONCLUSION

Implicit LES is a fuzzy concept in the sense that it is not based on well defined governing equations with a wide variety of techniques to obtain the expected regularization. The bet is that solving Navier-Stokes equations using a coarse mesh (by comparison with DNS) can provide a physically acceptable solution when the numerical errors are scale selective with high accuracy at LS and artificial dissipation at small scales. In this study, by considering two academic flows representative of turbulence with and without wall, it is shown that this pragmatic strategy can give more accurate results than conventional LES based on explicit SGS modelling, at least for the Smagorinsky model considered here.

The main message of this paper is that numerical accuracy is the most important condition to obtain reliable results by LES. The notion of numerical accuracy can be easily defined in the context of DNS through the feature of numerical convergence. In conventional LES based on explicit SGS modelling, this feature is preserved if the cell size  $\Delta x$  goes to zero while keeping constant the separation scale  $\Delta$ . In marginal conditions

where  $\Delta x$  is only adjusted on  $\Delta$ , as does the vast majority of LES users, it is shown that the solution is far from numerical convergence while being highly corrupted by spurious small-scale oscillations, a situation that corresponds to partial thermalization. The use of a more refined mesh can reduce these numerical errors but the numerical convergence is found to be very slow because even the condition  $\Delta x = \Delta/2.5$  is not enough to completely prevent partial thermalization. Moreover, even when the numerical convergence is reached, the Smagorinsky model has only a weak filtering effect with a resulting low potential for reduction of the number of degrees of freedom of the problem [9].

In implicit LES, the assessment of numerical convergence is more difficult because this approach is essentially discrete. The choice of the computational mesh determines the implicit LES solution without any other reference than  $\Delta x$  to estimate the separation scale  $\Delta$ . Note however that [9] have shown that, thanks to the ability of implicit LES to control the development of spurious small-scale oscillations, the resulting solution can be considered as numerically converged. This control is probably the main quality of any implicit LES. In this study, it is observed that the quality of LES predictions mainly depends on the ability of the SGS modelling to prevent thermalization. The more this thermalization is extended, the less accurate the results are. Since implicit LES is designed to avoid any thermalization, it has a natural advantage over conventional LES based on explicit SGS modelling.

One original conclusion of this work is that avoiding thermalization is also highly beneficial for the computation of wall turbulence, enabling the use of a very coarse mesh in the near-wall region. In this sense, the concept of implicit SGS modelling can be extended to wall-layer modelling with the ability to capture realistically near-wall dynamics, with, in particular, the correct prediction of basic turbulent statistics. The useful recommendation of mesh refinement near the wall can be overcome through a bypass of the viscous sublayer, a bypass that can be even extended beyond the turbulent production region. This unexpected feature needs to be further investigated to accurately determine what is missed by this straightforward implicit wall-layer modelling depending on the turbulent statistics considered. In particular, it would be interesting to compare the near-wall numerical dissipation with its molecular counterpart in the framework of a priori and a posteriori analysis as it is done here for the Taylor-Green vortex problem.

Finally, it has to be recognized that when the number of degrees of freedom of LES is strongly reduced by comparison to DNS, the implicit SGS modelling strategy is incomplete. The modelling of distant interactions between very LS and SGS is clearly missing because implicit SGS modelling is essentially inactive at very LS (vanishing feature of the numerical dissipation). Further development is required to ensure this specific modelling. Because by construction, numerical errors are minimum at very LS, it can be anticipated that the modelling of SGS effects on this range of scales has to be explicit. Then, a favourable option could be a mixed implicit/explicit SGS modelling. Thanks to the scale selectivity of the implicit modelling, which makes it inactive at LS, it can be simply superimposed on the explicit modelling. In the spectral range where both implicit

and explicit modelling are active (i.e. at small scale), it can be foreseen that implicit dissipation will dominate its explicit counterpart thanks to the hyperviscous feature. This straightforward implementation is tested in this study with the Smagorinsky model. No significant improvement has been observed for the reason that the Smagorinsky model is not a good candidate for SGS modelling at very LS. Further investigation is needed to establish the physical scaling of SGS dissipation at very LS and then propose a specific modelling term.

## ACKNOWLEDGEMENT

This work was granted access to the HPC resources of TGCC/CINES under the allocation A0052A07624 made by GENCI.

## REFERENCES

- [1] J. Berland, C. Bogey, and C. Bailly. A study of differentiation errors in large-eddy simulations based on the EDQNM theory. *J. Comp. Phys.*, 227:8314–8340, 2008.
- [2] J.P. Boris, F.F. Grinstein, E.S. Oran, and R.L. Kolbe. New insights into large-eddy simulation. *Fluid Dynamics Research*, 10:199–228, 1992.
- [3] J.-B. Chapelier, M. de la Llave Plata, and E. Lamballais. Development of a multiscale LES model in the context of a modal discontinuous galerkin method. *Computer Methods in Applied Mechanics and Engineering*, 307:275 – 299, 2016.
- [4] J. P. Chollet and M. Lesieur. Parameterization of small scales of the three-dimensional isotropic turbulence utilizing spectral closures. *J. Atmos. Sci.*, 38:2747–2757, 1981.
- [5] F. K. Chow and P. Moin. A further study of numerical errors in large-eddy simulations. *J. Comp. Phys.*, 184:366–380, 2003.
- [6] C. Cichowlas, P. Bonaïti, F. Debbasch, and M. Brachet. Effective dissipation and turbulence in spectrally truncated Euler flows. *Phys. Rev. Lett.*, 95(264502):1–4, 2005.
- [7] T. Dairay, V. Fortuné, E. Lamballais, and L.E. Brizzi. LES of a turbulent jet impinging on a heated wall using high-order numerical schemes. *Int. J. Heat and Fluid Flow*, 50:177–187, 2014.
- [8] T. Dairay, E. Lamballais, and S. Benhamadouche. Mesh node distribution in terms of wall distance for large-eddy simulation of wall-bounded flows. *Flow Turb. Combust.*, 100(3):617–626, 2018.

- [9] T. Dairay, E. Lamballais, S. Laizet, and C. Vassilicos. Numerical dissipation vs. subgrid-scale modelling for large eddy simulation. *J. Comp. Phys.*, 337:252–274, 2017.
- [10] R. Gautier, S. Laizet, and E. Lamballais. A DNS study of jet control with microjets using an immersed boundary method. *Int. J. Comp. Fluid Dynamics*, 28(6-10):1–18, 2014.
- [11] M. Germano. Turbulence : the filtering approach. *J. Fluid Mech.*, 238:325–336, 1992.
- [12] M. Germano, U. Piomelli, P. Moin, and W. H. Cabot. A dynamic subgrid-scale eddy viscosity model. *Phys. Fluids A*, 3(7):1760–1765, 1991.
- [13] B. Geurts. *Elements of direct and large-eddy simulation*. Edwards, 2004.
- [14] S. Ghosal. An analysis of numerical errors in large-eddy simulations of turbulence. *J. Comp. Phys.*, 125:187–206, 1996.
- [15] S. Ghosal and P. Moin. The basic equations for the large eddy simulation of turbulent flows in complex geometry. *J. Comp. Phys.*, 118:24–37, 1995.
- [16] F. F. Grinstein, L. G. Margolin, and W. J. Rider, editors. *Implicit Large Eddy Simulation: Computing Turbulent Fluid Dynamics*. Cambridge Univ. Press., 2007.
- [17] T.J.R. Hughes, L. Mazzei, and K.E. Jansen. Large eddy simulation and the variational multiscale method. *Computing and Visualization in Science*, 3(1):47–59, 2000.
- [18] G. K. El Khoury, P. Schlatter, A. Noorani, P. F. Fischer, G. Brethouwer, and A. V. Johansson. Direct numerical simulation of turbulent pipe flow at moderately high Reynolds numbers. *Flow Turb. Combust.*, 91(3):475–495, 2013.
- [19] R. H. Kraichnan. Eddy viscosity in two and three dimensions. *J. Atmos. Sci.*, 33:1521–1536, 1976.
- [20] S. Laizet and E. Lamballais. High-order compact schemes for incompressible flows: a simple and efficient method with quasi-spectral accuracy. *J. Comp. Phys.*, 228:5989–6015, 2009.
- [21] S. Laizet, E. Lamballais, and J. C. Vassilicos. A numerical strategy to combine high-order schemes, complex geometry and parallel computing for high resolution DNS of fractal generated turbulence. *Computers and Fluids*, 39(3):471–484, 2010.
- [22] S. Laizet and N. Li. Incompact3d: a powerful tool to tackle turbulence problems with up to  $o(10^5)$  computational cores. *Int. J. Numer. Methods Fluids*, 67(11):1735–1757, 2011.

- [23] E. Lamballais, T. Dairay, S. Laizet, and C. Vassilicos. Implicit/explicit spectral viscosity and large-scale SGS effects. In *Proc. DLES-11*, Pisa, Italy, 2017.
- [24] E. Lamballais, V. Fortuné, and S. Laizet. Straightforward high-order numerical dissipation via the viscous term for direct and large eddy simulation. *J. Comp. Phys.*, 230:3270–3275, 2011.
- [25] M. Lesieur. *Turbulence in fluids*. Springer, fourth edition, 2008.
- [26] J. Meyers, B. J. Geurts, and M. Baelmans. Database analysis of errors in large-eddy simulation. *Phys. Fluids*, 15(9):2740–2755, 2003.
- [27] J. Meyers, B. J. Geurts, and M. Baelmans. Optimality of the dynamic procedure for large-eddy simulation. *Phys. Fluids*, 045108:1–9, 2005.
- [28] J. Meyers, B. J. Geurts, and P. Sagaut. A computational error-assessment of central finite-volume discretizations in large-eddy simulation using a Smagorinsky model. *J. Comp. Phys.*, 227:156–173, 2007.
- [29] N. Park and K. Mahesh. Analysis of numerical errors in large eddy simulation using statistical closure theory. *J. Comp. Phys.*, 222:194–216, 2007.
- [30] P. Sagaut. *Large eddy simulation of incompressible flow: an introduction*. Springer-Verlag, second edition, 2005.
- [31] J. Smagorinsky. General circulation experiments with the primitive equations. *Mon. Weath. Rev.*, 91(3):99–164, 1963.

# Contraction of polymer gels due to the activity of molecular motors

Robert M. McMeeking<sup>1,2,3,4</sup>, Mattia Bacca<sup>5</sup>, Omar A. Saleh<sup>1,6</sup>

<sup>1</sup>*Materials Department, University of California, Santa Barbara, California, USA*

<sup>2</sup>*Mechanical Engineering Departments, University of California, Santa Barbara*

<sup>3</sup>*School of Engineering, University of Aberdeen, King's College, Aberdeen, UK*

<sup>4</sup>*INM—Leibniz Institute for New Materials, Campus D2 2, Saarbrücken, Germany*

<sup>5</sup>*Mechanical Engineering Department, University of British Columbia, Vancouver, BC, Canada*

<sup>6</sup>*Biomolecular Science & Engineering Program, University of California, Santa Barbara*

## Abstract

When molecular motors are present in the solvent of a polymer gel composed of DNA strands, it is observed that, when the motors are active, the gel shrinks. This is caused by the molecular motors attaching to the DNA strands and reeling them in. The power generated by these motors is obtained by ATP hydrolysis reaction, which transduces chemical energy into mechanical work. The process is controlled by signals of an electrochemical nature that trigger motor activity. Gel shrinkage is accompanied by a significant stiffening of its elastic modulus. The molecular motors separate into two families; one family remains permanently attached to the DNA chains and cause a steady-state shrinkage and stiffening. The other family of motors attaches to DNA chains, causes transient shrinkage and stiffening, and then detaches. We propose a theory based on non-equilibrium thermodynamics to describe this mechanical behavior. The phenomena are considered to occur due to the molecular motors increasing the effective cross-link density in the polymer network, thereby reducing system entropy. This outcome is shown to both shrink the gel and stiffen it. The theory is then applied to a swollen polymer network, with solvent diffusion and neo-Hookean elastic behavior used to describe the transient passive response of the gel. Results from simulation of active uniaxial contraction of a slab of gel is compared with experimental results for the behavior of a bead embedded in a gel. Good agreement is found.





# FINITE ELEMENT ANALYSIS OF A BARLOW MITRAL VALVE: PATIENT SPECIFIC GEOMETRY AND COMPARISON WITH THREE-DIMENSIONAL ECHOCARDIOGRAPHIC DATA.

Hans Martin Dahl Aguilera<sup>1</sup>, Victorien Prot<sup>1</sup>, Bjørn Skallerud<sup>1</sup> and Stig Urheim<sup>2</sup>

<sup>1</sup>Department of Structural Engineering, Faculty of Engineering Science  
The Norwegian University of Science and Technology, Norway  
e-mail: victorien.prot@ntnu.no

<sup>2</sup> Department of Heart Disease  
Haukeland University Hospital, Norway

**Key words:** Computational Methods, Finite element method, Barlow disease, Degenerative mitral valve disease.

**Abstract.** In this paper, a patient-specific finite element (FE) model is created for a mitral valve diagnosed with Barlow disease. The FE model is constructed from three-dimensional (3D) echocardiographic data. The mitral valve leaflets and the chordae tendineae are modelled with hyperelastic materials. Patient-specific annular and papillary muscle motions are used as boundary conditions in the analyses. The FE model of this Barlow mitral valve is used to predict the location of mitral regurgitation. The global response of the mitral valve model is compared with echocardiographic measurements, and with the patients lesions observed pre- and intraoperatively. The results showed regurgitation at both commissures, and the FE model aligned well with the echocardiographic measurements at peak systole.

## 1 Introduction

The mitral valve is a complex structure that separates the left atrium from the left ventricle, ensuring one-way blood flow between the two heart chambers. This valvular structure consists of several components: the anterior and posterior leaflets, the annulus, chordae tendineae and the papillary muscles. The annulus is situated at the intersection between the left atrium and the left ventricle, and functions as an attachment ring for the two leaflets. Moreover, from the ventricular wall, the papillary muscles originate. From the papillary muscles, the chordae tendineae branches out and insert into the posterior

and anterior leaflets. During the cardiac cycle, the components of the mitral valve work in concert in order to achieve proper closure at systole, enabling unidirectional blood flow. Furthermore, Carpentier et al.[1] divided the posterior and anterior leaflets into six different segments described in figure 1.

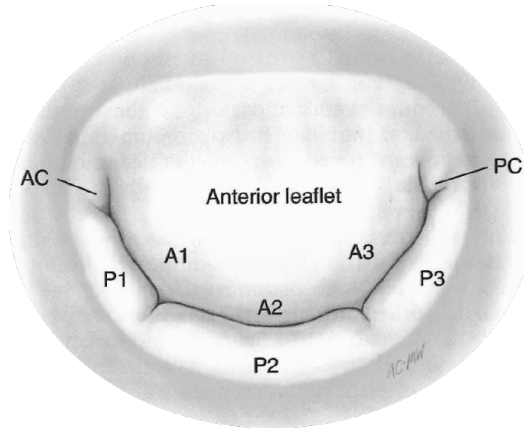


**Figure 1:** Atrial view of the mitral valve with leaflet segmentation. Anterolateral Commissure (AC), posteromedial Commissure (PC). Taken from [1].

The second most common valvular heart disease in European countries is mitral regurgitation [2]. Mitral regurgitation is predominantly caused by degenerative diseases such as Fibroelastic Deficiency or Barlow disease (BD), where the latter is the topic of this paper. BD affects the entire mitral valve apparatus, where a severely dilated annulus, excessive leaflet tissue, billowing or prolapse of the leaflets, myxomatous degeneration and chordae alterations are characteristic lesions. Another characteristic feature related to BD is that the annular saddle shape flattens, and overstretches at end systole[3]. Furthermore, Barlow disease is mainly observed in patients younger than the age of 60 [4]. The work by Hjortnaes et al.[5] studied the histological changes in the mitral valve due to Barlow's disease. It was observed that the thickening of the mitral valve leaflets was caused by gathering of water absorbent proteins (proteoglycans) in the spongiosa layer, and intimal thickening of the fibrosa and atrialis.

Repairing a Barlow mitral valve is a complex procedure, and often the whole mitral apparatus must be assessed. Reconstructive surgery of the mitral valve may include annuloplasty, different sliding and resection techniques and artificial chordal insertions. Sophisticated imaging techniques have in recent years become available, leading to a greater understanding of the mitral valve dynamics. The motivation for this paper is to develop a patient-specific finite element model of a Barlow mitral valve before surgical

treatment. The development of such a model will hopefully enable us to predict the location of mitral regurgitation. Furthermore, with a realistic model it should be possible to perform surgical procedures *in silico*, optimizing and creating a patient-specific repair procedure. To the authors' knowledge, this is the first time a Barlow mitral valve has been studied using a finite element model.

This paper is organized as follows. First, the patient's pathology is presented. Then the material models, the FE geometry and boundary conditions are described. Thereafter, the results are presented and discussed. Finally, conclusions from the study are given.

## 2 Methods

### 2.1 Patient and echocardiographic measurement

In this section the studied patient, his lesions and the surgical procedures performed are briefly described.

The patient is a 45 year old male who was diagnosed with Barlow's disease and operated in 2017 with mitral valve repair. The patient had a severely dilated annulus with excessive leaflet tissue and mitral regurgitation. From echocardiographic findings, multiple jets of mitral regurgitation in mid to late systole were observed. The most severe regurgitation was located in the posteromedial region with billowing (A2-A3-P3) and prolapse of the P3 segment. A less severe regurgitation jet was observed in the anterolateral region due to prolapse of P1. Mitral annular disjunction (MAD) of 10 mm was observed in the P1-P2 region.

The patient received an annuloplasty ring of size 38, triangular resection and sliding of P2 in order to reduce the height of the P2 segment. Furthermore, there was inserted 2x4 neo chordae (Goretex 5-0) from each papillary muscle and to the edge of the A2 and P2 segment. Lastly, there was performed a transposition of secondary P2 chordae to the free edge of the P2 segment.

### 2.2 Continuum mechanical framework and constitutive models

#### Kinematics

We consider a deformable body in two different instantaneous configurations  $\Omega_0$  and  $\Omega$ , representing the reference and current configuration, respectively. A particle in the reference configuration  $\Omega_0$  is defined by the position vector  $\mathbf{X}$ . The position of the same particle in the current configuration  $\Omega$  is further defined by the vector  $\mathbf{x}$ . The relationship between the two configurations is described by the deformation map relationship  $\mathbf{x} = \mathbf{x}(\mathbf{X}, t)$ . The deformation gradient  $\mathbf{F}$  is defined as

$$\mathbf{F} = \frac{\partial \mathbf{x}}{\partial \mathbf{X}}. \quad (1)$$

The volume ratio is defined as  $J = \det \mathbf{F}$ , where  $J = 1$  describes an isochoric transformation. Furthermore, the right and left Cauchy-Green tensors are defined as  $\mathbf{C} = \mathbf{F}^T \mathbf{F}$  and

$\mathbf{b} = \mathbf{F}\mathbf{F}^T$  respectively. Furthermore, the distortional part of the right and left Cauchy-Green can be written as  $\bar{\mathbf{C}} = J^{-\frac{2}{3}}\mathbf{F}^T\mathbf{F}$  and  $\bar{\mathbf{b}} = J^{-\frac{2}{3}}\mathbf{F}\mathbf{F}^T$

For an anisotropic material reinforced by a family of fibres, the fibre direction in the reference configuration is defined by the unit vector  $\mathbf{a}_0$ . The mapping of the fibre direction from the reference configuration to the current configuration is expressed as  $\mathbf{a} = \mathbf{F}\mathbf{a}_0$ .

### Strain-energy function and stress tensors

For hyperelastic materials a strain-energy function  $\Psi$  is introduced in order to describe the response of the material. The strain-energy function  $\Psi$  for incompressible materials can be expressed in terms of five invariants,  $I_1, I_2, J, I_4, I_5$  as,

$$\Psi = \tilde{\Psi}(I_1, I_2, I_4, I_5) + p(1 - J), \quad (2)$$

where the principal invariants of  $\mathbf{C}$  (i.e.,  $I_1, I_2, J$ ) are related to isotropic elasticity and defined as,

$$I_1 = \text{tr}(\mathbf{C}), \quad I_2 = \frac{1}{2}[I_1^2 - \text{tr}(\mathbf{C}^2)], \quad J = \sqrt{\det(\mathbf{C})}. \quad (3)$$

For an incompressible material the third invariant can be written as  $J = 1$ . The invariants  $I_4, I_5$  describe the transversely isotropic properties of the material, expressed by the fibre direction in the reference configuration  $\mathbf{a}_0$  and the right Cauchy-Green tensor  $\mathbf{C}$ ,

$$I_4 = \mathbf{a}_0 \cdot \mathbf{C}\mathbf{a}_0, \quad I_5 = \mathbf{a}_0 \cdot \mathbf{C}^2\mathbf{a}_0, \quad (4)$$

and  $p$  is the Lagrange multiplier. The second Piola-Kirchhoff stress tensor  $\mathbf{S}$  can be derived from 2 giving,

$$\mathbf{S} = 2 \sum_{\substack{i=1 \\ i \neq 3}}^5 \frac{\partial \Psi}{\partial \mathbf{I}_i} \frac{\partial \mathbf{I}_i}{\partial \mathbf{C}} + p\mathbf{C}^{-1}, \quad (5)$$

where the scalar  $p$  can be determined from the plane stress condition. In this work, we apply this constitutive model to mitral leaflets that may be considered as thin sheets, thus assuming that the stress in the out of plane direction (denoted 3-direction)  $S_{33}$  is zero leads to:

$$p = -2 \sum_{\substack{i=1 \\ i \neq 3}}^5 \frac{\partial \Psi}{\partial \mathbf{I}_i} \frac{\partial \mathbf{I}_i}{\partial \mathbf{C}_{33}} C_{33}. \quad (6)$$

Lastly the second Piola-Kirchhoff stress tensor  $\mathbf{S}$  can be transformed to the Cauchy stress tensor  $\boldsymbol{\sigma} = \frac{1}{J}\mathbf{F}\mathbf{S}\mathbf{F}^T$  by the push-forward operation of  $\mathbf{S}$  [6]. This was used for material parameter fitting presented in section 2.3.

## 2.3 Material models and parameters

The constitutive model used to analyse the response of the leaflets, is a hyperelastic anisotropic material model, which is available through the material library in Abaqus. The material model was originally developed in order to model the mechanical response of arterial layers with a distributed collagen fibre orientation [7]. The strain-energy function  $W$  is defined in terms of the deviatoric strain invariants  $\bar{I}_1$  and  $\bar{I}_4$ , which are defined as,

$$\bar{I}_1 = tr\bar{\mathbf{C}}, \quad \bar{I}_4 = \mathbf{a}_0 \cdot \bar{\mathbf{C}} \cdot \mathbf{a}_0. \quad (7)$$

Thus,

$$W(\bar{I}_1, \bar{I}_4) = C_{10}(\bar{I}_1 - 3) + \frac{1}{D} \left( \frac{(J^2) - 1}{2} - \ln(J) \right) + \frac{k_1}{2k_2} (exp^{k_2(\bar{E})^2} - 1), \quad (8)$$

with,

$$\bar{E} = \kappa(\bar{I}_1 - 3) + (1 - 3\kappa)(\bar{I}_4 - 1), \quad (9)$$

where  $C_{10}$ ,  $D$ ,  $k_1$ ,  $k_2$  and  $\kappa$  are temperature-dependent material parameters.  $C_{10}$  and  $k_1$  have the dimension MPa, while  $k_2$  is dimensionless. Furthermore,  $D$  is a material constant that controls compressibility[8]. The dispersion parameter  $\kappa$  describes the distribution of the fibres. When  $\kappa = 0$ , there is no dispersion of the fibres, while,  $\kappa = \frac{1}{3}$  describes an isotropic material where the fibres are randomly distributed [9].

In order to describe the mechanical response of the mitral valve leaflets, the constitutive model presented by [7] had to be fitted to experimental data. In the paper published by May-Newman and Yin [10], a strain-energy function derived from experimental data with corresponding material parameters is presented. The suggested model in [10] has an exponential form in terms of the invariants  $I_1$  and  $I_4$ .

$$\Psi(I_1, I_4) = c_0[exp^{c_1(I_1-3)^2+c_2(\sqrt{I_4}-1)^4} - 1] + p(J - 1), \quad (10)$$

where  $c_i$ ,  $i=0,1,2$ , are material parameters, and  $p$  is the Lagrange-multiplier.

The *lsqnonlin* function from the Optimization Toolbox of Matlab was used to perform a nonlinear least square fitting. In table 1, the acquired material parameters from the non-linear regression is presented. Furthermore, figures 2 and 2.3 show the stress-stretch relationship, comparing the obtained material parameters with the ones presented by May-Newman and Yin[10]. The leaflets were modelled with a density of 1000 kg/m<sup>3</sup>.

**Table 1:** Material parameters obtained from nonlinear data-fitting of experimental data provided by [10]

	$c_{10}(\text{MPa})$	$k_1(\text{MPa})$	$k_2$	$\kappa$
Anterior leaflet	0.001	0.0240	50.92	0.1728
Posterior leaflet	0.001	0.0207	52.35	0.2669

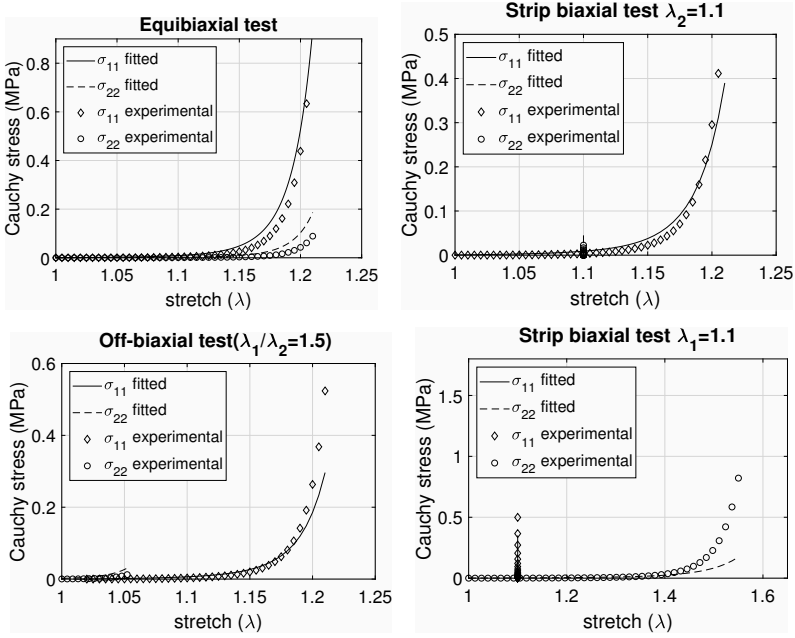


**Figure 2:** Cauchy-stress vs stretch curves for the anterior leaflet. Experimental data provided by [10] and nonlinear data-fitting of the constitutive model described by [7]. Note that the 1-direction is aligned with the collagen fiber. a) equibiaxial ( $\lambda_1 = \lambda_2$ ), b) strip biaxial ( $\lambda_2 = 1.1$ ), c) off-biaxial ( $\lambda_1/\lambda_2 = 1.5$ ), d) strip biaxial ( $\lambda_1 = 1.1$ ).

**Table 2:** Ogden model material parameters for modelling of chordae tendinae. Anterior Marginal(AM), Anterior Strut(AS) and Posterior Marginal(PM). Human and ovine material parameters.

	Human			Ovine		
	AM	AS	PM	AM	AS	PM
$\mu_1(MPa)$	8.91	9.61	9.57	0.37	0.85	0.66
$\alpha_1$	27.02	30.86	22.78	11.70	28.03	29.67
$\mu_2(MPa)$	12.19	7.99	10.61	1.79	0.21	1.37
$\alpha_2$	20.91	27.65	21.68	5.00	5.47	18.25
$\mu_3(MPa)$	12.78	7.81	10.65	0.33	0.16	1.46
$\alpha_3$	20.89	30.00	21.35	34.06	25.06	19.45

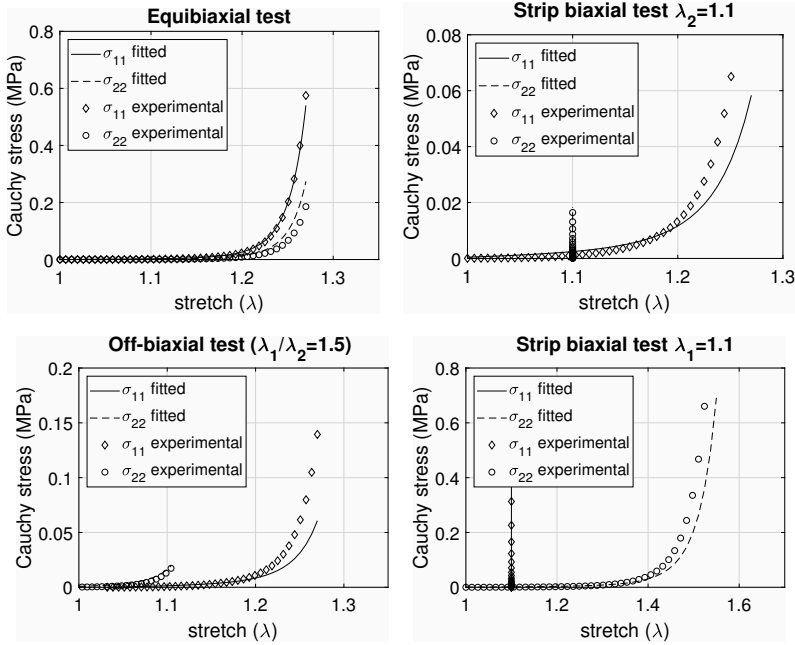


**Figure 3:** Cauchy-stress vs stretch curves for the posterior leaflet. Experimental data provided by [10] and nonlinear data-fitting of the constitutive model described by [7]. Note that the 1-direction is aligned with the collagen fiber. a) equibiaxial ( $\lambda_1 = \lambda_2$ ), b) strip biaxial ( $\lambda_2 = 1.1$ ), c) off-biaxial ( $\lambda_1/\lambda_2 = 1.5$ ), d) strip biaxial ( $\lambda_1 = 1.1$ ).

Lastly, the Ogden strain-energy function is used in order to describe the chordae tendineae. When assumed incompressible, the strain-energy function is,

$$\Psi = \sum_{i=1}^N \frac{2\mu_i}{\alpha_i^2} (\lambda_1^{\alpha_i} + \lambda_2^{\alpha_i} + \lambda_3^{\alpha_i} - 3), \quad (11)$$

where  $\mu_i$  and  $\alpha_i$  are material constants and  $\lambda_j^{\alpha_i}$  ( $j=1,2,3$ ) are the principal stretches. The material parameters used for the chordae are provided by Zuo et al.[11], and describe the response of human chordae tendineae. Material parameters provided by [11] of ovine chordae tendineae were also implemented in another analysis. Human chordae were shown to be significantly stiffer than ovine chordae [11], and myxomatous chordae were found to be 50% less stiff compared to human chordae [12]. Thus, ovine material parameters were studied to compare the global response between the two. In table 2, the material parameters for the marginal chordae and the strut chordae are presented. Lastly, the mechanical response of human and ovine marginal chordae are plotted in figure 4.

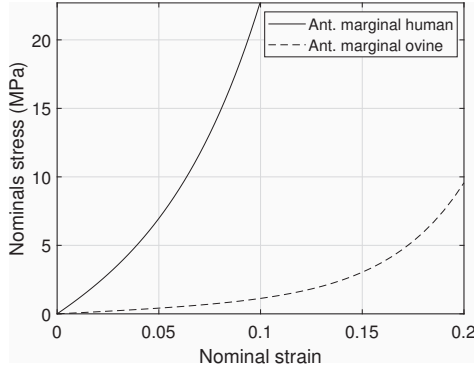


**Figure 4:** Nominal Stress vs Nominal Strain curves. Human and ovine chordae material parameteres implemented in the Ogden material model.

## 2.4 Geometry

The patient-specific geometry was created from 3D echocardiographic data of a patient diagnosed with Barlow disease. The recordings were imported into a Matlab GUI which enables manual extraction of geometrical points. At the end-diastolic configuration the annulus, leaflet edges and papillary muscle tips were identified (Figure 5).

The annulus was created by extracting points around the annular perimeter and performing a cubic spline interpolation. The anterior and posterior leaflets were constructed by identifying the leaflet edges and the tissue points as shown in figure 5, where the tissue points (white circles in figure 5) are defined as the points between the annulus and the free edge. For the free edge, a cubic interpolation is also performed, creating a continuous line at the margin (figure 6). The extracted points were then imported into the CAD software Rhino, where a non-uniform rational B-spline (NURBS) surface is created by using the tissue points to guide the surface between the annulus and the free edge lines. Furthermore, the papillary muscle tips are identified, and serve as the attachment points for the chordae.

## 2.5 Chordae modelling

The chordae tendineae originate from the papillary muscles and insert into either the leaflet edge, rough zone or the basal portion of the mitral valve leaflets. However, in this paper the basal chordae are not considered, hence only the marginal and strut chordae are modelled. The marginal chordae insert into the free edge of both the anterior and posterior leaflets, while the strut chordae insert into the anterior leaflet only.

Twelve marginal chordae were modelled to originate from each papillary muscle. Each marginal chordae was then split in a fan-like manner, inserting into the leaflet edge with



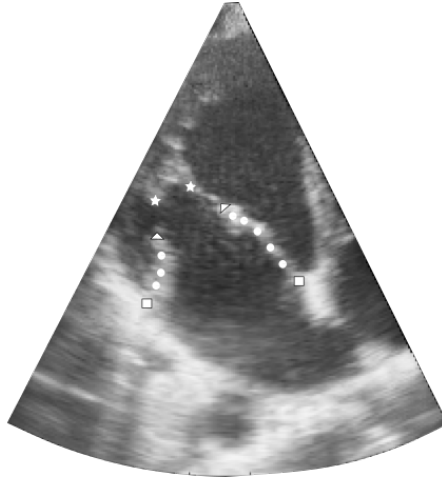


**Figure 5:** Explanation of the anatomical components on an echocardiographic image, end-diastolic configuration. Papillary Muscle Tips (stars), Posterior leaflet edge (left triangle), Anterior leaflet edge (right triangle), Annulus (squares). White circles represent the tissue points, extracted from the middle of the leaflets.

about five different insertion points as described by [13]. The branching was mainly done in order to simulate a more anatomically correct model, where the branch origin was set between the papillary muscle and the free edge (figure 7a). Moreover, the branching led to a redistribution of stress on the leaflet edge, hence preventing excessive distorted elements in the analysis. Lastly, the strut chordae is inserted into the rough zone of the anterior leaflet, which is situated between the annulus and the free edge. As with the marginal chordae, the strut chordae branches out in a fan-like manner. The branching is distributed to the nearby nodes of the main insertion point (figure 7a).

The cross-sectional areas for human marginal and strut chordae was modelled to be  $0.25 \text{ mm}^2$  and  $1.27 \text{ mm}^2$  respectively. While, for the ovine chordae the cross-sectional areas were modelled to be  $0.26 \text{ mm}^2$  and  $0.6 \text{ mm}^2$ . Here, the chordae were assumed to be circular and calculated with the cross-sectional diameter presented in the paper published by [11], which studied human and ovine cadaver hearts.

## 2.6 Finite element model

The end-diastolic finite element geometry constructed from the echocardiographic data is depicted in figure 7. For the anterior and posterior leaflets, four noded general-purpose shell elements (S4) were used. The chordae tendineae were modelled as two-noded 3D truss elements (T3D2). Furthermore, the overall leaflet thickness was set to be 3mm,

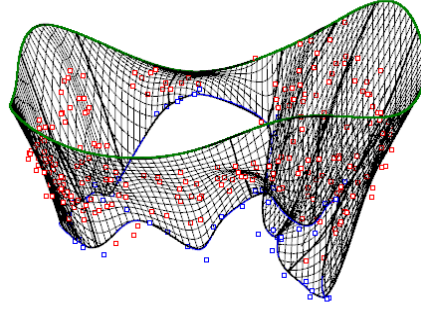


**Figure 6:** NURBS surface created from imported echocardiographic point cloud.  
Annulus - green line, Tissue points represented in red and leaflet free edge - blue line.  
NURBS surface

which is the average overall thickness of Barlow leaflets found by [5]. As for contact, a general contact algorithm available in Abaqus was applied. The tangential contact behaviour was set to frictionless and the normal contact behaviour was a hard contact condition [9].

The material orientation applied to the mitral valve leaflets is obtained from small angle light scattering (SALS) data presented by [14]. In [14], the mean collagen fibre direction is observed to be perpendicular to the annulus near the commissures, and parallel to the annulus at the middle of the leaflets. Moreover, the fibre direction is observed to gradually rotate from parallel to perpendicular towards the commissures. Implementation of the fibre direction in Abaqus is done by partitioning the leaflet into several regions. Then a material orientation was assigned to each individual partitioned region (figure 7b).

## 2.7 Boundary conditions and loading

In order to model the boundary conditions, the dynamics of the papillary muscle tips and the annulus were obtained using *in vivo* echocardiographic data. The geometry of the annulus and the positions of the PMs are recorded for all time-frames, between end-diastole and end-systole. As it is difficult to track material points from echocardiographic measurements, the motion of the annulus was prescribed using displacement boundary conditions determined from the acquired images, under the assumption that heterogeneity in annular strain is small. First, the annular geometries of each time step were modelled as periodic degree-3 spline curves parameterised by arc length. Then, the relative parameterisation of the annular curves was optimised to find the point-wise map that minimised the total displacement between two consecutive curves as described by Rego et al. [15]. Between each configuration a linear interpolation is performed, creating a continuous movement between the time-frames. These boundary conditions are then implemented

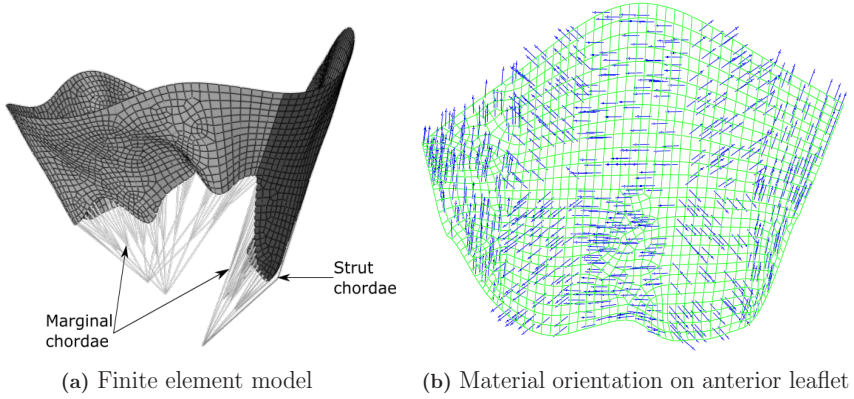


**Figure 7:** (a) - Finite element model created from echocardiographic data. Posterior leaflet (light gray), anterior leaflet (dark grey). (b) - Anterior leaflet material orientation.

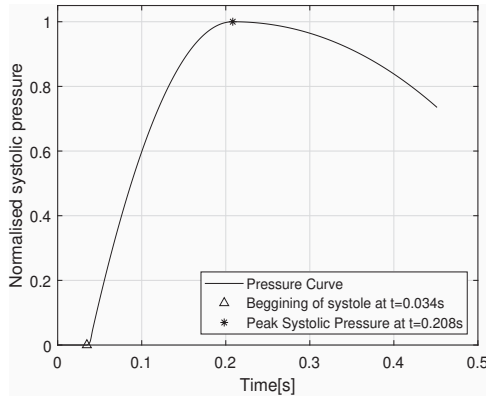


**Figure 8:** Load Amplitude Curve in the Cardiac Cycle

into the Abaqus user subroutine VDISP.

A uniformly distributed pressure was applied to the leaflets' ventricular surface, with a patient specific peak pressure of 18.13 kPa (136mmHg). Furthermore, the amplitude was modelled in order to follow a pressure curve similar to the one during the cardiac cycle [16]. The pressure curve is presented in figure 8, where the pressure is applied to the ventricular surface of the leaflets throughout systole.

### 3 Results

#### 3.1 Measurements of FE geometry

The geometry modelled from echocardiographic data has been compared with measurements obtained in literature of a Barlow mitral valve and a healthy mitral valve. The goal being to verify the geometry with anatomical measurements of Barlow mitral valves. Furthermore, the Barlow mitral valve studied herein shows abnormal features such as excessive tissue and a severely dilated annulus. The finite element model is measured in both the end-diastolic and end-systolic configuration. In table 3 the measurements are presented.

**Table 3:** Mitral valve measurements of the FE model, compared with measurements from literature both *in vitro* and from 3D echocardiography. [13, 17, 18, 3]

	FE model		From Literature		
	ED	PS	Barlow (S)	Barlow (D)	Healthy (D)
Annular perimeter (mm)	170	160	158 $\pm$ 19	148 $\pm$ 17	82 $\pm$ 7
IC diameter (mm)	50.83	-	45 $\pm$ 9	46.6 $\pm$ 5	39.5 $\pm$ 3.4
AP diameter (mm)	45.02	-	44 $\pm$ 8	37.3 $\pm$ 6	32.2 $\pm$ 3.6
Anterior leaflet height (mm)	32.07	-	-	-	20 $\pm$ 2
Posterior leaflet height (mm)	19.85	-	-	-	12 $\pm$ 1
AC height (mm)	10.03	-	-	-	7 $\pm$ 1
PC height (mm)	12.05	-	-	-	7 $\pm$ 1
3D annular area (mm <sup>2</sup> )	2100	1625	-	1500 $\pm$ 280	-
3D total leaflet area (mm <sup>2</sup> )	2645	-	2302 $\pm$ 455	1850 $\pm$ 490	-
Anterior leaflet area (mm <sup>2</sup> )	1145	-	1162 $\pm$ 276	-	-
Posterior leaflet area (mm <sup>2</sup> )	1500	-	1175 $\pm$ 306	-	-

IC- Intercommisural, AP-Anteroposterior, AC-Anterolateral Commissure,

PC-Posteriomedial commissure, ED-End Diastole, PS-Peak Systole, S-Systole, D-Diastole.

As can be seen in table 3, the FE model measurements coincide with the upper limits of the diastolic Barlow measures extracted from literature [3, 17]. Furthermore, for each time step, a mean annulus plane was calculated. Then, the annulus was projected onto this mean plane and a two-dimensional (2D) area was computed and plotted against time in figure 9a. This plot shows how much the annulus dilates throughout the whole cardiac cycle. Then, the mean squared distance of the annulus to this plane was computed and plotted in figure 9b, showing how much the annulus flattens during one full cardiac cycle. The t-wave on the ECG signal is observed prior to 0.5s, hence the measurements in figure 9 represent systole from 0 to 0.5s. As can be seen in figure 9b, the annulus is distinctly flattened during systole. Note that the end-diastolic configuration is the very last time step in figure 9.

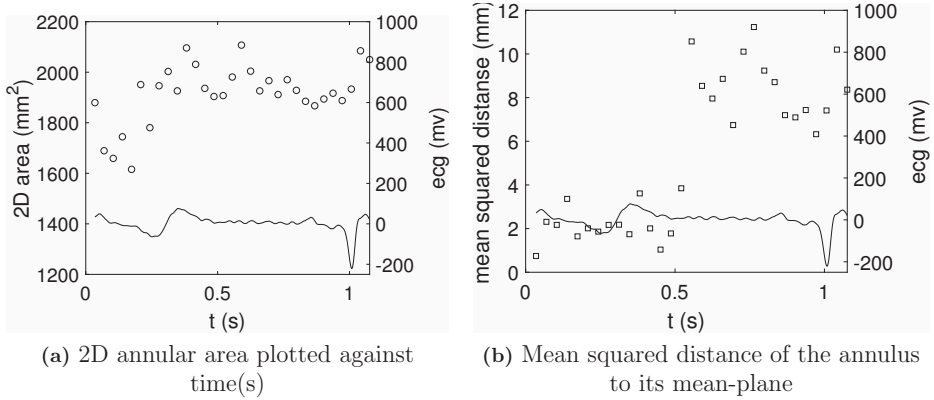


**Figure 9:** Annular measurements and shape. ECG signal(solid curve), 2D area (circles) and mean squared distance (squares).

### 3.2 Comparison with three-dimensional echocardiographic data

Figure 10 shows the global response at the A2-P2 region of the leaflet compared to echocardiography at peak systole. As can be seen, there is a very good correspondence between the echocardiographic measurements and the mitral valve models.

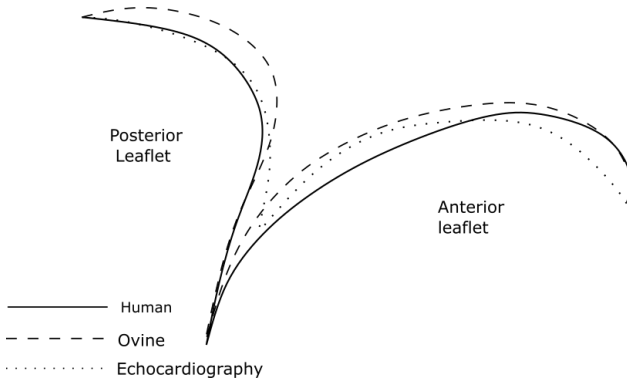


**Figure 10:** Comparison between finite element models and echocardiography along the A2-P2 leaflets at peak systolic pressure  $p=136\text{mmHg}$ , using human and ovine chordae material parameters.

### 3.3 Global Response

In this section, the global response of the finite element analysis is presented. Figure 11 depicts the valve closure from end-diastole to end-systole observed from the left atrium.

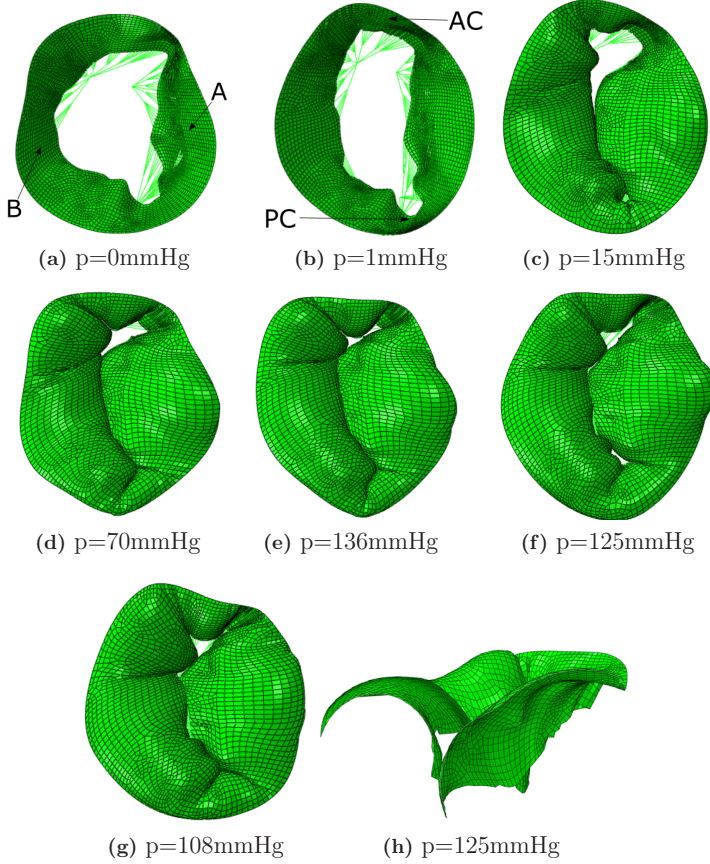


**Figure 11:** Valve closure of finite element model from end-diastole to end-systole. (a) End-diastolic configuration,  $p=0$  mmHg. (b)  $p=1$  mmHg. (c) First observation of coapting surfaces,  $p=15$  mmHg. (d)  $p=70$  mmHg. (e) Peak systolic pressure,  $p=136$ mmHg. (f) Late systolic regurgitation,  $p=125$ mmHg. (g) End-systolic configuration,  $p=108$  mmHg. (h) Cut-view of prolapse at the posteromedial side of the P2 segment

From figures 11(a-g) it can firstly be observed regurgitation at the anterolateral region (A1-P1) throughout the whole analysis. Secondly, the annular motion is clearly observed in figures 11(a-g). Lastly, in figure 11f, a late systolic regurgitation can be observed near the posteromedial commissure (A3-P3). Figure 11h depicts a cut-view, showing what appears to be prolapse at the posteromedial side of the P2 segment. The prolapse is observed at the same time as the late systolic regurgitation in figure 11f. Note that the prolapse is present until the end of systole.

### 3.4 Displacements

The norm of the displacement of points A and B (figure 12a) are plotted against time in figure 12. Prior to the pressure being applied, it is observed that points A and B move without any loading. These movements are due to the annular and papillary muscle dynamics. Moreover, figure 12 shows that as the analysis approaches 0.1s ( $p=81$  mmHg) the leaflets tend to oscillate very little for the rest of the analysis. Lastly, in figure 12, the displacements of points A and B are plotted to compare the leaflet response when ovine and human chordae material parameters are implemented.

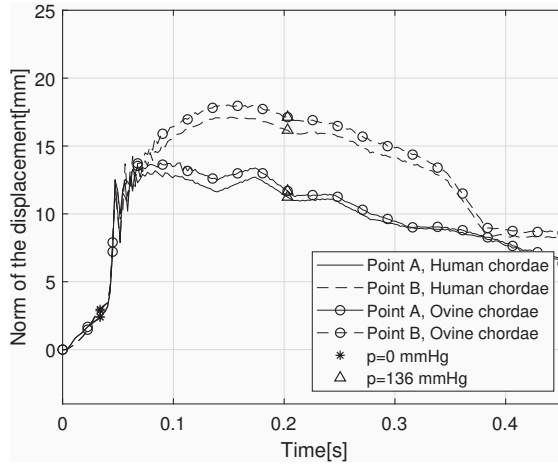


**Figure 12:** Norm of the displacement of points A and B, obtained with leaflet parameters from table 1, and human and ovine chordae material parameters from table 2.

### 3.5 Material parameter study

In this section the material parameters acquired from the nonlinear data-fitting is compared with stiffer and softer material parameters for the leaflets. This is done in order to

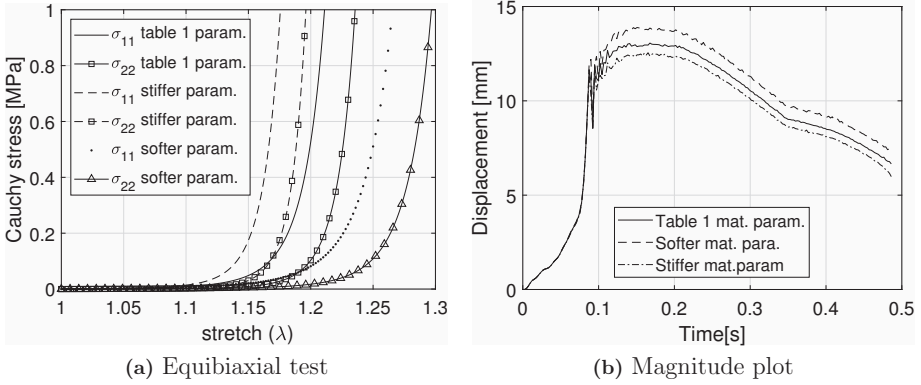


**Figure 13:** Displacement of point A obtained from analyses using stiffer and softer material parameters compared with material parameters from nonlinear data-fitting.

observe if there is any difference in global response, when changing these parameters. In figure 13a, the stress-stretch curves are plotted for an equibiaxial tensile test. Furthermore, in figure 13b the magnitude of point A is plotted, comparing the response from table 1 with the stiffer and softer material parameters.

From figure 13b, the response is as expected. For the stiffer material there are small oscillations during the analysis, and the displacement of point A at peak systole is 0.60mm less for the stiffer material, compared with the material parameters obtained in table 1. Moreover, the softer material clearly has higher oscillations throughout the analysis and displaces 0.75mm higher than the material parameters from table 1 at peak systole. Lastly, it is observed that during the first part of the analysis the response is similar for every analysis. Even for the large difference in stiffness in figure 13a, the difference in leaflet displacement in figure 13b is moderate.

### 3.6 Stresses

The leaflets von Mises stresses are plotted at peak systole (18.13 kPa) in figure 14. High stress regions are observed near the location where the strut chordae is inserted into the anterior leaflet and near the fibrous trigones. At the marginal chordae insertion points there are also observed large von Mises stresses. However, high stresses are also observed due to the implementation of material orientations, and is further discussed in the section 4.6.



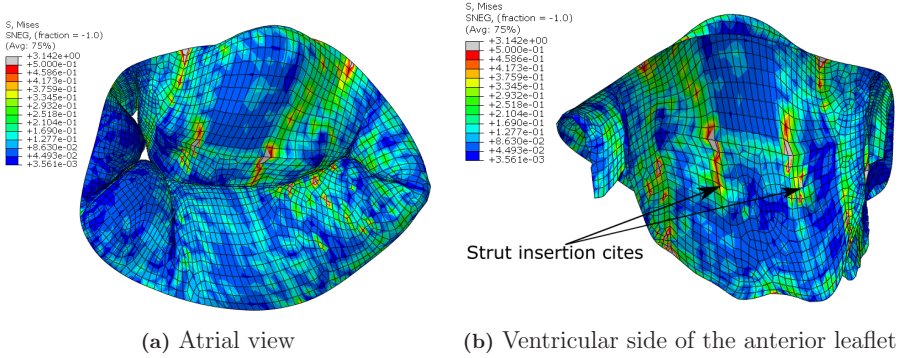


**Figure 14:** von Mises stress of the mitral valve leaflets (MPa).

The maximum principal stress direction is plotted on the deformed leaflets in figure 15. As can be seen from figure 15a, the maximum principal stress is aligned with the modelled material orientation for the anterior leaflet. The maximum principal stress for the entire posterior leaflet is observed in figure 15b to be perpendicular to the annulus. As a result, in the posterior leaflet, the maximum principal stress only aligns with the assigned material orientation near the commissures.

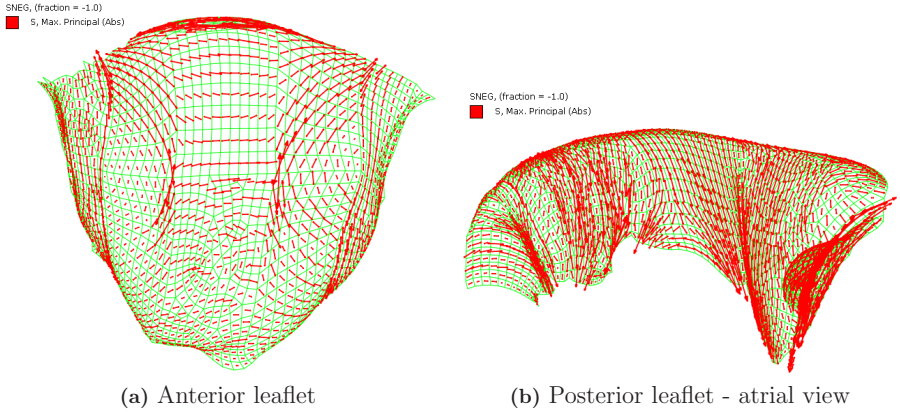


**Figure 15:** Maximum principal stress plotted on deformed mitral valve leaflets.

## 4 Discussion

### 4.1 Global Response

The global response presented in section 3.3 shows that there is regurgitation at the posteromedial region (A3-P3) at late-systole. Moreover, the posteromedial side of the P2 segment is observed to prolapse at late-systole causing the posterior leaflet to override the anterior leaflet. These results are highly consistent with what we know about the patient's lesions, where regurgitation was detected in the posteromedial region at late systole.

In the anterolateral region (A1-P1), lack of closure in the FE model is observed throughout the whole analysis. The severity of regurgitation in this region is high before and after peak systole for the model. However, comparing the anterolateral regurgitation observed in the patient, the obtained results did not fully coincide with the patient. The patient experienced regurgitation due to prolapse of the P1 segment from mid systole, which is not entirely what the FE model predicts. The echocardiographic modelling might be the reason for the inaccurate observation of regurgitation at this region, and is further discussed in section 4.2.

As can be seen from figure 9a, the annular area starts to increase prior to peak systole ( $t=0.17s$ ). The annulus continues to expand until the pressure has reached approximately 118mmHg (0.38s). Furthermore, the annular flattening observed during systole (figure 9b) is similar to what is written about Barlow diseased mitral valves [17, 3]. Comparing these findings with the global response (figure 11), it is evident that the annular changes must affect the coaptation of the leaflets. The late systolic regurgitation is observed when the annular area is at its highest. Thus, the dilation of the annulus may be a reason for regurgitation during this time interval.

### 4.2 Echocardiographic modelling

The patient-specific mitral valve geometry was modelled using echocardiographic data as described in section 2.4. The anterior leaflet and the P2 segment of the posterior leaflet were clearly visible on the echocardiographic images. However, locating the commissures was a more demanding process, where several echocardiographic views were needed. At the posteromedial commissure, the leaflets could be identified from the echocardiographic recording. Hence, the geometry obtained was satisfactory. For the anterolateral commissure the identification of the leaflet structure was cumbersome, leading to considerable uncertainty in the geometry at this region. As a consequence, the interpolated free edge at the anterolateral commissure was inaccurate.

As discussed in section 4.1 regurgitation is observed in the anterolateral region during systole. However, the patient did not experience similar severity of regurgitation near the anterolateral commissure. Thus, the observed regurgitation from the FE analysis is probably a consequence of the inaccurate modelling at the anterolateral region.

### 4.3 Comparison with 3D echocardiographic data

In figure 10, the correlation between the echocardiographic measurements and the mitral valve model response is observed to be very good. The bulging towards the left atrium is similar to that of the echocardiographic measurements. However, the FE response for both human and ovine chordae material parameters are shown to coapt further toward the left ventricle at peak systole compared to echocardiography. Furthermore, it is observed that both FE models bulge more than the echocardiographic measurements near the annulus, especially for the ovine material parameters.

Performing a similar comparison near the commissures at peak systole is difficult, as there is observed a lot of tissue on the echocardiographic images in this region. Collocating the echocardiographic measurements and the FE model at the commissures, show that the FE model bulges too little towards the atrium. The excessive tissue at this region is probably a combination of Barlow disease and calcifications near the annulus, making the comparison between the *in vivo* images and the FE model difficult in this region.

### 4.4 Material parameters

In order to use the Holzapfel-Gasser-Ogden material model, introduced in section 2.3, to model the response of the mitral valve, it is required that the material parameters implemented in the model show a similar response compared to experimental data presented by [10]. Obtaining a good fit between the experimental data and the material model provided by Abaqus, can make it possible to omit the usage of the subroutine VUMAT, where VUMAT is an Abaqus Explicit subroutine used for material models not directly available in Abaqus. The study performed in section 2.3, gave a sound fit comparing the experimental data from [10], with the Holzapfel-Gasser-Ogden strain-energy function.

Human mitral valve tissue has been shown to be stiffer than porcine mitral valve tissue [19]. Hence, it can be argued that using porcine material properties might not give a correct response when modelling a human mitral valve. However, in the study [12], myxomatous mitral valve leaflets were identified to be twice as extensible and less stiff compared to healthy human leaflets. As a consequence, porcine material parameters are assumed to be a better assumption than using the parameters from a healthy human, due to the difference in stiffness.

The chordae tendineae were modelled with both human and ovine material parameters. Comparing the global responses of these two cases, the coaptation and the location of regurgitation were observed to be nearly identical. From figure 12, the total displacements of points A and B are approximately  $1mm$  higher for the ovine chordae parameters. Furthermore, the difference in displacement is mainly observed when the ventricular surface is subjected to peak pressures leading to high chordae strains. As a consequence the human chordae is observed to displace less at high strains compared to the ovine chordae due to the nature of the material. In the study by [12], myxomatous chordae tendineae were found to be 50 % less stiff compared to human chordae. Studying the comparison

with 3D echocardiographic measurements, the ovine chordae parameters are observed to correlate less to the echocardiography than the model with human chordae parameters. Furthermore, there is observed little difference in coaptation between the models, but the ovine model prolapses more as both the leaflets displace towards the atrium.

In section 3.5, it was shown that the difference in displacements between the stiffer, softer and material parameters from table 1 was low. Hence, it appears that annulus and papillary muscle movements have more influence on the global response than the applied materials.

#### 4.5 Chordae modelling

The marginal chordae tendineae are modelled so that they originate from the papillary muscles and insert into the free edge of the mitral valve leaflets, while the strut chordae insert into the anterior leaflet rough zone. The chordae insertion sites at the free edge are prone to high stresses, and the splitting of the chordae helps redistributing the loads along the elements, preventing the elements from excessive distortion. The chordae modelling is not just important for anatomical correctness but also for the finite element analysis as a whole.

From echocardiographic images it is not possible to get a full representation of the chordae insertion site, nor the amount of chordae. As a consequence, for a patient-specific analysis, the amount of chordae and insertion sites has to be assumed from literature [13]. Furthermore, it is not possible to detect if the chordae are stretched or not in diastole. A characteristic feature for Barlow patients is the elongated chordae at systole [1], which might leave the chordae slack at diastole. It is therefore assumed that there is no pre-tension in the chordae for a Barlow patient. Hence, the chordae are modelled as straight lines without any form of pre-tension. The model managed to follow the echocardiographic measurements without any pre-tensions, which was not the case in the study performed by [20]. However, in the study by [20] the studied valve was a patient with functional mitral regurgitation (FMR), which is not a degenerative disease. It can be argued that some of the chordae should be modelled slack. However, this needs to be studied further.

#### 4.6 Material orientation

The material orientation applied in the FE model on the mitral valve leaflets is for a healthy porcine specimen. However, as stated in literature, the collagen fibres in Barlow leaflets are observed to be disoriented and disrupted [5]. In [21], this disruption is found to be due to myxomatous degeneration. Hence, the fibre direction used in this paper may not be entirely accurate. However, to the authors' knowledge little is known about the collagen orientation for Barlow mitral leaflets. The gradual rotation of the collagen fibres towards the commissures in the anterior leaflet is not fully accounted for, where instead each partitioned region is given one specific direction as described in section 2.6. This modelling technique leads to some abrupt changes where the modelled orientation changes

(figure 7b). This leads to the stress concentrations observed on the anterior leaflet, just above the chordae insertions (figure 14).

#### 4.7 Stresses

The von Mises stresses were found to be highest where the abrupt changes in material orientation were present. However, removing the elements with high stresses due to this feature, more reasonable stress values were observed. Regions of high stresses near the chordae insertion points, especially where the strut chordae is inserted, and the fibrous trigones are observed. This is consistent with previous studies [22, 23]. However, comparing stress values with literature, is not so beneficial, as an unusual thickness of 3mm is used in this study.

### 5 Conclusion

In this paper, a finite element model of a mitral valve with Barlow disease has been employed with annular and papillary muscle motions. Lack of closure were observed in both the anterolateral and posteromedial commissure for the model. This agrees, to some extent with the echocardiographic findings of the patient. The finite element model predicted regurgitation in the posteromedial region well, where late systolic regurgitation and prolapse were observed for both the patient and model. In the anterolateral region the model predicted regurgitation throughout systole, while echocardiography only showed regurgitation at mid-systole. An explanation for this discrepancy might be that the commissure geometry is difficult to define from echocardiography, especially for the anterolateral commissure. Refinement of the method used to localize these regions *in vivo* are necessary to create accurate models. In order to refine the geometrical modelling, an autostereoscopic 3D screen could be used to locate intricate points near the commissures [24]. Lastly, severe annular dilation seems to be one major cause of mitral regurgitation. In this study, the most severe lack of closure from mid- to late-systole appeared when the annulus dilated the most.

Creating accurate patient-specific models which can predict regurgitation correctly and reliably will in the future open up several exciting possibilities: for example, performing surgery *in silico* in order to optimize and create a patient-specific surgical procedure. Furthermore, it may facilitate the development of repair devices as they can be tested and refined numerically.

## REFERENCES

- [1] Carpentier, Alain and Adams, David H. and Filsoufi, Farzan *Carpentier's reconstructive valve surgery : from valve analysis to valve reconstruction*. Saunders Elsevier, Vol. I., (2010).
- [2] Iung, B., Baron, G., Tornos, P., Gohlke-Barwolf, C., Butchart, E. G. and Vahanian, A. Valvular heart disease in the community: a European experience. *Curr. Probl. Cardiol.* (2007) **32**:609–61.
- [3] Apor, A., Nagy, A. I., Kovacs, A., Manouras, A., Andrassy, P. and Merkely, B. Three-dimensional dynamic morphology of the mitral valve in different forms of mitral valve prolapse - potential implications for annuloplasty ring selection. *Cardiovasc. Ultrasound* (2016) **14**:32.
- [4] Jouan, J., Berrebi, A., Chauvaud, S., Menasche, P., Carpentier, A. and Fabiani, J. N. Mitral valve reconstruction in Barlow disease: long-term echographic results and implications for surgical management *J. Thorac. Cardiovasc. Surg.* (2012) **143**:517–20.
- [5] Hjortnaes, J., Keegan, J., Bruneval, P., Schwartz, E., Schoen, F. J., Carpentier, A., Levine, R. A., Hagege, A. and Aikawa, E. Comparative Histopathological Analysis of Mitral Valves in Barlow Disease and Fibroelastic Deficiency *Semin. Thorac. Cardiovasc. Surg.* (2016) **37**:757–767.
- [6] Prot, V., Skallerud, B. and Holzapfel, G. A. Transversely isotropic membrane shells with application to mitral valve mechanics. Constitutive modelling and finite element implementation. *Int. J. Numer. Meth. Engng.* (2007) **3**:987–1008.
- [7] Holzapfel, G. A., Ogden, R. W. and Gasser, T. C. Hyperelastic modelling of arterial layers with distributed collagen fibre orientations *J. R. Soc. Interface* (2006) **3**:15–35.
- [8] Prot, V. and Skallerud, B. Nonlinear solid finite element analysis of mitral valves with heterogeneous leaflet layers. *Comput. Mech.* (2008) **43**:353–368.
- [9] Abaqus *Abaqus Analysis User's Guide*. Dassault Systemes, Vol. (2014).
- [10] May-Newman, K. and Yin, F. C. A constitutive law for mitral valve tissue. *J Biomech Eng* (1998) **120**:38–47.
- [11] Zuo, K., Pham, T., Li, K., Martin, C., He, Z. and Sun, W. Characterization of biomechanical properties of aged human and ovine mitral valve chordae tendineae. *J. Mech. Behav. Biomed. Mater.* (2016) **62**:607–18.

- [12] Barber, J. E., Ratliff, N. B., Cosgrove, D. M., 3rd, Griffin, B. P. and Vesely, I. Myxomatous mitral valve chordae. I: Mechanical properties. *J. Heart Valve Dis.* (2001) **122**:955–62.
- [13] Kunzelman, K. S., Cochran, R. P., Verrier, E. D. and Eberhart, R. C. Anatomic basis for mitral valve modelling. *J. Heart Valve Dis.* (1994) **3**:449–58.
- [14] Cochran, R. P., Kunzelman, K. S., Chuong, C. J., Sacks, M. S. and Eberhart, R. C. Nondestructive analysis of mitral valve collagen fiber orientation *ASAIO Trans.* (1991) **37**:447–8.
- [15] Rego, B. V., A. H. Khalighi, A. Drach, E. K. Lai, A. M. Pouch, R. C. Gorman, J. H. Gorman, and M. S. Sacks. A noninvasive method for the determination of in vivo mitral valve leaflet strains. *Int. J. Numer. Method. Biomed. Eng.* (2018) **34**:e3142.
- [16] J. Levick *An Introduction to Cardiovascular Physiology*. Hodder Arnold, Vol. 5., (2010).
- [17] Grewal, J., Suri, R., Mankad, S., Tanaka, A., Mahoney, D. W., Schaff, H. V., Miller, F. A. and Enriquez-Sarano, M. Mitral annular dynamics in myxomatous valve disease: new insights with real-time 3-dimensional echocardiography. *Circulation* (2010) **121**:1423–31.
- [18] Chandra, S., Salgo, I. S., Sugeng, L., Weinert, L., Tsang, W., Takeuchi, M., Spencer, K. T., O'Connor, A., Cardinale, M., Settlemier, S., Mor-Avi, V. and Lang, R. M. Characterization of degenerative mitral valve disease using morphologic analysis of real-time three-dimensional echocardiographic images: objective insight into complexity and planning of mitral valve repair. *Circ. Cardiovasc. Imaging* (2011) **4**:24–32.
- [19] Prot, V., Skallerud, B., Sommer, G. and Holzapfel, G. A. On modelling and analysis of healthy and pathological human mitral valves: two case studies. *J. Mech. Behav. Biomed. Mater.* (2010) **3**:167–77.
- [20] Pham, T., Kong, F., Martin, C., Wang, Q., Primiano, C., McKay, R., Elefteriades, J. and Sun, W. Finite Element Analysis of Patient-Specific Mitral Valve with Mitral Regurgitation. *Cardiovasc. Eng. Technol.* (2017) **8**:3–16.
- [21] Anyanwu, A. C. and Adams, D. H. Etiologic classification of degenerative mitral valve disease: Barlow's disease and fibroelastic deficiency. *Semin. Thorac. Cardiovasc. Surg.* (2007) **19**:90–6.
- [22] Prot, V., Haaverstad, R. and Skallerud, B. Finite element analysis of the mitral apparatus: annulus shape effect and chordal force distribution. *Biomech. Model. Mechanobiol.* (2008) **8**:43–55.

- [23] Votta, E., Caiani, E., Veronesi, F., Soncini, M., Montecvecchi, F. M. and Redaelli, A. Mitral valve finite-element modelling from ultrasound data: a pilot study for a new approach to understand mitral function and clinical scenarios. *Philos. Trans. A Math. Phys. Eng. Sci.* (2008) **366**:3411–34.
- [24] Dumont, K. A., Kvitting, J. P., Karlsen, J. S., Remme, E. W., Hausken, J., Lundblad, R., Fiane, A. E. and Urheim, S. Validation of a Holographic Display for Quantification of Mitral Annular Dynamics by Three-Dimensional Echocardiography. *J. Am. Soc. Echocardiogr.* (2019) **32**:303–316 e4.



## PIPE FSI IN GENERALIZED COORDINATES

JAN CHRISTIAN ANKER

ANKER ZEMER Engineering AB  
Box 2005  
SE 702 02 ÖREBRO, Sweden.  
E-mail: [jc.anker@gmail.no](mailto:jc.anker@gmail.no)

**Key words:** Computational Methods, Boundary Elements

**Abstract:** Aspects of flow induced vibrations in piping systems due to internal flow are discussed, addressing Engineering Aspects, Computational Methods, and Vibration Problem Identification.

### 1 INTRODUCTION

Piping systems are used for conveying fluids (i.e. liquids and gases), the dominating cross section is circular. From an engineering point of view, piping systems seem, at a first glance, to be very simple systems: You determine the overall geometry ('from where to where'), the internal cross sections based on the amount of fluid to be conveyed per unit of time, and the structural properties (wall thicknesses, supports ...) based on allowable stresses. However, as a pipe failure may have consequences ranging from insignificant to catastrophic, it might be required to study all aspects of the behavior of a piping system, keeping mind that the pipe behavior is influenced by external sources and vice versa; this physical behavior is typically of dynamic nature. Hereinafter, the focus is on vibrations with respect to fatigue, noise, and influence on attached structures. In the literature, there are relative few papers addressing all three aspects; [1]. In this document, numerical methods for vibration analysis in piping engineering are discussed and a numerical concept based on the Boundary Element Method ("BEM") is presented.

### 2 ENGINEERING ASPECTS OF PIPING SYSTEMS

The problem of vibrations in piping systems conveying fluid can realistically be assessed by numerical methods only. A frequently applied concept is to iterate between structural analysis and fluid flow analysis, this is basically transferring the deflected geometry shape to the fluid flow software, then determining the fluid pressure distribution onto the structure and transferring it to the structural analysis software. After certain convergence-criteria are fulfilled, the simulation is halted and the solution is digested.

In the following, pipe vibrations are emphasized. A piping system must be designed such

that no critical vibrations with respect to noise, fatigue, and negative influence on other structures occur. The implication is that you have to do a simulation for each frequency of excitation you are capable of identifying. The discretization of the structure with supports and attached masses is straight forward and not discussed here; the discussion is about vibrations of pipes conveying fluids and what additional physical effects influences their behavior.

We are assuming the flow being one-phase, single medium, single phase, and continuous with or without disturbances in the flow field. Hence waterhammer effects, slugs, and cavitation are not considered, the purpose of the method presented is to determine whether disturbances in the internal flow field or time varying forces acting onto the pipe will cause insufficiently damped vibrations, i.e. vibrations of unacceptable amplitudes; one terms such behavior 'unstable'. One difficulty is to quantify 'unacceptable amplitude', as it is problem dependent. Some engineers are of the opinion that when the amplitude(s) stops growing, there is no problem, but this may only holds true when fatigue and/or noise are no issue(s).

A special case is 'the submerged pipe' as found in coolers/heaters, reactors, and with offshore installations. There are two additional effects to consider in this case: Hydrodynamic added mass and fluctuations in the surrounding medium, e.g. as a result of vortex shedding. Hydrodynamic added mass is pretty straightforward, fluctuations in the surrounding medium not, as the latter may require separate simulations to assess disturbances in the medium external to the pipe and interaction between pipe and surroundings.

The general procedure could be the following:

- i. Model the pipe for structural analysis utilizing solid elements (at least 36 elements over the circumference, account for masses attached, support stiffnesses, ...).
- ii. Identify any disturbances in the pipe flow and any time dependent forces from attached structures (e.g. pumps, motors) that could trigger vibrations.
- iii. Determine the characteristics of the fluid domain external to the pipe (if relevant) and decide if it must be accounted for.
- iv. Perform a series of computations for various speeds of medium internal to the pipe and for all relevant structural modes and frequencies; if there is a flowing medium external to the pipe, that must be accounted for as well.

What is outlined above is a brief sketch of what an analysis procedure could look like, result interpretation would presumably emphasize displacements, stresses and periods of events. The procedure above might be realistic in principle, but is not practical because of exorbitant computing times and the amount of data generated, which makes the interpretation cumbersome. In short: Another computational method is required to help the engineer remove a potentially serious problem.

### 3 A COMPUTATIONAL CONCEPT BASED ON GENERALIZED COORDINATES

For the analysis of the vibration of structures, the normal modes method is since long an accepted method for addressing their vibrational behavior. To understand the concept, consider the one spring, one mass system with or without damping that we can study with respect to steady and harmonic loads. Now, we ask us whether it is possible to represent the dynamic properties of the structure by sets of uncoupled ‘one mass, one stiffness’ systems? The answer is ‘yes’, we divide the structure in question in very many small chunks having mass and stiffness (called Finite Elements), and look for the *uncoupled* spring – mass systems. Since we need to keep track of every chunk in a structured way, we introduce matrices. We generate a Stiffness Matrix  $[\mathbf{K}]$  and a Mass Matrix  $[\mathbf{M}]$  representing the physical properties needed for (somehow) laying the foundation for our goal of describing the vibrational characteristics of the structure by a bunch of disconnected spring-mass systems. Now we want to apply Newton’s laws to our system: We call the directions of movement  $\{x_i\}$ , and – enforcing equilibrium – require that spring forces must be in equilibrium with mass times acceleration, and write in matrix notation

$$[\mathbf{K}]*\{x_i\}+[\mathbf{M}]*\{d^2x_i/dt^2\}=0 \quad (1)$$

then we substitute  $x_i = x_0*\sin(\omega t)$ , perform differentiation with respect to time ‘t’ two times, ( $dx_i/dt = x_0*\omega*\cos(\omega t)$ ,  $d^2x_i/dt^2 = -x_0*\omega^2*\sin(\omega t)$ ) and find

$$[\mathbf{K}]*\{x_0\}*\sin(\omega t)-\omega^2*[\mathbf{M}]*\{x_0\}*\sin(\omega t)=0, \quad \text{or} \\ ([\mathbf{K}]-\omega^2*[\mathbf{M}])* \{x_0\} = 0 \quad (2)$$

For any value of  $\omega$  there is a corresponding value of  $\{x_0\}$  giving a qualitative description of the shape of the structure vibrating; the system’s dynamics *without considering damping* may now be described in terms of uncoupled spring-mass systems.

Introducing Eigenvalues and the corresponding Eigenvectors as ‘Modal Coordinates’, we can describe the displacements and derived quantities as functions of the exiting frequencies.

### 4 FLUID STRUCTURE INTERACTION UTILIZING MODAL COORDINATES

In the previous section, we have discussed ‘Modal Coordinates’ for the pipe as a structure (with or without a fluid at rest). Our aim is to devise a method that describes the vibrational characteristics of a pipe conveying a fluid (liquid or gas) for the purpose of identifying any instable modes. Since all fluids have mass and elastic properties, they qualify for a modal analysis. In theory, you could do that by utilizing a model by Finite Elements, which is impractical (if not impossible).

LINFLOW (‘LF’) by ANKER – ZEMER Engineering AB is based on boundary elements (Boundary Element Method or BEM) and modal coordinates, the verified and surprisingly

effective concept is outlined below (a complete description does not fit in a conference paper, for a description in depth see [2]). For those who are technically interested, a brief presentation of the LF concepts is given below.

LF was originally developed as a tool for aeroelastic analyses for the air-craft industry. The concepts behind LF, however, differ from those used in classical aeronautical tools for aeroelastic analysis, so its is fair to describe the theoretical background and assumptions in some depth.

Firstly, derive the equations describing the inviscid fluid flow over a solid body. The frame of reference used is a body fixed coordinate system. A flow field can be characterized by the mass conservation or continuity equation (eq. (3)) and three Navier Stokes equations for momentum conservation (eq. (4)):

$$\frac{d\rho}{dt} + \nabla \cdot (\rho \vec{v}) = 0 \quad (3)$$

$$\rho \frac{d\vec{v}}{dt} = \rho \left( \frac{\partial \vec{v}}{\partial t} + \vec{v}(\nabla \cdot \vec{v}) \right) = -\nabla p + \mu \left[ \nabla^2 \vec{v} + \frac{1}{3} \nabla(\nabla \cdot \vec{v}) \right] + \rho \vec{f}_e \quad (4)$$

where  $t$  denotes time,  $\vec{v}$  the velocity vector,  $\rho$  the density,  $p$  the pressure,  $\mu$  the viscosity, and  $\vec{f}_e$  external bulk forces. As there are five unknowns ( $v_x, v_y, v_z, \rho$  and  $p$ ), a fifth equation is needed to make the equation system complete. This will be the classical isentropic relation for fluids ( $p^\gamma = \text{constant}$ , where  $\gamma$  denotes the constant ratio of specific mass). Unfortunately, solving eqs. (3) and (4) is very computer resource demanding. Approximations are needed if realistic fluid-structure interaction problems are to be solved with a minimum of computer resources and a minimum of man-hours for validation and interpretation.

As a first step in deriving the inviscid flow equations, we assume that the flow locally is irrotational (i.e.  $\nabla \times \vec{v} = 0$ ) and that the flow viscosity is zero ( $\mu = 0$ ). These assumptions are valid in flow domains with negligible boundary layer thickness and small shear layer regions so the influence from such layers can be neglected, assumptions that are well motivated for many other applications as well. However, LF is able to handle such limitations with additions to the governing set of equations, and the ability to address both inertial, viscous, and some non-linear effects not accounted for in the 'classical' but still approximate Reynold's equation.

We now introduce the velocity potential  $\Phi$  ( $\vec{v} = \nabla \Phi$ ) making it possible to reduce the five flow equations to three equations for the three unknowns  $\Phi, \rho$  and  $p$ . The momentum equation (2) can then be written as ( $\vec{f}_e = 0$ ):

$$\frac{\partial \nabla \Phi}{\partial t} + \nabla \left[ \frac{|\bar{v}|^2}{2} \right] = -\frac{\nabla p}{\rho} \quad (5)$$

Applying some vector algebra on equation (5) and applying far field conditions, with steady flow and straight streamlines, makes it possible to derive the Kelvin's (the unsteady version of Bernoulli's) equation, which is used in the following when deriving the pressure equation used in LF:

$$\frac{\partial \Phi}{\partial t} + \frac{|\bar{v}|^2}{2} + \int \frac{dp}{\rho} = \frac{U_{\infty}^2}{2} \quad (6)$$

where  $U$  is the free-stream part of the velocity vector  $\bar{v}$ , i.e. the flow with the 'disturbing' geometry of interest not present, and the subscript  $\infty$  indicates its far field (distant surrounding) value. Equation (6) differs from that used in the classical Double Lattice Method's ("DLM") approximation where the reference pressure ( $p_\infty$ ) is set to zero and the velocity potential is replaced with  $\phi = \Phi - U^2 t/2$ , leading to a modified Bernoulli's equation for the DLM:

$$\frac{\partial \phi}{\partial t} + \frac{|\bar{v}|^2}{2} + \int \frac{dp}{\rho} = 0 \quad (7)$$

Let us, for a moment, go back to the continuity equation (3) and introduce the velocity potential  $\Phi$  and the definition of the speed of sound,  $a$  ( $a^2 = dp/d\rho$ ). This yields, after some tedious mathematics, the following general vector equation:

$$\nabla^2 \Phi - \frac{1}{a^2} \left[ \frac{\partial}{\partial t} (\nabla \Phi \cdot \nabla \Phi) + \frac{\partial^2 \Phi}{\partial t^2} + \nabla \Phi \cdot \nabla \left( \frac{\nabla \Phi \cdot \nabla \Phi}{2} \right) \right] = 0 \quad (8)$$

This is the so-called full potential equation. Introduce the Mach number defined as  $M = U_\infty/a$ , and, assuming that the speed of sound,  $a$ , is constant and that the overall free-stream inflow ( $U_\infty$ ) is along the positive x-axis. An advantage is that  $M$  can be assumed constant for the entire flow field in the linear small deflection region. This will enable the derivation of the classical linear small disturbance velocity potential partial differential equation ("PDE"):

$$\nabla^2 \Phi - M^2 \left( \frac{1}{U_\infty} \frac{\partial}{\partial t} + \frac{\partial}{\partial x} \right)^2 \Phi = 0 \quad (9)$$

Interesting to note is that eq. (9) includes, as special cases, incompressible flow ( $d\rho/dp=0 \rightarrow \nabla^2 \Phi=0$ ) and the acoustic equation (harmonic  $\Phi$  and small perturbations  $\rightarrow \nabla^2 \Phi + (\omega/a)^2 \Phi = 0$ ).

Equation (9) is used as governing PDE for describing the fluid's dynamic behavior in LF. In the solution of the aeroelastic problem, the pressure is used as loads, and a linear expression for pressure as a function of the velocity potential,  $\Phi$ , is needed. This expression can be derived using the Kelvin's equation (6) and the isentropic relationship for the gas. The Kelvin's equation may now be rewritten into a linear expression for pressure as a function of  $\Phi$ :

$$p = p_{\infty} + \rho \left[ \frac{U_{\infty}^2}{2} - \left( \frac{|\vec{v}|^2}{2} + \frac{\partial \Phi}{\partial t} \right) \right] \quad (10)$$

Equation (10) is the incompressible version of the pressure equation used in LF. By using eq. (10), LF is not limited to applications and flow conditions that are based on thin structures oscillating around the zero degree angle of attack condition. As a comparison, the DLM is restricted to such conditions since the  $v^2/2$ -term is linearized about the free stream velocity components

$$\frac{|\vec{v}|^2}{2} = \frac{1}{2} U^2 + U \frac{\partial \tilde{\Phi}}{\partial x} \quad (11)$$

when deriving the expression for pressure, leading to the following DLM-pressure equation:

$$p - p_{\infty} = -\rho \left( \frac{\partial \tilde{\Phi}}{\partial t} + U \frac{\partial \tilde{\Phi}}{\partial x} \right) \quad (12)$$

with  $\tilde{\Phi}$  expressing the oscillatory part of the modified velocity potential. In the DLM,  $p_{\infty}$  describes the actual far field pressure, provided that the first term is removed from eq. (11), which is in agreement with the zero reference pressure assumption behind eq. (7). The reason why the  $U^2/2$ -term can be eliminated in the DLM is that this method's prime focus is on pressure differences between upper and lower surfaces (lift forces on wings, etc) and not on absolute pressures.

A key feature in LF is the representation of flow by harmonic oscillations around some general equilibrium point. This technique of variable separation and eigenmodes superposition is well proven and commonly used when analytically solving complicated, general PDEs. Normally, high accuracy solutions are obtained even with a very small number of eigenmodes. By assuming a harmonic velocity potential  $\Phi$  in the classical linear small disturbance velocity potential partial PDE (eq. (11)), one obtains:

$$\nabla^2 \Phi - M^2 \left( i \frac{\omega}{U_{\infty}} + \frac{\partial}{\partial x} \right)^2 \Phi = 0 \quad (13)$$

This is the PDE that is transformed into an integral formulation that is discretized utilizing the Boundary Element Method ('BEM') in LF. The steady and unsteady pressures are then calculated using the linearized pressure equation (10) derived above.

Problems involving interaction between structural and fluid dynamics can be described by the aeroelastic equation of motion. This equation is normally written in terms of modal coordinates that are based on the known structural eigenmodes. The benefit of using modal coordinates is that the number of degrees of freedom in the system is greatly reduced. In aeroelastic applications, only a few of the lowest frequency eigenmodes may be of interest, this also holds true when studying pipe vibrations. Another advantage with the LF concept is that the structural properties are computed once (without accounting for the fluid), and not over and over again in an iteration loop; required are eigenvalues and eigenmodes (and modal load vector for simulations not discussed here).

This concept outlined above has been implemented in the LF software; it is utilized for finding a modal representation of the "aeroelastic problem". With respect to piping problems, 'aeroelastic' is a misnomer, as that matrix covers gases as well as liquids. In any case, the concept allows us to derive the following equation describing the general FSI problem in modal coordinates:

The aeroelastic equation of motion expressed in modal coordinates is recognized as the structural dynamic equation with an additional term that includes the aeroelasticity matrix which describes the fluid - structure interaction; (14):

$$-\omega^2 [\mathbf{M}] \{ \mathbf{q} \} + i\omega [\mathbf{C}] \{ \mathbf{q} \} + [\mathbf{K}] \{ \mathbf{q} \} = [\mathbf{A}] \{ \mathbf{q} \} + \{ \mathbf{F} \} \quad (14)$$

with the left side representing the structure and the right side the fluid (gas or liquid), and where  $[\mathbf{M}]$  is the mass matrix,  $[\mathbf{C}]$  the damping matrix, and  $[\mathbf{K}]$  the stiffness matrix,  $[\mathbf{A}]$  is the aeroelastic matrix,  $\{ \mathbf{F} \}$  is the field strength, and  $\{ \mathbf{q} \}$  a displacement vector.

In LF, the above equation is used to solve stability problems. The method for identifying instabilities is to set the external force to zero, and check if there are eigenmodes in the system that are undamped or exponentially growing. Implemented in LINFLOW are the V-g method and the p-k method for finding inflow velocities that make the system unstable. These methods are iterative since the aeroelasticity matrix is velocity and frequency dependent, hence making the problem non-linear, convergence is usually obtained within two or three iterations. The methods is the way iterations are performed. In the V-g method a fictitious internal structural damping is introduced such that the stiffness and damping matrices are written in the form  $(1 + ig) [\mathbf{K}] \equiv i\omega [\mathbf{C}] + [\mathbf{K}]$ . In the V-g method one assumes a value for the critical velocity  $V$ , and solves for the value of the damping factor that makes the most unstable mode critical. Instabilities are identified by required damping factors that are greater than the available structural damping in the system. This solution gives a new value for the critical velocity  $V$ , and the procedure is repeated until the assumed and obtained values for  $V$  are consistent.

## 5 IDENTIFYING PIPING VIBRATION PROBLEMS

To better explaining the method for identifying piping vibration problems, we will expand on what is said on utilizing eigenfrequencies and eigenmodes in engineering above. Eigenvalue analysis as such gives valuable info about the dynamics of a structure. Moreover, it can be utilized as the foundation for linear transient dynamic analysis of structures (i.e. 'harmonic response by the normal modes method'). One of the big advantages of eigenvalue analysis is that the results are concise and easy to interpret, another advantage is that phase information may be considered with input as well as with output; eigenvalue analysis is well suited to optimize a structure with respect to vibrations. Assuming a perfectly straight and perfectly circular pipe geometry and corresponding supports, it is known that the eigenforms come in orthogonal pairs at the same eigenfrequency; this will describe the movement of the pipe in 3-D. If there is damping in the system, the pairs of orthogonal modes will no longer be in phase and the pipe will perform a rotating movement. All engineering materials have internal damping, so we have to account for damping in our evaluation of the vibrational characteristics of the pipe.

In pipe system engineering, there are two basic items of interest regarding the piping structure with respect to vibrations: The eigenfrequencies of the pipe as such, and whether the vibrational amplitudes due to force excitation by the flowing media internal and external to the pipe can be expected to be within limits. Further, the eigenfrequencies are essential for determining the response to excitation by outside forces. To assess the likelihood of growing amplitudes, we check whether material damping or other damping effects are sufficiently strong to inhibit amplitudes grow out of bounds.

The most pronounced physical effects in the context of harmonic vibrations or effects triggering vibrations we do not consider here, are: Water hammer effects or slugs (may trigger unwanted vibrations after the event), vortex shedding or cavitation internal and external to the pipe (triggering effect; may be introduced as concentrated, pulsating forces if applicable), and varying fluid mass densities. Further, the influence of a free surface is generally not considered.

We can safely assume that pipe material and medium have some internal damping. Damping means energy transfer to the material and to the medium. The energy loss due to material damping is increasing with growing amplitudes. As we are assuming small displacements and looking for growing amplitudes, the effects of growing amplitudes onto system damping will not be discussed henceforth.

There are several factors that directly or indirectly influence the vibrational characteristics. Some of the factors are depending on one or more of the other factors, this means that the problem is most likely nonlinear. Consider the following (extreme) example: A structure, connected to the submerged pipe to be checked for vibrations, has a part that may vibrate due to a farfield flow, this may influence the external fluid flowfield hitting the pipe; this implies that a) it must be considered whether there will be any influence from an unconnected structure on the flowfield reaching the pipe, b) how strong the influence superimposed on any flowfield influences from attached structures will be, and c) multiple simulations involving all



relevant combinations of items ‘a’ and ‘b’ should be performed. In reality, this example is most likely far fetched, but it shows the potentially complex physics that a pipe flow FSI analysis should take into account.

One factor not addressed above is the deviations between real and modeled physics, examples hereto would be perfectly straight and perfectly circular pipe geometry vs real geometry, assuming perfectly symmetric support vs real support characteristics, assumed material properties, etc. Neglecting such effects usually gives sufficiently accurate results with structural analysis, what effects small deviations will give in case of piping FSI are uncharted waters.

The assessment of vibrational behavior of the vibrations of a straight pipe is easy once you know the kind and frequencies of the excitation(s) and the eigenfrequencies of the pipe at rest. In the case you do not have data specific to a particular case, you have basically three options to remedy that, namely by performing a simulation with respect to fluctuations by utilizing a Navier-Stokes solver, using data based on on experience, and/or using intelligent assumptions. When modeling the pipe structure, it is recommended using at least 36 (solid) elements circumferentially, as the accuracy of the FSI simulation is strongly dependent on a correct pipe stiffness representation. The discretization of the system should also account for the mass density of the fluid, the higher the mass density, the coarser the discretization. It is mandatory that the discretization is such that it accurately captures structural eigenfrequencies near those exiting the system. To model the fluid, the interior of the pipe is covered with boundary elements matching the discretization of the structure. With the LF concept, computer time is not an issue for a system part, this having the effect that system changes can easily be simulated in a short time.

Finally: An often overlook fact is that the pipe eigenfrequencies are a function of the speed of the medium. Some maintain that this effect can be neglected; we disagree with this as we have seen changes of thirty percent and more with a changed medium speed.

## 6 CONCLUDING

The purpose of this paper is drawing attention to a disregarded (and often contested) fact, namely that the eigenfrequencies of pipes conveying a medium are depending on the speed of the medium, and to briefly hint onto the theoretical basis for a software that can address that phenomenon is given in [3]. References [4, 5, 6] point to the fact that such dependency really exists.

An efficient numerical concept based on The Boundary Element Method (‘BEM’) has been outlined, experience with the LINFLOW software shows that it yields engineering information with minimal computer resources; is remarkable in the sense that no error has been found in the software after approximately 20 years of usage.

## 7 REFERENCES

- [1] Shuaijun Lee, Bryan W. Karney, Gongmin Liu  
“FSI research in pipeline systems – A review of the literature”  
Journal of Fluids and Structures, 25 July 2015
- [2] Jari Hyvärinen  
"Generalized Methods for Aeroelastic Analysis"  
Licentiate Thesis, Aeronautical Engineering  
Swedish Royal Institute of Technology (KTH),  
TRITA-AVE 2003:02, ISSN 1651-7660
- [3] Jari Hyvärinen  
“LINFLOW Theory Manual”  
ANKER – ZEMER Engineering AB  
This manual is available from the author under a non-disclosure agreement.
- [4] Y L Zhang, D G Gorman and J M Reese  
"Analysis of vibrations of pipes conveying fluid"  
Department of Engineering, University of Aberdeen, Scotland, UK 1999
- [5] Murzin, A.N. Belousov, A.I.  
“Analysis of flexible metal hoses frequency characteristics”  
Dynamics and Vibroacoustics of Machines (DVM2016)  
Procedia Engineering 176 (2017) 66 – 70
- [6] Jari Hyvärinen  
“The Dynamics of Fluid Conveying Hydraulic Hose”  
ASME V&V2018-9352, ASME, 2018
- [7] Etim S Udoetok  
“Internal Fluid Flow Induced Vibration of Pipes”  
Journal of Mechanical Design and Vibration,  
vol. 6, no. 1 (2018): 1-8. doi: 10.12691/jmdv-6-1-1.

# NUMERICAL SIMULATION OF FATIGUE CRACK GROWTH IN OFFSHORE MOORING CHAINS

Mads Aursand<sup>1</sup> and Bjørn Skallerud<sup>1</sup>

<sup>1</sup>Norwegian University of Science and Technology (NTNU)  
Department of Structural Engineering  
Trondheim, Norway  
e-mail: mads.aursand@ntnu.no

**Key words:** Fatigue crack growth simulations, fracture mechanics, finite element analysis

**Abstract.** Numerical fatigue crack growth simulations are explored as a method for predicting the remaining fatigue life of offshore mooring chains. Polynomial solutions for calculating stress intensity factors along the front of a semi-elliptical crack in a curved cylindrical bar have been developed and included in a crack growth model. Stress intensity factor calculations based on superposition of polynomial solutions have been compared against non-linear finite element analysis results. Crack growth simulations highlighting the influence of residual stresses on predicted crack shape development and fatigue life are finally demonstrated.

## 1 BACKGROUND

Steel chains are extensively used in mooring systems for offshore oil&gas installations, as well as for floating wind turbines and fish farms. The dynamic motions of moored floating installation induced by e.g. wind and waves result in cyclic tensile loading of the mooring chains. Cyclic loading can over time potentially result in initiation and growth of fatigue cracks. In the marine environments where mooring chains are commonly used, this fatigue process may furthermore be significantly assisted by corrosion. Corrosion pits may aid crack initiation, while interactions between corrosive seawater and mechanical fatigue loading are known to enhance crack growth rates in steels [1, 2]. The problem of estimating remaining fatigue life under such conditions is consequently highly relevant for integrity management of offshore mooring systems [3].

In the present paper, the practical problem of predicting remaining fatigue lives of corroded offshore mooring chains will be approached using numerical fatigue crack growth simulations. A stud-less mooring chain design as illustrated in figure 1a will be considered. Each link in the chain is essentially a curved cylindrical bar joined with a single weld. Several studies involving full-scale fatigue testing on as-new as well as corroded

chains of this type can be found in published literature [4–6]. A general observation from these studies is that fatigue failures in mooring chains predominantly occur in the three locations highlighted in figure 1b. It can readily be found by stress analysis that these locations are hot-spots in terms of cyclic stress. Since standard requirements [7] for manufacture of offshore mooring chains specify a "proof-loading" that causes significant plastic deformation of the links, it can however also be shown that these same locations are characterized by compressive residual stresses [8]. For simulating fatigue crack growth in mooring chains, a fundamental element will accordingly be the fracture mechanical treatment of cracks in curved cylindrical bars containing compressive residual stresses.

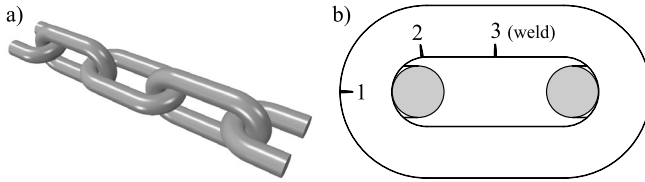


**Figure 1:** (a) Stud-less chain with (b) the three predominant fatigue fracture locations

Fatigue cracks in *straight* bars under simple load cases, i.e. combinations of pure tension and pure bending, is a problem that has been extensively covered in published literature [9–13]. A common approach is to fit polynomial functions to linear elastic stress intensity factors calculated using finite element analysis (FEA), and combining such functions using the principle of superposition. An extension of this approach aimed at geometries and loading situations relevant to cracks in mooring chains will be considered here.

The present paper explores a numerical model for computationally fast simulations of fatigue crack growth in offshore mooring chains. As part of this model, polynomial solutions for the stress intensity factor (SIF) along the front of a semi-elliptical crack in a generalized curved bar have been developed for stress distributions representative for proof loaded chains. Comparisons are made against non-linear finite element calculations performed on chain models containing cracks. Crack growth simulations have finally been demonstrated on a small selection of example fatigue cracks in a chain link.

## 2 MODELS AND METHODS

The fatigue crack growth model was developed by combining a generic crack growth model for semi-elliptical cracks (section 2.1) with stress intensity factor (SIF) solutions intended to be suitable for cracks in mooring chain links. Three different types of finite element analysis (FEA) models, as well as two polynomial fitting procedures, have been used in the development of the SIF solutions. Characterization of the stress distribution in a typical chain link before any crack has been introduced (sections 2.2-2.3) was performed

using non-linear FEA of a mooring chain model, with subsequent fitting of normal stresses to a cubic polynomial form. The SIF solutions (sections 2.4-2.5) were then developed using linear FEA of curved bar models containing cracks, with subsequent least-squares fitting to form polynomial solutions. Finally, non-linear FEA of a mooring chain model containing cracks (section 2.6) was performed for comparison and verification purposes.

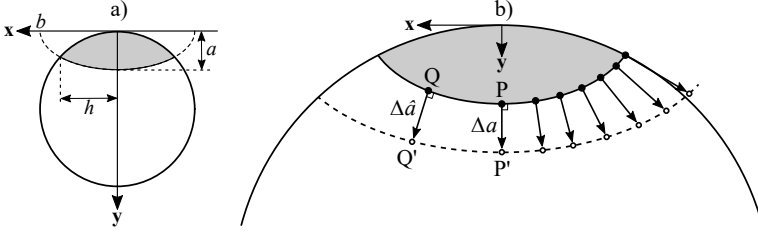


**Figure 2:** (a) Geometry definitions for semi-elliptical cracks and (b) crack growth model

## 2.1 Fatigue crack growth model

The numerical crack growth model is based on a model proposed by Couroneau and Royer [11] for semi-elliptical cracks in cylindrical bars. A semi-elliptical crack characterized by depth  $a$  and aspect ratio  $a/b$ , as defined in figure 2a, will be considered. The concept of an effective stress intensity factor range  $\Delta K_{eff}$  from linear elastic fracture mechanics will furthermore be used to characterize the cyclic stress conditions along the crack front under fatigue loading. Only mode I loading of the crack will be considered. In the case of a crack that is fully open throughout a constant-amplitude load sequence,  $\Delta K_{eff}$  will simply be equal to the difference between the stress intensity factors  $K_{max}$  and  $K_{min}$  calculated for the maximum- and minimum load values. Using the principle of superposition, these stress intensity factors can be calculated using linear combinations of solutions for different load cases. In the case of a crack that fully- or partially closes mid-cycle, which is a situation highly relevant for cracks growing in compressive residual stress fields, superposition of stress intensity factors may on the other hand result in physically meaningless negative values [14]. In the present work, a simple crack closure model that assumes  $K = 0$  when the crack faces are in contact has been used to handle the latter case. The effective stress intensity factor is consequently defined as follows:

$$\Delta K_{eff} = K_{max} - K_{min} \quad (K_{min} \geq 0) \quad (1a)$$

$$\Delta K_{eff} = K_{max} \quad (K_{min} < 0) \quad (1b)$$

Fatigue crack growth is simulated by propagating the crack front in small increments  $\Delta a$  while updating its aspect ratio  $a/b$ , as illustrated in figure 2b. In order to calculate the updated crack shape it is assumed that the local crack growth rate at any point P

or  $Q$  on the crack, as measured in a direction perpendicular to the crack front, can be described by an empirical crack growth law:

$$da/dN = f(\Delta K_{eff}) \quad (2)$$

The crack growth rate  $da/dN$  represents the local crack depth increment per load cycle  $N$ , and will generally vary over the width of the crack front. As long as the crack depth increment  $\Delta a$  from point  $P$  to  $P'$  along the crack centerline is small, the local increment  $\Delta \hat{a}$  from any point  $Q$  to  $Q'$  is approximated as follows:

$$\frac{\Delta \hat{a}}{\Delta a} \approx \frac{da/dN(\text{point } Q)}{da/dN(\text{point } P)} \quad (3)$$

For every point  $Q$  on the crack front with coordinates  $(x, y)$ , a new point  $Q'$  with coordinates  $(x', y')$  on the updated crack front can then be calculated by extending a normal vector of length  $\Delta \hat{a}$  from point  $Q$ . The shape of the updated crack front can finally be computed by fitting an ellipse to a distribution of  $n$  such  $Q'$  points. In the present work, this fitting was performed by finding the new ellipse parameters  $a$  and  $b$  that minimize the following sum-of-squares expression:

$$SS = \sum_n \left[ \left( \frac{x'_i}{b} \right)^2 + \left( \frac{y'_i}{a} \right)^2 - 1 \right]^2 \quad (4)$$

When  $\Delta a$  is given, the only unknown is  $b$ , and a solution for the aspect ratio of the updated crack front that minimizes the function  $SS$  can be readily shown to be:

$$\frac{a}{b} = \sqrt{\frac{a^2 \sum_n x'^2_i - \sum_n x'^2_i y'^2_i}{\sum_n x'^4_i}} \quad (5)$$

Growth of an initial semi-elliptical surface crack can thus be modeled by propagating it in small increments  $\Delta a$  while explicitly updating its aspect ratio  $a/b$  using the above equations. Number of fatigue cycles  $N$  accumulated throughout the simulation can furthermore be calculated by integration of the crack growth law (equation 2).

The crack growth law will generally depend on material and environment. For numerical examples in the present paper, a crack growth law based on statistical analysis of test results from various steels under freely corroding conditions in seawater performed by R.N. King [15] has been used. This two-stage law is defined as  $da/dN = 4.05 \times 10^{-12} \Delta K_{eff}^{3.42}$  [m/cycle] for  $\Delta K_{eff} \leq 42.2 \text{ Mpa}\sqrt{m}$ , and  $da/dN = 1.13 \times 10^{-8} \Delta K_{eff}^{1.3}$  [m/cycle] when  $\Delta K_{eff} > 42.2 \text{ Mpa}\sqrt{m}$ . In addition to the crack growth law, a vital component of this crack growth model is a method for calculating  $K_{max}$  and  $K_{min}$  along the crack front. Section 2.5 describes a polynomial  $K$  solution intended to be suitable for cracks in chain links.

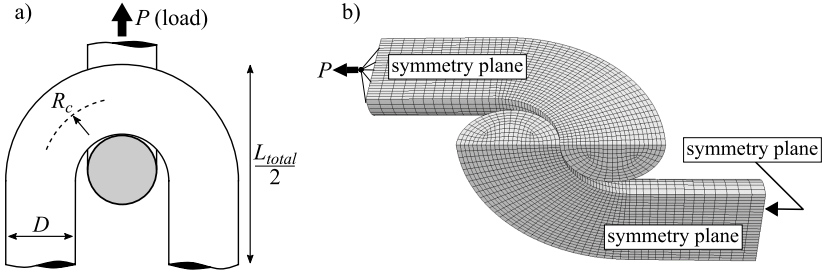


**Figure 3:** Chain link model (a) geometry and (b) FEA mesh

## 2.2 Chain model and stress calculations

The stress distribution in a typical chain link before any crack has been introduced was investigated by means of finite element analysis (FEA) of a mooring chain model. Figure 3a shows the assumed chain link geometry in its undeformed state. This geometry is defined by three parameters; diameter  $D$ , radius of curvature  $R_c$  and length  $L_{total}$ . The parameters given in table 1 will be used for numerical examples, and are intended to be representative of a chain used in permanent mooring of an offshore oil&gas installation. The chain is subjected to a tensile load  $P$ . For convenience, the load will be represented by a nominal cross-section stress  $\sigma_{nom}$  defined as follows:

$$\sigma_{nom} = 2P/\pi D^2 \quad (6)$$

Loading of the chain was modeled as a sequence starting with a simulated proof loading, followed by unloading and application of one or more service loads. A proof load level of  $\sigma_{nom} = 426$  MPa was used in the numerical examples, corresponding to standard requirements for a  $D = 114$  mm grade R4 mooring chain [7]. Significant plastic deformation of the chain accompanied by the introduction of residual stresses is expected to occur during proof loading. After unloading, a range of different service load levels up to  $\sigma_{nom} = 213$  MPa were included in the analysis. These service loads are assumed to be sufficiently small to not cause any further plastic deformation of the chain.

Material properties are important variables in FEA of chain models, particularly when the residual stresses caused by proof loading are of interest. Only a single elastic-plastic material model will however be considered in the present paper. The elastic modulus  $E$  and Poisson's ratio  $\nu$  define its linear elastic behavior, while a von Mises yield criterion and a Voce-law hardening rule define the plastic behavior. The yield stress magnitude can with this model be expressed as  $\sigma_y = \sigma_{y,0} + Q_\infty[1 - \exp(-\beta\epsilon_p)]$ , where  $\epsilon_p$  is the accumulated plastic strain. Values for the material parameters are given in table 2. These were chosen to produce a material model that could be reasonably representative for a grade R4 high-strength offshore mooring chain.

Finite element analysis was performed using the commercial software Abaqus 2017. The model (figure 3b) contains three symmetry planes and was meshed using 15120 quadratic hexahedral elements. Inter-link contact was modeled as a hard contact with Coulomb friction, assuming a friction coefficient of 0.35. Load was applied to a reference point coupled to the pulled end of the link via a constraint that prevented rotation of this face without limiting its translation in any direction. This was confirmed to ensure consistency/symmetry between neighboring links during loading.

**Table 1:** Chain link geometry parameters

$D[\text{mm}]$	$R_c[\text{mm}]$	$L_{total}[\text{mm}]$
114.0	134.0	684.0

**Table 2:** Material model parameters

$E[\text{GPa}]$	$\nu$	$\sigma_{y,0}[\text{MPa}]$	$Q_\infty[\text{MPa}]$	$\beta$
200.0	0.3	870.0	300.0	12.5

### 2.3 Polynomial approximation of stress distribution

Finite element analysis (FEA) results for the chain link model defined in section 2.2 were used to produce polynomial approximations for stress distributions in the predominant fatigue crack locations indicated in figure 1b. From theory of linear elastic fracture mechanics and the principle of superposition, the stress intensity factor associated with a given crack will be linearly dependent on the stresses that were acting over the crack plane before the crack was introduced. Since only mode I loading will be considered here, it is furthermore reasonable to assume that only the normal stress component will contribute to crack propagation. Expressing the normal stress field as a polynomial should therefore allow for calculation of linear elastic stress intensity factors via superposition of individual load cases.

By inspection of FEA results from the predominant fatigue crack locations it was found that the normal stress distributions  $\sigma_z$  in these regions, *before any crack has been introduced*, can be approximated by a cubic polynomial on the form:

$$\begin{aligned} \sigma_z(x, y) = & \sigma_0 + \sigma_1(1 - 2y/D) + \sigma_2(1 - 4y^2/D^2) + \sigma_3(1 - 8y^3/D^3) \\ & + \sigma_4(1 - 4|x|^2/D^2) + \sigma_5(1 - 8|x|^3/D^3) + \sigma_6(1 - 8|x|^2y/D^3) \end{aligned} \quad (7)$$

Note that two first terms in equation 7 represent the customary membrane- and bending stress components, and that the coordinate system is as defined in figure 2. The reference



stress values  $\sigma_\alpha = \sigma_0, \dots, \sigma_6$  are determined by least squares fitting of the polynomial function to FEA results. An example of such a polynomial fit is shown in figure 4. The normal stresses have here been calculated for the region representing location 1 in figure 1 after a load sequence consisting of proof loading, unloading, then re-loading to a moderately high service load level.

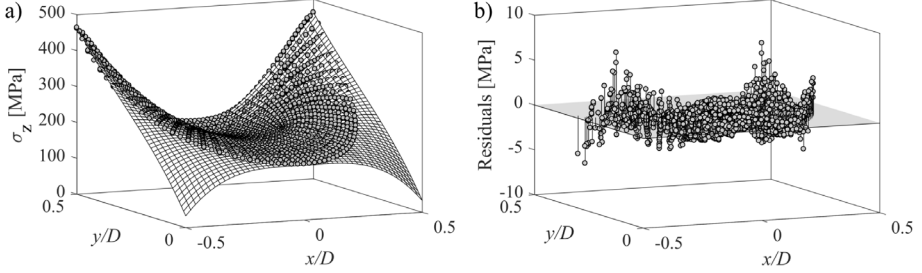


**Figure 4:** Example of polynomial stress field fitted to FEA results

## 2.4 Simplified curved bar model with crack

For the generalized case of a semi-elliptical crack in a curved bar where the stress distribution in the crack plane is defined by equation 7, stress intensity factor(SIF) calculations were performed using a parametric linear FEA model. The geometry of this model can be characterized by the three dimensionless parameters  $a/b$ ,  $a/D$  and  $D/R_c$ . Crack shape is defined by  $a$  and  $b$  as shown in figure 2, while the bar is defined by its diameter  $D$  and radius of curvature  $R_c$ . Two different directions of bar curvature relative to crack location were considered.  $R_c$  will here be denoted with a negative value if the crack is located on the interior side of the curvature, and a positive value if on the exterior side. See the example model geometries shown in figure 5.

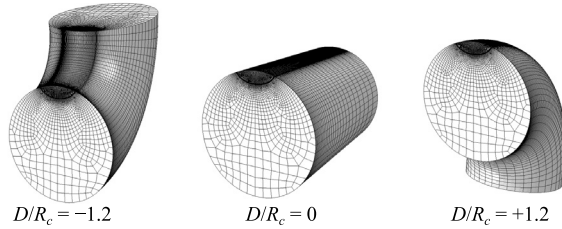


**Figure 5:** Examples of bar-with-crack models for different curvatures  $D/R_c$ , looking at the crack-face symmetry planes

Finite element analyses were performed on 448 individual geometries. Eight different crack depth ratios  $a/D$  between 0.03 and 0.4, eight different crack aspect ratios  $a/b$  between 0.0 and 1.5, and seven different bar curvature ratios  $D/R$  between  $-1.2$  and  $+1.2$  were considered. The length of the cylindrical bar was set to have a constant value of  $3D$ . Preliminary parametric studies indicated that the effect of bar length on calculated SIFs became insignificant when it exceeded about  $2.0D - 2.5D$ . Since very short bars are not of interest in this study, the bar length was consequently eliminated as a variable. For each geometry, seven separate load cases were applied, corresponding to each of the individual terms in the polynomial stress distribution defined by equation 7. The loads were applied as crack-face pressure fields  $p(x, y) = -\sigma_z(x, y)$  defined by setting the respective reference stress  $\sigma_\alpha$  to unit magnitude. For each analysis, SIFs were evaluated at 10 different crack front locations  $x/h$ . Since the intersection between a semi-elliptical crack and the free surface of a cylindrical bar in general cannot be characterized by a  $1/\sqrt{r}$  stress singularity [16], SIF evaluations were limited to the innermost  $\approx 85\%$  of the crack line.

The stress intensity factor calculations were performed using the virtual crack extension domain integral method [17,18], as implemented in the commercial software Abaqus 2017. Calculation of SIF from  $J$ -integral values were performed under an assumption of plane strain conditions. The material was assumed to be linear elastic with a Poisson's ratio of  $\nu = 0.3$ . Figure 6 shows a typical mesh for the crack front region. The domain integral volume comprised the innermost five layers of elements surrounding the crack tip, of which the innermost are collapsed-node elements with mid-side nodes moved to quarter-point positions. All elements were of 20-node hexahedral type. For verification, results were checked against SIF values calculated from the crack opening displacement field.

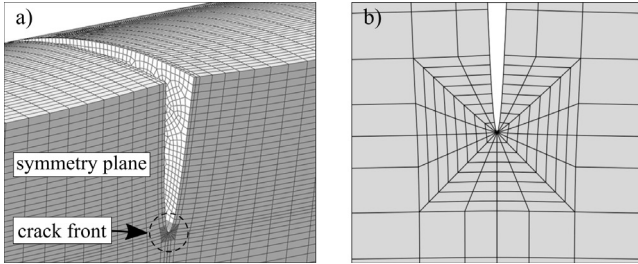


**Figure 6:** Finite element mesh in the crack front region of the simplified bar-with-crack model, looking at the center-of-crack symmetry plane

## 2.5 Polynomial stress intensity factor solution

For a semi-elliptical crack in a curved bar where the normal stress in the crack plane *before any crack is introduced* can be described by the cubic polynomial defined in equa-

tion 7, the SIF at any point on the crack front can be calculated as:

$$K_I = \sum_{\alpha=0}^6 F_{\alpha} \sigma_{\alpha} \sqrt{\pi a} \quad (8)$$

The above equation represents a superposition of SIFs contributed from each individual term in the stress field definition, and is theoretically only valid under the assumptions of linear elastic material and small deformations. Using FEA results from the generalized curved bar with crack model defined in section 2.4, polynomial solutions were developed for the geometry correction factors  $F_{\alpha}$ . A wide range of polynomial expressions were considered, using exhaustive leave-one-out cross validation for evaluation of fit-quality. The following polynomial expression was found to provide good fits without obvious indications of over-fitting:

$$F_{\alpha} = \sum_{i=0}^6 \sum_{j=0}^4 \sum_{k=0}^2 \sum_{l=0}^5 C_{ijkl}^{\alpha} (a/b)^i (a/D)^j (D/R_c)^k (x/h)^l \quad (9)$$

For each load case  $\alpha$ , least-squares fitting to the 4480 individual SIF values calculated by FEA was used to determine the 630 coefficients  $C_{ijkl}^{\alpha}$  in the corresponding polynomial.

## 2.6 Chain model with crack

Numerical stress intensity factor (SIF) calculations were performed by means of non-linear FEA of chain models containing cracks introduced after proof loading. The purpose of these simulations was to produce a set of reference SIF values for cracks in proof loaded offshore mooring chain links that could be used for comparison against the polynomial SIF solutions. Model geometries are illustrated in figure 7. The chain link geometry was defined by the parameters in table 1, while a variety of semi-circular cracks ( $a/b = 1$ ) with depths  $a$  in the range of 5 – 30 mm were introduced in locations 1 and 3. A sequence of (1) proof loading, (2) unloading, (3) crack introduction, and (4) service loading of the chain was simulated. Load levels and the elastic-plastic material model were as described in section 2.2. After proof loading and introduction of residual stresses, the material model was changed to linear-elastic and the crack introduced into the model by releasing a set of boundary conditions. Crack face contact due to compressive residual stresses was included in the simulation by defining a hard, friction-less contact condition between the crack face and the crack symmetry plane.

Stress intensity factor calculations were performed using the virtual crack extension domain integral method in Abaqus 2017, with conversion from  $J$ -value to linear elastic SIF performed under the assumption of plane strain. Note that due to the proof loading sequence and introduction of residual stresses, use of the original  $J$  definition by Rice [19] would in this case have lead to a path-dependent contour integral. A modified  $J$  definition based on the works of Lei et al. [20] that accounts for the initial residual stress field

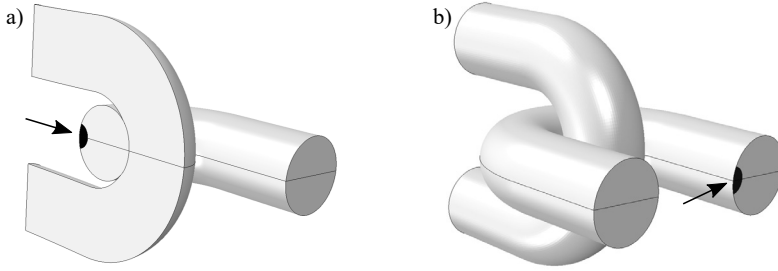


**Figure 7:** Example chain models with cracks in (a) location 1 and (b) location 3

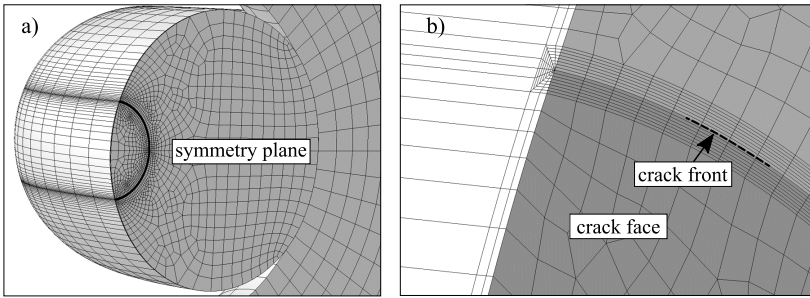


**Figure 8:** Finite element mesh for chain model with crack

has therefore been used. The finite element meshes consisted of approximately 26000-52000 quadratic hexahedral elements depending on crack geometry and location, with collapsed-node elements used at the crack tip. Figure 8 shows the refined mesh used in the crack front region. The domain integral volume comprised the innermost five layers of elements surrounding the crack tip. Verification of the SIF calculations was performed by comparing with SIF values calculated from the crack opening displacement field, as well as checking for possible path-dependencies in the  $J$ -integral values.

### 3 RESULTS AND COMPARISONS

#### 3.1 Stress intensity factors for cracks in curved bars

The polynomial stress intensity factor (SIF) solutions for semi-elliptical cracks in curved bars defined by equations 8 and 9 were fitted to results from linear FEA of simplified curved bar models, as detailed in sections 2.4 and 2.5. Coefficients of determination exceeded 0.9999 for all seven polynomial functions  $F_\alpha$ , with no single residual deviating more than 0.9 % from the corresponding FEA value. The computed coefficients  $C_{ijkl}^\alpha$  for

the polynomial SIF solution are provided as a separate dataset [21].

In the case of a straight bar subjected to a pure tension or bending load, considering only the  $x/h = 0$  crack front location, the present polynomial SIF solution may be directly compared with similar solutions published by Astiz [9], Couroneau and Royer [11], as well as Shin and Cai [12]. The solution by Astiz expresses the geometry correction factor  $F_0$  at the center of a semi-elliptical crack front in a cylindrical bar under tensile loading as a polynomial function of the two parameters  $a/D$  and  $a/b$ . Couroneau and Royer similarly expresses  $F_0$  and  $F_1$  at the center of the crack front under tensile- and bending loads as polynomial functions of  $a/D$  and  $a/b$ . The Shin-Cai solution adds crack front position as an independent parameter, expressing  $F_0$  and  $F_1$  along the crack front under tensile- and bending loads as polynomial functions of  $a/D$ ,  $a/b$  and  $x/h$ . Comparison plots for the corresponding geometry correction factors  $F_0$  and  $F_1$  are provided in figure 9. Note that the Shin-Cai solution was developed for  $a/D \geq 0.067$  and does not appear to be suitable for extrapolation to relative crack depths much smaller than that. Good agreement between the different polynomial solutions was otherwise observed.

In the limit where the relative crack depth  $a/D$  approaches zero, it can be argued that a crack with aspect ratio  $a/b > 0$  becomes equivalent to an identically shaped surface crack in a semi-infinite plate. Comparisons with the solution by Newman and Raju [22] for the latter geometry under tensile loading are shown in figure 10. Good agreement between computed geometry correction factors were observed over the crack front.

The effect of bar radius-of-curvature  $R_c$  on SIFs calculated for selected semi-elliptical crack shapes is demonstrated in figure 11. When the crack is located on the exterior side of the curved bar ( $D/R_c > 0$ ), the SIF was found to be enhanced by the curvature. When the crack is located on the interior side of the bar, a reduction in SIF was observed. As the relative crack depth approaches zero, the effect of curvature appears to vanish.

### 3.2 Stress intensity factors for cracks in chain links

Stress intensity factors (SIFs) calculated by non-linear FEA of chain models containing cracks introduced after simulated proof loading, as detailed in section 2.6, were compared against SIFs calculated using the polynomial solution for cracks in generalized curved bars. The corresponding polynomial solutions were computed by approximating the stress distribution in the crack plane according to equation 7 in section 2.3, and estimating the SIF by superposition of the polynomial functions defined by equations 8 and 9 in section 2.5.

Figure 12 shows a comparison for the case of an  $a = 10$  mm deep fatigue crack in location 1 (see figure 1) of a chain link. Figure 12a compares mean SIF values for the crack, as calculated over  $n = 10$  evenly distributed crack front positions, for a range of load levels  $\sigma_{nom}$ . Due to the considerable compressive residual stresses present in this region, a tensile load corresponding to  $\sigma_{nom} > 100$  MPa was needed to achieve complete opening of the crack. Figure 12b shows the corresponding mean of the differences between the calculated SIF values over the crack front. The SIFs calculated using the polynomial approximation

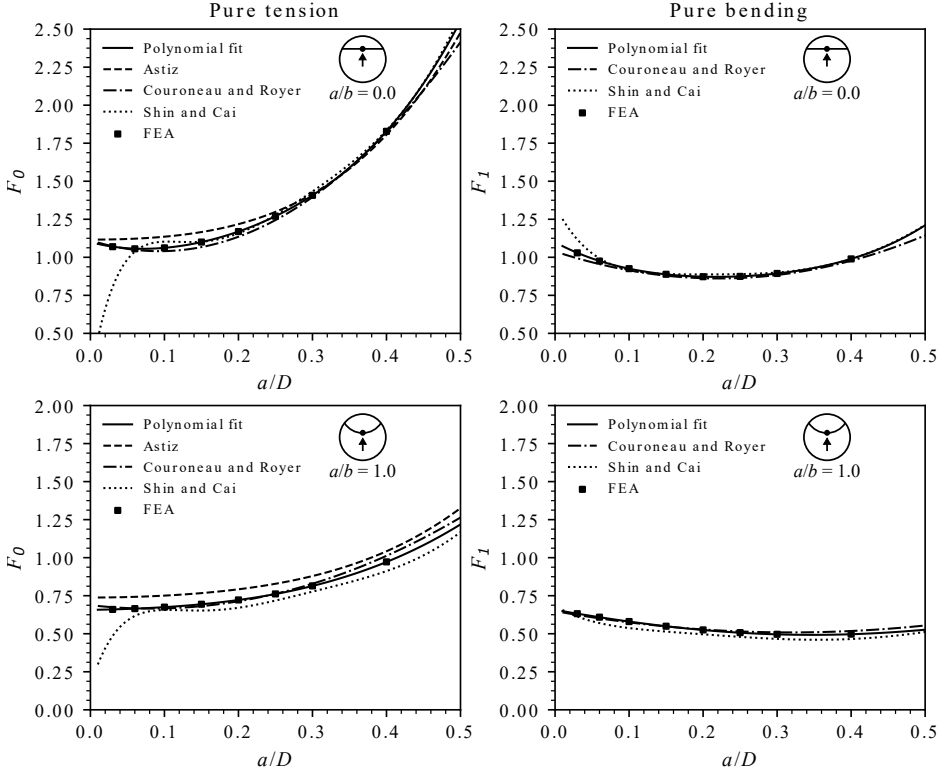


**Figure 9:** Geometry correction factors for cracks in straight bars under tension and bending loads

can be seen to agree well with FEA calculations, exhibiting a mean difference over the crack front of no more than  $1.5 \text{ MPa}\sqrt{m}$  for any of the investigated load levels. As demonstrated in figure 12c, the calculated variation in  $K$  with crack front position  $x/h$  furthermore appears consistent between the two SIF calculation methods.

Comparisons between the two SIF calculation approaches for cracks of various sizes in different locations are summarized in figure 13. Considering mean differences over the crack front, the SIFs calculated using the polynomial approximation were found to consistently be around 2 – 6 % higher than the corresponding SIFs from direct non-linear FEA calculations ( $K_{\text{FEA,mean}}$ ).

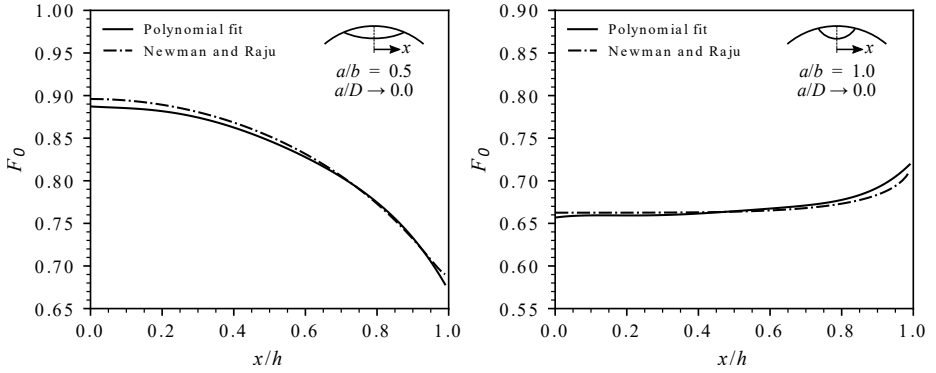


**Figure 10:** Crack front SIF variation in the limit when relative crack depth approaches zero

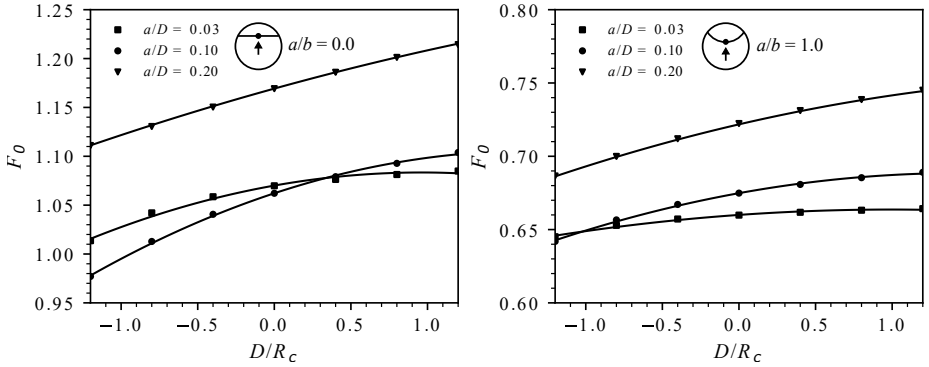


**Figure 11:** Influence of bar curvature on calculated SIF, showing FEA results with polynomial fits

### 3.3 Fatigue crack growth simulations

For the purpose demonstrating the fatigue crack growth simulation method defined in section 2.1, a selection of hypothetical initial surface defects in a chain link have been considered. The chain link geometry is as defined in table 1, while the cyclic load range was assumed to be  $\Delta\sigma_{nom} = 61$  MPa with a mean load of  $\sigma_{nom,mean} = 122$  MPa. Simulations were performed on four different initial cracks, all of which are characterized by an initial crack depth of  $a = 10$  mm. Comparisons are made between the two different aspect ratios  $a/b = 1$  and  $a/b = 1/3$ , and the two different crack locations labeled 1 and 3 in

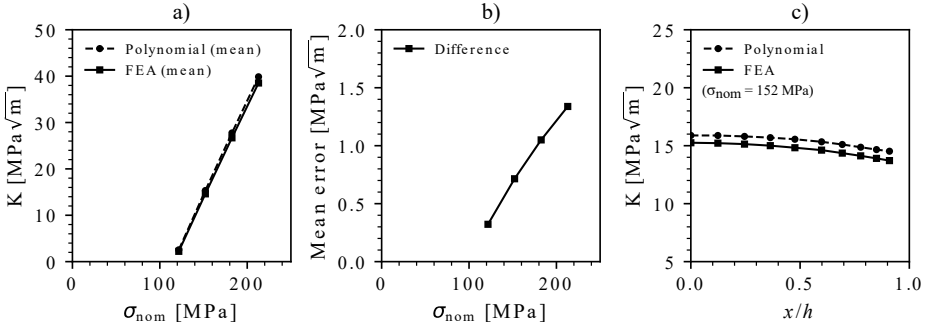


**Figure 12:** Stress intensity factor calculations for an  $a = 10$  mm semi-circular crack in location 1 of a chain link, comparing the polynomial SIF solution to the non-linear FEA calculation

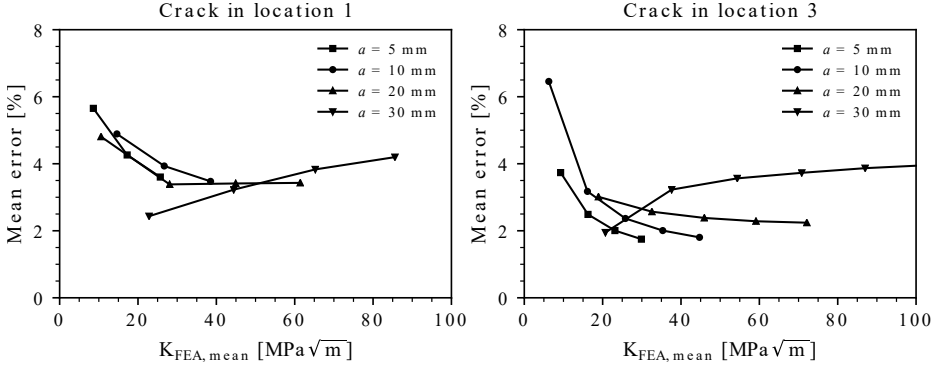


**Figure 13:** Stress intensity factor calculations for semi-circular cracks in chain link: Mean errors of the polynomial SIF solution relative to the non-linear FEA calculations

figure 1b. Each crack was propagated in 1000 increments, with the crack front represented by 25 nodes. Stress intensity factors were calculated using the polynomial solution from section 2.5. While limited in scope, these examples should be sufficient to demonstrate that the crack shape development predicted by the model is not unreasonable.

Results from the crack growth simulations are shown in figure 14. Crack front shape development during crack growth has been illustrated using a subset of crack front contours. Calculated number of cycles  $N$  for the crack to reach a final depth corresponding to  $a/D = 0.5$  are furthermore indicated. In all four calculation cases, the aspect ratio of the final crack front can be seen to converge to  $a/b \approx 0.7$  regardless of initial crack shape. Intermediate crack front shapes can however be seen to differ notably between the two



crack locations. Since crack front shape development largely is driven by the variation in  $\Delta K_{eff}$  along the crack front, compressive residual stresses in the chain link can be an important contributing factor to this variation.

The importance of compressive residual stresses for predicted crack front shape development and remaining fatigue life can be to some extent be demonstrated by ignoring crack closure in the crack growth simulations. Results from crack growth simulations where crack closure is ignored are shown in figure 15. The crack closure model defined in equation 1 has in this case been replaced with  $\Delta K_{eff} = K_{max} - K_{min}$  for any  $K_{min}$ . Comparison between figures 14 and 15 shows that the crack closure model has substantial effects on the simulation results for cracks growing from location 1. Under the influence of substantial compressive residual stresses, the crack closure model can be seen to considerably increase predicted fatigue life and notably influence the shape of intermediate crack contours. For cracks in location 3, where the residual stress magnitude is considerably lower and  $K_{min}$  in this particular case is non-negative over the full load range, the crack closure model is on the other hand found to be inconsequential.

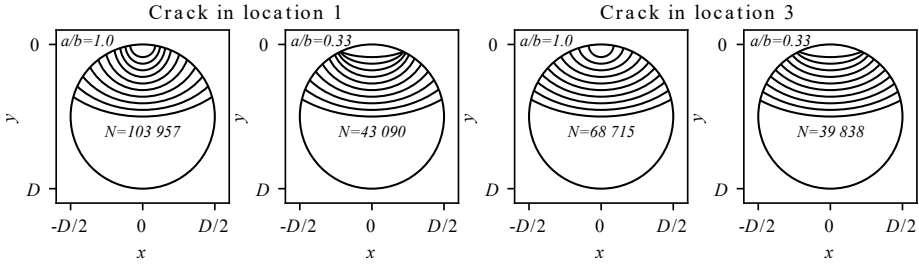


**Figure 14:** Crack growth simulation results for various initial cracks characterized by  $a = 10$  mm, showing subsets of crack front contours and calculated number of fatigue cycles  $N$

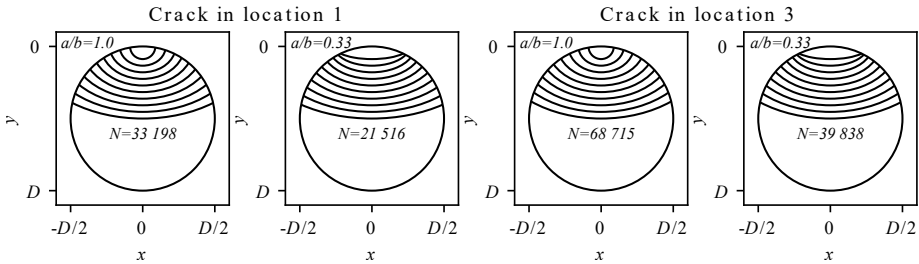


**Figure 15:** Crack growth simulation results for various initial cracks characterized by  $a = 10$  mm when ignoring crack closure from compressive residual stresses

## 4 DISCUSSION

A key question that this paper has attempted to address is whether the use of polynomial solutions and the principle of superposition is a suitable approach to calculating stress intensity factors (SIFs) for cracks in chain links. The polynomial solution presented here involves multiple layers of approximations: Complex stress distributions are simplified to polynomials, each term of this polynomial is assigned an approximate SIF solution, and the resulting SIF finally calculated by superposition. Comparisons between this approach and the computationally demanding approach of directly calculating the SIFs directly using non-linear FEA did however demonstrate reasonable agreement. The calculated SIFs were generally within  $\approx 2 - 6 \%$  of each other, with the polynomial method producing a more conservative result in all attempted comparisons. Considering the multitude of uncertainties that typically must be addressed in practical fatigue crack growth problems, these differences can arguably be characterized as minor.

An original contribution in the present paper is a polynomial solution developed for calculating SIFs along the front of a semi-elliptical crack in a curved cylindrical bar. For the special case of a straight bar subjected to tension- or bending loading, several similar solutions can be found in published literature. See e.g. Toribio et al. [13] for a comprehensive review. Comparisons presented in section 3.1 demonstrated that the present curved-bar solution should be suitable for this simpler straight-bar case as well, though at the cost of having to evaluate a comparably large polynomial expression. For a crack in a straight bar under tensile loading, the polynomial will contain 210 non-zero terms. For comparison, the straight-bar solution by Shin and Cai [12] contains 72 terms, and if only the center position on the crack front is of interest, the solution by Astiz [9] contains no more than 9 terms. With bar curvature included as an independent parameter, and by accommodating more complex stress distributions than simple tension and bending, the present polynomial solution is on the other hand intended to offer more refined SIF calculations for cracks in chain links.

Although somewhat outside the scope of this paper, it should perhaps also be noted that the use of linear elastic fracture mechanics for characterizing cracks growing in compressive residual stress fields is not without problems. The simple  $\Delta K_{eff}$  approach used in this work is widely known to be somewhat limited in its ability to characterize crack tip conditions under tension-compression type of loading [23]. Crack growth simulations presented in section 3.3 furthermore demonstrated that the crack closure model can have a significant effect on predicted remaining fatigue life. Since fatigue crack growth in compressive stress fields is of considerable importance for offshore mooring chain fatigue life predictions, an improved crack closure model suitable for steels in corrosive environments could be very valuable for the type of fatigue model used in the present work.

## 5 CONCLUSION

A numerical model for simulating fatigue crack growth in mooring chain links containing compressive residual stresses has been presented. Polynomial solutions for calculating stress intensity factors (SIFs) for semi-elliptical cracks in curved round bars have been developed as part of the model. SIFs calculated for semi-elliptical cracks in chain links by superposition of polynomial solutions developed for generalized curved bar geometries were found to compare well with SIFs calculated directly using non-linear FEA. For the range of crack sizes and tensile loads considered, results from the polynomial SIF solutions were found to consistently be  $\approx 2 - 6$  % higher than the corresponding non-linear FEA solutions. Fatigue crack growth simulations were finally demonstrated, highlighting the problem of characterizing the effective crack driving force ( $\Delta K_{eff}$ ) for cracks subjected to tension-compression loading.

## REFERENCES

- [1] T. W. Thorpe, P. M. Scott, A. Rance, and D. Silvester. Corrosion fatigue of BS 4360:50D structural steel in seawater. *International Journal of Fatigue*, 5(3):123–133, 1983.
- [2] N. O. Larrosa, R. Akid, and R. A. Ainsworth. Corrosion-fatigue: A review of damage tolerance models. *International Materials Reviews*, pages 1–26, 2017.
- [3] R. B. Gordon, M. G. Brown, and E. M. Allen. Mooring integrity management: A state-of-the-art review. In *Offshore Technology Conference*. Offshore Technology Conference, 2014.
- [4] A. Arredondo, J. Fernández, E. Silveira, and J. L. Arana. Corrosion fatigue behavior of mooring chain steel in seawater. In *ASME 2016 35th International Conference on Ocean, Offshore and Arctic Engineering*, Volume 1: Offshore Technology; Offshore Geotechnics. ASME.
- [5] J. Fernández, W. Storesund, and J. Navas. Fatigue performance of grade R4 and R5 mooring chains in seawater. In *ASME 2014 33rd International Conference on Ocean, Offshore and Arctic Engineering*, Volume 1A: Offshore Technology. ASME.
- [6] Ø. Gabrielsen, K. Larsen, and S-A. Reinholdtsen. Fatigue testing of used mooring chain. In *ASME 2017 36th International Conference on Ocean, Offshore and Arctic Engineering*, Volume 1: Offshore Technology. ASME.
- [7] Offshore Standard DNVGL-OS-E302 "Offshore mooring chain", 2015.
- [8] P. M. C. L. Pacheco, P. P. Kenedi, and J. C. F. Jorge. Elastoplastic analysis of the residual stress in chain links. In *ASME 2002 21st International Conference*

- on Offshore Mechanics and Arctic Engineering*, pages 39–46. American Society of Mechanical Engineers.
- [9] M. A. Astiz. An incompatible singular elastic element for two- and three-dimensional crack problems. *International Journal of Fracture*, 31(2):105–124, 1986.
  - [10] A. Carpinteri and R. Brighenti. Part-through cracks in round bars under cyclic combined axial and bending loading. *International Journal of Fatigue*, 18(1):33–39, 1996.
  - [11] N. Couroneau and J. Royer. Simplified model for the fatigue growth analysis of surface cracks in round bars under mode I. *International Journal of Fatigue*, 20(10):711–718, 1998.
  - [12] C. S. Shin and C. Q. Cai. Experimental and finite element analyses on stress intensity factors of an elliptical surface crack in a circular shaft under tension and bending. *International Journal of Fracture*, 129(3):239–264, 2004.
  - [13] J. Toribio, N. Álvarez, B. González, and J. C. Matos. A critical review of stress intensity factor solutions for surface cracks in round bars subjected to tension loading. *Engineering Failure Analysis*, 16(3):794–809, 2009.
  - [14] D. Schnubel and N. Huber. The influence of crack face contact on the prediction of fatigue crack propagation in residual stress fields. *Engineering Fracture Mechanics*, 84:15–24, 2012.
  - [15] R. King. A review of fatigue crack growth rates in air and seawater, HSE report OTH 511. Report, 1998.
  - [16] J. P. Benthem. State of stress at the vertex of a quarter-infinite crack in a half-space. *International Journal of Solids and Structures*, 13(5):479–492, 1977.
  - [17] D. M. Parks. The virtual crack extension method for nonlinear material behavior. *Computer Methods in Applied Mechanics and Engineering*, 12(3):353–364, 1977.
  - [18] C. F. Shih, B. Moran, and T. Nakamura. Energy release rate along a three-dimensional crack front in a thermally stressed body. *International Journal of Fracture*, 30(2):79–102, 1986.
  - [19] J. R. Rice. A path independent integral and the approximate analysis of strain concentration by notches and cracks. *Journal of Applied Mechanics*, 35(2):379–386, 1968.
  - [20] Y. Lei, N.P. O’Dowd, and G.A. Webster. Fracture mechanics analysis of a crack in a residual stress field. *International Journal of Fracture*, 106(3):195–216, 2000.

- [21] M. Aursand. Dataset from: Numerical simulation of fatigue crack growth in offshore mooring chains. <https://doi.org/10.5281/zenodo.3214401>, May 2019.
- [22] J. C. Newman and I. S. Raju. An empirical stress-intensity factor equation for the surface crack. *Engineering Fracture Mechanics*, 15(1):185–192, 1981.
- [23] C. Benz. Fatigue crack growth at negative stress ratios: On the uncertainty of using  $\Delta K$  and R to define the cyclic crack tip load. *Engineering Fracture Mechanics*, 189:194–203, 2018.



## THE LONG PERIODICITY OF VORTEX DISLOCATIONS IN THE WAKE BEHIND A STEP CYLINDER

Cai Tian<sup>\*1</sup>, Fengjian Jiang<sup>1</sup>, Bjørnar Pettersen<sup>1</sup> and Helge I. Andersson<sup>2</sup>

<sup>1</sup>Department of Marine Technology, Norwegian University of Science and Technology (NTNU)

<sup>2</sup> Department of Energy and Process Engineering, NTNU  
e-mail: cai.tian@ntnu.no

**Key words:** Grid independent study, direct numerical simulations, wakes, vortex dislocations, step cylinder

**Abstract.** By directly solving the three-dimensional unsteady Navier-Stokes equations, the wake flow behind a step cylinder with diameter ratio  $D/d = 2$  at Reynolds number  $Re_D = 150$  was investigated. The dominating frequency components and vortex interactions in the wake were studied in detail. Same as in previous studies, three spanwise vortex cells (the S-cell vortex behind the small cylinder, the L-cell vortex behind the large cylinder and the N-cell vortex between them) with different shedding frequencies were precisely captured in the present paper. Complex vortex interactions occur between these vortex cells. We focused on the vortex dislocations between the N- and L-cell vortices. A long periodicity of the vortex dislocation is reported and analyzed. Several long time numerical simulations (more than 3000  $D/U$  time units) were conducted to illustrate and analyze the wake flow. Benefit from it, a long period characteristic of the vortex dislocation was reported and analyzed. Additionally, the challenges of the grid resolution for investigating the long period phenomenon were discussed.

### 1 INTRODUCTION

In recent years, the wake flow behind a step cylinder has attracted more and more attention from researchers. Due to the abrupt change in diameter, the vortical structures in the near wake behind the step cylinder are complex even at a low Reynolds number, e.g.  $Re_D = 150$ , as shown in figure 7.

When considering flow past a step cylinder, there are two important parameters, i.e. the ratio between the large cylinder and the small cylinder (diameter ratio  $D/d$ ) and the Reynolds number ( $Re_D$ ). By doing laboratory experiments, Lewis & Gharib [1] observed and reported two vortex interaction modes, direct and indirect modes. When the diameter ratio is smaller than 1.25, only two dominating vortex shedding frequencies can be

captured in the wake of the step cylinder, corresponding to the vortices shed from the large cylinder and the small cylinder, respectively. These two vortex cells directly connect to each other, and the vortex interactions between them occur in a narrow region behind the step. This mode is called the direct mode. The indirect mode happens when the diameter ratio ( $D/d$ ) becomes larger than 1.55. Besides the two dominating vortex shedding frequencies of the small and large cylinder, a distinct frequency can be detected in the region downstream of the step. Lewis & Gharib [1] defined the region containing this distinct frequency as the modulation zone (the N-cell area in the present paper, see figure 1). Based on the shedding frequencies and locations of different vortex cells, Dunn & Tavoularis [2] defined three vortex cells behind the step cylinder with  $D/d = 2$ : (1) S-cell vortex shedding from the small cylinder with the highest vortex shedding frequency; (2) L-cell vortex shedding from the large cylinder; (3) N-cell vortex shedding near the step position between the S- and L-cell vortices, with the lowest vortex shedding frequency. The shedding areas of these three vortex cells are illustrated in figure 1. The terminologies S-cell, N-cell and L-cell were later used in many studies [3, 4, 5, 6], and are also used in the present study.

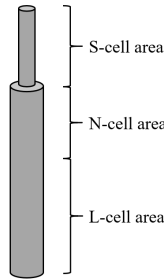


**Figure 1:** The shedding areas of the three vortex cells, i.e. S-, N- and L-cell area.

Due to the different shedding frequencies, neighbouring vortex cells move either in-phase or out-of-phase with each other. When they move out-of-phase, the contorted 'tangle' of vortices appears at the boundary between them, which looks like the dislocations that appear in solid materials. Williamson [8] defined this kind of vortex interaction as the vortex dislocation. The similar physical phenomena were also observed in the wake behind the step cylinder. In 1992, Lewis & Gharib [1] observed that an inclined interface between the N-cell and L-cell area appears at the beat frequency ( $f_L - f_N$ ). They suspected that this inclined interface might be caused by the variation of the actual spanwise length of the N-cell vortices. In 2010, Morton & Yarusevych [3] proved this suspicion. By doing numerical simulations, they clearly presented a cyclic variation of the N-cell vortices. In their studies, as N- and L-cell vortices move out-of-phase, in parallel with the appearances of the vortex dislocation, the spanwise length of the N-cell vortices



and the position of the N-L cell interface change periodically with the beat frequency ( $f_L - f_N$ ). Morton & Yarusevych [3] defined these cyclic variations as the N-cell cycle. In 2017, Tian et al. [6] further investigated the vortex dislocation between N- and L-cell vortices in detail. They identified two new loop structures: the NL-loop (the fake loop) structure formed between a N-cell and a L-cell vortex, and the NN-loop (the real loop) structure formed between two adjacent N-cell vortices. Based on careful observations of the formation processes of these loop structures, an antisymmetric vortex interaction was also reported between two adjacent N-cell cycles.

In 2015, McClure et al. [9] were the first reported the long period characteristic of the vortex dislocation by investigating flow past dual step cylinders ( $1 < D/d < 4$ ) at  $Re_D = 150$ . They found that there is a continuous variation in the vortex dislocations, i.e. the neighboring vortex dislocations are not exactly the same. They also defined the time period between two identical vortex dislocations as the fundamental dislocation cycle.

Compare to the interesting observations in this wake, what was much less focus on in the literature is the computational challenges in conducting simulations of the step cylinder wakes. Many complex and small vortical structures play important roles in the vortex interactions in this wake. These vortices are far more difficult to capture compared to the primary vortices. In addition, insufficient grid resolution may have little influence on the primary vortices, but will have strong effects on the vortex dislocations. When we discuss the long period phenomena, this becomes even more critical.

In the present paper, we investigate and report some interesting long period phenomena, and a subsequent computational challenge. In order to achieve this, the flow past a step cylinder ( $D/d = 2$ ) at  $Re_D = 150$  is studied by means of solving the full three-dimensional unsteady Navier-Stokes equations. The isosurface of  $\lambda_2$  and the time trace of velocity are plotted and observed for a relatively long time period (more than 2000  $D/U$ ). Last but not least, the challenges of investigating the long periodic phenomenon are discussed.

## 2 COMPUTATIONAL METHOD AND FLOW CONFIGURATION

### 2.1 Computational method

For all simulations in the present study, the full three-dimensional incompressible Navier-Stokes equations were directly solved by the code MGLET [10, 11]. In this second-order finite-volume solver, the governing equations are in integral form:

$$\int_A \mathbf{u} \cdot \mathbf{n} \, dA = 0 \quad (1)$$

$$\frac{\partial}{\partial t} \iiint_{\Omega} u_i \, d\Omega + \oint_A u_i \mathbf{u} \cdot \mathbf{n} \, dA = -\frac{1}{\rho} \oint_A p \mathbf{i}_i \cdot \mathbf{n} \, dA + \nu \oint_A \text{grad } u_i \cdot \mathbf{n} \, dA \quad (2)$$

where  $A$  and  $\Omega$  are the control surface and the control volume, respectively.  $\mathbf{n}$  is the unit vector on  $dA$  pointing out of  $\Omega$ , and  $\mathbf{i}_i$  is the Cartesian unit vector in  $\mathbf{x}_i$  direction.

All simulations are done on a staggered Cartesian mesh. After discretizing equation (2), we get

$$\frac{\partial u}{\partial t} = D(u) + C(u) + G(p) = f(u, p) \quad (3)$$

in which  $D(u)$  represents the discretized diffusive term,  $C(u)$  represents the discretized convective term, and  $G(p)$  represents the discretized pressure term. The midpoint rule is used to approximate the surface integral, leading to second-order accuracy in space. The diffusive term is approximated by a central-difference formulation, which preserves the second-order accuracy. The time integration of equation (3) is conducted by a third-order explicit low-storage Runge-Kutta scheme [12] (details can be found in [13]). The pressure term is corrected by solving a Poisson equation to fulfill a divergence-free velocity field:

$$\text{div}[(G(\delta p))]\Delta t = \text{div}(u^*) \quad (4)$$

where  $\delta p$  is the pressure correction,  $u^*$  is an intermediate velocity field calculated by omitting the pressure term in equation (3) and  $\Delta t$  is the constant time step that ensures a CFL number smaller than 0.7. At every marching time step, this discretized Poisson equation is represented by a linear equation system, which is solved by Stone's Strongly Implicit Procedure (SIP) [14].

The solid boundaries of the step cylinder is handled by an immersed boundary method (IBM). In MGLET, we use an unstructured triangular mesh to represent the surface of the geometry, and directly transfer information to IBM to block grid cells bounded by this surface. Then the grid cells at the fluid-solid interface will be set as internal cells by interpolating the flow variables from the surrounding cells. A more detailed description of the IBM used in MGLET can be found in [15].

## 2.2 Flow configuration

The geometry of the step cylinder investigated in the present paper is shown in figure 2 (a), in which  $D$  is the diameter of the large circular cylinder, and  $d$  is the diameter of the small cylinder.  $l$  and  $L$  are the length of the small and large cylinder, respectively. The origin locates at the center of the interface between the small and large cylinder. In figure 2 (b), the coordinate system and the computational domain are shown, where  $x$ -,  $y$ - and  $z$ -directions correspond to the streamwise, crossflow and spanwise direction, respectively. The computational domain is a rectangular box spanning  $20D$  in the crossflow direction,  $30D$  in the streamwise direction and  $45D$  in the spanwise direction. The total length of the step cylinder equals  $45D$ . These parameters are larger than that used by Morton and Yarusevych [3] for modeling a step cylinder with the same  $D/d$  and  $Re_D$ . Boundary conditions applied in the present study are as follow:

- The inlet boundary: uniform velocity profile  $u=U$ ,  $v=0$ ,  $w=0$ ;

- The outlet boundary: Neumann boundary conditions for velocity components ( $\partial u/\partial x = \partial v/\partial x = \partial w/\partial x = 0$ ) and constant zero pressure condition;
- The other four planes of the computational domain: free-slip boundary conditions. For the two vertical planes:  $v = 0, \partial u/\partial y = \partial w/\partial y = 0$ , For the two horizontal planes:  $w = 0, \partial u/\partial z = \partial v/\partial z = 0$ ;
- The step cylinder surfaces: no-slip and impermeable wall condition;

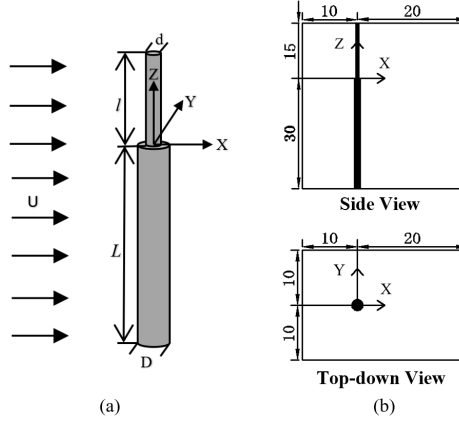


**Figure 2:** (a) The step cylinder geometry investigated in the present study; (b) Computational domain size, origin and coordinate system illustrated from different viewpoints. Diameter of the large cylinder,  $D$ , is the length unit. The origin locates at the center of the interface between the small and large cylinder.

### 3 Grid study

#### 3.1 Grid overview

**Table 1:** Grid information of all cases. The Reynolds number is 150 for all cases ( $Re_D = UD/\nu = 150$ ). Grid levels are illustrated in figure 3.

Case	Min grid cell size	Number of grid levels	Number of grid cells in one grid box	Time step $\Delta t$	Total number of grid cells (million)
1	0.025	5	$30 \times 30 \times 30$	0.0080	30.2
2	0.020	5	$36 \times 36 \times 36$	0.0067	48.8
3	0.015	6	$24 \times 24 \times 24$	0.0050	81.0
4	0.012	6	$30 \times 30 \times 30$	0.0040	173.8

Detailed grid information of all cases simulated is summarized in table 1. The Reynolds number is calculated based on the uniform free-stream velocity ( $U$ ) and the diameter of the large cylinder ( $D$ ), i.e.  $Re_D = UD/\nu = 150$  ( $\nu$  is the kinematic viscosity of the fluid). The computational domain is divided into many cubic Cartesian grid boxes. In each grid box,  $N \times N \times N$  cubic Cartesian grid cells are uniformly distributed. In the areas where complex flow phenomena take place, such as in the region around the 'step', the area where the vortex dislocation happens, etc., the grid is refined by equally splitting grid boxes (e.g. the level-1 box) into eight smaller cubic grid boxes (i.e. the level-2 box). Hence, the grid resolution on level-2 is two times better than that on level-1. This refinement process goes on automatically until the finest grid level (varies with cases shown in table 1) is reached. In figure 3, a schematic illustration of the grid for *Case2* is shown.

### 3.2 Grid convergence study

Motivated by ensuring that the grid resolution is good enough to resolve all important fluid phenomena, especially the complicated flow around the step, four grids were generated for the grid study, as shown in table 1.

First, we did a rough check by comparing vortex shedding frequencies of the three vortex cells in all cases. In table 2, by conducting Fast Fourier Transform of the time-series of the streamwise velocity  $u$  along a sampling line at  $(x/D, y/D) = (0.6, 0.2)$ , the Strouhal number ( $St$ ) of the three dominating vortex cells (S-cell  $St_S = f_S D/U$ , N-cell  $St_N = f_N D/U$  and L-cell  $St_L = f_L D/U$ ) in the wake of the step cylinder are calculated and presented. One can see that the differences in  $St$  of the same vortex cell are small among all cases. The largest difference is  $(St_S \text{ of } Case2 - St_S \text{ of } Case3) / (St_S \text{ of } Case3) = 1.7\%$ , which is considerably small. Moreover, the difference between *Case3* and *Case4* (the finest two cases) is smaller than 0.7%.

**Table 2:** The Strouhal number ( $St$ ) of three dominating vortex cells (S-cell  $St_S = f_S D/U$ , N-cell  $St_N = f_N D/U$  and L-cell  $St_L = f_L D/U$ ) for all cases investigated. The results of one previous numerical study [3] and two previous laboratory experiments [16, 17] are also shown. [Note: in our case,  $St_S$  is calculated based on the diameter of the large cylinder, a factor 2 is used when obtain data from [16, 17].]

Case	$St_S$	$St_N$	$St_L$
1	0.2943	0.1532	0.1769
2	0.2950	0.1531	0.1771
3	0.2895	0.1545	0.1780
4	0.2921	0.1549	0.1784
Morton and Yarusevych [3]	0.320	0.157	0.179
Norberg [16]	0.297	-	-
Williamson [17]	0.298	-	-

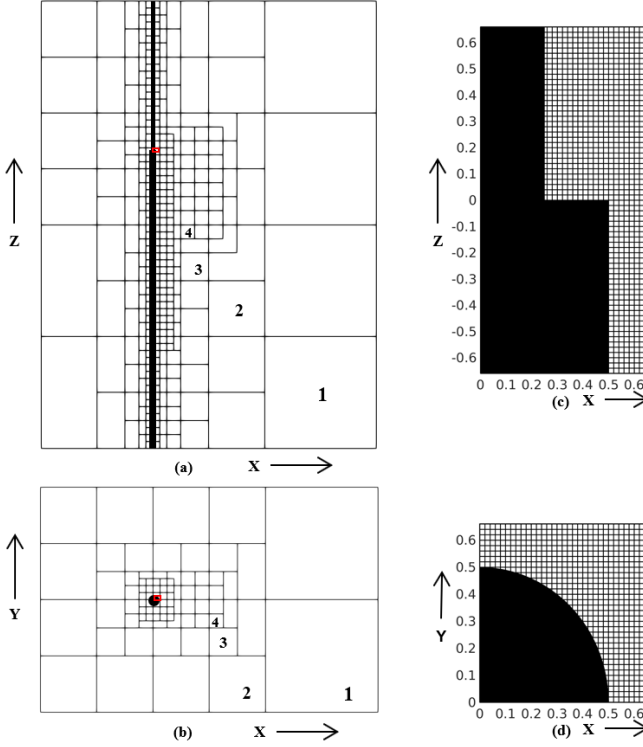


**Figure 3:** (a) A slice of the computational domain in the  $x-z$  plane at  $y/D = 0$ . Each square represents the slice of a corresponding cubic Cartesian grid box which contains  $N \times N \times N$  grid cells. In this figure, there are five levels of grid boxes, where the first four levels are indicated by numbers (1-4). Due to different minimum grid sizes, different cases have either five or six levels of grid boxes. (b) Same as (a) but the slice positioned in the  $x-y$  plane at  $z/D = 0^-$  (at the large cylinder area). (c) A zoom-in plot of the grid cells in the step region (red rectangle in (a)) for *Case2*; (d) Same as (c) but the zoom-in area is indicated by a red rectangle in (b).

Second, the mean streamwise velocity ( $\bar{u}/U$ ) distributions are checked along a line  $AB$  (as indicated in the subplot figure 4 (c)) and a line  $CD$  (as indicated in the subplot figure 5 (b)) to illustrate the time averaged flow conditions close to the step. The curves in figure 4 (a) are almost identical, and the zoom-in plot 4 (b) clearly shows a convergent tendency from *Case1* to *Case4*. Additionally, the difference between *Case3* and *Case4* is negligible. The flow field behind the step is more complicated than that in front of the step. As shown in figure 5 (a), the curve from *Case1* shows obvious differences compared with the curves from the other three cases. From the two zoom-in plots, figure 5 (c) and

(d), one can see that the maximum difference in  $\bar{u}/U$  between *Case2*, *Case3* and *Case4* is only around 0.005. This means that, except for *Case1*, the flow field from the other three cases fit each other well.

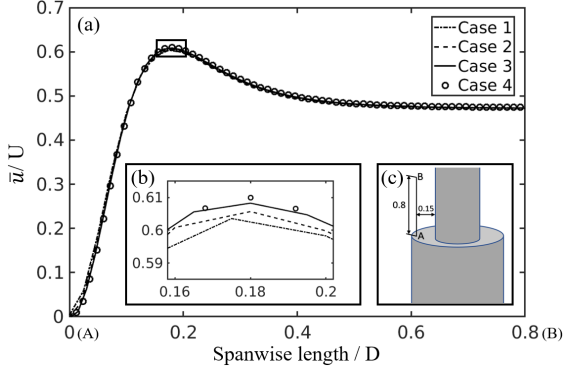


**Figure 4:** (a) Distributions of mean streamwise velocity  $\bar{u}/U$  along a sampling line AB in the  $x-z$  plane at  $y/D = 0$ ; (b) A zoom-in plot of the upper part of curves in (a) (black rectangle in (a)); (c) A sketch of the sampling line AB of length  $0.8D$ , positioned  $0.15D$  in front of the small cylinder.

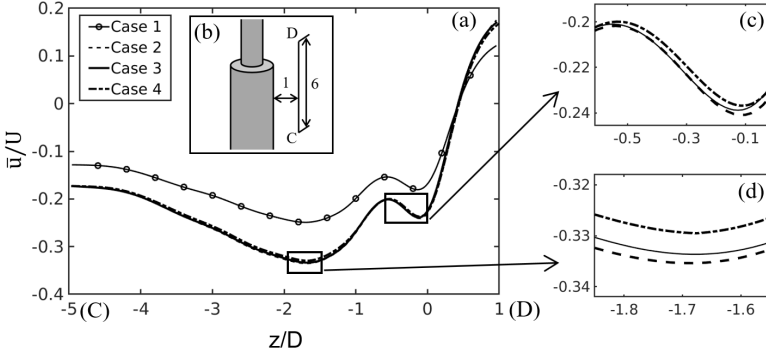


**Figure 5:** (a) Distributions of mean streamwise velocity  $\bar{u}/U$  along a sampling line CD in the  $x-z$  plane at  $y/D = 0$ ; (b) A sketch of the sampling line CD of length  $6D$ , positioned  $1D$  behind the large cylinder; (c) and (d) Zoom-in plots of the lower part of curves in (a) (black rectangles in (a)).

Furthermore, the time traces of the instantaneous spanwise velocity  $w$  in the N-cell area where the velocity varies dramatically with time are plotted for *Case2*, *Case1* and *Case4* in figure 6. The mean values and the fluctuations of these curves coincide well.

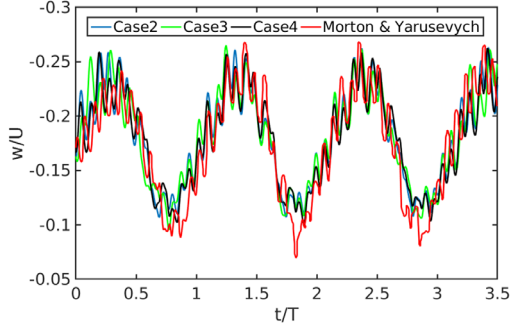


**Figure 6:** Time traces of the spanwise velocity ( $w/U$ ) at point  $(x/D, y/D, z/D)=(1, 0, -2.5)$  in the N-cell area. The red line is obtained from paper [3].  $T$  is the period of one N-cell cycle which is the same time scale as Morton and Yarusevych used in [3].

### 3.3 Comparing with previous studies

In figure 7 (a), an overview of the vortex structures behind the step cylinder is illustrated by plotting the isosurface of  $\lambda_2 = -0.05$  [7]. The overall vortical structures from previous numerical simulations [3] and laboratory experiments [2] are presented in figure 7 (b) and (c), respectively. The wake structures compare well with each other in these three plots. In figure 7 (a), three vortex cell areas (the S-, N- and L-cell areas) are also clearly illustrated. As Morton & Yarusevych [3], we also captured three dominating frequency components in the wake flow, as shown in table 2. The  $St_L$  from our simulations fits well with theirs. Our  $St_S$  and  $St_N$ , however, are somewhat lower than that from their simulations. As mentioned in previous papers [2, 18, 19], the shedding of S-cell vortices is seldomly affected by the step. Two laboratory experiments [16, 17] are introduced to validate our  $St_S$ . From table 2, one can see that our results compare better with the experimental values. Moreover, the spanwise velocity data from paper [3] is inserted in figure 6. The match between the present study and Morton & Yarusevych [3] is convincing, except for small differences in the lower part of the curves.

Based on all these careful comparisons, we believe that, except for *Case1*, the convergent tendency from *Case2* to *Case4* is clear. Moreover, the difference between *Case3* and *Case4* is small, and both of them fit well with previous results. However, due to the smaller time step size and large number of grid cells, the computational cost of *Case4* is significantly higher than that of *Case3*. All discussions in the present paper are therefore based on data from *Case3*.

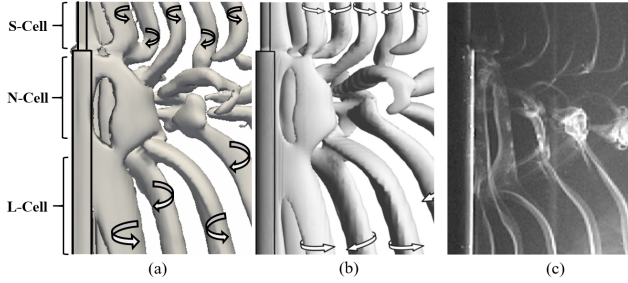


**Figure 7:** Vortex shedding in the wake behind a step cylinder: (a) Isosurfaces of  $\lambda_2 = -0.05$  [7] from our simulation,  $Re_D = 150$  and  $D/d = 2$ ; (b) Isosurfaces of  $Q \approx 2 \times 10^{-3}$  from [3],  $Re_D = 150$  and  $D/d = 2$ ; (c) Flow visualization image from [2],  $Re_D = 150$  and  $D/d = 2$ ;

## 4 RESULTS

### 4.1 Long periodicity of the vortex dislocations

In the present study, as in the previous investigations [2, 3], three vortex cells (S-, N- and L-cell vortices) are captured in the wake behind the step cylinder. Complex vortex interactions occur between them, especially between the N- and L-cell vortices. Due to different shedding frequencies, the N- and L-cell vortices move either in-phase or out-of-phase. During this process, vortex dislocations and vortex loop structures form. As shown in figure 8, the formation of the 1st N-cell cycle is illustrated by consecutive snapshots of isosurface of  $\lambda_2$ . The time  $t$  is set to  $t=t^*-2378.1D/U$ , where  $t^*$  is the actual time in the simulation (this applies through the paper). All N- and L-cell vortices are labeled by a combination of capital letters and numbers; 'N' and 'L' represent N- and L-cell vortices, respectively, while the number indicates the shedding order. To differentiate vortices shed from the different sides of the step cylinder, we use capital letters with primes (N' and L') to represent vortices shed from the '+Y' side; and capital letters (N and L) to represent vortices shed from the '-Y' side. From figure 8 (a) to (f), every N-cell vortex has one corresponding L-cell vortex shed from the same side (e.g. N0 and L0; N'1 and L'1...). As the phase difference between the N- and L-cell vortex accumulates [3], loop structures appear when corresponding N- and L-cell vortices are out of phase. From figure 8 (g) to (j), loop structures (N8-L'9) and (N'9-L10) form, and are indicated by green and red curves, respectively. Detailed descriptions of the formation process of those loop structures can be found in paper [6]. Based on the order of their appearances, we name the green curve as the NL-loop1, and the red curve as the NL-loop2. Meantime, we define the side of a NL-loop structure as the side of its N-cell vortex component. For example, the NL-loop1 N8-L'9 (shown by green curves) in figure 8 (h) is identified to form at the '-Y' side, because the N-cell vortex (N8) in this loop is at the '-Y' side.

In figure 9, by plotting the isosurface of  $\lambda_2 = -0.05$ , the NL-loop structures in the





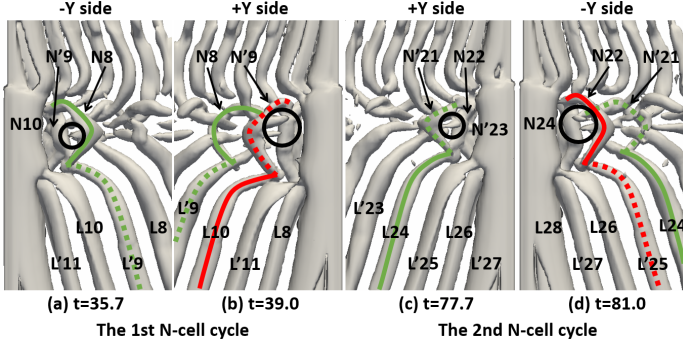


**Figure 9:** NL-loop structures at the 1st and 2nd N-cell cycles are plotted in [(a), (b)] and [(c), (d)], respectively. The same colors and definitions used in figure 8 are also used here.

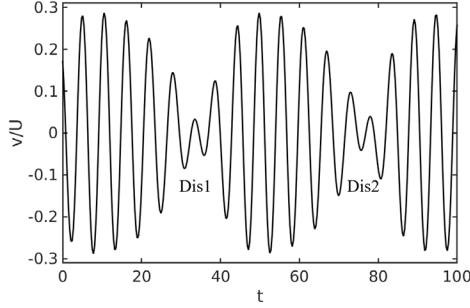


**Figure 10:** Time trace of the crossflow velocity ( $v$ ) at a sampling point  $(x/D, y/D, z/D)=(1.5, 0, -6)$ . "Dis1" represents the dislocation process that occurs in the 1st N-cell cycle defined in figure 9, same for "Dis2".

The different alignments of N- and L-cell vortices induce slightly different NL-loops and different reductions in the induced crossflow velocity in the 1st and 2nd N-cell cycles. From the NL-loop1 (N8-L'9) of the 1st N-cell cycle in figure 9 (a) to the NL-loop1 (N'21-L24) of the 2nd N-cell cycle in figure 9 (c), there are 13 N-cell and 15 L-cell vortices. Compared to the vortex pairs in the 1st N-cell cycle, the fact that  $15 \times \frac{1}{2f_L} - 13 \times \frac{1}{2f_N} = 0.064$  ( $f_N$  and  $f_L$  are obtained from table 2-Case3) induces a small phase shift to every vortex pair (a N-cell vortex and its counterpart L-cell vortex) in the 2nd N-cell cycle. It means that the vortex alignment varies from one N-cell cycle to another. Only when the vortex alignment becomes exactly the same in two N-cell cycles, the corresponding vortex dislocations can be exactly the same.

Considering vortices shed alternately from the '+Y' and '-Y' sides of the step cylinder, the exactly same vortex alignment can appear at the same side or different sides of the

step cylinder. When the same vortex alignment appears at the same side of the step cylinder in two N-cell cycles, their subsequent NL-loop structures should be identical (i.e. perfect symmetric). On the other hand, perfect antisymmetric NL-loop structures are expected. We assume that there are two neighboring vortex cells: vortex cell-1 with a shedding frequency  $f_1$ , and vortex cell-2 with a shedding frequency  $f_2$ . If the number of cell-1 and cell-2 vortices are 'k' and 'j' between the two N-cell cycles which have the same vortex alignment, expression 5

$$k \times \frac{1}{2f_1} = j \times \frac{1}{2f_2} \quad (5)$$

should be satisfied. We keep the number '2' as a factor in both sides of expression (5), because the shedding frequency should be doubled when we consider vortices from the '+Y' and '-Y' side separately (normally, the vortex shedding frequency in a Karman vortex street is the shedding frequency of a pair of vortices).

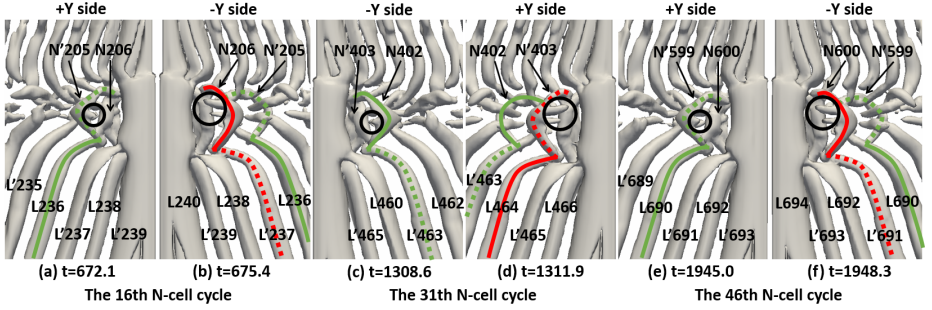


**Figure 11:** NL-loop structures at the 1st and 2nd N-cell cycles are plotted in [a), b)] and [c), d)], respectively. The same colors and definitions as in figure 8 are used here.

After long time of observation, we found that the corresponding NL-loop structures (NL-loop1: N8-L'9; NL-loop2: N'9-L10) in the 1st N-cell cycle, and (NL-loop1: N'205-L236; NL-loop2: N206-L'237) in the 16th N-cell cycle are perfect antisymmetric, as shown in figure 9 a), b) and figure 11 a) b). Details are highlighted by black circles. Between these two N-cell cycles, there are 183 N-cell vortices and 211 L-cell vortices which satisfy equation (5), i.e.  $183 \times \frac{1}{2f_N} = 211 \times \frac{1}{2f_L} = 592$  ( $f_N$  and  $f_L$  are obtained from table 2-Case3).

In addition, the NL-loop structures in the 31th and the 46th N-cell cycle are plotted in figure 11 (c), (d), (e) and (f). One can see that, after every 15 N-cell cycles, the perfect antisymmetric phenomenon appears. In figure 12, the time traces of the crossflow velocity  $v$  are plotted at the position  $(x/D, y/D, z/D) = (1.5, 0, -6)$ . The y-coordinate of figure 12 (b) is reversed (from  $v$  to  $-v$ ) to ease the comparison. The position where a vortex dislocation happens is marked by a combination of the capital letter 'D' and its series

number. One can see that these two plots almost coincide, which proves that all of the vortex alignments and the corresponding NL-loop structures are perfectly antisymmetric between D1-D15 and D16-D30.

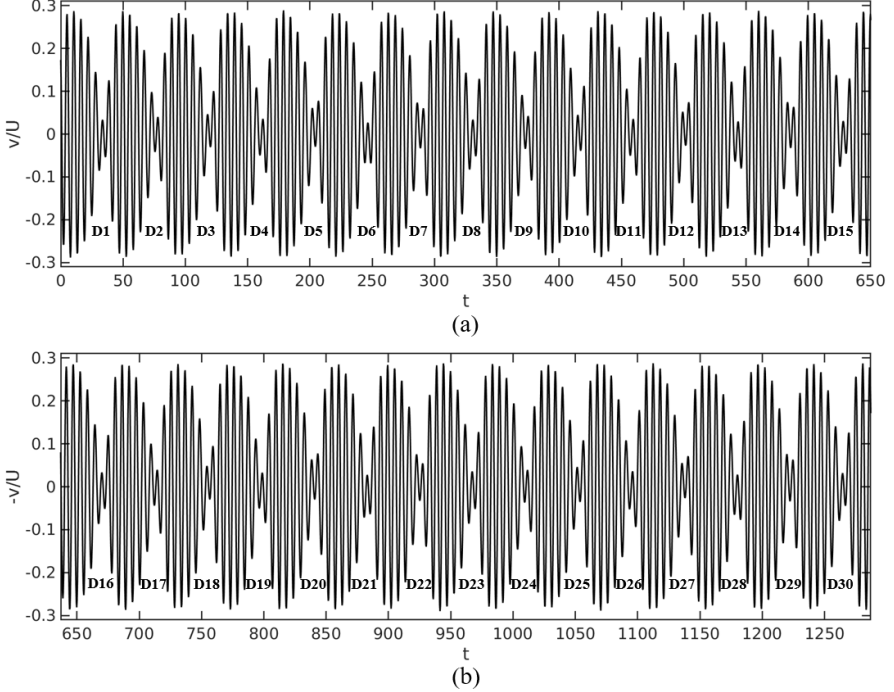


**Figure 12:** Time trace of the crossflow velocity ( $v$ ) at a sample point  $(x, y, z)/D=(1.5, 0, -6)$ . "D1" means the dislocation process that occurs in the 1st N-cell cycle defined in figure 9, same for "D2", etc.

This long cyclic process (around  $650 D/U$ ) is quite similar to the 'fundamental dislocation cycle' defined by McClure et al. [9]. They focused on the flow around a dual step cylinder. In their study, the same vortex dislocations appeared at the same side of the dual step cylinder at certain intervals, i.e. the perfect symmetry defined in the present paper. Moreover, they proposed equation (6) to measure the duration of the phase realignment process (the same assumption used in equation (5) is also used here).

$$\frac{f_1}{f_2} = \frac{m}{n} \quad (6)$$

The 'm' and 'n' are measured to the lowest possible integer value.

However, our observations clearly show that there is another type of the fundamental dislocation cycles, i.e. the perfect antisymmetric cycle. Behind the cylindrical structure, vortices alternately shed at the two sides of the structure. The alignment of vortices appears at one side of the structure is possible to repeat at either the same side or the other side of the structure. By using equation (6), the anticipated number of vortices in one fundamental vortex dislocation cycle can only be even ( $2m$  cell-1 vortices, and  $2n$  cell-2 vortices). It makes equation (6) only suitable for the cases with perfectly symmetric fundamental dislocation cycles. In addition, when  $f_1$  and  $f_2$  are close, it is impossible to get the accurate value of 'm' and 'n'. For example, in our case,  $f_1 = 0.1545$  and  $f_2 = 0.1780$ . It results in 197 N-cell vortices and 227 L-cell vortices in one fundamental vortex dislocation cycle. Without observations, it seems impossible to get the correct value of 'm' and 'n'.

In general, there are two types of the fundamental dislocation cycles, i.e. the perfect symmetric cycle and the perfect antisymmetric cycle. The different duration of 13 N-cell and 15 L-cell vortices brings the small phase shift to every vortex pair of the N- and L-cell vortex in neighboring N-cell cycles, and finally results in the 'fundamental dislocation cycle'. Ideally, the duration of the cycle can be measured by equation (5). But, in practice, it might be hard to get the accurate number of vortices without careful observations, especially when the shedding frequencies of neighboring vortices are close.

## 4.2 Computational challenges for investigating a long periodic phenomenon

As discussed in section 3.2, the results of our four cases show good convergence, and compare well with previous studies [3, 6]. However, considering the long periodicity of the fundamental dislocation cycle discussed in section 4.1, the simulation time of our convergence tests might not be long enough. Further investigations prove this.

Firstly, after another 1000 time units ( $D/U$ ) simulation of Case 4, the exact same fundamental vortex dislocation was observed. However, different from Case 3, in Case 4, the same vortex dislocation appears at the same side of the step cylinder, and there are 131 N-cell and 151 L-cell vortices in one fundamental vortex dislocation cycle.

Furthermore, we set up a new case (named as *Case5*) to continue refining our grid size from  $0.012D$  to  $0.010D$ . Still we cannot get exactly the same result as we obtained from the Case 4. In the Case 5, in one fundamental vortex dislocation cycle, the number of N- and L-cell vortices are 170 and 196, respectively.

Although, the number of vortices in one fundamental vortex dislocation cycle varies for different cases, further investigation proves that all the different cases converge to the same physical mechanism.

In figure 13, the isosurface of  $\lambda_2 = -0.05$  is plotted to illustrate the NL-loop structures for different cases. Details of the loop structures are highlighted by black circles. The figure is divided into three parts by two dashed black lines: the left, middle and right part. As shown in the left part of figure 13 ((a), (b), (g), (h), (m) and (n)), the same NL-loop structures are observed in all three cases (*Case3*, *Case4* and *Case5*). Even the details of

the loop structures highlighted by black circles are almost exactly the same. It means, at this moment, all the three grid resolutions are able to give the same vortex alignments, and the same vortex structures. For all three cases, the N-cell cycle containing the NL-loop structures shown in the left part of figure 13, is set up to the 1<sup>st</sup> N-cell cycle. By comparing the following N-cell cycles, we found that the differences between these three cases are gradually accumulated.

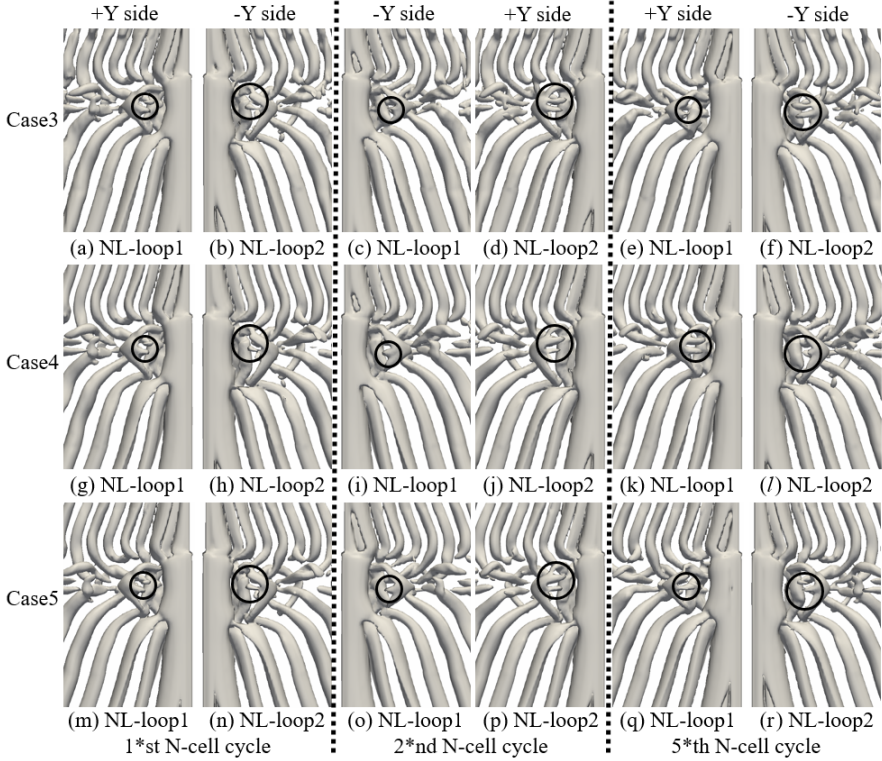


**Figure 13:** Isosurface of  $\lambda_2 = -0.05$  [7] showing the NL-loop structures in *Case3*, *Case4* and *Case5* on both '+Y' and '-Y' sides. The details of the loop structures are highlighted by black circles. Two dashed lines divide the figure into three parts: the left part (the NL-loop structures in the 1<sup>st</sup> N-cell cycle), the middle part (the NL-loop structures in the 2<sup>nd</sup> N-cell cycle) and the right part (the NL-loop structures in the 5<sup>th</sup> N-cell cycle).

In the middle part of figure 13, the NL-loop structures in the 2<sup>nd</sup> N-cell cycle are plotted for all three cases. One can see that the differences in details of the NL-loop



structures are still very small between the different cases. However, as shown in the right part of figure 13, the loop structures in the 5\*th N-cell cycle are completely different for all three cases. This transformation is caused by the accumulations of the minor differences in the vortex shedding frequencies ( $f_N$  and  $f_L$ ) between these three cases.

**Table 3:** The Strouhal number ( $St$ ) of N-cell vortex ( $St_N = f_N D/U$ ) and L-cell vortex ( $St_L = f_L D/U$ ) for *Case3*, *Case4* and *Case5*.

Case	Mean grid size (D)	$St_N$	$St_L$
3	0.015	0.1545	0.1780
4	0.012	0.1547	0.1783
5	0.010	0.1549	0.1784

As shown in table 3, the differences of the shedding frequencies ( $f_L$  and  $f_N$ ) are very small between these three cases. Normally, it is reasonable to claim that these three cases are already converged. Actually, in a relatively short time period, e.g. from the 1\*st N-cell cycle (the left part of the figure 13) to the 2\*nd N-cell cycle (the middle part of the figure 13), the wake flow and vortex structures agree well between *Case3*, *Case4* and *Case5*. But after long time accumulations, e.g. from the 1\*st N-cell cycle (the left part of figure 13) to the 5\*th N-cell cycle (the right part of the figure 13), even the small differences in the shedding frequencies can affect the wake flow. Only when the shedding frequencies of different grid cases are exactly the same, the vortex alignment and vortex structures can be exactly the same.

In general, we admit that even in *Case5*, the mesh resolution is still not fully converged for fundamental vortex dislocations. It is very difficult to get complete grid convergence when investigating the exceptionally long period phenomenon. After a long time accumulation, even a tiny difference could become big enough to affect the flow field. However we clearly show that *Case3*, *Case4* and *Case5* are all able to give the same instantaneous vortical structures in the near wake. The different detailed information (the number of N- and L-cell vortices) in one fundamental vortex dislocation cycle is caused by the accumulation of the minor difference in the vortex shedding frequencies between these cases. The mechanism and the existence of the two kinds of fundamental vortex dislocation cycles are valid for all cases.

## 5 CONCLUSION

The present results show good agreement with previous studies [3, 6, 9], such as the three dominating spanwise vortices (i.e. S-, N- and L-cell vortices), vortex dislocations between the N- and L-cell vortex, loop structures (NL-loop1 and NL-loop2) generated during the vortex dislocation process and the antisymmetric phenomena between the neighboring N-cell cycles. In addition, the long period characteristic of the vortex dislocation, i.e. the

fundamental dislocation cycle, was for the first time captured and analyzed in the wake of the single step cylinder. We have clearly shown that the different duration of 13 N-cell and 15 L-cell vortices during one N-cell cycle brings the small phase shift to every vortex pair of N- and L-cell vortex, and finally causes the 'fundamental vortex dislocation cycle'. In addition, there are two kinds of fundamental dislocation cycles, i.e. the symmetric fundamental dislocation cycle, and the antisymmetric fundamental dislocation cycle, which are determined by whether the same vortex alignment appears on the same side of the step cylinder or not. Last but not least, we discussed challenges of the grid resolution on investigating the long period characteristic. We found that, for the present case, although the detailed information (e.g. the number of N- and L-cell vortices) in one fundamental vortex dislocation cycle varies when continuing to refine the grid, the mechanism of the fundamental vortex dislocation cycle is valid for all cases.

In the future, other Reynolds numbers and diameter ratios will be investigated to explore how the vortex shedding frequencies of N- and L-cell vortices affect the formation and the length of the fundamental vortex dislocation cycle.

## 6 ACKNOWLEDGEMENTS

Computing time on Vilje was granted by the Norwegian Research Council (Program for Supercomputing, under project nn9191k). C.T. would like to thank China Scholarship Council (CSC) for financial support.

## REFERENCES

- [1] C.G. Lewis and M. Gharib *An exploration of the wake three dimensionalities caused by a local discontinuity in cylinder diameter*. Physics of Fluids A: Fluid Dynamics 4 (1992): 104-117.
- [2] W. Dunn and S. Tavoularis *Experimental studies of vortices shed from cylinders with a step-change in diameter*. Journal of Fluid Mechanics 555 (2006): 409-437.
- [3] C. Morton and S. Yarusevych. *Vortex shedding in the wake of a step cylinder*. Physics of Fluids 22 (2010): 083602.
- [4] C. Morton and S. Yarusevych *Vortex dynamics in the turbulent wake of a single step cylinder*. Journal of Fluids Engineering 136 (2014): 031204.
- [5] C. Tian, F. Jiang, B. Pettersen and H.I. Andersson *Numerical investigation of flow around a step cylinder*. In: 9th National Conference on Computational Mechanics MekIT'17. Ed. by B. Skallerud and H.I. Andersson. International Center for Numerical Methods in Engineering (CIMNE), Barcelona, Spain, 2017, pp. 369-384.
- [6] C. Tian, F. Jiang, B. Pettersen and H.I. Andersson *Antisymmetric vortex interactions in the wake behind a step cylinder*. Physics of Fluids 29 (2017): 101704.



- [7] J. Jeong and F. Hussain *On the identification of a vortex*. Journal of Fluid Mechanics 285 (1995): 69-94.
- [8] C.H.K. Williamson *Oblique and parallel modes of vortex shedding in the wake of a circular cylinder at low Reynolds numbers*. Journal of Fluid Mechanics 206 (1989): 579-627.
- [9] J. McClure, C. Morton and S. Yarusevych *Flow development and structural loading on dual step cylinders in laminar shedding regime*. Physics of Fluids 27 (2015): 063602.
- [10] M. Manhart and R. Friedrich *DNS of a turbulent boundary layer with separation*. International Journal of Heat and Fluid Flow 23 (2002): 572-581.
- [11] M. Manhart *A zonal grid algorithm for DNS of turbulent boundary layers*. Computers & Fluids 33 (2004): 435-461.
- [12] J.H. Williamson *Low-storage Runge-Kutta schemes*. Journal of Computational Physics 35 (1980): 48-56.
- [13] N. Peller *Numerische simulation turbulenter Strömungen mit immersed boundaries*. Diss. Universität München (2010).
- [14] H.L. Stone *Iterative solution of implicit approximations of multidimensional partial differential equations*. SIAM Journal on Numerical Analysis 5 (1968): 530-558.
- [15] N. Peller, A.L. Duc, F. Tremblay and M. Manhart *Highorder stable interpolations for immersed boundary methods*. International Journal for Numerical Methods in Fluids 52 (2006): 1175-1193.
- [16] C. Norberg *An experimental investigation of the flow around a circular cylinder: influence of aspect ratio*. Journal of Fluid Mechanics 258 (1994): 287-316.
- [17] C.H.K. Williamson *Defining a universal and continuous Strouhal–Reynolds number relationship for the laminar vortex shedding of a circular cylinder*. Physics of Fluids 31 (1988): 2742-2744.
- [18] M.K. Yagita, K. Yoshihiro and K. Matsuzaki *On vortex shedding from circular cylinder with step*. Bulletin of JSME 27 (1984): 426-431.
- [19] C. Norberg *An experimental study of the flow around cylinders joined with a step in diameter*. In: 11th Australasian Fluid Mechanics Conference. Hobart, Australia, 1992, Vol. 1, pp. 507-510.



## DEFINITION OF THE VERTICAL SPACING OF A SIGMA GRID BASED ON THE CONSTANT TRUNCATION ERROR

C. PAKOZDI<sup>1</sup>, W. WANG<sup>2</sup>, A. KAMATH<sup>2</sup> AND H. BIHS<sup>2</sup>

<sup>1</sup>Department of Civil and Environmental Engineering  
Norwegian University of Science and Technology  
Trondheim 7491, Norway  
e-mail: csaba.pakozdi@ntnu.no, web page: <https://reef3d.com/>

<sup>2</sup> Department of Civil and Environmental Engineering  
Norwegian University of Science and Technology  
Trondheim 7491, Norway

**Key words:** Potential theory, Numerical wave tank, Finite Differential Method, sigma-grid, REEF3D

**Abstract.** A new numerical wave model in the framework of REEF3D solves the Laplace equation for the flow potential and the nonlinear kinematic and dynamics free surface boundary conditions with HYPRE's massively parallel stabilized bi-conjugated gradient solver and a geometric multi-grid preconditioner. The validation of the new module is based on the comparison of measured time series against the simulation results. In the first phase of the validation regular wave experiments are compared, where the wave propagation is recorded over 160 m (model scale) using 19 wave probes placed at different locations in the long wave flume at Marintek, Trondheim [1]. The measured time series near the wavemaker in the flume is used to generate waves in the simulation. This gives the unique possibility to identify dispersion (phase) error in relation to the distance from the wavemaker with good accuracy. During the convergence studies, it was observed that the wave dispersion is sensitive to the variation of the vertical grid. In order to reduce the uncertainty around the choice of the best vertical distribution, a new method based on the constant truncation error was developed and validated. The new method is described in this paper as well as the improvement is also demonstrated.

### 1 INTRODUCTION

Several universities and research institutes are developing numerical wave tanks which can use today's hardware and software possibilities such as HOS [2], OceanWave3D [3] and HAWASSI [4]. One of them is developed under the framework of REEF3D [5]. REEF3D CFD module has already been used as numerical wave tank (NWT) [6]. The module solve

the Navier-Stoke Equations with a two-phase fluid model which makes the software able to simulate breaking waves [7], [8] and [9]. This module can be applied at all relevant scales as was demonstrated in [10] where sloshing is simulated with this module.

The new numerical wave model FNPF of REEF3D solves the Laplace equation for the flow potential and the nonlinear kinematic and dynamics free surface boundary conditions. This approach requires reduced computational resources compared to CFD based NWTs. This new module can use the already implement functionality of REEF3D [11], where solid boundaries are incorporated through a ghost cell immersed boundary method. Therefore it is capable of simulating wave-structure interaction such as complex sea bottom topography by solving the non-linear potential theory problem. The Laplace equation together with the enclosure of the boundary conditions are solved with a finite difference method on a stretched  $\sigma$ -coordinate system similar to OceanWave3D [12]. The stretching of the grid is applied to reduce the numerical error at the same number of the grid points. The vertical distribution of the grid points is defined at the Chebysev-Gauss-Loboto locations in OceanWave3D [3]. This grid is defined by several of parameters:

- the water depth  $d$
- the number of the vertical grid points  $N_z$ .

There are several stretching method implemented in REEF3D and therefore, two additional parameters must be given to define the vertical grid distribution:

- the stretching method
- the stretching factor.

In the first phase of the validation, regular wave experiments are compared. During the convergence studies it was observed that the vertical grid spacing has the largest influence on the regular wave propagation velocity in the numerical wave tank. Similar phenomena was reported in [12]. It was observed that the above mentioned stretching factor has the largest influence on the dispersion. Sometimes a simulation with a lower number of vertical grid points yields better results than the one with a larger number of  $N_z$ .

Grid stretching is introduced in order to reduce the numerical error from the same number of grid points. The main idea behind the new method is that this error can be linked to the truncation error of the applied numerical scheme and the vertical distribution of the error influences the wave propagation. This paper discusses the background of the method and shows the procedure which defines the location of the grid points for a given wave condition and a given truncation error.

## 2 MODEL TEST SETUP

The experiment was carried out in the long wave flume at Marintek, Trondheim, Norway (see [13] for details on the wave tank). The length of the tank is 270 m and its width



where  $h = h(\mathbf{x})$  is the water depth measured from the still water level to the seabed.

The Laplace equation with the boundary conditions is solved with a finite difference method on a  $\sigma$ -coordinate system. A  $\sigma$ -coordinate system deforms with the free surface and is also flexible in the handling of irregular boundaries. The relationship between a Cartesian grid and a  $\sigma$ -coordinate is as follows:

$$\sigma = \frac{z + h(\mathbf{x})}{\eta(\mathbf{x}, t) + h(\mathbf{x})}. \quad (5)$$

Several methods are implemented in REEF3D for grid stretching in horizontal and vertical direction. One of them uses the sinh function as the stretching function:

$$\tilde{z} = d \frac{\sinh(\delta z)}{\sinh(\delta)} \quad (6)$$

where  $z$  is the uniform vertical grid location,  $\delta$  is the above mentioned stretching factor and  $\tilde{z}$  is the new vertical location. This stretching method gives the closest grid location to the optimal grid positions and this is used in the simulations.

Once the velocity potential  $\Phi$  is obtained in the  $\sigma$ -domain, the velocities can be calculated as follows:

$$u(\mathbf{x}, z) = \frac{\partial \Phi(\mathbf{x}, z)}{\partial x} = \frac{\partial \Phi(\mathbf{x}, \sigma)}{\partial x} + \frac{\partial \sigma}{\partial x} \frac{\partial \Phi(\mathbf{x}, \sigma)}{\partial \sigma}, \quad (7)$$

$$v(\mathbf{x}, z) = \frac{\partial \Phi(\mathbf{x}, z)}{\partial y} = \frac{\partial \Phi(\mathbf{x}, \sigma)}{\partial y} + \frac{\partial \sigma}{\partial y} \frac{\partial \Phi(\mathbf{x}, \sigma)}{\partial \sigma}, \quad (8)$$

$$w(\mathbf{x}, z) = \frac{\partial \Phi(\mathbf{x}, z)}{\partial z} = \frac{\partial \sigma}{\partial z} \frac{\partial \Phi(\mathbf{x}, \sigma)}{\partial \sigma}. \quad (9)$$

Wave generation in the numerical wave tank is handled using a Neumann boundary condition. Here, the spatial derivatives of the velocity potential are prescribed according to the wavemaker kinematics. The velocity potential at the boundary can then be calculated as follows:

$$\varphi_{i-1} = -u(\mathbf{x}, z, t) \triangle x + \varphi_i \quad (10)$$

where  $u(\mathbf{x}, z, t)$  is the analytical horizontal velocity. The wavemaker motion is defined through a file where a time series of the angle of the flaps are defined. The measured flap angles are used in this paper to generate the waves.

The numerical beach uses the relaxation method [15] to mitigate wave reflection. The relaxation function used in the model is shown in Eqn. (11).

$$\Gamma(\tilde{x}) = 1 - \frac{e^{(\tilde{x}^{3.5})} - 1}{e - 1} \text{ for } \tilde{x} \in [0; 1]. \quad (11)$$

where  $\tilde{x}$  is scaled to the length of the relaxation zone.

The Laplace equation is discretized using a second-order central difference scheme and is solved using a parallelized geometric multigrid pre-conditioned conjugated gradient solver provided by HyPre [16].

The convection terms at the free-surface are discretized with the fifth-order Hamilton–Jacobi weighted essentially non-oscillatory (WENO) scheme [17]. A WENO discretization stencil is based on smoothness of three local ENO-stencils. The local stencil with the highest smoothness is assigned the highest weight and contributes the most significantly to the solution. The scheme is therefore capable of handling large gradients without instability.

For the time treatment, a third-order accurate TVD Runge-Kutta scheme [18] is used with constant time step.

The model is fully parallelized following the domain decomposition strategy. Ghost cells are used to exchange information between adjacent domains and are updated with the values from the neighboring processors using the Message Passing Interface (MPI).

## 4 THE NEW METHOD TO FIND AN OPTIMAL VERTICAL GRID DISTRIBUTION

### 4.1 Main idea

The solution of the Airy wave theory is based on the separation of variables method [19]:

$$\phi(x, z, t) = \Phi(z)\Xi(x)\Upsilon(t). \quad (12)$$

The main idea of the new procedure is based on the observation that the shape of the solution of the function  $\Phi(z)$ <sup>1</sup>:

$$\Phi(z) = Ce^{kz} \quad (13)$$

is governed only by the wave number  $k$  which value is defined by the linear dispersion relationship between the wave frequency  $\omega$  and the wave number:

$$\omega^2 = gk \quad (14)$$

where  $g$  is the gravity acceleration.

Due to numerical error, the numerically estimated values of the potential along a vertical line define a different shape than prescribed by theory. This has the consequence of changing the wave number in the numerical simulation, because the wave propagation velocity depends on the wave number and the wave frequency. The wave number changes the wave propagation velocity in the numerical simulation.

The truncation error of a finite differential scheme depends on the distance between the grid points ( $z$  and  $\zeta$ ) which can be seen from the Taylor series of a function  $f(z)$  (15)

---

<sup>1</sup>For simplicity, the linear deep water solution will be used in this paper.

:

$$f(z) = f(\zeta) + \frac{df(\zeta)}{dz}(z - \zeta) + \frac{1}{2} \frac{d^2 f(\zeta)}{dz^2}(z - \zeta)^2 + \frac{1}{6} \frac{d^3 f(\zeta)}{dz^3}(z - \zeta)^3 + \frac{1}{24} \frac{d^4 f(\zeta)}{dz^4}(z - \zeta)^4 + O((z - \zeta)^5) \quad (15)$$

Based on the observation that the variation of the vertical grid has the largest influence on the wave propagation, the error of the shape is considered to be directly related to the truncation error of the applied numerical scheme. The new method is based on the assumption that a constant absolute truncation error at every vertical location can preserve the correct shape of the function  $\Phi(z)$  and yield the correct wave number.

For example, the second order central differentiation scheme is a second-order scheme. This means that its residual can be estimated as an error of order  $O((z - \zeta)^3)$  of the Taylor series in (15) i.e., the truncation error at the location  $\zeta$  can be defined as:

$$E(z, \zeta) = f(z) - \left( f(\zeta) + \frac{df(\zeta)}{dz}(z - \zeta) + \frac{1}{2} \frac{d^2 f(\zeta)}{dz^2}(z - \zeta)^2 \right) \quad (16)$$

If the size of the absolute error is set to a constant  $E$  for every location  $\zeta$  and the function  $f(z)$  and its derivatives are known, one can find a maximum step  $\Delta z(\zeta) = z - \zeta$  to this condition at every location  $\zeta$ :

$$0 = E - f(\zeta + \Delta z) + \left( f(\zeta) + \frac{df(\zeta)}{dz}\Delta z + \frac{1}{2} \frac{d^2 f(\zeta)}{dz^2}\Delta z^2 \right). \quad (17)$$

## 4.2 Estimation of the vertical grid spacing based on the velocity potential function of the Airy wave theory for infinite water depth

Only the result for the infinite water depth case is presented for the second- and fourth-order schemes in this paper. According to the Airy wave theory for infinite water depth, the function of the solution which only depends on the variable  $z$  is defined as:

$$\Phi(z) = \frac{\zeta_A g}{\omega} e^{kz} \quad (18)$$

where  $\zeta_A$  is the wave amplitude. We can normalize this function with  $\frac{\zeta_A g}{\omega}$ , which gives a more general result for the analysis. The Taylor series of  $e^{kz}$  at  $z = \zeta + \Delta z$  is well known:

$$e^{k(\zeta + \Delta z)} = e^{k\zeta} + e^{k\zeta} k \Delta z + \frac{1}{2} e^{k\zeta} k^2 \Delta z^2 + \frac{1}{6} e^{k\zeta} k^3 \Delta z^3 + \frac{1}{24} e^{k\zeta} k^4 \Delta z^4 + O(\Delta z^5) \quad (19)$$

Using the condition defined in (17) with  $f(z) = e^{kz}$  we can define a grid size for each  $\zeta$  by solving:

$$0 = E e^{-k\zeta} - \sum_{n=O+1}^{\infty} \frac{(k \Delta z)^n}{n!} \quad (20)$$



for a scheme of order  $O$ . It is possible to generalize this equation for all wave numbers by introducing two dimensionless variables:  $kz = k\zeta$  and  $kdz = k\Delta z$ :

$$0 = Ee^{-kz} - \sum_{n=O+1}^{\infty} \frac{kdz^n}{n!} \quad (21)$$

This equation has no analytical solution and must be solved numerically. The series in (21) is calculated up to  $O + 20$ .

The solution for different  $E$  is presented in Figure 2a for the fourth order scheme ( $O = 4$ ). The  $x$ -axis defines the normalized grid height at the normalized  $z$  location shown on the  $y$ -axis of the diagram. Reduction of the error constant  $E$  yields a smaller grid height. Because  $\Phi$  exponentially decreases with increasing depth, the grid size can increase. The solutions are shown up to  $2\pi$  because one can assume that  $\Phi(z < -2\pi/k) = \text{const.}$  below one wavelength from the mean water level  $z = 0$  and the same grid size can be used below this depth. The solution for different  $E$  for the second order scheme ( $O = 2$ ) is shown in Figure 2b. One can see a reduction of the grid height for the fourth order scheme at an almost quadratic rate.

#### 4.3 Iterative procedure to estimate the vertical spacing for a given wave period

The ideal vertical spacing curves as a function of the normalized distance from the mean water level (MWL) at  $z = 0$  are shown in Figure 2. Using these solutions one can define the vertical grid spacing at  $z_1 = 0$ . This value defines the location of the next grid point  $z_2$  as  $z_1 - k\Delta z(kz = 0)$ . The location of the next grid point  $z_3$  can be estimated from the vertical grid spacing value at  $z_2$  from Figure 2 as  $z_3 = z_2 - k\Delta z(kz = z_2)$ . This way the vertical spacing can be estimated along the water depth generally for all waves:

$$kz_{i+1} = kz_i - k\Delta z(kz = z_i), \quad i = 1 \dots N_z. \quad (22)$$

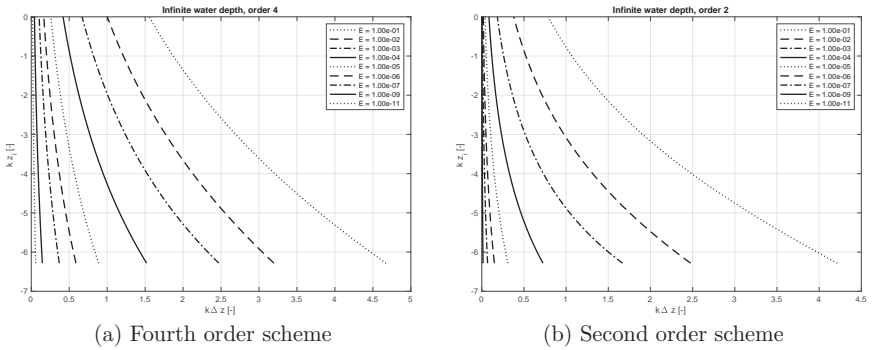


Figure 2: Grid size for different absolute error levels  $E$

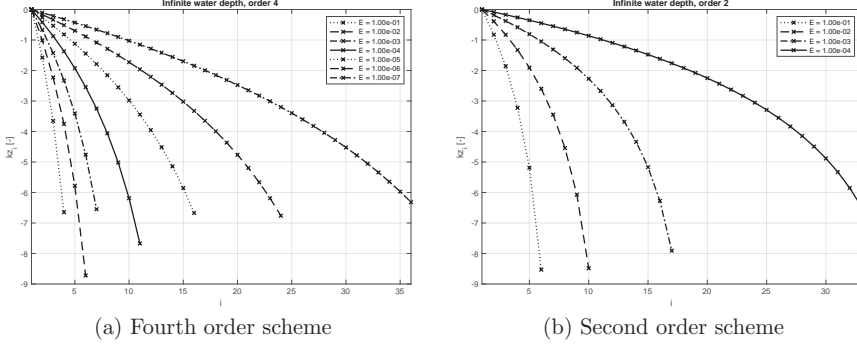


Figure 3: Locations of the vertical grid points for the second and fourth order schemes for different error levels  $E$

The normalized vertical locations of the grid for different truncation errors are shown in Figure 3. The horizontal axis shows the index of the grid locations and the vertical axis the normalized location. The use of the high-order scheme significantly reduces the number of the necessary vertical grid points for the same level of truncation error due to the larger grid spacing at the low error levels.

## 5 VALIDATION

### 5.1 Measurement of the similarity of the time series

Time series are compared each other with the magnitude of the signals and with their correlation to each other. In order to measure the magnitudes of the signal, several methods are used in this paper. One of this is the Fourier analysis where the amplitude spectrum is estimated for a given time window with help of the Fourier Transformation of the time series. However, this method does not show the change of the magnitude of the signal over time. Therefore, the Hilbert envelope of the full time series is calculated and compared. In these time series, the Hilbert envelope includes a minimal phase information too. The definition of these transformation is not shown in this paper.

In order to show how the time series are in phase to the measured time series, the cosine similarity is calculated [20] within a convolution window over the whole time series. The cosine similarity is defined for two vector of attributes, A and B, as:

$$\text{Correlation} = \frac{\sum_{i=1}^n A_i B_i}{\sqrt{\sum_{i=1}^n A_i^2} \sqrt{\sum_{i=1}^n B_i^2}} \quad (23)$$

where  $A_i$  and  $B_i$  are the components of vectors and A as well as B are the two time

series respectively. The resulting correlation ranges from -1 meaning anti-phase, to 1 meaning exactly in phase, with 0 indicating orthogonality or de-correlation, while in-between values indicate intermediate similarity or dissimilarity. This way the correlation between the time series can be displayed over the time axis.

## 5.2 Simulation setup

For testing the new procedure, a regular wave with a wave period of  $T = 1.5$  s is used. A setup of this wave was found before the development of this method which gives good agreement with the model test data. A uniform grid spacing in the horizontal direction with 35 cells per wavelength is used with the second-order central differences scheme solving the Laplace equation. The time step is constant and set to  $dt = 0.02$  s. The sinh stretching method defined in (6) is used in the simulation.

## 5.3 Results

The comparison of the applied grid distribution with the sinh method parameters against the "optimal" grid distribution defined by the new method is shown in Figure 4a. The vertical grid location  $Z_i$  is shown over the grid index number  $i$  for still water. One can see that the black curve, the "optimal" locations are very close to the applied grid distribution (green curve) down to one wavelength depth  $z = -3.5$  m. After this depth, the black line shows equidistant grid spacing where the green curve shows smaller grid spacing first up to  $i = 23$  and larger grid spacing afterwards compared to the black curve. After the development of the above described method, a new grid spacing based on the method estimated. The number of the vertical grid points  $N_z$  and the stretching factor  $\delta$  in REEF3D's sinh stretching method are tuned to obtaining the best match to the "optimal" distribution, shown in Figure 4b. The number of the grid points is reduced

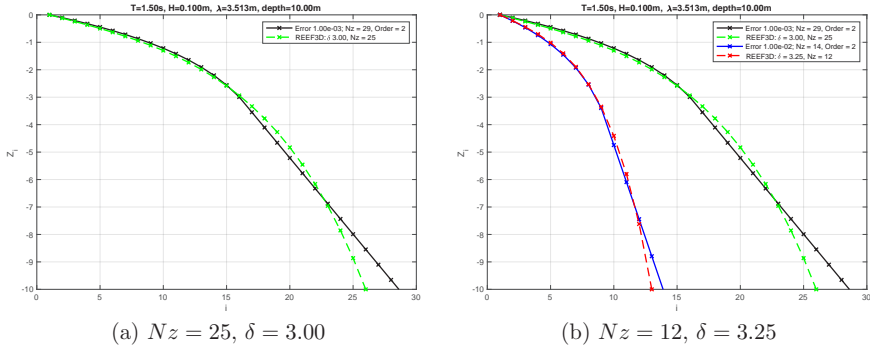


Figure 4: Comparison of the optimal grid spacing against the applied REEF3D's grid spacing

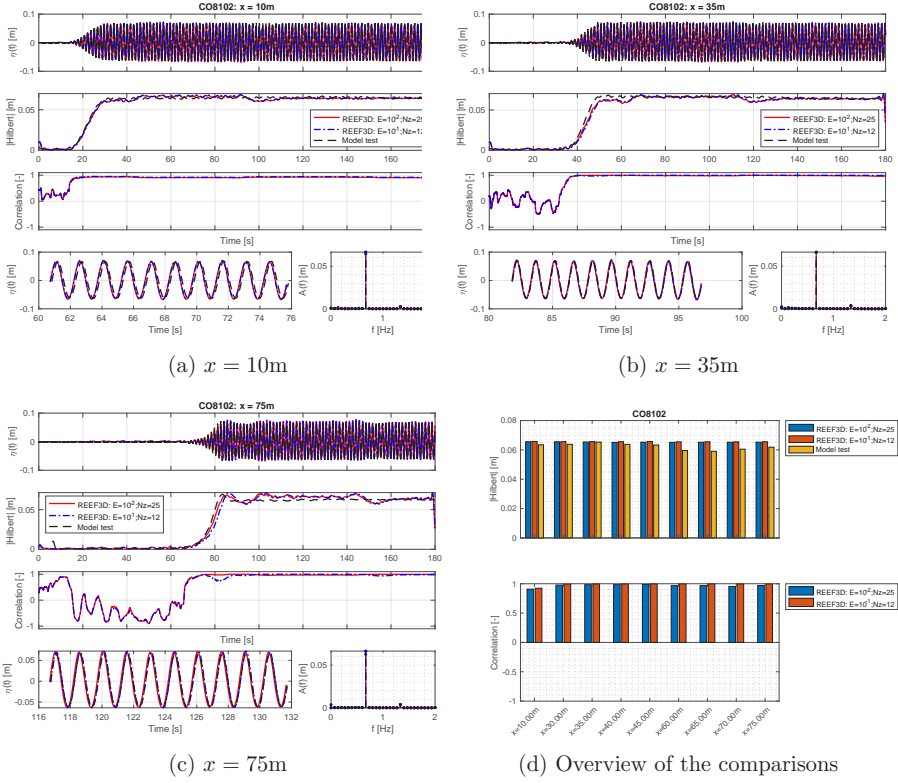


Figure 5: Validation of the simulations

which gives a ten times reduction of the error level  $E$ . However, the comparison of the simulations against the model test time series at different distances from the wavemaker gives almost the same good agreement with the model test time series as it shown in Figure 5. The top diagram in Figure 5a shows the whole time series of the simulation and the experiment at 10 m from the wave maker. The Hilbert envelopes of these time series in the next diagram show a good agreement between the simulations and the experiments regarding the magnitude of the time series, and the two curves of the numerical simulations are almost identical. The correlation curves, which quantify the similarity between the experiment and the two simulations show that the numerical simulations are in phase with the model test record. The lowest diagram shows the time windows where the Fourier analysis is applied and its results in the form of an amplitude spectrum is shown on the right. Here one can see some differences between the experiment and the numerical results.

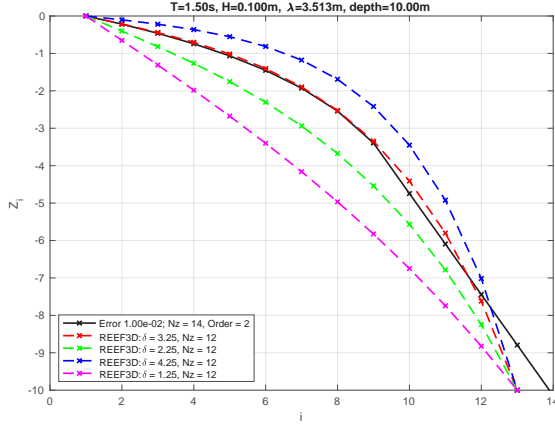


Figure 6: Comparison of the optimal grid spacing against the applied REEF3D's grid spacings

One can observe the trend at all other locations as shown in Figure 5b and 5c. The two bar diagrams in Figure 5d give an overview of the average of the Hilbert envelopes in the upper diagram and the average correlations at nine locations.

Based on this overview, one can conclude that the two simulations with different setups gives about the same accuracy regarding the magnitude and phase in spite of the different error levels. This supports the assumption regarding the importance of the constant error distribution in the vertical direction.

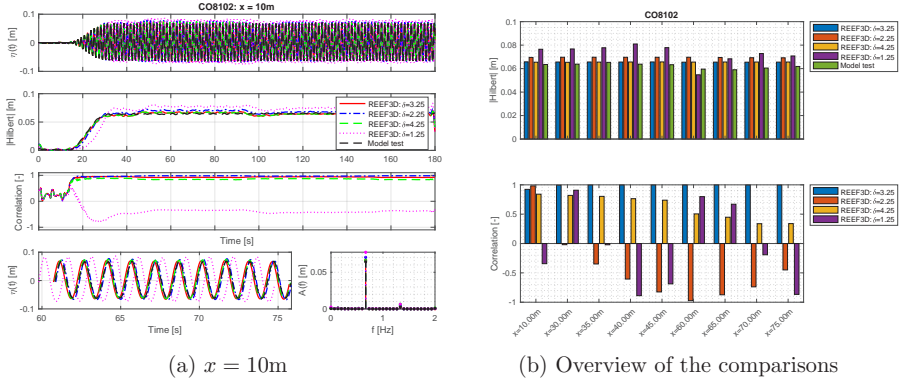


Figure 7: Validation of the simulations

In order to further investigate this assumption, a set of simulations with the same setup as the simulation with  $N_z=12$  except the stretching factor  $\delta$ , are run. The effect of the stretching factor on the vertical grid spacing is shown in Figure 6. The stretching factors which are less than 3.25 define the grid spacing with little variation in the grid height. The smallest one gives an almost uniform grid distribution (magenta curve). A stretching factor larger than 3.25 gives a more dense grid distribution compared to the "optimal" grid distribution. The comparison of the time series at 10 m from the wavemaker in Figure 7a shows that the almost uniform grid spacing gives a wrong wave propagation velocity. The value of the correlation to the model test time series is about -0.5, which indicates intermediate dissimilarity. However, the magnitude of the signal is over predicted based on the Hilbert envelopes and the amplitude spectrum, but the error is much lower than the phase error. One can see that with increasing distance from the wavemaker, the correlation decreases in all simulations. This indicates a numerical dispersion error, except in the simulation with the "optimal" stretching  $\delta = 3.25$  for the regular wave. The magnitude error of the simulations are less sensitive to the distance which indicates that the numerical dissipation is low.

## 6 CONCLUSIONS

The new potential theory based module of REEF3D is presented in this paper. The effect of the vertical grid distribution on the wave propagation is also demonstrated. A new method is described which finds the optimal vertical grid distribution and this method is validated against model test data. The comparison shows that the grid distribution based on the new method gives small phase error.

The validation is shown in this paper only for one regular wave. This method is used to define the grid in the vertical direction in several other simulations, where a regular wave with different periods and wave amplitude as well as three hours irregular sea state are simulated with similar good results as presented here. In the future work, it is necessary to find the mathematical background for the good performance of the presented method.

## Acknowledgement

This work is part of the "High Resolution Numerical Modelling of Flexible Fish Cage Structures" project and the authors gratefully acknowledge the support from the Norwegian Research Council (grant 267981). The authors are grateful to the model test data provided by the Transnational Access to Research Infrastructures Program of the European Commission under the contract HPRI-CT-2001- 00176. This study was supported in part with computational resources at the Norwegian University of Science and Technology (NTNU) provided by NOTUR, <http://www.notur.no>.

## REFERENCES

- [1] Onorato, M., Osborne, A., Serio, M., Cavaleri, L., Brandini, C. and Stansberg, C. Observation of strongly non-Gaussian statistics for random sea surface gravity waves in wave flume experiments. *Physical Review E* 2004. **70**(6).
- [2] Bonnefoy, F., Ducrozet, F., Le Touze, D. and Ferrant, P. Time-domain simulation of nonlinear water waves using spectral methods. *Advances in Coastal and Ocean Engineering* 2009. **11**:129–164.
- [3] Engsig-Karup, A.P., Bingham, H.B. and Lindberg, O. An efficient flexible-order model for 3D nonlinear water waves. *Journal of Computational Physics* 2009. **228**:2100–2118.
- [4] van Groesen and Andonowati. Time-accurate AB-simulations of irregular coastal waves above bathymetry. In: *Proceedings of the Sixth International Conference on Asian and Pacific Coasts* 2011. APAC, Hong Kong.
- [5] Kamath, A., Fleit, G. and Bihs, H. Investigation of free surface turbulence damping in RANS simulations for complex free surface flows. *Water* 2019. **11**(3):456.
- [6] Miquel, A.M., Kamath, A., Alagan Chella, M., Archetti, R. and Bihs, H. Analysis of different methods for wave generation and absorption in a cfd-based numerical wave tank. *Journal of Marine Science and Engineering* 2018. **6**(2). doi:10.3390/jmse6020073.
- [7] Ahmad, N., Bihs, H., Myrhaug, D., Kamath, A. and Øivind A. Arntsen. Numerical modeling of breaking wave induced seawall scour. *Coastal Engineering* 2019. **150**:108 – 120. doi:<https://doi.org/10.1016/j.coastaleng.2019.03.010>.
- [8] Chella, M.A., Bihs, H. and Myrhaug, D. Wave impact pressure and kinematics due to breaking wave impingement on a monopile. *Journal of Fluids and Structures* 2019. **86**:94 – 123. doi:<https://doi.org/10.1016/j.jfluidstructs.2019.01.016>.
- [9] Bihs, H., Kamath, A., Alagan Chella, M. and Arntsen, O.A. Extreme wave generation, breaking, and impact simulations using wave packets in REEF3D. *J. Offshore Mech. Arct. Eng.* 2009. **141**(4). doi:10.1115/1.4042178.
- [10] Grotle, E.L., Bihs, H. and Æsøy, V. Experimental and numerical investigation of sloshing under roll excitation at shallow liquid depths. *Ocean Engineering* 2017. **138**:73 – 85. doi:<https://doi.org/10.1016/j.oceaneng.2017.04.021>.
- [11] Moideen, R., Ranjan Behera, M., Kamath, A. and Bihs, H. Effect of girder spacing and depth on the solitary wave impact on coastal bridge deck for different airgaps. *Journal of Marine Science and Engineering* 2019.

- [12] Bingham, H.B. and Zhang, H. On the accuracy of finite-difference solutions for nonlinear water waves. *J Eng Math* 2007. **58**:211–228.
- [13] Onorato, M., Osborne, A., Serio, M., Cavaleri, L., Brandini, C. and Stansberg, C. Extreme waves, modulational instability and second order theory: wave flume experiments on irregular waves. *European Journal of Mechanics-B/Fluids* 2006. **25**(5):586–601.
- [14] Onorato, M., Osborne, A., Serio, M. and Cavaleri, L. Modulational instability and non-gaussian statistics in experimental random water-wave trains. *Physics of Fluids* 2005. **17**(7).
- [15] Mayer, S., Garapon, A. and Sørensen, L.S. A fractional step method for unsteady free-surface flow with applications to non-linear wave dynamics. *International Journal for Numerical Methods in Fluids* 1998. **28**(2):293–315. doi:10.1002/(SICI)1097-0363(19980815)28:2<293::AID-FLD719>3.0.CO;2-1.
- [16] Falgout, R.D., Jones, J.E. and Yang, U.M. Conceptual interfaces in hypre. *Future Gener. Comput. Syst.* 2006. **22**(1-2):239–251. doi:10.1016/j.future.2003.09.006.
- [17] Guang-Shan, J. and Chi-Wang, S. Efficient implementation of weighted eno schemes. *Journal of Computational Physics* 1996. **126**(1):202–228.
- [18] Chi-Wang, S. and Stanley, O. Efficient implementation of essentially non-oscillatory shock-capturing schemes. *Journal of Computational Physics* 1988. **77**(2):439–471.
- [19] Dean, R.G. and Dalrymple, R.A. *Water wave mechanics for engineers and scientists*, vol. 2 of *Advanced series on ocean engineering*. Singapore ; Teaneck, NJ : World Scientific, ©1991, 1991.
- [20] Bunnik, T. and de Ridder, E.J. Using nonlinear wave kinematics to estimate the loads on offshore wind turbines in 3-hour sea states. In: *ASME 2018 37th International Conference on Ocean, Offshore and Arctic Engineering* 2018. Madrid, Spain. OMAE2018-77807.



# EVALUATION OF SAFETY DISTANCES FOR STORAGE OF EXPLOSIVE MATERIALS USING A COMBINATION OF THERMOCHEMICAL COMPUTATIONS AND CFD

HANNIBAL E. FOSSUM<sup>1</sup>, ANDREAS N. OSNES<sup>2</sup> AND  
TOR E. KRISTENSEN<sup>1</sup>

<sup>1</sup>Norwegian Defence Research Establishment (FFI)  
P. O. Box 25, 2027 Kjeller, Norway  
e-mail (corresponding author): hannibal.fossum@ffi.no

<sup>2</sup> Department of Technology Systems, University of Oslo  
P. O. Box 70, 2027 Kjeller, Norway

**Key words:** TNT equivalency, detonation, explosives

**Abstract.** A novel approach to calculating TNT equivalencies and safety distances for explosives, using a combination of thermochemical computations and computational fluid dynamics, is presented. This enables the estimation of safety distances for specific explosives and charge geometries based on physical principles rather than empirical parametrizations. The methodology inherently allows for the simulation of subsequent shock propagation and interaction with surrounding structures, following the detonation of an explosive. Presented results include examples of computed TNT equivalencies for selected commercial explosives, as well as simulated pressure distributions around a detonating stack of dynamite.

## 1 Introduction

Globally, billions of kilograms of commercial explosives are used annually for purposes such as mining, quarrying, construction work, demolitions and weaponry. The manufacturing, transportation and storage of such materials pose considerable safety risks. Two aspects central to safe storage of explosive materials are investigated in this work by combining thermochemical computations and computational fluid dynamics (CFD).

The first part of this investigation details a novel approach for the establishment of robust TNT equivalency values in air for detonating explosives, including both pure substances or mixtures of several compounds (both being referred to herein simply as an *explosive*). The determination of reliable TNT equivalencies is essential for any realistic comparison of explosive materials with regards to evaluation of safety distances.

The concept of TNT equivalency is confusing because it may relate to various facets of relative explosive output [1, 2]. Firstly, the term can refer to a unit of energy, defined by convention and used typically to express the power of nuclear weapons or cosmic events. Secondly, it can be a relative measure for air blast phenomena (overpressure or impulse). Thirdly, TNT equivalency is often used rather arbitrarily as a relative effectiveness factor, in terms of “demolition power”, for comparison of explosives. Unfortunately, the second and third aspects are regularly mixed up.

It is the second aspect above that is relevant for evaluation of safety distances, in this context being defined as the amount of TNT (in pure form and shaped as a hemisphere) which, during detonation on the ground level and at a precise distance, yields the same blast overpressure or blast impulse as the mass unit of the considered explosive. Although strictly defined, TNT equivalencies for different explosives have traditionally been derived by simply comparing an easily obtained attribute of the performance of the explosive in question to that for TNT, e.g. directly relating the heats of detonations or the total energies of detonations.

In this work, more realistic TNT equivalencies are derived by carrying out one-dimensional gas-dynamic simulations of spherical-charge detonations (in air) for various explosives. The simulations are compared to corresponding simulations of TNT. This results in TNT equivalencies, either by peak overpressures or impulses, that are applicable for evaluation of the safety distances relevant to storage of explosives. The material properties and detonation parameters for specific explosives are obtained using a thermochemical code.

The second part of the study regards the detonation of pallets loaded with stacked cardboard boxes holding dynamite, this being the conventional way of storing such cartridge explosives. Gas-dynamic simulations are used to map peak pressures in the volume surrounding detonating stacks for different initiation scenarios. Geometrical effects, e.g. from corners, have large effects on the pressure distributions in the near-field of the detonation. These effects can possibly be exploited to improve safety or efficiency in storage facilities containing such palletized stacks.

The method detailed herein enables the estimation of safety distances for specific explosives and charge geometries based on physical principles rather than empirical parametrizations. Furthermore, the methodology inherently allows for the simulation of subsequent shock propagation and interaction with surrounding structures, following the detonation of an explosive.

This paper is structured as follows: Section 2 provides an overview of the thermochemical computations, the gas-dynamic simulation framework and the computational setup. Section 3 contains the simulation results. The results from the one-dimensional computations are presented first, followed by the simulations of dynamite stack detonations. Finally, concluding remarks are contained in section 4.

## 2 Method

### 2.1 General procedure

The simulations in this study have been performed via a two-step approach.

Firstly, a thermochemical code, EXPLO5 [3, 4], is used to compute material properties and detonation parameters for a specified explosive.

Secondly, the gas dynamics of the detonating explosive is simulated in a shock-capturing compressible-fluid flow solver, CharLES [5, 6]. Output from EXPLO5 is used to define the material properties of the explosive, as well as the initial conditions, in CharLES.

The output from the second step is a time-dependent, three-dimensional flow field describing the detonation by means of pressure, density and velocity fields. These data are post-processed in order to extract useful information, such as pressure levels at selected distances from the detonating explosive.

### 2.2 Thermochemical solution

EXPLO5, v6.03, is a thermochemical code that can estimate, among others, the equilibrium composition and thermodynamic parameters of state of detonation products along the shock adiabat of the detonation products for ideal detonations. The program contains a precompiled database with hundreds of chemical reactants and products with associated enthalpies of formation.

The detonation parameters are calculated based on a chemical-equilibrium, steady-state detonation model. The equilibrium composition of detonation products is calculated by applying the free-energy minimization technique of Dantzig, Johnson and White [7], giving a set of equations solved iteratively by a modified Newton-Raphson method.

The state of detonation products can be described by various equations of state (EOS), such as the Becker-Kistiakowsky-Wilson (BKW) EOS or the Jacobs-Cowperthwaite-Zwisler (JCZ3) EOS for gaseous products. The thermodynamic functions of the products are derived using the BKW EOS (for gases) or the Murnaghan EOS (for condensed products).

The thermochemical calculations assume that the detonation is well represented by a Chapman-Jouget (CJ) detonation. The CJ point is computed by numerical determination of the minimum value of the detonation velocity along the shock adiabat of the detonation products. Detonation parameters (pressure, velocity, heat, etc.) at the CJ point is found from the EOS for the products.

From the CJ point, the isentropic expansion of the products is calculated (by numerical integration), and non-linear curve-fitting [8] yields coefficients for the Jones-Wilkins-Lee (JWL) EOS. The JWL EOS enables the calculation of the released detonation energy which will be available to perform mechanical work. Highly resolved density domains were used both in the calculations of the detonation-products adiabat and the JWL coefficients.

The relevant parameters from EXPLO5 for subsequent gas-dynamics simulations are the JWL coefficients, the detonation velocity, and the released detonation energy.

### 2.3 Gas-dynamic solution

The motion of the gas phases are governed by the compressible Navier-Stokes equations. However, the equations of state describing the detonation-product gases and the ambient air are very different, and thus a multi-component model is required. Allaire's five equation model [9] is used for this purpose, with viscous terms included.

In index notation, with summation on double indices and  $i \in \{1, 2, 3\}$ , the governing equations can be written

$$\frac{\partial \rho_1 z_1}{\partial t} + \frac{\partial \rho_1 z_1 u_i}{\partial x_i} = 0, \quad (1)$$

$$\frac{\partial \rho_2 z_2}{\partial t} + \frac{\partial \rho_2 z_2 u_i}{\partial x_i} = 0, \quad (2)$$

$$\frac{\partial z_1}{\partial t} + u_j \frac{\partial z_1}{\partial x_j} = 0, \quad (3)$$

$$\frac{\partial \rho u_i}{\partial t} + \frac{\partial (\rho u_i u_j + p)}{\partial x_j} = \frac{\partial \tau_{ij}}{\partial x_j}, \quad (4)$$

$$\frac{\partial (\rho e + \frac{1}{2} \rho u_i u_i)}{\partial t} + \frac{\partial (\rho e u_j + \frac{1}{2} \rho u_i u_i u_j + u_j p)}{\partial x_j} = \frac{\partial (u_i \tau_{ij} - q_j)}{\partial x_j}, \quad (5)$$

where  $\rho_k$  and  $z_k = z_k(\mathbf{x}, t)$  are the phase-specific mass density and the volume fraction of component  $k$ , respectively.  $u_i = u_i(\mathbf{x}, t)$  is the velocity in the  $i$ 'th direction,  $p = p(\mathbf{x}, t)$  is the static pressure,  $\tau_{ij} = \tau_{ij}(\mathbf{x}, t) = \mu \left( \frac{\partial u_i}{\partial x_j} + \frac{\partial u_j}{\partial x_i} \right) - \frac{2\mu}{3} \delta_{ij} \frac{\partial u_i}{\partial x_i}$  is the viscous stress tensor,  $e = e(\mathbf{x}, t)$  is the specific internal energy and  $q = q(\mathbf{x}, t) = \lambda \partial T / \partial x_j$  is the heat flux, where  $\lambda$  is the heat conductivity. Viscosity is assumed to vary with temperature as a power law, so that  $\mu = \mu_0 (T/T_0)^{0.76}$ , where  $\mu_0$  and  $T_0$  are the kinematic viscosity and temperature at reference conditions. A constant Prandtl number of 0.7 relates the thermal conductivity and viscosity. The position vector is defined by  $\mathbf{x} = x_i = (x, y, z)$ .

Additionally, an equation of state is required for each gas component. In the current work, the Jones-Wilkins-Lee (JWL) equation of state (EOS) and the ideal gas EOS are used to model detonation gases and air, respectively.

The multi-component model described by (1)–(5) is implemented in the compressible fluid solver, resulting in a modified version of CharLES. In CharLES, the numerical method used for the gas phase is a finite-volume method with low dissipation and dispersion, developed for Large Eddy Simulations on unstructured grids [5]. The Harten-Lax-van Leer-Contact (HLLC) Riemann solver [10] is used to compute fluxes between neighbouring

cells, and the solution is advanced in time by a third order explicit Runge-Kutta scheme. The solver is highly parallelized.

For the one-dimensional simulations of spherical detonations, the face values are reconstructed using an Essentially Non-Oscillatory (ENO)-scheme to ensure sharp resolution of shocks. With the present implementation of the multi-component model, this scheme is not robust enough for general three-dimensional simulations. Therefore, a simpler first-order reconstruction of face values are used instead in this case.

### 2.3.1 Initial conditions from a similarity solution

For the spherical-detonation simulations, it is assumed that the detonation of the explosive is adequately described as a CJ detonation. The chemical reactions are assumed to occur within an infinitely thin layer immediately behind the shock front, and this layer terminates at the CJ point. The flow behind this point is assumed to be described by a similarity solution.

The similarity solution is described in e.g. [11]. Some of the results are repeated here for completeness. The basic assumptions required of this model are as follows:

- The flow is one-dimensional and self-similar.
- The adiabatic index (heat capacity ratio) of the detonation products is constant.

The latter assumption can be avoided, e.g., by using the phase-plane method of Kuhl [12]. However, the differences in density, pressure and velocity profiles between these methods are roughly between 1 and 2 % [12].

With these assumptions, the solution of the gas-dynamic equations is given in terms of a chosen set of similarity variables. Let  $\xi = r(Dt)^{-1}$  where  $r$  is the radial coordinate,  $D$  is the detonation velocity and  $t$  is time,  $\phi(\xi) = u/D$ , where  $u$  is the gas velocity,  $\eta(\xi) = c/D$ , where  $c$  is the speed of sound. Then the steady flow solution is given by:

$$\phi' = \left( \frac{j\phi}{\xi} \right) \frac{\eta^2}{(\phi - \xi) - \eta^2}, \quad (6)$$

$$\eta' = - \left( \frac{\gamma - 1}{2} \right) \left( \frac{j\eta\phi}{\xi} \right) \frac{\phi - \xi}{(\phi - \xi)^2 - \eta^2}, \quad (7)$$

where  $j = 0, 1, 2$  corresponds to planar, cylindrical and spherical geometry respectively, and  $\gamma$  is the adiabatic index. These equations can be integrated from the CJ-point, where  $\xi = 1$ ,  $\phi = \phi_1$  and  $\eta = \eta_1$ . For  $j = 1$  or  $j = 2$  the equations are singular at the front, and the solution in the immediate proximity of this point is instead computed by the first-order series expansion:

$$\phi(\xi) = \phi_1 - \sqrt{\frac{2j\phi_1\eta_1}{\gamma + 1}} (1 - \xi)^{1/2} + \dots, \quad (8)$$

$$\eta(\xi) = \eta_1 - \frac{\gamma - 1}{2} \sqrt{\frac{2j\phi_1\eta_1}{\gamma + 1}} (1 - \xi)^{1/2} + \dots \quad (9)$$

The series expansion is used to compute a single point behind the CJ point, and the rest of the profile follows by integration of equations 6 and 7. Since the expansion behind the CJ point is isentropic, pressure and density profiles are found by

$$p(\xi) = p(1) \left( \frac{\eta(\xi)}{\eta(1)} \right)^{2\gamma/(\gamma-1)}, \quad (10)$$

$$\rho(\xi) = \rho(1) \left( \frac{\eta(\xi)}{\eta(1)} \right)^{2/(\gamma-1)}. \quad (11)$$

### 2.3.2 Initial conditions from programmed burn

The evolution of a general detonation front in an explosive with complex charge geometry is difficult to compute accurately. Direct numerical simulations are infeasible, due to the conflicting requirements of high resolution of the reaction zone and the large amounts of explosives. Thus, programmed burn has emerged as an engineering solution. The programmed-burn approach has been shown to produce acceptable results without large computational cost [13, 14].

Based on the results from the thermochemical code, the detonation velocity is prescribed throughout the explosive. With this procedure, virtually no computational effort is spent on the detonation front and reaction zone calculations per se. Only the rest of the gas-dynamics problem, where the detonation energy performs mechanical work, is simulated directly.

In the present implementation, the programmed burn model is defined simply by a scalar field representing a local initiation time,

$$t_{\text{init}}(\mathbf{x}) = d_I/D.$$

Here,  $d_I = d_I(\mathbf{x})$  is the distance to the closest detonation initiation point. Once the simulation time reaches  $t_{\text{init}}$  for a given computational cell, the appropriate detonation energy (given by the thermochemical code) is released at that location.

## 3 Results

### 3.1 Spherical detonations

For the free-space spherical detonations, several common commercial explosives have been simulated. Selected coefficients for the JWL EOS for each (fully reacted) explosive are listed in Table 1, as are the detonation velocities and detonation-energy releases calculated in the thermochemical solver. Only parameters relevant to the gas-dynamics simulations are shown.

Table 1: Selected detonation parameters from the thermochemical code<sup>I</sup>; JWL constants ( $A$ ,  $B$ ,  $R_1$ ,  $R_2$ , and  $\omega$ ), detonation velocity ( $D$ ), and detonation energy ( $E_D$ ) are shown.

Explosive	$A$ [GPa]	$B$ [GPa]	$R_1$	$R_2$	$\omega$	$D$ [m/s]	$E_D$ [kJ/cm <sup>3</sup> ]
TNT	698.754	20.9134	5.30235	1.69442	0.425571	7158.2	7.1229
EGDN	635.736	16.3697	5.20740	1.47310	0.312138	7519.3	10.2795
HMX	1200.182	41.8148	5.14251	1.70474	0.516399	9194.8	11.2751
Nitroglycerine	802.456	19.4111	5.29319	1.51644	0.343281	7786.9	10.1127
PETN	812.029	24.8674	4.90760	1.53975	0.431519	8423.4	10.8304
Picric acid	789.910	23.2665	5.14538	1.67083	0.463379	7628.2	7.7859
RDX	906.164	31.5984	4.88605	1.60997	0.497743	8881.3	10.7488
Tetryl	743.711	24.1145	5.03631	1.61632	0.464622	7871.2	8.5857
AN	102.441	2.4722	5.65876	1.85368	0.390625	3723.5	1.5584
( $\rho = 800$ kg/m <sup>3</sup> )							
ANFO	94.244	3.2328	4.99013	1.42873	0.347341	4790.5	3.4817
( $\rho = 800$ kg/m <sup>3</sup> )							
Blasting gelatin	629.476	15.9885	5.21995	1.47715	0.316859	7408.6	9.8517
Comp. A-3	1139.844	34.2849	5.53357	1.71944	0.483375	8429.8	9.1571
Comp. B	867.256	28.3582	5.19281	1.65308	0.475931	8122.7	8.9343
Comp. C-4	1121.466	34.4409	5.47924	1.71300	0.488059	8455.1	9.2536
Octol 75-25	1072.979	34.6360	5.20599	1.66865	0.501066	8665.9	10.0424
Pentolite 50-50	657.216	23.8726	4.95074	1.59822	0.467663	7754.1	8.5708

<sup>I</sup> The EXPLO5 density increase ratio was set to 1.005 for the calculation of the shock adiabat of the products, and the density decrease ratio was set to 1.01 for the calculation of the expansion isentrope of the products (with a freeze temperature of 1800 K). Only formation of solid carbon as graphite (i.e., not diamond) was allowed in the EXPLO5 calculations. All explosives have densities close to their theoretical maximum densities unless otherwise noted.

For the gas-dynamics simulations, a series of expanding one-dimensional computational grids have been used, in which consecutive cell widths (and hence also cell volumes) expand in the  $x$ -direction, as shown in Figure 1. Cell widths in both  $y$ - and  $z$ -direction expand (corresponding to the two angular directions) with increasing  $x$ , though only one direction is visible in the figure. Using multiple meshes is significantly more efficient than using a single mesh for the entire simulation. Interpolation between meshes introduces a small error that a single mesh would avoid. However, that error was found to be insignificant for the current simulations.

The initial mesh represents a  $0.5^\circ$  spherical sector from  $x = 0.01R$  to  $x = 2R$ , where  $R = (3M/4*\rho*\pi)^{1/3}$ . Note that  $R$  is simply the radius of the explosive charge, based on  $M$ , the total mass of explosive (typically 1 kg in the present simulations), and  $\rho$ , the density of the explosive material. Once the shock wave reaches  $x = 0.85R$  in the initial mesh, the simulation data is interpolated to a new mesh with twice the resolution and domain size, and the simulation is continued. This interpolation procedure is repeated iteratively on successively coarser meshes until a desired distance (or time) of shock propagation has been calculated.

All the successive one-dimensional meshes comprise 1188 computational cells and use a spherical sector of  $0.5^\circ$  (in both angular directions). The meshes are uniformly spaced in the  $x$ -direction. The time-steps are determined based on a constant CFL number of 0.5, based on the cell width in the  $x$ -direction.

From the results of the simulated detonations, TNT equivalencies can be calculated as follows. The recorded shock pressure and impulse of the positive phase are recorded for all locations within  $5 \leq Z \leq 40$ . Then, these results are compared to a similar simulation of TNT. Since the results are a function of the scaled distance,  $Z = x/\sqrt[3]{M}$ , the TNT mass can be scaled so that the pressure or impulse at a certain (unscaled) distance matches for both explosives. The TNT equivalency is the ratio of the mass of the matching TNT charge to the mass of the other explosive. The TNT equivalency computed in this way is generally a function of scaled distance. The results of the calculations are listed in Table 2.

From a practical point of view, the TNT equivalency values in Table 2 for ammonium nitrate (AN) and ammonium nitrate/fuel oil (ANFO) hold particular importance with

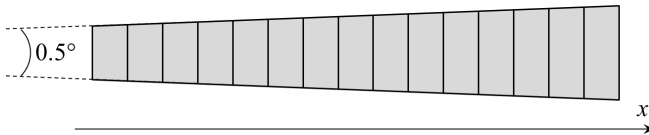


Figure 1: Schematic illustration of the one-dimensional mesh used in the spherical-detonation simulations.



Table 2: TNT equivalencies for selected commercial explosives, as computed with the two-step procedure. As the results did not depend significantly on distance,  $Z$ , only the average TNT equivalency is reported for each explosive.

Explosive	TNT equivalency by impulse	TNT equivalency by peak overpressure
TNT	1	1
EGDN	1.88	1.38
HMX	1.83	1.37
Nitroglycerine	1.71	1.31
PETN	1.76	1.34
Picric acid	1.09	1.05
RDX	1.79	1.35
Tetryl	1.31	1.15
AN ( $\rho = 800 \text{ kg/m}^3$ )	0.20	0.42
ANFO ( $\rho = 800 \text{ kg/m}^3$ )	0.69	0.80
Blasting gelatin	1.74	1.32
Comp. A-3	1.43	1.20
Comp. B	1.42	1.20
Comp. C-4	1.46	1.22
Octol 75-25	1.61	1.28
Pentolite 50-50	1.34	1.17

---

regard to explosives safety due to the enormous quantities of these materials being stored and transported at any time. For AN, which is by far the most important constituent of most civilian explosives, the TNT equivalency depends heavily on the choice of overpressure or impulse as the determining air-blast parameter. This may partly explain the difficulties associated with the establishment of robust equivalency values for this particular explosive.

In addition to the values in Table 2, we have also calculated the corresponding TNT equivalencies for a number of emulsion-matrix compositions (the non-sensitized precursor to emulsion explosives) obtained from a number of major producers of civilian explosives. All of these have TNT equivalencies, according to the method reported here, in the range of roughly 0.80 by overpressure and between approximately 0.65 and 0.70 by impulse.

When comparing the simulated pressure field for TNT to experimental data, shown in Figure 2, the results show good agreement; the underprediction of the simulated detonation pressure (between 20 % and 35 %) is acceptable given the wide pressure range (three orders of magnitude), and the results are in line with previously published simulation data [15]. The evolution of the pressure field with distance matches the experiment very well.

The peak pressure is underpredicted partly due to the finite size of the control volumes used in these simulations. However, since that effect will similarly reduce peak pressures for all explosives, it is not likely to have much impact on TNT equivalencies.

The results presented in the above is indicative of both the quality and usefulness of the two-step approach. In the following, an analogous procedure is applied to simulate detonations in more complicated cases, thereby assessing required safety distances for storage of explosive materials.

### 3.2 Detonating stacks of dynamite

Most calculations of detonation pressures, and hence related safety distances, are based on spherical detonations and TNT equivalencies. With the approach outlined in previous sections, case-specific calculations can be performed, allowing more accurate estimates of realistic pressure fields.

In the following, detonations of a stack of dynamite are simulated, with different points and planes of initiation. The particular dynamite formulation used in this study has been obtained from a leading European manufacturer. The composition contains ammonium nitrate (AN), ethylene glycol dinitrate (EGDN), nitrocellulose (NC) and various additives.

The simulation domain is illustrated in Figure 3a; the geometry represents a stack on a standard Euro-pallet (EUR 1; 1.2 by 0.8 m<sup>2</sup>) sitting on the ground, loaded with 1,000 kg of cartridge dynamite, contained in five layers of cardboard boxes. The pallet itself is 0.144 m tall, and the height of the stack of dynamite is 1.4 m. The ground surface is included as a fully shock-reflecting surface in the simulations, whereas the materials of the pallet and stack are not.

The coordinate system of the computational domain is defined such that the longer

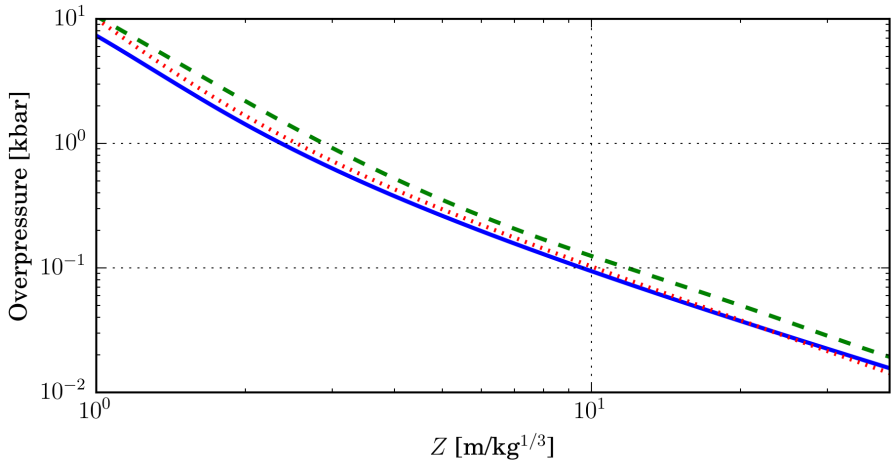
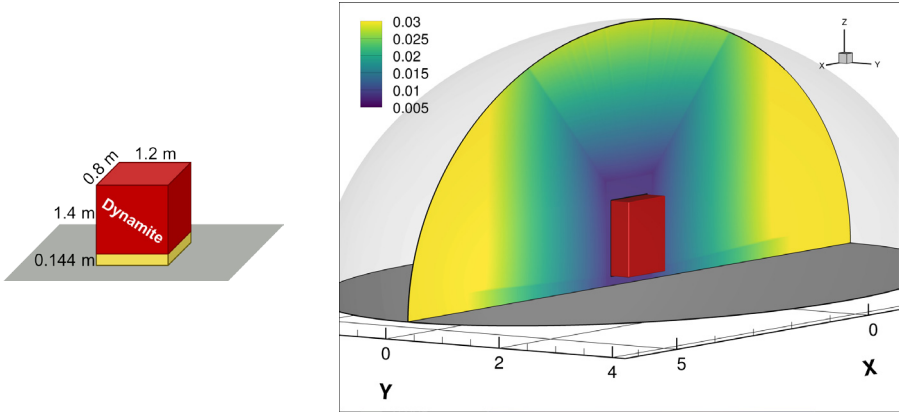


Figure 2: TNT-detonation pressure data from the present simulations (—), the experimental data compiled by Kingery and Bulmash [16] (---), and the numerical simulation of Grisaro [15] (.....).



(a) Schematic illustration of the pallet and stack geometry.

(b) Computational domain, with a cutplane at  $y = 0$ , colored by the cubic root of local cell volume. The stack of dynamite is marked in red.

Figure 3: The geometry (left) and computational domain (right) of the detonating-dynamite simulations.

edge of the pallet (1.2 m in length) runs along the  $x$ -direction, and  $z$  is the vertical coordinate. In the following, the *left* side of the stack detonates the side that is parallel to the  $y$ -axis and placed at the negative  $x$ -value. The *back* side of the stack detonates the side that is parallel to the  $x$ -axis and placed at the negative  $y$ -value. The *right* and *front* sides are defined analogously (and with opposite signs of the left and back side positions, respectively).

The computational domain is shown in Figure 3b, where the mesh resolution is also indicated; the cutplane at  $y = 0$  (through the middle of the stack) is colored by the cubic root of the local cell volume, i.e. an estimate of a typical local edge length for a computational cell. The smallest edge in the mesh, inside the explosive (i.e. inside the stack of dynamite) is 8.33 mm, whereas the largest edge, at the outer boundary, is 56.4 mm. The total number of computational cells is 25,666,560. Case L3 has a different resolution, to be discussed.

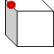
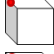
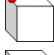
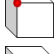
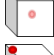
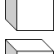
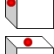




Given the three-dimensional nature of the problem, the mesh must also be three-dimensional. To allow reasonable computation times, the mesh resolution will be significantly reduced compared to the one-dimensional cases of Section 3.1, but the reduction in mesh density is somewhat mitigated by using a non-uniform mesh; as shown in Figure 3b, the mesh is most finely resolved in and near the explosive, where the peak pressures are highest.

All simulations, except L3, used a computational time step of  $\Delta t = 0.12 \mu\text{s}$ . 15,000 time steps were simulated, giving a total simulation time of 1.8 ms. Each simulation

required roughly 3,200 CPU-hours to complete.

Table 3 lists the 14 cases simulated. The simulations are divided into three case series; K, L, and M. The rationale and results for each of the series are discussed in the following.

Table 3: Overview of simulation cases and their initiation locations. Case L3 (\*) is a high-resolution ENO-reconstruction version of case K2.

Case	Initiation location	Illustration
K1	Point, center of upper-left edge	
K2	Point, center of upper-left edge	
K3	Point, center of upper-left edge	
L1	Point, upper-front-left corner	
L2	Point, centroid of stack	
L3*	Point, center of upper-left edge	
L4	Point, center of left side	
L5	Point, center of top side	
M1	Plane, left side	
M2	Plane, front side	
M3	Plane, top side	

### 3.2.1 Case series K: Worst-case pressure field

The cases in series K are simulated to determine the appropriate choice of density for the explosive material. Whereas the real density of the simulated dynamite is  $\rho_{\text{real}} = 1,500 \text{ kg/m}^3$ , the stack is not packed 100 % efficiently; only 49.6 % of the stack volume consists of dynamite. It is therefore possible to define a new pseudo-dynamite material with 49.6 % of the real density, i.e. use  $\rho_{\text{pseudo}} = 744 \text{ kg/m}^3$ . The pseudo-material density can be used both in the thermochemical and gas-dynamical simulations (case K1) or only for the gas dynamics (case K3). Alternatively, the real dynamite density can be used

in both steps, accompanied by a reduction in stack volume to account for the packing inefficiency (case K2). All of the K simulations are initiated in a point on the center of one of the upper edges of the stack.

Given the difficulty involved in determining which of the three K simulations represent the most realistic macroscopic model of a stack inefficiently packed with dynamite, the worst case (in terms of maximum pressure values) is used as a basis for the other case series (L and M).

Figure 4 shows the maximum pressure values,  $p_{\max}$  in the  $(x, z)$ -plane (with  $y = 0$ ) for the three cases in series K. In this and following figures,  $p_{\max}$  always refers to the maximum in time and in the vertical direction up to the stack height, i.e.,

$$p_{\max}(x, y) = \max_{t>0 \wedge z<1.544 \text{ m}} p(\mathbf{x}, t). \quad (12)$$

In the specific case of the present simulations,  $p_{\max}$  is an accurate estimate of the maximum of the peak pressure trailing the shock front, also referred to as the shock pressure.

From the data shown in Figure 4, it is clear that case K2 represents the highest maximum-pressure values. Hence, simulating a smaller stack with 100 % packing efficiency is the most conservative model for inefficient packing. For case series L and M, each stack dimension is thus reduced by a factor  $(\rho_{\text{pseudo}}/\rho_{\text{real}})^{1/3}$ , and  $\rho_{\text{real}}$  is used as the density of the explosive. The bottom of the stack remains at  $z = 0.144$  m above ground level and horizontally centered at  $(x, y) = (0, 0)$ .

### 3.2.2 Case series L: Point initiations

In case series L, various point initiations on the stack are considered, specifically in one corner, one of the edge centers, one of the side centers, and the stack centroid. Comparison of these simulations may reveal information about the dependence of the pressure field on initiation-point location. Note that case L3 is merely a high-resolution version of case K2, thereby allowing for an indicative mesh-resolution study, briefly discussed in Appendix A.

Figure 5 shows the maximum pressures,  $p_{\max}$  in the  $(x, z)$ -plane (with  $y = 0$ ) for cases L2, L4 and M1. As expected, the pressure field is symmetric for simulation L2. Within 4 meters from the center of the stack, the maximum pressure falls below 1 kbar. In comparison, case L4 yields higher pressure values on the right side of the stack relative to the left; at 4 m from the stack centroid, the pressure is more than twice as high on the right side. This is consistent with the fact that the rightward detonation propagates through more explosive material.

Another way of comparing the geometric effects of the initiation point on the pressure field is by considering isocurves in the  $xy$ -plane, as shown in Figure 6. The symmetry of case L5 is apparent, as expected. It is also worth noting that the highest pressure values (for a given distance from the stack) are encountered in the  $x$ - and  $y$ -directions

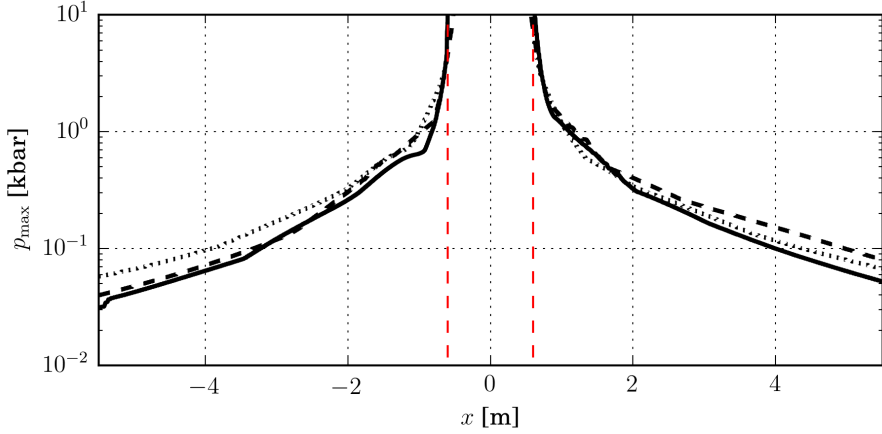


Figure 4: Maximum pressure,  $p_{\max}$ , as a function of  $x$ -distance (with  $y = 0$ ) from the center of the dynamite stack for cases K1 (—), K2 (---), and K3 (·····). The edges of the dynamite stack (real dimensions) are marked by vertical red (dashed) lines.

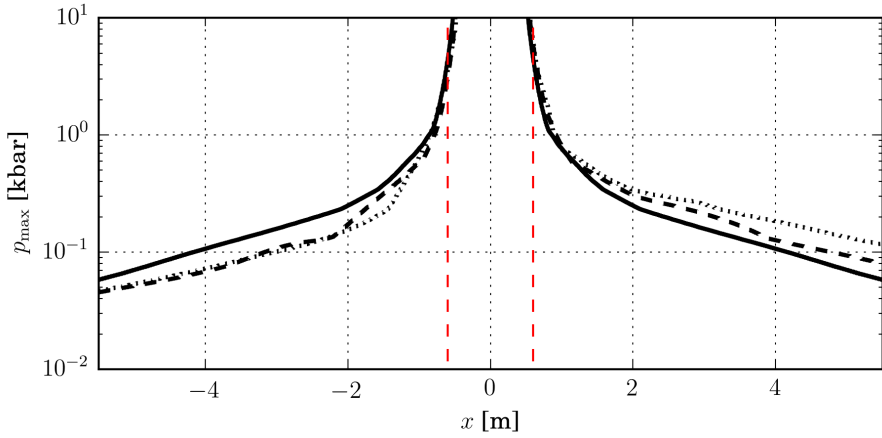


Figure 5: Maximum pressure,  $p_{\max}$ , as a function of  $x$ -distance (with  $y = 0$ ) from the center of the dynamite stack for cases L2 (—), L4 (---), and M1 (·····). The edges of the dynamite stack (real dimensions) are marked by vertical, red (dashed) lines.

(i.e. directly to the front, back, left and right of the stack), even for case L1, which is initiated in the upper-left-front corner.

From Figure 6, it appears that the initiation point is not critical for the evolution of the pressure field, although the effects of altering the initiation point are clearly visible. Case L4 generally seems to produce the smallest values of  $p_{\max}$ , whereas there is no clear “worst-case” for all the horizontal directions considered. Also, given how  $p_{\max}$  is defined, any high-pressure regions above the height of the stack are not accounted for in the data considered here.

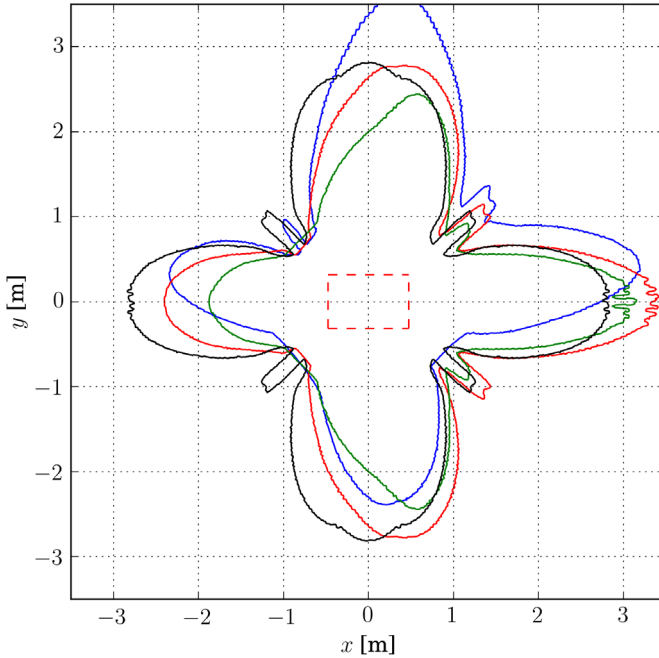


Figure 6: Isocurves in the  $xy$ -plane of  $p_{\max}(x, y) = 0.2$  kbar for cases K2 (red), L1 (blue), L4 (green), and L5 (black). The edges of the dynamite stack (real dimensions) are marked by red, dashed lines.

To obtain more information about the spatial structure of the detonation dynamics, density gradients can be considered. Figure 7 shows a representation of the density-gradient field at simulation time  $t = 0.612$  ms for cases L4 and M1. To improve the



visualization of the gradients, a pseudo-Schlieren technique is used; the shading in Figure 7 indicates the value of

$$F(\rho) = \exp\left(-30\frac{|\nabla\rho|}{|\nabla\rho|_{\max}}\right),$$

in which  $\nabla\rho = \partial\rho/\partial x_i$  is the density gradient, and  $|\nabla\rho|_{\max} = \max_{\text{plane}} |\nabla\rho|$  is the in-plane spatially maximal norm of the density gradient.

From Figure 7, the qualitative features of cases L4 and M1 look generally similar; several triple points can be identified, and a reflecting shock from the ground is seen as a black flattened structure in the lower part of the stack outline in both cases. However, the reflecting shock is more clearly seen in Figure 7b, indicating that the reflected shock is relatively (to the other pressure gradients in the domain) much stronger in case M1 than case L4.

The left part of the shock structure differs in the two cases; the shock front of case M1 is more smooth than that of case L4, which has a visible kink. The kink is a result of geometric effects of the explosive charge, specifically the effect of the upper-left edge of the stack. In the case of M1, the entire left side initiates the detonation, whereas for case L4 only a single point at the left side acts as a trigger. In the latter case, a shock front thus approaches the upper-left edge perpendicularly.

It can also be seen that the detonation front is closely followed by another density gradient, giving the front the appearance of an expanding shell. This second gradient is an inward propagating shock wave caused by overexpansion of the detonation gases. Eventually, that shock wave will implode towards the detonation center and create a secondary outward shock wave.

### 3.2.3 Case series M: Plane initiations

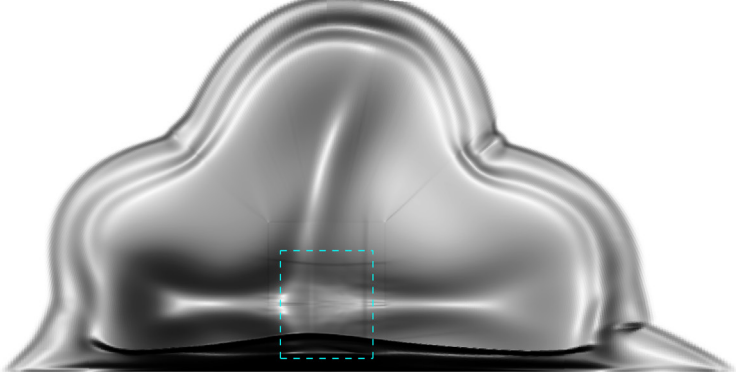
Case series M covers various full-plane initiations. By the symmetry of the problem, the simulations in this case series cover initiations from all possible sides of the stack (except the bottom).

From Figure 5, it is evident that the plane initiation, case M1, yields a higher maximum pressure than the two point initiations. This result also holds when considering all the point-initiation simulations as a whole compared to all the plane-initiation simulations as a whole; the plane initiations represent worst-case scenarios in terms of resulting maximum pressures.

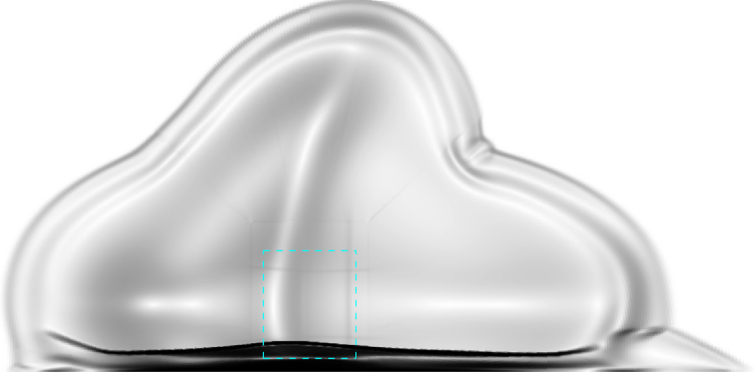
In order to estimate the highest possible peak pressure levels around a stack of dynamite, it is thus sufficient to consider only all possible plane initiations, i.e. cases M1–M3 and their relevant reflections. By accumulating data from all such initiations, a worst-case pressure field can be calculated simply by using the pointwise maximum over all the initiations<sup>1</sup>. Such a worst-case pressure field is shown in Figure 8.

---

<sup>1</sup>Of course, the computed  $p_{\max}$  field for each case is itself a casewise worst case, as defined by Equation (12).



(a) Case L4.



(b) Case M1.

Figure 7: Snapshots at time  $t = 0.612$  ms of the  $xz$ -plane (with  $y = 0$ ), colored by a function of the density gradient,  $F(\rho)$ . Dark shading indicates higher gradients. The edges of the dynamite stack (real dimensions) are marked by blue, dashed lines.

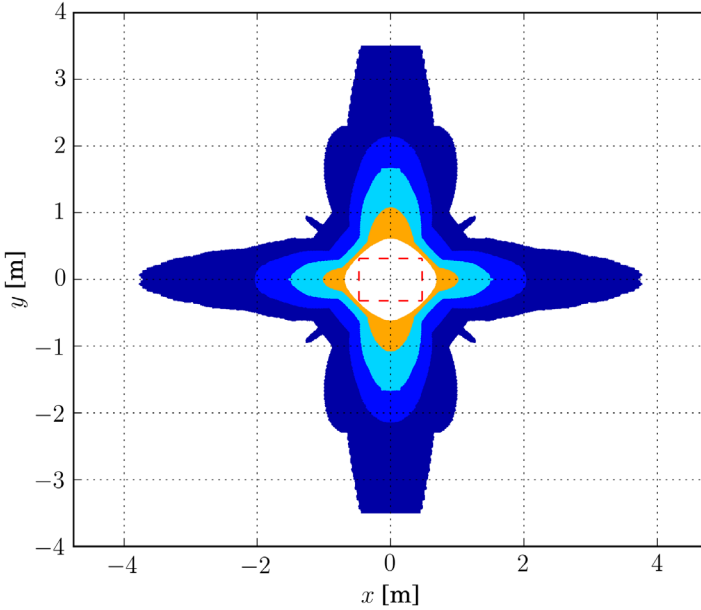


Figure 8: Contours in the  $xy$ -plane of the case-maximum of  $p_{\max}(x, y)$  for cases M1–M3 and their reflections. Contour levels increase by a factor two for each band and equal  $0.2 < p_{\max} < 0.4$  (dark blue),  $0.4 < p_{\max} < 0.8$  (blue),  $0.8 < p_{\max} < 1.6$  (turquoise) and  $1.6 < p_{\max} < 3.2$  (orange). The edges of the dynamite stack (real dimensions) are marked by red, dashed lines.

The contours in the figure are symmetric around the  $x$ - and  $y$ -axes, since plane initiations from all sides of the stack are included in the case-maximum. As seen earlier (in Figures 6 and 7), there are obvious corner effects in the pressure contours. The pressure quickly drops with distance, from more than 3 kbar (just outside of the stack) to less than 0.2 kbar (at around 3.5 m or less from the sides of the stack), consistent with previously shown data.

### 3.2.4 Discussion: Safety distances

The rationale for defining  $p_{\max}$  as a maximum up to stack height is as follows. Assuming a detonating stack in a storage of multiple stacks of equal height, it is only the pressure values occurring up to stack height that pose a risk to surrounding stacks. Potentially higher pressures above the level of the stack height is irrelevant. The definition of Equation (12) thus allows for the easy estimation of safety distances for storing multiple stacks alongside each other

If the sensitivity of a given explosive is known (e.g. based on gap-tests in air), it is thus trivial to estimate required safety distances based directly on the results of the previous section. Assuming the sensitivity of a hypothetical explosive to be, say, 0.4 kbar, a circular safety distance of 2.2 m can be determined based on Figure 8.

More useful information can also be extracted with regards to safety distances: It is clear from Figure 8 that the required safety distance is much larger in the directions perpendicularly from the sides of the stack than diagonally from the side edges. In the latter case, the required safety distance for the hypothetical explosive is merely 0.7 m. Hence, a staggered arrangement of stacks will allow for more compact storage without increasing the risk of sympathetic detonation.

Moreover, the simulation methodology presented in the above enables further testing of case-specific storage, such as effects of shock reflections from ceilings (for indoor storage), or quantitative investigations of clustered storage, in which several stacks are stored close together (allowing for a limited stack-to-stack propagation), but with correspondingly larger distances between stack clusters.

Note, however, that the pressure sensitivity of an explosive – if known – only constitutes one risk factor. Sensitivity to mechanical impacts, specifically from any solid fragments from nearby explosions, represents another real and considerable risk which has not been considered in the foregoing discussion.

## 4 Concluding remarks

A novel two-step approach to simulating detonations of explosives has been demonstrated, combining thermochemical calculations with gas-dynamical computations. The methodology allows for the simulated detonation of several different explosives and charge geometries, as well as subsequent shock interaction with surrounding structures, in up to three spatial dimensions.

The simulation methodology has been validated against earlier experimental and numerical work on TNT detonations. New TNT equivalencies have been computed for a selection of common commercial explosives.

Data has also been presented on simulated detonations of a stack of dynamite, using a variety of initiation locations, and resulting pressure fields and implied safety distances have been discussed.

For a detonating stack of dynamite, plane intitiations of the detonation generally yields the highest pressure levels. Furthermore, the pressures are significantly higher in the directions perpendicularly from the sides of the stack compared to the directions diagonally from the side edges of the stack. As expected, the pressure levels drop quickly with distance, from more than 3 kbar (just outside of the stack) to less than 0.2 kbar (at around 3.5 m or less from the sides of the stack).

The simulations and data processing demonstrated here can be easily used to determine required safety distances for storage of an explosive, given that empirical data on the pressure sensitivity of the explosive is available.

## Appendix

### A An indication of the mesh-resolution sensitivity

At this time, no rigorous study of the mesh-resolution sensitivity of the results has been carried out. Moreover, the effect of using first-order face-value reconstruction instead of the ENO scheme has not been evaluated, since this scheme was not stable for the three-dimensional simulations. These investigations will be included in future work.

That said, the comparison between case K2 (on a 26 million-cell mesh) and case L3 (on a 47 million-cell mesh) gives an important indication of the significance of the mesh resolution; as shown in Figure 9, the difference in pressure levels appear to be insignificant when comparing the high-resolution case to the low-resolution case.

More extensive studies should be carried out to ensure that also the *gradients* of pressure and density are well represented by the present choice of parameters. Furthermore, the differences might be more significant at higher pressure levels, such as if plane initiations or detonations of larger amounts of explosive were to be compared.

For now, however, it is tempting to conclude that the present choice of mesh resolution seems quite sufficient for the results which are the focus of this paper.

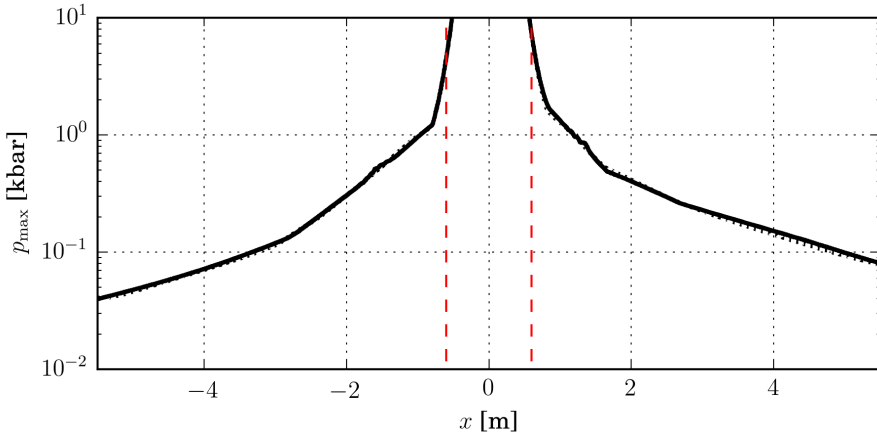


Figure 9: Maximum pressure,  $p_{\max}$ , as a function of  $x$ -distance (with  $y = 0$ ) from the center of the dynamite stack for cases K2 (—), and L3 (·····). The edges of the dynamite stack (real dimensions) are marked by vertical, red (dashed) lines.

## References

- [1] R. Jeremić and Z. Bajić, “An approach to determining the TNT equivalent of high explosives,” *Sci. Tech. Rev.*, vol. 56, no. 1, pp. 58–62, 2006.
- [2] R. Panowicz, M. Konarzewski, M. Trypolin, R. Panowicz, and M. K.-M. Trypolin, “Analysis of criteria for determining a TNT equivalent,” *Strojniški vestnik-Journal of Mechanical Engineering*, vol. 63, no. 11, pp. 666–672, 2017.
- [3] M. Sućeska, “Calculation of detonation parameters by EXPLO5 computer program,” in *Explosion, Shock Wave and Hypervelocity Phenomena in Materials*, vol. 465 of *Materials Science Forum*, pp. 325–330, Trans Tech Publications, 8 2004.
- [4] M. Sućeska, “EXPLO5 Version 6.02/2014 User’s Guide,” *OZM Research*, 2014.
- [5] G. Bres, Y. Khalighi, F. Ham, and S. Lele, “Unstructured large-eddy simulation technology for aeroacoustics of complex jet flows,” in *40th International Congress and Exposition on Noise Control Engineering (Inter-Noise 2011)*, Osaka, Japan, Sept, pp. 4–7, 2011.
- [6] Cascade Technologies Inc., *User’s and Developer’s Manual; Jefferson Release Version 4.1.0*, February 2014.

- [7] G. Dantzig, S. Johnson, and W. White, "A linear-programming approach to the chemical equilibrium problem," *Management Science*, vol. 5, no. 1, pp. 38–43, 1958.
- [8] S. Grys and W. A. Trzciński, "Thermodynamic modelling of processes of combustion, explosion, and detonation of non-ideal high energetic systems (in Polish)," *Biuletyn Wojskowej Akademii Technicznej*, vol. 59, no. 3, pp. 71–118, 2010.
- [9] G. Allaire, S. Clerc, and S. Kokh, "A five-equation model for the simulation of interfaces between compressible fluids," *Journal of Computational Physics*, vol. 181, pp. 577–616, Sep 2002.
- [10] E. F. Toro, M. Spruce, and W. Speares, "Restoration of the contact surface in the HLL-Riemann solver," *Shock waves*, vol. 4, no. 1, pp. 25–34, 1994.
- [11] J. H. S. Lee, *The Detonation Phenomenon*. Cambridge University Press, 2008.
- [12] A. Kuhl, "On the structure of self-similar detonation waves in TNT charges," *Combustion, Explosion, and Shock Waves*, vol. 51, no. 1, pp. 72–79, 2015.
- [13] J. Bdzil, D. S. Stewart, and T. L. Jackson, "Program-burn algorithms based on detonation shock dynamics: discrete approximations of detonation flows with discontinuous front models," *Journal of Computational Physics*, vol. 174, no. 2, pp. 870–902, 2001.
- [14] A. Kapila, J. B. Bdzil, and D. S. Stewart, "On the structure and accuracy of programmed burn," *Combustion Theory and Modelling*, vol. 10, no. 2, pp. 289–321, 2006.
- [15] H. Y. Grisaro and I. E. Edri, "Numerical investigation of explosive bare charge equivalent weight," *International Journal of Protective Structures*, vol. 8, no. 2, pp. 199–220, 2017.
- [16] C. N. Kingery and G. Bulmash, *Airblast parameters from TNT spherical air burst and hemispherical surface burst*. US Army Armament and Development Center, Ballistic Research Laboratory, 1984.





## USE OF THE FINITE VOLUME FRAMEWORK OPENFOAM FOR SIMULATION OF TUMOR GROWTH

KNUT ERIK TEIGEN GILJARHUS<sup>1</sup>, STEINAR EVJE<sup>2</sup>

<sup>1</sup>University of Stavanger  
PB 8600 Forus, 4036 Stavanger, Norway  
e-mail: knut.e.giljarhus@uis.no, web page: <http://www.ux.uis.no/~keg/>

<sup>2</sup>University of Stavanger  
PB 8600 Forus, 4036 Stavanger, Norway  
e-mail: steinar.evje@uis.no, web page: <http://www.ux.uis.no/~sevje/>

**Key words:** Computational Methods, Finite Volume, Tumor Growth, OpenFOAM

**Abstract.** We present implementations of tumor growth models in the open source finite volume framework OpenFOAM. Three different models are implemented, the Keller–Segel chemotaxis model, a haptotaxis model for cell invasion and the Chaplain–Lolas model for cell invasion. The implementation is shown to be straight-forward using the equation-mimicking interface of OpenFOAM. Numerical experiments indicate that with proper choices for discretization schemes and solvers, OpenFOAM is a suitable framework for studying tumor growth models.

### 1 INTRODUCTION

Cancer is the second leading cause of death globally, with close to 10 million deaths each year. The application of mathematical modelling to the study of tumor growth can lead to improved understanding of the underlying biological behavior and help design efficient treatment methods.

Tumor growth is a complex topic due to the many biological processes involved and the wide range of spatial and temporal scales. Models have been applied at various level of complexity to understand these processes. On the tissue scale, the tumor growth process often involves transport processes that lend themselves to formulations based on systems of conservation equations. Such models typically require numerical methods in order to compute reliable solutions, with the most common methods being the finite volume method and the finite element method. Particular care must be taken to ensure that the cell concentrations remain positive throughout the simulation. Negative values can be caused by numerical oscillations near steep gradients due to the discretization of the convective terms. Examples of the use of the finite volume method are found in e.g. [1], where they used a fractional-step method with high-resolution advection schemes, in [2], where they used a second-order, positivity preserving discretization scheme and in [3], where a higher-order scheme with a non-linear limiter was used. The finite element method was used in [4], where a Galerkin scheme with TVD flux limiting was used and in [5], where they applied a local discontinuous Galerkin method. Most previous work has been performed on uniform grids with simple geometries. A notable exception is [6] who used medical images to generate geometries for simulating breast tumor growth. They used a standard finite element method with triangular grid elements, since their mathematical model was a biomechanical model that did not include the numerically challenging convection terms.

In this work, we investigate the use of the OpenFOAM [7] software for tumor growth problems. OpenFOAM is an open source library for solving partial differential equations using the finite

volume method. The built-in applications and models are primarily intended for computational fluid dynamics, but the underlying library can be applied to any continuum mechanics problem. The potential benefits of using OpenFOAM are

- easy implementation of new models due to the equation-mimicking interface that tries to keep close correspondance between the equations and the solver code
- one implementation for 1D, 2D and 3D geometries
- wide range of discretization schemes and equation solvers to choose from
- support for polyhedral, unstructured meshes and built-in mesh generators
- efficient, parallelized code that scales to a large number of cores

Three different models are implemented and the results compared against results from the literature.

## 2 TUMOR GROWTH MODELS

### 2.1 Chemotaxis

Chemotaxis is the movement of a cell due to a gradient of a particular substance. This is an important process in many biological processes, such as cell pattern formation and cell aggregation. The most well-known mathematical model for this process is the Keller–Segel model [8–10]. This model can be written in a generic way as

$$u_t + \underbrace{\nabla \cdot (B(v)u\nabla v)}_{\text{chemotaxis}} = \underbrace{\nabla \cdot (D(u)\nabla u)}_{\text{cell motility}} + \underbrace{f(u)}_{\text{cell growth/death}} \quad (1)$$

$$v_t = \underbrace{\nabla \cdot (D(v)\nabla v)}_{\text{diffusion}} + \underbrace{g(u)u}_{\text{production}} - \underbrace{s(u)v}_{\text{decay}} \quad (2)$$

Here,  $u$  is the cell density and  $v$  is the chemoattractant. We see that chemotaxis term in the transport equation for the cell density is essentially a convection term where the gradient of the chemoattractant represents the velocity. Particular choices for the general functions  $D$ ,  $A$ ,  $B$ ,  $C$ ,  $q$ ,  $g$  and  $s$  yield specific models. In this work, we consider the following specific model, which was used in [1] to describe aggregating bacteria behavior,

$$u_t + \chi \nabla \cdot \left[ \frac{u}{(1+v)^2} \nabla v \right] = d_u \Delta u \quad (3)$$

$$v_t = \Delta v + w \frac{u^2}{1+u^2} - v \quad (4)$$

### 2.2 Haptotaxis

Haptotaxis is a similar process to chemotaxis, but for tumor growth haptotaxis can be understood as cell movement due to gradients of cellular adhesion sites. These gradients are naturally present in the extracellular matrix (ECM) of the body, which is considered to be stagnant, but can also be generated by the tumor by the production of an enzyme which degrades the ECM.

We consider the following specific model here [11],

$$u_t + \underbrace{\nabla \cdot (\chi u \nabla v)}_{\text{haptotaxis}} = \underbrace{d_u \Delta u}_{\text{cell motility}} - \underbrace{\Psi u}_{\text{cell death}} + \underbrace{\frac{2w}{1+w} u}_{\text{cell division}} \quad (5)$$

$$v_t = - \underbrace{\alpha m v}_{\text{degradation}} \quad (6)$$

$$m_t = \underbrace{d_m \Delta m}_{\text{diffusion}} + \underbrace{\delta u}_{\text{production}} - \underbrace{\beta m}_{\text{decay}} \quad (7)$$

$$w_t = \underbrace{d_w \Delta w}_{\text{diffusion}} + \underbrace{\gamma v}_{\text{production}} - \underbrace{\epsilon w}_{\text{decay}} - \underbrace{\eta w}_{\text{uptake}} \quad (8)$$

Here,  $u$  is the tumor cell density,  $v$  is the extracellular matrix density,  $m$  is the matrix-degradative enzyme concentration and  $w$  is the oxygen concentration. The remaining variables are model constants.

### 2.3 Chaplain-Lolas model

The final model considered is the model from [3], which is developed for modelling cancer cell invasion of tissue. The main element of the model is the inclusion of the urokinase plasminogen activation system (uPA), which is believed to be important for the regulation of tumor invasion. A full description of the model is beyond the scope of this work, but the full system of equations is as follows,

$$c_t = - \underbrace{d_c \Delta c}_{\text{cell motility}} + \nabla \cdot \left[ \underbrace{\chi_u c \nabla u}_{\text{uPA-chemo}} + \underbrace{\chi_p c \nabla p}_{\text{PAI-1-chemo}} + \underbrace{\chi_v c \nabla v}_{\text{VN-hapto}} \right] + \underbrace{\mu_1 c (1 - c)}_{\text{proliferation}} \quad (9)$$

$$v_t = - \underbrace{\delta v m}_{\text{degradation}} + \underbrace{\phi_{21} u p}_{\text{uPA/PAI-1}} - \underbrace{\phi_{22} v p}_{\text{PAI-1/VN}} + \underbrace{\mu_2 v (1 - v)}_{\text{remodelling}} \quad (10)$$

$$u_t = \underbrace{d_u \Delta u}_{\text{diffusion}} - \underbrace{\phi_{31} p u}_{\text{uPA/PAI-1}} - \underbrace{\phi_{33} c u}_{\text{uPA/uPAR}} + \underbrace{\alpha_{31} c}_{\text{production}} \quad (11)$$

$$p_t = \underbrace{d_p \Delta p}_{\text{diffusion}} - \underbrace{\phi_{41} p u}_{\text{PAI-1/uPA}} - \underbrace{\phi_{42} p v}_{\text{PAI-1/VN}} + \underbrace{\alpha_{41} m}_{\text{production}} \quad (12)$$

$$m_t = \underbrace{d_m \Delta m}_{\text{diffusion}} + \underbrace{\phi_{52} p v}_{\text{PAI-1/VN}} + \underbrace{\phi_{53} c u}_{\text{uPA/uPAR}} - \underbrace{\phi_{54} m}_{\text{degradation}} \quad (13)$$

$$(14)$$

Here,  $c$  is the cancer cell density,  $v$  is the ECM density,  $u$  is the uPA concentration,  $p$  is the PAI-1 concentration and  $m$  is the plasmin concentration. The remaining variables are model constants, a full description can be found in [3]. We see that the cancer cell density equation contains both two chemotaxis terms and one haptotaxis term. Also, the source terms in the equations are both coupled and non-linear.

## 3 IMPLEMENTATION IN OPENFOAM

OpenFOAM is built for solving continuum mechanics problems using the finite volume method [7]. It is implemented using object-oriented techniques in C++, and the underlying idea is to have close to 1:1 mapping between the partial differential equations and the source code.

For instance, the solution of the cell concentration equation of the Keller-Segel system, Equation 1, is done by the source code shown in Figure 1. The `fvm` namespace contains implicit methods,

---

```

phi = fvc::snGrad(v)*mesh.magSf()*fvc::interpolate(model.B(v));
solve
(
    fvm::ddt(u)
    ==
    fvm::laplacian(model.Du(), u)
    - fvm::div(phi, u)
    + fvm::Sp(model.f(u), u)
);

```

---

Figure 1: C++ source code for solving the cell concentration equation in OpenFOAM

which means that each function returns a sparse matrix with the finite volume operator applied to the supplied field. The `fvc` namespace contains explicit methods, which returns a new field with the operator applied directly. The specific discretization scheme to use for each operator is selected at run-time.

Of particular interest is the convective term, since this is numerically the most challenging aspect of the models. In the finite volume method, this is treated as

$$\int_V \nabla \cdot (B(v)u \nabla v) dV = \sum_f \mathbf{S}_f \cdot (\nabla v)_f B(v)_f u_f, \quad (15)$$

where  $V$  represents the cell volume,  $f$  denotes a cell face and  $\mathbf{S}_f$  is the cell surface vector, which points in the normal direction with magnitude equal to the cell face area.

OpenFOAM uses a polyhedral mesh with co-located variables, meaning all variables are stored in the cell centres. The `fvm::div` operator takes  $\phi_f$  as input, i.e. a field stored at the cell faces. To calculate this, we apply the `fvc::snGrad` operator to the  $v$  field, which calculates the surface normal gradient on the cell faces. The `mesh.magSf` function returns the cell surface area, while the `fvc::interpolate` function interpolates a field from the cell centre to the cell faces. This is typically done using linear interpolation, but other schemes are also available. For the divergence operator, multiple discretization schemes are available. In this work, best results were obtained using the `limitedLinear` scheme. This is a second-order central-upwind scheme which is total variation diminishing, using the Sweby limiter [12, 13].

The source term is linearized by lagging the  $f(u)$  function, and then treated in an implicit manner, which is handled automatically by the `fvm::Sp` function. Note that this is a crude way of handling the source term and could lead to problems with stiff source terms.

As seen in Figure 1, the implementation in OpenFOAM also takes advantage of object-orientated features in the C++ programming language. The solver is implemented for the generic Keller-Segel model. Specific submodels are then implemented by subclassing the Keller-Segel model base class and supplying the functions required by the general model. This allows the solver to only be implemented once, and new models can be added by just specifying these functions.

For time discretization, the Crank-Nicolson scheme is used. The linear equation systems arising from the discretization are solved with an algebraic multigrid solver.

## 4 RESULTS

### 4.1 Chemotaxis

For testing the implementation of the Keller-Segel model from Equation 4, we consider a cubic 3D domain  $\Omega = [0, 8]^3$  with homogeneous Neumann boundary conditions on  $\partial\Omega$ . The parameters

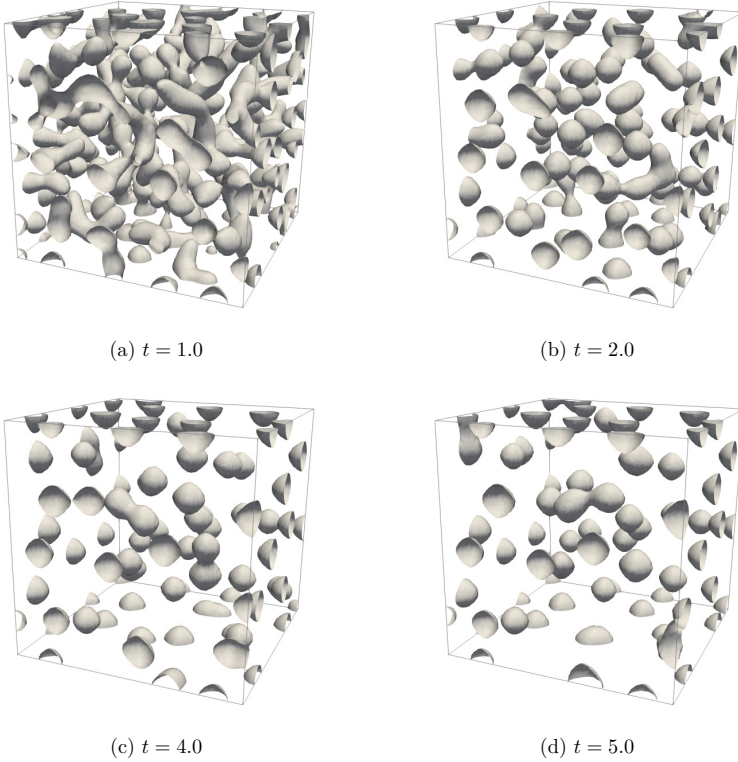


Figure 2: Time evolution of bacteria concentration for Keller-Segel model. Contour plot of  $u = 0.9$ .

of the model are chosen as  $d_u = 1$ ,  $\chi = 80$  and  $w = 1$ . The initial conditions are set to

$$u_0 = 0.9 + 0.2 \cdot \text{random}[0, 1] \quad (16)$$

$$v_0 = 0 \quad (17)$$

Here, the random function returns a random float between 0 and 1. The domain is divided into uniform cells with size  $h = 0.1$  and the time step is set to  $\Delta t = 0.01$ .

Figure 2 shows the time evolution of the bacteria concentration by visualizing the contour field with value 1. We see that the initially randomly distributed bacteria gather into spherical clusters. The concentrations inside these clusters continue to grow with time. These results are in good agreement with results presented in [4] using a TVD finite element method. No negative cell concentrations were observed in the results.

## 4.2 Haptotaxis

For testing the implementation of the haptotaxis model, we consider a square 2D domain  $\Omega = [0, 6]^2$  with homogeneous Neumann boundary conditions on  $\partial\Omega$ . The parameters of the model are chosen as  $d_u = d_w = d_m = 0.01$ ,  $\chi = 0.4$ ,  $\Psi = 1.0$ ,  $\delta = 1.0$ ,  $\beta = 0.01$ ,  $\alpha = 5.0$ ,  $\gamma = 5.0$  and  $\eta = 1.0$ .

The initial conditions are set to

$$u_0 = 5 \max[0.3 - (x - 3)^2 - (y - 3)^2, 0], \quad (18)$$

$$v_0 = 0.05 \cos\left((10\pi/36)x^2\right) \sin\left((13\pi/72)y^2\right) + 0.3, \quad (19)$$

$$m_0 = u_0, \quad (20)$$

$$w_0 = 4v_0. \quad (21)$$

The domain is divided into uniform cells with size  $h = 0.01$  and the time step is set to  $\Delta t = 0.001$ .

Figure 3 shows the time evolution of the tumor cell concentration. The degradation of the ECM due to the matrix-degenerative enzyme leads to a large gradient, which in turn makes the tumor cells propagate outwards. The fluctuations in the density are caused by the initial variation in the ECM density and oxygen concentration, with higher variation in the upper right corner compared to the lower left. The results are in good agreement with the results presented in [11].

### 4.3 Chaplain–Lolas model

For testing the Chaplain–Lolas model from Equation 14, we consider a square 2D domain  $\Omega = [0, 5]^2$  with homogeneous Neumann boundary conditions on  $\delta\Omega$ . In the top 20 % of the domain, the following values are used as initial conditions:  $c = 0$ ,  $v = 0$ ,  $u = 0.5$ ,  $p = 0.05$ ,  $m = 0$ . The ECM density is correspondingly set to  $v = 1$  in the remainder of the domain, with the rest of the fields set to 0. The remaining values for the parameters of the model can be found in [3].

Figure 4 shows the evolved cancer cell density and ECM density after  $t = 200$ . The model exhibits a complex behavior, with cancer cells invading the domain in a heterogeneous and fragmented pattern. The ECM density is correspondingly heterogeneous with severe degradation. The results are in good agreement with the numerical results from [3].

## 5 CONCLUSIONS

This work investigated the implementation of various models relevant to tumor growth modelling in the finite-volume framework OpenFOAM. The implementation of the models was shown to be straight-forward, utilizing the equation-mimicking interface of OpenFOAM. Simulations of test cases from the literature were performed, and the results were in good agreement with results obtained with other numerical methods.

Future work will be implementation of further models, of particular interest are models taking into account the multiphase fluid dynamic behavior such as the model developed in [14]. The present study only considered simple geometries with uniform meshes, future work will also test the implementation on more complex geometries arising from medical imaging, such as [6]. Additionally, other numerical schemes such as the high-resolution Kurganov–Tadmor schemes [15] could be interesting to apply for further accuracy and stability. These schemes were used for tumor growth modelling in [2]. An implementation of these schemes is already available in OpenFOAM for compressible flow modelling in the `rhoCentralFoam` solver, and these could be adapted to the models used in this work. Finally, a more rigorous study of the convergence behavior of the implementation should be performed.

## REFERENCES

- [1] R. Tyson, L. Stern, R. J. LeVeque, Fractional step methods applied to a chemotaxis model, *Journal of mathematical biology* (2000) 455–475.
- [2] A. Chertock, A. Kurganov, A second-order positivity preserving central-upwind scheme for chemotaxis and haptotaxis models, *Numerische Mathematik* (2008) 169.

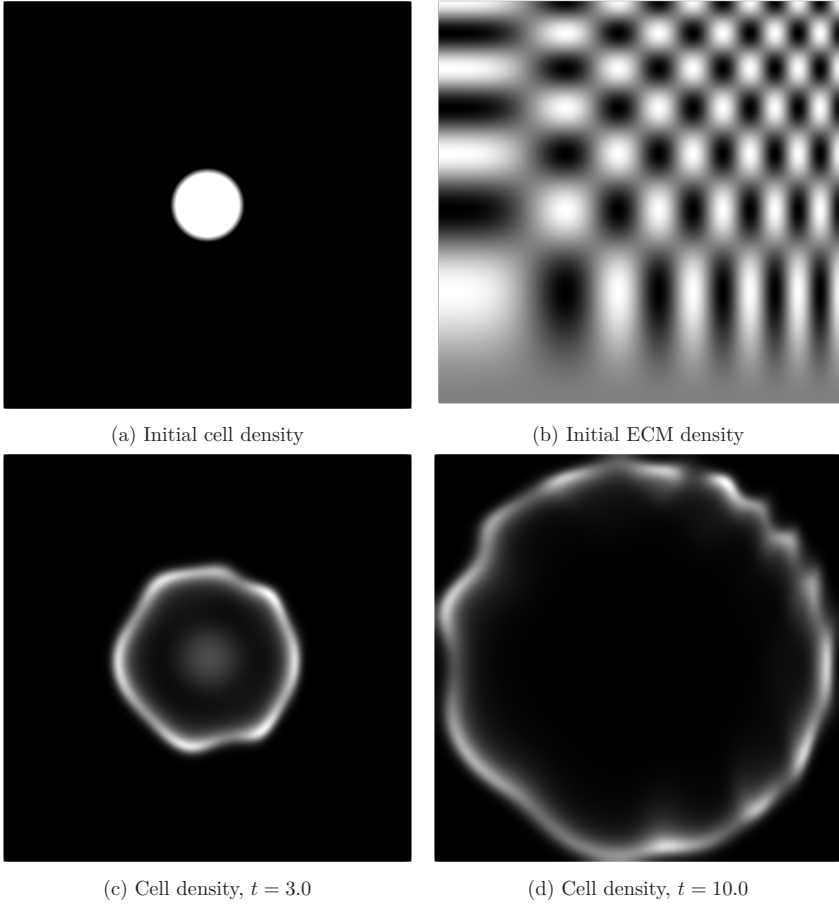
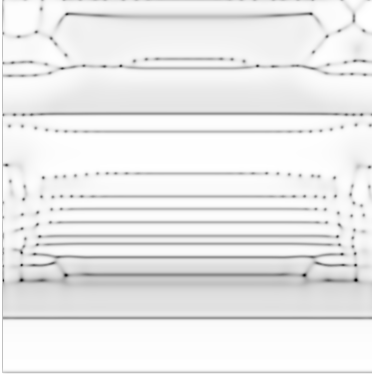
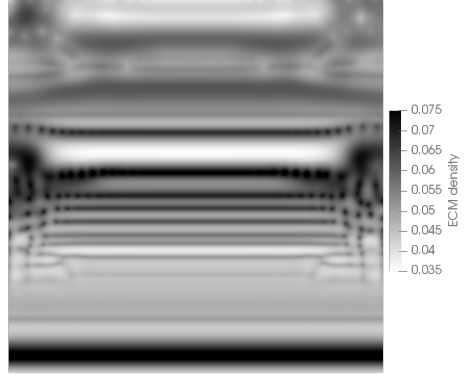


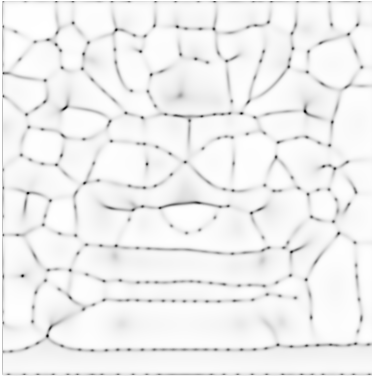
Figure 3: Time evolution of cell concentration for haptotaxis model.



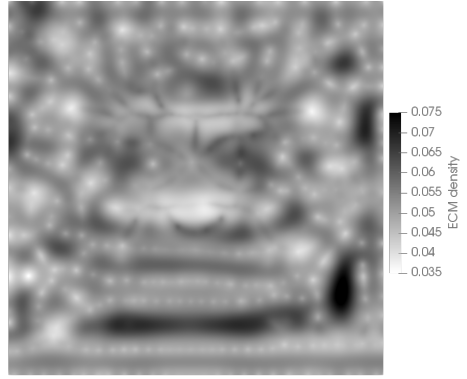
(a) Cell density,  $t = 100.0$



(b) ECM density,  $t = 100.0$



(c) Cell density,  $t = 200.0$



(d) ECM density,  $t = 200.0$

Figure 4: Time evolution of cell density (left) and ECM density (right) for Chaplain-Lolas model.



- [3] V. Andasari, A. Gerisch, G. Lolas, A. South, M. Chaplain, Mathematical modeling of cancer cell invasion of tissue: biological insight from mathematical analysis and computational simulation, *Journal of Mathematical Biology* (2011) 141–171.
- [4] R. Strehl, A. Sokolov, D. Kuzmin, D. Horstmann, S. Turek, A positivity-preserving finite element method for chemotaxis problems in 3d, *Journal of Computational and Applied Mathematics* (2013) 290–303.
- [5] L. Guo, X. H. Li, Y. Yang, Energy dissipative local discontinuous galerkin methods for keller–segel chemotaxis model, *Journal of Scientific Computing* (2019) 1387–1404. doi:10.1007/s10915-018-0813-8.  
URL <https://doi.org/10.1007/s10915-018-0813-8>
- [6] J. A. Weis, M. I. Miga, T. E. Yankeelov, Three-dimensional image-based mechanical modeling for predicting the response of breast cancer to neoadjuvant therapy, *Computer methods in applied mechanics and engineering* (2017) 494–512.
- [7] H. G. Weller, G. Tabor, H. Jasak, C. Fureby, A tensorial approach to computational continuum mechanics using object-oriented techniques, *Computers in physics* (1998) 620–631.
- [8] E. F. Keller, L. A. Segel, Initiation of slime mold aggregation viewed as an instability, *Journal of Theoretical Biology* (1970) 399–415.
- [9] D. Horstmann, From 1970 until present : the Keller-Segel model in chemotaxis and its consequences I., *Jahresbericht der Deutschen Mathematiker-Vereinigung* (2003) 103–165.
- [10] T. Hillen, K. J. Painter, A user’s guide to pde models for chemotaxis, *Journal of Mathematical Biology* (2009) 183.
- [11] C. Walker, G. F. Webb, Global existence of classical solutions for a haptotaxis model, *SIAM Journal on Mathematical Analysis* (2007) 1694–1713.
- [12] P. K. Sweby, High resolution schemes using flux limiters for hyperbolic conservation laws, *SIAM Journal on Numerical Analysis* (1984) 995–1011.
- [13] H. Jasak, Error analysis and estimation for the finite volume method with applications to fluid flows., Ph.D. thesis, Imperial College London (University of London) (1996).
- [14] S. Evje, An integrative multiphase model for cancer cell migration under influence of physical cues from the microenvironment, *Chemical Engineering Science* (2017) 240–259.
- [15] A. Kurganov, E. Tadmor, New high-resolution central schemes for nonlinear conservation laws and convection–diffusion equations, *Journal of Computational Physics* (2000) 241–282.



## SIMULATION OF BLAST-LOADED ALUMINIUM PLATES WITH CRACK-LIKE DEFECTS

Henrik Granum<sup>1</sup>, David Morin<sup>1,2</sup>, Tore Børvik<sup>1,2</sup>, Odd Sture Hopperstad<sup>1,2</sup>

<sup>1</sup>Structural Impact Laboratory (SIMLab), Department of Structural Engineering, Norwegian University of Science and Technology (NTNU), Trondheim, Norway

<sup>2</sup>Centre for Advanced Structural Analysis (CASA), NTNU, Trondheim, Norway

**Key words:** Computational mechanics, Shell elements, Ductile failure, Through-thickness regularization

**Abstract.** This paper presents a numerical study on the response of blast-loaded AA6016 T4 aluminium plates with crack-like defects. Explicit finite element simulations were performed with LS-DYNA, using an uncoupled plasticity and fracture model with through-thickness damage regularization valid for shell elements. Uniaxial tensile tests are used to determine the parameters of the constitutive model by inverse modelling. Four different crack-like defects are considered at a load level resulting in failure and crack propagation in all the plates. The simulation results obtained with different mesh sizes are evaluated against experiments conducted in a shock tube facility. The shell element model is able to predict failure and crack propagation with good accuracy for the finest mesh, i.e., shell elements with length-to-thickness ratio of 1/3, while the accuracy decreases rapidly as the mesh size is increased.

### 1 INTRODUCTION

When modelling structural problems using the finite element method (FEM), shell elements have been the standard in industrial applications due to their superior computational efficiency compared to solid elements. They benefit from a versatile formulation and are especially suitable for structures where two dimensions are much larger than the third one. Even though shell elements provide good results in the elastic and plastic domains, predicting failure and crack propagation has always been a challenge. Local necking is often a precursor to failure in thin-walled structures. In the necking process, the local stress state of the plate changes from plane stress to a three-dimensional stress state. Computationally efficient simulations often require large element sizes, which makes it difficult to capture strain localization. This is due to the local characteristic of a necking process, where a coarse spatial discretization in a simulation will even out the strain gradients. To overcome the aforementioned problems, different empirical relationships have

been proposed in an attempt to couple the failure strain to the element size. However, many of the proposed regularization models are limited to membrane loading. This is a problem due to the lower ductility exhibited by a plate in stretching compared to bending, linked to the local neck which is formed in a membrane dominated problem. To account for this challenge, the damage evolution due to stretching and bending should be accounted for in problems involving combined loading actions. The uncoupled plasticity and fracture model used in this study was proposed by Costas et al. [1] and comprises a through-thickness damage regularization scheme valid for shell elements. The model has been validated against experiments on a two-chamber extruded profile of the aluminium alloy AA6005 T6 subjected to quasi-static and dynamic axial crushing and quasi-static three-point bending. The results showed that the model was able to predict failure in tests involving both local necking and severe bending of the material. The mesh sensitivity was found to be reduced with the proposed scheme, providing a more realistic prediction of the local necking. The simple calibration of the model from a single tensile test using two-dimensional digital image correlation (2D-DIC) and inverse modelling makes it suitable for industrial applications.

Numerical simulations of ductile failure using shell elements have been presented in a number of studies (see e.g. [2, 3, 4]). Woelke et al. [5] investigated an idealized ship grounding scenario where both phenomenological damage and cohesive zone models for ductile failure were evaluated. Stiffened and unstiffened steel plates, where the loading was dominated by biaxial stretching, were considered. Both models were able to reproduce the experimentally observed behaviour, despite the differences between them. Pack and Mohr [6] proposed the concept of Domain of Shell-to-Solid Equivalence (DSSE) to account for the onset of localized necking with shell elements. Marciniak-Kuczynski type of localization analyses were used in the calibration of the model and combined with the Hosford-Coulomb fracture initiation model. The proposed model was validated against five different tests on DP780 steel, and the displacement at fracture was successfully predicted in all the tests. The authors emphasized that the DSSE concept should be confined to the domain where the plane-stress assumption of the shell element solution is meaningful. Morin et al. [7] investigated the behaviour and failure of stiffened aluminium panels subjected to quasi-static and low-velocity impact loading conditions. A regularized failure criterion was employed and the effect of mesh size was investigated. The numerical results showed a good correlation with the experiments for the fine meshes, while the larger meshes failed to initiate and propagate cracks as observed in the experiments. The mesh dependence was reduced by employing the regularization model, where five different length-to-thickness ratios were employed.

Blast-loaded aluminium plates with crack-like defects presented in [8] are investigated numerically in this study. This is done using an uncoupled plasticity and fracture model with through-thickness damage regularization. A simplified finite element model of the blast test set-up is made with shell elements, and the numerical results are evaluated against blast tests conducted in a shock tube facility on 1.5 mm thick AA6016 T4 plates

with four different configurations of crack-like defects. The effect of varying the mesh size is investigated, where the in-plane dimensions of the elements varied from 1/3 to 5 times the thickness of the plate.

## 2 MATERIAL AND EXPERIMENTAL WORK

The material considered in this study is the aluminium alloy AA6016 in temper T4, which is an Al-Mg-Si alloy often used in the automotive industry. The material was delivered as 1.5 mm thick sheets with in-plane dimensions 625 mm  $\times$  625 mm by Hydro Aluminium Rolled Products in Bonn, Germany. The chemical composition of the alloy as provided by the supplier is given in Table 1.

**Table 1:** Chemical composition of AA6016 in wt%.

Si	Mg	Fe	Cu	Mn	Cr	Zn	Ti	Al
1.3160	0.3490	0.1617	0.0081	0.0702	0.0025	0.0084	0.0175	Balance

Uniaxial tensile tests were carried out on specimens with tensile axis at 0°, 45° and 90° to the rolling direction of the sheet, see Granum et al. [8]. The tests revealed a slight difference in elongation to failure with the tensile direction and minor scatter was observed between the repeat tests. The flow stress was practically independent of the tensile direction. In contrast, the Lankford coefficient, defined as the ratio of the plastic strain in the width direction to that in the thickness direction, was consistently higher in the rolling direction than in the other two directions, but always less than unity. The material exhibits a moderate plastic anisotropy, where the tendency for thinning is stronger than for an isotropic material.

The blast tests were conducted in the SIMLab Shock Tube Facility at NTNU [9]. The test program, setup and experimental results are presented in Granum et al. [8], and the reader is referred to this article for details. In total, four different initial defect geometries were tested with peak pressure at impact of the blast wave approximately equal to 600 kPa. The clamping of the plate in the shock tube and the different plate configurations are shown in Figure 1, where each plate configuration is given an abbreviation on the form X-Y, where X is the number of defects and Y indicates the orientation of the defect(s). These abbreviations are used in the rest of this study. The defects were cut with wire erosion as thin slits with an approximate width of 0.1 mm. The blast event was recorded by two synchronized Phantom v1610 high-speed cameras positioned in a stereovision setup, recording at 24 000 fps with an image resolution of 768  $\times$  800 pixels.

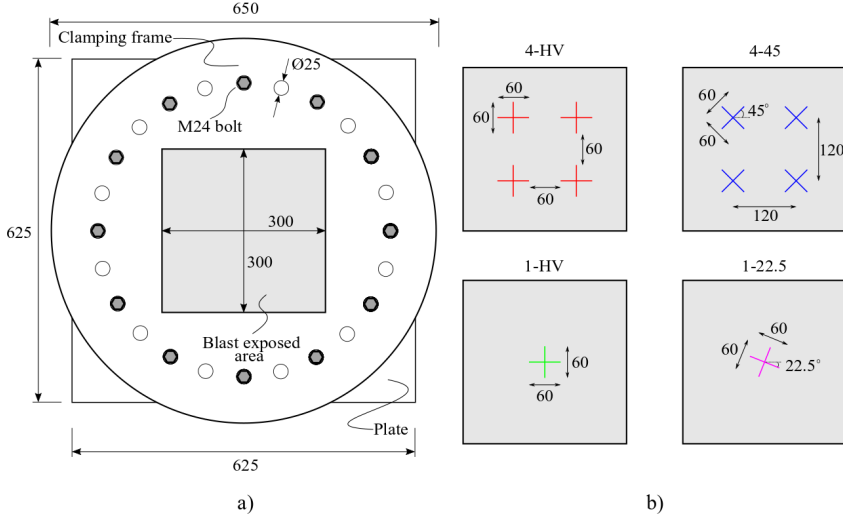


**Figure 1:** Sketch of a) plate and clamping frame, and b) blast exposed area of the plates depicting the four different initial defect geometries. Measurements are in mm.

### 3 MATERIAL MODELLING

#### 3.1 Constitutive model

Even though the plate material exhibits moderate plastic anisotropy, the assumption of isotropic material behaviour was employed for simplicity in the constitutive modelling. The yield surface was defined by the high-exponent Hershey-Hosford yield function [10, 11], which has been shown to be suitable for isotropic Face Centered Cubic (FCC) and Body Centered Cubic (BCC) materials. The yield surface is expressed as

$$f = \varphi(\boldsymbol{\sigma}) - (\sigma_0 + R) = 0 \quad (1)$$

where  $\varphi$  is the equivalent stress,  $\boldsymbol{\sigma}$  is the stress tensor,  $\sigma_0$  is the initial yield stress and  $R$  is the isotropic hardening variable. A rate-independent formulation was selected due to the low rate sensitivity reported for 6000-series aluminium alloys [12]. Also the temperature dependence was omitted, as this proved to give negligible differences in the results [8]. The Hershey-Hosford equivalent stress is expressed as

$$\varphi(\boldsymbol{\sigma}) = \left[ \frac{1}{2} (|\sigma_1 - \sigma_2|^m + |\sigma_2 - \sigma_3|^m + |\sigma_3 - \sigma_1|^m) \right]^{\frac{1}{m}} \quad (2)$$

where  $\sigma_1$ ,  $\sigma_2$  and  $\sigma_3$  are the principal stresses and  $m$  is a parameter controlling the curvature of the yield surface. Studies on FCC materials like aluminium alloys suggest

to set  $m$  equal to 8, based on polycrystal plasticity calculations [13]. This value was adopted without further investigation in this study. The hardening variable is given by the extended Voce hardening rule on the form

$$R(p) = \sum_{i=1}^3 R_i(p) = \sum_{i=1}^3 Q_i(1 - \exp(-C_i p)) \quad (3)$$

where  $R_i$  are hardening terms that saturate at different levels of equivalent plastic strain  $p$ , and  $Q_i$  and  $C_i$  represent the saturation value and the rate of saturation of the hardening term  $R_i$ , respectively.

### 3.2 Failure model

Failure was modelled by the Cockcroft-Latham failure criterion [14]. Accordingly, the damage variable  $D$  is defined as

$$D = \frac{1}{W_C} \int \langle \sigma_I \rangle dp \leq 1 \quad (4)$$

where  $W_C$  is the fracture parameter,  $\sigma_I$  is the major principal stress and  $\langle \cdot \rangle$  are the Macaulay brackets, defined as  $\langle \sigma_I \rangle = \frac{1}{2}(|\sigma_I| + \sigma_I)$ . The failure criterion has been modified as proposed by Costas et al. [1] where the fracture parameter  $W_C$  is divided into two parts responsible for pure membrane loading and pure bending. The reader is referred to Costas et al. [1] for a detailed description of the modified failure criterion. The fracture parameter  $W_C^b$  governing pure bending is retrieved from a finite element simulation of a tensile test using a fine solid element mesh. By conducting similar simulations with shell elements, the fracture parameter governing membrane loading  $W_C^m$  is obtained for a range of element sizes. The influence of element size is then included by making  $W_C^m$  a function of the element's aspect ratio  $l_e/t_e$ , where  $l_e$  is the element length and  $t_e$  is the initial thickness of the plate [7]

$$W_C^m = W_C^l + (W_C^s - W_C^l) \cdot \exp\left(-c \cdot \left(\frac{l_e}{t_e} - 1\right)\right) \quad (5)$$

where  $W_C^l$  is the fracture parameter for large shell elements,  $W_C^s$  is the fracture parameter for an element with aspect ratio equal to unity, and  $c$  is a model parameter. In elements subjected to combined membrane loading and bending, the fracture parameter is calculated as

$$W_C = \Omega W_C^b + (1 - \Omega) W_C^m \quad (6)$$

where  $\Omega$  is a deformation mode indicator determining the relative amount of membrane loading and bending an element is subjected to. The deformation mode indicator is defined by the through-thickness plastic strain as

$$\Omega = \frac{1}{2} \frac{|\varepsilon_{p,33}^T - \varepsilon_{p,33}^B|}{\max\{|\varepsilon_{p,33}^T|, |\varepsilon_{p,33}^B|\}} \quad (7)$$

where  $\varepsilon_{p,33}^T$  and  $\varepsilon_{p,33}^B$  are the through-thickness plastic strains at the top and bottom integration point of the shell element, respectively. This gives  $\Omega = 1$  for pure bending and  $\Omega = 0$  for pure membrane loading.

### 3.3 Parameter identification

The yield stress  $\sigma_0$  and the hardening parameters  $Q_i$  and  $C_i$  were calibrated based on a representative tensile test in the rolling direction of the sheet. An initial estimate of the hardening parameters was obtained in a spreadsheet, using the true stress-strain curve up to necking. A finite element model of the tensile test was made in Abaqus/Standard, where only 1/8 of the specimen was modelled, assuming isotropic material behaviour. The gauge section was modelled with solid elements with characteristic element size of 0.15 mm, resulting in 10 elements over the thickness. Reduced integration with hourglass control was employed. An extensometer of length 50 mm was used to extract displacements from the simulation, coinciding with the virtual extensometer used to extract displacements from the DIC. Inverse modelling by use of the optimization tool LS-OPT was used to improve the accuracy of the hardening parameters, where sequential simulations on the same model with different values of the hardening parameters were conducted. The engineering stress-strain curve obtained from the test was used as the target curve, and the mean squared error between the target curve and the simulated curve was calculated and used in the optimization. The result of the optimization is shown in Figure 2 a) in terms of the force-displacement curves from the representative tests and the simulation, where the marker illustrates the assumed point of failure in the simulation. The figure demonstrates good agreement between the experiments and the simulation all the way to failure. The equivalent stress-equivalent plastic strain curve from the experiment is plotted up to necking in Figure 2 b) together with the calibrated flow stress curve. The moderate anisotropy exhibited by the material suggests that the fit may not be as good when plotted against test data in the other tensile directions.

The calibrated material parameters for the extended Voce hardening rule are presented in Table 2. The elastic material properties were taken as standard values for aluminium: Young's modulus  $E = 70000$  MPa and Poisson's ratio  $\nu = 0.3$ . The failure parameter governing bending  $W_C^b$  was obtained from a simulation using a fine solid element mesh and estimated to  $W_C^b = 245.2$  MPa. In Costas et al. [1], the failure parameter governing membrane loading  $W_C^m$  was obtained by use of a virtual extensometer to extract DIC measurements at different length-to-thickness ratios  $l_e/t_e$  of a uniaxial tensile test. In this study,  $W_C^m$  was found by use of a finite element simulation of the uniaxial tensile test with a refined solid element mesh. Vectors of different length  $l_e$  spanned across the neck were used to extract elongations. These elongations were then applied as boundary conditions



to a single shell element simulation with the same element size  $l_e$  until the point where fracture occurred in the test. The fracture parameters  $W_C^m$  for the different element sizes  $l_e$  were found by numerical integration. The obtained fracture parameters then served as discrete points which Equation (5) was curve fitted to, where the optimized parameters came out as  $W_C^l = 79.1$  MPa,  $W_C^s = 116.1$  MPa and  $c = 0.36$ .

**Table 2:** Parameters for the extended Voce hardening rule for AA6016 T4.

$\sigma_0$	$Q_1$	$C_1$	$Q_2$	$C_2$	$Q_3$	$C_3$
[MPa]	[MPa]		[MPa]		[MPa]	
112.5	78.6	32.80	109.8	4.9	325.7	0.5

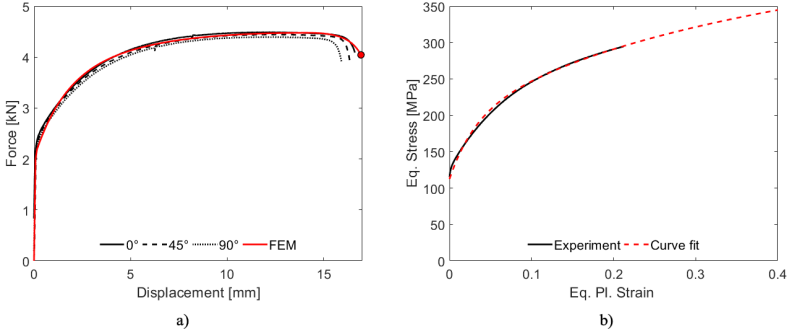


**Figure 2:** a) Force-displacement curves from representative tests in each direction together with the curve from the calibrated FE model, and b) experimental and calibrated flow stress curves in terms of the equivalent stress and equivalent plastic strain.

## 4 NUMERICAL RESULTS

### 4.1 Finite element model

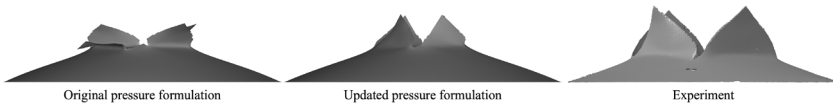
The numerical simulations of the blast-loaded plates were conducted in the explicit solver of LS-DYNA. The edge of the plate was fixed in an attempt to mimic the effect of the clamping frames in the test setup. Shell elements with reduced integration and five integration points through the thickness were used, denoted type 2 in LS-DYNA. This is a Belytschko-Lin-Tsay shell formulation which is based on the Reissner-Mindlin kinematic assumption [15]. Four different length-to-thickness ratios of the shell elements were used in the model ( $l_e/t_e = 1/3, 1, 3, 5$ ). A sweep meshing technique was used to

obtain a random mesh, resulting in approximately 450 000 elements for  $l_e/t_e$  equal to 1/3 and below 2000 elements for  $l_e/t_e$  equal to 5. The slits were modelled star shaped, resulting in a single node at each slit end to simplify the meshing of the plate.

The blast load was obtained from blast tests on a massive steel plate, where pressure sensors mounted directly on the plate recorded the loading [9], and applied to the AA6016 T4 plates as a tabulated uniform pressure-time curve. In addition to the built-in pressure definition in LS-DYNA, a user-defined subroutine was employed where the magnitude of the applied pressure was multiplied by the cosine of the angle between the initial load direction and the normal of the shell element. This allowed the pressure to "slide off" as the plate deformed, preventing situations where the pressure pointed in the opposite direction of the initial pressure load. Failure was handled by element erosion, where the stress tensor is set to zero in all integration points when the damage variable  $D$  is equal to unity in two integration points on either side of the mid through-thickness integration point.

## 4.2 Results and discussion

The effect of updating the pressure magnitude as described above in the simulations was significant for some defect geometries. In Figure 3, this effect is shown for the 1-HV configuration with  $l_e/t_e$  equal to 1. The "flaps" in the simulation with the original pressure formulation have folded considerably and the pressure on the flaps is pointing in the opposite direction of the initial loading direction in the last part of the simulation due to the Lagrangian description of the loading. In the simulation with the updated pressure formulation, the pressure "slides off" as the flaps deform in a petal mode, i.e., the pressure is reduced with the rotation of the shell normal. By comparing the two approaches to the corresponding experiment also shown in the figure, it is concluded that the correct behaviour is somewhere in-between the two approaches, yet much closer to the updated pressure formulation. However, to properly account for fluid-structure interactions, coupled Eulerian-Lagrangian simulations are needed, increasing the complexity and computational cost of the simulations significantly.



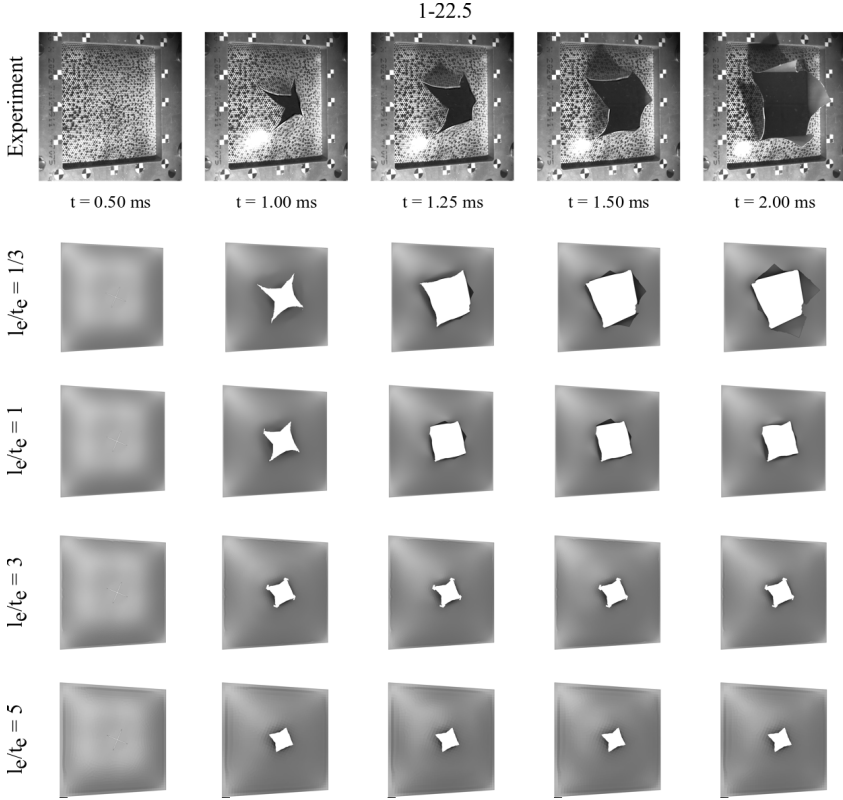
**Figure 3:** The effect of the two pressure formulations on a plate with a slit oriented along the plate axis compared to the corresponding experiment.

Image series comparing the 1-22.5 simulations to the experiment are shown in Figure 4 at selected points in time, where  $t = 0$  indicates the time of impact of the blast load. Similar trends were seen for the other geometries and they are omitted for brevity. In the

experiment, cracks propagate from the slit ends towards the corner of the plate and the flaps deform in a petal mode. As expected, the discretization of the mesh is important when modelling failure and crack propagation. For a length-to-thickness ratio  $l_e/t_e = 5$ , no failure or cracking is seen as the flaps just deform in a petal mode. The plastic zones in front of the slit ends are smeared out over the coarse elements, preventing the failure criterion to be triggered. In the simulation with  $l_e/t_e = 3$ , the overall response is similar to the coarsest model. However, failure initiation is predicted, but the mesh discretization is not fine enough for the cracks to propagate. Failure of two elements in front of each slit end resulted in a substantial increase in the crack width and led to the sudden arrest of the crack. First in the simulation with  $l_e/t_e = 1$  crack propagation is predicted, where the experimental behaviour up to  $t = 1.00$  ms is accurately recreated. The cracks are arrested at  $t = 1.25$  ms and the flaps fold in a petal mode. Further reduction of the length-to-thickness ratio to  $l_e/t_e = 1/3$  proved to enhance the results even more. Shell elements with smaller in-plane dimension than the thickness are usually not recommended and the results should be evaluated carefully. However, the smaller in-plane element size makes the width of the crack narrower when an element is eroded, which is advantageous for the crack to propagate. Eventually, the cracks are arrested slightly prematurely compared to the experiment, but the agreement up to  $t = 1.50$  ms is deemed good.

The last frame from the four 1-22.5 simulations is shown from the side in Figure 5. From the figure it is evident that the global displacement is predicted equally well in the simulations with  $l_e/t_e = 5$  and  $l_e/t_e = 1$ . Even though the amount of crack propagation varies between these simulation, the final shape of the plates is almost identical. However, in the simulation with  $l_e/t_e = 1/3$ , the flaps have folded considerably and there is a significant opening of the plate. As seen from the image series in Figure 4, this simulation gives the most accurate failure mode when compared to the experiment.

The simulations with the different length-to-thickness ratios are compared to the experiments at  $t = 2.0$  ms in Figure 6. The simulations with  $l_e/t_e = 5$  are not able to capture failure in any of the four configurations due to the coarse discretization. Contour plot of the damage variable  $D$  shows that  $D = 0.76$  in the most critical element, substantiating the difficulty to capture localization of plastic strain with a coarse mesh. Even with  $l_e/t_e = 3$  the predictive capability of the model is insufficient. The two elements in front of the slit ends for the 1-HV and 1-22.5 configurations have failed in these simulations, but no crack propagation is observed. For the 4-HV and 4-45 configurations, no failure is observed, even though the damage variable  $D$  is close to unity in the elements in front of the slits in the 4-HV simulation. For  $l_e/t_e = 1$ , the 4-HV simulation is in good agreement with the experiment, where the centre part of the plate is correctly ejected from the rest of the plate. However, the 4-45 simulation is not able to predict crack propagation particularly well and the agreement with the experiment is less good. The 1-HV and 1-22.5 configurations are predicted with acceptable accuracy. The simulations with the finest mesh ( $l_e/t_e = 1/3$ ) were able to replicate the experiments with reasonable accuracy for all configurations, where the crack propagation is especially impressive in



**Figure 4:** Image series from test 1-22.5 and corresponding simulations with different length-to-thickness ratios ( $l_e/t_e$ ) at selected points in time.



**Figure 5:** Side view of 1-22.5 simulations with different length-to-thickness ratios ( $l_e/t_e$ ).

the 4-HV and 4-45 simulations. The cracks were arrested slightly too early in the 1-HV and 1-22.5 simulations, but the overall response was predicted. The crack propagation in the simulations was always less than what was seen in the experiment apart from the 4-HV simulation. In many structural applications, the occurrence of failure is of interest,

which the two finest meshes were able to predict with satisfying accuracy. However, if crack propagation is of interest, only the finest mesh is able to give reliable results.

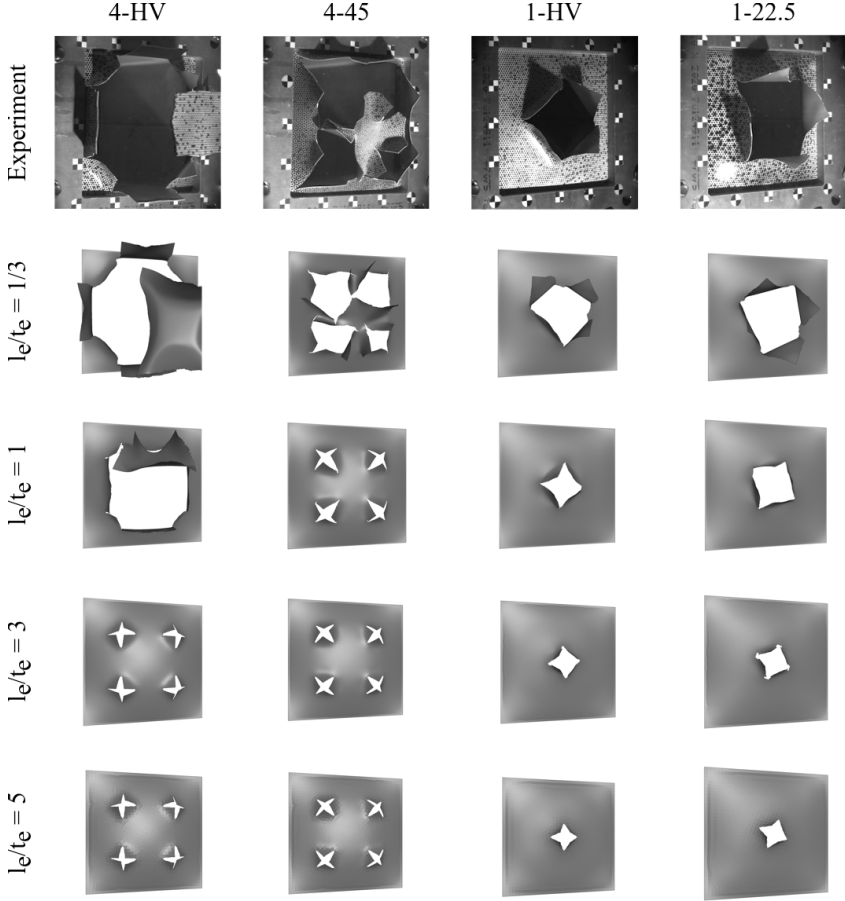


**Figure 6:** Comparison of tests and simulations with different length-to-thickness ratios ( $l_e/t_e$ ) at  $t = 2.0$  ms.

Figure 7 shows a contour plot of the deformation mode indicator  $\Omega$  given in Equation (7) for simulations with  $l_e/t_e = 1$  at  $t = 1.25$  ms. The figure shows that the loading is dominated by membrane actions, but near the defects and the boundary there are areas with mixed loading. Such a thin plate is not expected to have particularly high bending

stiffness compared to the membrane capacity. In front of the cracks, the deformation mode indicator is close to zero in all simulations, indicating pure membrane loading. However, the 4-HV and 4-45 simulations exhibit areas near the defects where the deformation mode varies and significant bending is observed. On the other hand, in the 1-HV and 1-22.5 simulations the loading is mostly membrane dominated near the slits. The corners are the most confined part of the plate, as seen by the bending dominated loading in this region.

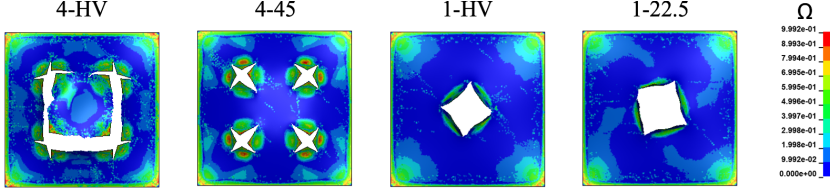


**Figure 7:** Contour plots of the deformation mode indicator  $\Omega$  for simulations with  $l_e/t_e = 1$  at  $t = 1.25$  ms.

In modelling of ductile failure and crack propagation, solid elements are usually the preferred option as long as it is computationally feasible. The simulation time with shell elements ranged from 17 seconds for  $l_e/t_e = 5$  to above 13 hours for  $l_e/t_e = 1/3$  using 8 cores on an Intel Xeon Gold 5120 CPU. To assess the efficiency of the shell element model, a comparison to a solid element model with the same in-plane dimension as the finest shell model was conducted. The characteristic element size was set to 0.5 mm, resulting in three elements over the thickness and around 1 000 000 elements in total. The model was equivalent to the shell element model apart from the modelling of failure, where the standard Cockcroft-Latham failure criterion was employed (Equation (4)). The simulation time was approximately 6 hours on 28 cores, making the computational cost about 60 % more expensive than for the finest shell element model. The results from the two simulations are compared to the experiment in Figure 8 at selected points in time. By inspection of the figure, the shell element model gives similar results as the solid element simulation. The same trend is observed as in the shell element mode, where the propagating cracks were arrested too early compared to the experiment. However, Granum et al. [8] showed that the solid element model overall gave satisfactory results with regards to fracture initiation and crack propagation for various geometries and materials.

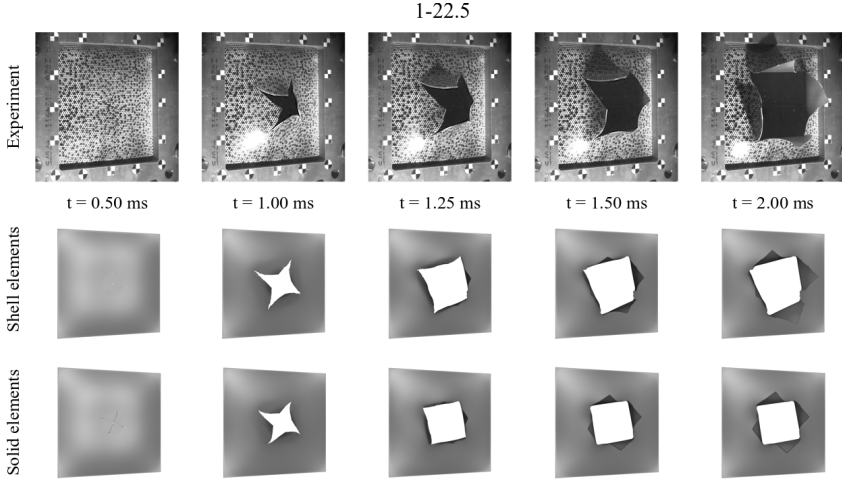


**Figure 8:** Comparison of a shell element simulation ( $l_e/t_e = 1/3$ ) and a solid element simulation to test 1-22.5 at selected points in time.

## 5 Conclusions

The behaviour of aluminium plates with crack-like defects subjected to blast loading was investigated numerically and compared to experiments presented by Granum et al. [8]. The finite element analyses employed an uncoupled plasticity and fracture model with through-thickness damage regularization developed for shell elements. The conclusions from the study are summarized in the following.

- The simulated global displacement field of the plates was similar for all mesh sizes.
- A length-to-thickness ratio of the shell elements equal to unity was sufficient to describe initiation of failure in the simulations.
- Initiation and crack propagation were only predicted in the simulations with the finest mesh, i.e., a length-to-thickness ratio of the shell elements equal to  $1/3$ .
- A simulation with solid elements using three elements over the plate thickness gave similar results as the shell element simulation with the finest mesh, but at a higher computational cost.

## Acknowledgements

The authors appreciate the financial support from NTNU and the Research Council of Norway through the FRINATEK Programme, Project No. 250553 (FractAl). The

authors would also like to thank Dr. Olaf Engler at Hydro Aluminium Rolled Products in Bonn, Germany, for providing the materials.

## REFERENCES

- [1] Costas, M., Morin, D., Hopperstad, O.S., Børvik, T. and Langseth, M. A through-thickness damage regularization scheme for shell elements subjected to severe bending and membrane deformations. *Journal of the Mechanics and Physics of Solids* 123 (2019) 190-206.
- [2] Alsos, H.S., Amdahl J. and Hopperstad, O.S. On the resistance to penetration of stiffened plates, Part II: Numerical analysis. *International Journal of Impact Engineering* 36 (2009) 875-887.
- [3] Storheim, M., Alsos, H.S., Hopperstad, O.S and Amdahl J. A damage-based failure model for coarsely meshed shell structures. *International Journal of Impact Engineering* 83 (2015) 59-75.
- [4] Simonsen, B.C. and Törnqvist R. Experimental and numerical modelling of ductile crack propagation in large-scale shell structures. *Marine Structures* 17 (2004) 1-27.
- [5] Woelke, P.B., Shields, M.D., Abboud N.N. and Hutchinson J.W. Simulations of ductile fracture in an idealized ship grounding scenario using phenomenological damage and cohesive zone models. *Computational Materials Science* 80 (2013) 79-95.
- [6] Pack, K. and Mohr, D. Combined necking & fracture model to predict ductile failure with shell finite elements. *Engineering Fracture Mechanics* 182 (2017) 32-51.
- [7] Morin, D., Kaarstad, B.L., Skajaa, B., Hopperstad, O.S. and Langseth, M. Testing and modelling of stiffened aluminium panels subjected to quasi-static and low-velocity impact loading. *International Journal of Impact Engineering* 110 (2017) 97-111.
- [8] Granum, H., Aune, V., Børvik T. and Hopperstad O.S. Effect of heat-treatment of the structural response of blast-loaded aluminium plates with pre-cut slits. *International Journal of Impact Engineering* 132 (2019) 103306.
- [9] Aune, V., Fagerholt, E., Langseth, M. and Børvik, T. A shock tube facility to generate blast loading on structures. *International Journal of Protective Structures* 7 (2016) 340-366.
- [10] Hershey, A.V. The plasticity of an isotropic aggregate of anisotropic face centred cubic crystals. *Journal of Applied Mechanics* 76 (1954) 241-9.
- [11] Hosford, W.F. A generalized isotropic yield criterion. *Journal of Applied Mechanics* 39 (1972) 607-9.



- [12] Vilamosa, V., Clausen, A.H., Børvik, T, Skjervold S.R. and Hopperstad O.S. Behaviour of Al-Mg-Si alloys at a wide range of temperatures and strain rates. *International Journal of Impact Engineering* 86 (2015) 223-239.
- [13] Hosford, W.F. On the crystallographic basis of yield criterion. *Textures and Microstructures* 26-27 (1996) 479-493.
- [14] Cockcroft, M. and Latham D. Ductility and workability of metals. *Journal of the Institute of Metals* 96 (1968) 33-9.
- [15] Belytschko, T., Lin, J.I. and Tsay, C.S. Explicit algorithms for nonlinear dynamics of shells. *Computer Methods in Applied Mechanics and Engineering* 42 (2) (1984) 225-251.



# ACCIDENTAL LOAD ASSESSMENT OF PROCESS PIPE SYSTEMS

TORRE HOLMAS<sup>1</sup> AND INGAR FOSSAN<sup>2</sup>

<sup>1</sup> AkerSolutions  
5253 Sandsli, Norway.  
e-mail: [tore@holmas.com](mailto:tore@holmas.com)

<sup>2</sup> Safetec  
Trondheim, Norway.  
e-mail: [ingar.fossan@safetec.no](mailto:ingar.fossan@safetec.no)

**Key words:** Process Pipe System, Structural Engineering, Computational Techniques.

**Abstract.** This document describes the typical accidental load requirements of process pipe systems and the use of non-linear tools, which describes the physics better than the conventional linear elastic methods normally used by the industry.

## 1 INTRODUCTION

An offshore platform processes oil and gas with high pressure. Stricter requirements regarding accidental loads have resulted in increased weight and costs of the process pipe systems. The main reason why the accidental loads have become the governing parameter (“design driver”) is the use of simplified linear elastic models and methods.

This document describes how use of non-linear analysis tools and more advanced analysis models could give substantial weight and cost reductions of pipe systems. Enhanced modelling of both the dynamic characteristics of the accidental loads and the structure gives more cost efficient design without compromising the target level of safety.

## 2 PIPE SYSTEMS

Processing oil and gas involves a large number of pressurized pipe systems. The pressure levels range typically from 10 to 300bar, and the pressure levels are defined in “pressure classes” specified in pound per square inch, denoted #150 (low pressure) to #2,500 (high pressure).

A pipe system is composed by many components (see Figure 1), and the components are standardized within the different pressure classes. The components connecting the straight pipes are in general stronger (ultimately) than the pipe itself, and this simplifies the assessment.

High-Pressure (HP) pipes are thick-wall, and diameter to thickness ratios (D/T) could be as low as 10. The Low Pressure (LP) pipes could be thin-wall with D/T ratio in the order of 100.

HP pipe systems are robust and less vulnerable for extreme loads than the LP pipe systems, (e.g. the explosion drag loads are not dependent on the pipe thickness, only the outer diameter). Extreme heating is also less severe for a thick-wall pipe since the heating process goes slower. Focus is therefore normally set on the LP systems regarding assessment for extreme accidental loads, such as explosion and fire.

Pipe Supports carry the pipes, but are also supporting the pipes in case of explosion drag load. Yielding and even fracture of a pipe support is not critical as such, but in conventional design, the linear elastic stress in a single support is often the governing parameter, and has become the design driver. The weight of the pipe supports has therefore almost doubled (since the early 2000) as a result of the “linear elastic” explosion assessment.

Heavy items attached to the pipes (e.g. safety critical valves) need special attention. In a fire situation, the weight of such objects (could be more than 10ton) is normally too big to be carried by the pipe, and extra supports under the heavy items are inserted. The additional drag loads on the eccentric (to the pipe) valve area needs to be accounted for.

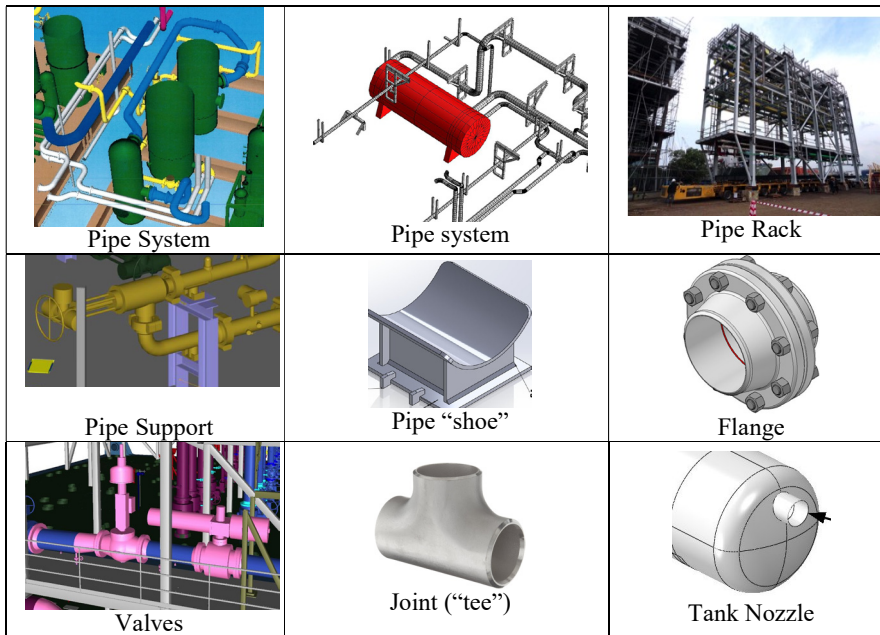


Figure 1 - Pipe system components and details

### 3 CONVENTIONAL LINEAR RESPONSE ASSESMENT

A pipe system shall withstand both the operation loads caused by the different conditions of the internal fluid such as temperature variation, pressure changes and extreme flow.

Normally the pipes are modelled without the flexible pipe supports included, and the boundary conditions free/fix (0/1) are used. The maximum reaction forces are then handed over to a separate group of engineers being responsible for designing sufficiently strong supports. Both the ultimate limit state loads ULS (e.g. extreme fluid flow) and the fatigue limit state FLS (e.g. vibrations and thermal/pressure cycling) are assessed.

Since the pipe system shall withstand both the ULS and FLS loads for the entire design life of the pipe system (e.g. 20 years), the system has to respond elastically to these loads. These methods are therefore based on linear elastic stress.

In connection with accidental limit state loads ALS, however the use of these *simplified linear elastic procedures cannot* describe the physical response of a complete pipe system.

The simplified linear assessment has two main limitations:

- 1 : No plasticity is included: neither in the supports nor in the pipes.
- 2 : The interaction with the pipes and the supports cannot be described, see Figure 2.

On top of this, the explosion is treated as a *static* load with different load factors.

This kind of assessing pipe systems exposed to accidents results in unnecessary amount of steel for the supports (to handle the explosion) and requirements regarding passive fire protection (PFP) on the supports (to handle the pre-defined weight loads during fire).

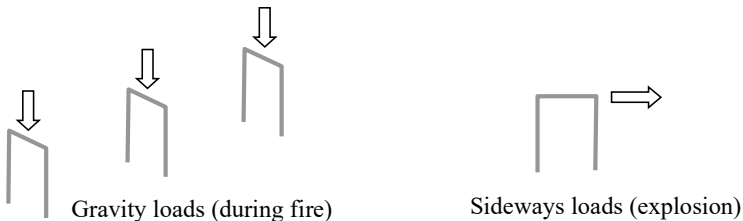


Figure 2 – The presence of the pipe as a structure is ignored in conventional design.

#### 4 DESIGN ACCIDENTAL LOAD (DAL) REQUIREMENTS

In a design project, the accidental load requirements are established in an early phase. These loads depend on the choice of concept regarding of the process modules (e.g. ventilation conditions) and characteristics of the process system (e.g. time to de-pressurize the pipe systems).

Normally, the most severe accidental loads are:

- Explosion
- Fire

It is required that a pipe system is able to withstand the explosion loads, and then, after the explosion, to handle the defined fires.

The definition of “withstand” in this context is that the pipes do not rupture and thus feed more fuel into the module (escalating the accident).

However, after a certain time (when personnel has evacuated the area), some escalation is often accepted. The longer time since the start of the accident, the larger amount of fuel is accepted. (The main structures are designed to withstand such escalated fires).

#### 5 ACCEPTANCE CRITERIA

In the conventional assessment, the linear elastic stress in “most extreme fibre” is used as the main criterion. This stress is checked vs. a certain limiting stress level.

Linear elastic stress based criterion is not recommended in connection with accidental loads. Instead, since steel is a *ductile* material, *the strain level* is better to describe failure (fracture) of a pipe system.

In order to avoid conflict with other pipe assessment (internal pressure and “time to burst”) the maximum accepted strain level in the pipe is set to a moderate level, e.g. 5%. The corresponding level for the supporting structures (pipe support and pipe rack) is set to a higher level, e.g. 15%.

It could be argued to use stricter requirements in Design in order to have extra reserves for future modifications. (More congested process areas tend to increase the explosion loads). For example: to accept that the pipe supports yield, but ensure (in design) that the pipes remain elastic in connection with explosion.

## 6 EXPLOSION LOADS

The impact from an explosion will not occur simultaneously along the whole length of the pipe, see Figure 3. The peak travels fast and each element experiences a short pulse. The total duration (rise + decay) is typically in the order of 20-100ms. When one element experiences the peak drag load, the neighbour elements have almost no load. This means that the loads acting on a pipe system are localized and activates only a fraction of the pipe and support at the time. This is normally **not** accounted for in an analysis.

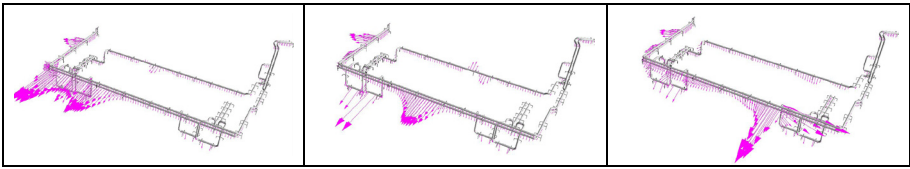


Figure 3 Drag loads from CFD analysis. The peaks occur on different times along the pipe

The magnitude of the explosion drag load is normally computed as:  $Force = p D$ , where “ $p$ ” is the design accidental drag pressure (with typical levels from 0.2-0.5bar), and “ $D$ ” is the drag diameter of the pipe (accounting for the extra projected area due to e.g. insulation). The result is a force per unit length of the pipe.

The normal design load considers simultaneous drag loads on all the pipe members within the same blast area. Drag loads on pipes parallel with the drag load direction are set to zero, see Figure 4 for example of explosion loads in positive X- and Y-directions.

The design drag pressure gives the *maximum* level after a certain time after ignition, and a linear rise and decay is normally used (triangular pulse).

Since the explosion loads have short durations, it is recommended to perform dynamic simulations, where the substantial inertia forces are accounted for.

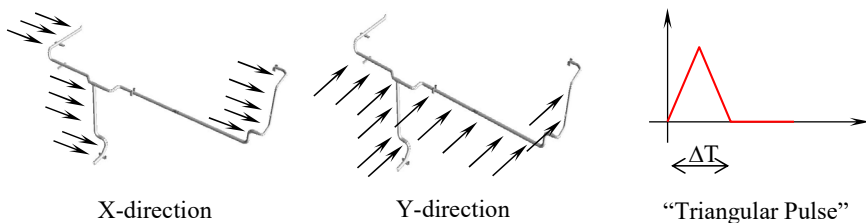


Figure 4: Typical DAL Drag Pressure Loads acting on pipe

## 7 FIRE LOADS

It is essential to have agreed design fires. The fires need to describe the heat flux or temperature in addition to the extent of the fire.

Turbulent combustion in a large-scale industrial environment due an ignited release of a combustible fluid is a dynamic and time-dependent phenomenon inherently coupled to the properties of the environment of which the phenomena take place. An important parameter is for example the ventilation conditions deciding the supply of oxygen to the chemical reaction. Other parameters are the properties of the process system (e.g. pressure and temperature) and the safety systems initiated upon detection (Emergency Shut Down, ESD and Blowdown, BD) controlling how the leak scenario feeding the fire unfolds.

The heat load history during a hydrocarbon fire is therefore not easily described. The common approach for equipment and secondary structures is to apply generic heat loads found in NORSOK S-001. Such simple methods generally leads to over prediction of the heat transferred to the objects as it does not reflect the time-dependent behaviour of the phenomena.

A fire fed by a leak from a process system equipped with a depressurisation system possess a dynamic behaviour, both in time and space. An ignited jet or spray (most liquid leaks generates spray fires) fire expands from the leak point until it reaches a maximum size. Upon initiation of the ESD and BD-systems, the rate feeding the fire starts to decrease according to the decrease in pressure. Depending on the ratio between hydrocarbon leak rate and ventilation rate, the fire size will start to decrease immediately in most cases. If the module is under ventilated (the air supply controls the fire), the fire may continue to grow for some time after initiation of blow down, but will eventually start to decrease.

In Figure 5 the incident thermal radiation and gas temperatures for decreasing leak rate from 32 to 2 kg/s is presented (simulations performed with Kameleon FireEx, KFX®). The initial large release rate (32 kg/s) generates too rich gas mixture inside the module leading to limited fire loads. At the late phase of the fire scenario, the heat loads are quite local, but for the intermediate stage, substantial heat loads acts on a much larger fraction of the module. This example demonstrates that the fire load exposure experienced by the various objects inside the module will vary throughout the lifetime of a fire scenario.



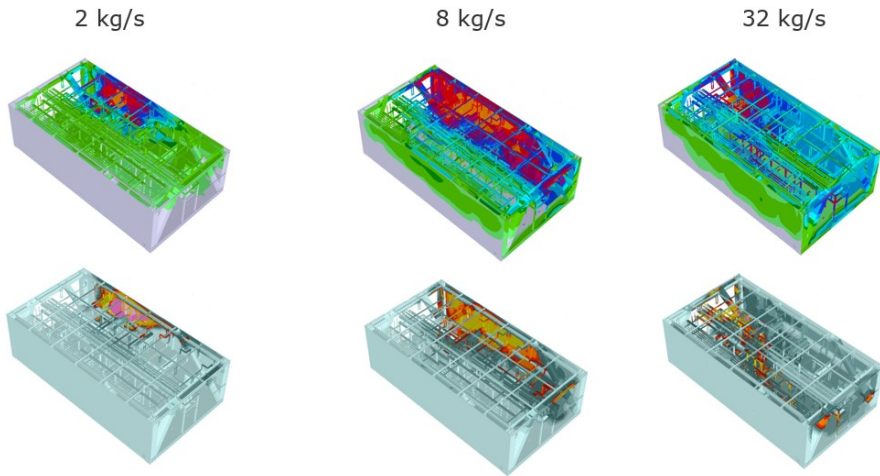


**Figure 5: CFD simulation with Kameleon FireEx KFX®: incident radiation flux to objects (top) and walls and gas temperatures projected on objects in module (bottom) (Ref. /1/)**

To analyse the consequences of a transient heat load resulting from a time-dependent fire without reflecting the temperature transfer to the objects may result in inaccurate assessment of the vulnerability of the objects. The aggregated fire heat load acting on the exposed objects is built up of two contributors; radiation and convection. For small objects inside the flame, the contribution from convection (i.e. heat transferred between the gas and the solid surface) can be equal to the radiation heat flux. In areas where the flow rate is less (typically outside the reaction zone), the radiation heat flux is dominating the heat load and convective heat transfer may contribute to heat transfer from the object to the surrounding atmosphere rather than heating (i.e. the temperature of the object surface is higher than surrounding gas). Hence, the fire heat load can hardly be described by a generic heat for all locations inside a fire.

In order to capture the dynamic behaviour of the fire outlined above, and at the same time provide basis for effective structural response analysis, it is suggested to apply a method based on a volumetric temperature distribution describing the resulting temperature of the various objects at hand. The relationship between temperature and volume could be established based on results for fire simulations using CFD tools (such as KFX). A unique distribution should be developed for the various types of objects based on their temperature response when subjected to the potential fire scenarios in the area. The size and thickness of the objects are the decisive parameters in addition to the parameters governing the fire behaviour.

The shape of the volume can be represented by a sphere for effective mathematical modelling in the response analysis. The real shape will typically deviate somewhat from the ideal shape. However, developing the distribution based on the most severe fire scenarios will ensure that a simplified shape is an adequate idealisation. The developed volumetric temperature distribution (denoted “matruska fire”) can be effectively applied at various locations in a response model to check the fire integrity for the various systems. The “matruska fire” can alternatively be described as a volumetric heat load distribution, but in this case the temperature response has to be computed in the structural response tool.

Hence, the suggested method facilitates effective and consistent reflection of the fire characteristics of the module and the response of the exposed critical objects in the design process.

Figure 6 shows how to construct a simplified fire using smaller volumes inside bigger (like the Russian matruska doll), where each circle represents a certain volume.

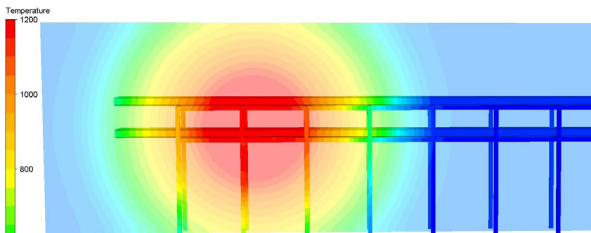
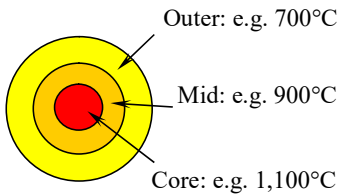


**Figure 6 – Illustration simplified “matruska fire” to be used for sec-steel. Top: illustration of principle; Below: example temperature response of pipe rack for typical “matruska fire” at an offshore installation.**

## 8 MODELS FOR ACCIDENTAL LOAD ASSESSMENT OF PIPE SYSTEMS

In order to perform realistic assessments of pipe systems exposed to e.g. explosion and fire, models suited for the purpose is needed. The (over) simplified “component-by-component” checks *cannot* be used.

The models of a pipe system will *always* require that the pipes are included in the analysis models. The presence of the pipes makes it possible to simulate the force-redistribution if/when one single pipe support becomes weak (fire) or yields (explosion).

An additional benefit is that the loads used in the ALS assessment become as correct as possible when the actual pipes are included (since the weight of a given pipe is computed accurately). The loads used in an early concept study are often far higher than what is reality in a final design. (e.g. if the pressure-class is not 100% settled in the concept phase, a thick-wall alternative is used to estimate the weights, and this could result in 2-3 times higher loads).

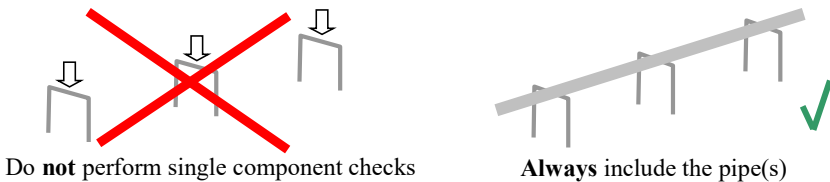


Figure 7 – Models for Accidental Limit State Assessment of pipe systems.

The pipe has different fixations to the support structure, such as “rest”, “hold”, “guide” and “line stop” in order to let the pipe expand/contract as the temperature and pressure of the internal fluid changes. It is essential that correct boundary conditions are used: in particular in connection with explosion assessment. Since some fixations are non-symmetric (e.g. transfers vertical downwards loads only, the rest function), 2-node non-linear springs are recommended.

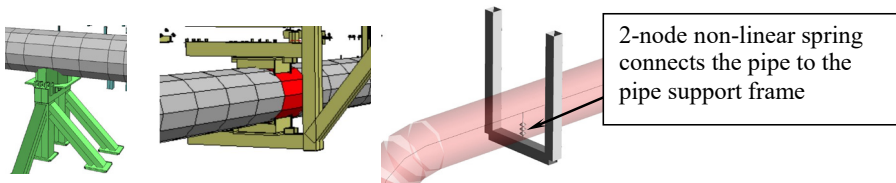


Figure 8 – Misc. Support frames and how to model the connection between the pipe and the supports.

Beam elements could be used for both pipes and support frames.

## 9 EXPLOSION RESPONSE ANALYSIS

In order to get a realistic response of a pipe system exposed to explosion loads, both non-linear material and geometry effects have to be included.

It is always useful to start with a non-linear static analysis. Here, the impact from the self-weight and the internal pressure is found. By scaling the drag forces up to failure (one explosion direction at the time) an early indication of the performance of the system is found. Mistakes regarding modelling (supporting, etc.) are also easier to detect from a static analysis.

The final simulations use a non-linear dynamic solver. The pipe is exposed to the actual drag forces and durations described in the DAL specifications.

A pipe system does not have a “1/0, OK/notOK” response when non-linear methods are used, (In contrast to linear elastic methods, where exceeding the yield strength in a single component becomes the limit for the entire system). It is therefore useful to divide the non-linear response into several main groups or “Damage Levels”. Simulations are repeated with *increasing* drag pressures and the response is monitored for the different drag pressure levels:

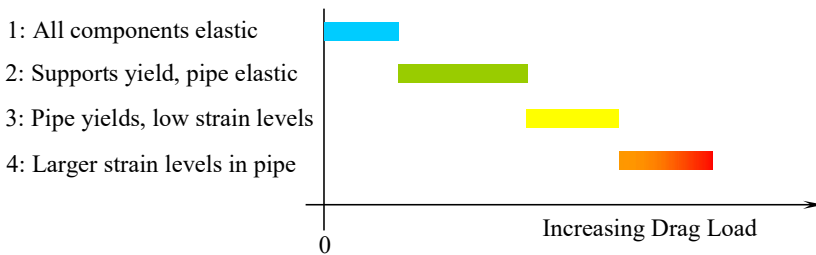


Figure 9 – “Damage Levels” for a Pipe System exposed to explosion loads

Such “damage level” figures for the different pipe systems are easy to communicate with the “safety discipline”, (which is responsible for the total safety of a platform).

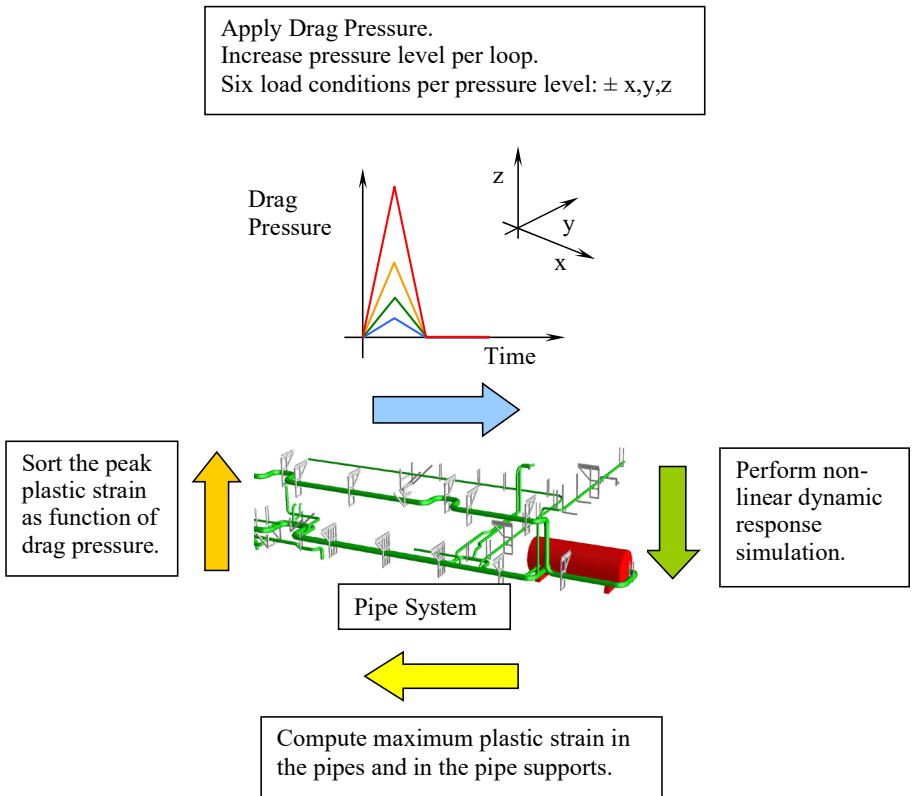
As mentioned under “acceptance criteria”, it is recommended to use stricter criterion in design (easier to change components) compared with a platform modification project later (when changes are expensive). Such modifications tend to cause higher explosion loads (more congested). If a pipe system handles the DAL loads within the “green zone” in the design, the “yellow zone” becomes the margin for future projects.

By accepting that the steel exceeds the elastic range it is found that a given pipe system has the order of 3 times higher resistance compared with conventional linear assessment.

The Simulation Loop needed to establish the “Damage Levels” is shown on the next page.

**Simulation Loop:**

1. Define drag pressure load level. Start with a low level for the first loop and increase gradually per loop. Keep the explosion load duration constant. Check for all load-directions:  $\pm x$ ,  $\pm y$  and  $\pm z$ .
2. Perform non-linear dynamic simulation of the pipe system exposed to the actual drag pressure load.
3. Compute the maximum plastic strain during the entire simulation length. Both for the pipes and the pipe supports.
4. Find the max strain among all pipes and pipe supports for each simulation. Store as function of pressure.



## 10 FIRE RESPONSE ANALYSIS

The main purpose of the fire response analysis of the pipe systems is to identify need for thermal insulation (Passive Fire Protection, PFP) of the support structures.

When steel is heated, the performance degrades (becomes both softer and weaker). The degraded material parameters (E-mod and Yield stress) are found by using the “degradation vs. temperature” curves, which are established for all relevant pipe- and structural -steels. At temperature e.g. 1,100°C the steel has yield strength of 2% compared with the performance at room temperature.

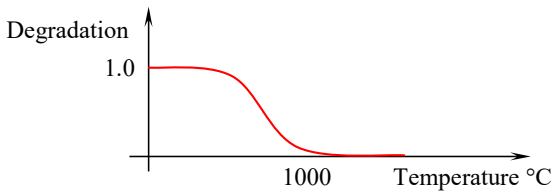


**Figure 10 – Typical degradation vs. time for the yield strength.**

It should be emphasized that the stress levels caused by the self-weight of the pipes (gravity) are very low, and many systems remain stable also at high temperatures. The deformations may increase, but this will introduce beneficial 2<sup>nd</sup> order effects such as membrane action (the pipe carries the vertical loads by axial tension, not bending).

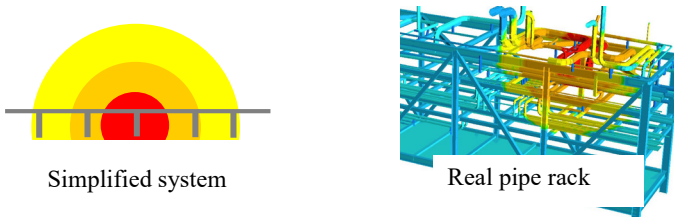


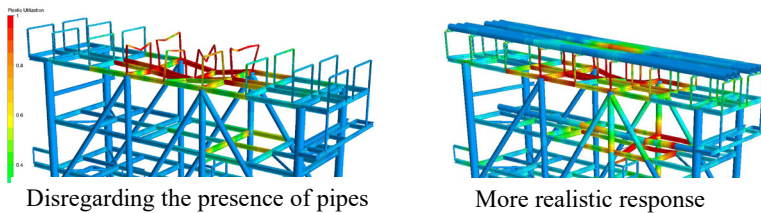
**Figure 11 – Simplified assessment (left) and complete FE modelling (right)**

Simplified systems could be assessed without use of temperature simulations. Since the simplified “matruska” fire gives the temperature directly, the E-mod and yield strength could be modified manually based on the components’ location vs. the different temperature levels.

For more complex systems like the pipe rack the use of general finite element tools could be beneficial.

The importance of including the pipes (and not just the forces from them) is illustrated in Figure 13. This is a case where the pipe rack is exposed to an extreme jet fire hitting the upper part including the pipes. In the model to the left, the loads from the pipes are introduced as concentrated weights on the “tiny” pipe supports. In this case, the supports fail, and the conclusion would be that the supports need PFP.

In the model to the right, the actual pipes are included, and no concentrated weights are needed. When the most exposed supports become weak, the pipes will shed the loads to the neighbour supports, which are less exposed to the fire. The pipes (which are heated too) handle such “free” spans without fracturing, but could deform up to  $\sim \frac{1}{2}$  diameter in order to find equilibrium. Here, the conclusion is that the supports **do not** need PFP.



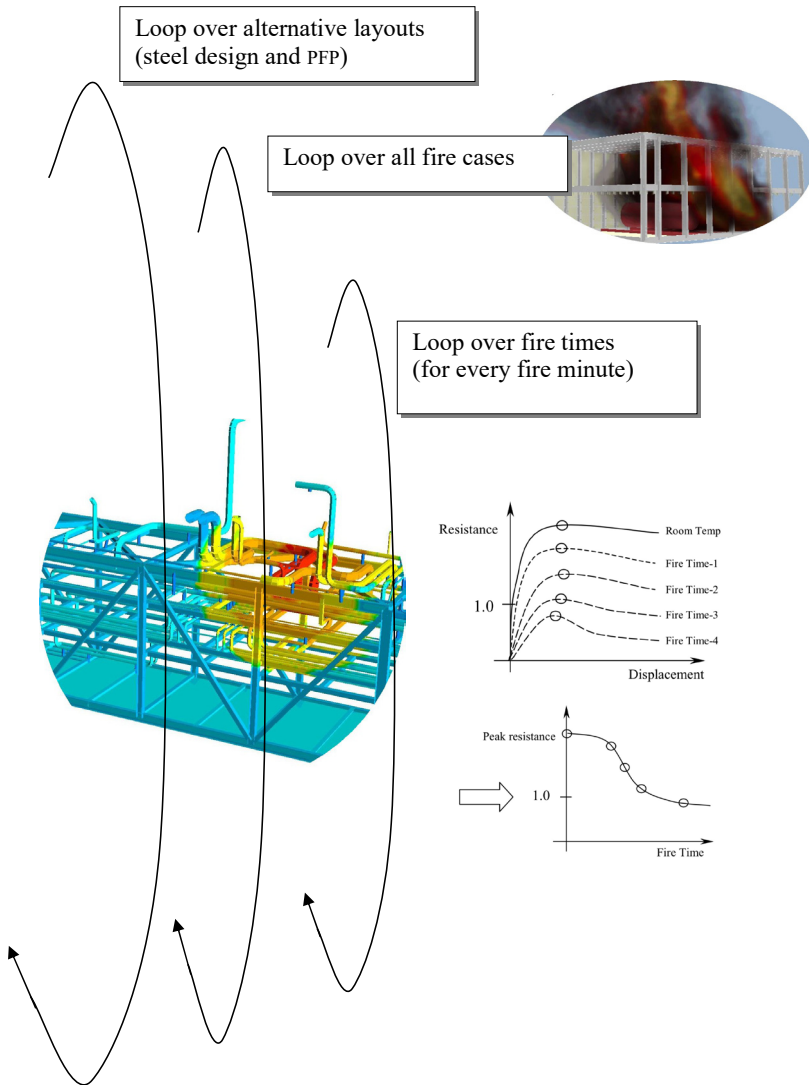
**Figure 13 – Response (plastic utilization) without pipe (left) and with the pipes included (right)**

Figure 14 (on next page) shows the general, full simulation loop for a fire assessment:

- For every design layout (steel and PFP):
  - For every fire design case:
    - For every fire time (e.g.: every minute):
      - Find the ultimate resistance of the pips system
      - Compute the plastic strain of the pipes

Each simulation (ref the load vs. deformation curve) gives one point in the resistance vs. fire time curve, which gives an overview of how the structural system degrades over time due to the heating.

If the pipe system demonstrates sufficient resistance the required time (and within the acceptance criteria) the system layout is accepted.



**Figure 14 – General fire assessment simulation loop, (finding resistance vs. fire time).**



## 10 CONCLUSIONS

Enforcement of stricter safety requirements of pipe systems (which means that the response for accidental loads are investigated in detail) has resulted in increased costs.

One main reason for the increased costs is that linear elastic methods are used for the accidental limit state (ALS) assessment.

By accepting that the steel exceeds the elastic range and using non-linear analysis tools in combination with a realistic description of the accidental loads, it is found that a given pipe system performs far better than found from a linear elastic assessment.

This opens for substantial cost and weight savings for both new design and in connection with modification of existing platforms.

## REFERENCES

- [1] FABIG–TM95-June 2018: “*CFD analysis of the effects of ventilation on the fire loads in enclosed and partly enclosed modules*”



## FLOW-INDUCED VIBRATION OF TANDEM CYLINDERS IN THE VICINITY OF A HORIZONTAL PLANE WALL

Marek Jan JANOCHA<sup>1</sup>, Muk Chen ONG<sup>2</sup>

<sup>1</sup>Department of Mechanical and Structural  
Engineering and Materials Science  
University of Stavanger  
Stavanger 4036, Norway  
e-mail: marek.j.janocha@uis.no

<sup>2</sup> Department of Mechanical and Structural  
Engineering and Materials Science  
University of Stavanger  
Stavanger 4036, Norway  
e-mail: muk.c.ong@uis.no

**Key words:** Flow-induced vibration, Tandem cylinders, Wall proximity effects, CFD

**Abstract.** Flow mechanisms around two cylinders in tandem close to a horizontal plane wall are investigated using the 2D Unsteady Reynolds-averaged Navier-Stokes (URANS) equations with a  $k-\omega$  SST turbulence model. The Reynolds number based on the free stream velocity ( $U_\infty$ ) and cylinder diameter ( $D$ ) is  $Re = 13100$ , and the normalised boundary layer thickness is set to  $\delta/D = 2.98$ . The objective of the present study is to investigate numerically the flow-induced vibrations of two cylinders free to vibrate in two degrees-of-freedom with center-to-center spacing ratio  $L/D = 5$  located near plane wall at a gap-to-diameter ratio  $e/D = 2$  ( $e$  is defined as the distance from the cylinder's bottom surface to the wall). The present numerical model results are compared with available experimental data. A good agreement is found between the predicted hydrodynamic force coefficient values, maximum vibration amplitudes and the published experimental and numerical studies. Flow field characteristics are computed and discussed. Three distinct regimes in the VIV response of the tandem cylinders are found. Complex response behaviour of the downstream cylinder is analysed with respect to the hydrodynamic forcing induced by the upstream cylinder. The extended lock-in range indicates that in the presence of the wake interference, the downstream cylinder might experience resonance and large vibration amplitudes outside of the typical reduced velocity range employed in the design codes for subsea pipelines.

## 1 INTRODUCTION

The flow around two cylinders in proximity is of practical engineering and academic interest and was studied extensively in the past. A comprehensive review of the influence of the configuration on the flow was carried out by Zdravkovich [21] and updated based on the more recent advances in the field by Sumner [17]. The most widely adopted classification of the wakes of two-cylinder configurations was proposed by Zdravkovich [20]. Four main regions can be distinguished, i.e. the proximity interference region, the proximity and wake interference region, the wake interference region and no interference region. In the proximity interference region the two cylinders are placed close to each other in a side-by-side configuration or at a high angle  $\alpha$  defined as the angle between the freestream flow direction and the line connecting the centres of the cylinders. Characteristic coupled vortex shedding occurs in this region resulting in the formation of a single vortex street. Considering two cylinders with identical diameters ( $D_1 = D_2 = D$ ) in tandem arrangement the relative position of the cylinders can be defined as a non-dimensional spacing ratio ( $L/D$ ) where  $L$  is the centre-to-centre distance between the two cylinders. For tandem arrangements and slightly staggered arrangements ( $\alpha < 10^\circ$ ) the proximity and wake interference region occurs at  $1 < L/D < 4$  and transitions into the wake interference region after exceeding the critical value of the spacing ratio,  $L/D > 4$ . In those regions, the downstream cylinder is strongly affected by the wake of the upstream cylinder. The upstream cylinder is affected by the feedback mechanism for  $L/D$  values up to 8, as demonstrated by Alam et al. [1]. However, the feedback effects become less significant after exceeding spacing of  $L/D = 4$ .

A special class of flow interference problems occurs in the configurations in which the cylinders are placed near the horizontal plane wall and are free to vibrate in two degrees-of-freedom (2DoF). An example of such configuration is the case of two free-spanning subsea pipelines laid next to each other. Near-wall effects were investigated experimentally by numerous authors (see e.g., Lei et al. [10], Price et al. [16]). Experiments conducted by Bearman and Zdravkovich [2] revealed that vortex shedding is suppressed when  $e/D < 0.3$  for a static cylinder case. Wang et al. [19] investigated an elastically mounted cylinder and reported vibrations even at very small gap ratios,  $e/D \geq 0.05$ .

More recently, Computational Fluid Dynamics (CFD) methods have increasingly been applied in the area of marine hydrodynamics. The flow mechanism around the marine pipeline close to a plane wall was investigated by Ong et al. [14] using standard  $k-\epsilon$  model and a satisfactory agreement with published experimental data was found. Li et al. [11] performed a similar study using Large Eddy Simulations with Smagorinsky subgrid-scale model. Results reported by Li et al. [11] confirmed that 3D scale resolving simulations are capable of predicting the hydrodynamic quantities with higher accuracy than 2D RANS at the expense of significantly higher computational cost. RANS-based turbulence models are known to yield less accurate predictions of flows with strong anisotropic turbulence (Ong et al. [13]). When the Reynolds number is large, the numerical response of the

lift coefficient of flow around a circular cylinder is often smaller than the experimental values. A common problem occurring in simulations of vortex-induced vibration based on 2D URANS is manifested by smaller than the experimental values of the transverse amplitudes of vibration and too fast decay of the amplitude in the lower branch. However, as evidenced by numerous published studies on vortex-induced vibration employing 2D numerical simulations (see, e.g., Guilmineau and Queutey [4]; Pan et al. [15]; Wanderley et al. [18], Kang et al. [8]; Han et al. [5]), prediction of the essential VIV characteristics shows reasonable agreement with the experimental data.

Majority of the published numerical studies investigating flow around tandem cylinders are concerned with two stationary cylinders at low  $Re$  (see e.g., Bhattacharyya and Dhinakaran [3], Harichandan and Roy [6]). Relatively little attention has been given to the configuration of two tandem cylinders vibrating near the horizontal plane wall. The complexity of the flow is increased due to the interaction with the bottom boundary layer and large vibration amplitudes caused by VIV and wake-induced vibrations (WIV) lock-in phenomena.

In this study flow around two elastically mounted cylinders in tandem close to a plane boundary, undergoing 2DOF vibrations is investigated numerically. The present study focuses on the wake interference regime with centre-to-centre spacing set to  $L/D = 5$ , boundary layer thickness ratio  $\delta/D = 2.89$  and gap-to-diameter ratio  $e/D = 2$ . The considered Reynolds number is  $Re = 13100$  and corresponds to the sub-critical regime. The governing equations and the numerical methodology are presented in Section 2. Grid and time step convergence study is presented in Section 3. Validation tests are shown in Section 4, and the results and discussion are presented in Section 5.

## 2 NUMERICAL MODEL

### 2.1 Governing equations

The governing equations for the fluid flow considered in this paper are the two dimensional incompressible Reynolds-averaged Navier-Stokes equations. The equations of continuity and momentum conservation, are given by:

$$\frac{\partial u_i}{\partial x_i} = 0, \quad (1)$$

$$\frac{\partial u_i}{\partial t} + u_j \frac{\partial u_i}{\partial x_j} = -\frac{1}{\rho} \frac{\partial p}{\partial x_i} + \frac{\partial}{\partial x_j} \left[ (\nu + \nu_t) \left( \frac{\partial u_i}{\partial x_j} + \frac{\partial u_j}{\partial x_i} \right) \right], \quad (2)$$

where  $i, j = 1, 2$ ;  $x_1, x_2$  are streamwise and wall-normal directions respectively;  $u_1, u_2$  are the mean flow velocity components corresponding to directions  $x_1$  and  $x_2$ ;  $\nu$  denotes the kinematic viscosity of the fluid;  $\nu_t$  is the eddy viscosity,  $\rho$  is the density of the fluid;  $p$  is the dynamic pressure. The shear stress transport (SST)  $k-\omega$  turbulence model with updated coefficients according to Menter et al. [12] is used in the present study to calculate eddy

viscosity by solving the two variables namely, the turbulent kinetic energy ( $k$ ) and the specific turbulent dissipation ( $\omega$ ).

In the present study, two elastically supported cylinders experiencing VIV are considered as shown in Figure 1. Flow direction is parallel to the horizontal plane wall. The dynamic behavior of the cylinders vibrating with 2DOF is modeled via a mass-spring-damper system. The equations of motion of cylindrical structure are as follows:

$$m \frac{\partial^2 x}{\partial t^2} + c \frac{\partial x}{\partial t} + kx = F_x(t) \quad (3)$$

$$m \frac{\partial^2 y}{\partial t^2} + c \frac{\partial y}{\partial t} + ky = F_y(t) \quad (4)$$

where  $x$  and  $y$  denote the in-line and transverse displacements respectively,  $k$  is the structural stiffness,  $c$  is the structural damping,  $m$  is the structural mass,  $F_x$  and  $F_y$  are the fluid forces per unit length acting in the streamwise and transverse directions on the cylinder. The mass ratio  $m^*$  and damping coefficient  $\zeta$  are expressed as:

$$m^* = \frac{m}{m_d}, \quad \zeta = \frac{c}{2\sqrt{km}}, \quad (5)$$

where  $m$  is the mass of the cylinder,  $m_d$  is the mass of displaced fluid. The reduced velocity,  $U_r$  is defined as  $U_r = U_\infty / (f_n D)$ , where  $f_n$  is the structural natural frequency,  $U_\infty$  is free stream flow velocity.  $C_D$  and  $C_L$  are the drag and lift coefficients, respectively, computed by integrating the fluid forces  $F_x$  and  $F_y$  acting on the cylinder.

Simulations are conducted using the open source CFD library OpenFOAM. Pressure-velocity coupling is solved using PIMPLE algorithm combining Semi-Implicit Method for Pressure Linked Equations (SIMPLE) and Pressure Implicit with Split Operators (PISO) methods. The implicit second-order Crank-Nicolson scheme is used for the time integration. The divergence and gradient terms are discretised using Gauss linear integration scheme. The Laplacian and surface normal gradients are discretised using Gauss linear integration with limited non-orthogonal correction. All of the schemes used have second-order accuracy.

## 2.2 Computational domain and boundary conditions

Problem definition schematic is presented in Figure 1. In the present study, a rectangular computational domain is established with dimensions of  $35D$  by  $12.5D$ , where  $D$  is the diameter of the cylinder. The upstream cylinder centre is located at a distance of  $10D$  from the inlet. The centre-to-centre spacing between the cylinders is set to  $L = 5D$ . The downstream cylinder centre is located at a distance of  $20D$  from the outflow. The upper boundary is located at a distance  $10D$  from the centres of the cylinders, and the bottom wall is located  $2.5D$  from the centres of the cylinders. Therefore, the gap-to-diameter ratio is  $e/D = 2$ .

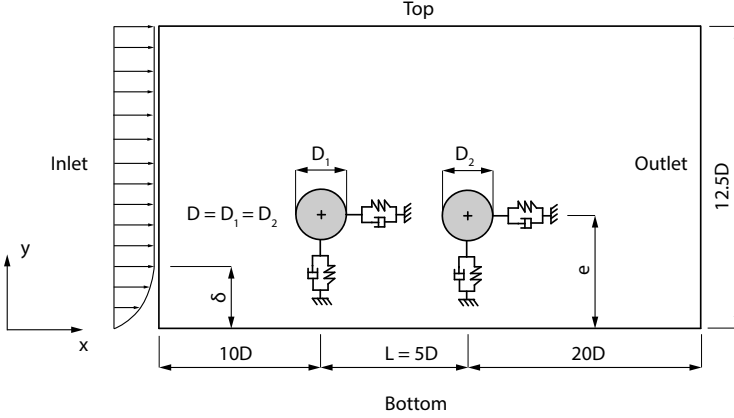


**Figure 1:** Problem definition and computational domain settings.

Boundary layer thickness  $\delta$  of the inflow is expressed in terms of nondimensional boundary layer to diameter ratio ( $\delta/D$ ) and is set to  $\delta/D = 2.89$ . The boundary conditions imposed at the inlet are adapted from Ong et al. [14]. The boundary conditions imposed on the domain are as follows:

1. At the inlet a fully developed boundary layer flow is specified using the expressions for  $u$ ,  $k$ , and  $\omega$ :

$$u_1(y) = \min \left[ \frac{u_*}{\kappa} \ln \left( \frac{y}{z_w} \right), U_\infty \right] \quad (6)$$

$$u_2(y) = 0 \quad (7)$$

$$k(y) = \max \left[ C_\mu^{-1/2} \left( 1 - \frac{y}{\delta} \right)^2 u_*^2, 0.0001 U_\infty^2 \right] \quad (8)$$

$$\omega(y) = \max \frac{k(y)^{1/2}}{\beta_*^{1/4} l(y)} \quad (9)$$

$$l(y) = \min \left[ \kappa y \left( 1 + 3.5 \frac{y}{\delta} \right)^{-1}, C_\mu \delta \right] \quad (10)$$

where  $y$  is the wall-normal direction starting from the bottom as illustrated in Figure 1;  $l$  is the estimated turbulent length scale;  $C_\mu = 0.09$  is the model constant;

$\kappa = 0.41$  is the von Kármán constant;  $u_*$  is the friction velocity expressed as:

$$u_* = \frac{\kappa U_\infty}{\ln\left(\frac{\delta}{z_w}\right)} \quad (11)$$

$U_\infty$  denotes the free stream velocity;  $z_w = 1 \times 10^{-6}$  m is the imposed seabed roughness.

2. At the outlet of the domain  $u$ ,  $k$  and  $\omega$  are prescribed with zero normal gradient condition, the reference pressure is set  $p = 0$ .
3. At the top boundary  $u$ ,  $k$ ,  $\omega$  and  $p$  are set to zero normal gradient.
4. On the bottom and on the cylinders walls a "no-slip" condition is imposed:  $u_1 = 0$ ,  $u_2 = 0$ ,  $k = 0$ , and  $\omega = \frac{60\nu}{\beta_1(h_p)^2}$  where  $\beta_1 = 0.075$  is the model constant,  $h_p$  is the radial distance from the wall to the first cell center.

Reynolds number based on the free stream velocity  $U_\infty$ , diameter of the larger cylinder  $D$  and kinematic viscosity  $\nu$  is kept constant at  $Re = 13100$ . The movement of the boundary of the cylinders is realized using the dynamic grid method.

### 3 GRID AND TIME STEP CONVERGENCE STUDY

The spatial domain is discretized with a block-structured hexahedral grid. Figure 2 shows the typical mesh used in the present study. The grid is refined in the high gradient areas of the domain and close to the walls. The near-wall grid expansion ratio is kept smaller than  $r_e \leq 1.05$  for the first 20 cell layers. The grid expansion ratio in the remainder of the domain is smaller than  $r_e \leq 1.2$ . In the present study, numerical simulations are first performed to confirm the grid and time step independence. For this purpose, a set of three meshes with different cell densities using constant refinement factor  $r_F = 1.4$  is generated. The dimensionless wall distance  $y^+$  is defined as  $y^+ = h_p u_* / \nu$ . Maximum and average values of  $y^+$  are calculated on respective walls based on  $u_*$  extracted from the simulations. The first cell layer height near the cylinders surface is set to  $0.0005D$  corresponding to  $y_{max,1}^+ = 0.615$  and  $y_{avg,1}^+ = 0.323$  on the upstream cylinder,  $y_{max,2}^+ = 0.416$  and  $y_{avg,2}^+ = 0.242$  on the downstream cylinder. The first cell layer near the plane wall was set to  $0.002D$  corresponding to  $y_{max,bot}^+ = 1.02$  and  $y_{avg,bot}^+ = 0.55$ . The near-wall mesh resolution is therefore, sufficient to resolve the laminar sublayer. The hydrodynamic force coefficient results for the cases with different grid and time resolutions are shown in Table 1. The relative difference in computed quantities with respect to the results obtained on the mesh M1A are given in the brackets. It is observed that for the case of a dense mesh (M3A) and medium mesh (M1A), the differences in the predicted hydrodynamic quantities are within the acceptable range, namely under 2%. The time step sensitivity study shows relatively small sensitivity of the computed quantities to the variation of  $\Delta t$  in



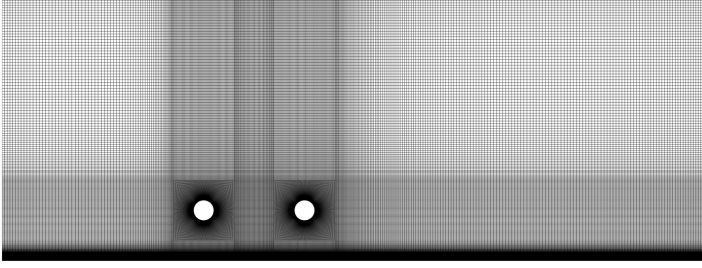


**Figure 2:** Example of a computational mesh for flow around a tandem cylinders vibrating with 2DOF (134 394 elements,  $L/D = 5$ ,  $e/D = 2$ ).

the investigated range. Time step  $\Delta t = 0.002$  is therefore selected and is expected to give a good balance between accuracy and computational efficiency. Overall, it appears that the mesh with 134 394 elements (M1A) with the time step  $\Delta t = 0.002$  can provide satisfactory spatial and time resolution for the simulations of tandem cylinders at  $Re = 13100$ .

**Table 1:** Results of the cases with different grid and time resolutions.

MESH	TIME STEP	ELEMENTS	$\overline{C}_{D,1}$	$\overline{C}_{L,1}^{rms}$	$\overline{C}_{D,2}$	$\overline{C}_{L,2}^{rms}$
M1A	$\Delta t = 0.002$	134394	1.537 (-)	1.149 (-)	0.122 (-)	1.261 (-)
M2A	$\Delta t = 0.002$	68033	1.468 (4.51%)	1.289 (12.23%)	0.114 (6.7%)	1.475 (16.94%)
M3A	$\Delta t = 0.002$	265616	1.540 (0.23%)	1.161 (1.04%)	0.123 (1.13%)	1.285 (1.94%)
M1B	$\Delta t = 0.004$	134394	1.559 (1.43%)	1.168 (1.74%)	0.124 (1.23%)	1.289 (2.18%)
M1C	$\Delta t = 0.001$	134394	1.524 (0.83%)	1.142 (0.64%)	0.121 (0.45%)	1.244 (1.33%)

#### 4 VALIDATION STUDY

The present model is used to simulate the flow around a single near-wall cylinder. The calculated hydrodynamic forces are compared with the experiential data from Lei et al. [10] and Kiya [9]. The domain size is the same as shown in Fig. 1, and the boundary layer thickness is set to  $\delta/D = 2.89$ . The investigated Reynolds number is  $Re = 13100$ , matching the  $Re$  reported in Lei et al. [10]. Figure 3 shows the variation of the mean drag coefficient ( $\overline{C}_D$ ) with gap ratio. A good agreement is found between the predicted  $\overline{C}_D$  values and experimental results by Lei et al. [10]. Overall, a good fit to the experimental data is reported and the present simulations are capable of capturing the drag force reduction on the downstream cylinder due to the interaction with the wake of the upstream cylinder.

The model ability to predict the vortex-induced vibration amplitudes and frequencies is validated by performing a set of simulations of an isolated cylinder vibrating with 2DOF at selected range of reduced velocities  $3 \leq U_r \leq 13$ . The present numerical study is set up according to the experiment settings reported by Jauvtis and Williamson [7]

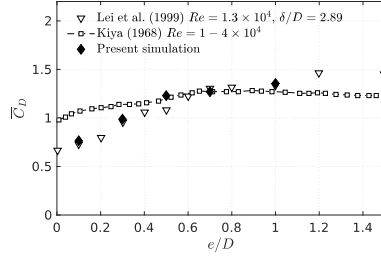


**Figure 3:** Comparison of mean drag coefficient predicted by the present model with the experimental data.

**Table 2:** Summary of the physical properties used in the simulations of an isolated cylinder vibrating with 2DOF.

Parameter	Value
Cylinder diameter $D$ [m]	0.0381
Cylinder mass [kg]	1.13
Added mass [kg]	1.13
Water density [kg/m <sup>3</sup> ]	1000
Mass ratio $m^*$ [-]	2.6
Damping ratio $\zeta$ [-]	0.0036
Natural frequency of the system [Hz]	0.4
Turbulent intensity $I$ [%]	0.7
Turbulent length scale $\ell$ [m]	0.0027

which are summarized in Table 2. Figure 4 shows the normalized maximum cross-flow vibration amplitudes ( $A_{Y,max}/D$ ) versus  $U_r$  predicted by the present numerical model compared to the experimental data. As the natural frequency of the cylinder approaches the vortex shedding frequency, the lock-in phenomenon is observed in which the response amplitude of the cylinder is amplified significantly. In both analysed settings the present model appears to predict the onset of the lock-in with reasonable accuracy. The branching behaviour described by Jauvtis and Williamson [7] is clearly visible in Fig. 4 with three distinguishable branches, namely the initial branch, the super upper branch, and the lower branch. The present numerical model results of the response amplitude agree well with earlier experimental data across the range of  $U_r$  considered. There are some discrepancies between the numerical results and experiment for displacement amplitudes corresponding to the peak response in the super upper branch. The predicted maximum of cross-flow non-dimensional amplitude is  $A_{Y,max}/D \approx 1.4$  which is slightly lower than  $A_{Y,max}/D = 1.5$  reported by Jauvtis and Williamson [7]. Generally, the present approach seems to provide reasonable accuracy and performance in capturing essential physics of flow-induced vibrations.

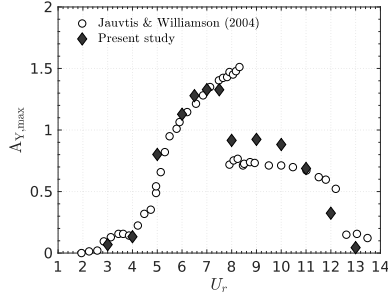


**Figure 4:** Comparison of response amplitudes in cross flow direction with experimental data.

## 5 RESULTS

The case matrix established in the present study is summarized in Table 3. The configuration of tandem cylinders with  $L/D = 5$  and  $e/D = 2$  is investigated over the range of reduced velocities  $3 \leq U_r \leq 14$  with increments of 0.5. For each analysed case the simulations are performed for  $tU/D = 250$  units of non-dimensional time. The mass ratio is kept constant at  $m^* = 3$ , and the damping factor value is set to  $\zeta = 0.005$ . Figure 5 shows the  $A_{Y,max}/D$  (a) and normalized root-mean-square in-line displacement

**Table 3:** Range of parameters investigated in the present study.

PARAMETER	VALUE
Cylinder diameters $D_1, D_2$	$D_1 = D_2 = D$
Mass ratio $m^*$	3
Damping ratio $\zeta$	0.005
Center-to-center spacing $L/D$	5
Gap ratio $e/D$	2
Reduced velocity range $U_r$	3 - 14

( $A_{X,rms}/D$ ) versus  $U_r$  for the upstream and the downstream cylinder. The cross-flow response of the upstream cylinder in the range of  $3 \leq U_r \leq 8$  clearly resembles the three branches identified in the response of the single cylinder (see Fig. 5 (a)). The main difference can be spotted in the lower branch for  $8.5 \leq U_r \leq 9.5$  where a sudden drop in the  $A_{Y,max}/D$  is observed. This indicates that despite being formally in the wake interference regime, the upstream cylinder is affected by the presence of the downstream cylinder. For the upstream cylinder the peak in the  $A_{X,rms}/D$  response coincides with the peak in  $A_{Y,max}/D$  response. In comparison to the upstream cylinder, the lock-in onset of the downstream cylinder is delayed and can be observed approximately at  $U_r = 5.5$ . The reason for that is the shielding effect due to the upstream cylinder presence which is amplified by its large vibration amplitude in the range of  $4 \leq U_r \leq 5.5$ , corresponding to

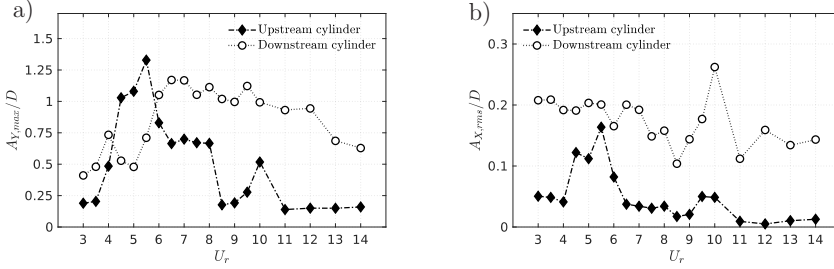


**Figure 5:** Normalized maximum cross-flow displacement  $A_{Y,max}/D$  (a) and normalized root-mean-square in-line displacement  $A_{X,rms}/D$  (b) for tandem cylinders vibrating with 2DOF versus reduced velocity  $U_r$ .

the initial and the super upper branch of the upstream cylinder response. The vibrating upstream cylinder disturbs the flow field in front of the downstream cylinder, causing a reduction in the mean flow velocity. The "true" reduced velocity experienced by the downstream cylinder is, therefore, lower than the nominal reduced velocity based on the free stream velocity  $U_\infty$ . In addition to the delay in the lock-in onset, the downstream cylinder shows much wider lock-in width in terms of  $U_r$  range. The peak  $A_{Y,max}/D$  amplitudes close to  $1D$  are observed in the range of  $6 \leq U_r \leq 12$ .

The  $A_{X,rms}/D$  of the downstream cylinder is generally much larger than that of the upstream cylinder. This is the consequence of the wake-induced vibrations caused by the vortices shed from the upstream cylinder impinging on the downstream cylinder, which will be shown in the subsequent flow field analysis. The  $A_{X,rms}/D$  response of the downstream cylinder shown in Fig. 5 (b) decreases monotonically with  $U_r$ , except for  $U_r = 10$  where a large increase of the in-line displacement is observed. This sudden increase is correlated with a smaller secondary peak in  $A_{X,rms}/D$  of the upstream cylinder. In order to explain the dynamics of the downstream cylinder the instantaneous non-dimensional vorticity ( $\omega D/U_\infty$ ) contour plots shown in Figs. 6 - 8 are presented and discussed. The solid line indicates counterclockwise vorticity and the dashed line indicates the negative vorticity, ten equispaced isocontours  $-4 \leq \omega D/U_\infty \leq 4$  are plotted. The dynamics of the vibrating tandem cylinders can be classified based on the vibration responses and the flow field characteristics. Regime A is identified in the range of  $U_r$  where the downstream cylinder vibration amplitude is small  $U_r < 5$ . Regime B is found at  $U_r \approx 4.5 - 5.5$  corresponding to the super upper branch of the upstream cylinder lock-in. Regime C is the regime where the vibration amplitude of the downstream cylinder is large, i.e.  $U_r \geq 6.5$ . In Regime A, the downstream cylinder is submerged in the wake of the upstream cylinder during the oscillation cycle (see Fig. 6). The phase lag of the downstream cylinder oscillation with respect to the upstream cylinder oscillation is approximately  $\tau = \pi$ . Vorticity that forms on the upstream cylinder merges with the vorticity of the same sign

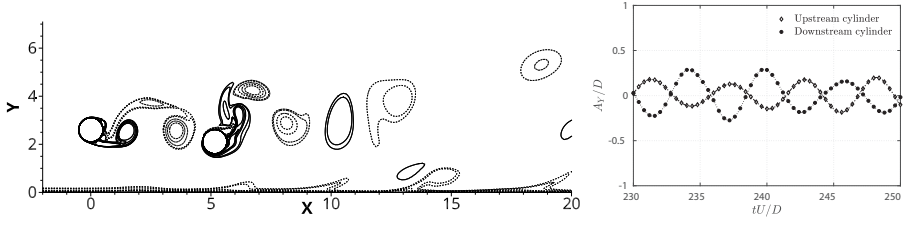


Figure 6: Vorticity contours and cross-flow displacement time series at  $U_r = 3$ .

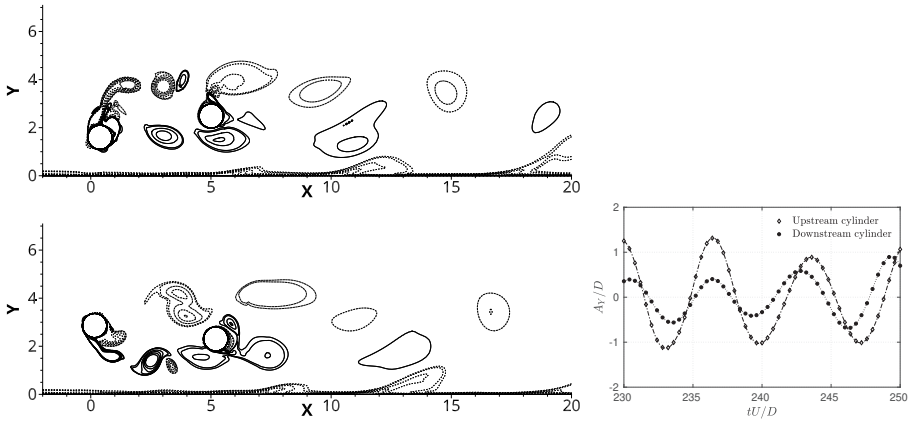
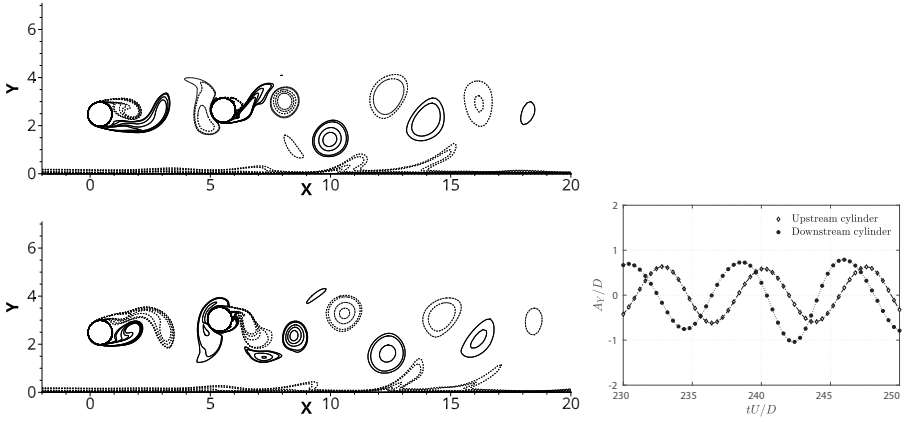


Figure 7: Vorticity contours and cross-flow displacement time series at  $U_r = 5.5$ .



**Figure 8:** Vorticity contours and cross-flow displacement time series at  $U_r = 8.5$ .

on the rear cylinder. One vortex of each sign is shed forming a regular vortex street.

Regime B exists for  $U_r \approx 4.5 - 5.5$ . For the cases in this  $U_r$  range, the upstream cylinder experiences large vibration amplitudes. The characteristic 2T vortex shedding mode is found in the wake of the upstream cylinder as evidenced by the vorticity contours shown in Fig. 7. The 2T shedding mode was first observed and described by Jauvtis and Williamson [7] who associated it with the super upper branch of the VIV response. In Regime B the cylinders oscillate in phase,  $\tau \approx 0$ . Large oscillation amplitude of the upstream cylinder is the reason for the wide wake formed behind it. The downstream cylinder is entrenched in the wake of the upstream cylinder, and its motion is governed by the strong vorticity formed and convected from the surface of the upstream cylinder.

Regime C exists for  $U_r \geq 6.5$  and is characterised by large oscillation amplitudes of the downstream cylinder, with the oscillation of the downstream cylinder lagging the front cylinder by  $\tau \approx \pi/2$ . Figure 8 shows the vorticity contours for the case of  $U_r = 8$ . Compared to the Regime A the increased vortex formation length is observed. Upstream cylinder oscillation amplitudes are much lower than that in Regime B. In consequence, a narrow wake is formed behind the upstream cylinder, and the vortices shed directly impinge the downstream cylinder. In a complex interaction, negative and positive vorticity from the front cylinder is subsumed by the vortex formation on the rear cylinder each half cycle. Within each cycle, this vortex interaction creates two pairs of unequal strength vortices.

## 6 CONCLUSIONS

Wake-induced vibrations of two tandem cylinders near a horizontal plane wall with centre-to-centre spacing  $L/D = 5$  and gap ratio  $e/D = 2$  have been investigated numerically.

ically. The simulations have been performed at  $Re = 13100$  and normalized boundary layer thickness  $\delta/D = 2.89$ . The results for the flow around tandem cylinders vibrating with two degrees-of-freedom have been presented. Three distinct regimes of oscillation and vortex-shedding have been identified in the range of investigated  $U_r$ . The oscillation regimes have been characterised based on the vibration amplitudes, a phase difference between the two cylinders oscillations and flow field analysis using vorticity contours. The extended resonant range of the downstream cylinder has been observed and has been attributed to the interaction with the upstream cylinder's wake. In comparison to the single cylinder VIV response, the onset of the lock-in of the downstream cylinder is shifted to higher  $U_r$  value. The lock-in width in terms of  $U_r$  range is significantly increased for the downstream cylinder. The in-line vibration amplitudes of the downstream cylinder are largely increased due to the flow disturbances introduced by the vibrating upstream cylinder.

A series of numerical simulations have been performed in order to validate the model. The simulation results reveal that the present model predicts the drag coefficient with good accuracy. The present model provides reasonable accuracy with respect to the prediction of the vibration amplitudes.

## ACKNOWLEDGEMENTS

This study was supported in part with computational resources provided by the Norwegian Metacenter for Computational Science (NOTUR), under Project No: NN9372K.

## REFERENCES

- [1] ALAM, M., MORIYA, M., TAKAI, K., AND SAKAMOTO, H. Fluctuating fluid forces acting on two circular cylinders in a tandem arrangement at a subcritical reynolds number. *Journal of Wind Engineering & Industrial Aerodynamics* 91, 1 (2003), 139 – 154.
- [2] BEARMAN, P., AND ZDRAVKOVICH, M. Flow around a circular cylinder near a plane boundary. *Journal of Fluid Mechanics* 89 (1978), 33 – 47.
- [3] BHATTACHARYYA, S., AND DHINAKARAN, S. Vortex shedding in shear flow past tandem square cylinders in the vicinity of a plane wall. *Journal of Fluids and Structures* 24, 3 (2008), 400 – 417.
- [4] GUILMINEAU, E., AND QUEUTEY, P. Numerical simulation of vortex-induced vibration of a circular cylinder with low mass-damping in a turbulent flow. *Journal of Fluids and Structures* 19, 4 (2004), 449 – 466.
- [5] HAN, X., LIN, W., WANG, D., QIU, A., FENG, Z., TANG, Y., AND WU, J. Numerical simulation of super upper branch of a cylindrical structure with a low mass ratio. *Ocean Engineering* 168 (2018), 108 – 120.

- [6] HARICHANDAN, A., AND ROY, A. Numerical investigation of flow past single and tandem cylindrical bodies in the vicinity of a plane wall. *Journal of Fluids and Structures* 33, Supplement C (2012), 19 – 43.
- [7] JAUVTIS, N., AND WILLIAMSON, C. H. K. The effect of two degrees of freedom on vortex-induced vibration at low mass and damping. *Journal of Fluid Mechanics* 509 (2004), 23 – 62.
- [8] KANG, Z., NI, W.-C., ZHANG, X., AND SUN, L.-P. Two improvements on numerical simulation of 2-dof vortex-induced vibration with low mass ratio. *China Ocean Engineering* 31, 6 (Dec 2017), 764–772.
- [9] KIYA, M. Study on the turbulent shear flow past a circular cylinder. *Bulletin of the Faculty of Engineering* 50 (1968), 1 – 100.
- [10] LEI, C., CHENG, L., AND KAVANAGH, K. Re-examination of the effect of a plane boundary on force and vortex shedding of a circular cylinder. *Journal of Wind Engineering & Industrial Aerodynamics* 80, 3 (1999), 263 – 286.
- [11] LI, Z., ABRAHAMSEN-PRSIČ, M., ONG, M. C., AND KHOO, B. C. Large eddy simulations of flow around two circular cylinders in tandem in the vicinity of a plane wall at small gap ratios. *Journal of Fluids and Structures* 76 (2018), 251 – 271.
- [12] MENTER, F. R., KUNTZ, M., AND LANGTRY, R. Ten years of industrial experience with the sst turbulence model. *Heat and Mass Transfer* 4 (2003), 625 – 632.
- [13] ONG, M. C., UTNES, T., HOLMEDAL, L. E., MYRHAUG, D., AND PETTERSEN, B. Numerical simulation of flow around a smooth circular cylinder at very high reynolds numbers. *Marine Structures* 22, 2 (2009), 142 – 153.
- [14] ONG, M. C., UTNES, T., HOLMEDAL, L. E., MYRHAUG, D., AND PETTERSEN, B. Near-bed flow mechanisms around a circular marine pipeline close to a flat seabed in the subcritical flow regime using a  $k - \epsilon$  model. *ASME. Journal of Offshore Mechanics and Arctic Engineering* 134, 2 (2011), 021803 – 021803–11.
- [15] PAN, Z., CUI, W., AND MIAO, Q. Numerical simulation of vortex-induced vibration of a circular cylinder at low mass-damping using rans code. *Journal of Fluids and Structures* 23, 1 (2007), 23 – 37.
- [16] PRICE, S., SUMNER, D., SMITH, J., LEONG, K., AND PAIDOUSSIS, M. Flow visualization around a circular cylinder near to a plane wall. *Journal of Fluids and Structures* 16, 2 (2002), 175 – 191.
- [17] SUMNER, D. Two circular cylinders in cross-flow: A review. *Journal of Fluids and Structures* 26, 6 (2010), 849 – 899.



- [18] WANDERLEY, J. B., SOUZA, G. H., SPHAIER, S. H., AND LEVI, C. Vortex-induced vibration of an elastically mounted circular cylinder using an upwind tvd two-dimensional numerical scheme. *Ocean Engineering* 35, 14 (2008), 1533 – 1544.
- [19] WANG, X., HAO, Z., AND TAN, S. Vortex-induced vibrations of a neutrally buoyant circular cylinder near a plane wall. *Journal of Fluids and Structures* 39, Supplement C (2013), 188 – 204.
- [20] ZDRAVKOVICH, M. Classification of flow-induced oscillations of two parallel circular cylinder in various arrangements. *ASME Winter Annual Meeting, Symposium on Flow-Induced Vibrations 2* (1984), 1 – 18.
- [21] ZDRAVKOVICH, M. *Flow Around Circular Cylinders: Volume I: Fundamentals*. Oxford University Press, 1997.



# NUMERICAL SOLUTION OF POISSON EQUATION USING SHERMAN-MORRISON ALGORITHM IN TAYLOR-GREEN VORTEX FLOW

ROHITH JAYARAM<sup>1</sup>, JURRIAAN J.J. GILLISSEN<sup>2</sup>, LIHAO ZHAO<sup>3</sup> AND  
HELGE I. ANDERSSON<sup>1</sup>

<sup>1</sup>Department of Energy and Process Engineering  
Norwegian University of Science and Technology  
Trondheim, Norway  
e-mail: rohith.jayaram@ntnu.no  
e-mail: helge.i.andersson@ntnu.no

<sup>2</sup> Department of Mathematics  
University College London, United Kingdom  
e-mail: jurriaangillissen@gmail.com

<sup>3</sup> AML, Department of Engineering Mechanics  
Tsinghua University, China  
e-mail: zhaolihao@mail.tsinghua.edu.cn

**Key words:** Taylor-Green vortex, Sherman-Morrison algorithm, Poisson equation, Solver code validation, Spherical particles

**Abstract.** The validation of the Sherman-Morrison algorithm to solve the Poisson equation with periodic boundary conditions constitutes the essence of the study. The solver code of channel flow case (no-slip boundary condition) is changed to include the periodic boundary conditions to simulate the Taylor-Green vortex (TGV) flow using Sherman-Morrison algorithm. The kinetic energy, dissipation rate and energy spectra are examined along with the evolution of vortex break-up and decay. Results are in reasonable agreement with the standard reference solution. The study is further extended by examining the particle concentration with the Q criterion. But, the main focus of the paper is the validation of the algorithm and particle statistics just serves as motivation for the future study.

## 1 INTRODUCTION

Turbulence is a ubiquitous phenomenon which always offer its share of surprises in its understanding. Understanding the dynamics of turbulent flow has its own challenges from

the numerical and mathematical point of view. All fluid flows are described by the Navier-Stokes equations and time dependent solutions of the Navier-Stokes equations represent the turbulent motion of the flow. Such solutions are still an unsolved problem from the mathematical point of view and hence numerical simulations have their advantage.

Direct numerical simulations (DNS) solve the unsteady Navier-Stokes equations to compute all the scales of turbulent motion. This is an accurate method to predict the turbulent motion since no modelling is required at any stage. Reynolds number of the flow in nature is quite high and hence to simulate the same using DNS requires huge computing capacities. To capture the smallest eddy, DNS needs high resolution computational mesh and time step which indeed leads to a huge consumption of memory and CPU hours. In general, DNS is a costly numerical experiment and only restricted to low or moderately high Reynolds numbers.

The Taylor-Green vortex flow is one of the simplest and classic flow systems to study the vortex dynamics, energy dissipation process, transition and decay [1, 2, 3]. It is also one of the classic systems to study the generation of excitations at small scales and the resulting turbulence [4]. Initially it consists of a smooth vortex distribution. As time advances, since there is no external forcing, vortex rolls up, stretch and eventually break down into turbulence [1]. Small scale turbulent motion eventually loses all its energy and dies out. The periodic 3D TGV flow is computed from an initial condition in terms of its velocity field at  $t = 0$ . Periodic boundary conditions are applied to all the boundary surfaces. As time advances, vortices start to break down and energy is cascaded to smaller scales and eventually dies out. The TGV problem is simple and a good benchmark to test and validate numerical schemes [1, 5].

Suspensions of particles in a turbulent flow have been extensively studied in the view to better understand the transport mechanisms, dispersion and other mechanisms [6]. It is interesting to study the particle motion in response to the breaking down of the vortices in TGV flow. Spherical particles are considered in this study. The complexity can be increased by looking into non-spherical particles and also by the addition of forces like gravity, lift etc. The focus of this work is only to study the validation and use of the Sherman-Morrison algorithm to solve the Poisson equation with periodic boundary conditions and hence the study of particles in TGV flow just serves as a motivation for the future study.

In the present study, a spectral scheme is applied in two directions while a finite-difference scheme in the other to solve the Navier-Stokes equations. The Sherman-Morrison algorithm is used to solve the Poisson equation originating from the standard projection method. The motivation to validate the solver code (using Sherman-Morrison algorithm) in TGV flow is to extend the present code to simulate homogeneous shear turbulent flow (HST) in the near future. In simulating HST, using spectral schemes in all three directions leads to remeshing the flow periodically to keep the numerical errors in check [7, 8]. This indeed leads to loss of enstrophy and energy that degrade the accuracy of the solution. This can be avoided by using 'shear-periodic' boundary conditions in

which periodicity is enforced between shifting points of the upper and bottom boundaries of the computational box using finite-difference scheme [8]. Thus, the Sherman-Morrison algorithm solving the Poisson equation with periodic boundary conditions in TGV flow, will be further extended to solve the same with shear-periodic boundary conditions to simulate HST provides the motivational background for the current work.

## 2 NUMERICAL METHODOLOGY

### 2.1 Governing equations

In the present work, 3D TGV flow is considered. The fluid flow is assumed to be incompressible, Newtonian and isothermal which is governed by the mass and momentum conservation equations,

$$\frac{\partial u_i}{\partial x_i} = 0 \quad (1)$$

$$\frac{\partial u_i}{\partial t} + u_j \frac{\partial u_i}{\partial x_j} = -\frac{\partial p}{\partial x_i} + \frac{1}{Re} \frac{\partial^2 u_i}{\partial x_j \partial x_j}, \quad (2)$$

where  $u_i$  is the  $i^{\text{th}}$  component of the velocity vector,  $\frac{\partial p}{\partial x_i}$  is the pressure gradient and  $Re$  is the Reynolds number defined in the next section is used to normalise the above equation. Equations (1) and (2) are solved fully in DNS and hence without the involvement of any modelling.

### 2.2 Flow conditions

A cubical domain with sides of length  $2\pi L$  is considered. Initial conditions for the simulation are specified by the following relations

$$u = V_0 \sin\left(\frac{x}{L}\right) \cos\left(\frac{y}{L}\right) \cos\left(\frac{z}{L}\right) \quad (3)$$

$$v = 0 \quad (4)$$

$$w = -V_0 \cos\left(\frac{x}{L}\right) \cos\left(\frac{y}{L}\right) \sin\left(\frac{z}{L}\right), \quad (5)$$

where,  $u, v, w$  are the three components of the velocity vector  $u_i$  and  $V_0$  is the large scale velocity of the vortex at the start of the simulation. These initial conditions satisfy the continuity equation (1) and the momentum equations (2).  $Re$  used in equation (2) is defined by  $V_0$ ,  $L$  and kinematic viscosity  $\nu$ .  $Re$  is set to be 1600, which is the Reynolds number used in the reference solution [4].

## 2.3 Code description

Initially, the code was intended to simulate channel flow cases with no-slip boundary conditions. So, the main focus of the work is to convert the code from channel flow problem to TGV flow problem. In the channel flow case, periodic boundary conditions are imposed in homogeneous streamwise ( $x$ ) and spanwise ( $y$ ) directions while no-slip boundary condition is imposed in the wall-normal ( $z$ ) direction. A standard projection method is employed for the time advancement of the Navier-Stokes equations and the resulting Poisson equation is solved eventually using a tri-diagonal matrix algorithm (TDMA).

But in TGV flow, the periodic boundary condition alters the coefficient matrix of the Poisson equation and hence direct usage of TDMA is not possible. This necessitates to find a new algorithm to solve the linear system of equations of the new Poisson equation. All sections of the channel flow code is retained the same for the TGV flow case as well, except changing the solver. Staggered grid is used in the code with velocity components  $u, v$  and pressure  $p$  defined at the cell center and velocity component  $w$  is defined at the cell-face center.

### 2.3.1 Numerical method

A pseudo-spectral method is used to compute spatial derivatives in the homogeneous  $x$  and  $y$  directions. Second order central finite-difference method is used to compute spatial derivatives in  $z$  direction. In the pseudo-spectral method, spatial derivatives are computed by transforming variables into spectral space using Fourier series representation. So, the velocity vector is expressed as follows

$$u_i(x_i, t) = \sum_k \hat{u}_k(t) e^{ikx_i}, \quad (6)$$

where,  $x_i$  is the position vector in physical space, while  $k$  is the wave number in spectral space. First and second derivatives are computed by multiplying the transformed terms with  $ik_x$  and  $-k_x^2$  and then transformed back to physical space. This forward and backward transformation is done using FFT (Fast Fourier transform).

The Navier-Stokes equations are advanced in time using the second-order explicit Adams-Bashforth scheme. The standard projection method is summarized in steps,

Step 1: Intermediate velocity  $u_i^*$  is computed at time between  $t^n$  and  $t^{n+1}$  by neglecting the pressure  $p^n$  as

$$\frac{u_i^* - u_i^n}{\Delta t} = \frac{3}{2}T(u_i^n) - \frac{1}{2}T(u_i^{n-1}), \quad (7)$$

where,  $T(u_i^n) = -u_j^n \frac{\partial u_i^n}{\partial x_j} + \frac{1}{Re} \frac{\partial^2 u_i^n}{\partial x_j \partial x_j}$ , is the transport terms, i.e. convection and diffusion.

Step 2: Solving the Poisson equation to compute pressure at the new time level

$$\nabla^2 p^{n+1} = \frac{\nabla \cdot u^*}{\Delta t} \quad (8)$$

Step 3: Velocity at the new time level is updated from the computed pressure at the new time level by,

$$u_i^{n+1} - u_i^* = -\Delta t \frac{\partial p^{n+1}}{\partial x_i}. \quad (9)$$

The Poisson equation is solved at every time step to calculate the velocity at each instant by maintaining the mass conservation. It is solved using FFT in  $x$  and  $y$  directions. While in  $z$  direction, it leads to a system of linear equations of tri-diagonal matrix form with two extra entries in the upper and the lower diagonal corner of the coefficient matrix due to the periodic boundary condition of the TGV flow. This facilitates to use Sherman-Morrison algorithm to solve the Poisson equation.

### 3 Sherman-Morrison algorithm

The Sherman-Morrison formula is one of the attractive methods to solve linear systems of equations arising from elliptical partial differential equations. It is a direct method and uses a finite iterative process [9]. Linear system of equations of the discrete Poisson equation is denoted as,

$$\tilde{A}p = d, \quad (10)$$

where,  $\tilde{A}$  is the coefficient matrix of size  $n \times n$ ,  $p$  denotes the pressure matrix and  $d$  denotes the RHS of the equation (8). The expansion of equation (10) is,

$$\begin{bmatrix} b_1 & c_1 & 0 & \dots & & & \beta \\ a_2 & b_2 & c_2 & \dots & & & \\ & & & \dots & & & \\ & & & \dots & a_{N-1} & b_{N-1} & c_{N-1} \\ \alpha & & & \dots & 0 & a_N & b_N \end{bmatrix} \begin{bmatrix} p_1 \\ p_2 \\ \dots \\ p_{N-1} \\ p_N \end{bmatrix} = \begin{bmatrix} d_1 \\ d_2 \\ \dots \\ d_{N-1} \\ d_N \end{bmatrix}. \quad (11)$$

In the coefficient matrix  $\tilde{A}$ ,  $(b_1, b_2, \dots, b_n)$  are the diagonal elements,  $(c_1, c_2, \dots, c_{n-1})$  are the upper-diagonal elements and  $(a_2, a_3, \dots, a_n)$  are the lower-diagonal elements. It would have been a perfect tri-diagonal matrix without the two cornered elements  $\alpha$  and  $\beta$ . The extra two elements in the coefficient matrix are due to the periodic boundary conditions of TGV flow. The Sherman-Morrison algorithm to solve equation (11) is summarized in three steps,

Step 1:  $\tilde{A}$  is re-written as  $\tilde{A} = \hat{A} + l \otimes m$

where,

$$\hat{A} = \begin{bmatrix} 2b_1 & c_1 & 0 & \dots & & 0 \\ a_2 & b_2 & c_2 & \dots & & \\ & & \dots & & & \\ & & \dots & a_{N-1} & b_{N-1} & c_{N-1} \\ 0 & & \dots & 0 & a_N & b_N + \frac{c_N a_1}{b_1} \end{bmatrix} \quad (12)$$

$$l = \begin{bmatrix} \gamma \\ 0 \\ \cdot \\ \cdot \\ \cdot \\ 0 \\ \alpha \end{bmatrix} \quad m = \begin{bmatrix} 1 \\ 0 \\ \cdot \\ \cdot \\ \cdot \\ 0 \\ \beta/\gamma \end{bmatrix}. \quad (13)$$

Step 2: Solving the two auxiliary equations using TDMA to find  $y$  and  $z$  column vectors. TDMA is summarized in the Appendix A.

$$\hat{A}y = d \quad \hat{A}z = l \quad (14)$$

Step 3: In terms of the above, the pressure matrix is obtained as,

$$p = y - \left[ \frac{m^T \cdot y}{1 + m^T \cdot z} \right] z \quad (15)$$

The main idea of the algorithm is to re-write the coefficient matrix in such a way that it remains tri-diagonal and hence TDMA could be applied. TDMA is applied twice to solve the auxiliary equations which increases the number of operations. But, the simplicity of implementation is rewarded in return.

## 4 RESULTS

### 4.1 TGV flow simulation

The primary method for evaluating the TGV solutions is to examine the rate at which the fluid dissipates the kinetic energy in the domain [4]. Volume averaged kinetic energy is computed in the cubic domain  $\Omega$  by

$$E_k = \int_{\Omega} \frac{u'_i u'_i}{2} d\Omega, \quad (16)$$



where,  $u'_i$  denotes the velocity. The volume averaged energy dissipation rate is computed in two ways. One way is to compute directly from the first principles,

$$\langle \epsilon_{iso} \rangle = \nu \langle \frac{\partial u'_i}{\partial x_j} \frac{\partial u'_i}{\partial x_j} \rangle, \quad (17)$$

where,  $\langle \rangle$  represents the volume average of the physical quantity in the cubic domain  $\Omega$ . The other way to calculate  $\epsilon$  is from the decay rate of the kinetic energy  $E_k$  as

$$\epsilon(E_k) = -\frac{dE_k}{dt}. \quad (18)$$

$\epsilon(E_k)$ , kinetic energy dissipation rate (KEDR), is written as function of  $E_k$  to emphasise that it is computed directly from the kinetic energy in the domain [1]. All the physical quantities like kinetic energy, energy dissipation rate, vorticity and time are normalized using the velocity scale  $V_0$  and length scale  $L$ .

In figure 1(a), the evolution of volume averaged kinetic energy is plotted in comparison with the reference solution [4]. A small discrepancy is seen owing to the accuracy of the second order central finite-difference in  $z$  direction in comparison with the spectral accuracy in  $x$  and  $y$  directions. Accuracy can be further increased by increasing the number of grid points in  $z$  direction to 256 and 512 from the current 128. In figure 1(b), evolution of volume averaged  $\epsilon$  is plotted in comparison with the reference solution [13]. The reference solution of  $\epsilon$  is computed as  $\epsilon(E_k)$ , i.e. kinetic energy dissipation rate (KEDR). The peak of the energy dissipation is seen at around  $t=9$  in the reference solution.

Evolution of iso-contours of the  $y$ -component vorticity ( $\omega_y$ ) is presented in figure 3, where  $\omega_y = (\frac{\partial u}{\partial z} - \frac{\partial w}{\partial x})$ , where  $u$  and  $w$  are the  $x$  and  $z$  component of the velocity vector  $u_i$ . This illustrates the evolution breaking down of vortices as depicted in the reference solution [1]. It starts with the smooth vortices and as time advances, vortex structure starts to undergo structural changes. The flow is more or less inviscid till  $t = 5$ . At  $t = 7$ , coherence starts to break down and eventually the flow becomes turbulent and finally the smaller structures slowly decay until the flow comes to rest.

The progression of energy spectra is shown in figure 2. At  $t = 3$ , the energy is confined to small wave numbers  $k$ . Energy begins to cascade down to smaller and smaller scales as time progresses. It can be observed in figure 2 that the peak of the energy dissipation is around  $t = 9$ . This is clearly seen in the figure 1b, where the energy in the smallest scales peaks at  $t = 9$ , which is consistent with the maximum energy dissipation rate.

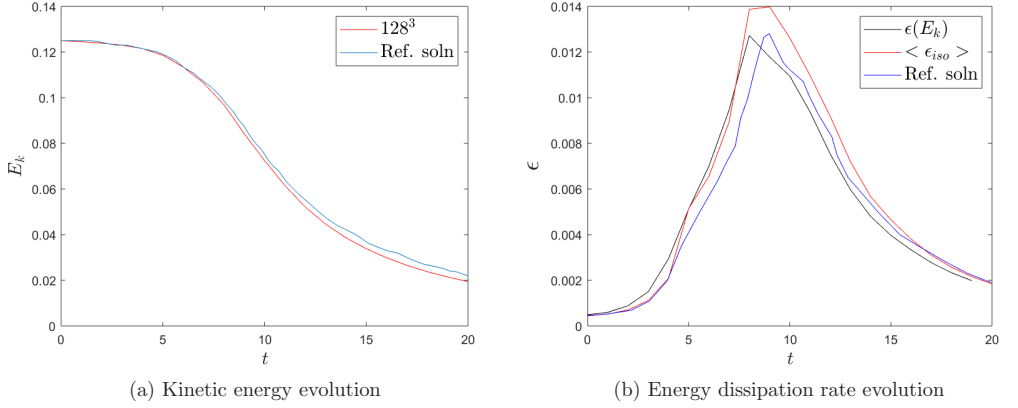


Figure 1: Kinetic energy and dissipation rate evolution on the  $128^3$  grid compared with the reference solutions [4, 13].

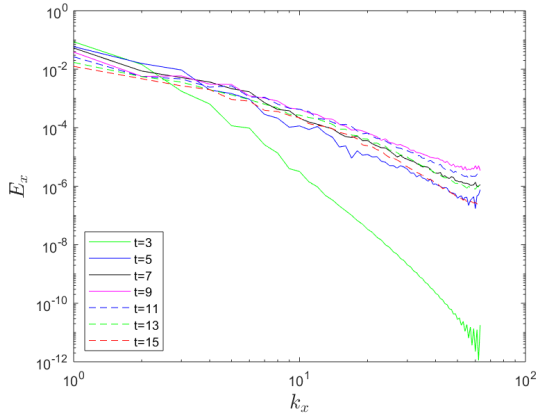


Figure 2: Evolution of energy spectra in  $x$  direction on the  $128^3$  grid.

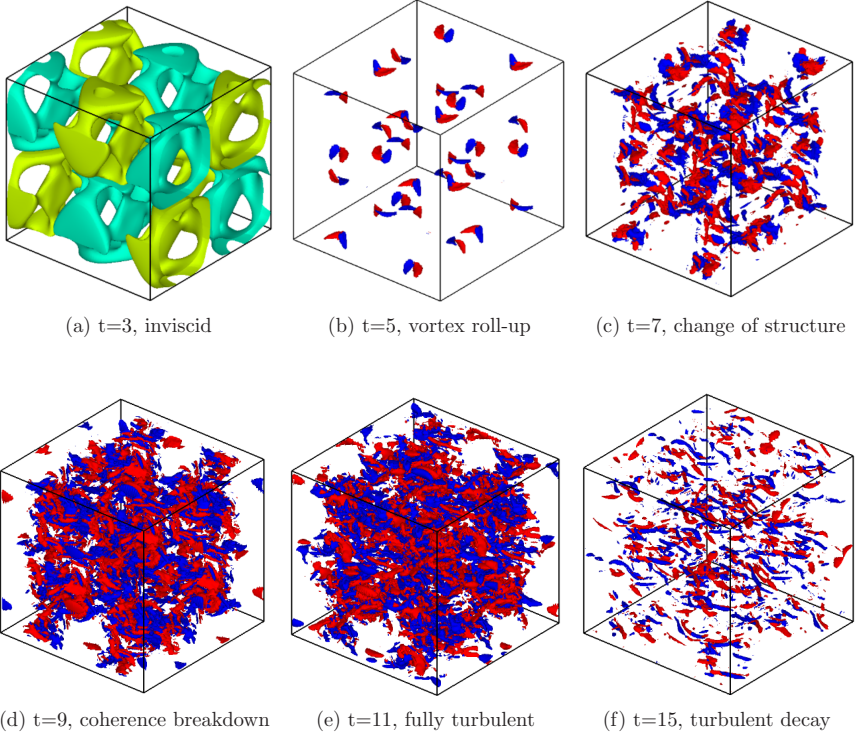


Figure 3: Iso-surfaces of  $y$ -vorticity ( $\omega_y$ ) on the  $128^3$  grid in comparison with the reference [1]. The colours distinguish between ( $\omega_y > 0$ ) and ( $\omega_y < 0$ )

## 4.2 Particles in TGV flow

TGV flow is one of the simplest turbulent flows to realise computationally and it is quite interesting to look at particle motion in the flow. The scope of the result presented in this article related to particles is just to show a glimpse of the particle motion in TGV flow without going further deep, since the main focus of this article is about the Sherman-Morrison algorithm for the Poisson equation. Particle concentration contours are presented at time  $t = 5$  in comparison with the contour of  $z$ -component of vorticity and the second invariant of the velocity gradient tensor  $Q$  at the midplane sliced at  $z = \pi$ .

$Q$  represents the balance between the strain rate and rotation rate magnitude [10],

$$Q = \frac{1}{2}[\|\Omega_{ij}\|^2 - \|S_{ij}\|^2], \quad (19)$$

where,  $\Omega_{ij} = \frac{1}{2}(\frac{\partial u_i}{\partial x_j} - \frac{\partial u_j}{\partial x_i})$  and  $S_{ij} = \frac{1}{2}(\frac{\partial u_i}{\partial x_j} + \frac{\partial u_j}{\partial x_i})$  represent the rotation rate tensor and strain rate tensor, respectively. Strain rate is dominating if  $Q < 0$  and vice-versa if  $Q > 0$ .  $Q$  characterises the velocity field in terms of its strain rate and high vortex regions.

Inertial spherical particles are represented by means of a Lagrangian point-particle approach where each individual particle is tracked at every time-step [6, 11]. One-way coupling is considered to see the effect of the flow on the particle motion. The Stokes number is defined as the ratio of particle response time to a characteristic time of the flow. Here, the flow time is based on the velocity scale  $V_0$  and length scale  $L$ .  $St = 1$  is considered in the current case.

A Voronoï diagram is one of the powerful tools to quantify the preferential concentration/clustering of particles [12]. A Voronoï diagram is the unique decomposition of  $nD$  space into independent cells associated to each particle. One Voronoï cell is defined as the ensemble of points that are closer to the particle than any other [12]. Sample 2D-Voronoï diagram for the instantaneous distribution of particles in the slice  $z = \pi$  is shown in figure 5. From the definition of Voronoï diagram, the inverse of the volume  $V$  of a Voronoï cell is the local concentration of the particles.

It is observed from figure 4 that particles are concentrating at  $Q < 0$ , which is strain rate dominant region. Also, no concentration of particles is observed inside the strong vortex regions. This is consistent with previous research about the particle inertia producing a bias in its trajectory towards regions of high strain rate or low vorticity [14]. This indeed is due to the fact that a centrifugal force of the vortex flow will throw the particles outside its region. The above result just serves as a teaser to the potential study left on particles in TGV flow.

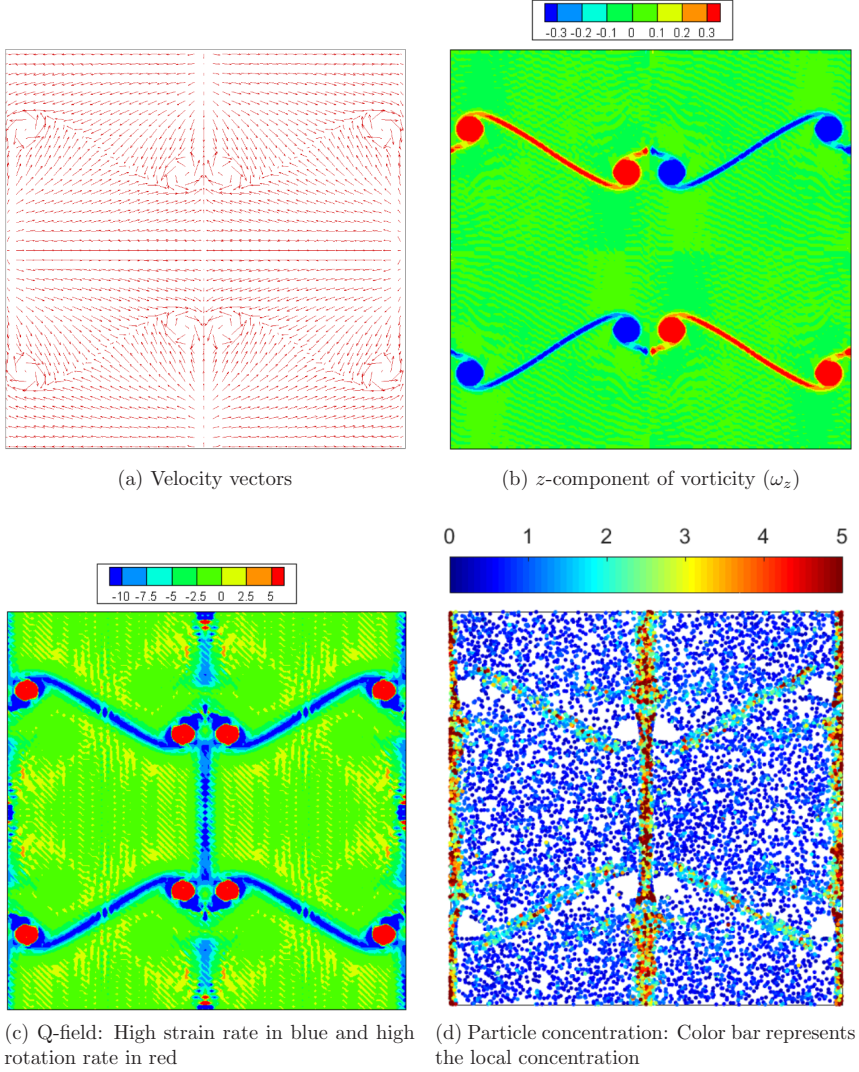


Figure 4: Comparison of particle concentration with Q-field at  $(x,y)$  midplane, sliced at  $z = \pi$  for all the four plots

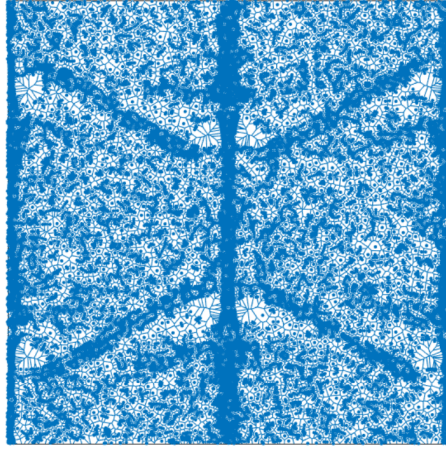


Figure 5: 2D Voronoï volumes at  $(x,y)$  midplane, sliced at  $z = \pi$

## 5 CONCLUSION

The validation of the Sherman-Morrison algorithm in solving the Poisson equation with periodic boundary conditions in TGV flow is undertaken in this study. As an extension of the study, concentration of particles in the context of TGV flow is presented to observe the regions of the flow where the particles are getting concentrated.

The Sherman-Morrison algorithm serves as a good tool to solve the Poisson equation with the periodic boundary conditions in all the three directions. It essentially uses TDMA twice to solve the auxiliary equations by modifying the coefficient matrix. This is simple in execution.

The algorithm is validated by solving the Poisson equation in TGV flow incorporating the periodic boundary conditions. A  $128^3$  grid is considered in the simulation. The time evolution of kinetic energy and energy dissipation rate is in reasonable agreement with the reference solution. The error can be reduced by increasing the number of grid points in  $z$  direction to 256, 512 and so on. The study of energy spectrum showed that the energy in the smallest scales peaks at  $t = 9$ . This is consistent with the fact that maximum energy dissipation occurs at the time  $t = 9$ . A more qualitative picture of vortex breaking down is studied by the evolution of iso-surfaces of  $y$ -vorticity. The coherence breaks down at  $t = 7$  and the vortical structures further breaks down to become turbulent which eventually dies out.

As an extension of this study, particle concentration is examined using Voronoï volumes. To facilitate the study,  $Q$  criterion is used to characterize the velocity field into high vortex and high strain rate dominant regions. In the back-drop of the  $Q$  field, it is observed that

the particles are more concentrated in the strong strain rate regions ( $Q < 0$ ) and almost zero at the high vortex regions ( $Q > 0$ ). With the validation of the solver code in TGV flow, the study on particles in TGV flow can be further extended.

## 6 ACKNOWLEDGMENTS

We thank Yucheng Jie for useful discussions on particle concentration using Voronoi volume method. This work has been supported by The Research Council of Norway through research grant no. 250744 and computational resources through grant no. NN2694K.

## REFERENCES

- [1] J.R. DeBonis. *Solutions of the Taylor-Green vortex problem using high-resolution explicit finite difference methods*. AIAA paper: 0382, 2013.
- [2] N. Sharma and T.K. Sengupta. *Vortex dynamics of the three-dimensional Taylor-Green vortex problem*. Physics of Fluids 31: 035106, 2019.
- [3] M.E. Brachet, D.I. Meiron, S.A. Orszag, B.G. Nickel, R.H. Morf and U. Frisch. *Small-scale structure of the Taylor-Green vortex*. Journal of Fluid Mechanics 130: 411-452, 1983.
- [4] M.E. Brachet. *Direct simulation of three-dimensional turbulence in the Taylor-Green vortex*. Fluid Dynamics Research 8: 1-4, 1991.
- [5] T. Dairay, E. Lamballais, S. Laizet and J.C. Vassilicos. *Numerical dissipation vs. subgrid-scale modelling for large eddy simulation*. Journal of Computational Physics 337: 252-274, 2017.
- [6] L. Zhao and H.I. Andersson. *Computation of particle-laden turbulent flows*. The 23rd Nordic seminar on Computational Mechanics, Stockholm: 2010.
- [7] T. Gerz, U. Schumann and S.E. Elghobashi. *Direct numerical simulation of stratified homogeneous turbulent shear flows*. Journal of Fluid Mechanics 200: 563-594, 1989.
- [8] A. Sekimoto, S. Dong and J. Jiménez. *Direct numerical simulation of statistically stationary and homogeneous shear turbulence and its relation to other shear flows*. Physics of Fluids 28: 035101, 2016.
- [9] N. Egidi and P. Maponi. *A Sherman-Morrison approach to the solution of linear equations*. Journal of Computational and Applied Mathematics 189: 703-718, 2006.
- [10] J.C.R. Hunt, A.A. Wray and P. Moin. *Eddies, streams, and convergence zones in turbulent flows*. Center for Turbulence Research Report CTR-S88: 193-208, 1988.

- [11] P.H. Mortensen, H.I. Andersson, J.J.J. Gillissen and B.J. Boersma. *Dynamics of prolate ellipsoidal particles in a turbulent channel flow*. Physics of Fluids 20: 093302, 2008.
- [12] R. Monchaux, M. Bourgoïn and A. Cartellier. *Analyzing preferential concentration and clustering of inertial particles in turbulence*. International Journal of Multiphase Flow 40: 1-18, 2012.
- [13] W.M. van Rees, A. Leonard, D.I. Pullin and P. Koumoutsakos. *A comparison of vortex and pseudo-spectral methods for the simulation of periodic vortical flows at high Reynolds numbers*. Journal of Computational Physics 230: 2794-2805, 2011.
- [14] M.R. Maxey. *The gravitational settling of aerosol particles in homogeneous turbulence and random flow fields*. Journal of Fluid Mechanics 174: 441-465, 1987.

## Appendix A Tri-diagonal matrix algorithm

The tri-diagonal matrix algorithm (TDMA) is a simple method to solve a linear system of equations. It is one of the special cases of Gaussian elimination. Consider the system of linear equations in the form,

$$Ap = d. \quad (20)$$

Expanding equation (20),

$$\begin{bmatrix} b_1 & c_1 & 0 & \dots & & 0 \\ a_2 & b_2 & c_2 & \dots & & \\ & & \dots & \dots & \dots & \\ & & \dots & a_{N-1} & b_{N-1} & c_{N-1} \\ 0 & & \dots & 0 & a_N & b_N \end{bmatrix} \begin{bmatrix} p_1 \\ p_2 \\ \dots \\ p_{N-1} \\ p_N \end{bmatrix} = \begin{bmatrix} d_1 \\ d_2 \\ \dots \\ d_{N-1} \\ d_N \end{bmatrix}. \quad (21)$$

TDMA to solve (21) in two steps:

Step 1: Forward elimination

$\forall i = 2, 3, \dots, N$

$$k_1 = b_1, \quad Q_1 = \frac{d_1}{k_1}, \quad k_i = b_i - \frac{a_i c_{i-1}}{k_{i-1}}, \quad Q_i = \frac{d_i - a_i Q_{i-1}}{k_i}; \quad (22)$$

Step 2: Backward substitution

$$p_N = Q_N, \quad p_i = Q_i - \frac{c_i p_{i+1}}{k_i}. \quad (23)$$



## ADAPTIVE MESH REFINEMENT ON UNSTRUCTURED CARTESIAN GRIDS FOR THE EULER EQUATIONS

FREDERIK KRISTOFFERSEN<sup>1</sup> AND BERNHARD MÜLLER<sup>2</sup>

<sup>1</sup> Department of Energy and Process Engineering  
Norwegian University of Science and Technology  
7491 Trondheim, Norway  
e-mail: frederik.regi@gmail.com

<sup>2</sup> Department of Energy and Process Engineering  
Norwegian University of Science and Technology  
7491 Trondheim, Norway  
e-mail: bernhard.muller@ntnu.no - Web page: <http://folk.ntnu.no/bmuller/>

**Key words:** Computational Methods, Adaptive Mesh Refinement, Euler Equations, Gas Dynamics, Shock Reflection, 2D Riemann Problem

**Abstract.** A finite volume solver that utilizes adaptive mesh refinement (AMR) on unstructured Cartesian grids has been developed for the two-dimensional Euler equations of gas dynamics. The solver uses the explicit Euler method and the Rusanov method for time and flux discretization, respectively. The rectangular cells can be refined by quadrisecution through their centers. This preserves their aspect ratios and doubles the spatial resolution locally. Four cells that were created from the same cell refinement can be merged by reversing the refinement process. The criteria for refinement and merging is based on the absolute differences of the density and velocity components in neighboring cells. For triggering adaptation, i.e., for deciding when to perform AMR, a new criterion is proposed. It is based on accumulating the absolute rate of change of mass relative to its initial value.

The development of a regular oblique shock reflection from a plane wall is simulated, starting from an initial condition corresponding to a Riemann problem. For comparison, the Euler equations of gas dynamics are also solved by a standard finite volume solver on a structured Cartesian grid. Using AMR, the number of cells can be reduced by up to 95%, i.e. a factor 20, to achieve the same error as the standard finite volume solver. Even though mesh adaptation impairs convergence to steady state and there is some overhead related to the data structure, the AMR solver takes only 36% of the computing time needed by the standard solver, in the most beneficial cases. The potential of the AMR solver for unsteady flow is demonstrated for the simulation of a 2D Riemann problem.

## 1 INTRODUCTION

In computational fluid dynamics (CFD), the demand for high mesh resolution is not equal throughout the computational domain. High gradients or discontinuities in flow variables are not adequately resolved in a coarse mesh with large cells. On the other hand, areas with smaller gradients can be resolved by coarser meshes without increasing the error much. To reduce the computational cost, it is therefore common to vary the cell sizes throughout the mesh. It is possible to do this adaptation before simulating if a priori knowledge or justified assumptions are available for the flow. In many flows the regions that require high resolution are moving. Examples are vortex shedding, and moving shocks. It would be possible to resolve the vortices or shock by refining the mesh in the entire region the features traverse before they dissipate. Another approach, that can lower the computational cost further, is to detect resolution demanding features while simulating, and refine or coarsen accordingly [1] [2] [3] [4]. This approach is known as *Adaptive Mesh Refinement*, or AMR for short.

An adaptation strategy describes how the AMR is executed on an algorithmic level. It should answer the questions: When, where and how to adapt? [5] The choice of adaptation strategy is closely linked with the choice of mesh, and affects how the mesh should be generated. The AMR solver developed for this project, uses an unstructured Cartesian mesh. The reason for limiting the mesh to be Cartesian, was to reduce the computation overhead related to the data structure, as explained in [6]. Marsha J. Berger has contributed to the field of AMR using unstructured Cartesian meshes in cooperation with Michael J. Aftosmis and John E. Melton [6]. This work has laid the basis for locally refining AMR softwares such as NASA's Cart3D project [7].

One method for refining a Cartesian mesh locally, is to quadrisect the cells through their centers [3]. This allows the refinement state of the cells to be classified by *levels* [8] [9]. These refinement levels  $L$  correspond to cell sizes, as shown in Figure 1. The largest permitted cell size corresponds to level  $L = 0$ , and gives the lowest possible resolution. The smallest allowed cell size corresponds to  $L = L_{max}$ , which gives the highest possible resolution. Each time  $L$  increases by one, the spatial resolution is locally doubled in all dimensions. This means that when a 2D cell is refined, it is split into four geometrically similar cells [3], as can be seen in Figure 1. In other words, all the cells have equal aspect ratio, regardless of the refinement level. For three-dimensional meshes, refined cells are split into eight cells. Only 2D cases are considered in this project.

An advantage of using this refinement approach is that one can refine very locally. Any cell can be split into four, as can be seen in Figure 1. Conversely, four cells that were created by the same cell refinement can be merged. However, it is advantageous to limit this freedom with a constraint called *grading* [8]. This constraint sets the lower limit, denoted by  $q$ , for how many cells must come between two level changes. With a grading degree of  $q = 0$ , there is no limit to how close two level changes can be. Essentially, this means that the refinement level can change multiple times from one cell to another, i.e.

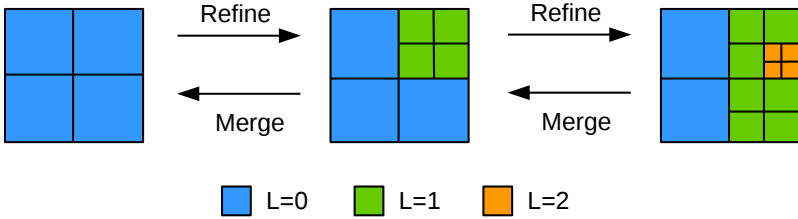


Figure 1: Principle sketch of local grid refinement and merging using quadrissection.  $L$  is the cell refinement level. The grading degree is  $q = 1$ , which means that between a cell at  $L = 0$  and a cell at  $L = 2$ , there must be at least one cell at  $L = 1$ . This figure is taken from [10] and adapted slightly.

a very small cell can be adjacent to a big cell. This can negatively affect accuracy, and it can make the local refining and coarsening algorithms more intricate. With a grading degree of  $q = 1$ , like in Figure 1, there needs to be at least one cell between level changes. This means that the resolution level can change for every traversed cell, but only *one* level at a time.

Another approach of mesh refinement is known as structured AMR, or S-AMR for short [1] [6] [3]. This method involves organizing the computational domain into patches. All the cells that belong to the same patch have the same resolution. This makes the detection and refinement procedures much simpler [1], which is an advantage. It also makes it much easier to implement methods with a higher order of accuracy in space, due to the fact that each patch is a structured sub-mesh. However, many cells will get a higher resolution than they require, unless the patches are very small. If the patches are too small, then the maximum cell size is limited, and the inter-patch communication becomes costly. The work of Marsha J. Berger must be mentioned here as well. She has contributed to the field of S-AMR, collaborating with Randall J. LeVeque. Their work in this field is utilized in the AMRCLAW software package [1], which is part the CLAWPACK package [11].

A third alternative is to refine locally using a tree structure, instead of an unstructured mesh. For a 2D solver it would be a quadtree structure. This approach allows for a relatively simple data structure if combined with the quadrissection method discussed above. However, tree data structures are more costly to traverse. Neither S-AMR or quadtrees are used in this project, but they are mentioned as alternatives.

There are multiple ways to detect where the mesh needs refinement, and where it can be coarsened. One way is to compare the entire solution from the latest time step, with a solution calculated on a coarsened mesh [1]. If the error of a cell, or patch of cells, is above

a given threshold then the cell or patch is marked for refining. Another way is to evaluate the gradients in the solution, in pairs of neighbor cells. Then the cell or patch could be flagged for refinement or merging based on gradient thresholds. An even simpler approach is used in this project. We check the differences between flow variables in neighboring cells. Regardless of how the detection is done, it will consume CPU time. Therefore it is common not to detect at every time step, but to have a criterion for *when* to adapt. A simple criterion is to specify a number of time steps between each detection routine [1], or a time interval. The AMR-solver in this project decides when to adapt, by accumulating an approximated mass redistribution rate. We will elaborate this in subsection 4.1.

This paper is based on the first author's master's thesis [12], and continues with the following sections: In section 2, the 2D Euler equations and their initial and boundary conditions for two test cases involving shocks are stated. The explicit finite volume method (FVM) for the discretization of the 2D Euler equations is given in section 3. The present AMR approach based on unstructured Cartesian grids is outlined in section 4. Results for a regular oblique shock reflection from a plane wall and for a 2D Riemann problem are discussed in section 5. The accuracies and efficiencies of the AMR solver and a standard solver are compared. In section 6, conclusions are drawn.

## 2 GOVERNING EQUATIONS

### 2.1 2D Euler Equations

The 2D Euler equations of gas dynamics read:

$$\frac{\partial \mathbf{U}}{\partial t} + \frac{\partial \mathbf{F}(\mathbf{U})}{\partial x} + \frac{\partial \mathbf{G}(\mathbf{U})}{\partial y} = 0, \quad (1)$$

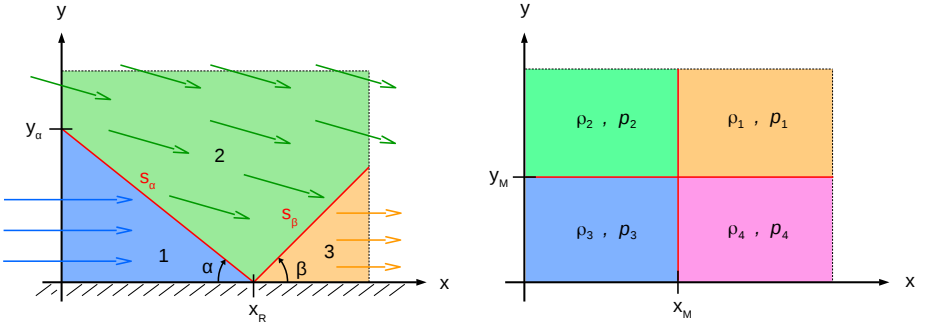
where

$$\mathbf{U} = \begin{bmatrix} \rho \\ \rho u \\ \rho v \\ \rho E \end{bmatrix} \quad (2)$$

is the vector of conservative variables,

$$\mathbf{F}(\mathbf{U}) = \begin{bmatrix} \rho u \\ \rho u^2 + p \\ \rho uv \\ u(p + \rho E) \end{bmatrix} \quad \text{and} \quad \mathbf{G}(\mathbf{U}) = \begin{bmatrix} \rho v \\ \rho vu \\ \rho v^2 + p \\ v(p + \rho E) \end{bmatrix} \quad (3)$$

are the flux vectors in the x- and y-directions, respectively. The density is denoted by  $\rho$ , the x- and y-components of the velocity by  $u$  and  $v$ , respectively, the specific total energy by  $E$ , and the pressure by  $p$ . For perfect gas considered here the pressure is related to



(a) Steady-state solution for the shock reflection case. The numbers denote regions 1, 2 and 3 respectively. The red lines represent the shocks. The colored arrows represent the velocity vectors.

(b) Initial conditions for the 2D Riemann problem. The red lines represent diaphragms, which are instantaneously removed at  $t = 0$ .

Figure 2: Principle sketches of the two test cases.

the conserved variables by

$$p = (\gamma - 1) \left[ \rho E - \frac{1}{2} \rho (u^2 + v^2) \right] , \quad (4)$$

using  $u = \frac{\rho u}{\rho}$  and  $v = \frac{\rho v}{\rho}$ .  $\gamma$  is the constant ratio of specific heats. We shall consider air with  $\gamma = 1.4$ . The vector of the primitive variables is defined by:

$$\mathbf{V} = \begin{bmatrix} \rho \\ u \\ v \\ p \end{bmatrix} . \quad (5)$$

## 2.2 Initial and Boundary Conditions

We will examine two test cases: regular shock reflection, cf. Figure 2a, and a 2D Riemann problem, cf. Figure 2b.

### 2.2.1 Regular Oblique Shock Reflection

The shock reflection case seen in Figure 2a, is a steady-state problem. The figure shows how the steady solution can be divided into regions 1, 2 and 3. Inside each region, the

flow variables are constant:

$$\mathbf{V}(x, y) = \begin{cases} \mathbf{V}_1 & \text{for } x < x_R \quad \text{and } y < s_\alpha(x) \\ \mathbf{V}_2 & \text{for } y > s_\alpha(x) \quad \text{or } y > s_\beta(x) \\ \mathbf{V}_3 & \text{for } x > x_R \quad \text{and } y < s_\beta(x) \end{cases}, \quad (6)$$

where subscripts 1, 2 and 3 denote regions illustrated in Figure 2a.  $s_\alpha(x)$  and  $s_\beta(x)$  are the shock graphs in the same figure.  $\mathbf{V}_1$  describes the uniform incoming flow at  $M_1 > 1$ .  $\mathbf{V}_2$  describes the flow behind the oblique shock  $s_\alpha$  with shock angle  $\alpha$ .  $\mathbf{V}_3$  describes the flow behind the reflected shock  $s_\beta$ . The analytical solution for the variables in (6) is given in [12].

We use the following initial conditions (IC) for the shock reflection case:

$$\mathbf{V}(x, y, t = 0) = \begin{cases} \mathbf{V}_1 & \text{for } y < y_\alpha \\ \mathbf{V}_2 & \text{for } y > y_\alpha \end{cases}, \quad (7)$$

where  $\mathbf{V}_1$ ,  $\mathbf{V}_2$  and  $y_\alpha$  are shown in Figure 2a. We use the following boundary conditions (BC) for this case:

$$\mathbf{V}(x = 0, y, t) = \begin{cases} \mathbf{V}_1 & \text{for } y < y_\alpha \\ \mathbf{V}_2 & \text{for } y > y_\alpha \end{cases}, \quad (8)$$

$$\mathbf{V}(x, y = y_{max}, t) = \mathbf{V}_2, \quad (9)$$

$$v(x, y = 0, t) = 0. \quad (10)$$

### 2.2.2 2D Riemann Problem

The second test case is a 2D Riemann problem. This case is defined by its initial condition:

$$\mathbf{V}(x, y, t = 0) = \begin{cases} \mathbf{V}_1 & \text{for } x > x_M, \quad y > y_M \\ \mathbf{V}_2 & \text{for } x < x_M, \quad y > y_M \\ \mathbf{V}_3 & \text{for } x < x_M, \quad y < y_M \\ \mathbf{V}_4 & \text{for } x > x_M, \quad y < y_M \end{cases}, \quad (11)$$

which is illustrated in Figure 2b. Subscripts 1-4 in (11) denote the regions in the latter figure. Physically, we envision this IC being achieved by diaphragms. At time  $t = 0$  the diaphragms are removed, causing different types of waves to interact with each other. We will see this in the results.

The boundaries enclosing the domain,  $[0, x_{max}] \times [0, y_{max}]$ , are considered artificial boundaries.

## 3 NUMERICAL APPROACH

In this section the numerical method is outlined.



(a) The cell  $i$  is in focus. It has 6 enclosing faces, whose normal vectors point away from the cell  $i$ . The vertical faces  $k_{F,i}$  are colored blue, and the horizontal faces  $k_{G,i}$  are colored red. There can be one or two enclosing faces on each side, giving a minimum of 4 and a maximum of 8 faces in total.

(b) Two examples where a face  $k$  is in focus. Its adjacent cells are denoted by subscripts  $L$  and  $R$ . For vertical faces the subscripts denote cells on the left and right side of the face, respectively. For horizontal faces the subscripts  $L$  and  $R$  denote cells below and above the face, respectively.

Figure 3: Notation for cells and faces, depending on focus.

### 3.1 Spatial Discretization

We use Cartesian grids with rectangular cells. This means that all cell faces are either vertical or horizontal. We also set the cell sizes  $\Delta x = \Delta y$  for all cells, meaning that all cells are squares. The finite volume method (FVM) is used to approximate the cell averages of the conserved variables.

The fluxes (3) are approximated at the cell faces by the Rusanov method, also known as the local Lax-Friedrichs method. The flux approximations at a face  $k$  are:

$$\mathbf{F}_k = \frac{1}{2} [(\mathbf{F}(\mathbf{U}_R) + \mathbf{F}(\mathbf{U}_L)) - a_k(\mathbf{U}_R - \mathbf{U}_L)] \quad , \quad (12)$$

$$\mathbf{G}_k = \frac{1}{2} [(\mathbf{G}(\mathbf{U}_R) + \mathbf{G}(\mathbf{U}_L)) - b_k(\mathbf{U}_R - \mathbf{U}_L)] \quad , \quad (13)$$

where  $\mathbf{F}_k$  and  $\mathbf{G}_k$  are the flux approximations at the vertical and horizontal faces, respectively. Subscripts  $L$ ,  $R$  and  $k$  are explained in Figure 3b.  $a_k$  and  $b_k$  are determined by the spectral radii of the Jacobian matrices  $\frac{\partial \mathbf{F}(\mathbf{U})}{\partial \mathbf{U}}$  and  $\frac{\partial \mathbf{G}(\mathbf{U})}{\partial \mathbf{U}}$ , respectively, in the cells  $i_L$  and  $i_R$ .

$$a_k = \max\{|u_L| + c_L, |u_R| + c_R\} \quad , \quad b_k = \max\{|v_L| + c_L, |v_R| + c_R\} \quad , \quad (14)$$

where  $c = \sqrt{\gamma p / \rho}$  is the speed of sound.

At the inflow boundaries at  $x = 0$  and  $y = y_{max}$  in the shock reflection test case, the fluxes are computed analytically using  $\mathbf{F}(\mathbf{U})$  and  $\mathbf{G}(\mathbf{U})$  (3), respectively.  $\mathbf{U}$  is then set using  $\mathbf{V}_1$  and  $\mathbf{V}_2$ , respectively, cf. Figure 2a and equation (6). At  $x = x_{max}$  in the same test case, the fluxes are computed using the variables from the upwind cell:  $\mathbf{F}_k = \mathbf{F}(\mathbf{U}_L)$ . At the symmetry boundary  $y = 0$  in the shock reflection case, the numerical flux is

approximated by the Rusanov flux (13) with the ghost cell values  $\rho_L = \rho_R$ ,  $u_L = u_R$ ,  $v_L = -v_R$  and  $p_L = p_R$ .

The numerical fluxes at the artificial boundaries for the 2D Riemann problem are approximated by the upwind fluxes, i.e., by setting  $\mathbf{U}_L = \mathbf{U}_R$  at  $x = 0$  and  $y = 0$  and  $\mathbf{U}_R = \mathbf{U}_L$  at  $x = x_{max}$  and  $y = y_{max}$  in the Rusanov fluxes (12) and (13). Outgoing waves are thereby properly treated. For incoming waves, the boundary treatment corresponds to approximately nonreflecting artificial boundary conditions.

### 3.2 Time Discretization

The discretization in time is done by the explicit Euler method,

$$\mathbf{U}_i^{n+1} = \mathbf{U}_i^n - \frac{\Delta t^n}{V_i} \left( \sum_{k \in k_{F,i}} [F_k^n A_k \hat{x}_k] + \sum_{k \in k_{G,i}} [G_k^n A_k \hat{y}_k] \right), \quad (15)$$

where  $i$  is a cell index, superscript  $n$  denotes time level,  $V_i$  is the volume of the cell  $i$ ,  $k_{F,i}$  contains the vertical faces enclosing cell  $i$ , and  $k_{G,i}$  contains the horizontal faces enclosing cell  $i$ , as shown in Figure 3a.  $A_k$  is the area of face  $k$ ,  $\hat{x}_k$  and  $\hat{y}_k$  are the x- and y-components, respectively, of the normal vector of face  $k$ , which always points away from cell  $i$ , as shown in Figure 3a. The time step size  $\Delta t^n$  is set at every time level to give the Courant number,

$$C_{max} = \frac{\max_i \{|u_i| + c_i\} \Delta t}{\min_i \{\Delta x_i\}} + \frac{\max_i \{|v_i| + c_i\} \Delta t}{\min_i \{\Delta y_i\}} \leq 1. \quad (16)$$

### 3.3 Stopping Criterion for the Steady-State Solution

Steady state is assumed if

$$\left\| \frac{\Delta \rho^n}{\Delta t^n} \right\|_1 \leq 10^{-4} \left\| \frac{\Delta \rho^0}{\Delta t^0} \right\|_1, \quad (17)$$

where

$$\|\Delta \rho^n\|_1 = \sum_i [V_i |\rho_i^{n+1} - \rho_i^n|] \quad (18)$$

is the 1-norm of the density change, corresponding to the sum of the modulus of the mass change in all cells  $i$ , from time level  $n$  to time level  $n + 1$ .

$$\left\| \frac{\Delta \rho^n}{\Delta t^n} \right\|_1 = \frac{\|\Delta \rho^n\|_1}{\Delta t^n} \quad (19)$$

approximates the rate of mass redistribution between time levels  $n$  and  $n + 1$ . It is required to be lower equal to its initial value by the factor  $10^{-4}$ .



## 4 AMR APPROACH

In this section we will see how the mesh is adapted in 4 sub-procedures: Flagging, grading, refining and merging. The data structure of the AMR-solver will not be discussed here, but can be found in [12]. We note that the cell- and face objects are stored in doubly linked lists.

### 4.1 Adaptation Trigger

An adaptation strategy should specify when, where and how to adapt [5]. The answer to the *when* is what will be referred to as the adaptation trigger. When the trigger activates, the flagging, grading, refining and merging procedures are run, in that order. The trigger is related to the mass redistribution rate  $\|\Delta\rho^n\|_1 / \Delta t^n$ , as defined in (19) and (18).

The first mesh adaptations are triggered at time level  $n_0 = 0$ , i.e., based on the initial condition (IC). The number of initial adaptations is equal to the upper limit  $L_{max}$  for the refinement level. Thus, if there are large gradients or discontinuities in the IC, the nearby cells will be refined to the highest level before the first time step starts. After an adaptation, say at  $n = n_a$ , the subsequent values of  $\|\Delta\rho^n\|_1 / \Delta t^n$  are accumulated until

$$\sum_{n=n_a}^{n_{a+1}-1} \frac{\|\Delta\rho^n\|_1}{\Delta t^n} \geq 5 \frac{\|\Delta\rho^0\|_1}{\Delta t^0} \quad . \quad (20)$$

Then, mesh adaptation is triggered at time level  $n = n_{a+1}$ . The factor 5 above was found by trial and error and can be expected to be case specific. However, it has given good results for both test cases in all the simulations this far.  $\|\Delta\rho^n\|_1 / \Delta t^n$  approximates the sum of the absolute rates of mass change in all the cells. Therefore, it reacts to mass entering or leaving the domain through the boundaries, and more important: mass being redistributed within the domain. The idea is that if flow structures or gradients are moving then mass is being redistributed. When enough mass has been redistributed, the large gradients might have moved towards the end of the refined areas. If little or no mass has been redistributed we are sure that the gradients haven't moved much. Therefore we sum up  $\|\Delta\rho^n\|_1 / \Delta t^n$  at each time level until the sum exceeds the threshold given in (20).

### 4.2 Flagging

The flagging procedure is the first step of each mesh adaptation. It decides *where* the mesh will be refined, and where it can be coarsened. To decide this, refinement criteria, based on absolute differences in the flow variables  $\rho$ ,  $u$  and  $v$  is used. These 3 variables will be referred to as the indicators.

The flagging procedure is a loop over all the interior faces. For each face  $k$  we check the absolute difference in all the indicators, between the 2 adjacent cells.

$$\Delta\rho_k = |\rho_R - \rho_L| \quad , \quad \Delta u_k = |u_R - u_L| \quad , \quad \Delta v_k = |v_R - v_L| \quad , \quad (21)$$

where subscripts  $R$  and  $L$  denote values in the right and left adjacent cells if the face is vertical. For horizontal faces, the subscripts  $R$  and  $L$  denote the cells above and below the face, respectively, like in Figure 3b. By looping over interior faces we check all combinations of adjacent cell pairs exactly once. The differences (21) are compared to the refinement thresholds,

$$\delta_{r,\rho} = \eta_r \Delta\rho_{max} \quad , \quad \delta_{r,u} = \eta_r \Delta u_{max} \quad , \quad \delta_{r,v} = \eta_r \Delta v_{max} \quad , \quad (22)$$

and the merging thresholds,

$$\delta_{m,\rho} = \eta_m \Delta\rho_{max} \quad , \quad \delta_{m,u} = \eta_m \Delta u_{max} \quad , \quad \delta_{m,v} = \eta_m \Delta v_{max} \quad , \quad (23)$$

where

$$\begin{aligned} \Delta\rho_{max} &= \max_{i,0 \leq m \leq n} \{\rho_i^m\} - \min_{i,0 \leq m \leq n} \{\rho_i^m\} \\ \Delta u_{max} &= \max_{i,0 \leq m \leq n} \{u_i^m\} - \min_{i,0 \leq m \leq n} \{u_i^m\} \\ \Delta v_{max} &= \max_{i,0 \leq m \leq n} \{v_i^m\} - \min_{i,0 \leq m \leq n} \{v_i^m\} \end{aligned} \quad (24)$$

are the largest spreads for all the indicators, evaluated over all cells  $i$  and all time levels  $m$  until  $n$ . That is,  $\max_{i,0 \leq m \leq n} \{\rho_i^m\}$  is the largest density that has existed in any cell  $i$  at any time level  $m$  until time level  $n$ . Conversely,  $\min_{i,0 \leq m \leq n} \{\rho_i^m\}$  is the lowest cell density until time level  $n$ . The same applies for the other indicators. Thus, the largest spreads (24) define the scales of the problem.

$\eta_r$  is a multiplier that affects all the refinement thresholds (22). It sets the thresholds  $\delta_r$  as fractions of the largest spreads (24). We will refer to  $\eta_r$  as the refinement tolerance. In a similar way,  $\eta_m$  sets the *merging* thresholds  $\delta_m$  in (23), also as fractions of the largest spreads (24).  $\eta_m$  will be referred to as the merging tolerance. Both these tolerances are given as constant parameters for the AMR solver to adjust the strictness of the refinement criteria. That is, adjusting the tolerances affects the balance between CPU-time and solution accuracy.

The comparisons between absolute differences and thresholds are used to flag the cells in the following way:

- Cells are flagged for refinement if *any* of the indicators has large absolute differences, over *any* of the enclosing faces, *and* the cell is not at the maximum refinement level  $L_{max}$ . That is, cell  $i$  with refinement level  $L_i < L_{max}$  is flagged for refinement, if at least one of its enclosing faces  $k$  has  $\Delta\rho_k > \delta_{r,\rho}$  or  $\Delta u_k > \delta_{r,u}$  or  $\Delta v_k > \delta_{r,v}$ .
- Cells are flagged for merging if *all* of the indicators have small absolute differences, over *all* of the enclosing faces, *and* the cell is not at the minimum refinement level 0. That is, cell  $i$  with refinement level  $L_i > 0$  is flagged for merging, if all of its enclosing faces  $k$  have  $\Delta\rho_k < \delta_{m,\rho}$  and  $\Delta u_k < \delta_{m,u}$  and  $\Delta v_k < \delta_{m,v}$ .
- No cell has both the refine flag and the merge flag. They have either one of them, or none of them.



Figure 4: Examples of illegal flag and level combinations, and following countermeasures to avoid size ratio 4.  $m$  and  $r$  denote the merge and refine flags. The figures are taken from [10], with small changes.

### 4.3 Grading

As discussed in the introduction, we will use mesh grading to prevent adjacent cells to be more than 1 refinement level apart. Thus, we require

$$\Delta x_L \in \left\{ \frac{1}{2} \Delta x_R, \Delta x_R, 2 \Delta x_R \right\} \quad (25)$$

at all interior faces, where  $\Delta x_L$  and  $\Delta x_R$  are the cell sizes of the adjacent cells. To achieve it we adjust the flags in a another loop over interior faces, which we call the grading loop. Examples of this are shown in Figure 4. We limit the number of combinations to handle, by assuming that (25) holds when the grading loop starts.

If the adjacent cells are at equal levels  $L_L = L_R$  there is only one illegal flag combination, which is shown in Figure 4a. The figure also shows how it is solved. If the cells are at different levels, there are multiple illegal flag combinations that call for different countermeasures. These are given in [12] and so are the implementation details.

### 4.4 Refining and Merging

The refining and merging of cells are done separately in two loops. The refine loop is a loop over all the cells in the mesh, where we check the refine flag  $r_i$  for each cell  $i$ . If  $r_i = 1$  we split cell  $i$  into four new cells, where the flow variables are copied from the refined cell. Similarly, the merge loop checks the merge flag  $m_i$  for all cells  $i$ . However, cells are only allowed to merge if all the four cells that came from one cell refinement have merge flags. When four cells merge, the flow variables in the resulting cell is set to the average from the merging cells,  $i$ ,  $i + 1$ ,  $i + 2$  and  $i + 3$ ,

$$\frac{\mathbf{U}_i + \mathbf{U}_{i+1} + \mathbf{U}_{i+2} + \mathbf{U}_{i+3}}{4} . \quad (26)$$

This changes the solution, but still conserves  $\mathbf{U}$ . The implementation of the refine and merge loops are detailed in [12].

## 5 RESULTS AND DISCUSSION

In this section, the obtained results will be presented and discussed.

A simple structured solver was implemented to act as a basis for comparison. This solver uses the same numerical approach as the AMR-solver, but its data structure is based on arrays. The mesh in this solver will always be structured and equidistant and cannot be adapted. However, the grid spacing can be varied from one simulation to another. This was done to provide a justified comparison that will show the potential overhead of the AMR data structure.

### 5.1 Development of Shock Reflection

The shock reflection test case was introduced in subsection 2.2. We set the incoming Mach number  $M_1 = 2.5$  and the shock angle  $\alpha = \frac{\pi}{5}$ . In this subsection we will examine how the shock reflection flow develops from the initial condition to the steady-state solution. The main reasons for studying this are:

1. To check that the mesh adapts as intended by checking whether the fine resolution areas follow the shocks.
2. To provide intuitive understanding of the flow.
3. To control that the solution actually converges and achieves a steady state.

We will primarily study the results from a simulation by the AMR-solver, with parameters as shown in Table 1. The allowed refinement levels and cell sizes are listed in Table 1b. These are driven parameters, dictated by  $\Delta x_{max}$  and  $L_{max}$ . For later simulations, only  $\Delta x_{max}$ ,  $L_{max}$  and  $\Delta x_{min}$  will be listed. All the results displayed in this subsection will be from the AMR simulation with the parameters in Table 1, unless something else is specified.

Figures 5 and 6 are cell plots of the density  $\rho$  and the velocity component  $u$ . They show the development of these variables, from their initial conditions in figures 5a and 5b, until steady state in figures 6c and 6d. For both  $\rho$  and  $u$  we see that the incoming shock moves towards the lower boundary wall, but with a higher speed for  $\rho$  than for  $u$ . Since the refinement criteria discussed in subsection 4.2 is based on differences (21) of  $\rho$ ,  $u$  and  $v$ , we see two distinct branches of highly refined cells. The reflected shocks start to form in figures 5e and 5f. These figures, and figures 6a and 6b show that the reflected shocks form differently for  $\rho$  than for  $u$ . The converged solutions are shown in figures 6c and 6d, where the shock locations for  $\rho$  and  $u$  coincide. The developments of the second velocity component  $v$  and the pressure  $p$  are not plotted in this paper, but are examined in [12]. For  $v$  and  $p$ , the shock locations are almost identical to the shock location for the density  $\rho$ , during the entire development.

To check that the solutions discussed above achieve steady states, the convergence history of the AMR simulation cf. Table 1 is plotted in Figure 7. Another simulation was executed, by the standard finite volume solver, using a grid spacing  $\Delta x_{str} = \Delta x_{min}$ , i.e., equal to the smallest cell size allowed in the AMR-simulation. This standard

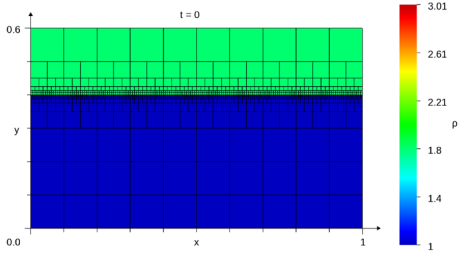
Table 1: Parameters and derived parameters used by the AMR-solver to simulate the development of the shock reflection.  $M_1$  is the Mach number in the uniform incoming flow, and  $\alpha$  is the incoming shock angle, cf. Figure 2a.  $\Delta x_{max}$  is the largest allowed cell size corresponding to the lowest refinement level  $L = 0$ .  $L_{max}$  is the highest permitted refinement level.  $\eta_r$  and  $\eta_m$  are the refinement and merging tolerances, respectively, defined in subsection 4.2.

(a) Given parameters.

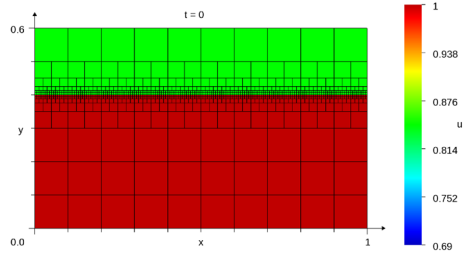
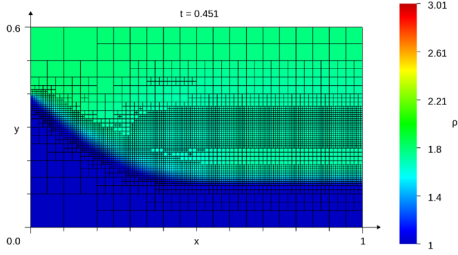
$M_1 :$	2.5
$\alpha :$	$\frac{\pi}{5}$
$\Delta x_{max} :$	$\frac{1}{10}$
$L_{max} :$	4
$\eta_r :$	0.04
$\eta_m :$	0.0182

(b) Available refinement levels and corresponding cell sizes. These can always be derived from  $\Delta x_{max}$  and  $L_{max}$ .

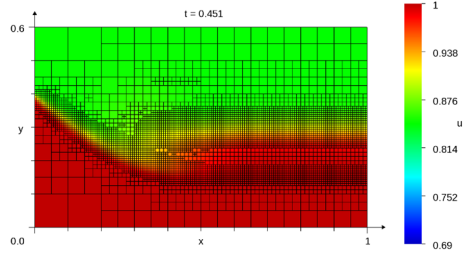
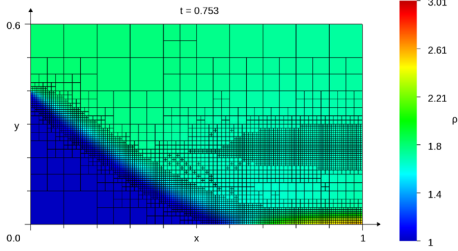
					$L_{max}$
$L :$	0	1	2	3	4
$\Delta x_{amr} :$	$\frac{1}{10}$	$\frac{1}{20}$	$\frac{1}{40}$	$\frac{1}{80}$	$\frac{1}{160}$
	$\Delta x_{max}$				$\Delta x_{min}$



(a) IC for density.


 (b) IC for velocity component  $u$ .


(c) Density. The shock moves downwards, and the area around it has high resolution.


 (d) Velocity component  $u$ . The discontinuity moves downwards, but slower than for  $\rho$ . Thus there are two branches of highly refined cells.


(e) Density. The shock has reached the wall, and starts to reflect.

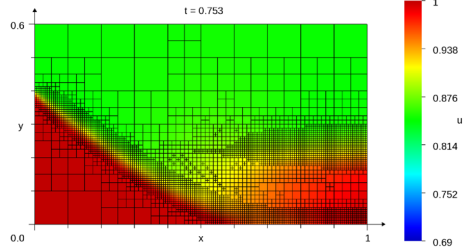
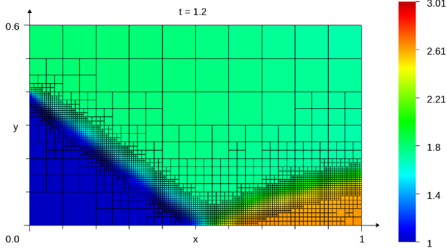
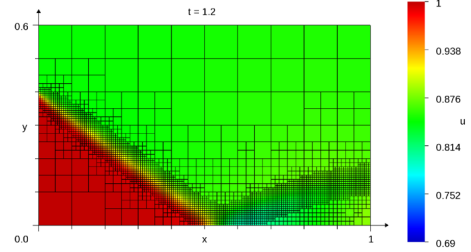

 (f) Velocity component  $u$ . The left part of the wave has reached the wall. The right part has become diffuse and exits through the right boundary.

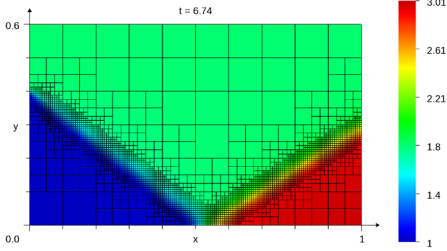
Figure 5: Cell plots of the developments of density  $\rho$  and velocity component  $u$ , from initial conditions until the shock reaches the wall at  $y = 0$ . The black lines are the faces in the mesh. The most highly refined cells, at level  $L = L_{max}$ , follow the discontinuities of both  $\rho$  and  $u$ .



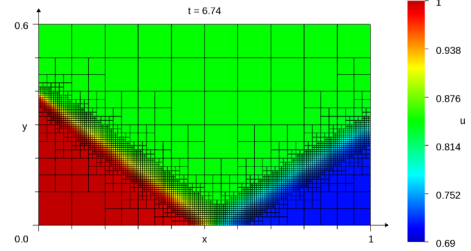
(a) Density. The reflected shock is bending upwards, while the reflection point moves leftwards.



(b) Velocity component  $u$ . The reflected shock forms extensionally, like a telescope, while bending upwards.



(c) Converged solution for the density.



(d) Converged solution for the velocity component  $u$ .

Figure 6: Cell plots of the developments of density  $\rho$  and velocity component  $u$ , from time  $t = 1.2$  until steady state, at  $t = 6.74$ . The black lines are the faces in the mesh. The most highly refined cells, at level  $L = L_{max}$ , follow the discontinuities of both  $\rho$  and  $u$ .

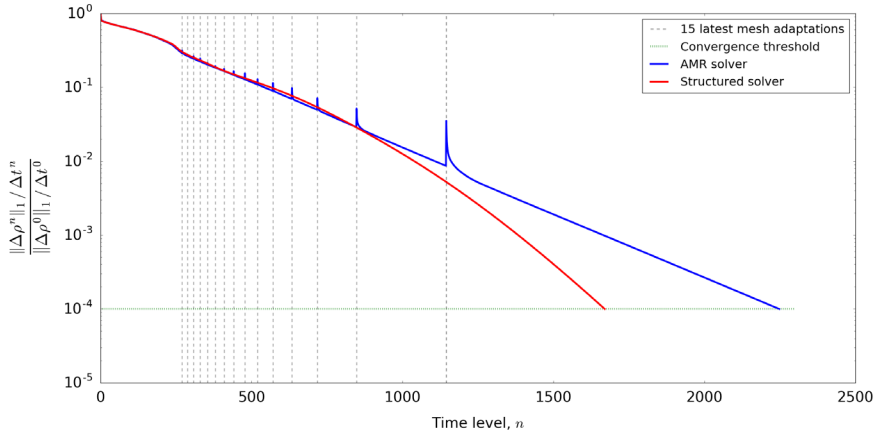


Figure 7: Convergence history plot with logarithmic ordinate axis. The red and blue graphs show the development of the convergence indicator  $\|\Delta\rho^n\|_1 / \Delta t^n$ , normalized by its initial value. The dashed gray vertical lines show the time levels when the last 15 of the total 42 adaptations occurred. Both solvers used  $\Delta x_{min} = \Delta y_{min} = \frac{1}{160}$ .

simulation is also included in the convergence history plot in Figure 7. In said figure, the red graph shows that the convergence indicator  $\|\Delta\rho^n\|_1 / \Delta t^n$ , scaled by its initial value, decreases monotonically for the structured solver, until reaching the threshold,  $10^{-4}$ . For the AMR simulation the convergence indicator is indicated by the blue graph in Figure 7. It jumps up at the time levels indicated by the dashed vertical lines, because the mesh is adapted at those times, causing disturbances of the numerical solution. In this particular case, the convergence threshold is reached at  $n = 2248$  for the AMR solver, and at  $n = 1671$  for the standard solver. This means that the AMR-solver takes 1.35 times as many time steps as the structured solver, which is a recurring trend. Although the factor varies between 1.3 and 1.6, the AMR-solver required more time steps to converge in all simulations.

Figure 7 makes yet another important point, if we observe the spacing between the dashed gray lines. It is evident that the mesh adaptations happen much more seldom later in the simulation. This relates to the adaptation trigger that was introduced in subsection 4.1. As  $\|\Delta\rho^n\|_1 / \Delta t^n$  decreases, more time steps are required before mesh adaptation is triggered.

## 5.2 Comparing Error versus Runtime

To measure the gains from the AMR approach, we will compare the runtime, error and number of cells in multiple simulations. These simulations are grouped into 6 series, where



Table 2: Parameters that vary within an AMR simulation series.  $\Delta x_{max}$  is the size of all the cells when the mesh is created and  $L_{max}$  is the highest permitted refinement level.  $\Delta x_{min}$  is the smallest permitted cell size, and follows directly from  $\Delta x_{max}$  and  $L_{max}$ .

Sim. number:	1	2	3	4	5	6	7	8	9	10	11
$\Delta x_{max}$ :	$\frac{1}{10}$	$\frac{1}{15}$	$\frac{1}{10}$	$\frac{1}{15}$	$\frac{1}{10}$	$\frac{1}{15}$	$\frac{1}{10}$	$\frac{1}{15}$	$\frac{1}{10}$	$\frac{1}{15}$	$\frac{1}{20}$
$L_{max}$ :	2	2	3	3	4	4	5	5	6	6	6
$\Delta x_{min}$ :	$\frac{1}{40}$	$\frac{1}{60}$	$\frac{1}{80}$	$\frac{1}{120}$	$\frac{1}{160}$	$\frac{1}{240}$	$\frac{1}{320}$	$\frac{1}{480}$	$\frac{1}{640}$	$\frac{1}{960}$	$\frac{1}{1280}$

Table 3: Refinement and merging tolerances for the 5 AMR series.  $\eta_r$  and  $\eta_m$  are defined in subsection 4.2.

Series no.:	$\eta_r$	$\eta_m$
1	0.08	0.0364
2	0.06	0.0273
3	0.04	0.0182
4	0.02	0.0091
5	0.01	0.0045

1 series was executed by the structured solver and the remaining 5 series were simulated by the AMR-solver. In each of the 5 AMR series, there are 11 simulations, giving a total of 55 AMR simulations. Inside the series, the parameters that control the available cell sizes are varied according to Table 2.

The 5 AMR series use different tolerances for the refinement and merging criteria that were introduced in subsection 4.2. The tolerances are given in Table 3, where the merging tolerances have been set as  $\eta_m = \frac{\eta_r}{2.2}$ . The first series has high tolerances. This gives relaxed refinement and merging criteria, meaning that fewer cells will be refined and more cells will merge. The last series has low tolerances. This gives stricter criteria, forcing more cells to be refined and permitting fewer cells to merge.

The structured series consist of 13 simulations executed by the structured solver using equidistant grids. The 13 simulations use different mesh resolutions listed as grid spacings in Table 4. These chosen cell sizes are similar to  $\Delta x_{min}$  in Table 2, which was intended to give errors in the same range. The error considered here is the volume averaged density error

$$\varepsilon_\rho = \frac{1}{V_D} \|\rho - \bar{\rho}_{exact}\|_1 \quad , \quad (27)$$

Table 4: Cell sizes, i.e. grid spacings for the structured solver.

Sim. number:	1	2	3	4	5	6	7	8	9	10	11	12	13
$\Delta x$ :	$\frac{1}{35}$	$\frac{1}{40}$	$\frac{1}{60}$	$\frac{1}{80}$	$\frac{1}{120}$	$\frac{1}{160}$	$\frac{1}{240}$	$\frac{1}{320}$	$\frac{1}{480}$	$\frac{1}{640}$	$\frac{1}{960}$	$\frac{1}{1100}$	$\frac{1}{1200}$

where  $V_D = \sum_i V_i$  is the domain volume and

$$\bar{\rho}_{exact,i} = \frac{1}{V_i} \int_{\Omega_i} \rho_{exact}(x, y) dx dy \quad (28)$$

is the exact average density in cell  $i$ .

From these 55 AMR simulations and 13 standard simulations, the computation times  $T_R$ , density errors  $\varepsilon_\rho$ , and cell counts  $N_{cell}$  were logged and presented in plots. In Figure 8 we see that the AMR solver uses much fewer cells than the standard solver to achieve the same error. The AMR simulation with the lowest error (leftmost blue circle) used only about 5% of the cells the standard solver used. This simulation also showed a large saving in runtime, using only about 36% of the time used by the standard solver. The comparisons of runtime versus error is shown in Figure 9. In this plot the runtimes were normalized as

$$T_R^* = \frac{T_R}{T_{R,str}} \quad , \quad (29)$$

where  $T_R$  is the runtime the simulation in focus, and  $T_{R,str}$  is the runtime of a simulation from the structured solver, that gives the same error as the simulation in focus. Since no two simulations have equal errors,  $T_{R,str}$  is found by interpolation between structured simulations:

$$T_{R,str} = T_R^{right} + (\varepsilon_\rho - \varepsilon_\rho^{right}) \frac{T_R^{left} - T_R^{right}}{\varepsilon_\rho^{left} - \varepsilon_\rho^{right}} \quad , \quad (30)$$

where the superscripts *left* and *right* denote the closest structured solution on each side, in terms of error. The most obvious trend in Figure 9 is that the AMR solver mostly uses less runtime to achieve the same error as the standard solver. However, the red graph shows that if the tolerances are too relaxed, we will not achieve this gain in the left part of the plot. Even though the high tolerance  $\eta_r = 0.08$  gives low runtimes and cell counts, it increases the error so much, that the standard solver could achieve the same error using less runtime. Comparing the AMR series we see that the series with the highest tolerance gets the largest runtime gain in the right part of the plot. The simulations in the right part of the plot have larger cells overall and thus higher errors. Conversely, small tolerances giving strict criteria, seem to give lower gain with fewer larger cells, and the highest gains with smaller cells, i.e. in the left part of the figure, where the errors are lower. If this relationship holds, the refinement and merging tolerances should be set depending on the smallest allowed cell size.

Table 5: Comparison between an AMR simulation and a standard simulation, where we see a large benefit from AMR. For the standard solver the refinement tolerance  $\eta_r$  is not applicable, and  $\Delta x_{min}$  was the size of *all* the cells.  $N_{cell}$  is the final number of cells in the mesh.  $\varepsilon_\rho$  is the density error. The ratios are the values from the standard solver divided by the AMR values.

	$\eta_r$	$\Delta x_{min}$	$N_{cell}$	$T_R$ [s]	$\varepsilon_\rho$
AMR:	0.01	$\frac{1}{1280}$	35 433	327	0.00742
Standard:		$\frac{1}{1100}$	726 000	903	0.00735
Ratio:			20.5	2.76	0.991

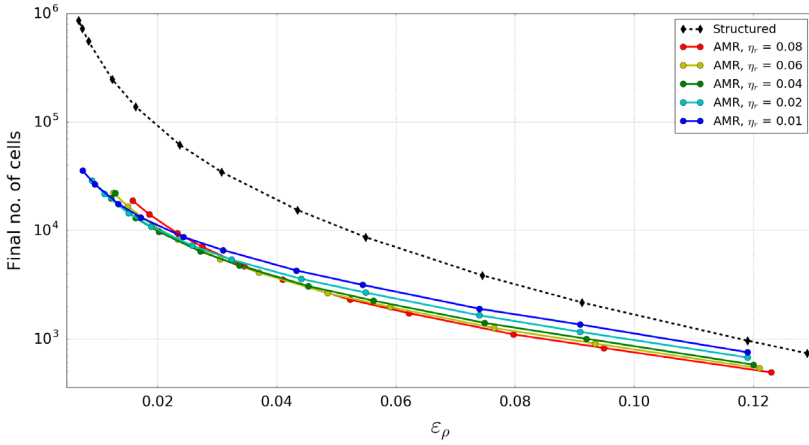


Figure 8: Number of mesh cells  $N_{cell}$  plotted versus the density error  $\varepsilon_\rho$ . Ordinate axis is logarithmic.

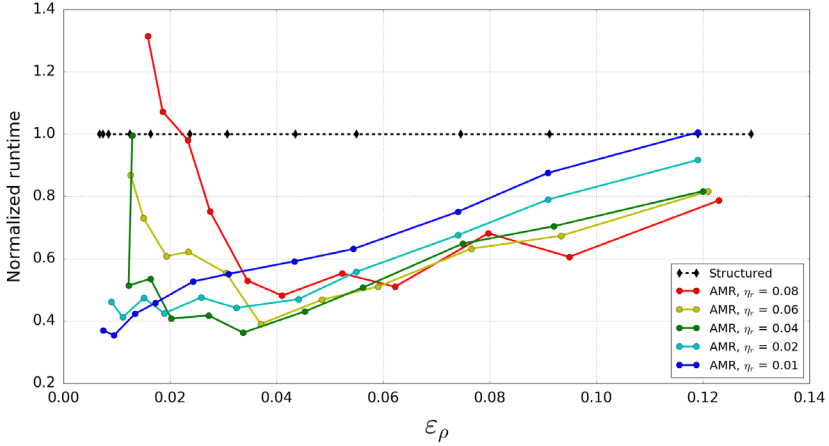


Figure 9: Normalized runtime  $T_R^*$  plotted versus density error  $\varepsilon_\rho$ . The scaling factor for the runtimes are the runtimes from the structured simulations. Therefore  $T_R^* = 1$  for all structured simulations.

### 5.3 Simulation of a 2D Riemann Problem

The second test case that was studied is a 2D Riemann problem. It was introduced in subsection 2.2. For this flow case we do not have an analytical solution to verify the solution. However, there are other gains from simulating this test case:

1. We will check that the AMR-solver finds the same solution as the structured solver.
2. We will check that the mesh adaptation algorithm detects high gradients in a more complicated flow.
3. We will still compare runtimes between the AMR-solver and the structured solver.

For the initial conditions given in equation (11) and Figure 2b we set the following numerical values:

$$\rho_1 = p_1 = 4 \quad , \quad \rho_2 = p_2 = 3 \quad , \quad \rho_3 = p_3 = 1 \quad , \quad \rho_4 = p_4 = 2 \quad , \quad (31)$$

$$u(x, y, t = 0) = v(x, y, t = 0) = 0 \quad . \quad (32)$$

The parameter settings that were used to simulate this test case with the AMR-solver are given in Table 6. The refinement and merging tolerances  $\eta_r$  and  $\eta_m$ , and the smallest cell size  $\Delta x_{min} = \Delta y_{min}$  are set relatively small, if compared to the parameters used in subsection 5.2. This was done to ensure that all the different wave types were resolved.

Table 6: Parameters used by the AMR-solver to simulate the 2D Riemann problem.

$\Delta x_{max}$ :	$\frac{1}{20}$
$L_{max}$ :	6
$\Delta x_{min}$ :	$\frac{1}{1280}$
$\eta_r$ :	0.015
$\eta_m$ :	0.0068

---

For the structured solver, the uniform grid spacing  $\Delta x_{str}$  was set equal to the smallest allowed cell size  $\Delta x_{min}$  for the AMR-solver. We limit the test case to the time  $0 \leq t \leq 0.2$ , before any of the waves reach the domain boundaries.

Figures 10 and 11 show cell plots of the simulation results from the 2D Riemann problem test case. The time instant is shown at the top, and the size and symbol of the plotted variable is shown by the colorbar. Figure 10a shows the initial condition (31) for the density. Figure 10b shows the final density solution at  $t = 0.2$ , computed by the AMR-solver. In this density field we can identify several different waves. We see the vertical shock at  $x \approx 0.23$  and the horizontal shock at  $y \approx 0.2$ . The contact discontinuities at  $x \approx 0.48$  and  $y \approx 0.43$  are not as distinct, especially near the center of the domain. At  $x \approx 0.7$  and  $y \approx 0.7$  we find the rarefaction waves, which are wider than the other waves. We can also see that the flow variables are constant in the corners, and that we have 1D Riemann problems along the boundaries. In the central part of the domain we see complex interactions between the different waves in the form of non-linear wave fronts. Figure 10c shows that these different waves are all detected, because their surrounding areas have been refined. The contact discontinuities are not as highly refined as the shocks and rarefaction waves. Figure 10d shows the solution from the standard solver, which looks very similar to the AMR solution in Figure 10b.

Figure 11 shows the AMR solutions of the velocity components and pressure. We can see that none of these plots show all the waves. Conversely, there is no wave front that we find in Figure 11, that we do not find in Figure 10. This demonstrates that the density is a very good indicator to use in the criteria for *where* to refine.

Finally for this test case, we will examine some technical output from the AMR-solver, and compare some of it with data from the structured solver. Table 7 shows selected values from the reports that the two solver produced when simulating the 2D Riemann problem.

The runtime is the measured time that the CPU used to execute the simulation. We see that the structured solver used about twice as much time as the AMR-solver. This ratio is lower than the values we found for the shock reflection case, indicating that the efficiency gain is a little lower for this case.

19% of the total 92.6 seconds were consumed by mesh adaptation in the AMR simulation. The remaining 81% is used for computing and transferring fluxes, computing

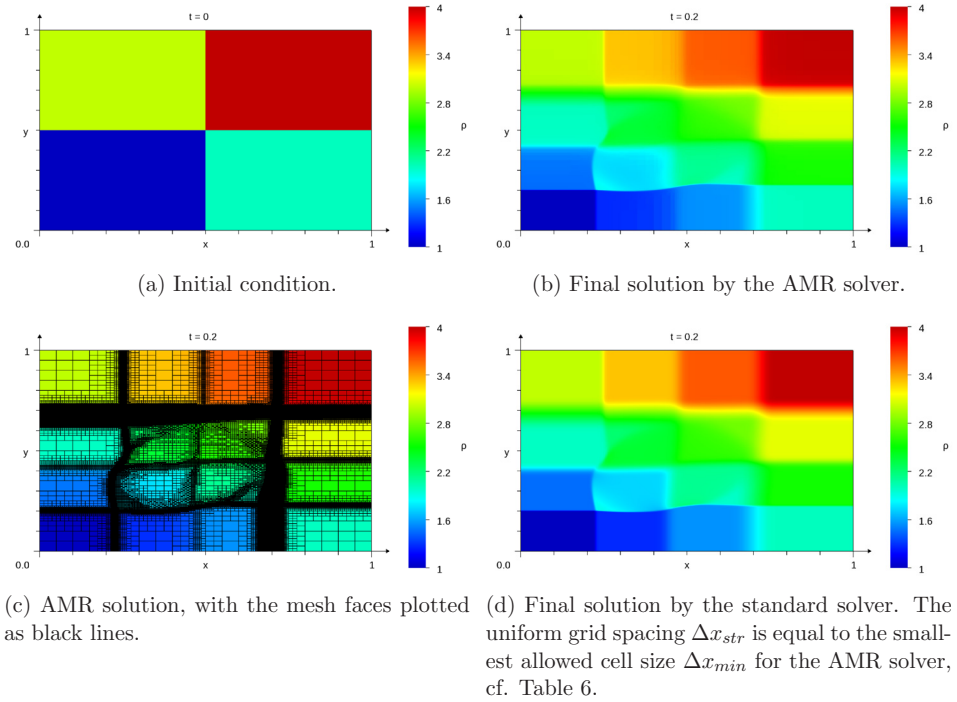


Figure 10: Cell plots of the density in the 2D Riemann problem.

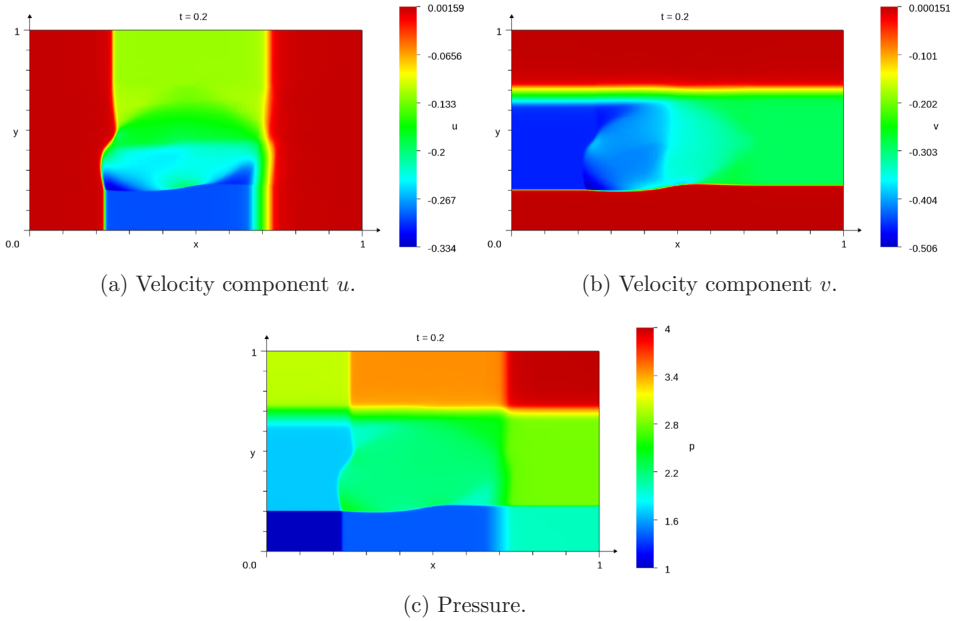


Figure 11: Cell plots of the velocity components and pressure in the 2D Riemann problem. These are solutions by the AMR solver.

Table 7: Miscellaneous technical output from the AMR solver. Values from the structured solver are given where applicable, for comparison. The right column is the ratio between the left and middle columns. The meaning of each row is explained when commented in the text.

	AMR	Structured	$\frac{\text{Structured}}{\text{AMR}}$
Total Runtime [s]:	92.6	187	2.02
Numerical method time [s]:	75.0	(81% of 92.6 s)	
Mesh adaptation time [s]:	17.6	(19% of 92.6 s)	
Average no. of cells:	200 321	1 638 400	8.18
Final no. of cells:	206 677	1 638 400	7.93
No. of time steps:	891	891	1
No. of mesh adaptations:	133		

primitive variables, etc, which is definitely the main time consumer.

The time-level-averaged number of cells and the final number of cells are approximately 8 times higher for the structured solver. This ratio was typically much higher for the shock reflection case, as we saw in Figure 8. The many waves that appear in the 2D Riemann problem require a larger portion of the domain to be well resolved. This decreases the gain from the AMR approach, as expected. Similar to the shock reflection case, we see much higher ratios in cell count than in runtime. This indicates that there is much overhead related to the data structure, since the actual mesh adaptation only used 19% of the CPU time. In turn this means that there is potential to increase the efficiency gain considerably, e.g. by optimizing the data structure. The number of time steps is how many times the explicit Euler method was applied to march the solution forward. The number of mesh adaptations is how many times the complete procedure of flagging, grading, refining and merging was executed. We can see that the mesh was adapted much more often for this test case:

$$\frac{N_{adapt,Riemann}}{n_{max,Riemann}} = \frac{133}{891} = 0.149 \quad , \quad (33)$$

than for the first shock reflection case (cf. Table 1 in subsection 5.1):

$$\frac{N_{adapt,reflect}}{n_{max,reflect}} = \frac{42}{2248} = 0.0187 \quad . \quad (34)$$

$N_{adapt}$  is the number of adaptations and  $n_{max}$  is the number of time steps computed. We also see that the solvers used the same number of time steps, as opposed to the steady-state case in sections 5.1 and 5.2, which we saw in Figure 7.

## 6 CONCLUSIONS

An AMR finite volume solver using unstructured Cartesian grids has been developed for the 2D Euler equations of gas dynamics. The adaptation trigger, i.e., the criterion for *when* to adapt, is based on accumulating an approximated mass redistribution rate, cf. subsection 4.1. To the best of our knowledge, this is a new approach. The results indicate that this approach works well for both steady-state problems and transient simulations, though many more flow cases must be tested before we can assert this. For the transient test case of a 2D Riemann problem, and the development of a regular shock reflection, the new adaptation trigger keeps the mesh updated, avoiding that large gradients leave the highly resolved areas. If the resolution demanding features slow down or stop moving, the trigger activates more seldom. During convergence of the steady-state simulations, this is especially evident. This adaptation trigger is also very easy to implement and inexpensive in terms of CPU time.

The benefit from the AMR approach was measured by comparing the number of cells and the CPU time of simulations that give similar errors. The cases that benefit the most from AMR are the simulations where we allow the smallest cells, i.e., the simulations with the smallest errors and highest CPU times. In these cases, the number of cells for



the AMR solver was only about 5% of the number of cells for the standard solver. The efficiency gain for CPU time is much lower, but still significant. The AMR solver used 36-40% of the runtime of the standard solver to give similar errors in the most beneficial cases. The difference between these percentages is most likely related to the mesh data structure. The mesh adaptation procedures only comprise 3-20% of the AMR solver's total runtime, whereas the numerical method consumes the rest of the runtime.

The criteria for *where* to refine and coarsen the mesh was varied. This proved to have a big effect when examining runtime, number of cells and error. Relaxed criteria give lower cell counts and runtimes and higher errors than strict criteria, as expected. The results indicate that to maximize the benefits from this AMR approach, the refinement and merging tolerances should be set depending on the smallest allowed cell size. Specifically, with smaller cells the tolerances should be smaller, and with larger cells the tolerances should be larger, to give a good balance between CPU time and error.

## References

- [1] M. J. Berger and R. J. Leveque. "Adaptive Mesh Refinement Using Wave-Propagation Algorithms for Hyperbolic Systems". *SIAM Journal on Numerical Analysis* 35.6 (1998), pp. 2298–2316. ISSN: 0036-1429.
- [2] R. Löhner. *Applied computational fluid dynamics techniques : an introduction based on finite element methods*. 2nd ed. Chichester: Wiley, 2008. ISBN: 9780470519073.
- [3] G. W. Zumbusch. *Parallel multilevel methods : adaptive mesh refinement and load-balancing*. Ed. by H. G. Bock et al. 1st ed. Wiley-Teubner series, advances in numerical mathematics. Stuttgart, Germany: Teubner, 2003. ISBN: 3-322-80063-6.
- [4] T. Linde T. Plewa and V. G. Weirs. "Adaptive mesh refinement, theory and applications : proceedings of the Chicago Workshop on Adaptive Mesh Refinement Methods, Sept. 3-5, 2003". Vol. 41. Lecture notes in computational science and engineering. Chicago Workshop on Adaptive Mesh Refinement Methods. Berlin: Springer, 2005. ISBN: 1-280-41225-9.
- [5] O. P. Jacquotte. "Grid Optimization Methods for Quality Improvement and Adaptation". N. P. Weatherill J. F. Thompson B. K. Soni. *Handbook of Grid Generation*. Boca Raton Fla: CRC Press, 1998.
- [6] M. J. Aftosmis, M. J. Berger, and J. E. Melton. "Adaptive Cartesian Mesh Generation". J. F. Thompson, B. K. Soni, and N. P. Weatherill. *Handbook of Grid Generation*. Boca Raton Fla: CRC Press, 1998.
- [7] Michael J. Aftosmis. *What is Cart3D?* 2018. URL: <https://www.nas.nasa.gov/publications/software/docs/cart3d/pages/cart3Dhome.html>.
- [8] S. Müller. *Adaptive Multiscale Schemes for Conservation Laws*. Ed. by T. J. Barth et al. Lecture Notes in Computational Science and Engineering. Berlin, Heidelberg: Springer, 2003. ISBN: 978-3-540-44325-4.

- [9] M. Paszynski, D. Pardo, and V. M. Calo. “A direct solver with reutilization of LU factorizations for h-adaptive finite element grids with point singularities”. *Computers and Mathematics with Applications* 65.8 (2013), pp. 1140–1151. issn: 0898-1221.
- [10] F. Kristoffersen. “Adaptive Mesh Refinement for Conservation Laws”. Pre-Master Project. Norwegian University of Science and Technology, 2018.
- [11] R. J. LeVeque. *Finite volume methods for hyperbolic problems*. eng. Cambridge, 2002.
- [12] F. Kristoffersen. “Adaptive Mesh Refinement for the Euler Equations of Gas Dynamics”. Master thesis. Norwegian University of Science and Technology, 2019.

## ADAPTIVE ISOGEOMETRIC METHODS FOR THIN PLATES

TROND KVAMSDAL<sup>1,2</sup>, KNUT M. OKSTAD<sup>2</sup>, MUKESH KUMAR<sup>3</sup>,  
ARNE M. KVARVING<sup>2</sup>, KJELL M. MATHISEN<sup>4</sup>

<sup>1</sup>NTNU, Department of Mathematical Sciences  
N-7491 Trondheim, Norway  
e-mail: [Trond.Kvamsdal@ntnu.no](mailto:Trond.Kvamsdal@ntnu.no) - web page: <http://www.ntnu.no>

<sup>2</sup>SINTEF Digital, Department of Mathematics and Cybernetics  
N-7465 Trondheim, Norway  
e-mail: [Trond.Kvamsdal@sintef.no](mailto:Trond.Kvamsdal@sintef.no), [Knut.Morten.Okstad@sintef.no](mailto:Knut.Morten.Okstad@sintef.no),  
[Arne.Morten.Kvarving@sintef.no](mailto:Arne.Morten.Kvarving@sintef.no) - web page: <http://www.sintef.no/>

<sup>3</sup>College of Charleston, South Carolina, USA  
e-mail: [kumarm@cofc.edu](mailto:kumarm@cofc.edu)

<sup>4</sup>NTNU, Department of Structural Engineering  
N-7491 Trondheim, Norway  
e-mail: [Kjell.Mathisen@ntnu.no](mailto:Kjell.Mathisen@ntnu.no) - web page: <http://www.ntnu.no>

**Key words:** Error Estimation, Isogeometric Analysis, Thin Plate Problems.

**Abstract.** Recovery-based error estimation for thin plate problems (the bi-harmonic equation) is revisited in the context of Isogeometric analysis. A posteriori energy-norm error estimates based on global  $L_2$  recovery of the bending moments is shown to enable optimal convergence rates for both smooth and non-smooth problems.

### 1 INTRODUCTION

Through the isogeometric finite element analysis concept [1] using splines as basis functions instead of traditional Lagrange/Hermitian polynomials, the Kirchhoff-Love thin plate equations can efficiently be solved numerically without the introduction of rotational degrees of freedom, since the inter-element continuity is of order  $p-1$  for elements of order  $p$ . Using the recently proposed Locally Refined B-splines [2], we may also perform adaptive analyses of such problems based on a posteriori error estimates.

In the current study, the recovery techniques studied by the authors earlier [3, 4, 5] are revisited and developed for handling Kirchhoff-Love thin plate theory.

## 2 THE THIN PLATE PROBLEM

The partial differential equation based on Kirchhoff-Love plate theory for a thin plate with a constant bending stiffness  $D = \frac{Et^3}{12(1-\nu^2)}$ , where  $E$  is the Young's modulus,  $\nu$  the Poisson's ratio, and  $t$  the plate thickness, can be written

$$w_{,\alpha\alpha\beta\beta} = \frac{p}{D} \quad \forall x_\alpha \in \bar{\Omega} \quad (1)$$

$$m_{\alpha\beta}n_\beta = \bar{M}_\alpha \quad \forall x_\alpha \in \partial\Omega_m \quad (2)$$

$$D w_{,\alpha\alpha\beta}n_\beta = -\bar{Q} \quad \forall x_\alpha \in \partial\Omega_q \quad (3)$$

$$w = \bar{w} \quad \forall x_\alpha \in \partial\Omega_w \quad (4)$$

$$w_{,\alpha}n_\alpha = \bar{\theta} \quad \forall x_\alpha \in \partial\Omega_\theta \quad (5)$$

where Einsteins summation convention over repetitive indices is assumed and  $\alpha$  and  $\beta$  are running indices over coordinate directions, i.e.,  $w_{,\alpha\alpha\beta\beta} := w_{,xxxx} + 2w_{,xxyy} + w_{,yyyy}$ . The bending moments,  $m_{\alpha\beta}$ , are related to the unknown transverse displacement field  $w$ , through  $m_{xx} = -D(w_{,xx} + \nu w_{,yy})$ ,  $m_{yy} = -D(w_{,yy} + \nu w_{,xx})$  and  $m_{xy} = -D(1 - \nu)w_{,xy}$ . Furthermore,  $n_\alpha$  is the outward-directed normal vector on the boundary  $\partial\Omega$ ,  $\bar{M}_\alpha$  denote some applied edge torque and moment in the local axes directions of  $\partial\Omega_m = \partial\Omega \setminus \partial\omega_\theta$ , and  $\bar{Q}$  denotes the applied transverse shear force on  $\partial\Omega_q = \partial\Omega \setminus \partial\omega_w$ . Finally,  $p = p(x_\alpha)$  is the distributed transverse load, whereas  $\bar{w}$  and  $\bar{\theta}$  denote the prescribed transverse displacement and normal rotation at the boundaries  $\partial\Omega_w$  and  $\partial\Omega_\theta$ , respectively.

The weak form is obtained by multiplying Equation (1) by a test function  $v(x_\alpha) \in \mathcal{V}(x_\alpha)$  and then integrating over the domain  $\Omega$ . Then, after applying Green's identity twice and some manipulations, we arrive at the following. Find  $w \in \mathcal{W}(x_\alpha)$  such that

$$a(w, v) = l(v) \quad \forall v \in \mathcal{V}(x_\alpha) \quad (6)$$

where we introduce the bilinear form  $a(w, v)$  and the linear functional  $l(v)$  as follows

$$a(w, v) := D \int_{\Omega} w_{,\alpha\beta} v_{,\alpha\beta} dA \quad (7)$$

$$l(v) := \int_{\Omega} p v dA + \int_{\partial\Omega_q} \bar{Q} v dS + \int_{\partial\Omega_m} \bar{M}_\alpha v_{,\alpha} dS \quad (8)$$

Proper function spaces for the trial- and test displacements  $w$  and  $v$  are, respectively

$$\mathcal{W} = \{w \in H^2(\Omega) \mid w = \bar{w} \text{ on } \partial\Omega_w \text{ and } v_{,\alpha}n_\alpha = \bar{\theta} \text{ on } \partial\Omega_\theta\} \quad (9)$$

$$\mathcal{V} = \{v \in H^2(\Omega) \mid v = 0 \text{ on } \partial\Omega_w \text{ and } v_{,\alpha}n_\alpha = 0 \text{ on } \partial\Omega_\theta\} \quad (10)$$

and we then introduce finite dimensional sub-spaces of  $\mathcal{W}^h \subset \mathcal{W}$  and  $\mathcal{V}^h \subset \mathcal{V}$  to obtain our finite element (FE) formulation. In the current study, tensor-product splines with polynomial order  $p \geq 2$  are used in the discretization, as well as LR B-splines, see [2] for more details.

### 3 ERROR ESTIMATES

An estimate of the discretization error in the FE solution is obtained by projecting the secondary solution,  $w_{,\alpha\beta}^h$  onto the basis used for the the primary solution  $w^h$ , resulting in the recovered solution,  $w_{,\alpha\beta}^*$ . Herein, we use continuous global  $L_2$ -projection to obtain this recovered solution. An error indicator based on the energy norm is then

$$\eta^* = \|w^* - w^h\|_E \quad (11)$$

where  $\|w\|_E := \sqrt{a(w, w)} = \sqrt{l(w)}$ .

Continuous global  $L_2$ -projection (CGL2) of the bending moment field goes like this: Find  $m_{\alpha\beta}^* \in \mathcal{S}_p^r$  such that

$$(m_{\alpha\beta}^* - m_{\alpha\beta}^h, v_h)_\Omega = 0 \quad \forall v_h \in \mathcal{S}_p^r \quad (12)$$

That is, we project the FE bending moments  $m_{\alpha\beta}^h \in \mathcal{S}_{p-2}^{r-2}$  onto the same basis as used for the displacement,  $\mathcal{S}_p^r$ , for convenience. It is possible to also chose a separate basis  $\mathcal{S}_p^{r-1}$  or  $\mathcal{S}_p^{r-2}$  with reduced regularity in the  $L_2$ -projection, motivated by the fact that in the real solution the bending moments do have lower regularity than the displacement field. However, we have not done this in the present study.

The error estimate given by Equation (11) will underestimate the true error, defined as  $\|w - w^h\|_E$ , which is bounded by

$$\|w - w^h\|_E \leq \|w^* - w^h\|_E + \|w - w^*\|_E \quad (13)$$

If the recovered solution  $w^*$  is *superconvergent*, i.e., has higher order convergence rates than  $w$ , the error estimator defined by Equation (11) will be asymptotic exact.

## 4 NUMERICAL EXAMPLES

### 4.1 Beam with parabolic load

Consider a simply supported beam subjected to a parabolic distributed transverse load  $q(x) = \frac{q_0}{L^2}4x(x - L)$ , as depicted in Figure 1. This 1D problem is governed by the differential equation

$$w_{xxxx}(x) = -\frac{q(x)}{EI} \quad (14)$$

where  $EI = \frac{Ebh^3}{12}$  assuming a rectangular cross section with height  $h$  and width  $b$ , and  $w(x)$  is the unknown transverse displacement. The bending moment  $M(x)$  is given by

$$\frac{M(x)}{EI} = w_{xx}(x) \quad (15)$$

Integrating Equation (14) twice, while imposing boundary conditions  $w_{xx}(0) = w_{xx}(L) = 0$  yields the analytical bending moment

$$M(x) = \frac{q_0}{3L^2}(L^3 - 2Lx^2 + x^3)x \quad (16)$$

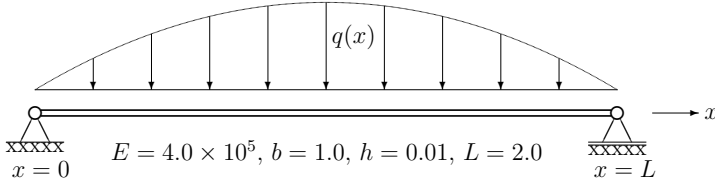


**Figure 1:** Simply supported beam with parabolic load: Geometry and properties.

Integrating Equation (16) twice, while imposing boundary conditions  $w(0) = w(L) = 0$ , yields the analytical displacement

$$w(x) = \frac{q_0}{90EIL^2}(3L^5 - 5x^2L^3 + 3x^4L - x^5)x \quad (17)$$

We can then find the analytical energy norm value  $\|w\|_E$  as

$$\|w\|_E^2 = a(w, w) = (q, w) = \int_0^L q(x)w(x)dx = \frac{31q_0^2L^5}{5670EI} \quad (18)$$

which for our choice of parameters from Figure 1 and  $q_0 = 2.0$  yields the analytical energy norm value  $\|w\|_E = 4.58199836258253$ .

Since this problem has a smooth solution, doing adaptive refinement is not likely to produce better convergence compared to a pure uniform refinement. However, we may use it to compare the convergence rates for different polynomial order of the splines basis, and to verify that we can reproduce the analytical solution with a 6'th order spline basis since the analytical displacement field of Equation (17) is of polynomial order 6. For such a smooth problem we expect to observe the convergence rates  $N_{\text{dof}}^{-(p-1)/2}$  for all polynomial orders  $p \geq 2$ .

In Figure 2 we present the estimated and exact error for polynomial orders 2, 3, 4, 5 and 6 and the associated effectivity indices. We observe that we get the expected convergence rates according to the polynomial order, except for the  $p = 6$  simulation. For the latter, the calculated discretization error instead increases as we refine the model. However, the values are very small and we assume that this is due to accumulation of truncation errors in the finite precision calculations, and not discretization errors as such.

## 4.2 Square plate with point load

Figure 3 depicts a simply supported square plate subjected to a transverse point load  $P_z$  at its center. The material properties are taken from Gustafsson *et. al* [6], who studied adaptive simulation of this problem using a fifth-order plate bending finite element.

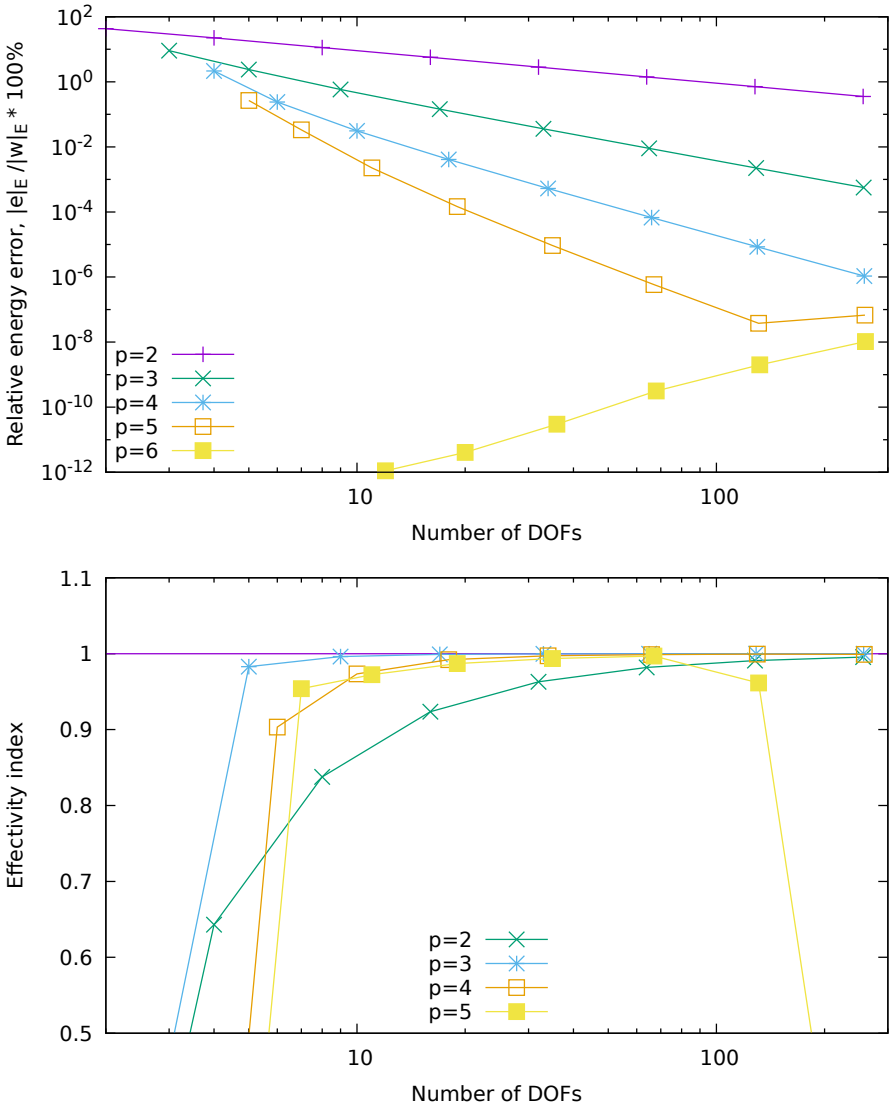


**Figure 2:** Simply supported beam with parabolic load: Exact errors for  $p = 2 \dots 6$  and associated effectivity indices for  $p = 2 \dots 5$  when doing uniform mesh refinements.

The exact error in strain energy for this problem can easily be computed from the exact displacement under the point load,  $w(\frac{1}{2}, \frac{1}{2})$ , through

$$\begin{aligned} \|e\|_E &= \|w - w^h\|_E = \sqrt{a(w - w^h, w - w^h)} = \sqrt{l(w - w^h)} \\ &= \sqrt{P_z \left( w \left( \frac{1}{2}, \frac{1}{2} \right) - w^h \left( \frac{1}{2}, \frac{1}{2} \right) \right)} \end{aligned} \quad (19)$$

with [6]

$$w \left( \frac{1}{2}, \frac{1}{2} \right) = \frac{P_z}{2D\pi^3} \sum_{m=1}^{\infty} \frac{\sin^2 \frac{m\pi}{2} (\sinh m\pi - m\pi)}{m^3 (1 + \cosh m\pi)} \quad (20)$$

resulting from the classical Navier thin plate solution. With our choice of parameters as in Figure 3, this yields  $w(\frac{1}{2}, \frac{1}{2}) = 0.12668117031255$ .

With this at hand, we can now perform convergence studies for this problem using adaptive mesh refinement based on the estimated error distribution, and compare with uniform mesh refinement simulations. All simulations are started from an uniform mesh with 8 by 8 elements. In Figure 4 we display, as an example, the initial mesh and the final adapted mesh for one of the quintic simulations.

According to [6] the analytical solution for the problem with a point load is in  $H^{3-\epsilon}(\Omega)$ , i.e., for uniform mesh refinement we can expect to observe convergence rates  $N_{\text{dof}}^{-1/2}$  for all  $p \geq 2$ . However, using a posteriori driven adaptive mesh refinement our goal is to achieve optimal convergence rates determined by the polynomial order, i.e.,  $N_{\text{dof}}^{-(p-1)/2}$  for all polynomial orders  $p \geq 2$ .

The results are shown in Figures 5–8 for quadratic, cubic, quartic and quintic splines basis, respectively. Here we also include some adaptive simulations with reduced regularity

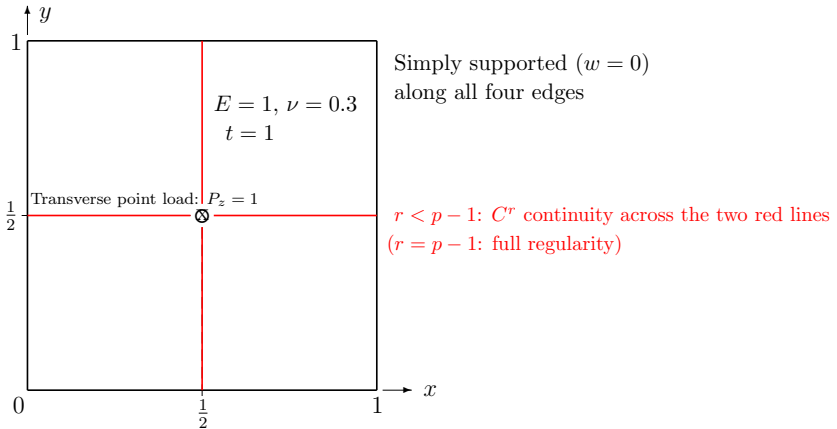


**Figure 3:** Square plate with point load: Geometry and properties (from Gustafsson *et. al* [6]).



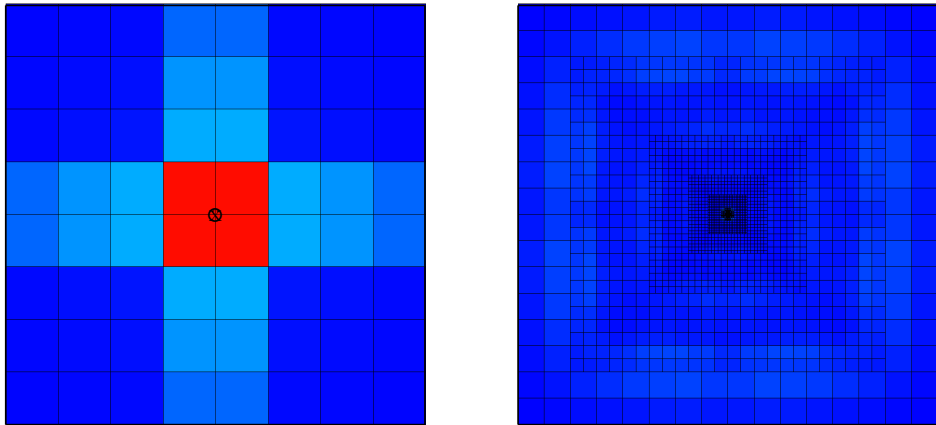


**Figure 4:** Square plate with point load: Initial and final adaptive mesh with error distribution for  $p = 5$ .

under the point load ( $r < p - 1$ ), to demonstrate that increased accuracy in terms of lower error can be obtained with this choice as the analytic solution is  $C^2$  at the center point. The reduced regularity is achieved by introducing multiple knots in the splines basis along the two orthogonal red lines passing through the centre point, as illustrated in Figure 3.

For the lowest polynomial order ( $p = 2$ ), we observe from Figure 5 that we get slightly less than expected convergence rate for UMR, whereas for AMR we achieve the optimal rate. The effectivity index for UMR approaches slowly 1.0, whereas for AMR it is much closer to 1.0.

For cubic polynomials ( $p = 3$ ) the results in Figure 6 clearly demonstrate that for UMR the convergence rate is suboptimal, i.e., it is governed by the regularity of the analytical solution. The adaptively refined meshes (AMR) give optimal convergence rate with slightly better results for full regularity ( $r = 2$ ) than for reduced regularity in the center point ( $r = 1$ ). The effectivity index for UMR converges very slowly from below towards 1.0, whereas AMR gives indices much closer to 1.0 and again slightly better results for regularity  $r = 2$  than  $r = 1$ .

In Figure 7 the results obtained with  $p = 4$  are displayed. The difference in the convergence rates between UMR and AMR are pronounced and the results obtained with full regularity  $r = 3$  everywhere gives significantly larger error than for locally reduced regularity  $r = 2$  and  $r = 1$  normal to the two orthogonal centre lines. Here, we get the lowest error and best effectivity indices for AMR using locally reduced regularity  $r = 2$ . For the adaptive refined meshes we obtain good effectivity indices for the case with locally reduced regularity  $r = 1$  but for full regularity the effectivity indices are below 0.5. For UMR we get both suboptimal convergence rates and the effectivity indices seem to diverge away from 1.0.

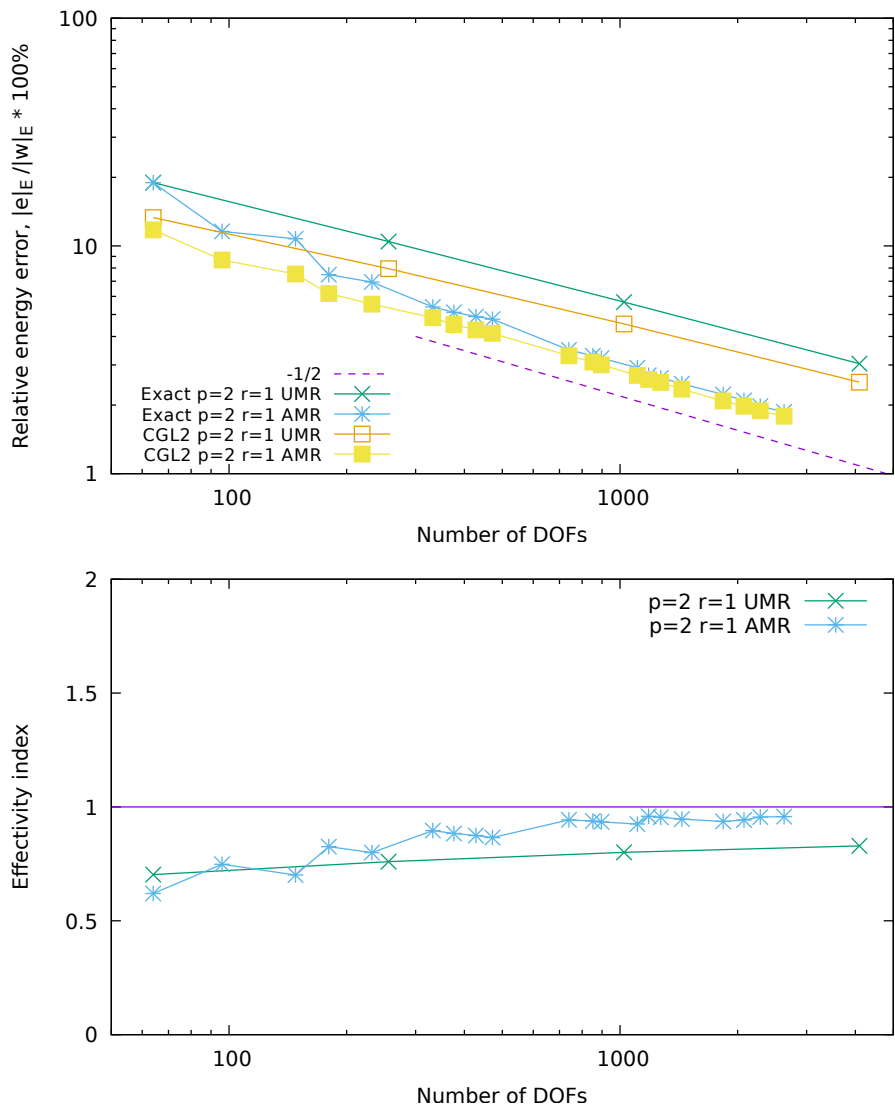


**Figure 5:** Square plate with point load: Exact and estimated errors and associated effectivity indices for  $p = 2$ , for uniform (UMR) and adaptive (AMR) mesh refinements.

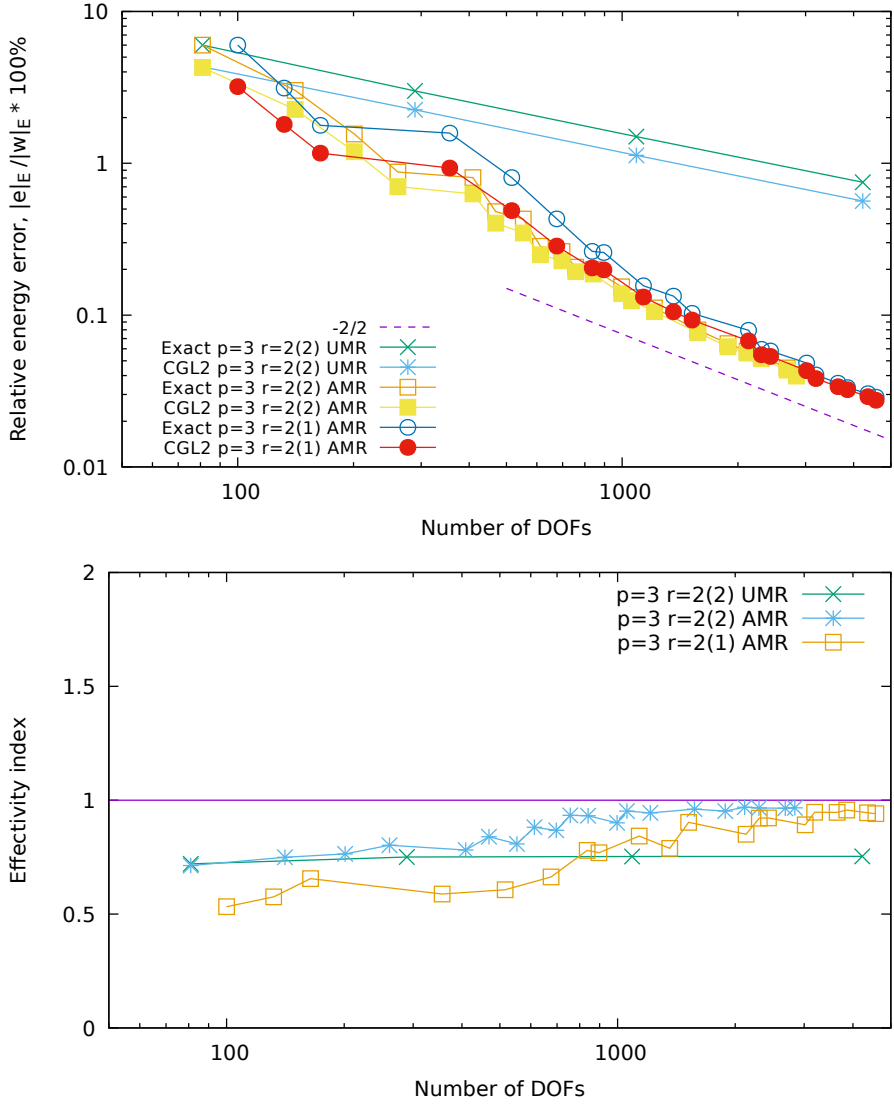


**Figure 6:** Square plate with point load: Exact and estimated errors and associated effectivity indices for  $p = 3$ , with full (2(2)) and locally reduced (2(1)) regularity, for uniform (UMR) and adaptive (AMR) mesh refinements.

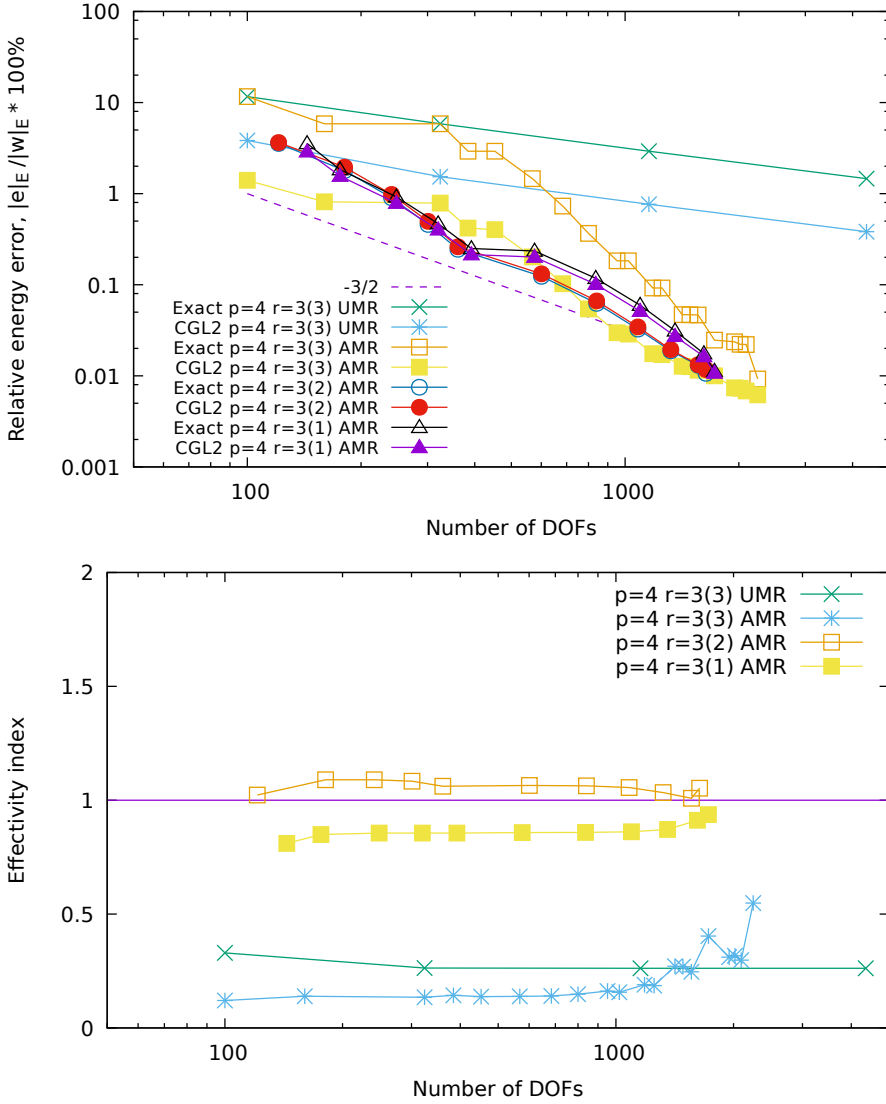


**Figure 7:** Square plate with point load: Exact and estimated errors and associated effectivity indices for  $p = 4$ , with full  $(3(3))$  and locally reduced  $(3(r \leq 2))$  regularity, for uniform (UMR) adaptive (AMR) mesh refinements.

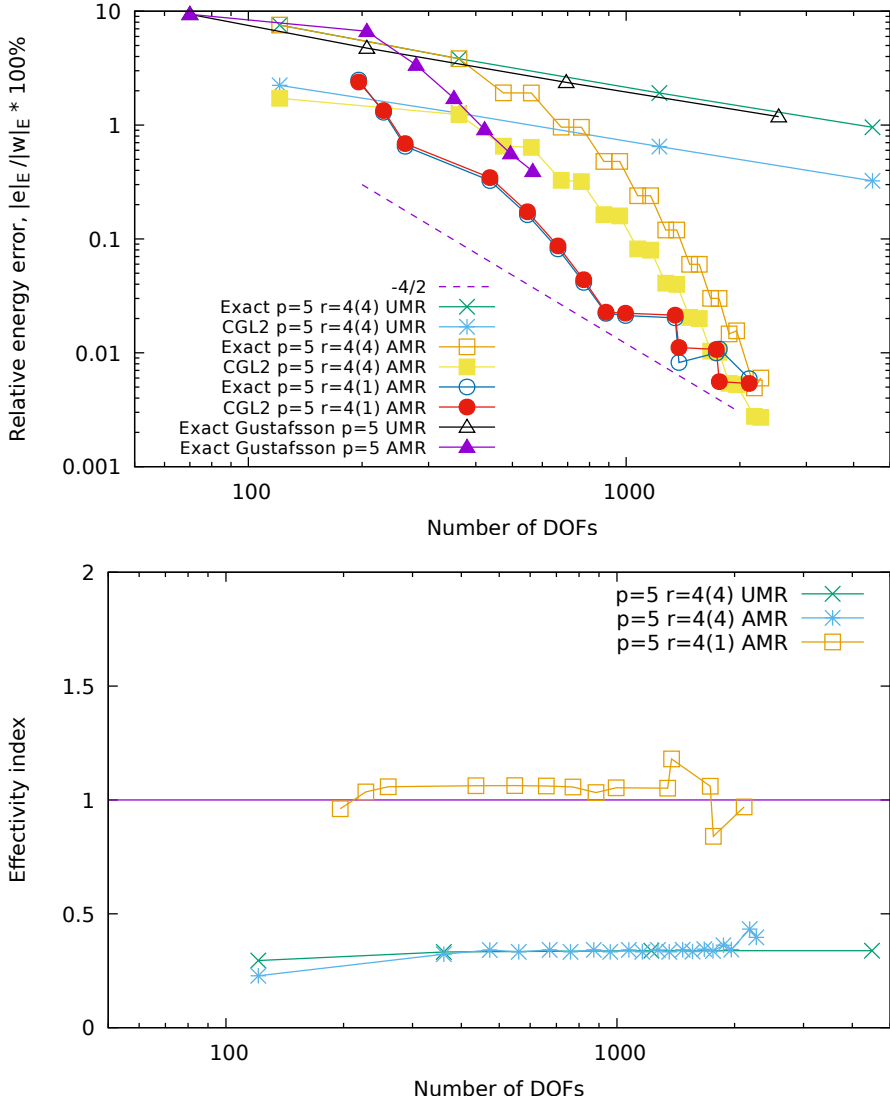


**Figure 8:** Square plate with point load: Exact and estimated errors and associated effectivity indices for  $p = 5$ , full (4(4)) and locally reduced (4(1)) regularity, for uniform (UMR) adaptive (AMR) mesh refinements. Comparison with exact errors from Gustafsson *et. al* [6].

Finally, we run this case with  $p = 5$  to be able to compare our results with those obtained by Gustafsson *et. al* [6]. Firstly, we observe in Figure 8 that our results obtained with UMR and full regularity ( $r = 4$ ) are very close (slightly less accurate) to their results obtained with  $C^1$  (i.e.,  $r = 1$  everywhere) compatible classical finite elements. For the adaptive refined meshes our results are better than theirs when we use (local) regularity normal to the center lines less or equal to  $r = 2$ , whereas for  $r = 3$  and  $r = 4$  the opposite is true. For clarity, we have only showed our results for full regularity everywhere (i.e.,  $r = 4$ ), and local regularity  $r = 1$ . The effectivity indices for AMR and local regularity  $r = 1$  is quite close to 1.0, whereas for full regularity the indices are below 0.5 for both AMR and UMR.

## 5 CONCLUSIONS

We have developed adaptive methods for isogeometric Kirchhoff-Love thin plates. The main finding is that using a posteriori error estimate based on global  $L_2$  projection for recovery of a *superconvergent* moment field to drive adaptive mesh refinement, achieves optimal convergence rates for challenging non-smooth problems.

## REFERENCES

- [1] Hughes, T. J. R., Cottrell, J. A. & Bazilevs, Y. Isogeometric Analysis: CAD, Finite Elements, NURBS, Exact Geometry and Mesh Refinement. *Computer Methods in Applied Mechanics and Engineering* **194**, 4135–4195 (2005).
- [2] Johannessen, K. A., Kvamsdal, T. & Dokken, T. Isogeometric Analysis using LR B-splines. *Computer Methods in Applied Mechanics and Engineering* **269**, 471–514 (2014).
- [3] Kvamsdal, T. & Okstad, K. M. Error Estimation based on Superconvergent Patch Recovery using Statically Admissible Stress Fields. *International Journal for Numerical Methods in Engineering* **42**, 443–472 (1998).
- [4] Okstad, K. M., Kvamsdal, T. & Mathisen, K. M. Superconvergent Patch Recovery for Plate Problems using Statically Admissible Stress Resultant Fields. *International Journal for Numerical Methods in Engineering* **44**, 697–727 (1999).
- [5] Kumar, M., Kvamsdal, T. & Johannessen, K. A. Superconvergent Patch Recovery and a Posteriori Error Estimation Technique in Adaptive Isogeometric Analysis. *Computer Methods in Applied Mechanics and Engineering* **316**, 1086–1156 (2017).
- [6] Gustafsson, T., Stenberg, R. & Videman, J. A Posteriori Estimates for Conforming Kirchhoff Plate Elements. *SIAM Journal on Scientific Computing* **40**(3) (2018).

## AN ANISOTROPIC GROWTH MODEL FOR FIBROUS TISSUES: CONTINUUM FORMULATION AND COMPUTATIONAL ASPECTS

Xuyan Liu<sup>1</sup>, Bjørn H. Skallerud<sup>1</sup>, Victorien E. Prot<sup>1</sup> and Gerhard A. Holzapfel<sup>1,2</sup>

<sup>1</sup>Department of Structural Engineering, Faculty of Engineering  
Norwegian University of Science and Technology (NTNU), 7491 Trondheim, Norway  
e-mail: {xuyan.liu|bjorn|victorien.prot|gerhard.holzapfel}@ntnu.no

<sup>2</sup> Institute of Biomechanics, Graz University of Technology, Stremayrgasse 16/II, 8010 Graz, Austria

**Key words:** In-stent Restenosis, Growth Model, Anisotropy, Damage, FE Simulation

**Abstract.** In-stent restenosis (ISR) is one of the most common reasons for failure of stent implementation. It is hypothesized that during angioplasty arterial tissues suffer from weakening (softening) due to supraphysiological loading. In a clinical context these inelastic effects are described as ‘controlled vessel injury’. From the materials science point of view tissue damage occurs, and because the tissues are living, healing is triggered which in some cases lead to a re-blocking of the diseased artery, to ISR. Arterial walls consist of three layers which behave mechanically anisotropic, because at least two families of collagen fibers are embedded in an isotropic matrix. In the present study we propose an anisotropic growth model for fibrous (collagenous) soft tissues and consider distributed collagen fiber orientations. In particular we analyze a comparison between isotropic and anisotropic growth models, which shows that the fiber reinforcement helps with the adaptation to the new mechanical environment. Finally, we provide a numerical simulation of a simplified ISR using a quarter of an artery modeled as a regular cylinder using three layers.

### 1 INTRODUCTION

Cardiovascular diseases (CVDs) are by far the leading cause of death in the world, although great developments in medical, surgical and pharmacological interventions have been made, see, e.g., the recent reviews [1, 2]. One of the major types of CVDs is atherosclerosis in which fibrous and fatty materials build up at the artery walls and cause a blocking situation in the vessel. Such materials are called plaques. There are several ways to unblock the arterial vessels, and angioplasty with stenting is one of the most frequently used treatments. However, due to the difference of the stiffness between the arterial wall and the inserted stent, and due to a supraphysiological loading condition that occurs during angioplasty, there is always some damage involved in the biological tissues, even in the healthy tissues. In order to cure the injury, tissues start to grow and heal. Unfortunately, in several cases, this healing and growth

processes may block the lumen again, and may also obstruct the blood flow, which is known as in-stent restenosis (ISR) [3].

Techniques of cardiovascular surgeries and post-surgical treatments have been developed rapidly, however, ISR remains a significant clinical problem. Though, different stents have been put into use such as better-structured bare metal stents and newer-generation drug-eluting stents (DES). The treatment of ISR remains a challenge and the long-term clinical outcome of the treated patients may be complicated by recurrences [4]. Various efforts have been pursued to reduce ISR, and a significant focus has been put on DESs. Interestingly, according to the recent study [5], in patients undergoing percutaneous coronary intervention, *'there were no significant differences between those receiving DESs and those receiving bare-metal stents in the composite outcome of death from any cause and nonfatal spontaneous myocardial infarction'*. Given that situation, scientists started to look into the mechanisms behind ISR so that an effective therapy can be found which completely, or at least, as much as possible, prevents ISR from taking place after intervention. However, as it turns out, the underlying mechanism of restenosis is complicated. The lumen can enlarge in some cases, which is known as positive tissue remodeling [6]. On the contrary, the lumen can also have a narrowing, i.e. restenosis. The mechanism of restenosis after angioplasty is a combination of elastic recoil, arterial vessel remodeling, and neointimal hyperplasia [7, 8]. The stimuli for the restenosis process are disruption of the endothelial barrier layer and the mechanical stretch and disruption of the intima/media, and partly also of the adventitia. This mechanical injury of the vessel wall stimulates migration of smooth muscle cells (from the media) and myofibroblasts (from the adventitia) to the intima where they proliferate [9]. In other words, the tissue may grow and re-block the lumen when an injury occurs to the vessel wall.

Growth is an individually distinguished feature of existing living systems. Throughout the past century, growth of living systems has fascinated plenty of physiologists, biologists, clinical scientists, mathematicians, physicists, computer scientists, and engineers alike [10]. An intriguing feature of growth is the interplay of form and function, or, more specifically, the ability of the growing system to manipulate its micro-environment and, *vice versa*, the ability of the micro-environment to manipulate the micro-structural architecture of growth [11]. The latter is what we are interested in. It is associated with an exploration of the mechanisms which cause a system to grow, stretch, strain, or to stress. In particular we want to better understand how mechanics can trigger biology [12]. For biological growth, a number of mechanical models have been proposed [12]. Some of them are based on the isotropic theory, by assuming that growth of arterial tissue is isotropic, see, e.g., [13]. Anisotropic growth has also been proposed and studied, see, e.g., [14]. Arterial tissues are characterized by an anisotropic material, with (at least) two families of fibers embedded in an isotropic matrix [15] (for each layer of human aortas). Given this fact, it is more meaningful to use anisotropic growth models.

In this study, we present an anisotropic growth model. In Section 2 we provide the constitutive framework and the specifics of the model. In Section 3, we present the stress and elasticity tensors, illustrate biaxial extension tests and compare between isotropic and anisotropic models. Finally, in Section 4, a regular cylinder with stent inflation is used to simulate ISR.



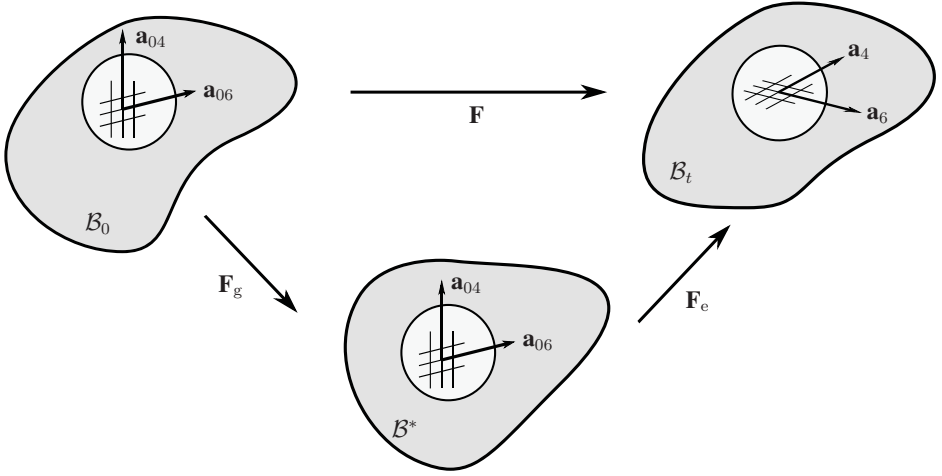


**Figure 1:** Reference configuration  $\mathcal{B}_0$  describes the undeformed state of a solid body, and the current configuration  $\mathcal{B}_t$  the deformed state. The multiplicative decomposition of the deformation gradient  $\mathbf{F} = \mathbf{F}_e \mathbf{F}_g$  into an elastic ( $\mathbf{F}_e$ ) and a growth part ( $\mathbf{F}_g$ ) is realized by introducing an imaginary configuration  $\mathcal{B}^*$ . The anisotropic micro-structure of the material is rendered by two families of fibers with directions  $\mathbf{a}_{0i}$ , and  $\mathbf{a}_i$ ,  $i = 4, 6$ , in the reference and the current configuration, respectively.

## 2 METHOD

Let  $\mathcal{B}_0$  be a solid body (piece of tissue) in the reference configuration, and  $\mathcal{B}_t$  be the body in the current configuration, see Fig. 1. An imaginary configuration  $\mathcal{B}^*$  is introduced so that the deformation gradient  $\mathbf{F}$  can be multiplicatively decomposed into a growth deformation gradient, say  $\mathbf{F}_g$ , and an elastic deformation gradient, say  $\mathbf{F}_e$ , [16], i.e.

$$\mathbf{F} = \mathbf{F}_e \mathbf{F}_g. \quad (1)$$

The micro-structure of the anisotropic material is rendered by two families of symmetric fibers in the reference and the intermediate configurations, with directions  $\mathbf{a}_{0i}$ , while  $\mathbf{a}_i$ ,  $i = 4, 6$ , are the related directions in the current configuration. The determinants of the deformation gradient  $\mathbf{F}$  and its growth and elastic parts are denoted by  $J$ ,  $J_g$  and  $J_e$ , respectively. Thus,

$$J = J_e J_g, \quad J = \det \mathbf{F}, \quad J_e = \det \mathbf{F}_e, \quad J_g = \det \mathbf{F}_g. \quad (2)$$

In addition, we introduce the right and left Cauchy-Green tensors of the elastic part according to

$$\mathbf{C}_e = \mathbf{F}_e^T \mathbf{F}_e, \quad \mathbf{B}_e = \mathbf{F}_e \mathbf{F}_e^T. \quad (3)$$

The first invariant  $I_{1e}$ , which we will later use in the free-energy function, is given by

$$I_{1e} = \text{tr} \mathbf{C}_e = \text{tr} \mathbf{B}_e. \quad (4)$$

Next, the unimodular elastic deformation gradient is defined by  $\bar{\mathbf{F}}_e = J_e^{-1/3} \mathbf{F}_e$ , with  $\det \bar{\mathbf{F}}_e \equiv 1$ . Similarly, the unimodular counterparts of the Cauchy-Green tensors are  $\bar{\mathbf{C}}_e = J_e^{-2/3} \mathbf{C}_e$  and  $\bar{\mathbf{B}}_e = J_e^{-2/3} \mathbf{B}_e$ , [17].

Arterial walls are anisotropic and incompressible materials; for a review of constitutive models see, e.g., [18]. They consist of three layers, and each of them is equipped by two (or more) families of collagen fibers with both in-plane and out-of-plane dispersion embedded in an isotropic matrix material (in particular for human aortas); for a more recent constitutive framework see [19], although we are here not pursuing this approach. In the present study we rather use the proposed model [13], however for the anisotropic part of the free energy we are not using just the isochoric part of the deformation gradient; for a recent study of this point in regard to its numerical efficiency and physical interpretation of the fiber stretches see [20]. The free-energy function  $\Psi$  is then proposed as

$$\Psi(\mathbf{C}_e, \mathbf{a}_{04}, \mathbf{a}_{06}) = U(J_e) + \Psi_{\text{iso}}(\bar{\mathbf{C}}_e) + \Psi_{\text{ani}}(\mathbf{C}_e, \mathbf{a}_{04}, \mathbf{a}_{06}), \quad (5)$$

where

$$U(J_e) = \frac{1}{D_1} \left( \frac{J_e^2 - 1}{2} - \ln J_e \right) \quad (6)$$

serves as a penalty term to constrain the incompressibility condition, and  $D_1$  is a penalty coefficient chosen to be  $2 \times 10^{-7} / \mu$ . The energy stored in the isotropic matrix material is assumed to be neo-Hookean, i.e.

$$\Psi_{\text{iso}}(\bar{\mathbf{C}}_e) = \mu(\bar{I}_{1e} - 3), \quad (7)$$

where  $\bar{I}_{1e} = \text{tr} \bar{\mathbf{C}}_e = J_e^{-2/3} I_{1e}$ , and  $\mu$  is a material parameter. We then provide the free energy  $\Psi_{\text{ani}}$  for the anisotropic contribution according to [21] (here we do not use the volumetric/isochoric split for  $\Psi_{\text{ani}}$ ), i.e.

$$\Psi_{\text{ani}}(\mathbf{C}_e, \mathbf{a}_{04}, \mathbf{a}_{06}) = \frac{k_1}{2k_2} \sum_{i=4,6} [\exp(k_2 E_i^2) - 1], \quad (8)$$

$$E_i = \kappa I_{1e} + (1 - 3\kappa) I_{ie} - 1, \quad I_{ie} = \mathbf{C}_e : \mathbf{a}_{0i} \otimes \mathbf{a}_{0i}, \quad i = 4, 6, \quad (9)$$

where  $k_2 > 0$  is a dimensionless parameter and  $k_1 > 0$  is a stress-like parameter to be determined from mechanical tests of the tissue, while  $\mathbf{a}_{0i}$ ,  $i = 4, 6$ , and  $\kappa \in [0, 1/3]$  are structure parameters to be determined from histological data of the tissue.

As mentioned in the introduction, after stent placement, healthy and scar tissues build around the stent over time, which may lead to a new narrowing of the artery called ISR. The healing process works against tissue damage. We assume now that if a damage identifier defined as

$$D = \frac{1}{r_1} \text{erf} \left[ \frac{1}{m_1} (\Psi_{\text{iso}} + \Psi_{\text{ani}})_{\text{max}} \right] \quad (10)$$

exceeds a threshold, say  $D_{\text{th}}$ , which is again a material parameter, then tissue growth is triggered [13]. In (10)  $\text{erf}(\bullet)$  is the error function of  $(\bullet)$ , and  $r_1$ ,  $m_1$  are damage parameters. For a different constitutive approach to capture the inelastic phenomena associated with tissue stretches beyond the physiological domain see [22].

We propose anisotropic growth by defining the growth deformation gradient  $\mathbf{F}_g$  as

$$\mathbf{F}_g = \mathbf{F}_{g,\text{iso}} \mathbf{F}_{g,\text{ani}}, \quad (11)$$

where

$$\mathbf{F}_{g,\text{iso}} = \lambda_g \mathbf{I}, \quad \lambda_g = \exp \left\{ \frac{k}{3\alpha^2} [1 - (1 + \alpha t) \exp(-\alpha t)] \langle D - D_{\text{th}} \rangle \right\}. \quad (12)$$

The material parameters  $k$ ,  $\alpha$  and  $D_{\text{th}}$  need to be identified from experiments or clinical data, while  $\mathbf{I}$  denotes the second-order identity tensor. From clinical observations, the growth behavior of most biological tissues should have the property that growth finally approaches to a stable state, which means no further growth should happen. Equation (12)<sub>2</sub>, the isotropic growth factor  $\lambda_g$ , is an ascending function in time. However, the first derivative of  $\lambda_g$  with respect to time, i.e.  $\dot{\lambda}_g$ , is a descending function. When the time goes to infinity,  $\dot{\lambda}_g$  is infinitely close to zero and  $\lambda_g$  is close to a constant. Similar properties should be possessed by the anisotropic growth factor as well.

The anisotropic growth deformation gradient  $\mathbf{F}_{g,\text{ani}}$  is proposed to taken on the form

$$\mathbf{F}_{g,\text{ani}} = \mathbf{I} + (\nu_4 - 1) \mathbf{a}_{04} \otimes \mathbf{a}_{04} + (\nu_6 - 1) \mathbf{a}_{06} \otimes \mathbf{a}_{06}, \quad (13)$$

where  $\nu_4$  and  $\nu_6$  are two anisotropic growth factors for the two fiber families. Instead of using a different function, the anisotropic growth factors are formulated in the same way as the isotropic growth factor  $\lambda_g$ , i.e.

$$\nu_i = \exp \{ c_{1,i} [1 - (1 + c_{2,i} t) \exp(-c_{2,i} t)] \langle D - D_{\text{th}} \rangle \}, \quad i = 4, 6, \quad (14)$$

where  $c_{1,i}$  and  $c_{2,i}$  are material parameters. In this way, anisotropic growth can be included.

### 3 FINITE ELEMENT IMPLEMENTATION, TEST EXAMPLES

#### 3.1 Stress and elasticity tensors

First we derive the stress tensor on the basis of the proposed model of Section 2, which we implemented into the UMAT-routine of Abaqus [23]. In the frame of continuum mechanics, the second Piola-Kirchhoff stress tensor  $\mathbf{S}$  is the derivative of free-energy function  $\Psi$  with respect to the right Cauchy-Green tensor  $\mathbf{C}$  according to  $\mathbf{S} = 2\partial\Psi/\partial\mathbf{C}$ . Given Eq. (5), the stress tensor  $\mathbf{S}$  has then the form

$$\mathbf{S} = 2 \frac{\partial U(J_e)}{\partial \mathbf{C}} + 2 \frac{\partial \Psi_{\text{iso}}(\bar{\mathbf{C}}_e)}{\partial \mathbf{C}} + 2 \frac{\partial \Psi_{\text{ani}}(\mathbf{C}_e, \mathbf{a}_{04}, \mathbf{a}_{06})}{\partial \mathbf{C}}. \quad (15)$$

By applying the chain rule to (15) we obtain

$$\begin{aligned} \mathbf{S} &= 2 \frac{\partial U(J_e)}{\partial J_e} \frac{\partial J_e}{\partial \mathbf{C}} + 2 \frac{\partial \Psi_{\text{iso}}(\bar{\mathbf{C}}_e)}{\partial \bar{\mathbf{C}}_e} : \frac{\partial \bar{\mathbf{C}}_e}{\partial \mathbf{C}} + 2 \sum_{i=4,6} \frac{\partial \Psi_{\text{ani}}(\mathbf{C}_e, \mathbf{a}_{04}, \mathbf{a}_{06})}{\partial E_i} \frac{\partial E_i}{\partial \mathbf{C}} \\ &= \mathbf{F}_g^{-1} \mathbf{S}_e \mathbf{F}_g^{-T}, \end{aligned} \quad (16)$$

where we have used the definition

$$\mathbf{S}_e = 2 \frac{\partial \Psi}{\partial \mathbf{C}_e} = 2 \frac{\partial U(J_e)}{\partial J_e} \frac{\partial J_e}{\partial \mathbf{C}_e} + 2 \frac{\partial \Psi_{\text{iso}}(\bar{\mathbf{C}}_e)}{\partial \bar{\mathbf{C}}_e} : \frac{\partial \bar{\mathbf{C}}_e}{\partial \mathbf{C}_e} + 2 \sum_{i=4,6} \frac{\partial \Psi_{\text{ani}}(\mathbf{C}_e, \mathbf{a}_{04}, \mathbf{a}_{06})}{\partial E_i} \frac{\partial E_i}{\partial \mathbf{C}_e}. \quad (17)$$

A more detailed derivation of the stress relation can be found in the Appendix A.

The numerical computation of the elasticity tensor  $\mathbb{C}$  in the material description is also needed, which, with (16)<sub>2</sub>, is given by

$$\mathbb{C} = 2 \frac{\partial \mathbf{S}}{\partial \mathbf{C}} = 2 \frac{\partial (\mathbf{F}_g^{-1} \mathbf{S}_e \mathbf{F}_g^{-T})}{\partial \mathbf{C}} = (\mathbf{F}_g^{-1} \otimes \mathbf{F}_g^{-1}) : \mathbb{C}_e : (\mathbf{F}_g^{-T} \otimes \mathbf{F}_g^{-T}), \quad (18)$$

with

$$\mathbb{C}_e = 2 \frac{\partial \mathbf{S}_e}{\partial \mathbf{C}_e}, \quad (19)$$

where the symbol  $\otimes$  denotes a non-standard tensor product between two second-order tensors according to  $(\mathbf{A} \otimes \mathbf{B})_{ijkl} = A_{ik} B_{jl}$ , see, e.g., [24]. Note that (18)<sub>3</sub> may be written in the index notation as

$$(\mathbb{C})_{ijkl} = F_{gim}^{-1} F_{gjn}^{-1} (\mathbb{C}_e)_{mnrq} F_{gkr}^{-1} F_{glq}^{-1}. \quad (20)$$

For a detailed derivation see [13]. What remains is a detailed expression for  $\partial \mathbf{S}_e / \partial \mathbf{C}_e$ , where explicit terms for  $\mathbf{S}_e$  are provided in the Appendix A.

### 3.2 Biaxial extension test

In order to show the difference between the isotropic model ( $\mathbf{F}_{g,\text{ani}} = \mathbf{I}$ ) and the proposed anisotropic growth model we perform a biaxial extension test on a cube with size  $1 \times 1 \times 1$  mm. The fibers are symmetrically embedded in the  $(x, y)$ -plane. A stretch  $\lambda$  of 1.5 is applied both in  $x$ - and  $y$ -directions; for the related sketch including the boundary conditions see Fig. 2. For this example we have just used one finite element, in particular the C3D8H element within Abaqus (8-node linear brick, hybrid with constant pressure). The material of the cube is set to an intima, and the related properties are summarized in Table 1. In the table,  $\gamma$  denotes the angle between the mean fiber direction and the  $x$ -direction.

During  $t \in [0, 0.5]$  the material is loaded until the desired stretch is achieved, and a damage of the material occurs. Then the material is unloaded during  $t \in (0.5, 1]$  until its original shape

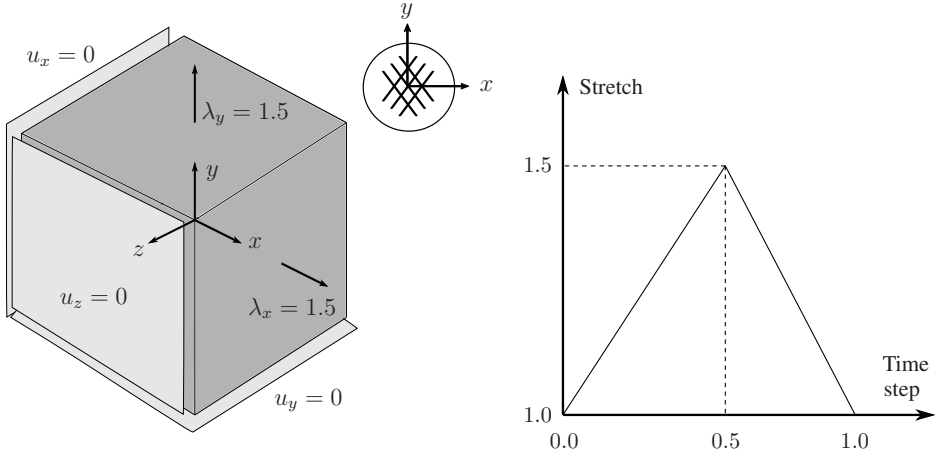


**Figure 2:** Undeformed cube with boundary conditions and a zoom-up of the symmetrically disposed fibers in the  $(x, y)$ -plane shown on the left. A stretch  $\lambda_x = \lambda_y = 1.5$  is applied in the  $x$ - and  $y$ -directions within the first half of the time step, and then the cube is unloaded to its original shape. The function of the stretching within the time step is shown on the right.

**Table 1:** Material and structural parameters of the intima, the media and the adventitia used in the simulations of the present study. With the exception of  $D_{th}$  (intima) and  $k$  (media and adventitia) the values are taken from [13].

	Intima	Media	Adventitia
$\mu$ [MPa]	0.049	0.020	0.016
$k_1$ [MPa]	15.467	0.180	0.845
$k_2$ [-]	2.085	100.0	22.30
$\gamma$ [°]	43.9	5.76	56.3
$\kappa$ [-]	0.23	0.314	0.32
$r_1$ [-]	1.37	3.36	3.29
$m_1$ [MPa]	0.0198	0.0191	0.045
$D_{th}$ [-]	0.2	0.01	0.01
$\alpha$ [day <sup>-1</sup> ]	0.05	0.05	0.05
$k$ [day <sup>-2</sup> ]	0.005	0.005	0.005
$c_{1,i}$ [day <sup>-1</sup> ]	0.5	0.5	0.5
$c_{2,i}$ [day <sup>-2</sup> ]	0.05	0.05	0.05

is restored. Instead of using the same formulations for  $\nu_4$  and  $\nu_6$ , as provided in (14), we select here specific anisotropic growth factors according to

$$\nu_4 = \nu_6 = 1 + \frac{-1 + \sqrt{1 + \sin^2 2\gamma (\lambda_g^3 - 1)}}{\sin^2 2\gamma}, \quad (21)$$

where we assume that the growth factors for the two families of fibers are the same (symmetry) and  $\lambda_g$  is adopted from Eq. (12)<sub>2</sub>. In this way we obtain an isotropic growth and a pure anisotropic growth of the material under the condition of equal volume change, however, different geometrical patterns, as shown in Fig. 3.

In order to see the difference between an isotropic model and an anisotropic model, we carefully selected two different total growth deformation gradients, see Table 1. In this way we can obtain a pure isotropic growth and a pure anisotropic growth of the material under the condition of equal volume change, however, different geometry patterns, as shown in Fig. 3

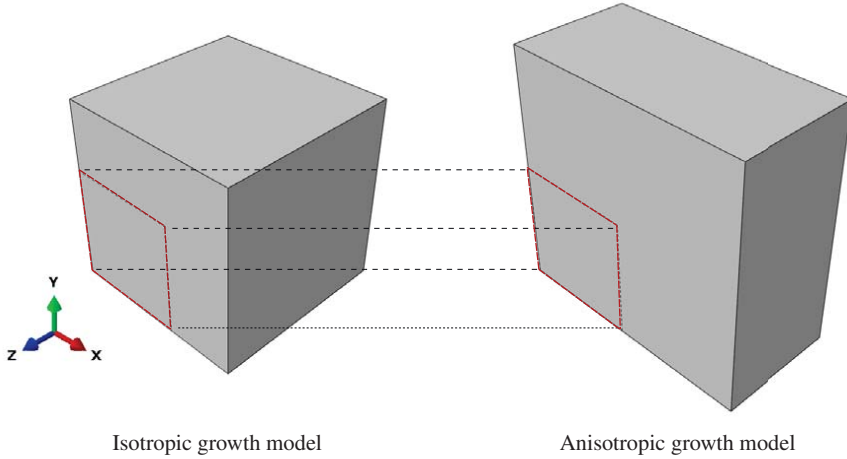


**Figure 3:** Red dashed lines show the geometry of the material before the growth. The growth pattern occurring due to isotropic growth is shown on the left side, while on the right side the shape of the material is shown after anisotropic growth.

Figures 4 and 5 provide the numerical data obtained from these simulations of the biaxial extension tests. The determinants of the elastic deformation gradient for the two cases, i.e.  $J_{e,iso}$  and  $J_{e,ani}$ , remain 1, which implies that the volume change of the material is purely due to growth, as shown in the left plot of Fig. 4. As assumed the volume change of the anisotropic and isotropic models are the same. At the beginning of the growth the volume  $v$  of the element

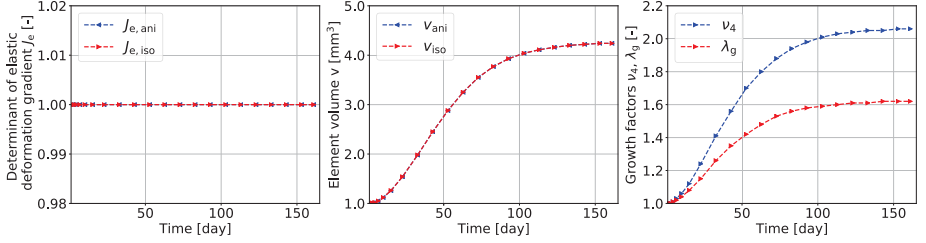


**Figure 4:** Left figure illustrates the determinant of the elastic deformation gradient  $J_e$  over time. During intimal growth  $J_e$  remains 1 in both cases (isotropic, anisotropic), which agrees with the assumption we have made; the middle and the right figures provide changes in the element volume  $v$ , the anisotropic growth factor  $\nu_4$  and the isotropic growth factor  $\lambda_g$  over time.

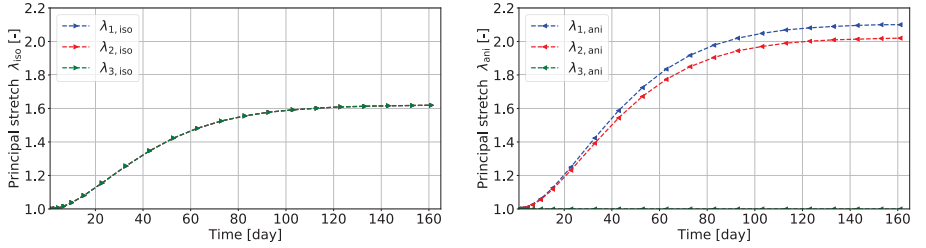


**Figure 5:** Evolution of principal stretches of the intima over time for the isotropic growth model (left) and the anisotropic growth model (right).

is  $1 \text{ mm}^3$  and at the end it has reached more than  $4.0 \text{ mm}^3$ ; for the volume change over time see the middle plot of Fig. 4. The right plots of Fig. 4 show the anisotropic and isotropic growth factors ( $\nu_4$  and  $\lambda_g$ ), as discussed in Section 2, as a function of time. The growth factors are ascending functions of time and become asymptotic when time goes to infinity.

With the same volume growth, the isotropic and anisotropic growth models result into significantly different geometries; for the evolution of the principal stretches  $\lambda_1, \lambda_2, \lambda_3$  over time see Fig. 5. The stretches in the isotropic model are equal in all principal directions, while in the anisotropic model the stretches in the first and second principal directions grow significantly larger, while  $\lambda_{3,\text{ani}} = 1$ .

Arterial tissues with their specific structure adopt and remodel to new conditions when the mechanical environment within the tissue changes. It is reasonable to assume that the collagenous reinforcement, hence the particular structure, drives the growth mechanism. Consequently, the used anisotropic growth model, in which the fiber directions are considered, may actually lead to a more realistic prediction of tissue growth – a comparison with experimental growth data is still of urgent need.

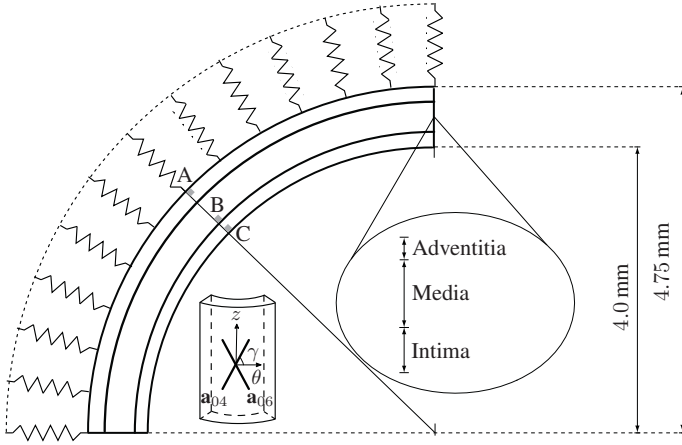


**Figure 6:** Quarter of a regular cylinder considering three layers, intima, media and adventitia, and constrained by equally distributed strings at the outer boundary surface. The fibers are embedded in the  $(\theta, z)$ -plane and their directions are characterized by  $\mathbf{a}_{04}$  and  $\mathbf{a}_{06}$ . The locations A, B and C are related to Figs. 8 and 9.

#### 4 NUMERICAL SIMULATION OF RESTENOSIS

This section provides a numerical simulation of a simplified restenosis process using a quarter of an artery modeled as a regular cylinder considering three layers, intima, media and adventitia, see Fig. 6. The inner radius of the cylinder is 4.0 mm, while the thickness of the wall is 0.75 mm. The thicknesses of the intima, media and adventitia are 0.25 mm, 0.375 mm and 0.125 mm, respectively. We assumed 13 identical groups of linear springs that are equally distributed around the outer surface of the cylinder, which we take as an elastic foundation towards the tissues around the arterial wall. It is assumed that the springs only give a radial constraint to the cylinder. The stiffness of the spring is set to 0.33 kPa. For each individual layer, in the circumferential direction 120 elements are used and 8 elements in the axial directions, while three elements discretize the thickness of the intima and media, and two elements are used along the thickness direction of the adventitia, i.e. a total of 7 680 hexahedral elements of C3D8H type. The tissue properties of the individual layers are summarized in Table 1. Six equally spaced stent struts are modeled along the quarter of the cylinder, as illustrated in Fig. 7, while a displacement boundary condition is applied onto the respective nodes for inflating the stent. The ends of the cylinder are fixed in the axial direction.

The simulation includes two steps: (i) expansion of the cylinder during which the damage occurs and (ii) tissue growth, triggered by the damage accumulated in the first step. For the numerical analysis the general anisotropic growth model, with the expressions (11)–(14), is



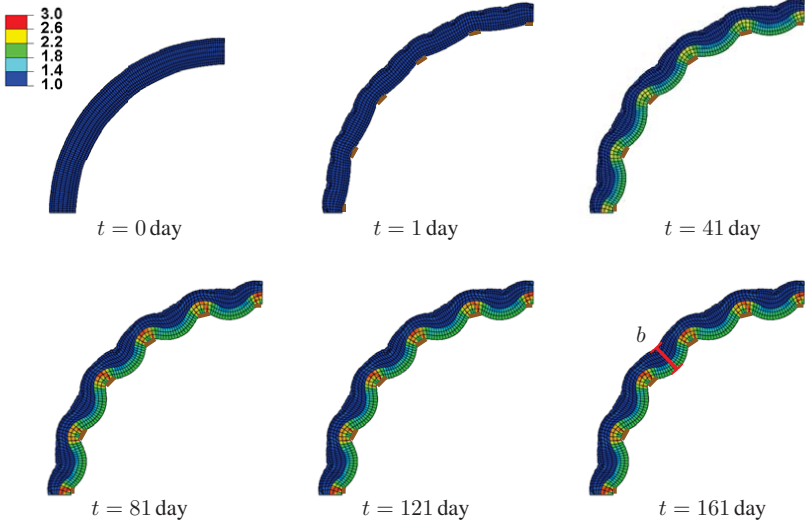


**Figure 7:** Deformed configurations at different time points  $t$  (days). The brown bars illustrate the locations of the stent struts. The red line in the configuration at  $t = 161$  days indicate the thickness of the wall at a stent strut (compare also the plot on the right side of Fig. 9 showing the evolution of  $b$  over time). The different colors visualize the determinant of the growth deformation gradient  $J_g$  computed for each element.

used. The time used for the first step is 1 day and for the second step 160 days. The arterial wall is expanded linearly during the first day by a radial displacement of 1.3 mm at the locations of the stent struts, activating the resistance of the springs. For some specific time points the element volumes are illustrated in Fig. 7 in terms of the determinant of the growth deformation gradient  $J_g$ . Tissue growth starts from  $t = 1$  day. Initially, the tissue grows slightly towards the surrounding tissues (positive remodeling), which is also observed in clinics. This may happen due to the geometry of the model, as growing outwards gives a more stable state. Since the springs, which are used to simulate the surrounding tissues, become stiffer as the outwards growth proceeds, the tissue starts to grow inwards (towards the lumen), where less resistance exists. As time goes by, the growth slows down and finally achieves an almost constant value. From  $t = 1$  to 121 days a relatively strong change in  $J_g$  occurs. However, from  $t = 121$  to 161 days quite little changes are observed.

From the locations as indicated in Fig. 6 by the labels A, B and C (at the cross-section on one end of the cylinder) we then pick out elements from the adventitia, the media and the intima, and plot the growth factors  $\lambda_g$  and  $\nu_4$  during step (ii), see Fig. 8. All investigated growth factors are ascending functions of time. The velocities and accelerations of both isotropic and anisotropic growth factors for all three layers are the same due to the identical values for  $\alpha$  and  $k$ . Hence,

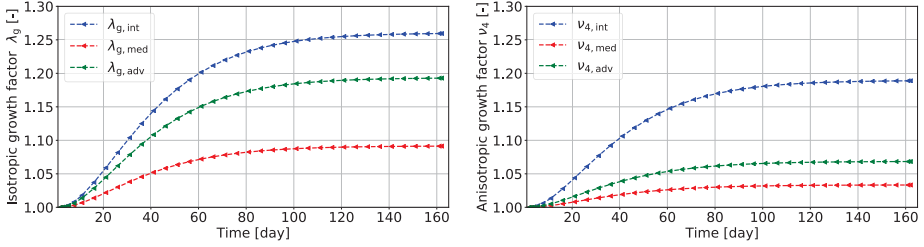


**Figure 8:** Isotropic growth factor  $\lambda_g$  (left) and anisotropic growth factor  $\nu_4$  as a function of time for the locations A, B and C in the three layers, as indicated in Fig. 6. The subscripts int, med, and adv refer to intima, media, and adventitia, respectively.

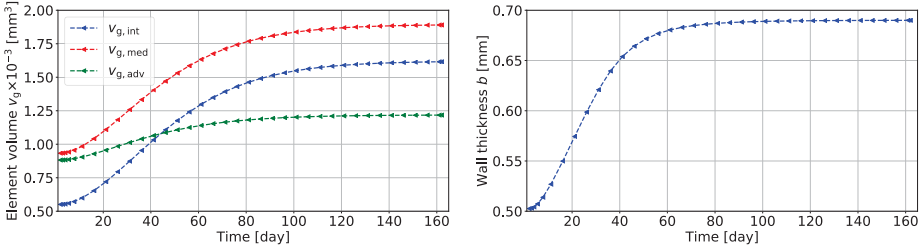


**Figure 9:** Volume  $v_g$  as a function of time for the locations A (adventitia), B (media) and C (intima) in the three layers (left), as indicated in Fig. 6, and evolution of the wall thickness  $b$  over time (right); for the respective location of the wall thickness see the right side of Fig. 7.

by changing the values of  $\alpha$  and  $k$ , one can easily modify the growth velocity and acceleration. By analyzing the volumes  $v_g$  of the elements located at A, B and C, see Fig. 6, and by plotting them over time, as can be seen in Fig. 9 (left side), we find that the volumes have grown by 33% for the adventitia, by 110% for media and by 220% for intima. The wall thickness  $b$  has significantly increased with respect to the growth initiation, as can be seen in Fig. 9 (right side) – compare also with the final configuration shown in Fig. 7, which also illustrates that the tissue has a tendency to enclose the struts.

## 5 CONCLUSION

We have presented a constitutive model and a specific form of the growth deformation gradient to capture isotropic/anisotropic growth of fibrous (collagenous) soft tissues triggered by damage. The first example, a comparison of growth between simulations using an isotropic and an anisotropic growth model shows that the fiber structure plays an important role in the re-adaptation to the new environment after damage. Given the same elastic volume change the anisotropic growth model results in a completely different growth pattern, which we suggest to

fit better than an isotropic growth model when comparing with real tissue growth observed in clinics.

In the second example, i.e. Section 4, we numerically simulate restenosis in an arterial segment considering three layers by using the Abaqus software. We use equally distributed springs to model the surrounding tissues around the blood vessel, and observe a tendency of re-blocking the lumen. However, a regular cylinder is too ideal compared to a real blocked blood vessel, and the material properties for the growth also needs a refinement. As mentioned above, the narrowing includes multiple factors such as elastic recoil, arterial vessel remodeling, and neointimal hyperplasia. The blood pressure is also excluded in the simulations presented here. In future, more realistic conditions should be taken into account to obtain more accurate results, in particular a realistic plaque morphology needs to be considered. A growth model should also consider in-plane and out-of-plane dispersions of the collagen fibers (and not axisymmetric dispersion, as used here). The influence of the fiber directions/dispersions should also be carefully analyzed.

At the moment, we have no access to clinical data that could be used to calibrate the growth parameters. There is hope to obtain patient-specific data so that more accurate material properties can be used, which is the basis for predicting in-stent restenosis more realistically.

## APPENDIX A

Here we want to provide more details of the second Piola-Kirchhoff stress tensor  $\mathbf{S}_e$ , which is according to (17)<sub>2</sub>

$$\mathbf{S}_e = 2 \left( \underbrace{\frac{\partial U(J_e)}{\partial J_e} \frac{\partial J_e}{\partial \mathbf{C}_e}}_{\text{Term 1}} + \underbrace{\frac{\partial \Psi_{\text{iso}}(\bar{\mathbf{C}}_e)}{\partial \bar{\mathbf{C}}_e} : \frac{\partial \bar{\mathbf{C}}_e}{\partial \mathbf{C}_e}}_{\text{Term 2}} + \underbrace{\sum_{i=4,6} \frac{\partial \Psi_{\text{ani}}(\mathbf{C}_e, \mathbf{a}_{04}, \mathbf{a}_{06})}{\partial E_i} \frac{\partial E_i}{\partial \mathbf{C}_e}}_{\text{Term 3}} \right). \quad (\text{A.1})$$

To derive term 1 we use (6) and the property for  $\partial J_e / \partial \mathbf{C}_e$ , see [17], i.e.

$$\frac{\partial U(J_e)}{\partial J_e} = \frac{1}{D_1} (J_e - J_e^{-1}), \quad \frac{\partial J_e}{\partial \mathbf{C}_e} = \frac{J_e}{2} \mathbf{C}_e^{-1}. \quad (\text{A.2})$$

Hence,

$$\text{Term 1} = \frac{1}{2D_1} (J_e^2 - 1) \mathbf{C}_e^{-1}. \quad (\text{A.3})$$

We continue to derive term 2 by recalling (7) and the property for  $\partial \bar{\mathbf{C}}_e / \partial \mathbf{C}_e$ , see [17], so that

$$\frac{\partial \Psi_{\text{iso}}(\bar{\mathbf{C}}_e)}{\partial \bar{\mathbf{C}}_e} = \mu \mathbf{I}, \quad \frac{\partial \bar{\mathbf{C}}_e}{\partial \mathbf{C}_e} = J_e^{-2/3} \left( \mathbb{I} - \frac{1}{3} \mathbf{C}_e \otimes \mathbf{C}_e^{-1} \right), \quad (\text{A.4})$$

where  $\mathbb{I}$  is fourth-order identity tensor. Consequently, with (4) we get

$$\text{Term 2} = \mu \mathbf{I} : J_e^{-2/3} \left( \mathbb{I} - \frac{1}{3} \mathbf{C}_e \otimes \mathbf{C}_e^{-1} \right) = \mu J_e^{-2/3} \left( \mathbf{I} - \frac{1}{3} I_{1e} \mathbf{C}_e^{-1} \right). \quad (\text{A.5})$$

Finally, to derive term 3 we recall (8) and (9). Thus,

$$\frac{\partial \Psi_{\text{ani}}(\mathbf{C}_e, \mathbf{a}_{04}, \mathbf{a}_{06})}{\partial E_i} = k_1 \sum_{i=4,6} E_i \exp(k_2 E_i^2), \quad \frac{\partial E_i}{\partial \mathbf{C}_e} = \kappa \mathbf{I} + (1 - 3\kappa) \mathbf{a}_{0i} \otimes \mathbf{a}_{0i} \quad (\text{A.6})$$

so that

$$\text{Term 3} = k_1 \sum_{i=4,6} E_i \exp(k_2 E_i^2) [\kappa \mathbf{I} + (1 - 3\kappa) \mathbf{a}_{0i} \otimes \mathbf{a}_{0i}]. \quad (\text{A.7})$$

A push-forward of the second Piola-Kirchhoff stress tensor  $\mathbf{S}$  results in the Kirchhoff stress tensor  $\boldsymbol{\tau} = \mathbf{F} \mathbf{S} \mathbf{F}^T$ . Thus, with (16)<sub>2</sub> and the multiplicative decomposition (1) we obtain

$$\boldsymbol{\tau} = \mathbf{F}_e \mathbf{S}_e \mathbf{F}_e^T. \quad (\text{A.8})$$

Hence, by inserting (A.1) into (A.8) and by using the results (A.3), (A.5)<sub>2</sub> and (A.7) we finally get

$$\begin{aligned} \boldsymbol{\tau} = & \frac{1}{2D_1} (J_e^2 - 1) \mathbf{I} + \mu J_e^{-2/3} \left( \mathbf{B}_e - \frac{1}{3} I_{1e} \mathbf{I} \right) \\ & + \sum_{i=4,6} k_1 E_i \exp(k_2 E_i^2) [\kappa \mathbf{B}_e + (1 - 3\kappa) \mathbf{a}_i \otimes \mathbf{a}_i] \end{aligned} \quad (\text{A.9})$$

for the Eulerian stress relation, where  $\mathbf{B}_e$  is defined in (3)<sub>2</sub> and  $\mathbf{a}_i$ ,  $i = 4, 6$ , denote the two fiber directions in the current configuration.

## REFERENCES

- [1] E. J. Benjamin, S. S. Virani, C. W. Callaway, A. M. Chamberlain, A. R. Chang, S. Cheng, S. E. Chiuev, M. Cushman, F. N. Delling, R. Deo, S. D. de Ferranti, J. F. Ferguson, M. Fornage, C. Gillespie, C. R. Isasi, M. C. Jiménez, L. C. Jordan, S. E. Judd, D. Lackland, J. H. Lichtman, L. Lisabeth, S. Liu, C. T. Longenecker, P. L. Lutsey, J. S. Mackey, D. B. Matchar, K. Matsushita, M. E. Mussolino, K. Nasir, M. O’Flaherty, L. P. Palaniappan, A. Pandey, D. K. Pandey, M. J. Reeves, M. D. Ritchey, C. J. Rodriguez, G. A. Roth, W. D. Rosamond, U. K. A. Sampson, G. M. Satou, S. H. Shah, N. L. Spartano, D. L. Tirschwell, C. W. Tsao, J. H. Voeks, J. Z. Willey, J. T. Wilkins, J. H. Wu, H. M. Alger, S. S. Wong, P. Muntner, and American Heart Association Council on Epidemiology and Prevention Statistics Committee and Stroke Statistics Subcommittee. Heart Disease and Stroke Statistics – 2018 Update: A Report From the American Heart Association. *Circulation*, 137:e67–e492.

- [2] K. Mc Namara, H. Alzubaidi, and J. K. Jackson. Cardiovascular disease as a leading cause of death: how are pharmacists getting involved? *Integr. Pharm. Res. Pract.*, 8:1–11, 2019.
- [3] M. S. Lee and G. Banka. In-stent restenosis. *Interv. Cardiol. Clin.*, 5:211–220, 2016.
- [4] F. Alfonso. Treatment of in-stent restenosis – past, present and future. *Eur. Cardiology*, 5:74–78, 2009.
- [5] K. H. Bønaa, J. Mannsverk, R. Wiseth, L. Aaberge, Y. Myreng, O. Nygård, D. W. Nilsen, N. E. Kløw, M. Uchto, T. Trovik, B. Bendz, S. Stavnes, R. Bjørnerheim, A. I. Larsen, M. Slette, T. Steigen, O. J. Jakobsen, Ø. Bleie, E. Fossum, T. A. Hanssen, Ø. Dahl-Eriksen, I. Njølstad, K. Rasmussen, T. Wilsaard, J. E. Nordrehaug, and NORSTENT Investigators. Drug-eluting or bare-metal stents for coronary artery disease. *N. Engl. J. Med.*, 375:1242–1252, 2016.
- [6] A. M. Varnava, P. G. Mills, and M. J. Davies. Relationship between coronary artery remodeling and plaque vulnerability. *Circulation*, 105:939–943, 2002.
- [7] R. S. Schwartz, K. C. Huber, J. G. Murphy, W. D. Edwards, A. R. Camrud, R. E. Vliestra, and D. R. Holmes. Restenosis and proportional neointimal response to coronary artery injury: results in a porcine model. *J. Am. Coll. Cardiol.*, 19:267–274, 1992.
- [8] G. S. Mintz, J. J. Popma, A. D. Pichard, K. M. Kent, L. F. Satler, C. Wong, M. K. Hong, J. A. Kovach, and M. B. Leon. Arterial remodeling after coronary angioplasty: a serial intravascular ultrasound study. *Circulation*, 94:35–43, 1996.
- [9] N. A. Scott, G. D. Cipolla, C. E. Ross, B. Dunn, F. H. Martin, L. Simonet, and J. N. Wilcox. Identification of a potential role for the adventitia in vascular lesion formation after balloon overstretch injury of porcine coronary arteries. *Circulation*, 93:2178–2187, 1996.
- [10] L. A. Taber. Biomechanics of growth, remodelling, and morphogenesis. *Appl. Mech. Rev.*, 48:487–543, 1995.
- [11] D. Ambrosi, G. A. Ateshian, E. M. Arruda, S. C. Cowin, J. Dumais, A. Goriely, G. A. Holzapfel, J. D. Humphrey, R. Kemkemer, E. Kuhl, J. E. Olberding, L. A. Taber, and K. Garikipati. Perspectives on biological growth and remodeling. *J. Mech. Phys. Solids*, 59:863–883, 2011.
- [12] A. Menzel and E. Kuhl. Frontiers in growth and remodeling. *Mech. Res. Commun.*, 42:1–14, 2012.
- [13] B. Fereidoonhezad, R. Naghdabadi, S. Sohrabpour, and G. A. Holzapfel. A mechanobiological model for damage-induced growth in arterial tissue with application to in-stent restenosis. *J. Mech. Phys. Solids*, 101:311–327, 2017.

- [14] A. Menzel. Modelling of anisotropic growth in biological tissues. A new approach and computational aspects. *Biomech. Model. Mechanobiol.*, 3:147–171, 2005.
- [15] A. J. Schriefl, G. Zeindlinger, D. M. Pierce, P. Regitnig, and G. A. Holzapfel. Determination of the layer-specific distributed collagen fiber orientations in human thoracic and abdominal aortas and common iliac arteries. *J. R. Soc. Interface*, 9:1275–1286, 2012.
- [16] E. K. Rodriguez, A. Hoger, and A. D. McCulloch. Stress-dependent finite growth in soft elastic tissues. *J. Biomech.*, 27:455–467, 1994.
- [17] G. A. Holzapfel. *Nonlinear Solid Mechanics. A Continuum Approach for Engineering*. John Wiley & Sons, Chichester, 2000.
- [18] G. A. Holzapfel and R. W. Ogden. Constitutive modelling of arteries. *Proc. R. Soc. Lond. A*, 466:1551–1597, 2010.
- [19] G. A. Holzapfel, J. A. Niestrawska, R. W. Ogden, A. J. Reinisch, and A. J. Schriefl. Modelling non-symmetric collagen fibre dispersion in arterial walls. *J. R. Soc. Interface*, 12:20150188, 2015.
- [20] O. Gültekin, H. Dal, and G. A. Holzapfel. On the quasi-incompressible finite element analysis of anisotropic hyperelastic materials. *Comput. Mech.*, 63:443–453, 2019.
- [21] T. C. Gasser, R. W. Ogden, and G. A. Holzapfel. Hyperelastic modelling of arterial layers with distributed collagen fibre orientations. *J. R. Soc. Interface*, 3:15–35, 2006.
- [22] T. C. Gasser and G. A. Holzapfel. Finite element modeling of balloon angioplasty by considering overstretch of remnant non-diseased tissues in lesions. *Comput. Mech.*, 40:47–60, 2007.
- [23] *Abaqus: Dassault Systèmes Simulia Corp., Providence, RI, USA*, 2019.
- [24] A. Javili, B. Dortdivanlioglu, E. Kuhl, and C. Linder. Computational aspects of growth-induced instabilities through eigenvalue analysis. *Comput. Mech.*, 56:405–420, 2015.

## VISUALIZING HYDRODYNAMIC FLUID SIMULATIONS WITHIN AN IMMERSIVE EXPERIENCE AS A SCIENTIFIC DISSEMINATION STRATEGY

ADINA MORARU<sup>1</sup>, ODDBJØRN BRULAND<sup>1</sup>, ANDREW PERKIS<sup>2</sup> AND NILS  
RÜTHER<sup>1</sup>

<sup>1</sup>Department of Civil and Environmental Engineering  
Norwegian University of Science and Technology (NTNU)  
7491 Trondheim - Norway

e-mail: adina.moraru@ntnu.no; oddbjorn.bruland@ntnu.no; nils.ruther@ntnu.no

<sup>2</sup>Department of Electronic Systems  
Norwegian University of Science and Technology (NTNU)  
7491 Trondheim - Norway

e-mail: andrew.perkis@iet.ntnu.no

**Key words:** Visualization of Natural Hazards, Flash Floods in Steep Rivers, Hydrodynamic Fluid Simulations, Immersive Experience, Quality of Experience, Risk Perception.

**Abstract.** Visualizing results is more important than ever in scientific dissemination. Natural hazards are complex phenomena; their examination and illustration call for a holistic approach when studying them and improving their communication in order to save lives and cost. In this paper, we present an overview of different methodologies ruling the visualization of flash floods and a proposal for integrated workflow for a more immersive experience and better risk perception. Our proposal will contribute to the current state-of-the-art on visualization of flash floods with an integrated visualization platform where precise and realistic flood simulations will be implemented. The contributions will affect small, ungauged steep rivers by the development of a model with a more precise and robust predictive capability at a local scale. The target of the hydraulic modelling executed in this research project is to achieve optimized simulations that could be carried out in the prototype of a serious gaming engine. The incentive for such optimized simulations is that complex hydrodynamic and morphodynamic flood simulations are data and computationally greedy. This contradicts the necessity for low complexity solutions needed in the real-time based scenarios that an immersive experience and on-site decision-making requires. Concluding remarks are that advanced fluid solvers integrated within computer graphics suites would provide the best results in terms of realistic visualization of reliable hydrodynamic simulations. Virtual reality engines can provide an experience arena or visualization, where different disciplines can meet and combine resources and knowledge for a common goal, such as the study and communication of natural hazards.

### 1. INTRODUCTION

Natural disasters are responsible for fatalities and economic losses worldwide and, among them, floods are the most widespread and have caused the highest damages in recent years [1]. Human actions have become a dominant influence on fluvial systems and, together with potential effects of climate change on flood regime (e.g. spatially restricted extreme rainfalls

affecting especially steep and ungauged rivers), predicting where major geomorphic changes may occur is very challenging. Associated geomorphic processes cause a significant amount of the damages related to floods and river response to floods can vary significantly [2]. Research efforts have fruitfully focused on major rivers, while thorough flood risk assessment (*i.e.* including full hydro- and morphodynamic approaches) in small and steep ungauged rivers has been constrained by the inadequacy of fluid solvers to tackle the complexity of the dynamics affecting such rivers in more affordable applications [3]. New environmental changes introduce new and more complex scenarios that translate into expertise demands (such as detecting these changes promptly and increase social awareness of the problem at hand) that researchers need to address.

Risk perception not only has an important role in shaping natural hazards policies. In order to increase public knowledge and influence its opinion, it is crucial to understand why people have diverging attitudes and perceptions related to natural hazards and their possible consequences. The perception to an extreme event is explained to a certain degree by the direct personal experience of the damage caused by climate-related events, such as flooding or landslides, as shown by Lujala *et al.* [4]. This has the largest impact on the subjects' belief that there will occur more natural hazards locally than nationally or globally. It is noteworthy that merely living in a more exposed area, but not having a personal experience of the phenomenon, does not affect the population's concern towards natural hazards.

Available models for flood hazard assessment in steep and ungauged rivers converge in outcomes that do not convey the estimated risk based on a user-friendly and relatable three-dimensional real world nor is the analysis often based on the most recent and highly accurate data at hand [5]. Therefore, the risk perception achieved is hardly ever in accordance with the hydraulic model presented. In order to fill this gap, the World of Wild Waters (WoWW) project aims at being the future tool for analyzing and communicating the potential causes and effects of natural hazards, where the end user is not a scientist, but a land manager or any other user with no background in hydrology and hydraulics. Its orientation towards the gamification of natural disasters and its aim at bringing together knowledge on the physical properties of these with knowledge on digital storytelling and human behaviour emerges into an immersive experience based on real data, realistic scenarios and simulations. WoWW project acts as a framework for the setting of the research strategy here presented. As part of WoWW's work packages, the investigation scheme described in this document targets the Visualization of Flash Floods as a strategy to improve the scientific dissemination of one of the most recurring and of highest impact natural disasters affecting small, ungauged steep rivers in Norway and worldwide. Particularly, it is aiming to dynamically visualize water flow in small, ungauged steep catchments and the effect of water forces on their riverbanks and structures in and along these watercourses based on knowledge about hydraulics and hydraulic modelling and enable more efficient hydrodynamic fluid simulations for better flood risk assessment and communication. The latest trends in realistic data presentation and scientific visualization go hand in hand with the implementation of a flooding scenario in Extended Reality (XR, *i.e.* the combination of Augmented/Mixed/Virtual Reality; AR/MR/VR, respectively). Immersive technologies require very advanced visualization modalities. The outcome of this project will be implemented into the prototype for a serious gaming (*e.g.* VR/MR) flood engine.

The aim of the present document is to highlight the need of a holistic approach when studying natural hazards and improving the communication of these in order to save life and cost. Hereinto is presented an overview of different methodologies and a proposal of integrated workflow that will contribute to the current state-of-the-art on visualization of flash floods affecting small, ungauged steep rivers by developing a model with an improved predictive capability at a local scale. An efficient and robust flood simulation model should conceive high-quality and most updated data retrieval from the Internet of Things (IoT), precise flood



area estimation and representation, reduced computational time scale (*i.e.* currently of one to several hours in the case of 2D hydraulic simulations), on-site application and analysis accuracy [6]. The model will be calibrated with monitoring data collected through the environmental IoT and further tested within WoWW. Regarding the visualization of the results, this research will include the development of a system with a geo-referenced 3D environment on which the model can be implemented and coupled into a virtual reality gaming engine.

In the following sections, we will address key concepts regarding the visualization of natural hazards. We will also describe the characteristics of numerical models and visualization trends affecting flash floods and propose an integrated workflow scheme for the visualization of natural hazards. The implementation of this workflow scheme will be addressed in a step-wise fashion and we will discuss the suitability of the methodology for WoWW's purpose.

## 2. KEY CONCEPTS ON THE VISUALIZATION OF NATURAL HAZARDS

The multidisciplinary aspect of WoWW give rise for a need to unify common terminology. The most controversial concepts identified were, for instance, simulation, modelling, real-time, visualization and gamification. Other useful concepts regarding the currently presented topic, yet not often used in the field of hydraulic engineering (*e.g.* immersive experience, quality of experience), are also defined in this section.

A *simulation* is carried out when a particular set of conditions are created artificially in order to study or experience something that could exist in reality. In this study, this concept will be handled in the context of fluid (*i.e.* water, specifically) simulation and the analysis of its flow patterns, directions, forces and physical characteristics and properties. We will address, therefore, hydrodynamic simulations throughout the following sections. For instance, *hydrodynamic modelling* has been defined as the mathematical application of momentum, continuity and transport conservation equations to represent evolving fluid flow in terms of velocity, density and scalar fields [7] [8].

*Real-time* refers to an immediate computational response to input data. In the context of hydrodynamic fluid simulations, real-time refers to the simulation speed being equal to the speed of the simulated event when occurring in real life. Real-time visualization refers, on the other hand, to the display of the simulated scenario at real life speed. In this sense, it is noteworthy that the temporal perception is human-relative, and not computer-relative. As suggested by Henonin *et al.* [6], real-time flood assessment may be classified into three categories depending on the role of hydrodynamic fluid modelling in the hazard evaluation: i) empirical scenarios-based (*i.e.* no hydraulic model is used), ii) pre-simulated scenarios-based (*i.e.* hydraulic models are used as pre-study tools) and iii) real-time simulations-based (*i.e.* real-time forecast with online and real-time simulation models). Although previous hydrodynamic simulations are often used to assess flood hazard, we will aim at developing an integrated real-time simulation-based model that can be scaled and reproducible in future prototypes.

*Scientific visualization* is often mentioned regarding the representation of three-dimensional phenomena, where the efforts are committed to realistic *renderings* (*i.e.* the processing of an image using colour and shading to translate it into a solid and three-dimensional look) of volumes, surfaces, illumination sources, and so forth, often with a dynamic (temporal) component and oriented to subsequent analysis [9]. This interdisciplinary branch is frequently also considered a subset of computer graphics and its goal is to depict scientific data graphically so that scientists understand, illustrate and gain insight from their data.

The visualization of flash floods facilitates disclosing information regarding their analysis and management in a universal fashion. In our case, the display is predominantly of geographical data, which may overlay a map, terrain model, or even an orthophoto. Traditionally, experts working on risk assessment have based its representation on colour-coded maps. Some numerical models use maps or orthophotos to texture the Digital Elevation

Model (DEM; *i.e.* represent the land use on the DEM). However, even though the DEM is three-dimensional, the calculated parameters are visualized as two-dimensional colour-codes if the model used solved equations only in two dimensions. The suitability of the models used in hydrodynamic fluid simulations will be discussed further sections.

*Gamification* is the process of arranging non-game content by means of game mechanics with the main objective of positively influencing behavior and enhancing the user's motivation [10]. This is usually done by incorporating elements that the user must interact with in order to achieve certain goals provided by the game instructions. In serious gaming, the purpose is to create a better understanding of a certain concept or topic; hence, it is often aligned to educational or business goals. Although the gamification of natural hazards will not be discussed in the present document, the gamification of floods is contemplated as one-step beyond the visualization of floods. Therefore, the visualization scheme here presented must ensure the potential of gamifying its results in order to facilitate an improved immersive experience.

*Immersive Experience* is a representation of the (virtually created) reality that allows the audience to be engaged with the visualized content to the extent of perceiving themselves as being present in the displayed surrounding environment. An immersive experience ought to be, among others, accurate, realistic if relevant, emotional, context adaptive, engaging, useful, interactive, intuitive, etc. [11] [12] [13]. This definition goes very much on the lines of the updated concept of *Quality of Experience* (QoE), defined by the Qualinet group of experts as "the degree of delight or annoyance of the end user of an application or service. It results from the fulfillment his or her expectations with respect to the utility and/or enjoyment of the application or service in the light of the user's personality and current state". In fact, the concept of immersive experiences has evolved into the QoE concept, and the trends have shifted in favor of the latter. QoE better differentiates related terminology such as performance, Quality of Service and application acceptance, and it focuses its efforts on evaluating the user experience based on a rigorously designed methodology that contemplates both objective and subjective metrics. As the Quality of Experience is inherently dependent on system-, human- and context-influencing factors [14], the content design and its display shall be carefully conducted taking into account all these factors and their interrelations.

Immersive Media Technology Experiences (IMTE) are game changers when it comes to transferring knowledge and influencing lifestyles as they tackle these tasks with a human-centred designed approach [15]. IMTE have been used so far in fields such as entertainment, medical and biosciences, art, oil and gas, aerospace and naval, automotive, power and traffic, gaming industries, etc. Nevertheless, this science has not been overly applied in natural hazards, risk perception and risk assessment-related studies. A recent experiment [16] has proven that, if the user related emotionally to the experience evaluated, the level of immersion was higher than that of when being spatially immersed. A thorough content design process, where risk perception and system factors are interlaced, and with a visualization of natural hazards that presents the characteristics needed to achieve an immersive experience (*e.g.* accurate and context-adaptive in terms of physics; relevant and realistic in terms of scenario selection; engaging, interactive and able of creating an affinity between the user and the displayed content) will result in a more effective communication of flood risk.

### **3. CHARACTERISTICS OF NUMERICAL MODELS AND VISUALIZATION TRENDS APPLIED TO FLASH FLOODS**

The vast advances technology has experienced in the last decades provide a limitless array of tools when it comes to studying flash floods and river's response to them. Flash floods are studied through the definition and characterization of spatial and temporal parameters. In this

sense, Geographic Information Systems (GIS) and related technology help representing and visualizing data in real-time and in an understandable way (see for example [17] [18] [19] [20]). A quick display of information allows a more effective and competent implementation of alleviation measures and flood management practices. Experts are looking for ways to integrate the existing tools and use them in interdisciplinary projects in order to make the best of the immense possibilities these tools provide.

### 3.1. Characteristics of numerical models for flash flood simulation

Numerical simulations have become a common tool to approach engineering problems for which there is no available similar analytical solution. One possible criterion when selecting a suitable model is to see if our approach considers an analysis dependent on field observations and the statistical analysis of the relationship between these and other characteristics of the phenomenon (*i.e.* empirical), regards the total phenomenon at a given point in space (*i.e.* is purely analytical) or if it is based on Computational Fluid Dynamics (CFD) and solves numerically once the parameters are discretized in time and space (*i.e.* numerical models). In this research, numerical models will be used and contrasted afterwards with either empirical or different numerical models. Moreover, we will rather refer to the different models, their characteristics and suitability based on the continuum mechanics approach and spatial dimensions the model is contemplating (Table 1). This approach allows taking into consideration the target and level of simplification required by the analysis in question.

If discretized numerical models into 1-, 2- and 3-dimensional, the most extended form of CFD equations concerning flood simulations are the Reynolds-Averaged Navier-Stokes equations (also referred to as RANS) and the Shallow-Water Equations (SWE), which are derived from the Navier-Stokes equations considering simplifications on the third dimension [21] [22]. They allow the prediction of the fluid dynamics, *e.g.* water velocity, water elevation, water forces, shear stress, stream power, travelled distance by the fluid, hence, if there is overflow of the riverbanks and where would the overflowing areas be. A recent comparative study of 1D, 2D and combined 1D/2D models applied to the same study case in HEC-RAS [23] showed that all three models could successfully reproduce a historic flooding event. Moreover, the 2D and 1D/2D model could also provide relatively detailed information regarding flood propagation and velocities on the floodplain.

A detailed comparison of 2D hydraulic modelling packages is provided in [21]. On the other hand, two-dimensional modelling is not very comprehensive in incorporating secondary circulation at bends and three-dimensional modelling is favoured to study that behavior (Table 1). For instance, HEC-RAS is unable to work with falls and steps and changing flow regimes, which is reflected in 2D hydrodynamic simulations of steep slopes [22]. Furthermore, the slope limitation in one-dimensional numerical simulations carried out in this software is, basically, because the 1D St. Venant equation is derived with the assumption that the bed slope is very small and higher slopes come in contradiction with this assumption.

Regarding 3D modelling, often applied to short river stretches in order to solve complex specific issues, such as vertical turbulence, vortices, secondary circulation, bed mobilization and bank erosion, the reference frame utilized also differentiates models. For instance, an Eulerian reference frame is grid-based and fixed in space while the Lagrangian reference frame is particle-based and takes into account the movement with the local velocity. The advantage of Lagrangian models is that they do not require spatial discretization and are able to represent smaller features than the grid size. Moreover, particle-based models provide a higher accuracy and non-diffusive prediction of convection. Different models use different fluid assumptions, nevertheless.

Table 1. Comparison of hydrodynamic models (based on [8] [21] [22] [23] [24] [26]). A model with more dimensions includes also the features of that with less dimensions.

Criterion	1D models	2D models	3D models
Governing equations	Bernoulli (steady flow); 1D Saint Venant (unsteady flow)	2D Saint Venant (SWE); 2D Reynolds-Averaged Navier Stokes (RANS)	3D Reynolds-Averaged Navier-Stokes (RANS)
Assumptions/ simplifications	Cross-sectional averaged velocity, topography is discrete, constant lateral variables	Hydrostatic pressure distribution, Reynolds averaged over shallow depth, uniform vertical distribution of velocity, incompressible fluid with uniform density	Conservation of momentum and continuity (incompressible fluid), Turbulence is modelled instead of assumed
Features	Needs a predefined flow path, subjective to cross-sectional spacing, orientation and location. Free surface calculated with pressure	Topography is continuous over the cross-section. Takes into account viscosity, shear stress, wall friction, inflow volume and momentum, turbulence is incorporated through Manning's equation. Free surface is calculated with level set	Grid-based or Particle-based, includes a "multi-physics" environment. Free surface is calculated with volume of fluid
Applications	Little spatial variation and uniform flow simulations (e.g. deep flooding in narrow streets, long reaches (>100km), etc.)	Large spatial variability and non-uniform flow (e.g. steep rivers, urban and coastal areas, wide flood plains). Also used in morphodynamic studies	In short river stretches and localized complex dynamics in 3D (e.g. vertical turbulence, vortices, secondary circulation). Suitable for simulation of weirs. Also in morphodynamic studies
Accuracy	Less accurate if the processes prime in more than 1D	More accurate than 1D in terms of lateral diffusion of flood wave and flow recirculation	More detailed information on flow behavior, provides detailed analysis on streamlines
Advantages	Computationally more efficient, possibility to couple with 2D models, extensive literature available. Ideal as a preliminary approach to more complex problems	Makes better use of topographic information than 1D models, ability to represent more detailed changes in velocity and flow depth and direction, flexible meshes, time discretization, shock-capture schemes	Solves full RANS equations directly, mass and momentum conservation equations contemplate additional terms, incorporates tuning parameters of energy dissipation. Possibility to propose and check changes in structures (design-oriented)
Limitations	Does not simulate lateral flood wave diffusion, averages velocity and topography is discrete, cannot describe different water levels at the same section, does not describe local hydraulic behavior, turbulence is disregarded	Does not represent channel bend-induced secondary circulation, not suitable for large-scale systems (>100km) or topographic discontinuities, as it neglects vertical velocity by averaging it. Requires calibration on discharge coefficient (in case of weirs) which is laborious and complex	Requires the calibration of the turbulence model and roughness value (which are key in energy dissipation)
Speed and cost	Quick and inexpensive	Computational speed and cost dependent on problem complexity	Computational greedy and expensive
Available Software	e.g. HEC-RAS, Flood Modeller-TUFLOW, Mike 11, IDSS	e.g. Iber, HEC-RAS, Telemac-Mascaret, Flood Modeller-TUFLOW, Flow2D, Mike 21, ANUGA, Dual SPHysics, REEF3D, Autodesk InfraWorks, Gerris,	e.g. REEF3D, Gerris, OpenFOAM, Blender, Flow3D, Maya-GLU3D, Bifrost

Depending on the degree of complexity of the pondered scenario, new and more sophisticated demands have called for new and more integrated models. These models differ depending on the required scope of the analysis, the scale, available input data and the extent of the output aimed for. In Figure 1, different numerical models, such as Direct Numerical Simulation (DNS), Large Eddy Simulation (LES), RANS, Double-Averaged Navier-Stokes equations (DANS), SWE and Diffusive Wave Equation (DWE), are plotted based on their applicability to new and more complex fluid modelling demands (*i.e.* their role in real-time flood risk assessment and the level of simplification that they include). Often enough, these involve combining hydrodynamic fluid simulations with algorithms that increase their efficiency or improve their precision (see for example [27] [28]). The computational cost of 3D models is still a noteworthy disadvantage.

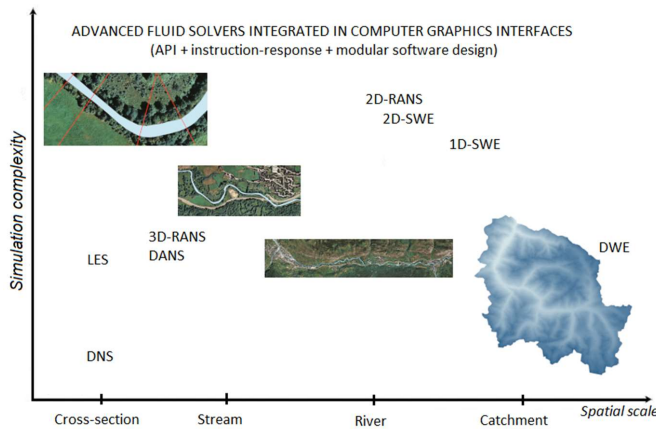


Figure 1. Numerical models according to the analysed spatial scale and their usability in flood risk analysis (modified after [6] and [29]). The level of complexity of the model is linearly correlated with that of the simulated scenario and the scale at which this is studied. See text for abbreviations.

### 3.2. Trends in the visualization of flash floods

Several studies tackle the visualization of flood events (see for example [30] [31] [32] [33] [34] [35] [36] [37] [38]). However, the tools presented until now lack common principles and approach to visualization, as well as the unification of data formats due to the wide-ranging amount of software offered in the market. Suhr [39] defined *sound decision-making* as a reality-based, congruent and effective decision-making, as it is founded on “the correct use of correct data”. Widely used nowadays, sound decision-making consists not only on the accurate selection of data, but also on the comparison of these in order to detect the best alternative (*i.e.* the most advantageous alternative). In flood risk management, sound decision-making requires the use of reliable decision-support tools; nonetheless, worldwide there is currently no integrated model [19] [30] [35] for both excellent risk assessment and effective communication of the potential impact of flood risk in small steep rivers to the stakeholders.

Visualizing large and realistic flood scenarios is, in fact, complex and requires the use of excellent state-of-the-art graphic tools that allow rendering these as quasi real-time scenarios. The display of grid computation results obtained in flood modelling arises the need of a unified visualization scheme with unified standards, *e.g.* integration of input data formats [31]. If grid computation is required, it is fundamental to have a pre-designed input workflow, as this

controls the efficient execution of the visualization tool. The visualization scheme should integrate visualization requests of any type of application oriented on the computation of natural hazards.

Recent developments in the visualization of floods include numerical computations and simulations in 3D. For instance, Ghazali and Kamsin [17] used the combination of SPH (through the GLU3D plug-in) and 3D computer graphics (in this case, Maya) to simulate and model flash floods on a three-dimensional geo-referenced environment (*i.e.* LiDAR DEM). Moreover, they used most of the software's potential by testing the realistic visualization of natural hazards in real-time through an Application Programming Interface (API) in Maya. Later on, Li *et al.* [32] used OpenGL for flood simulations in 3D by first creating the 3D terrain and sky background, and later simulating the water flow and its depth overlaid on the terrain. Parallel, Ye *et al.* [40] used SPH to model the water flow during a dam break and their computational output was embedded in a 3D spatio-temporal GIS application where this and other flood scenarios were dynamically visualized. Additionally, specific layers could be added to show public infrastructures within the system. Demir and Krajewski [34] juxtaposed in their research flood analysis, adaptive real-time communication of flooding conditions and the interactive visualization of results. Nevertheless, the data provided was very complex, including river conditions, flood maps, forecasting and related information. Cartoon-style displays of results in an online platform made the data easily accessible and understandable to the end user.

Most recently, Macchione *et al.* [37] represented 2D hydraulic simulations within a so-called 3D virtual reality environment while aiming at presenting a product potentially useful for hydraulic engineers for risk communication purposes. Their workflow contemplated a sensible compromise between the inherent complexity of virtual reality and the need to represent flooding events in 3D environments to improve the interaction with decision-makers and to engage people with natural hazards. Zhang *et al.* [36] [41] went a step further and aimed to improve data visualization, increase simulation speed and allow real-time interaction during the simulation process. This led in the development of a 3D flood simulation platform with VR technology. They analyzed flood processes, simulated the flow field as well as the breach flood process and contemplated the emergency plan making. Moreover, their digital platform not only represented the real-time changing process through the "instruction-response" method and data interpolation, but also combined the virtual visualization of the data with numerical modelling in a 3D visual form based on modular software design. Although their methods involved the use of coding techniques, numerical modelling and virtual reality tools (*e.g.* C++, FORTRAN, OSG, VPB, osgGIS, intranet, middleware, etc.) altogether, the simulation speed and the interaction between numerical models had room for improvement regarding the achieved level of immersion and complexity of interactive functions.

Wang *et al.* [5] tackled the need for an improvement of flood risk communication and the real-time flood risk assessment through a combined simulation-visualization approach somewhat similar to that of Macchione *et al.* [37] in terms of presenting 2D hydraulic simulations in an improved 3D environment. They enhanced decision support by including the analysis of the uncertainties of such model as well as by increasing the computational efficiency in data assimilation and calculation with the help of algorithms. Their study did not limit to the presentation of aesthetically attractive scenarios, where the 3D model was rendered by means of computer graphic-assisted improvement. A gamification process adds value to their study and is noteworthy. They added interactive elements, such as user-interactive features *e.g.* 3D "drag-and drop" icons, design analysis, 3D stereo panorama, storyboards or online shared view. These elements allow the user of their application to position elements wherever they want, measure the inundated area, share the experience as a web link or QR code that displays a 360  rendered panoramic view, follow a tour of static and dynamic specified

views or even capture their comments of design plans. All these tools permit a greater immersive experience and a much more effective communication of the presented hazardous scenarios. The interaction of user-model through virtual reality increases the stakeholders' implication in planning and decision-making and provides instant feedback on how to increase the model's potential and effectiveness.

The most suitable model should be selected based not only on the most advanced technologies and the attempts to tackle very complex problems. The model choice should be ruled by what works best in the given context, considering the level of investment needed (*i.e.* data and financially speaking), the hydraulic context and the precision needed for decision-making. Characteristics of numerical models and model-selection criteria are described in section 3.1. WoWW is aiming at potential real-time simulation-based solutions, where the output is both physically and visually realistic and enables an accurate flood risk assessment and its communication to the stakeholders, whom are oftentimes not part of the scientific community. For such purpose, the most suitable approach is a combination of that adopted by Wang *et al.* [5], implemented in suites that integrate advanced hydrodynamic fluid solvers and computer graphic rendering that will upgrade the fluid simulations into visually relatable scenarios (*e.g.* see [42]).

#### 4. INTEGRATED WORKFLOW SCHEME FOR VISUALIZING NATURAL HAZARDS

In the present section, we propose a working scheme (Figure 2) that will allow an integrated study and visualization of Flash Floods in small and ungauged steep rivers and a more immersive experience for a better risk perception. This will result in a simplified, reproducible and scalable prototype that can be embedded in a serious gaming engine and help a non-expert user make decisions based on intuitive and more precise data than that provided by current gaming engines, often based on computer graphics rather than real hydraulics. In summary, the objectives of this working scheme are to:

- Optimize existing fluid simulation models.
- Progress towards real-time simulations of flash floods in steep rivers.
- Incorporate optimized simulations in a serious gaming engine.
- Design realistic and dynamically evolving flood scenarios in steep rivers.
- Implement realistic, hydraulics-based scenarios in a prototype that will be furtherly executed in a gamifying engine.

The first step is to review the imminent trends on serious gaming (VR/MR) applied to the study of natural hazards. Also, to exhaustively overview the state-of-the-art on hydrodynamic and morphological simulation models (*i.e.* CFD) solving the Reynolds Averaged Navier-Stokes (RANS) equations, the numerical flood models available today, and the visualization models (2D and 3D) of flash floods that are currently in use within the scientific community. In doing so we will be able to i) understand what possibilities and limitations the current simulation models have, ii) chose and/or combine available models in order to achieve speedier results, iii) gain knowledge on how to couple available CFD models within a serious gaming engine. The hereby-presented state-of-the-art (see section 3.2) on visualization of floods results from a first attempt of completing the first branch of the workflow scheme.

Once familiar with the characteristics, potential and limitations of available hydrodynamic and morphological models, the most suitable numerical model will be chosen based on testing and comparison of currently used ones among the scientific community (see section 3.1), such



as grid-based and particle-based (e.g. Smoothed-Particle Hydrodynamics, SPH) models. Furthermore, an integrated model based on state-of-the-art will be developed given the new demands on higher simulation speed without compromising the achieved level of complexity. Developing sharpened hydraulic modelling permits to focus, simplify and standardize the simulation methods before mentioned, thus, optimize risk assessment studies, as it will display the main factors controlling river response to flood events and allow to direct the efforts towards the parameters that are most relevant to study. Another reason to optimize the fluid simulations is to reduce the simulation time needed in order to achieve increasingly precise although not necessarily as accurate scenarios. By doing so, we will be one step closer to real-time simulations in future prototypes. The need of this simplification will be verified through statistical comparison (R and RStudio) of simplified to full hydrodynamic fluid simulations.

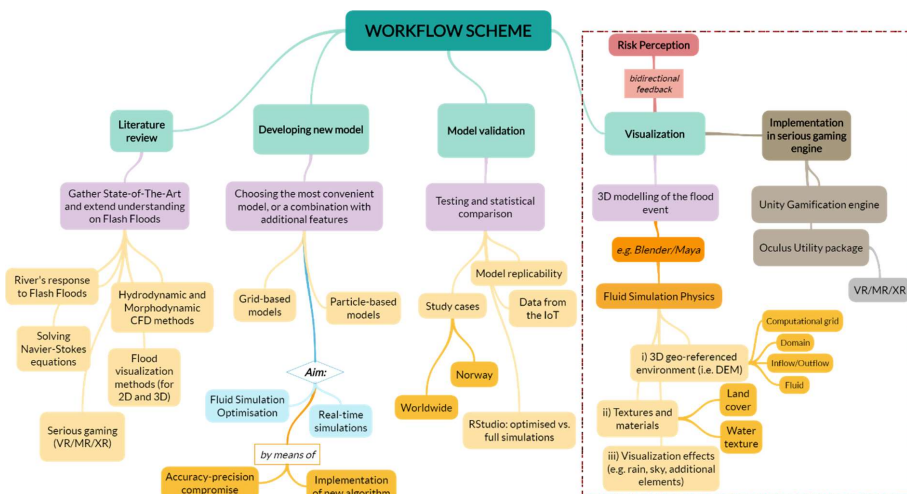


Figure 2. Approximate workflow diagram proposed for the research project. The pink and gray sections correspond to the link between the output of this investigation and the Human Behaviour and Risk Perception and Immersive and Interactive Experience of Natural Hazards work packages, respectively. The red dashed rectangle contains the implementation stage of the resulting model in WoWW.

The model will first be developed and further tested in existing study cases affecting Norwegian rivers (e.g. Tokke in 2009, Flåm in 2014, Utvik and Innvik in 2017, etc.) within WoWW's umbrella. Identifying critical locations along steep watercourses by integrating Geographical Information Systems (GIS) and existing 2D and 3D hydrodynamic fluid simulation models (e.g. see Table 1 for examples of trending software) will result in simplified flood simulations that contribute to a more efficient risk assessment. The reconstructed flood event will be based on steep mountainous areas, where hydrological data will be input and the fluid simulation will be run in a 3D geo-referenced environment (i.e. terrain, in most cases a DEM). Afterwards, the elements will be visualized by texturing and adding materials, as well as incorporating visualization effects such as rain or sky (i.e. world). The information needed in order to perform numerical simulations will be collected and implemented through field and experimental work, or from environmental sources available in the IoT. The data collected and modelled will need testing and validation with field observations.



Additionally, the simplified and validated numerical hydrodynamic model will be integrated in a serious gaming engine (by means of *e.g.* Unity), as represented in the red dashed rectangle on the right-hand side of Figure 2. As mentioned above, a prototype for a serious gaming engine will be created in 3D computer rendering software such as Blender or Maya. Available open source software will be employed during the research, as far as these have enough functionality (*i.e.* efficiency and compatibility with needed add-ons). However, certain adjustments might be required, as existing fluid solvers might need to be complemented with the development of additional material descriptions and customized computer algorithms in order to achieve the optimal fluid simulation.

Furthermore, two to four scenarios, if not more, will be tested and presented in a Virtual Flood Game (*i.e.* Serious Gaming Engine), which will allow testing the prototype in selected watercourses. Certainly, the research could be extended to investigating worldwide study cases, validating the resulting optimized model in any river that might be interesting and meets the eligibility criteria (*i.e.* small steep catchment that has flood risk potential and with available data of the required resolution for further study and implementation in the Serious Gaming Engine).

In order to achieve the World of Wild Waters' goal of communicating the implications of natural hazards as a phenomenon and helping decision-making by means of reaching an end user without scientific background in a very relatable approach, the research carried out in this work package is very much interrelated with creating an immersive experience and will use risk perception as a basis during the content design, hence, contributing to the creation of a good Quality of Experience (QoE). For this purpose, it is expected to have a close collaboration with other work packages of the World of Wild Waters (*i.e.* WP4: Immersive and Interactive Experience of natural hazards, and WP5: Human Behaviour and Risk Perception of natural hazards). The results of this investigation will be used in a serious gaming engine and tested in selected subjects for the purpose of iteration and improving the communication of natural hazards and the pursue of a proactive and preventive response in the end user.

The application of both 2D and 3D hydrodynamic models to flood risk assessment in small, ungauged steep rivers, as well as the visualization of results will be exemplified in the following section. Their suitability for the scope of this research will also be discussed.

## **5. RESULTING VISUALIZATION OF HYDRODYNAMIC FLUID SIMULATIONS USING AN INTEGRATED WORKFLOW SCHEME**

For clarification purposes of the workflow scheme proposed in this document (Figure 2), in this section, we will describe an example applied on a step-wise fashion.

A flooding event is characterized in terms of hydrologic and geographic parameters that are used as an input in hydrodynamic fluid simulations (Figure 3). These are the initial conditions and define the geometry and boundary conditions defined in the plan set up in any two- or three-dimensional numerical model. The computational grid needs to respect singularities present in the terrain and adapt in function of the level of interest of each section (*i.e.* denser mesh, break lines and refinement regions shall be used for a higher precision in the fluid simulation). To go one step closer to real-time flood simulations, hydrological data resulting from WoWW's statistics of extremes and hydrologic work packages will be connected to the IoT and retrieved by means of algorithms included in the developed model. This previous stage is not shown in the workflow scheme, as it is resulting from simultaneous research within the World of Wild Waters project.



Figure 3. Documentation of the flood event that affected the municipalities of Utvik and Innvik in 2017, a study case for this project. Water flow direction is from South to North. See [3] for further reference on the case.

The most suitable numerical model will be selected based on the state-of-the-art and model comparison presented in section 3, and implemented on open-source fluid simulation software, when feasible. Figure 4 shows a 2D hydrodynamic simulation in HEC-RAS, whereas figure 5 presents a 3D overly simplified hydrodynamic simulation in Blender. The two-dimensional hydrodynamic simulation is solving the Shallow Water Equations (SWE) through a combination of Finite Difference (for orthogonal mesh sections) and Finite Volume (for local non-orthogonal sections) methods for unsteady flow (see computational mesh in Figure 4, right), while the three-dimensional fluid simulation is using the Lattice-Boltzmann free surface Method (LBM) on a quadrangular mesh (Figure 5, right). For further reference, see the manuals of HEC-RAS and Blender, respectively.

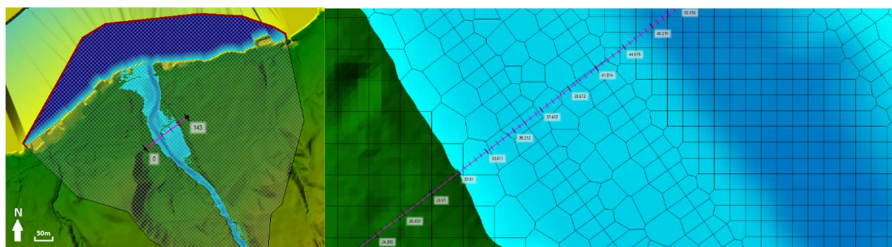
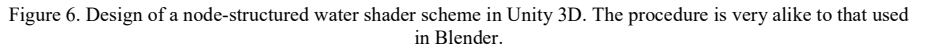
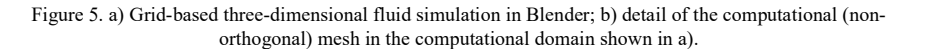


Figure 4. Left: 2D simulation of Utvik flood event (2017) in HEC-RAS (v.5.0.6), where the water depth is represented in blue tones (darker tones correspond to larger water depths), and cross-section (red line in a) of the river channel and the flooded riverbanks. Scale is 50m. Right: close-up of the computational mesh, where different cell sizes and shapes (orthogonal and non-orthogonal) are observed due to the use of mesh-refinement and break lines.

The resulting hydrodynamic simulations will consider real-time and an increased efficiency will be sought out. The knowledge gathered will result in the development of a model that shall be replicable; hence, the comparison of several study cases will provide an insight on how to optimize the fluid simulation speed without compromising on precision. Hydrodynamic fluid simulations can be connected to the environmental data available in the IoT and optimized with the help of algorithms embedded in the numerical simulation model [5] [20] [28]. The level of optimization achieved relative to currently existing full hydrodynamic simulations will be estimated through statistical analysis.



Efforts are being focused on integrating more complex fluid solvers into these creation suites. For instance, the 3D solver for the two-phase incompressible Navier-Stokes equations NaSt3DGPf was successfully coupled with Maya in a toolkit that enables the user to control the full fluid simulation within Maya's interface [42] [43]. The solver uses high-order Finite Difference discretization methods and the rendering techniques result in realistic CFD visualizations. Moreover, the limitations of the discretization methods seem to be overcome by introducing an approximation method in stochastic space, with a high convergence order and a very small pre-asymptotic error, outperforming methods such as Monte Carlo. The use of coupled toolkits as such is desirable and is contemplated in the workflow scheme here proposed.

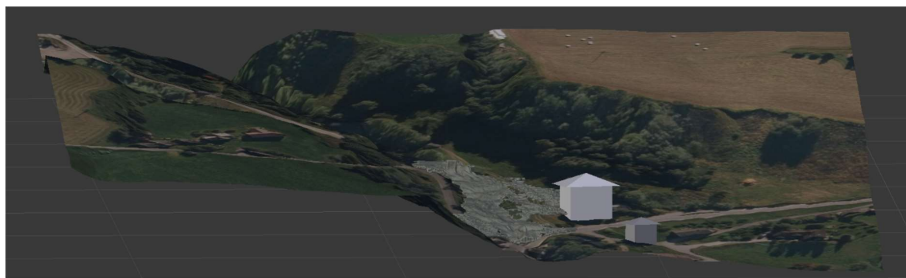


Figure 7. Hydrodynamic fluid simulation in Blender, with textures and materials on terrain and water.

Once the textures and materials have been incorporated to the hydrodynamic fluid simulation, visualization effects such as rain, a panoramic 360 degrees sky or buildings will make the resulting scenario more relatable to the non-expert user, hence, ready to use in further experiments (such as risk perception and QoE) or for direct decision-making.

## 6. DISCUSSION

Simulating flood scenarios allows iterating research objectives and potential answers to these. A quick display of information allows a more effective and competent implementation of alleviation measures and flood management practices. The comparison of frequently used fluid simulation models (Table 1, Figure 1), as well as the overview on recent related work on the visualization of flash floods gives an insight into the selection of an optimal model to simulate flash floods in small, ungauged steep rivers. The suitability of the model depends on the problem definition and the scale of analysis. For instance, for visualization purposes and further research on achieving an outstanding immersive experience, the main goal is to obtain optimized hydrodynamic fluid simulations and of increasing precision.

Two-dimensional hydrodynamic modelling is the best alternative in terms of compromise between precision and computational expense. Even though 2D models are not very comprehensive in incorporating complex hydrodynamics, such as secondary circulation at bends, this feature is not required for a realistic visualization. Therefore, three-dimensional modelling is not necessarily favoured to represent flood scenarios in a precise and more understandable fashion. On the other hand, HEC-RAS solves 2D-SWE and is unable to work with falls and steps and changing flow regimes, which leads to shocks and instabilities when modelling flash floods in steep slopes [22]. Shock-capturing algorithms (*e.g.* Total Variation Diminishing) are not included in this and generally in most of the open-source modelling packages, with exception of, *e.g.* Telemac-Mascaret. Nevertheless, three-dimensional solutions seem to give the most realistic representation, although the computational cost of 3D models is still a noteworthy disadvantage.

Advanced solvers are often present in modelling packages without a graphical user interface (e.g. Telemac-Mascaret for 2D or REEF3D for both 2D and 3D). These tools have the advantage of solving complex physics at optimal speeds and with very satisfactory reliability. On the other hand, they need to be coupled to post-processors (e.g. Blue Kenue, Paraview) in order to visualize results. This means additional work for the researcher, often significantly time-consuming, in order to analyse, interpret and build up based on the simulated outcome. The lack of an integrated interface obviously hinders decision-making, as the user needs to be familiar with multiple platform, generally not user-friendly. Therefore, experts are looking for ways to integrate the existing tools and even use them in interdisciplinary projects in order to save cost and make the best of the immense possibilities these tools provide. Research efforts are currently oriented towards combining advanced two- and three-dimensional fluid solvers with algorithms that increase their efficiency or improve their precision for visualization purposes (see for example [27]).

Realistic portrayal of flash floods in small steep rivers requires advanced hydrodynamic simulations and outstanding rendering of these, which is expected to be computationally expensive, anyhow. Hadimlioglu and King [28], for example, used a flexible mapping engine to visualize 3D-simulated water depth, which allowed adaptive resolution and the possibility to select the representation type dynamically. This resulted in an increased efficiency. The simulations were particle-based (Lagrangian), which seemed to provide more stable outcomes than grid-based fluid simulations. Their flexible mapping engine also provided increasing precision of the water level description by means of quadrees (which is also used in signal processing in High Efficiency Video Coding, HEVC) and allowing the system to select the most suitable representation based on the demanded level of detail. Their model is efficient, provides good precision and has spatial scalability. However, it does not permit a dynamic change of parameters over time (e.g. changes in discharge, and no adaptive real-time response), although this could be potentially implemented. Their study alludes to the benefits of using 2D visualization over more complex and realistic 3D visualization, as it is easier to use. The visualization of such model is very promising, despite the fact that the sense of being there (*i.e.* good immersive experience) will not be achieved unless using three-dimensional visualization tools.

It is noteworthy that computer graphics specifications are rarely included in fluid modelling packages, and the latter generally prioritize computational sources destined to the fluid solver, leaving the display of results in a secondary position. Although accuracy in terms of mathematics and physics is crucial when representing a realistic scenario, the data representation should not require the extensive post-processing that rendering often implies. When it comes to communication of flood risk to the stakeholders, not only precision is needed, but also an intuitive display of results. The step-wise workflow scheme hereinto presented (Figure 2) highlights the need to master diverse software, sometimes open-source and user-friendly, but most of the times insufficient alone for a reliable and integrated presentation of the risk assessed. This is inefficient and leads to compatibility issues at times, as well as unsuited for real-time decision-making. Ideally, a unified visualization platform shall be used in such case. This means to combine, in a unique platform, advanced hydrodynamic fluid solvers with algorithms that increase their computational speed, and computer graphic rendering, achieving solid and optimized hydrodynamic fluid simulations that are immediately depicted into visually relatable scenarios (e.g. see [5] [42] [43]).

Some visual scenarios are too complex or transitory, and an honest representation of them faces challenges that might be overcome by their implementation through a holistic approach. The use of risk perception-based knowledge together with a correctly represented content, in a well-studied context, will provide the unexperienced user the best Quality of Experience. Natural hazards concern many different target groups, thus, designing a valuable



communication of the assessed risk, as well as successfully guiding and influencing their choices, requires a level of interaction, usability, immersion, and compromise in the methodology used that is only comprehended by the concept of QoE. Quality of Experience, in the context of flash flood risk assessment and communication, evaluates the user experience on the serious gaming engine within WoW by contemplating both objective and subjective metrics. QoE does not only evaluate the content presented to the end user, but is rather inherently dependent on system-, human- and context-influencing factors. It is, nonetheless, essential to provide precise and usable content, which has been designed taking into account the rest of the influencing factors (*i.e.* that fulfills the user's needs and expectations and is provided in an intuitive manner), in order to achieve the best communication of flash flood risk to the stakeholders and support sound decision-making.

## 7. CONCLUSIONS

- The target of the hydraulic modelling executed in this research project is to achieve optimized simulations of flash floods affecting small, ungauged steep rivers that could be carried out in a realistic, scalable and reproducible prototype in a serious gaming engine.
- Developing an integrated mathematical model with modern 3D graphics combined in a user-friendly model engine for satisfactory impact assessment will emphasize the potential use of visualization technology to enhance understanding of engineering problems for non-experts on hydraulic engineering.
- Visualization results from the study can be self-sustaining and used in the analysis and estimation of the consequences of flash floods by a vast array of decision-maker profiles, such as emergency agencies, government, risk managers, risk consultants, and for educational purposes, risk communication and awareness, gaming industry, and users with no-scientific background among others.
- The implementation of optimized fluid simulations in other applications will save time and cost to those seeking for a compromise between precise and accurate simulation results, such as researchers, companies and the administration. The data obtained from simplified simulations could be potentially used as a preliminary orientation in decision-making, permitting to narrow down the research focus when tackling a very complex problem, hence, increase efficiency by saving time and cost.
- Soil erosion and sediment transport are important parameters to take into account, but not enclosed in hydrodynamic simulations. Most of the visualized models available do not include morphodynamics of small and steep ungauged rivers due to their complexity to be reproduced successfully even in two-dimensional numerical simulations. Sediment transport is studied parallel in WoW and the feasibility to include morphodynamics in the visualization engine will be discussed in future work.
- Developing virtual scenarios gives the opportunity to replicate and analyze complex real-life models and the human experiences that accompany them. Virtual reality engines can provide a laboratory of visual experience where different disciplines can meet and combine resources and knowledge for a common goal, such as the study and communication of natural hazards. Using Quality of Experience and Immersive Media Technology Experiences in the context of natural hazards will improve risk assessment and its delivery for better decision-making.

## ACKNOWLEDGEMENTS

The authors thank two anonymous reviewers for their improving suggestions. This publication is part of the World of Wild Waters (WoWW) project, which falls under the umbrella of Norwegian University of Science and Technology (NTNU)'s Digital Transformation initiative.

## REFERENCES

- [1] UNISDR - United Nations Office of Disaster Risk Reduction. United Nations Office for Disaster Risk Reduction: 2018 annual report, (2019) 107pp. + annex I (24pp.).
- [2] Moraru, A., Ruiz-Villanueva, V. and Furdada, G. Factors controlling streambank erosion and channel widening: implications for flood hazard. In: Garcia, C.; G  mez-Pujol, L.; Mor  n-Tejeda, E.; Batalla, R. J. (Eds.), *Geomorfolog  a del Antropoceno: efectos del cambio global sobre los procesos geomorfol  gicos*. Palma de Mallorca, Balearic Islands: Universitat de les Illes Balears, Sociedad Espa  ola de Geomorfolog  a. (2018) 247–252, ISBN: 978-84-09-04850-2
- [3] Pavli  ek, M. and Bruland, O. Mapping areas exposed to erosion and water forces during extreme floods in steep terrain. In: European Geosciences Union (EGU), EGU2019-19167. Available at: [https://presentations.copernicus.org/EGU2019-19167\\_presentation.pdf](https://presentations.copernicus.org/EGU2019-19167_presentation.pdf); last accessed: 24<sup>th</sup> May 2019. (2019)
- [4] Lujala, P., Lein, H. and R  d, J.K. Climate change, natural hazards, and risk perception: the role of proximity and personal experience. *Local Environment*, (2015) 20(4): 489–509. DOI: 10.1080/13549839.2014.887666
- [5] Wang, C., Hou, J., Miller, D., Brown, I. and Jiang, Y. Flood risk management in sponge cities: The role of integrated simulation and 3D visualization. *International Journal of Disaster Risk Reduction*, *In Press*, (2019) 101139. DOI: 10.1016/j.ijdr.2019.101139
- [6] Henonin, J., Russo, B., Mark, O. and Gourbesville, P. Real-time urban flood forecasting and modelling – a state of the art. *Journal of Hydroinformatics*, (2013), 15(3):717–36. DOI: 10.2166/hydro.2013.132
- [7] Hodges, B.R. Hydrodynamical Modeling. In: Elias, S.A. (Ed.). *Reference Module in Earth Systems and Environmental Sciences*. Elsevier, (2014), 22pp.
- [8] Teng, J., Jakeman, A.J., Vaze, J., Croke, B.F. W., Dutta, D. and Kim, S. Flood inundation modelling: A review of methods, recent advances and uncertainty analysis. *Environmental Modelling & Software*, (2017) 90: 201–216. DOI: 10.1016/j.envsoft.2017.01.006
- [9] Friendly, M., and Denis, D.J. Milestones in the history of thematic cartography, statistical graphics and data visualization. *Statistical Consulting Service and Institute for Social Research of the University of York (Ontario, Canada)*, (2006) 71pp.
- [10] Muntean, C.I. Raising engagement in e-learning through gamification. In: 6<sup>th</sup> International Conference on Virtual Learning (ICVL), Cluj-Napoca, Romania, (2011) 323–329.
- [11] Ebrahimi, T., Foessel, S., Pereira, F. and Schelkens, P. JPEG Pleno: Toward an Efficient Representation of Visual Reality. *IEEE Multimedia*, (2016) 23(4):14–20. DOI: 10.1109/MMUL.2016.64
- [12] Timmerer, C., Ebrahim, T. and Pereira, F. Toward a New Assessment of Quality. *Computer Journal*, (2015) 48(3): 108–110. ISSN: 0010-4620
- [13] Perkis, A., Hameed, A. Immersive media experiences - what do we need to move forward? In: *Society of Motion Picture and Television Engineers (SMPTE)*. Los Angeles, USA, (2018). 1–12.

- [14] Qualinet (European Network on Quality of Experience in Multimedia Systems and Services). Qualinet white paper on definitions of quality of experience, Dagstuhl seminar 12181, (2012) 24pp.
- [15] Perkis, A. A QoE cross layer approach to model media experiences. IEEE COMSOC MMTTC E-Letter, (March 2013) 8(2): 6–9.
- [16] Zhang C, Perkis A, Arndt S. Spatial immersion versus emotional immersion, which is more immersive? In: 9th International Conference on Quality of Multimedia Experience (QoMEX). Erfurt, Germany: IEEE, (2017) 1–6. DOI: 10.1109/QoMEX.2017.7965655
- [17] Ghazali, J. and Kamsin, A. A real time simulation and modeling of flood hazard. In: 12<sup>th</sup> WSEAS International Conference on Systems, Heraklion, Greece, (2008) 438–443. ISBN: 978-960-6766-83-1
- [18] Wang, L. and Cheng, Q. Web-based hydrological modeling system for flood forecasting and risk mapping. Geoinformatics 2008 and Joint Conference on GIS and Built Environment: Monitoring and Assessment of Natural Resources and Environments, (2008) 7145(November 2008): 71450A. DOI: 10.1117/12.812986
- [19] Al-Sabhan, W. Designing a Human-Centred, Mobile Interface to Support Real-time Flood Forecasting and Warning System. PhD Thesis, University of Brunel (UK), (2016) 419pp.
- [20] Krajewski, W.F., Ceynar, D., Demir, I., Goska, R., Kruger, A., Langel, C., Mantilla, R., Niemeier, J., Quintero, F., Seo, B.C., Small, S.J., Weber, L.J. and Young, N.C. Real-time flood forecasting and information system for the state of Iowa. Bulletin of the American Meteorological Society, (2017) 98(3): 539–554. DOI: 10.1175/BAMS-D-15-00243.1
- [21] Néelz, S. and Pender, G. Benchmarking the Latest Generation of 2D Hydraulic Modelling Packages. Environment Agency (Bristol, UK), (2013) 182pp.
- [22] Brunner, G.W. HEC-RAS 5.0 Hydraulic Reference Manual. (2016) 538pp. Last access: 10<sup>th</sup> May 2019; retrieved from: [www.hec.usace.army.mil/software/hecras/documentation.aspx](http://www.hec.usace.army.mil/software/hecras/documentation.aspx)
- [23] Betsholtz, A. and Nordlöf, B. Potentials and limitations of 1D-2D-coupled 1D-2D flood modelling in HEC-RAS - A case study on Høje river. MSc Thesis, University of Lund, (2017) 128pp.
- [24] Gómez, M. and Martínez, E. 1D, 2D, and 3D Modeling of a PAC-UPC Laboratory Canal Bend. In: SimHydro: Modelling of rapid transitory flows, Sophia Antipolis, (2014) 12pp. DOI: 10.1007/978-981-287-615-7\_29
- [25] Gharbi, M., Soualmia, A., Dartus, D. and Masbernat, L. Comparison of 1D and 2D hydraulic models for floods simulation on the medjerda river in tunisia. Journal of Materials and Environmental Science, (2016) 7(8): 3017–3026. ISSN: 2028-2508
- [26] Glock, K., Tritthart, M., Habersack, H. and Hauer, C. Comparison of hydrodynamics simulated by 1D, 2D and 3D models focusing on bed shear stresses. Water (Switzerland), (2019) 11(226): 19pp. DOI: 10.3390/w11020226
- [27] Annis, A., Gonzalez-Ramirez, N., Nardi, F., Castelli, F. Integrating a 2D Hydraulic Model and GIS Algorithms into a Data Assimilation Framework for Real Time Flood Forecasting and Mapping. In: La Loggia, G., Freni, G., Puleo, V., De Marchis, M. (Eds.), 13<sup>th</sup> International Conference on Hydroinformatics (HIC). Palermo, Italy: EPiC Series in Engineering, (2018) 36–44. DOI: 10.29007/29nd
- [28] Hadimlioglu, I.A. and King, S.A. Visualization of Flooding Using Adaptive Spatial Resolution. ISPRS International Journal of Geo-Information, (2019) 8(5): 204. DOI: 10.3390/ijgi8050204
- [29] Zinke, P. Modelling of flow and levee depositions in a freshwater delta with natural vegetation. PhD Thesis, Norwegian University of Science and Technology (NTNU), (2011) 309pp.



- [30] Lee, J.H.W., Cheung, V., Kuang, C.P., Choi, D.K. W., Wang, W.P., Tu, C.H., Chan, B. and Choi, Y.K. VISJET & VISFLOOD: Software for Environmental Hydraulic Modeling and Visualization. In: S. H. Winoto (Ed.), 7<sup>th</sup> Asian symposium on visualization, Singapore: Springer, (2003) conf24a155, 1–6.
- [31] Pajorov  , E., Hluch  y, L., Halada, L. and Sl        , P. 3D visualization tool for Virtual models of natural disasters. In: Aravossis, K., Brebbia, C.A., Gomez, N. (Eds.), Environmental Economics and Investment Assessment II WIT Press, (2008) 105–114. DOI: 10.2495/EEIA080111
- [32] Li, X., Wan, W., Li, L., Zhang, X., Gan, C. and Yu, X. Realization of flood simulation visualization based on OpenGL. In: 2012 International Conference on Audio, Language and Image Processing (IEEE), (2012a) 1151–1154. DOI: 10.1109/ICALIP.2012.6376790
- [33] Li, Y., Pan, L., Liu, T. and Wei, C. Three-dimensional GIS based dynamic visualization simulation system for flood routing. In: Proceedings of 2<sup>nd</sup> International Conference on Computer Science and Network Technology (ICCSNT), (2012b) 1409–1412. DOI: 10.1109/ICCSNT.2012.6526184
- [34] Demir, I. and Krajewski, W.F. Towards an integrated Flood Information System: Centralized data access, analysis, and visualization. Environmental Modelling and Software, (2013) 50: 77–84. DOI: 10.1016/j.envsoft.2013.08.009
- [35] Haynes, P.S. and Lange, E. In-situ flood visualisation using mobile AR. Proceedings of the IEEE Symposium on 3D User Interfaces (3DUI), (2016) 243–244. DOI: 10.1109/3DUI.2016.7460061
- [36] Zhang, S.H., Yuan, R. and Zhang, T.X. Development and Application of a Three-Dimensional Flood Simulation Platform. In: 11<sup>th</sup> International Symposium on Ecohydraulics, Melbourne, Australia, (2016) 8pp.
- [37] Macchione, F., Costabile, P., Costanzo, C. and De Santis, R. Moving to 3-D flood hazard maps for enhancing risk communication. Environmental Modelling and Software, (2019) 111(January 2019): 510–522. DOI: 10.1016/j.envsoft.2018.11.005
- [38] Gissler, C., Peer, A., Band, S., Bender, J. and Teschner, M. Interlinked SPH Pressure Solvers for Strong Fluid-Rigid Coupling. ACM Transactions on Graphics, (2019) 38(1):1–13. DOI: 10.1145/3284980
- [39] Suhr J. Basic Principles of Sound Decisionmaking [Internet]. Utah, USA; 1981. Available from: <http://leanconstruction.org/media/docs/deliveryGuide/Appendix13b.pdf>
- [40] Ye, F., Wang, H., Ouyang, S., Tang, X., Li, Z and Prakash, M. Spatio-temporal analysis and visualization using SPH for dam-break and flood disasters in a GIS environment. In: 2012 International Symposium on Geomatics for Integrated Water Resource Management (IEEE), (2012) 1–6. DOI: 10.1109/GIWRM.2012.6349636
- [41] Zhang, S.H., Xia, Z.X. and Wang, T.W. A real-time interactive simulation framework for watershed decision making using numerical models and virtual environment. Journal of Hydrology, (2013) 493: 95–104. DOI: 10.1016/j.jhydrol.2013.04.030
- [42] Zaspel, P. and Griebel, M. Photorealistic visualization and fluid animation: Coupling of Maya with a two-phase Navier-Stokes fluid solver. Computing and Visualization in Science (2011), 14(8): 371–83. DOI: 10.1007/s00791-013-0188-1
- [43] Griebel, M., Rieger, C. and Zaspel, P. Kernel-based stochastic collocation for the random two-phase Navier-Stokes equations. *In Press*, (2019) 1–21. ArXiv ID: 1810.11270, last access: 8<sup>th</sup> August 2019.



# NUMERICAL INVESTIGATION OF SHOCK WAVE PARTICLE CLOUD INTERACTION IN CYLINDRICAL GEOMETRIES

Andreas N. Osnes<sup>1</sup>, Magnus Vartdal<sup>2</sup>, Marianne G. Omang<sup>3,4</sup>, and Bjørn A.  
P. Reif<sup>1</sup>

<sup>1</sup> Department of Technology Systems, University of Oslo (UiO)  
PO Box 70 Kjeller, 2027 Kjeller  
e-mail (A. N. Osnes, corresponding author): a.n.osnes@its.uio.no  
e-mail (B. A. P. Reif): b.a.p.reif@its.uio.no

<sup>2</sup>Norwegian Defence Research Establishment (FFI)  
PO Box 25 Kjeller, 2027 Kjeller  
e-mail: magnus.vartdal@ffi.no

<sup>3</sup>Norwegian Estates Research Agency  
PO Box 405 Sentrum, 0103 Oslo

<sup>4</sup>Institute of Theoretical Astrophysics, University of Oslo (UiO)  
PO Box 1029 Blindern, 0315 Oslo  
e-mail: m.g.omang@astro.uio.no

**Key words:** Diverging flow, shock wave, particle-resolved simulation, dense particle suspension

**Abstract.** This study investigates the interaction of a shock wave with a fixed layer of particles in cylindrical geometries using particle-resolved large eddy simulations. The curvature radius of the particle layer is varied and effect on the flow is analyzed. The mean flow field depends strongly on the curvature radius, but this is not the case for flow fluctuations or particle drag coefficients. The results indicate that particle scale flow phenomena are insensitive to geometric expansion within the range investigated here. This is an encouraging result from a modeling perspective, since it means that results and observations of particle scale phenomena obtained in planar configurations can likely be extrapolated to diverging geometries.

## 1 INTRODUCTION

The interaction of shock waves with particle clouds plays an important role in a number of natural phenomena, industrial applications, and safety measures such as volcanic

eruptions [1], shock wave mitigation using porous barriers [2, 3], and ejection of stellar dust from supernovae [4]. The primary motivation for the present work is the role of shock wave particle cloud interaction in heterogeneous explosives [5] and explosive dissemination of powders and liquids [6, 7, 8]. The latter applications typically include significant geometric expansion effects. The effect of this expansion on the interaction process is the topic of this work.

Dispersal of cylindrical particle shells by shock waves has previously been studied experimentally using both explosives [7, 6, 9] and shock tubes [10, 8]. In both cases, the particle layers have initially been very dense, with volume fractions approaching the random packing limit. The initial dispersion of these shells are therefore subject to strong particle collision effects. As the powders are accelerated outward, the particle volume fraction quickly decreases as a result of geometric expansion. Consider for instance a layer of initial thickness  $L$  and inner curvature radius  $R_0 = L$  that initially has a particle volume fraction,  $\alpha_p$ , of 0.5. If this layer is accelerated outwards without changing thickness, it will have  $\alpha_p = 0.3$  when the inner radius is  $2L$ , and  $\alpha_p \approx 0.2$  at  $R_0 = 3L$ . Thus, despite having a large initial volume fraction, the particle cloud rapidly enters the intermediate volume fraction regime ( $\alpha_p = 0.01 - 0.5$ ) and remain there for a substantial part of the dispersal process in such scenarios. Furthermore, one of the primary flow features of this dispersal process is the formation of particle jets [9, 11]. The preferential concentration of the particles in jets tends to increase the time during which particles remain in the intermediate volume fraction regime. During this time, the flow periodically over-expands. This results in implosions that generate secondary shock waves which propagate outwards through the particle cloud. Interactions between shock waves and particle clouds in the intermediate volume fraction regime is therefore one of the primary flow features in this dispersal process.

From a modelling perspective, the intermediate volume fraction regime is especially challenging because the dynamics are affected by a complex interaction between the flow field and the particle distribution [12]. Each particle interacts with the incoming shock wave and subsequent flow in a manner that depends on the local particle configuration. The interaction generates reflected shocks, shear layers, and wakes that in turn interact with nearby flow features. These flow perturbations result in large particle drag force variations that alter the configuration of particles. Consequently, any modeling effort where the interaction between the particles and the flow is assumed to consist of a sum of interactions with isolated particles is unlikely to succeed. It is therefore necessary to perform detailed investigations of the flow around and forces on the particles, and relate the observations to available model quantities, in order to establish suitable simplified models for this regime.

Experimental investigation of flow features at the particle scale inside particle clouds is challenging. It is, however, possible to conduct particle-resolved simulations for this purpose, and several recent studies have done just that [13, 14, 15, 16, 17, 18, 19]. Such simulations are computationally expensive, since a large number of particles must be

used to obtain meaningful statistics. In addition to yielding physical insight, particle resolved simulations can be used to investigate closures for unresolved terms that appear in simpler dispersed flow models. The unclosed terms are a result of averaging of products of fluctuations. What the fluctuation products represent depends on the averaging type. For shock wave particle cloud interaction it is convenient to apply volume averaging. With this approach, both turbulent fluctuations and laminar flow effects around particles, often referred to as pseudo-turbulent fluctuations, contribute to fluctuation correlations. In addition, new terms appear due to averaging over volumes containing gas and particles, as discussed in e.g. [20]. Particle-resolved simulation data can be utilized to examine all of these terms. This is particularly useful for development of Eulerian-Eulerian and Eulerian-Lagrangian dispersed flow models [21, 12, 22, 23]. Furthermore, the results of resolved simulations can be used directly as validation data for the simplified models.

In this work, we examine the effect of flow expansion on the passage of shocks through particle clouds in the intermediate volume fraction regime ( $\alpha_p = 0.1$ ). Flow expansion causes rapid spatial variation of mean flow fields, and this work explores how this affects the flow through particle clouds. We conduct particle resolved large eddy simulations of a shock wave passing through a cylindrical shell of randomly positioned stationary particles. We vary the radius of curvature of the cylindrical shell and keep the shell thickness constant. For each curvature radius we perform an ensemble of simulations to obtain statistically representative results.

This paper is organized as follows. In Section 2 the governing equations and the volume averaged equations used for analysis are presented. Section 3 describes the computational method and the set-up of the problem. Section 4 contains results from grid and ensemble convergence studies. Section 5 presents the simulation results. We examine wave trajectories, mean flow fields, flow fluctuations and particle forces. We also investigate the relative importance of the terms in the volume averaged momentum equation in different regions. Finally, concluding remarks are given in section 6.

## 2 GOVERNING EQUATIONS

The governing equations for the gas dynamics in this work are the conservation equations of mass, momentum and energy

$$\partial_t \rho + \partial_k (\rho u_k) = 0, \quad (1)$$

$$\partial_t (\rho u_i) + \partial_k (\rho u_i u_k) = -\partial_i p + \partial_j \sigma_{ij}, \quad (2)$$

$$\partial_t (\rho E) + \partial_k (\rho E u_k + p u_k) = \partial_j (\sigma_{ij} u_i) - \partial_k (\lambda \partial_k T). \quad (3)$$

Here,  $\rho$  is the mass density,  $u$  is the velocity,  $p$  is the pressure,  $\sigma_{ij} = \mu(\partial_j u_i + \partial_i u_j - 2\partial_k u_k \delta_{ij}/3)$  is the viscous stress tensor,  $E = \rho e + 0.5\rho u_k u_k$  is the total energy per unit volume,  $\lambda$  is the thermal conductivity,  $T$  is the temperature,  $\mu$  is the dynamic viscosity and  $e$  is the internal energy per unit mass. A calorically perfect ideal gas equation of state

with  $\gamma = 1.4$  is employed. Furthermore, we assume a power law dependence of viscosity on temperature with an exponent of 0.76 and a constant Prandtl number of 0.7.

Due to the strong spatial variation within the particle cloud, the above equations are inconvenient for analysis of the simulation results. Instead, the volume averaged equations of motion are used for analysis. These are obtained by averaging eqs. (1) to (3) over a volume, and carefully accounting for the effect of the dispersed phase within that volume. In this study,  $\bar{\cdot}$  will be used to denote volume averaging,  $\langle \cdot \rangle$  denotes phase-averaging, and  $\tilde{\cdot}$  denotes Favre-averaging. The deviations from Favre-averaged values are denoted by  $\cdot''$ . Phase and volume averaging are related by  $\alpha \langle \cdot \rangle = \bar{\cdot}$ , where  $\alpha$  is the gas phase volume fraction. The problem under consideration is statistically homogeneous in the axial ( $z$ ) and azimuthal ( $\theta$ ) directions. Therefore, the only component of the volume averaged momentum equation that is of interest is the radial ( $r$ ) one. Assuming stationary inert particles, the volume averaged mass and momentum equations in the radial direction are

$$\partial_t (\alpha \langle \rho \rangle) + \partial_r (\alpha \langle \rho \rangle \tilde{u}_r) = -\frac{\alpha \langle \rho \rangle \tilde{u}_r}{r}, \quad (4)$$

$$\begin{aligned} \partial_t (\alpha \langle \rho \rangle \tilde{u}_r) + \partial_r (\alpha \langle \rho \rangle \tilde{u}_r \tilde{u}_r + \alpha \langle p \rangle) &= -\frac{\alpha \langle \rho \rangle}{r} \tilde{u}_r \tilde{u}_r + \partial_r (\alpha \langle \sigma_{rr} \rangle) + \frac{\alpha \langle \sigma_{rr} \rangle}{r} \\ -\partial_r (\alpha \langle \rho \rangle \tilde{R}_{rr}) - \frac{\alpha \langle \rho \rangle}{r} \tilde{R}_{rr} &+ \frac{1}{V} \int_S p n_r dS - \frac{1}{V} \int_S \sigma_{rk} n_k dS. \end{aligned} \quad (5)$$

Here, the boundary between the gas and the particles is denoted by  $S$ ,  $V$  is the averaging volume and  $n_k$  is the particle surface normal. The integrals represent the forces acting on the particle surfaces.  $\tilde{R}_{rr} = \widetilde{u_r'' u_r''}$  is the radial component of the average stress due to velocity fluctuations. The full tensor,  $\tilde{R}_{ij}$ , is the single-point, density weighted (Favre averaged), velocity fluctuation correlations, i.e.

$$\tilde{R}_{ij} = \frac{\langle \rho u_i'' u_j'' \rangle}{\langle \rho \rangle}. \quad (6)$$

$\tilde{R}_{ij}$  contains both the classical turbulent stresses and the pseudo turbulent stresses mentioned in the introduction. Its role is analogous to that of the classical Reynolds stress in the RANS equations and we thus refer to this term as Reynolds stress in the rest of the paper.

### 3 COMPUTATIONAL METHOD AND SET-UP

#### 3.1 Computational method

The governing equations are solved numerically using the compressible flow solver "CharLES" from Cascade Technologies. It employs an entropy stable scheme on a Voronoi-mesh with third order Runge-Kutta time stepping [24]. For more information on of entropy stable schemes, consult e.g. [25, 26].

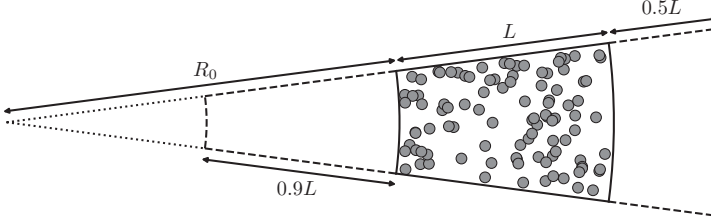


Figure 1: Sketch of the computational domain. The dashed lines indicate the domain being simulated.  $R_0$  is the radius of curvature and  $L = 1.2\sqrt[3]{4}$  mm is the particle layer thickness. The particle cloud is located between  $R_0$  and  $R_0 + L$ . The particle diameter is  $D_p = 4^{-1/3} \times 10^{-1}$  mm.

### 3.2 Problem set-up

This work considers the effect of geometric expansion on the passage of shocks through particle clouds. To this end, we conduct simulations in a cylindrical geometry, where the particle cloud is a cylindrical shell. We consider spherical particles with diameter  $D_p = 4^{-1/3} \times 10^{-1}$  mm. The shell-thickness is denoted  $L$ , and is kept constant at  $1.2\sqrt[3]{4}$  mm  $\simeq 30.2D_p$ . We consider three different radii of curvature defined such that the inner particle shell radius,  $R_0$ , takes the values  $L$ ,  $2L$  and  $\infty$ . Figure 1 shows a sketch of the computational domain. The arc-length of the inner shell edge is kept constant at  $8\sqrt[3]{4}D_p$  by considering cylindrical sectors with different angles. In the axial direction, a constant domain size of  $8\sqrt[3]{4}D_p$  is used. For each curvature radius, the inner boundary is located  $0.9L$  upstream of the particle shell edge.

The particles occupy a volume fraction  $\alpha_p = 0.1$  within the layer, and their positions are drawn randomly with the condition that none of the particles are closer than  $0.05D_p$  to another particle. Furthermore, the particles are not allowed to touch the boundaries of the computational domain. This gives a number of particles ranging between approximately 900 and 1400, depending on the given radius of curvature. For a discussion on the effect of particle distribution regularity, consult [19]. For each radius of curvature, five simulations with different particle distributions are conducted to reduce the effect of fluctuations introduced by the particle distribution realizations. The effect of the number of realizations considered is discussed in section 4.2.

Each simulation is initiated as a diverging shock tube. The initial state consists of a high-pressure, high-density region and a region containing air at atmospheric conditions. These are separated by a discontinuity, located  $0.156L$  upstream of the particle cloud. The driver section conditions are  $p^0 = 3.6619$  MPa,  $\rho^0 = 12.508$  kg/m<sup>3</sup>, and the gas is initially at rest. This choice of driver section conditions yields a shock wave with Mach number

Table 1: Control volume length scale ( $\Delta_{CV}$ ) and total number of control volumes used in the grid study ( $N_{CV}$ ).

$\Delta_{CV}$ [ $\mu\text{m}$ ]	$D_p/\Delta_{CV}$	$N_{CV}$
7.5	8.4	$3.99 \times 10^6$
5	12.6	$13.5 \times 10^6$
3.35	18.8	$41.3 \times 10^6$
2.25	28.0	$14.5 \times 10^7$
1.5	42.0	$49.8 \times 10^7$

$M = 2.6$  followed by a contact discontinuity without any density jump. The flow state behind the incident shock wave in the planar case is used for normalization purposes and is denoted by the subscript  $IS$ . Based on these conditions, the particle Reynolds number  $Re_p = \rho_{IS} u_{IS} D_p / \mu_{IS} \simeq 5000$ . The position of the initial gas state discontinuity is chosen such that the time when the shock wave arrives at the outer shell edge coincides with the arrival time of the head of the rarefaction wave at the inner boundary of the computational domain. A symmetry boundary condition is employed at the inner and axial boundaries and periodic boundary conditions are used in the azimuthal direction.

The results are analyzed using the volume averaged equations (eqs. (4) and (5)). We define averaging volumes spanning the domain in the axial and azimuthal directions, with a radial extent of  $L/60$ . The flow quantities are averaged over these bins and over the ensemble of simulations at the same radius of curvature. A timescale based on the initial shock wave velocity and layer thickness

$$\tau_L = L \left( M \sqrt{\gamma \frac{p^0}{\rho^0}} \right)^{-1}, \quad (7)$$

is used to compare the simulation results.

## 4 GRID AND ENSEMBLE CONVERGENCE

### 4.1 Grid convergence

To assess the effect of grid size, we perform a grid convergence study for  $R_0 = L$ . This study uses a slightly different set-up than the results presented below, with an initial condition corresponding to a  $M = 2.6$  shock wave located at  $r = R_0$  and a corresponding inflow at  $r = R_0 - 0.9L$ . The flow pattern for this configuration is similar to the configuration described in section 3.2 for the initial part of the simulation and we therefore expect the grid dependence to be similar in both cases. Five different grids were utilized, and each new grid had a length scale of roughly  $2/3$  of the previous grid length scale. The grid length scales and total number of control volumes are listed in table 1. These grid length scales are used for regions within a distance  $0.5D_p$  from any particle. Outside of those regions, the grid length scale is doubled, and for  $r > R_0 + 1.5L$  the length scale is doubled once more.



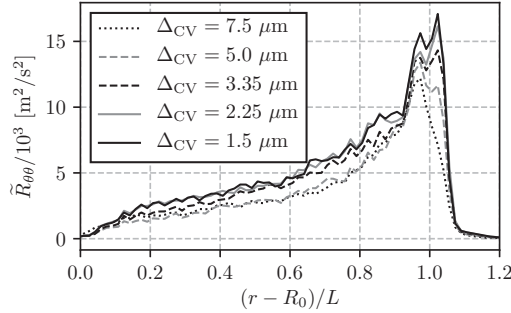


Figure 2: Grid convergence results for  $\tilde{R}_{\theta\theta}$  in the case  $R_0 = L$  at  $t/\tau_L = 1.5$ .

The volume averaged quantities in eqs. (4) and (5) that have the strictest requirement on the computational grid are the Reynolds stresses and the particle forces. By inspection, we find that the azimuthal component of the Reynolds stress is the slowest to converge. Figure 2 shows the convergence of  $\tilde{R}_{\theta\theta}$  at  $t/\tau_L = 1.5$ . We do not achieve completely converged results within the range of grid length scales used here. Due to the extreme computational cost for the simulations with the finest length scale, we find it necessary to choose  $\Delta_{CV} = 2.25 \mu\text{m}$  for the simulations within this work. By extrapolating the trend observed in fig. 2, we expect the converged Reynolds stresses to be slightly higher than those obtained in our simulations.

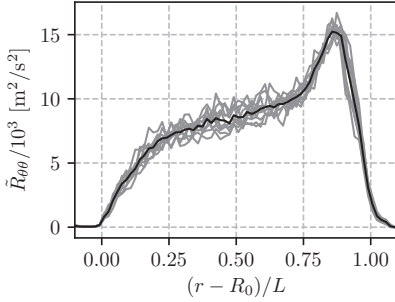
## 4.2 Ensemble convergence

In order to minimize the effect of random particle distribution fluctuations, we perform multiple simulations for each  $R_0$  and average the results over the simulation ensemble. We determine the number of simulations needed to achieve reasonably converged results based on how  $\tilde{R}_{\theta\theta}$  converges with the number of simulations in the case with  $R_0 = L$ . This estimate is based on a grid with  $\Delta_{CV} = 3.35 \mu\text{m}$ , which is coarser than that used for the final simulations.

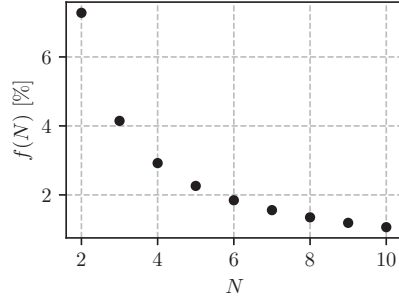
Figure 3a shows  $\tilde{R}_{\theta\theta}$  at  $t/\tau_L = 1.5$  for ten different realizations. It is clear that the general shape of all the curves is quite similar and impressions about the trend can be obtained from single simulations. The variation is up to one third of the mean value, and there is a lot to gain from performing an ensemble average.

We quantify the convergence by examining the relative change as we go from  $N$  to  $N + 1$  simulations. This is expressed by the function

$$f(N) = \left[ \frac{1}{2.9L} \int_{R_0-0.9L}^{R_0+2L} \left( \frac{\frac{1}{N} \sum_{i=1}^N \tilde{R}_{\theta\theta}^i(r) - \frac{1}{N-1} \sum_{i=1}^{N-1} \tilde{R}_{\theta\theta}^i(r)}{\frac{1}{N-1} \sum_{i=1}^{N-1} \tilde{R}_{\theta\theta}^i(r)} \right)^2 dr \right]^{1/2}. \quad (8)$$



(a)  $\tilde{R}_{\theta\theta}$  at  $t/\tau_L = 1.5$  for the ten different simulations (gray) and their mean value (black).



(b) Relative difference between averaging  $\tilde{R}_{\theta\theta}$  over  $N$  and  $N - 1$  simulations.

Figure 3: Ensemble convergence results.

We compute  $f(N)$  for every permutation of the simulation order and average the results over these combinations. The results are shown in fig. 3b. At five realizations, the average relative change in  $\tilde{R}_{\theta\theta}$  from adding one more simulation is about 2%. At ten realizations, it is 1%. Due to the high computational cost and relatively small gain in increasing the number of simulation beyond this point, we use  $N = 5$  for all subsequent results presented in this study.

## 5 RESULTS

Due to similar initial conditions, the simulations for the different radii of curvature display the same basic flow pattern. The discontinuity at the outer boundary of the driver section generates an outward moving shock wave and a rarefaction wave with a head moving inwards and a tail moving outwards. As the shock wave impacts the particle cloud, a reflected shock wave is set up. Subsequently, the tail of the rarefaction also interacts with the upstream boundary of the particle cloud. Thereafter, the head of the rarefaction interacts with the cloud after having reflected off the inner boundary. Finally, the reflected shock wave interacts with the cloud after having reflected off the inner boundary. An  $x - t$  diagram showing the position of the above mentioned waves, obtained numerically, is found in fig. 4. This figure also contains the acoustic characteristic  $\tilde{u}_r - c$  generated as the shock wave exits the particle cloud. The right-ward trajectory of these signals for  $R_0 = 2L$  and  $R_0 = \infty$  indicates that the flow becomes supersonic immediately at the downstream edge, but we do not observe the same phenomenon for  $R_0 = L$ .

The interaction of the shock wave with the particle cloud results in a continuous weakening of the shock that slows it down. The geometric expansion also attenuates the shock and slows it down further. If we correct for the weakening of the shock wave due to the

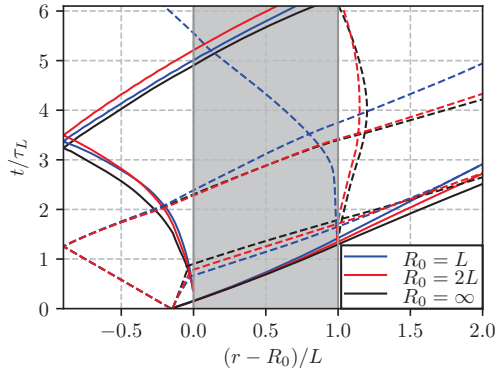


Figure 4:  $x-t$  diagram showing the propagation of the primary shock wave (solid), acoustic signals resulting from the head and tail of the initial rarefaction (dashed), reflected shock wave generated at the upstream particle cloud edge (solid) and acoustic signals generated by the shock wave exiting the particle cloud (dashed).

geometric expansion, by comparing with simulation results obtained without particles, no significant difference in shock weakening between the three curvature radii is observed.

Based on the wave system described above, we chose  $t/\tau_L = 0.75, 1.5, 3$  and  $4.5$  to compare the results for the different cases. At  $t/\tau_L = 0.75$  the state inside the particle cloud is only affected by the initial shock wave, while at  $t/\tau_L = 1.5$  both the tail of the rarefaction and the shock wave are involved. At  $t/\tau_L = 3$ , the head of the rarefaction is part way through the cloud. Finally, at  $t/\tau_L = 4.5$  the flow has developed further but is not yet affected by the reflected shock wave. For the last two times an expansion region is present at the downstream edge of the particle cloud. The strength of this expansion is important for the process of particle dispersion. Its dependence on the radius of curvature will also be discussed below.

Figure 5 contains a visualization of the radial velocity and density gradients within the particle cloud at  $t/\tau_L = 1$ . It illustrates the complexity of the flow field resulting from the interaction. The refracted initial shock wave is visible to the right and directly behind it, the reflected shock waves from the particles. Further upstream, we see the development of particle wakes and shear layers. Upstream of the particle cloud, the reflected shock wave is clearly visible.

### 5.1 Mean flow

In this section, we examine the mean flow fields for the three curvature radii at the four times  $t/\tau_L = 0.75, 1.5, 3.0$  and  $4.5$ . Figure 6 shows the mean radial velocity. It increases with distance within the particle cloud. At the two earliest times, there is a

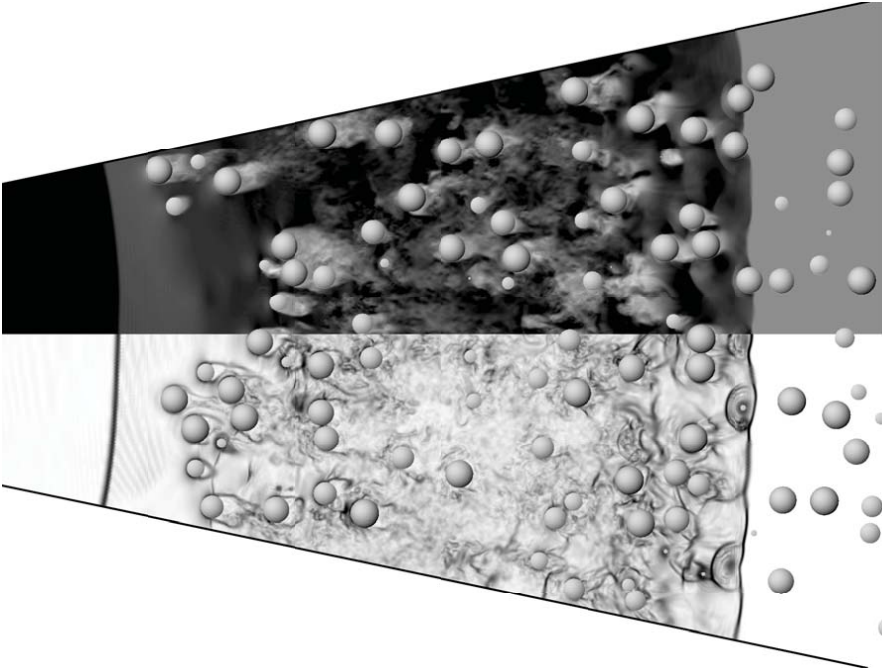
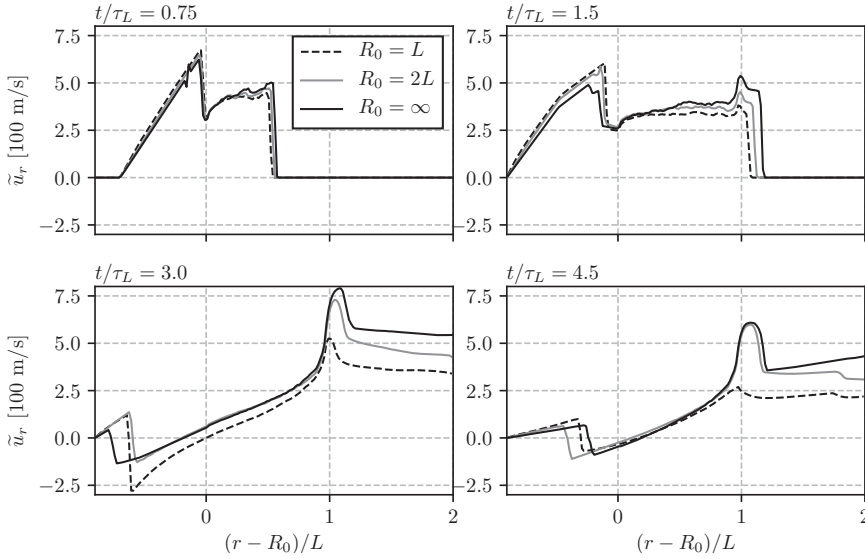


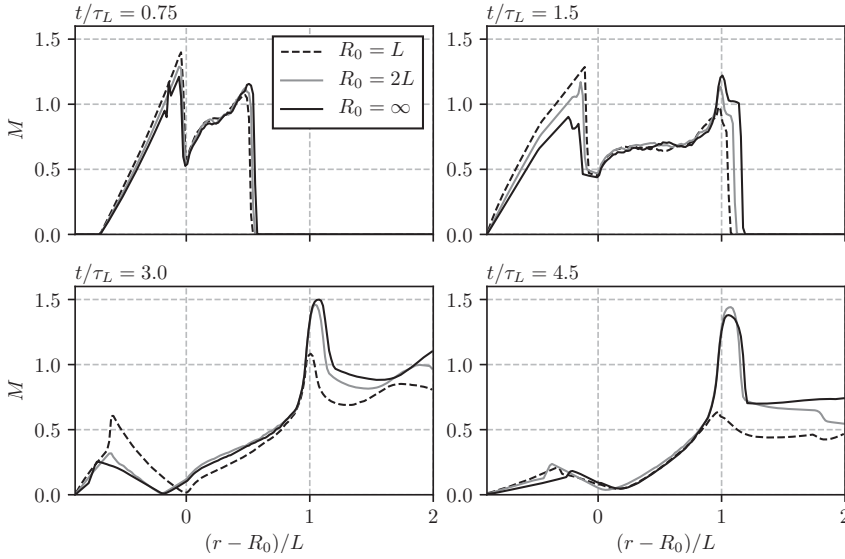
Figure 5: Flow snapshot for  $R_0 = L$  at  $t/\tau_L = 1$ . The top half displays the radial velocity ( $u_r$ ) and the bottom half displays density gradients using numerical schlieren.


 Figure 6: Mean radial velocity as a function of  $r$  at  $t/\tau_L = 0.75, 1.5, 3.0$  and  $4.5$ .

steep gradient just downstream of the inner cloud edge. This is expected since the flow is locally subsonic when it enters the cloud due to the reflected shock. Therefore, the area contraction at the particle cloud edge causes a flow acceleration. The region upstream of the reflected shock has higher radial velocities for smaller  $R_0$  due to the geometric expansion. A small numerical artifact can be seen at about  $r - R_0 \approx -0.2$ , which is a result of the discontinuous initial condition on the Voronoi-grid. This effect is present also for smaller  $R_0$ , but is dampened much faster in those simulations.

At  $t/\tau_L = 1.5$ , the shock wave has exited the particle cloud, and the flow accelerates towards the downstream cloud edge. The head of the rarefaction wave has reflected off the inner domain boundary, and can be seen as a kink in the velocity profiles around  $(r - R_0)/L \approx -0.5$ . At later times, the flow slows down due to the reflected rarefaction wave. Indeed, the gas flows inwards in parts of the cloud at  $t/\tau_L = 3.0$ . We also observe that the expansion region at the downstream edge is stronger for larger  $R_0$  and persists for a long time. At  $t/\tau_L = 4.5$ , the reflected shock wave is moving outwards, having reflected off the inner boundary, and is visible at  $(r - R_0)/L \approx -0.25$ .

The local flow Mach numbers are shown in fig. 7. At  $t/\tau_L = 0.75$  and  $t/\tau_L = 1.5$ , the region inside the particle cloud has locally higher Mach numbers for smaller curvature radii. In contrast, the local Mach number is larger for larger curvature radii at the downstream cloud edge. For all cases, there is a transition to supersonic flow which occurs just before the edge of the of the particle layer. For  $R_0 = L$ , the flow only becomes


 Figure 7: Local Mach number as a function of  $r$  at  $t/\tau_L = 0.75, 1.5, 3.0$  and  $4.5$ .

supersonic for a very limited time, with a Mach number just above one at  $t/\tau_L = 3.0$ , while for larger  $R_0$  local Mach numbers up to 1.5 are observed for extended periods of time. For the latter cases, we observe that the expansion region is terminated by a quasi-steady shock located at  $(r - R_0)/L \approx 1.25$  at the two latest times.

The density profiles are shown in fig. 8. When the gas expands outwards the mass is distributed over relatively larger volumes for smaller  $R_0$ . This leads to lower mass densities. It can be seen that the relative jump in density over the reflected shock is higher for lower  $R_0$ , which means that the reflected shock wave is stronger for smaller curvature radii. This is in accordance with the path of the reflected shocks in fig. 4, where it can be seen that the reflected shock for  $R_0 = L$  accelerates strongly until it reflects off the inner domain boundary.

The pressure profiles, found in fig. 9, display much of the same properties as the density profiles. There is an almost constant gradient through the particle layer after the shock wave has passed, and this state lasts until the rarefaction wave has reflected off the inner boundary and begins to decelerate the flow within the particle cloud. The pressure drops sharply in the expansion at the downstream cloud edge. This is most prominent for larger curvature radii.

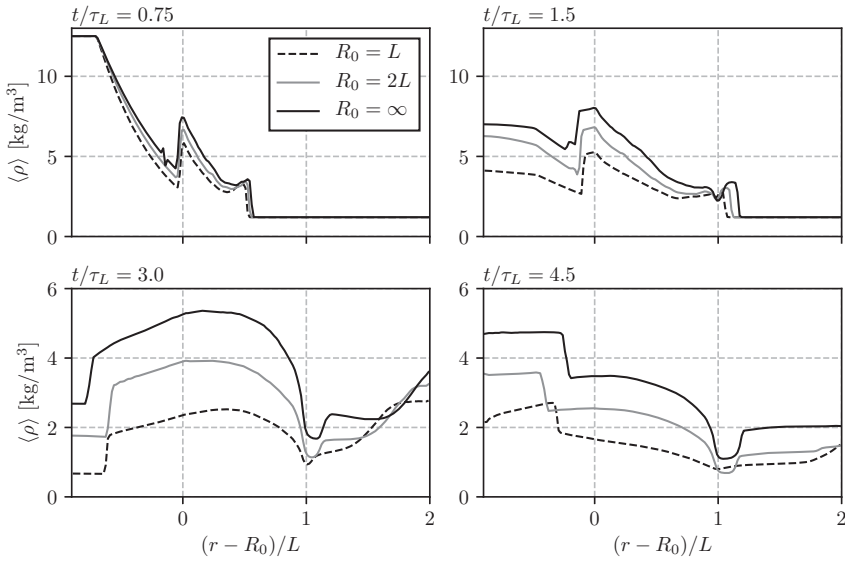


Figure 8: Mean density as a function of  $r$  at  $t/\tau_L = 0.75, 1.5, 3.0$  and  $4.5$ . Note the difference in scaling of the vertical axis for the top and bottom.

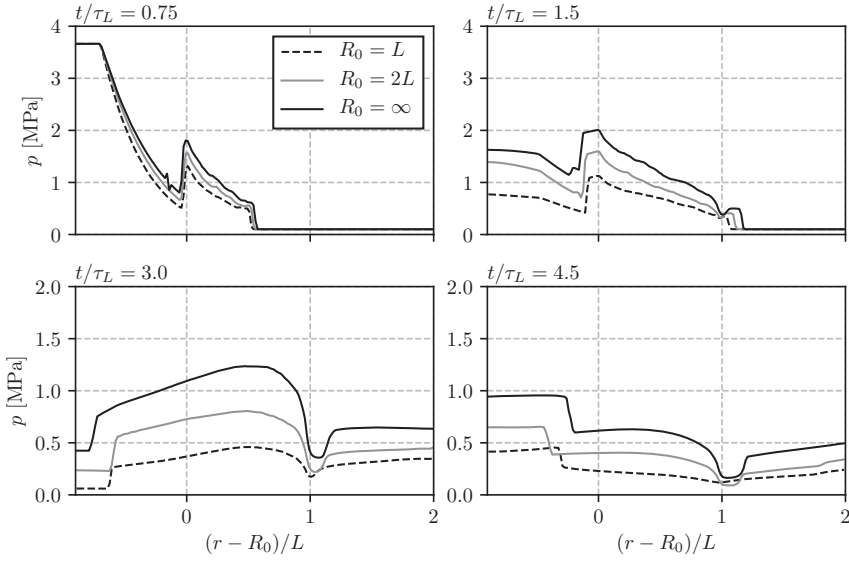


Figure 9: Mean pressure as a function of  $r$  at  $t/\tau_L = 0.75, 1.5, 3.0$  and  $4.5$ . Note the difference in scaling of the vertical axis for the top and bottom.



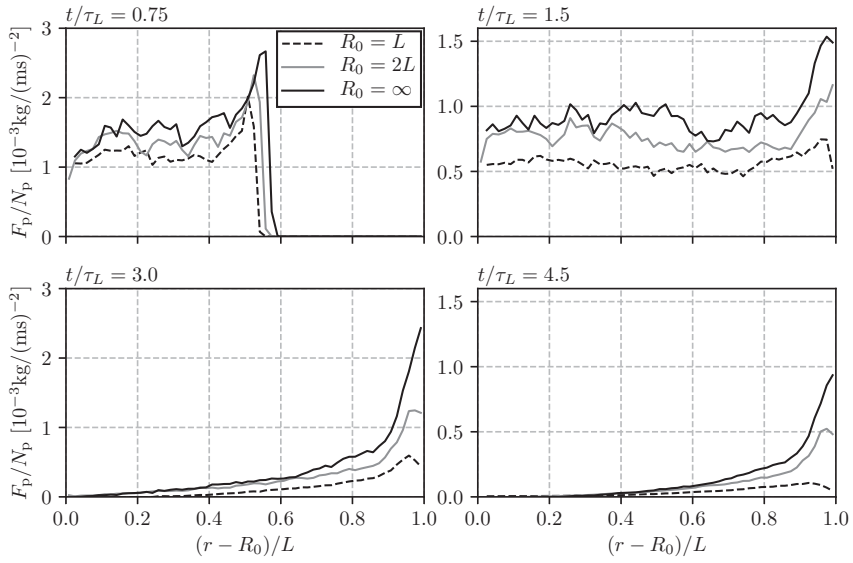
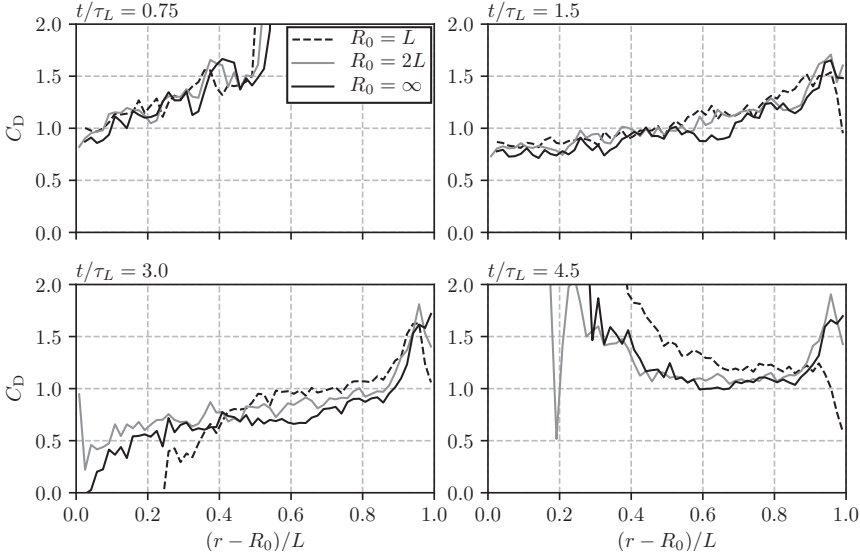


Figure 10: Average force on the particles as a function of  $r$  at  $t/\tau_L = 0.75$ ,  $1.5$ ,  $3.0$  and  $4.5$ . Note the difference in scaling of the vertical axis for the left and right columns.


 Figure 11: Mean drag coefficient as a function of  $r$  at  $t/\tau_L = 0.75, 1.5, 3.0$  and  $4.5$ .

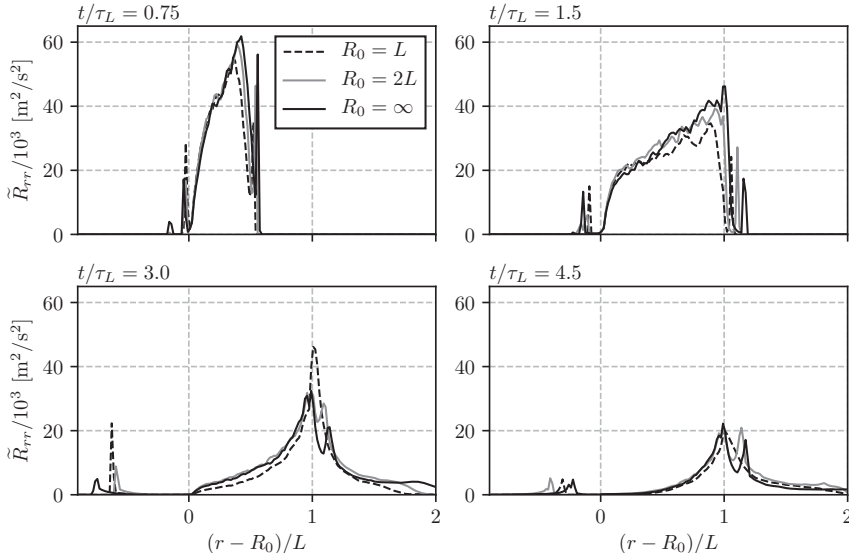
## 5.2 Particle forces

Average particle forces are shown in fig. 10. Smaller  $R_0$  lead to lower particle forces, primarily as a result of the lower mean kinetic energy of the flow. At  $t/\tau_L = 0.75$ , it is clear that the largest forces on the particles are imposed during their interaction with the shock wave. Subsequently, the forces tend to a roughly constant value through the particle cloud, except for the drastic increase at the downstream cloud edge. This state lasts until the passage of the rarefaction wave. Interestingly, for  $R_0 = L$  and  $R_0 = 2L$  there is a slight dip in the forces on the particles towards the end of the particle cloud at the later time intervals. This is in accordance with the distribution of the pressure gradient, which is steepest at the location of the peak particle forces. At the end of the particle layer, the pressure gradient is gentler and therefore contributes less to the forces on the particles.

The drag coefficients, shown in fig. 11, also increase at the downstream particle cloud edge. The particle drag coefficient is defined as

$$C_D = \frac{\int_{S_i} (-p\delta_{rk} + \sigma_{rk}) n_k dS_i}{0.5\langle\rho\rangle\tilde{u}_r^2 A_p}, \quad (9)$$

where  $\delta_{ij}$  is the Kronecker delta,  $A_p$  is the projected area of the particle in the direction of the flow, and  $S_i$  denotes the surface of the particle. The increase in drag coefficient


 Figure 12: Radial Reynolds stress as a function of  $r$  at  $t/\tau_L = 0.75, 1.5, 3.0$  and  $4.5$ .

signifies that the increase in particle forces is not merely an effect of an increased kinetic energy of the flow. Instead, the increase is a result of the increased Mach number, cf. fig. 7. This is consistent with findings in studies of single-particle drag as a function of Mach number [27, 28].

In contrast to the particle forces, the drag coefficient does not vary much with curvature radius. The minor variation is consistent with standard drag correlations, which predict decreasing  $C_D$  with increasing particle Reynolds numbers.

Compared to the isolated particle case, the average drag coefficients obtained here are significantly higher. This has also been observed in previous studies [16, 19]. These studies have shown that there is a wide distribution of drag coefficients, centered higher than isolated particle drag correlations predicts, for particle clouds consisting of randomly distributed particles. In addition to the Mach number effect, a likely contributing factor to this result is the flow blockage effects of nearby particles. Blockage effects have experimentally been shown to significantly increase drag for single particles in ducts [29, 30].

### 5.3 Velocity fluctuations

Figure 12 shows the radial component of the Reynolds stress. It can be seen that  $\tilde{R}_{rr}$  increases rapidly immediately behind the shock wave. While the shock wave is inside the particle layer, its peak value occurs a few particle diameters behind the shock wave. After

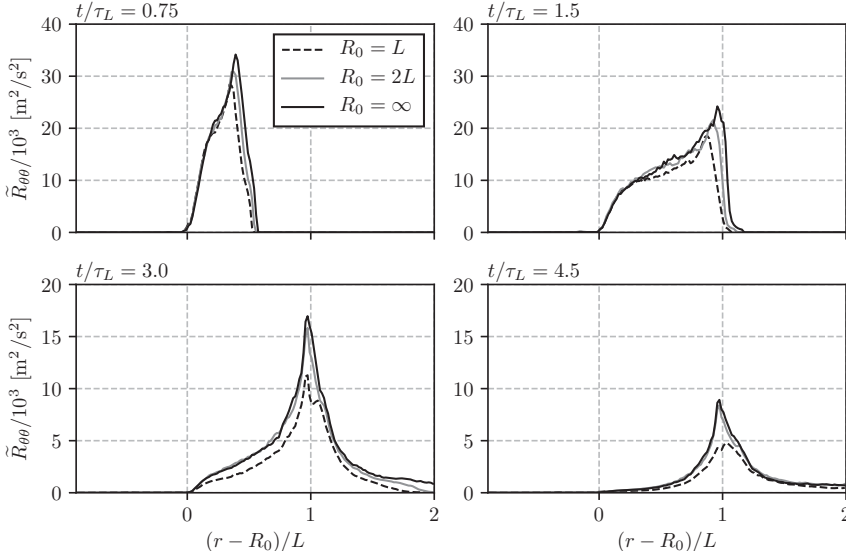


Figure 13: Azimuthal Reynolds stress as a function of  $r$  at  $t/\tau_L = 0.75, 1.5, 3.0$  and  $4.5$ . Note the difference in scaling of the vertical axis for the top and bottom.

the shock exits the layer, the peak value is at the downstream layer edge. The variation with curvature appears to only manifest in the magnitude of  $\tilde{R}_{rr}$  at  $t/\tau_L = 0.75$  and  $t/\tau_L = 1.5$ . At later times this is no longer the case. Two peaks can be seen for  $R_0 = L$  and  $R_0 = 2L$  at the two latest times. The second peak is the result of the standing shock wave at the end of the expansion. For  $R_0 = L$ , the two peaks merge because this shock wave is closer than one bin-length to the particle layer. The radial component of the Reynolds stress drops sharply over the downstream particle cloud edge. This is expected, because particle wakes is the primary source of  $\tilde{R}_{rr}$  in this problem. It does, however, not vanish completely as flow fluctuations are advected downstream from the cloud. Interestingly, apart from the previously mentioned shocks, the distribution seems to become more symmetric around the edge at late times.

We note that the magnitude of the streamwise Reynolds stress is significant. It corresponds to root-mean square velocity fluctuations of up to 50% of the local mean flow velocity. The relation between the mean flow velocity and radial velocity fluctuations will be further discussed below.

The azimuthal component of the Reynolds stress, seen in fig. 13, behaves in much the same way as  $\tilde{R}_{rr}$ . At  $t/\tau_L = 0.75$  and  $t/\tau_L = 1.5$ , it increases slower with downstream distance than the radial component. Its magnitude is about 50% of  $\tilde{R}_{rr}$ . Surprisingly, the azimuthal and axial (not shown) components of the Reynolds stress are almost indis-

tinguishable. This adds credibility to the claim that the majority of the fluctuations are pseudo-turbulent in nature and that the flow at the particle scale is largely unaffected by the expansion. This result is encouraging from a modeling perspective as it means that results obtained for planar configurations are likely to hold for curvature radii within the range considered here.

It has been observed that the correlation of streamwise velocity fluctuations (when the fluctuations are defined as deviations from volume averages) is approximately proportional to the square of the volume averaged velocity after the strong shock-induced transient has decayed [19]. It is interesting to investigate whether this also holds in the current configurations, which differs from the previous study both in domain geometry and initial conditions. The proportionality factor was defined as

$$\alpha_{\text{sep}} = \alpha \left(1 + \tilde{u}^2 / \tilde{R}_{rr}\right)^{-1}, \quad (10)$$

and is plotted in fig. 14. It can be seen that this factor varies only slightly with  $R_0$  at the two earliest times. The basis of the model is that the main flow effect that contributes to  $\tilde{R}_{rr}$  is the separated flow behind each particle, and  $\alpha_{\text{sep}}$  represents the volume fraction of separated flow. It is clear that this is not a reasonable assumption when the flow decelerates and eventually changes direction, because the particle wakes no longer have the simple behavior required by the model. This effect can be seen at  $t \geq 3\tau_L$ . It does however appear that as long as the velocity remains fairly high, the model is a decent approximation, cf.  $\alpha_{\text{sep}}$  at  $t/\tau_L = 3.0$  for  $R_0 = 2L$  and  $R_0 = \infty$ , and even at  $t/\tau_L = 4.5$  in the outer half of the particle layer.

The derivation of this model approximates the flow field as two different homogeneous regions. One region is the separated flow behind each particle, where the velocity is approximated as zero. The second region is the flow between particles, where the velocity is assumed to be constant. Improvements to the model can be obtained by analysis of the flow fields around each particle. Such studies could extend the model to include the effects of flow deflection and acceleration around particles, as well as particle volume fraction dependency and particle acceleration. These are topics for future works.

One of the appealing aspects of this Reynolds stress model is that it is easily applicable to simplified dispersed flow models. It is an algebraic fluctuation model, and thus computationally efficient. Beyond the direct addition of the Reynolds stress, the model also implies corrections to mean flow properties due to the non-negligible volume fraction of the separated flow, as well as the appropriate velocities for computing drag coefficients on the particles. For a more thorough discussion, consult [19].

## 5.4 Momentum balance

The time-dependence and radial distribution of flow statistics have been presented above. Here, the relative importance of the terms in the volume averaged momentum balance equation is investigated. Figure 15 shows the most important terms in the momentum balance as a function of time for the three curvature radii at  $r = R_0 + L/20$ . This

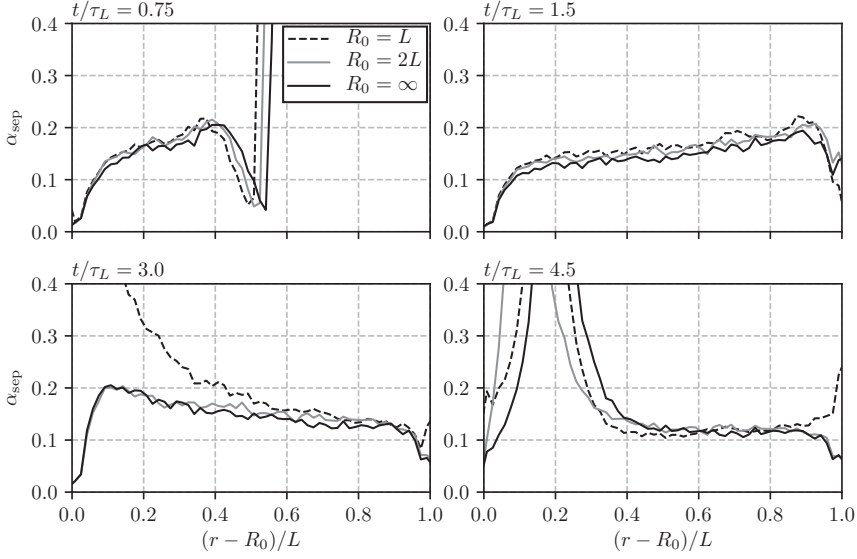


Figure 14: Separation volume as a function of  $r$  at  $t/\tau_L = 0.75, 1.5, 3.0$  and  $4.5$ .

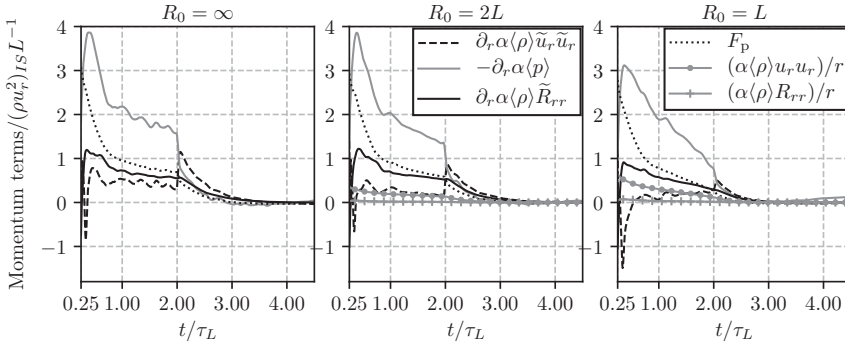


Figure 15: Main terms in the momentum balance close to the upstream edge of the particle cloud ( $r = R_0 + 0.05L$ ).

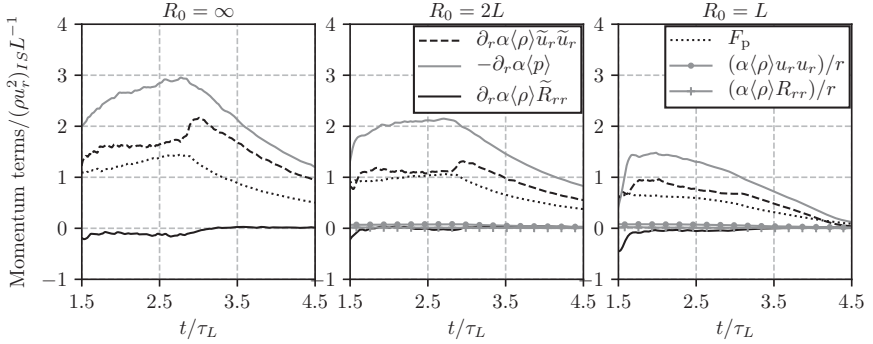


Figure 16: Main terms in the momentum balance close to the downstream edge of the particle cloud ( $r = R_0 + 0.95L$ ).

specific location is chosen for a reason: the momentum balance around the inner cloud boundary has a strong effect on the reflected shock wave. The strength of this shock determines the incoming flow which subsequently interacts with the particle cloud. Therefore, capturing this reflected shock wave correctly is essential for all simplified models for this problem.

It was shown in fig. 12 that around the inner particle cloud edge, the gradient of  $\tilde{R}_{rr}$  is initially sharp, and it is therefore likely to play an important role in the momentum balance. Figure 15 confirms that this is the case. For all radii of curvature,  $\partial_r \alpha \langle \rho \rangle \tilde{R}_{rr}$  is the same order of magnitude as the pressure force,  $F_p$ , acting on the particles. Both of these terms are at least 25% of the pressure gradient, which is the most dominant. The variation of the Reynolds stress gradient with curvature radius is insignificant. The advection term decreases in importance with decreasing curvature radius, but this effect is partially compensated for by its geometric expansion term. The results indicate that geometric expansion becomes important at small  $R_0$ , but does not cause any significant changes in flow fluctuations or particle forces.

It can be seen that for  $R_0 = \infty$  and  $R_0 = 2L$ , there is an abrupt change in the momentum balance around  $t/\tau_L = 2.0$ . The same phenomenon also occurs for  $R_0 = L$ , but the effect is much smaller. This time coincides with the arrival time of the reflected rarefaction, which initiates a strong flow deceleration. This mainly affects the advection term and the pressure gradient. The remaining terms have a delayed response to the deceleration.

Figure 16 shows the momentum balance close to the downstream cloud edge. Here, the Reynolds stress is not very important, but we note that this is very close to the peak Reynolds stress, and therefore the gradient is gentler at this point than further downstream. That the important terms in this region are the pressure gradient, the advection term and the particle forces. The order of importance of these terms is similar

for all  $R_0$ , and the geometric expansion terms are insignificant.

To complete this discussion, we note that within the interior of the particle cloud, the particle force is the dominant term. The Reynolds stress is non-negligible, but significantly less important than at the upstream cloud edge since its slope is gentler. The pressure gradient and advection terms remain important at all locations.

## 6 CONCLUDING REMARKS

The effect of geometric expansion on shock induced flow through stationary particle clouds has been investigated using viscous particle-resolved simulations in cylindrical domains with differing radii of curvature.

The main effect of the geometric expansion was found in the mean flow quantities. Density, velocity and pressure were significantly affected, which also translated to differences in the magnitudes of forces experienced by the particles. Analysis of the volume averaged momentum balance equations at the upstream particle cloud edge showed that the Reynolds stresses (products of velocity fluctuations) play an important role during the initial part of the flow. During this phase, the Reynolds stress contribution is of the same order as the pressure forces acting on the particles. This means that the Reynolds stresses cannot be ignored in simplified models of shock particle cloud interaction.

The flow fluctuations varied with curvature radius, but mainly due to differences in the mean fields with which they are interacting. This observation is supported by the fact that no significant difference in the axial and azimuthal components of the Reynolds stresses were observed. This indicates that the geometric expansion rates considered in this work are insufficient to affect the flow at the particle scale. It also supports the hypothesis that the primary contributions to velocity fluctuations are the pseudo turbulent structures at the particle scale.

We also examined whether the Reynolds stress model introduced in [19] holds for the present configurations. Indeed, a remarkable agreement was obtained for the regions where the mean velocity of the gas was substantial. From a modeling perspective, the results concerning the velocity fluctuations are encouraging because they indicate that results from planar geometries are likely to hold for diverging flows within the range considered here. Furthermore, the relatively simple correlation between mean flow and Reynolds stress is easy to transfer to simpler dispersed flow models.

Finally, the current results can be used to improve simplified models for shock wave particle cloud interaction. The data from resolved simulations allow comparison of flow fields within the particle cloud. The current data set includes stronger transient effects than e.g. the simulations in [19], and can therefore be used as a more challenging verification case for simplified models.



## REFERENCES

- [1] S. M. Bower and A. W. Woods, “On the dispersal of clasts from volcanic craters during small explosive eruptions,” *J. Volcanol. Geotherm. Res.*, vol. 73, no. 1-2, pp. 19–32, 1996.
- [2] K. Suzuki, H. Himeki, T. Watanuki, and T. Abe, “Experimental studies on characteristics of shock wave propagation through cylinder array,” tech. rep., The Institute of Space and Astronautical Science, 2000.
- [3] A. Chaudhuri, A. Hadjadj, O. Sadot, and G. Ben-Dor, “Numerical study of shock-wave mitigation through matrices of solid obstacles,” *Shock Waves*, vol. 23, no. 1, pp. 91–101, 2013.
- [4] D. W. Silvia, B. D. Smith, and J. M. Shull, “Numerical simulations of supernova dust destruction. II. Metal-enriched ejecta knots,” *Astrophys. J.*, vol. 748, no. 1, p. 12, 2012.
- [5] F. Zhang, S. Murray, and K. Gerrard, “Aluminum particles–air detonation at elevated pressures,” *Shock Waves*, vol. 15, no. 5, pp. 313–324, 2006.
- [6] F. Zhang, D. Frost, P. Thibault, and S. Murray, “Explosive dispersal of solid particles,” *Shock Waves*, vol. 10, no. 6, pp. 431–443, 2001.
- [7] A. Milne, C. Parrish, and I. Worland, “Dynamic fragmentation of blast mitigants,” *Shock Waves*, vol. 20, no. 1, pp. 41–51, 2010.
- [8] V. Rodriguez, R. Saurel, G. Jourdan, and L. Houas, “Impulsive dispersion of a granular layer by a weak blast wave,” *Shock Waves*, vol. 27, no. 2, pp. 187–198, 2017.
- [9] D. L. Frost, Y. Grégoire, O. Petel, S. Goroshin, and F. Zhang, “Particle jet formation during explosive dispersal of solid particles,” *Phys. Fluids*, vol. 24, no. 9, p. 091109, 2012.
- [10] V. Rodriguez, R. Saurel, G. Jourdan, and L. Houas, “External front instabilities induced by a shocked particle ring,” *Phys. Rev. E*, vol. 90, no. 4, p. 043013, 2014.
- [11] D. L. Frost, “Heterogeneous/particle-laden blast waves,” *Shock Waves*, vol. 28, pp. 439–449, May 2018.
- [12] T. G. Theofanous and C.-H. Chang, “The dynamics of dense particle clouds subjected to shock waves. Part 2. Modeling/numerical issues and the way forward,” *Int. J. Multiph. Flow*, vol. 89, pp. 177–206, 2017.

- [13] J. D. Regele, J. Rabinovitch, T. Colonius, and G. Blanquart, “Unsteady effects in dense, high speed, particle laden flows,” *Int. J. Multiph. Flow*, vol. 61, pp. 1–13, 2014.
- [14] Z. Hosseinzadeh-Nik, S. Subramaniam, and J. D. Regele, “Investigation and quantification of flow unsteadiness in shock-particle cloud interaction,” *Int. J. Multiph. Flow*, vol. 101, pp. 186–201, 2018.
- [15] O. Sen, N. J. Gaul, S. Davis, K. K. Choi, G. Jacobs, and H. S. Udaykumar, “Role of pseudo-turbulent stresses in shocked particle clouds and construction of surrogate models for closure,” *Shock Waves*, vol. 28, pp. 579–597, May 2018.
- [16] Y. Mehta, C. Neal, K. Salari, T. L. Jackson, S. Balachandar, and S. Thakur, “Propagation of a strong shock over a random bed of spherical particles,” *J. Fluid Mech.*, vol. 839, pp. 157–197, 2018.
- [17] T. G. Theofanous, V. Mitkin, and C.-H. Chang, “Shock dispersal of dilute particle clouds,” *J. Fluid Mech.*, vol. 841, pp. 732–745, 2018.
- [18] M. Vartdal and A. N. Osnes, “Using particle-resolved LES to improve Eulerian-Lagrangian modeling of shock wave particle cloud interaction,” in *Proceedings of the Summer Program 2018*, pp. 25–34, Center for Turbulence Research, Stanford University, 2018.
- [19] A. N. Osnes, M. Vartdal, M. G. Omang, and B. A. P. Reif, “Computational analysis of shock-induced flow through stationary particle clouds,” *Int. J. Multiph. Flow*, vol. 114, pp. 268 – 286, 2019.
- [20] J. D. Schwarzkopf and J. A. Horwitz, “BHR equations re-derived with immiscible particle effects,” tech. rep., Los Alamos National Laboratory, 2015.
- [21] G. S. Shallcross and J. Capecelatro, “A parametric study of particle-laden shock tubes using an Eulerian-Lagrangian framework,” in *2018 AIAA Aerospace Sciences Meeting*, p. 2080, 2018.
- [22] T. P. McGrath, J. G. S. Clair, and S. Balachandar, “A compressible two-phase model for dispersed particle flows with application from dense to dilute regimes,” *J. Appl. Phys.*, vol. 119, p. 174903, 2016.
- [23] R. Saurel, A. Chinnayya, and Q. Carmouze, “Modelling compressible dense and dilute two-phase flows,” *Phys. Fluids*, vol. 29, no. 6, p. 063301, 2017.
- [24] G. A. Bres, S. T. Bose, M. Emory, F. E. Ham, O. T. Schmidt, G. Rigas, and T. Colonius, “Large-Eddy Simulations of co-annular turbulent jet using a Voronoi-based mesh generation framework,” in *2018 AIAA/CEAS Aeroacoustics Conference*, p. 3302, 2018.

- [25] E. Tadmor, “Entropy stability theory for difference approximations of nonlinear conservation laws and related time-dependent problems,” *Acta. Numer.*, vol. 12, pp. 451–512, 2003.
- [26] P. Chandrashekar, “Kinetic energy preserving and entropy stable finite volume schemes for compressible Euler and Navier-stokes equations,” *Commun. Comput. Phys.*, vol. 14, no. 5, pp. 1252–1286, 2013.
- [27] A. Bailey and J. Hiatt, “Free-flight measurements of sphere drag at subsonic, transonic, supersonic, and hypersonic speeds for continuum, transition, and near-free-molecular flow conditions,” tech. rep., Arnold Engineering Development Center, 1971.
- [28] T. Nagata, T. Nonomura, S. Takahashi, Y. Mizuno, and K. Fukuda, “Investigation on subsonic to supersonic flow around a sphere at low Reynolds number of between 50 and 300 by direct numerical simulation,” *Phys. Fluids*, vol. 28, no. 5, p. 056101, 2016.
- [29] E. Achenbach, “The effects of surface roughness and tunnel blockage on the flow past spheres,” *J. Fluid Mech.*, vol. 65, no. 1, pp. 113–125, 1974.
- [30] S. Krishnan and A. Kaman, “Effect of blockage ratio on drag and heat transfer from a centrally located sphere in pipe flow,” *Eng. Appl. Comp. Fluid.*, vol. 4, no. 3, pp. 396–414, 2010.



## APPLICATION OF DIFFERENT RANS TURBULENCE MODELS FOR BREAKING WAVES PAST A VERTICAL CIRCULAR CYLINDER

Sen Qu<sup>1</sup>, Shengnan Liu<sup>2</sup> and Muk Chen Ong<sup>2</sup>

<sup>1</sup> College of Shipbuilding Engineering  
Harbin Engineering University, 150001, Harbin, China  
e-mail: qusen@hrbeu.edu.cn

<sup>2</sup> Department of Mechanical and Structural Engineering and Materials Science  
University of Stavanger, 4036 Stavanger, Norway  
e-mail: shengnan.liu@uis.no, muk.c.ong@uis.no

**Key words:** Breaking Wave; Turbulence Model; Vertical Cylinder; CFD; OpenFOAM.

**Abstract.** *In the present work, two turbulence models are evaluated for predicting the interaction of breaking waves with a vertical cylinder. The numerical simulations are conducted by solving the Reynolds-Averaged Navier-Stokes (RANS) equations using the open-source Computational Fluid Dynamic (CFD) software OpenFOAM. The Volume of Fluid (VOF) method is employed to capture the free surface. Grid and time-step refinement studies have been carried out. The numerical results are compared with the experimental data from Irschik et al. [1]. It is found that the  $k-\omega$  SST turbulence model [2] gives better predictions in term of wave elevation and wave force. The stabilized  $k-\omega$  SST turbulence model [3] gives a good prediction for the surface elevation; however, the predicted horizontal breaking wave force is smaller than the published experimental data.*

## 1. INTRODUCTION

The circular cylinder, as an elementary structure, is one of the most commonly used structures in the field of marine engineering. When the structure is installed in shallow water area, a large nonlinear breaking wave force will occur. It is of great importance to accurately predict breaking wave forces on structures for the design purpose. With the increase in computational capabilities, Computational Fluid Dynamics (CFD) based method by solving the Reynolds-Averaged Navier-Stokes (RANS) equations has become more and more popular in marine engineering. Xiao and Huang [4] employed the  $k-\varepsilon$  turbulence model with the Volume of Fluid (VOF) method to simulate solitary wave run-up and breaking wave force on a vertical cylinder located at different positions of a slope. The relative variation between the maximum numerical run-up height in vertical direction and experimental measurement was 1.96% and breaking wave force on the cylinder showed a satisfactory agreement with the experiment in the validation study. Kamath et al. [5] used the  $k-\omega$  turbulence model with the level set method to investigate the influences of breaking locations on the breaking wave forces on a vertical cylinder. In their study, the largest total horizontal wave force was observed when the overturning wave tongue was just below the wave crest level and impact the cylinder. Liu et al. [6] investigated breaking wave past a vertical cylinder using the  $k-\omega$  SST turbulence model in combination with the VOF method. Both the surface elevation and breaking wave force on the cylinder showed a good agreement with the experimental measurement.

However, one of the weaknesses of traditional two-equation turbulence models is that the turbulent kinetic energy (TKE) is generally over-estimated for the breaking wave, which will cause an under-prediction of the breaking wave elevation. Xie [7] investigated spilling and plunging breakers in the surf zone using  $k-\varepsilon$  turbulence model with the VOF method to capture the free surface. As compared to the experimental data, the numerical breaking wave heights were under-estimated in both spilling and plunging breakers. Devolder et al. [8] evaluated the performances of buoyancy-modified  $k-\omega$  and  $k-\omega$  SST turbulence model for both spilling and plunging breakers. They pointed out that the buoyancy-modified turbulence models significantly reduce the common over-estimation of TKE in the flow field and numerical results agreed well with the experimental data. Recently, in order to overcome the overprediction of turbulent kinetic energy, Larsen and Fuhrman [9] proposed a new formulation by a modification to the stress-limiting feature for the commonly used two-equation turbulence models. The new model gave a satisfactory prediction for the surface elevation, TKE, as well as undertow velocity.

To the authors' knowledge, evaluation of different turbulence models for simulating the breaking waves past a vertical cylinder has not been performed thoroughly. In this paper, the  $k-\omega$  SST [2], and stabilized  $k-\omega$  SST [3] turbulence models are selected to evaluate the performance of each for the surface elevations and horizontal breaking wave forces on the vertical cylinder. The air-water surface is captured by VOF method. The paper is organized as follows. First, the equations of two turbulence models are presented,

followed by the grid and time-step refinement studies. Then, the numerical results with different turbulence models are compared to the experimental measurements. Finally, the conclusions are drawn based on the present numerical results.

## 2. METHODOLOGY

### 2.1. Numerical model

The numerical simulations are conducted using OpenFOAM along with a wave generation toolbox waves2Foam developed by Jacobsen et al. [10]. The governing equations for the incompressible air and water phases are expressed as follows:

$$\frac{\partial u_i}{\partial t} + u_j \frac{\partial u_i}{\partial x_j} = -\frac{1}{\rho} \frac{\partial p}{\partial x_i} + \frac{\partial}{\partial x_j} \left[ (\nu + \nu_t) \left( \frac{\partial u_i}{\partial x_j} + \frac{\partial u_j}{\partial x_i} \right) \right] + g_i \quad (1)$$

$$\frac{\partial u_i}{\partial x_i} = 0 \quad (2)$$

where  $u_i$  are the Cartesian components of the velocity,  $\rho$  is the fluid density,  $p$  is the pressure,  $\nu$  is the kinematic viscosity,  $\nu_t$  is the turbulent kinematic viscosity and  $g_i$  is the acceleration due to gravity.

#### 2.1.1. The $k-\omega$ SST model

The  $k-\omega$  SST turbulence model was proposed by Menter [2] to effectively blend the  $k-\varepsilon$  turbulence model in the far field and  $k-\omega$  turbulence model in the near-wall region. It avoids the problem that the  $k-\omega$  turbulence model is very sensitive to the inlet free-stream turbulence properties. In addition, the  $k-\omega$  SST turbulence model provides good behavior in adverse pressure gradients and separation flow. Two advection-diffusion equations for turbulent kinetic energy  $k$  and turbulent characteristic frequency  $\omega$  are expressed as

$$\frac{\partial(\rho k)}{\partial t} + \frac{\partial(\rho k u_j)}{\partial x_j} = \frac{\partial}{\partial x_j} \left[ (\mu + \sigma_k \mu_t) \frac{\partial k}{\partial x_j} \right] + \rho P_k - \beta^* \rho \omega k \quad (3)$$

$$\frac{\partial(\rho \omega)}{\partial t} + \frac{\partial(\rho \omega u_j)}{\partial x_j} = \frac{\partial}{\partial x_j} \left[ (\mu + \sigma_\omega \mu_t) \frac{\partial \omega}{\partial x_j} \right] + \frac{\gamma}{\nu_t} \rho G - \beta \rho \omega^2 + 2(1 - F_1) \frac{\rho \sigma_{\omega 2}}{\omega} \frac{\partial k}{\partial x_j} \frac{\partial \omega}{\partial x_j} \quad (4)$$

The dynamic turbulent viscosity is calculated by

$$\mu_t = \frac{\rho a_1 k}{\max(a_1 \omega, SF_2)} \quad (5)$$

The details of model parameters definitions and coefficients can be found in Menter [2].

### 2.1.2. The stabilized $k-\omega$ SST model

Larsen et al. [3] proposed a stabilized  $k-\omega$  SST closure model recently, which added stress-limiting modifications to the  $k-\omega$  SST model. The aim of new turbulence model is to avoid non-physical exponential growth of the turbulent kinetic energy and eddy viscosity in the nearly potential flow region. The eddy viscosity is redefined according to

$$\nu_t = \frac{a_1 k}{\max \left( a_1 \omega, F_2 \sqrt{P_0}, a_1 \lambda_2 \frac{\beta}{\beta^* \alpha} \frac{P_0}{P_\Omega} \omega \right)} \quad (6)$$

where  $P_0 = 2S_{ij}S_{ij}$ ,  $P_\Omega = 2\Omega_j\Omega_j$ ,  $\lambda_2 = 0.05$ . The other parameters definitions are the same as the  $k-\omega$  SST [2] turbulence model.

### 2.2. Free surface capture

The free surface is captured by the VOF method [11]. The method is based on a volume fraction coefficient  $\alpha$ , which is 0 for air and 1 for water. The volume fraction is solved by following the advection equation:

$$\frac{\partial \alpha}{\partial t} + \frac{\partial (\alpha u_i)}{\partial x_i} - \frac{\partial [\alpha (1-\alpha) u_{ir}]}{\partial x_i} = 0 \quad (7)$$

where  $u_{ir}$  is the relative velocity between the water and the air. The density and kinematic viscosity at the interface are obtained by a weighted value based on the volume fraction coefficient  $\alpha$ .

$$\begin{cases} \rho = \alpha \rho_w + (1-\alpha) \rho_a \\ \nu = \alpha \nu_w + (1-\alpha) \nu_a \end{cases} \quad (8)$$

where  $\rho_w$  and  $\rho_a$  denote the densities of water and air;  $\nu_w$  and  $\nu_a$  are the kinematic viscosity coefficients of water and air.

### 2.3. Boundary conditions

The three-dimensional numerical wave tank (NWT) is 120.0 m long, 5 m wide and 8 m height, as shown in Fig.1. A cylinder with the diameter of  $D = 0.7$  m was installed with its central axis at the edge of the slope (1:10). The water depth in the NWT is fixed to  $d = 3.8$  m. Fifth-order Stokes wave with a wave height of  $H = 1.3$  m and wave period of  $T = 4.0$  s is generated. A wave gauge (WG) is set at near the wall along the frontline of the cylinder. At the inlet boundary, the velocity of water and phase fraction are given according to wave theory while the pressure is set to normal zero-gradient condition. At the outlet of domain, a Neumann condition is set for the pressure  $p$ ,  $k$ ,  $\varepsilon$  and  $\omega$ , and the



velocities of water and air are zero. The top boundary of the computational domain is set to a mixed Dirichlet-Neumann boundary condition for the velocity, pressure and volume fraction. The no-slip wall boundary condition is used at the front, back, bottom boundaries of NWT and the cylinder's surface. Meanwhile, wall functions are applied to capture the boundary layer characteristics. The dimensionless wall distance  $y^+$  for the present simulations is at the range of 45~200.

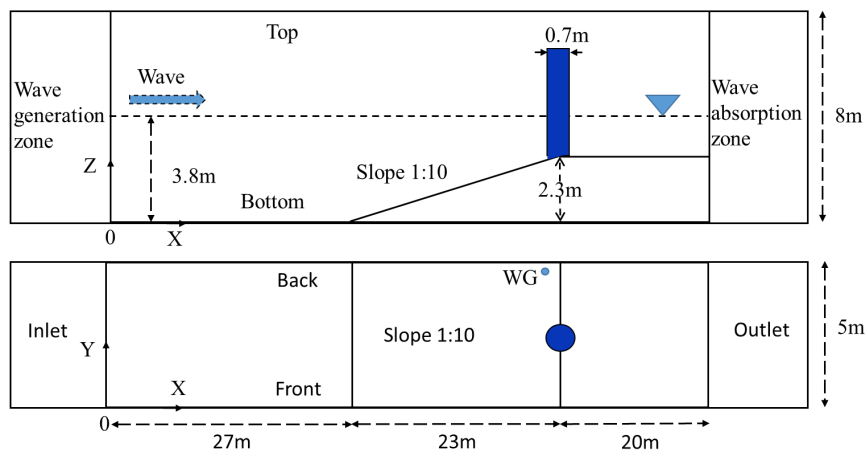


Fig. 1. Sketch of the numerical wave tank: front view (top); overlook view (bottom).

3. NUMERICAL IMPLEMENTATION

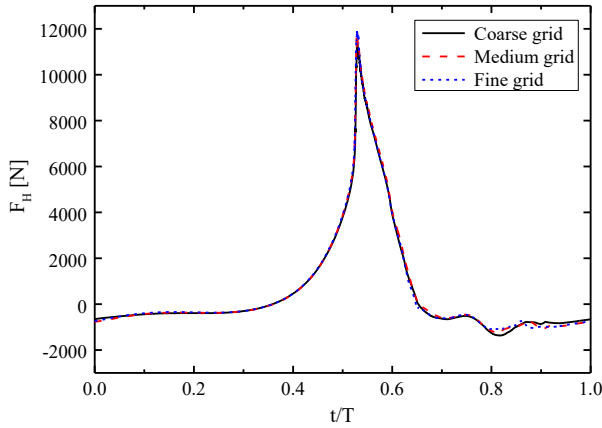
In the present simulations, both the wave generation zone and the absorption zone of NWT are one wavelength long. The Navier–Stokes equations are solved using the finite volume method. The PIMPLE algorithm is used for the pressure-velocity coupling. Second-order implicit Crank-Nicolson scheme is used for the time derivatives. The grid and time-step refinement studies are carried out by examining the total horizontal wave forces on the cylinder with  $k-\omega$  SST turbulence model. Three different meshes with refined areas in the vicinity of the cylinder and the free surface are shown in Table 1.

Table 1: The resolutions of three different grids

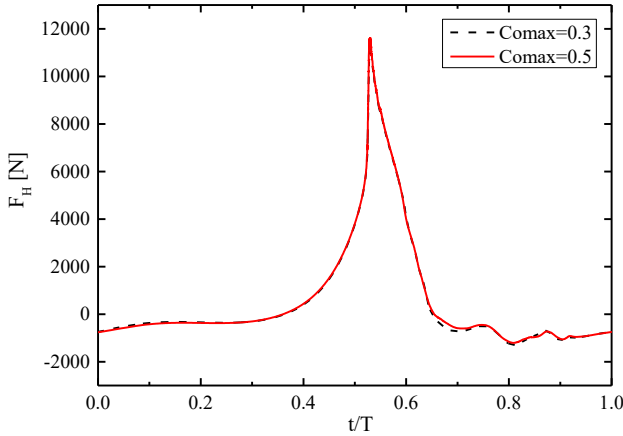
Grid	Coarse grid	Medium grid	Fine grid
Total number of cells	4791152	6371680	8564864

Figure 2 shows the horizontal breaking wave forces  $F_H$  on the cylinder with three different grid resolutions over one wave period. The relative variation of the peak

horizontal wave forces between medium grid and fine grid is 2.6%. Moreover, a time-step refinement study is also conducted by decreasing the maximum Courant number from 0.5 to 0.3. The relative variation of the peak horizontal breaking wave forces between two time-steps is 2.1% in Fig. 3. Therefore, the medium grid with the Courant number 0.5 is considered to give sufficient accuracy to capture the variation of horizontal wave forces on the cylinder and will be used for the present simulations.



**Fig. 2.** Horizontal wave forces on the cylinder with different grid resolutions.



**Fig. 3.** Horizontal wave forces on the cylinder with different Courant number.

## 4. RESULTS AND DISCUSSION

In this section, the characteristics of free surface elevations  $\eta$  and horizontal wave forces  $F_H$  on the cylinder are investigated using  $k-\omega$  SST and stabilized  $k-\omega$  SST turbulence models. Meanwhile, these two quantities are compared with the experimental data from Irschik et al. [1] to evaluate the performances of different models. All the present numerical simulations are conducted for a minimum duration of 140 s (35 wave periods), which ensures that the stable results can be obtained.

### 4.1. Free surface elevation

Figure 4 shows the comparison of surface elevations at WG (see Figure 1) between the numerical results with two turbulence models and experimental data [1]. The horizontal axis denotes the normalized time, where  $T$  is the incident wave period. It can be seen that the stabilized  $k-\omega$  SST turbulence model gives an accurate prediction at the peak of the wave elevation. However, it does not give sufficient accuracy for the wave elevation in the wave initiation and termination stages. The wave elevation calculated by the  $k-\omega$  SST turbulence model is in good agreement with the experimental data over one wave period. The relative different between the peak wave elevations of the numerical result and the experimental data is 1.9%.

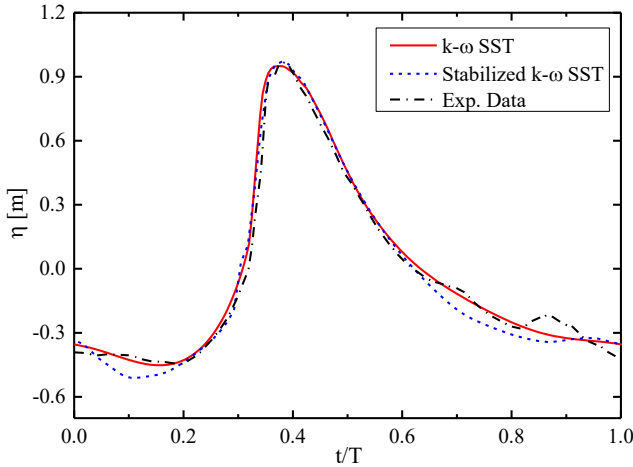
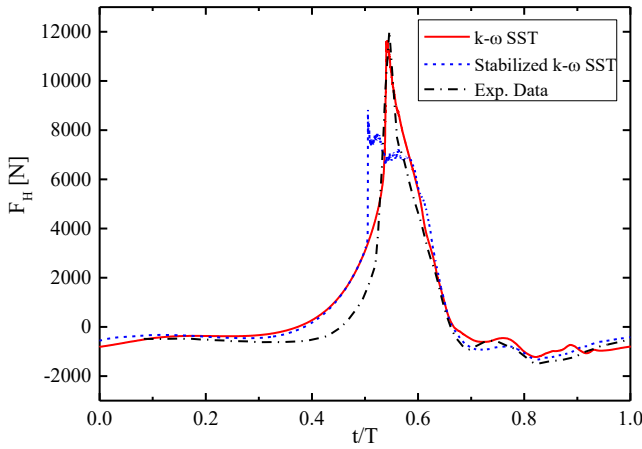


Fig. 4. Comparison of surface elevations between the numerical results and experimental data.

### 4.2. Breaking wave force on the cylinder

The horizontal breaking wave forces  $F_H$  on the cylinder using two turbulence models

are shown in Fig. 5. It clearly indicates that the breaking wave force predicted by the  $k-\omega$  SST turbulence model agrees best with the experimental data. The stabilized  $k-\omega$  SST turbulence model produce a lower value of wave forces as compared to the experimental data. In addition, the peak value of wave force on the cylinder predicted by the stabilized  $k-\omega$  SST turbulence model appears earlier than experimental measurement. The reason for this is that the stabilized  $k-\omega$  SST turbulence model modifies the turbulent kinetic energy and it is smaller than the other turbulence models. The energy is concentrated at the crest, which results in the wave crest to overturn prematurely and hit the cylinder. The details of the wave shapes can be seen in Fig. 6.



**Fig. 5.** Comparison of the horizontal breaking wave forces between the numerical results and experimental data

#### 4.3. The processes of breaking waves past a vertical cylinder

Figure 6 shows the variations of predicted the free surface shapes with the horizontal velocity using the two turbulence models at the middle transverse section of NWT. It clearly shows that the crest is almost vertical at time instant  $t/T=0.525$  using the  $k-\omega$  SST turbulence model. Meanwhile, the cylinder will subject to a large dynamic pressure. For the case of the stabilized  $k-\omega$  SST turbulence model, the wave already breaks before reaching the cylinder. The overturned wave tongue hits the cylinder and a smaller breaking wave force on the cylinder is obtained as compared with the experimental data.

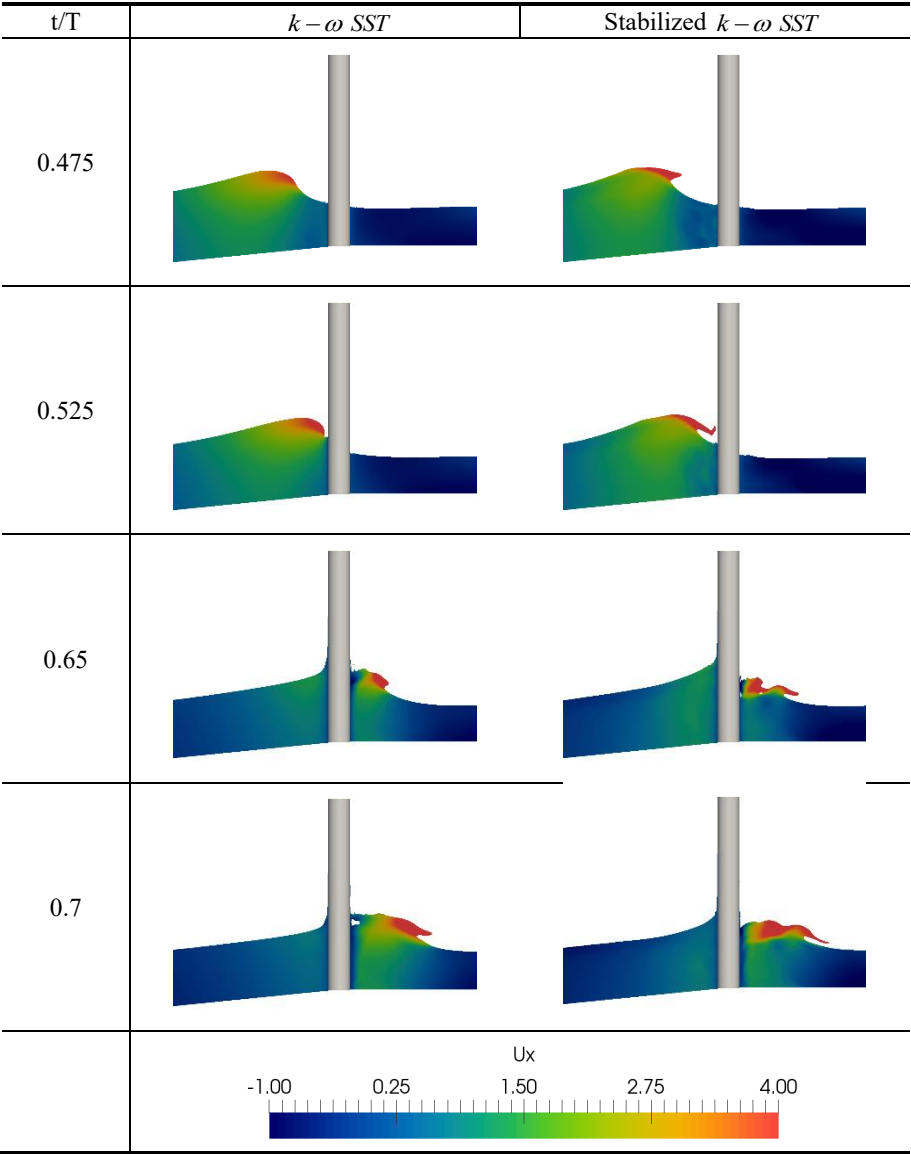


**Fig. 6.** Snapshots of the waves past the cylinder with the horizontal velocity magnitude contours at different time instants using different turbulence models.

## 5. CONCLUSIONS

In this paper, two different turbulence models have been evaluated for breaking wave past a vertical cylinder using OpenFOAM. The obtained numerical results of the surface elevations and breaking wave forces on the cylinder are compared to the experimental data. The main conclusions can be drawn from the present study:

- (1) The breaking wave force on the cylinder not only depends on the wave elevation but also on the wave shape, i.e., the extent of crest overturn, as well as the hitting degree between the wave crest and the cylinder.
- (2) The stabilized  $k-\omega$  SST turbulence model predicted the peak of wave elevation well. However, it caused the waves to overturn prematurely, resulting in smaller breaking wave force than the experimental value.
- (3) The  $k-\omega$  SST turbulence model shows a better agreement with the experimental measurement for the both wave elevation and wave force.

However, each RANS turbulence model has its own applicable scope, and there are also no available general guidelines on the application of turbulence model for free surface wave simulations. Therefore, different turbulence models can be chosen according to different research situations.

## ACKNOWLEDGMENTS

This study was supported in part with computational resources provided by the Norwegian Metacenter for Computational Science (NOTUR), under Project No: NN9372K.

## REFERENCES

- [1] Irschik, K. Breaking wave loads on a slender pile in shallow water. Proc., 29th Int. Conf. on Coastal Engineering. (2004) Vol. 2: 1778–1790.
- [2] Menter, F.R., Kuntz, M. and Langtry, R. Ten years of industrial experience with the SST turbulence model. In Proceedings of the fourth international symposium on turbulence, heat and mass transfer, Antalya, Turkey, (2003) 625–632.
- [3] Larsen, B. E., and Fuhrman, D. R. On the over-production of turbulence beneath surface waves in Reynolds-averaged Navier–Stokes models. Journal of Fluid Mechanics. (2018) 853, 419–460.
- [4] Xiao, H, and Huang, W. Three-Dimensional Numerical Modeling of Solitary Wave Breaking and Force on a Cylinder Pile in a Coastal Surf Zone. Journal of Engineering Mechanics. (2015) 141 (8), A4014001.
- [5] Kamath, A, Chella, M.A., Bihs, H., Arntsen, Ø.A. Breaking wave interaction with a vertical cylinder and the effect of breaker location. Ocean Engineering. (2016) 128, 105–115.
- [6] Liu, S., Jose, J., Ong, M.C., Gudmestad, O.T. Characteristics of higher-harmonic breaking wave forces and secondary load cycles on a single vertical circular

- cylinder at different Froude numbers. *Marine Structures*. (2019) 64, 54-77.
- [7] Xie, Z. Two-phase flow modelling of spilling and plunging breaking waves. *Appl. Math. Model.* (2013) 37, 3698–3713.
  - [8] Devolder, B., Troch, P., Rauwoens, P. Performance of a buoyancy-modified  $k-\omega$  and  $k-\omega$  SST turbulence model for simulating wave breaking under regular waves using OpenFOAM®. *Coastal Engineering*. (2018) 138, 49-65.
  - [9] Larsen, B. E., and Fuhrman, D. R. On the over-production of turbulence beneath surface waves in Reynolds-averaged Navier–Stokes models. *Journal of Fluid Mechanics*. (2018) 853, 419-460.
  - [10] Jacobsen, N.G., Fuhrman, D.R., Fredsøe, J. A wave generation toolbox for the open-source CFD library: OpenFoam®. *International Journal for Numerical Methods in Fluids*. (2012) 70 (9), 1073-1088.
  - [11] Hirt, C.W., Nichols, B.D. Volume of fluid (VOF) method for the dynamics of free boundaries. *Comput. Phys.* (1981) 39, 201–225.





# HIGH-RESOLUTION CFD MODELLING AND PREDICTION OF TERRAIN-INDUCED WIND SHEAR AND TURBULENCE FOR AVIATION SAFETY

Mandar V. Tabib<sup>1</sup> , Adil Rasheed<sup>1</sup> and Trond Kvamsdal<sup>1</sup>

<sup>1</sup>SINTEF Digital, Computational Science and Engineering group, Mathematics and  
Cybernetics, Klæbuvein 153, Trondheim, Norway.  
Email: mandar.tabib@sintef.no and adil.rasheed@sintef.no

**Key words:** Aviation safety, Terrain-induced turbulence, Atmospheric flow, Alert system

**Abstract.** The paper describes the ability of a high-resolution Computational Fluid Dynamics model to predict terrain-induced turbulence and wind shear close to the ground for aviation safety. The capabilities of the model are demonstrated by applying it to the Sandnessjøen Airport, Stokka, in Norway, an airport that is located in a mountainous area. The model is able to forecast turbulence in real time and trigger an alert when atmospheric conditions might result in high wind shear and turbulence. It is nested with two coarser grid mesoscale meteorological models, and constitute an hourly operational turbulence forecast system for 20 Norwegian airports at the time of writing.

## 1 INTRODUCTION

Atmospheric flows in mountainous regions are often characterized by high level of turbulence and wind shear. In the context of aviation science, wind shear refers to spatio-temporal variations of wind speed and direction experienced by an aircraft. The definition covers an extremely wide range of meteorological phenomena including jet streams, microbursts, gust fronts, internal gravity waves, vertical shears, hydraulic jumps, terrain effects, rotor formations etc. Presence of strong wind shear might result in a sudden gain or loss of altitude by the aircraft if the latter does not respond quick enough, resulting in passenger's discomfort and increased pilot's work load. Generally, such a change of altitude is compensated without any risk at higher altitudes when the pilot and the aircraft has enough time to execute corrective measures. However, situation can turn potentially hazardous when the aircraft is close to the ground in mountainous regions where strong wind shear almost always prevails. Every year a number of accidents and incidents linked to turbulence and wind shear are reported (<http://planecrashinfo.com>). It then goes without saying that an alarm system capable of predicting and identifying the zones of high wind shear and turbulence will be very much appreciated by the aviation community. In

fact several alarm systems are already in operation throughout the world. But generally these low level wind alert systems are based upon the hypothesis that the most hazardous flows are associated with relatively large coherent and deterministic structures. In fact several alarm systems are already in operation throughout the world. But generally these low level wind alert systems are based upon the hypothesis that the most hazardous flows are associated with relatively large coherent and deterministic structures. Such structures are commonly related to convective or gravity flows and classified as wind shear, gust fronts, thunderstorms and micro-bursts. It is implicitly understood that when the flow field is represented in terms of such structures, the number of degrees of freedom is so limited that a few local data can be interpreted rationally with respect to actual hazardous flying conditions. Alert systems based on this assumption are discussed by [1, 2, 3].

But in the context of present work when we talk about low level wind shear we are generally implying the shear existing due to terrain variations in the first couple of kilometers in the vertical direction, containing valleys and fjords (in a country like Norway). Such terrain induced flow variations include coherent flow structures that may be particularly hazardous to flying, such as recirculation, mountain waves, hydraulic transitions, rotors and vortices. These kind of flows are quite complicated and therefore cannot be represented efficiently by a few degrees of freedom. This may be illustrated by referring to experimental and numerical results for flow over and around a single model hill ([4] and [5]). A few local data alone will, in most cases, contain insufficient information about the local flow in a mountainous terrain. Hence, from aviation safety point of view, there are reasons to assume that a high resolution numerical wind and turbulence prediction system could be very useful along with the traditional alert systems in cases of mountainous terrain near airports.

In this paper we present the potential of an turbulence alarm system that has been developed in our group. We start with a brief description of the theories and equations that form the basis of the modeling code. Then we apply the model to a real site containing the Sandnessjøen Airport, Stokka, where the terrain variations are very sharp. We investigate some of the issues related to domain size, orientation, resolution, practicality of the work, and potential of the model to model main characteristics of flows in a complex terrain. A comparison of forecasts for one landing and one takeoff at Trondheim Airport, Værnes, with processed *Flight Data Recorder* (FDR) data is included, and finally, so is the communication of the results to pilots and the air traffic management.

## 2 Theory

### 2.1 Governing Equations

The general equations of motion for incompressible flow may be adapted to atmospheric flows by the use of so-called anelastic approximation. This formulation is often applied

in meteorological models, and may be written in the following conservative form :

$$\nabla \cdot (\rho_s \mathbf{u}) = 0 \quad (1)$$

$$\frac{D\mathbf{u}}{Dt} = -\nabla \left( \frac{p_d}{\rho_s} \right) + \mathbf{g} \frac{\theta_d}{\theta_s} + \frac{1}{\rho_s} \nabla \cdot \boldsymbol{\tau} + \mathbf{f} \quad (2)$$

$$\frac{D\theta}{Dt} = \nabla \cdot (\gamma \nabla \theta) + q \quad (3)$$

Here  $(\mathbf{u}, p, \theta, \rho)$  represent velocity, pressure, potential temperature and density, respectively. Furthermore,  $\boldsymbol{\tau}$  is the stress tensor,  $\mathbf{f}$  is a source term that may include rotational effects,  $\mathbf{g}$  is the gravitational acceleration,  $\gamma$  is the thermal diffusivity and  $q$  is the energy source term. Subscript  $s$  indicates hydrostatic values and subscript  $d$  the deviation between the actual value and its hydrostatic part, i.e.  $p = p_s + p_d$ ,  $\theta = \theta_s + \theta_d$ ,  $\rho = \rho_s + \rho_d$ , where the hydrostatic part is given by  $\partial p_s / \partial z = -g\rho_s$ . In addition, the following expression for hydrostatic density may be derived from the state equation and the definition of potential temperature:

$$\rho_s = \frac{p_s}{R\theta_s} \left( \frac{p_o}{p_s} \right)^{R/C_p} \quad (4)$$

where  $R$  is the gas constant and  $C_p$  is the specific heat at constant pressure. Hence, once the hydrostatic (potential) temperature profile is given, the hydrostatic pressure and density may be calculated, and then substituted into Equations 1 and 2.

It may be noted that the Boussinesq approximation is obtained from the system of Equations 1 and 2 by assuming constant values  $(\rho_o, \theta_o)$  instead of the hydrostatic values, and that formulation may well be used for incompressible flow and ordinary temperature.

The aim of the present study is to solve these equations for high Reynolds-number flows. For this purpose we apply an unsteady Reynolds-averaged modelling of the equation system, together with a turbulence model. Presently a standard high-Reynolds ( $k - \epsilon$ ) turbulence model is used for this purpose. With these assumptions the model equations take the following form:

$$\nabla \cdot (\rho_s \mathbf{u}) = 0 \quad (5)$$

$$\frac{D\mathbf{u}}{Dt} = -\nabla \left( \frac{p_d}{\rho_s} \right) + \mathbf{g} \frac{\theta_d}{\theta_s} + \frac{1}{\rho_s} \nabla \cdot \mathbf{R} + \mathbf{f} \quad (6)$$

$$\frac{D\theta}{Dt} = \nabla \cdot (\gamma_T \nabla \theta) + q \quad (7)$$

$$\frac{DK}{Dt} = \nabla \cdot (\nu_T \nabla K) + P_k + G_\theta - \epsilon \quad (8)$$

$$\frac{D\epsilon}{Dt} = \nabla \cdot \left( \frac{\nu_T}{\sigma_\epsilon} \nabla \epsilon \right) + (C_1 P_k + C_3 G_\theta) \frac{\epsilon}{k} - C_2 \frac{\epsilon^2}{k} \quad (9)$$

where turbulent viscosity is given by  $\nu_T = C_\nu \frac{k^2}{\epsilon}$ . The Reynolds stress tensor is given by

$$R_{ij} = \nu_T \left( \frac{\partial u_i}{\partial x_j} + \frac{\partial u_j}{\partial x_i} \right) - \frac{2}{3} k \delta_{ij} \quad (10)$$

while the eddy diffusivity appearing in the energy equation is  $\gamma_T = \nu_T / \sigma_T$ ,  $\sigma_T$  being the turbulent Prandtl number. The production and stratification terms in the turbulence model are given by

$$P_k = \nu_T \left( \frac{\partial u_i}{\partial x_j} + \frac{\partial u_j}{\partial x_i} \right) \frac{\partial u_i}{\partial x_j}, \quad G_\theta = -\frac{g}{\theta} \frac{\nu_T}{\sigma_T} \frac{\partial \theta}{\partial z} \quad (11)$$

Conventional constants for the high-Reynolds ( $k - \epsilon$ ) model are given by

$$(C_\nu, C_1, C_2, \sigma_\epsilon) = (0.09, 1.44, 1.92, 1.3) \quad (12)$$

The value for  $C_3$  is more uncertain. In the present study we assume  $C_3 G_\theta = \max(G_\theta, 0)$ , i.e.  $C_3 = 0$  in stably stratified flows, else  $C_3 = 1$ .

## 2.2 Safety Analysis

$F$ -factor or wind shear and turbulence represented by  $\epsilon^{1/3}$  given by Equations 13 and 14 are the two simplest meteorological variables considered most important for aviation safety.

$$F = -\frac{c}{g} \frac{\partial u}{\partial x} + \frac{w}{c} = -\frac{c}{g \ell_f} [u(x + \ell_f/2) - u(x - \ell_f/2)] + \frac{\bar{w}^{\ell_f}}{c} \quad (13)$$

$$\epsilon^{1/3} \approx \left( \frac{(C_\mu^{1/2} K)^{3/2}}{\ell_t} \right)^{1/3} \approx 0.67 K^{1/2} \ell_t^{-1/3} \quad (14)$$

Here  $c$  is the fly path,  $g$  is the acceleration due to gravity,  $u$  is the wind component along the fly path,  $w$  is the vertical wind component,  $\epsilon$  is the turbulent dissipation,  $K$  is turbulent kinetic energy,  $\ell_t$  turbulent length scale and  $\ell_f$  is the minimum response distance for landing configuration and is of the order of  $\sim 500$  m, which corresponds to a time interval of about  $t = O(7$  s). Averaging over this distance is indicated by the overline. Coefficient  $C_\mu$  is given by  $C_\mu \approx 0.09$ .

Prevalence of the two conditions  $F < -0.1$  and  $\epsilon^{1/3} > 0.5 \text{ m}^{2/3} \text{ s}^{-1}$  correspond to severe turbulence for commercial aircrafts and represent potential danger ([6]). These conditions are easily met when  $\sqrt{K} > 3.5 \text{ m s}^{-1}$ . We refer to this quantity as *turbulence intensity*  $u_t$ .

## 3 Results and discussion

### 3.1 Validation with Benchmark Bolund Hill

Bolund Hill [7] is considered a challenging validation case owing to its (a) geometric shape which features an sudden vertical escarpment with almost 90 degree crest (see

Figure 1) and owing to (b) abrupt change in terrain roughness (from a flat sea level to grass dominated land above the Bolund hill terrain). It has now become a popular benchmark with the modeling community to test their models as care has been taken by experimentalists to reduce the modelling input related uncertainty by quantifying the terrain roughness parameters used in describing the ground boundary condition in numerical models and by ensuring that the inflow neutral boundary condition do not change much for westerly wind as it is surrounded by sea-water with a long uniform fetch. Hence, the experimental velocity and turbulence data measured at a reference mast (located about one hill height upstream) can be specified as a model boundary condition. The high certainty in input values enables us to judge the performance of our computational model vis-a-vis other computational models and experiment.

The details of simulations and results are given below :

### **3.1.1 Bolund Terrain and Computational domain with measurements point location**

Bolund hill is a 12 m high peninsula located at Roskilde Fjord, 1 km north of Ris DTU as shown in Figure 1. The hill topography is approximately 130 m long and 75 m wide and it is surrounded by sea on all sides (assumed to have a constant sea-surface height of 0.75 m). This results in sharp change in surface roughness length ( $z_0$ ) at the point of transition from water ( $z_0 = 0.0003$  m) to grass ( $z_0 = 0.015$  m), which are used as inputs in the numerical model. The field experimental measurements were conducted here in 2007-2008 at various masts for four wind directions. The values of velocity components and turbulence at different heights along the masts were collected for validation of models. Figure 1 shows the location of four such measurement masts (M7,M6,M3,M8) for 270 degree wind direction and this data is used for validation in the work. The computational domain (figure 1) used for simulation has a size of 400 m (in stream-wise direction) x 270 m (in span-wise-direction) x 150 m (in vertical direction). The meshing details are given below :

### **3.1.2 Meshing Details**

Figure 2 shows the mesh used for simulation. The mesh is dominated by hexahedral cells and mesh size is 6.6 Million cells. The finest mesh size is the near the terrain surface ( about 0.0663 m mesh size). A refinement zone is used in the vicinity of terrain to capture terrain induced flows i.e. the flow separation at crest and at downstream end of hill. Using three different zones of different refinement levels, the mesh grid spacing is slowly increased away from terrain to reach 10 m grid resolution in upper regions of domain where the flow is expected to be uniform and without velocity gradients. The boundary conditions are given below next :

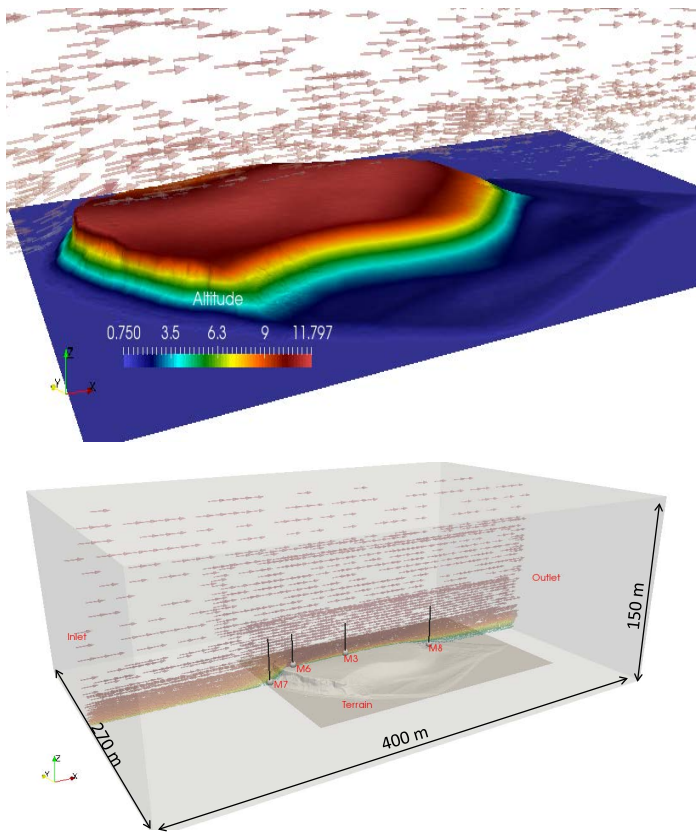


**Figure 1:** Terrain of Bolund and computational domain with measurement location

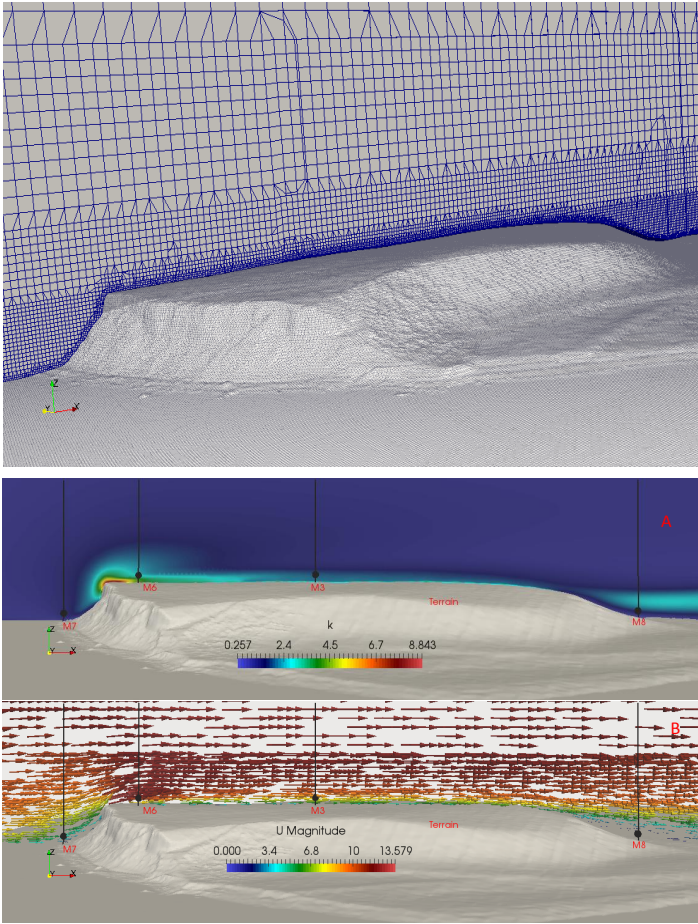


**Figure 2:** Mesh near terrain boundary, and, Results from simulations : contour of velocity and turbulent kinetic energy

### 3.1.3 Boundary conditions

A standard logarithmic atmospheric boundary velocity profile is used as the inlet velocity boundary condition and this fits the experimental data at Mast M0 (located 150m away from Bolund hill). The friction velocity used here is 0.4 for defining the input velocity profile. A constant turbulence value as suggested by experimental data is used. The ground condition involves no-slip boundary for velocity and use of wall function. The wall function uses the roughness values as suggested before. The side and top boundary conditions for the computational domain involve slip boundary condition.

### 3.1.4 Results - comparison between simulation and experiments

Figure 2(b) shows simulation predicted contours of turbulent kinetic energy (TKE) and velocity vectors along a plane across the terrain for 270 degree wind-direction. The vertical black lines in figure 2(b) are locations of masts (M7,M6,M3,M8) and the black spheres represents the measurement points which are located 2 m above the ground on these masts. Experimental data on velocity and turbulence are measured at these measurement points and are compared with simulation predicted results (see figure 3 and figure 3(b) for comparisons). The measurement locations are located so as to understand the complex physics and fluid dynamics and provide dataset for validation of numerical models. The measurement locations are : (a) Just upstream of steep escarpment of the Bolund hill (Measurement M7), (b) immediately downstream of steep 90 degree escarpment (Measurement M6) , (c) in middle of flatter terrain above hill (Measurement M3) and (d) immediately downstream of Bolund hill (Measurement M8). The regions of 90 degree escarpment and Bolund downhill are high turbulence regions (as seen in TKE contour of figure 2(b)-A top figure) with high velocity gradients (as seen in vector plot of figure 2(b)-B the bottom figure). The field experiments reveal that the 90 degree escarpment causes wind to increase suddenly and lead to flow separation at the crest edge (thus resulting in the high velocity gradients and turbulence), while as the Bolund hill slopes downward steeply at the end, the wind speeds-down and the resulting shear generates higher turbulence. The numerical model captures this trend in an expected manner (see figures 2(b) - 3). Numerical results (figure 2(b)) shows that : (a) at the M7 location (in hill upstream), there is not much turbulence and the boundary layer is attached to the ground, (b) at M6 location (downstream of escarpment) very high turbulence values and wind-speed up is seen (as compared to M7) which is owing to the separation at escarpment, (c) the flow attaches to the ground by the time it reaches the M3 location in the middle of the hill but the turbulence is still higher as compared to M7 location and (d) as the flow descends across the sharp slope, it detaches and creates a low velocity wake with high turbulence that can be seen near M8 location. These results can also be seen in figure 3(a) and figure 3(b), where the comparison is presented. Regarding results in comparison, for any RANS turbulence model to accurately capture the velocity magnitude and TKE values at M6 and M8 regions is a challenge due to the highly anisotropic nature of flow in these



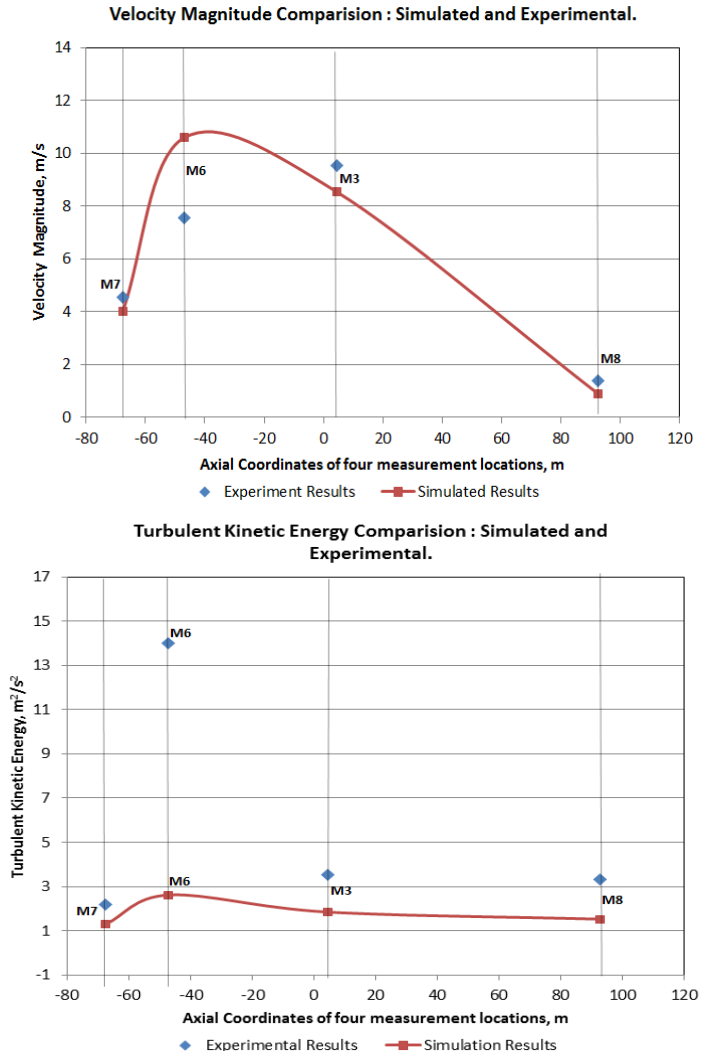


Figure 3: Comparison of velocity magnitude and turbulent kinetic energy.

regions (as seen in deviations predicted by various turbulence models for the Bolund hill in [7]). The current results should be seen in this context. In our case, the numerical model has been able to capture the velocity magnitude with around 10% deviation from the field experimental values at M3 and M7 locations while the deviations at M6 and M8 regions are in order of 30-40% (as seen in figure 3(a)). This is along expected lines for the RANS turbulence model as reported in [7]. For TKE, the simulations are consistently under predicting the turbulent kinetic energy with deviations of the order of 40-80% from experimentally measured value (as seen in figure 3(b)). This trend of under-prediction of TKE is consistent with that reported by other RANS models for Bolund hill ([7]) and the range of deviations are comparable with other numerical models.

#### **4 Sandnessjøen Airport : Model Verification for simulating a realistic condition involving the impact of terrain-induced turbulence on flight safety**

Sandnessjøen Airport, Stokka is a regional airport serving Sandnessjøen in Norway. The airport is operated by AVINOR and served by Widerøe with Dash 8 aircraft connecting the community to Bodø and Trondheim. The routes are operated on public service obligation with the Norwegian Ministry of Transport and Communication. The airport is located on a relatively flat area close to the sea with a runway oriented parallel to the shoreline. The nearby terrain on the east side is hilly with heights up to 100 – 150m. Further away in the E-SE sector, at a distance of about 5km, lays the rugged mountain chain named the *Seven Sisters*. This mountain chain where all the seven peaks rise up to a height of about 1000m above the sea level, offers ideal conditions for the generation of rotors, recirculation, flow separations and mountain waves.

On 15<sup>th</sup> September 2010, DHC-8-103B LW-WIF of Widerøe Flyveselskap was substantially damaged in a hard landing when the undercarriage collapsed. The aircraft was operating a domestic scheduled passenger flight from the Bodø Airport. Most of such incidents appear to be associated with the turbulence generated due to the presence of the Seven Sisters on the south-east side of the airport. The pilots operating at the airport report their experiences after the arrival. Based on the reports we found the following facts:

1. Moderate turbulence occurs frequently at Stokka for the south-easterly wind and the turbulence may be quite strong around 1000m above sea level for stronger wind fields.
2. The turbulence is damped significantly below 150m. Under these conditions the wind close to the ground is often changing rapidly and significantly, with low mean wind speed values, strong gusts, and variable wind direction.
3. Sometime it is difficult to choose the landing or takeoff direction due to the prevalence of tail winds on both the ends of the runway.

In the absence of detailed measurement data in this article, we rely solely on these observations. Here we want to evaluate the performance of the model in a realistic setup.

## 5 Simulation setup

Most of the pilot experiences reported in section 4 are related to the south-easterly wind. The orientation of the Seven Sisters mountain chain with respect to the runway, giving an impression that the south-easterly wind direction has the potential of creating the worst flight conditions. We therefore have chosen this wind direction for a detailed investigation presented in this work and for the optimization of the numerical simulation procedure. Best practice guidelines for CFD simulations give elaborate guidelines for conducting such simulations. However, most of those are applicable to very idealized cases of flow around an isolated hill, ridge or any other simplified flow obstacle. The requirements posed by the kind of realistic problem we deal with here hardly allows those guidelines to be followed by words. We have therefore, used reasonings and numerical experiments for the choice of domain size, its orientation, grid resolution and specification of boundary conditions, keeping in mind the computational constraints. We discuss each of these aspects in the following subsections.

### 5.1 Domain size and orientation

In the absence of any constraint one would like to have a domain as big as possible, but the limitation imposed by computational constraints (in a forecasting context) on the number of grid cells means that any expansion of the domain will come at the loss of grid resolution. In short, by increasing the domain size, one will be able to capture the large scale phenomena at the expense of under-resolution of the small scale ones. We therefore settled for a domain large enough to include the airport, mountain chain comprising of the Seven Sisters and the smaller chain of hills on the north-northwesterly side of the airport. This resulted in a domain of  $30km \times 30km$  with the airport occupying almost the central position as shown in Figure 4.

Any deviation from this size would result in the vertical boundary plane cutting the complex terrain, a situation we tried to avoid as it makes the specification of boundary conditions on the plane complicated. The domain was further rotated by an angle of 30 degrees in order to align the inlet plane of the domain normal to the wind direction. This is known to improve robustness, minimize numerical errors and speed up convergence of the solution.

### 5.2 Grid resolution

The importance of grid resolution is well known. Mesh resolution is critical to an accurate estimate of wind shear and turbulence intensity. In the code we have developed, the non-orthogonal terms in the discretized equations of turbulent kinetic energy and dissipation are ignored to make the solver fast and robust. In order to negate the

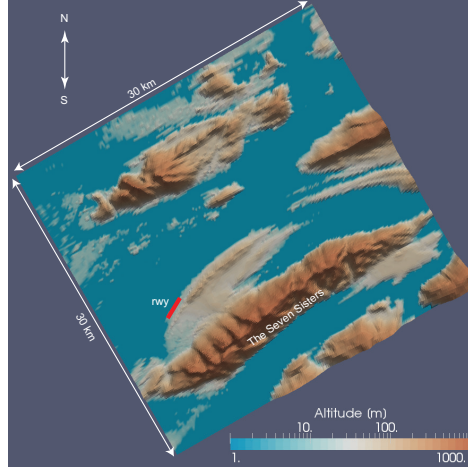


**Figure 4:** Terrain close to the airport in meters above sea level. Note that the legend is log-scaled.

effects of the approximation, mesh cells with mutually orthogonal faces are required. The orthogonality criteria close to the wall is satisfied by forcing the vertical lines to be incident normal to the ground surface. Away from the ground surface the imposition of orthogonality condition is trivial. The imposition of orthogonality helps in improving the mesh quality which results in lesser discretization error, increased robustness and faster solutions but at the same time, depending upon the complexity of the terrain, imposes a constrain on the finest achievable resolution. It is worth emphasizing here that although we are presenting off-line simulations in this article, the final goal is to reproduce similar results in real time. Hence, we conducted three simulations with different resolutions:  $71 \times 61 \times 41$ ,  $101 \times 97 \times 41$  and  $201 \times 191 \times 41$  with the grids stretching in the vertical direction in a geometric progression with a ratio of 1.02. A comparison of the turbulence intensity in the vertical direction at the middle of the runway and in the horizontal direction along the runway at a height of 100m above the ground is presented in the figure 5. It can be concluded from the figure that coarse mesh resolutions lead to under-prediction of turbulent intensity both the horizontal and vertical directions. Also the troughs and crests in the profile are closely related to the seven peaks of the Seven Sisters. This can be attributed either to the numerical errors associated with the discretization of the numerical equations or with the smoothening of the terrain due to its coarse representation. However, the difference in the predicted turbulence intensity by almost doubling the resolution from  $101 \times 97 \times 41$  to  $201 \times 191 \times 41$  is only about 5% while the computation time increases several times. This is critical to forecasting and hence the rest of the simulations presented here are with  $101 \times 97 \times 41$  grid points giving an average horizontal resolution

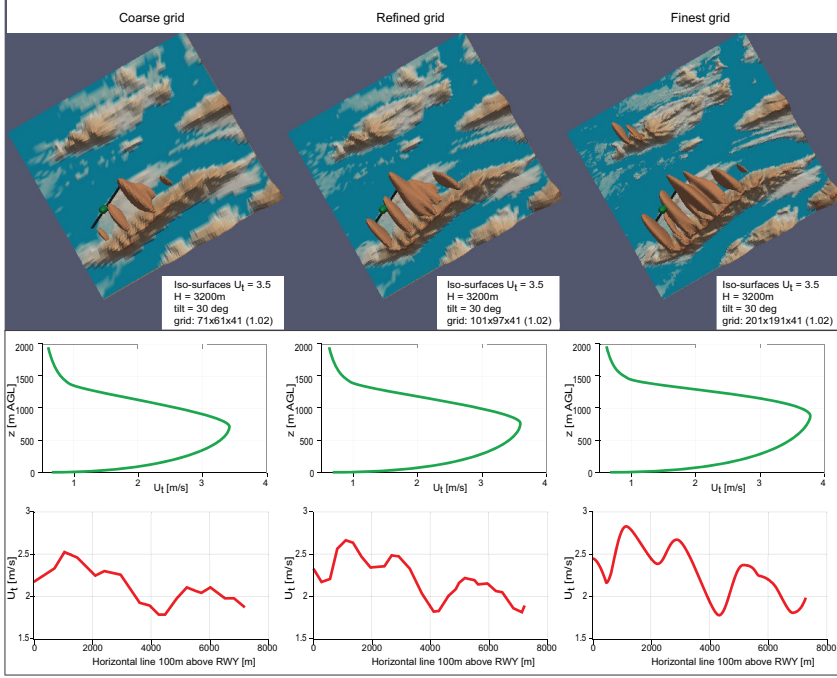


**Figure 5:** Effects of grid resolution on  $u_t$ . Uppermost row shows the 3D contour of  $u_t = 3.5$  for three different resolutions. Middle rows shows the vertical  $u_t$  profile at the middle of the runway. Lowermost row shows the  $u_t$  along a line passing through the runway.

of  $300m \times 300m$  which we think is a good trade-off between accuracy and computational time. A terrain adapted mesh is utilized giving a horizontal mesh resolution of  $30 - 100m$  in regions of steep terrain variations. Resolution of  $30m$  is also the resolution of the digital elevation data (Figure 4) that is being used. Any higher resolution simulation would require artificial interpolation of the terrain data which might not necessarily translate into the actual terrain. Also, in a complex terrain it is almost impossible to generate a mesh which accurately satisfies the  $y^+$  criteria imposed by the turbulence model ( $k - \epsilon$  in this case). The case of the airport under investigation is an extreme one with very steep terrain variations (more than  $45^\circ$ ). The choice was thus to either work with coarser mesh close to the ground or work with severely skewed mesh (which would break the assumption of orthogonal vertical lines) close to the ground. We chose the former option as it has the potential to reduce the simulation time considerably and increase robustness of the code.

### 5.3 Boundary conditions and influence of Froude Number

In a complicated mountainous terrain it is generally difficult to specify a realistic inlet profile. Therefore, a standard profile for wind speed and turbulent kinetic energy was used to specify the boundary conditions and initialize the domain. The profiles for the wind speed  $u(z)$ , the turbulent kinetic energy  $k(z)$  and dissipation of turbulent kinetic energy  $\epsilon(z)$  are given by

$$u(z) = \frac{u_*}{\kappa} \left( \ln \frac{z}{z_0} + W \left( \frac{z}{D} \right) \right) \quad (15)$$

$$k(z) = C_\mu^{-1/2} u_*^2 \left( 1 - \frac{z}{D} \right) \quad (16)$$

$$\epsilon(z) = C_\mu^{0.75} k(z)^{3/2} / \ell; \ell = \frac{\kappa z}{1 + 4z/D} \quad (17)$$

where  $u_*$ ,  $z_0$ ,  $z$  and  $D$  represent friction velocity, surface roughness, height above the ground surface and boundary layer thickness, respectively. The so-called wake function  $W$  is defined by the formula  $W(z/D) = (A - 1)(z/D) - A/2(z/D)^2$  such that  $W(1) = 1$ . The coefficients  $\kappa = 0.42$  and  $A = 4.0$ . Synoptic wind (mesoscale)  $U$  is given by  $U = u(D)$ . In the present simulations we have used  $(z_0, D, U) = (0.3 \text{ m}, 1500 \text{ m}, 20 \text{ m/s})$  such that the friction velocity  $u_* \approx 0.9 \text{ m/s}$  and wind speed  $10 \text{ m}$  above the ground is  $u_0 \approx 7.5 \text{ m/s}$ . A surface roughness value of  $0.001$  have been used for the sea surface. Along with the magnitude, direction of the synoptic wind is also specified. For a proper imposition of the inlet boundary condition give by equations 15 - 17 the vertical inlet plane should lie on the sea surface. Also a zero gradient boundary condition is applied at the exit boundaries which again requires that the vertical exit plane should lie on the sea surface for the satisfaction of the boundary conditions mathematically. These conditions are rarely satisfied in the case of flow in a complex terrain. Some researchers have resorted to using a periodic boundary condition for such simulations. This according to us is not correct physically hence, we have tried to place the boundary planes on the sea surface. By doing so we satisfy the boundary conditions accurately, but make a compromise with the placement of the inlet boundary closer to the Seven Sisters than is what is allowed by the best practice guidelines.

Atmospheric flows are significantly influenced by atmospheric stability and hence we did a test to evaluate the significance. We simulated the effects using a potential temperature profile corresponding to a stable stratification given by figure 6 which is typical in the region and gives a Froude number of 1 based on the free stream speed of  $20 \text{ m/s}$  and average mountain height of  $1000 \text{ m}$ .

### 5.4 Verifying pilot observations : Sensitivity analysis of Froude Number

Buoyancy perturbations develop when stably stratified air ( $d\theta/dz > 0$ ) ascends a steep mountain barrier. These perturbations often trigger disturbances that propagate away

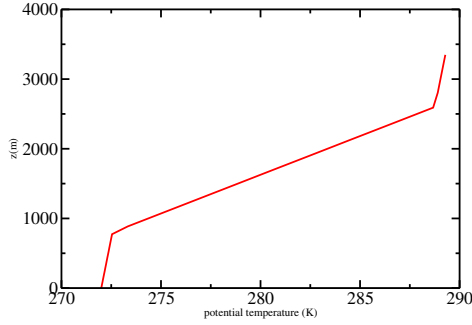


**Figure 6:** Vertical potential temperature profile used for simulations.

from the mountain as gravity (or buoyancy) waves. When these waves are triggered by the flow over a mountain, they are referred to as mountain waves. Large-amplitude mountain waves can generate regions of clear-air-turbulence that pose a hazard to aviation. A relevant non-dimensional number to characterize mountain waves is the Froude number defined as

$$Fr = \frac{U}{NL} \quad (18)$$

where  $U$  is a reference velocity and  $L$  a reference length.  $N$  is called the buoyancy frequency (also called the Brunt-Väisälä frequency) given by

$$N^2 = \frac{g}{\theta} \frac{d\theta}{dz} \quad (19)$$

The relevant quantities for mountain waves are the free stream wind velocity, vertical potential temperature profile and mountain width or height distributing the flow, or actually a natural length of the mountain(s) that can create an internal wave of wavelength  $2L$ . Mountain waves may occur if the actual Froude number is of the order of one,  $Fr = O(1)$ . A detailed behavior of these waves can be found in [8].

Simulations were also conducted for different Froude numbers by changing the free stream speed to see if the terrain induced flow structures could be modeled in a realistic terrain. The Froude number being a ratio of the inertial to buoyant forces is a good parameter to categorize the flow and predict the expected behavior. In the subsequent simulations we have used the boundary conditions given by equations 15 - 17.

Generally, the stable stratification significantly dampens the turbulence and prevents the formation of big rotors close to the foot hills. This "flows approaching the mountain range" can be interpreted in the light of the analogy of a moving ball as given by [9]. He concluded that an air parcel must overcome a gravity force to reach the crest of a mountain. The parcel might not ascend up to the top of a hill if it does not have enough kinetic energy or the height of the mountain is large. Relative to a neutral state, an approaching

fluid parcel must also overcome a potential energy deficit due to stratification. Blocking or stagnation and separation of the flow on the upwind side of a hill occurs when the air doesn't have enough energy to surmount the hill.

Four different simulations were conducted for  $Fr = 0.25, 0.5, 1, 1.5$ . Figure 7 show the evolution of flow in the vicinity of the Seven Sisters as a function of the  $Fr$  number.  $Fr = 0.25$  represents light wind and a stable atmosphere. This leads to the stagnation of air on the upwind side of the mountain chain. It shows the lateral movement of the flow at low  $Fr$  numbers.  $Fr = 0.5$  represents slightly faster winds and weaker stability. Air in such cases flows both around and over the mountain. The air that flows over is perturbed by the mountains to form lee waves above non-oscillating wind that flows around the hill. When  $Fr = 1$  most of the air flows over the hill and in the event of doing so, produces large amplitude lee waves and rotor circulations close to the ground on the lee side. When the  $Fr$  increases to 1.5, the winds are even stronger and the stability is relatively weaker. Boundary layer separation is observed on the lee-side of the hill, which creates a reversal of the surface flow close to the ground on the lee side. The formation of rotors and vertical perturbation of the flow on the leeward side results in strong wind shear consequently giving rise to shear generated turbulence close to the height of the mountain peaks. From the figures it is also easy to visualize the presence of three-dimensional eddies which are more pronounced at lower Froude numbers. At this point it is interesting to look at the figure 7 which presents the projection of the three-dimensional turbulence intensity field on a conical surface centered at the middle of the runway and containing the glide path of the aircrafts that operate in the region. The two dotted circles in each figure correspond to the altitudes of 400m and 800m above the sea level. For smaller  $Fr = 0.25$  corresponding to calm wind condition there is no zone of high turbulence intensity. Figure 7 further reveals low turbulence intensity below an altitude of 200m. However, at high wind speed (or  $Fr$  number), the rotors formed on the leewards side of the mountain gets stronger and stronger resulting in large wind shear at an altitude of 800m. The pilots report quote the zones close to an altitude of 1000m as the most turbulent zone. The streaks of high turbulence zone shown in the figure 7 is closely related to the seven peaks. It appears that flow accelerates in the gaps between the peaks resulting in horizontal wind shear in addition to the vertical wind shear resulting from the ascend and descend of the flow. These streaks at  $Fr = 1$  itself starts creating turbulent zones along the trajectory of the aircrafts.

## 6 Conclusion

In this article we have shown the capability of a high resolution CFD code to predict flow behavior in a complex terrain by validating it with both benchmark problem (Bolund Hill) and realistic turbulence alert system for Norwegian Airports. Several simulations for different Froude numbers were conducted and the flow characteristics were analyzed. Below we enumerate the most important findings from the study.



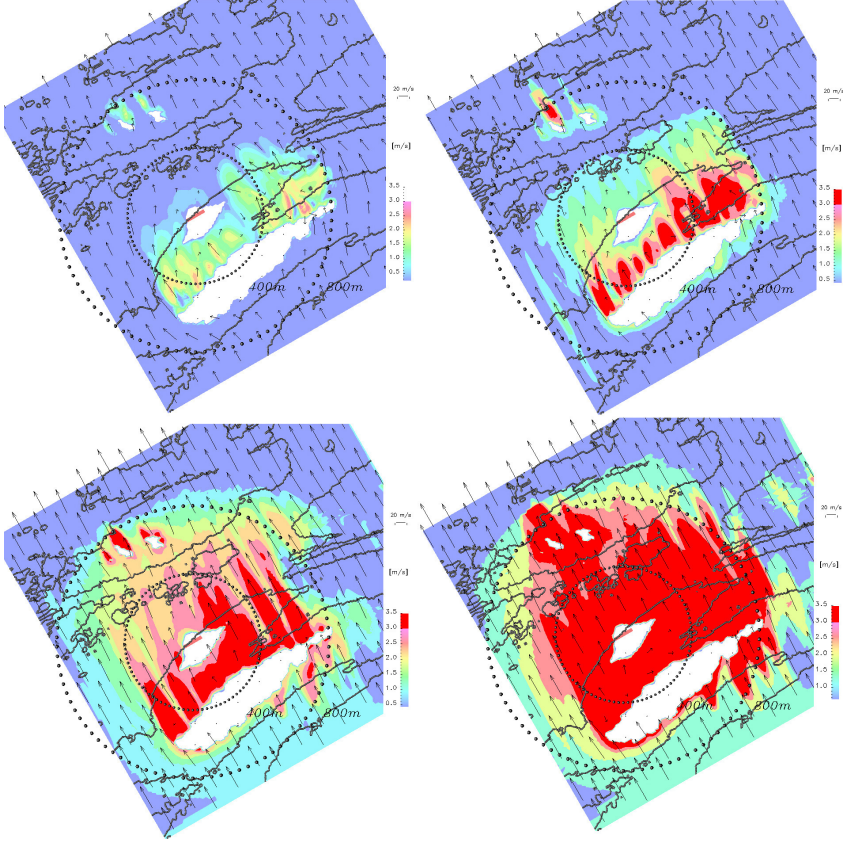


**Figure 7:**  $u_t$  contour on the conical section containing the glide path. Top-Left  $Fr = 0.25$ , Top-Right  $Fr = 0.5$ , Bottom-Left  $Fr = 1.0$ , Bottom-Right  $Fr = 1.5$ .

1. Confirmation of models ability to predict aviation safety : The pilots' reports of observing turbulence at Stokka Airport has been confirmed by the CFD model that captures the terrain-induced turbulence. The model has verified that the turbulent intensity can be very high for the south-easterly wind. The long streaks of high turbulence intensity intersect the gliding plane and can pose potential danger for aviation activities. It was also observed that for the south-easterly wind, flight operations can be quite dangerous when the free wind speed reaches about 20 – 30m/s, a value that is reached frequently.
2. Identification of high risk zones using the CFD model: The study resulted in ability of the model to identify zones where turbulence can be maximum. It was shown that a zone quite safe in a calm situation (low wind speed) can turn hazardous with increasing free stream speed.
3. At low wind speed the tendency of the flow to go around the mountain chain results in the propagation of tail winds at both the ends of the runway, a conclusion that is confirmed by the pilots reports.

Having concluded the above list, it is worth mentioning here that we have not accounted for the large scale phenomena which might also influence the flight conditions significantly. However, in the meteorological communities there are good mesoscale models existing which are more suited for the purpose. The model explained in this article, coupled with such a mesoscale model are complementary to each other, and it comprises a turbulence alert system for the aviation community. Such a system is presently undergoing a thorough validation process using data from Flight Data Recorders (FDR) as well as ground-based measurement data.

### Acknowledgement

We are thankful to AVINOR for funding the work done in this study. Also we are thankful to Erling Bergersen from AVINOR and Knut Helge Midtbø from the Norwegian Meteorological Office for their valuable inputs.

### REFERENCES

- [1] Sinclair, P.C. and Kuhn, M.P. *Aircraft Low Altitude Wind Shear Detection and Warning System*. Journal of Applied Meteorology. 1991. 30. 3-16.
- [2] Politovich, M.K. and Goodrich, R.K. and Morse, C.S. and Yates, A. and Barron, R. and Cohn, S.A. *The Juneau Terrain-Induced Turbulence Alert System*. Bull. Amer. Meteor. Soc. 2011. 92. 299-313.
- [3] Wai-Kin Wong and Cheong-Shing Lau and Pak-Wai Chan. *Aviation Model: A Fine-Scale Numerical Weather Prediction System for Aviation Applications at the Hong*

- Kong International Airport*. Advances in Meteorology, Hindawi Publishing Corporation. 2013. 11 pages.
- [4] Hunt J.C.R. and Snyder, W.H. *Experiments on Stably and Neutrally Stratified Flow over a Model Three Dimensional Hill*. Journal of Fluid Mechanics. 1980.96. 671-704.
  - [5] Utne, T. and Eidsvik, K.J. *Turbulent Flows over Mountainous Terrain Modelled by the Reynolds Equations*. Boundary-Layer Meteorology. 1997. 79.393-416.
  - [6] Clark, T.L. and Keller, T. and Coen, J. and Neille, P. and Hsu, H-M. and Hall, E.D. *Terrain-Induced Turbulence over Lantau Island: 7 June 1994 Tropical Storm Russ Case Study*. Journal of Atmospheric Science. 1997. 54. 1795-1814.
  - [7] Bechmann, A. and Berg, J. and Courtney, M. and Mann, J. and Sørensen, N.N. *The Bolund experiment, Part II: Blind Comparison of microscale models*. Boundary-Layer Meteorology. 2011. 141. 245-271.
  - [8] Doyle, J.D. and Durran, D.R. *The dynamics of Mountain-Wave-Induced Rotors*. Journal of Atmospheric Sciences. 2001. 59. 186-201.
  - [9] Sheppard, P.A. *Airflow over mountains*. Quarterly Journal of the Royal Meteorological Society. 1956. 82. 528-529.
  - [10] Roland L. Bowles and Bill K. Buck. *A Methodology for Determining Statistical Performance Compliance for Airborne Doppler Radar with Forward-Looking Turbulence Detection Capability*. NASA. 2009.
  - [11] Sharman, R. and Cornman, L.B. and Meymaris, G. and Pearson, J.M. and Farrar, T. *Description and derived climatologies of automated in situ eddy-dissipation-rate reports of atmospheric turbulence*. Journal of Applied Meteorology and Climatology. 2014. 53. 1416-1432.



## A SLENDER BODY MODEL FOR THIN RIGID FIBERS: VALIDATION AND COMPARISONS

Laurel Ohm<sup>1</sup>, Benjamin K. Tapley<sup>2</sup>, Helge I. Andersson<sup>3</sup>, Elena Celledoni<sup>2</sup>,  
and Brynjulf Owren<sup>2</sup>

<sup>1</sup> School of Mathematics, University of Minnesota, Minneapolis, MN 55455

<sup>2</sup> Department of Mathematical Sciences, The Norwegian University of Science and Technology,  
7491 Trondheim, Norway

<sup>3</sup> Department of Energy and Process Engineering, The Norwegian University of Science and  
Technology, 7491 Trondheim, Norway

**Key words:** Slender body theory; Multiphase flows; Fiber suspensions; Anisotropic particles

**Abstract.** In this paper we consider a computational model for the motion of thin, rigid fibers in viscous flows based on slender body theory. Slender body theory approximates the fluid velocity field about the fiber as the flow due to a distribution of singular solutions to the Stokes equations along the fiber centerline. The velocity of the fiber itself is often approximated by an asymptotic limit of this expression. Here we investigate the efficacy of simply evaluating the slender body velocity expression on a curve along the surface of the actual 3D fiber, rather than limiting to the fiber centerline. Doing so may yield an expression better suited for numerical simulation. We validate this model for two simple geometries, namely, thin ellipsoids and thin rings, and we compare the model to results in the literature for constant and shear flow. In the case of a fiber with straight centerline, the model coincides with the prolate spheroid model of Jeffery. For the thin torus, the computed force agrees with the asymptotically accurate values of Johnson and Wu and gives qualitatively similar dynamics to oblate spheroids of similar size and inertia.

### 1 Introduction

Understanding the dynamics of particles immersed in viscous fluids is of importance in many areas of nature and industry. The first problem one encounters when simulating the dynamics of particles with complicated shapes is determining an appropriate model. As the forces and torques of arbitrarily shaped particles are not known in general, one must make a number of assumptions on the particle size and shape to accurately and cheaply specify the forces and torques on the particle. If the particle length scale is small (for

example, smaller than the Kolmogorov scale in turbulent flows), the local fluid velocity can be accurately approximated by creeping Stokes flow and then the problem is amenable to a number of mathematical techniques that are available in the literature. One popular technique involves implementing slender body theories to model long and thin particles. An advantage of using slender body models is that they have the freedom to model flexible and arbitrarily shaped particles (with free ends or closed loops) provided that the particle is thin and the parametrization of centerline is known. The theoretical assumptions on which slender body models are based are also valid for long particles whose centerline lengths are comparable or extend beyond the limiting length scales of the fluid field. In particular, slender body theory has the potential to model particles that are longer than the Kolmogorov scale, where conventional models such as the Jeffery model for ellipsoids are not valid. This is a major advantage over current state-of-the-art particle simulations in, for example, [23, 30]. We also refer to [28] and references therein for a review of other available models and methodologies for treating anisotropic particles in turbulent flows.

In this article, we will consider a model based on slender body theory for rigid fibers that have either free ends or are closed loops. The purpose of this paper is primarily to provide a numerical validation of the proposed slender body model. For this reason, we will primarily focus on two simple geometries: long ellipsoids and thin rings (also referred to as thin tori). These geometries are chosen as there are verified ellipsoid and torus models available in the literature with well-studied dynamics, see for example [29, 23] for prolate ellipsoids and [15] for thin torus models. This will serve as grounding for future work that will focus on more interesting and complex particle shapes (e.g., helical particles, complex closed loops or very long particles) in more complex flows (e.g., 3D numerical turbulence) that can be approached with more advanced numerical methods [25, 26]. Such studies could impact our understanding of the transport and deposition of microplastics in the ocean, since a large percentage of these microplastics are thin fibers [20].

The slender body approximation expresses the fluid velocity away from the fiber centerline as an integral of singular solutions to the Stokes equations along the fiber centerline. As such, the approximation itself is singular along the fiber centerline, and there exist various methods to obtain a limiting integral expression for the velocity of the slender body itself [17, 16, 7]. For the purposes of particle simulations, we are primarily interested in solving for the forces and torques on the particle given a flow about the body. In the case of slender body theory, this involves inverting the limiting integral expression for the fiber velocity to find the force per unit length. Thus we need to be careful that the limiting expression is suitable for numerical inversion. In particular, we hope to avoid the high wavenumber instabilities that arise in some of the existing centerline expressions which require additional regularization to overcome. Often the methods for regularization lack a physical justification.

Here we consider approximating the fiber velocity by simply evaluating the slender body fluid velocity expression on a curve along the actual slender body surface, away from the

fiber centerline. Numerical evidence suggests that this method does not require further regularization to yield an invertible matrix equation for any discretization level or fiber centerline shape. We also show that our model agrees well with exact or asymptotically accurate expressions for the forces and torques on fibers with simple geometries in simple flows.

The next section presents the mathematical theory for the slender body formalism, as well as a brief review of rigid body mechanics and spheroidal particle models. Section 3 is dedicated to numerical experiments, and the final section is for conclusions.

## 2 Particle modeling

We begin by reviewing the rigid body dynamics that are relevant to particle modeling. The theoretical basis for the slender body model is then presented for rigid free ended fibers and rigid closed loops. Finally, we present the Jeffery model for torques on an ellipsoid, which is used for comparison purposes.

### 2.1 Dynamics

The angular momentum  $\mathbf{m}$  of a rigid particle with torque  $\mathbf{N}$  is governed by the ordinary differential equation

$$\dot{\mathbf{m}} = \mathbf{m} \times \boldsymbol{\omega} + \mathbf{N}, \quad (1)$$

where  $\boldsymbol{\omega} = J^{-1}\mathbf{m}$  is the angular velocity and  $J$  is the diagonal moment of inertia tensor. All the above quantities are given in the particle frame of reference. The particle orientation (with respect to a fixed inertial frame of reference) is specified using Euler parameters  $q \in \mathbb{R}^4$  which satisfy the constraint  $\|q\|_2 = 1$  and are determined by solving the ODE

$$\dot{q} = \frac{1}{2}q \cdot w,$$

where  $w = (0, \boldsymbol{\omega}^T)^T \in \mathbb{R}^4$  and  $\cdot$  here denotes the Hamilton product of two quaternions [10]. A vector in the particle reference frame  $\mathbf{x}_p$  can be rotated to a vector in an inertial co-translating reference frame  $\mathbf{x}_T = Q\mathbf{x}_p$  where  $Q$  is the rotation matrix that is the image of  $q$  under the Euler-Rodriguez map. We refer the reader to [10] for details on quaternion algebra and rigid body mechanics.

### 2.2 Slender body theory

We begin by describing the slender body geometries that will be considered in the free end and closed loop settings. To condense notation, we will use  $\mathcal{I}$  to denote the interval  $[-1/2, 1/2]$  in the free end setting and the unit circle  $\mathbb{T} = \mathbb{R}/\mathbb{Z}$  in the closed loop setting. We take  $\mathbf{X} : \mathcal{I} \rightarrow \mathbb{R}^3$  to be the coordinates of an open or closed non-self-intersecting  $C^2$  curve in  $\mathbb{R}^3$ , parameterized by arclength  $s$ . We let  $\mathbf{e}_s(s) = \frac{d\mathbf{X}}{ds}$  denote the unit tangent vector to  $\mathbf{X}(s)$ . The curve  $\mathbf{X}(s)$  will be the centerline of the slender body, and we assume that all cross sections of the slender body are circular.

Let  $0 < \epsilon \ll 1$ . In the closed loop setting, we consider fibers with uniform radius  $\epsilon$  on each cross section. In the free end setting, we consider the actual endpoints of the fiber to be  $\pm\sqrt{1/4 + \epsilon^2}$  rather than  $\pm 1/2$ , and define a *radius function*  $r \in C^2(-\sqrt{1/4 + \epsilon^2}, \sqrt{1/4 + \epsilon^2})$  such that  $0 < r(s) \leq 1$  for each  $s \in [-1/2, 1/2]$ , and  $r(s)$  decays smoothly to zero at the fiber endpoints  $\pm\sqrt{1/4 + \epsilon^2}$ . We will mostly be concerned with the prolate spheroid, for which we have

$$r(s) = \frac{1}{(\frac{1}{4} + \epsilon^2)^{1/2}} \left( \frac{1}{4} + \epsilon^2 - s^2 \right)^{1/2}. \quad (2)$$

Notice that the interval  $[-1/2, 1/2]$  extends from focus to focus of this prolate spheroid, and that  $r = \mathcal{O}(\epsilon)$  at  $s = \pm\frac{1}{2}$  (see figure 1). In numerical applications, we will also briefly consider the case of a free end fiber with uniform radius (except for hemispherical caps at the fiber endpoints – see section 3.2), but we note that the slender body approximation is better suited for the prolate spheroid. Throughout this paper, for the sake of conciseness, we will often write one expression to encompass both the free end and closed loop settings, in which case we note that in the closed loop setting we define  $r(s) = 1$  for each  $s \in \mathbb{T}$ .

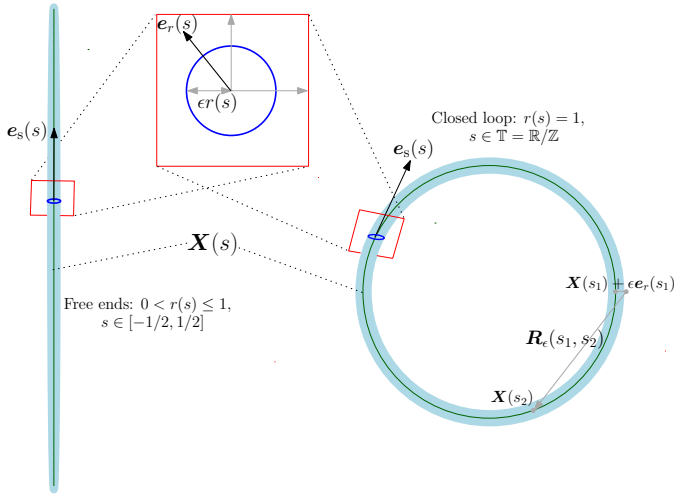


Figure 1: A depiction of the geometries under consideration in the free end and closed loop settings.

The idea behind slender body theory is to approximate the fluid velocity about the fiber as the Stokes flow due to a one-dimensional curve of point forces in  $\mathbb{R}^3$ . The basic theory



originated with Hancock [12], Cox [8], and Batchelor [2] with later improvements by Keller and Rubinow [16] and Johnson [14]. Here we will consider specifically the slender body theory of Johnson, which was further studied by Götz [11] and Tornberg and Shelley [27]. Let  $\mathbf{u}_0(\mathbf{x}, t)$  denote the (known) velocity of the fluid in the absence of the fiber at time  $t$ , and let  $\mu$  denote the viscosity of the fluid. The classical slender body approximation  $\mathbf{u}^{\text{SB}}(\mathbf{x}, t)$  to the fluid velocity at any point  $\mathbf{x}$  away from the fiber centerline  $\mathbf{X}(s, t)$  is then given by

$$8\pi\mu(\mathbf{u}^{\text{SB}}(\mathbf{x}, t) - \mathbf{u}_0(\mathbf{x}, t)) = - \int_{\mathcal{I}} \left( \mathcal{S}(\mathbf{R}) + \frac{\epsilon^2 r^2(s')}{2} \mathcal{D}(\mathbf{R}) \right) \mathbf{f}(s', t) ds', \quad \mathbf{R} = \mathbf{x} - \mathbf{X}(s', t);$$

$$\mathcal{S}(\mathbf{R}) = \frac{\mathbf{I}}{|\mathbf{R}|} + \frac{\mathbf{R}\mathbf{R}^T}{|\mathbf{R}|^3}, \quad \mathcal{D}(\mathbf{R}) = \frac{\mathbf{I}}{|\mathbf{R}|^3} - \frac{3\mathbf{R}\mathbf{R}^T}{|\mathbf{R}|^5}. \quad (3)$$

Here  $\frac{1}{8\pi\mu}\mathcal{S}(\mathbf{R})$  is the Stokeslet, the free space Green's function for the Stokes equations in  $\mathbb{R}^3$ , and  $\frac{1}{8\pi\mu}\mathcal{D}(\mathbf{R}) = \frac{1}{16\pi\mu}\Delta\mathcal{S}(\mathbf{R})$  is the doublet, a higher order correction to the velocity approximation. The force density  $\mathbf{f}(s, t)$  is here considered as the force per unit length exerted by the fluid on the body. The sign convention is opposite if we instead consider  $\mathbf{f}$  to be the force exerted by the body on the fluid. Note that in the free end case, this force density is only distributed between the generalized foci of the slender body ( $s = \pm 1/2$ ) rather than between the actual endpoints of the fiber.

In the stationary setting, Mori et al. in [21] (closed loop case) and [22] (free end case) prove a rigorous error bound for the difference between the velocity field given by (3) and the velocity field around a three-dimensional flexible rod satisfying a well-posed *slender body PDE*. In particular, for the closed loop, given a force density  $\mathbf{f} \in C^1(\mathbb{T})$ , the difference between  $\mathbf{u}^{\text{SB}}$  and the PDE solution exterior to the slender body is bounded by an expression proportional to  $\epsilon |\log \epsilon|$ . In the free end case, given a force density  $\mathbf{f} \in C^1(-1/2, 1/2)$  which decays like a spheroid at the fiber endpoints ( $\mathbf{f}(s) \sim \sqrt{1/4 - s^2}$  as  $s \rightarrow \pm 1/2$ ), the difference between the free end slender body approximation  $\mathbf{u}^{\text{SB}}$  and the well-posed PDE solution of [22] is similarly bounded by an expression proportional to  $\epsilon |\log \epsilon|$ . Thus the Stokeslet/doublet expression (3) is quantitatively a good approximation of the flow field around a slender body.

To approximate the velocity of the slender body itself, we would like to use (3) to obtain an expression for the relative velocity of the fiber centerline  $\frac{\partial \mathbf{X}(s, t)}{\partial t}$  depending only on the arclength parameter  $s$  and time  $t$ . In the case of a rigid fiber, given the velocity  $\frac{\partial \mathbf{X}(s, t)}{\partial t} = \mathbf{v} + \boldsymbol{\omega} \times \mathbf{X}(s, t)$ ,  $\mathbf{v}, \boldsymbol{\omega} \in \mathbb{R}^3$ , of the filament centerline, we would like to then be able to invert the centerline velocity expression to solve for the force density  $\mathbf{f}(s, t)$  along the fiber. We use this  $\mathbf{f}(s, t)$  to compute the total force  $\mathbf{F}(t)$  and torque  $\mathbf{N}(t)$  exerted on the body as

$$\int_{\mathcal{I}} \mathbf{f}(s, t) ds = \mathbf{F}(t), \quad \int_{\mathcal{I}} \mathbf{X}(s, t) \times \mathbf{f}(s, t) ds = \mathbf{N}(t).$$

Since the expression (3) is singular at  $\mathbf{x} = \mathbf{X}(s, t)$ , deriving a limiting expression for the fiber centerline must be done carefully. There are various ways to use (3) to obtain a centerline expression depending on  $s$  only, including the methods of Lighthill [17], Keller and Rubinow [16], and the method of regularized Stokeslets [3, 6, 7]. Each method expresses the velocity of the slender body centerline  $\frac{\partial \mathbf{X}(s, t)}{\partial t}$  as an integral operator acting on the force density  $\mathbf{f}(s, t)$ . A brief overview of these methods is given in appendix A.

Because solving for the force density  $\mathbf{f}(s, t)$  given  $\frac{\partial \mathbf{X}(s, t)}{\partial t}$  involves inverting an integral operator at each time step, we need to take particular care that the operator – at least when discretized – is suitable for inversion. In particular, we need to avoid the high wavenumber instabilities that limit discretization of the integral operator and hinder some of the asymptotic methods described in appendix A. At the same time, we would like the centerline expression to have a clear physical meaning and connection to the Stokeslet/doublet expression (3).

Thus we will use the following expression to approximate the velocity  $\frac{\partial \mathbf{X}(s, t)}{\partial t}$  of the slender body itself. Taking  $\mathbf{e}_r(s, t)$  to be a particular unit vector normal to  $\mathbf{X}(s, t)$  (we will discuss the choice of  $\mathbf{e}_r$  later), we essentially evaluate (3) at  $\mathbf{x} = \mathbf{X}(s, t) + \epsilon r(s) \mathbf{e}_r(s, t)$ , a curve along the actual surface of the slender body. For  $\mathcal{S}, \mathcal{D}$  as in (3), we have

$$8\pi\mu \left( \frac{\partial \mathbf{X}}{\partial t} - \mathbf{u}_0(\mathbf{X}(s, t), t) \right) = - \int_{\mathcal{I}} \left( \mathcal{S}_\epsilon(s, s', t) + \frac{\epsilon^2 r^2(s')}{2} \mathcal{D}_\epsilon(s, s', t) \right) \mathbf{f}(s', t) ds'; \quad (4)$$

$$\mathcal{S}_\epsilon = \mathcal{S}(\mathbf{R}_\epsilon(s, s', t)) - \frac{\epsilon^2 r^2 \mathbf{e}_r \mathbf{e}_r^T}{|\mathbf{R}_\epsilon(s, s', t)|^3}, \quad \mathcal{D}_\epsilon = \mathcal{D}(\mathbf{R}_\epsilon(s, s', t)) + \frac{3\epsilon^2 r^2 \mathbf{e}_r \mathbf{e}_r^T}{|\mathbf{R}_\epsilon(s, s', t)|^5},$$

$$\mathbf{R}_\epsilon(s, s', t) = \mathbf{X}(s, t) - \mathbf{X}(s', t) + \epsilon r(s) \mathbf{e}_r(s, t).$$

Here we are relying on the fact that for any point  $\mathbf{x}$  on the actual fiber surface, the expression (3) for  $\mathbf{u}^{\text{SB}}(\mathbf{x})$  is designed to depend only on arclength  $s$  to leading order in  $\epsilon$  – in particular, on each cross section of the slender body, the angular dependence about the fiber centerline is only  $\mathcal{O}(\epsilon \log \epsilon)$  (see [21], proposition 3.9, and [22], proposition 3.11). This is because the leading order angular-dependent terms (the  $\epsilon^2 r^2 \mathbf{e}_r \mathbf{e}_r^T$  term in both the Stokeslet and the doublet, which is  $\mathcal{O}(1)$  at  $s = s'$ ) cancel each other asymptotically to order  $\epsilon \log(\epsilon)$  (see estimates 3.62 and 3.65 in [21] and estimates 3.40 and 3.43 in [22]). We therefore eliminate these two terms from the formulation (4), in part due to this cancellation and in part because their omission appears to improve the stability of the discretized integral operator (4) when  $n$ , the number of discretization points, is large. This apparent improvement in stability merits further study in future work.

Thus to approximate the velocity of the fiber centerline, we evaluate (3) on the actual slender body surface along a normal vector  $\mathbf{e}_r(s, t) \in C^2(\mathcal{I})$  extending from  $\mathbf{X}(s, t)$  but cancel the  $\epsilon^2 r^2 \mathbf{e}_r \mathbf{e}_r^T$  terms that would otherwise appear. Note that the choice of normal vector  $\mathbf{e}_r$  is somewhat arbitrary, and does have an  $\mathcal{O}(\epsilon \log \epsilon)$  effect on the resulting approximation. These effects can and should be studied further in future work. However, we use this normal vector as a physically meaningful means of avoiding the high wavenumber

instabilities that appear in other asymptotic methods (see appendix A). Numerical evidence suggests that the discretized centerline equation (4) yields a matrix equation that is solvable for  $\mathbf{f}(s, t)$  given  $\frac{\partial \mathbf{X}(s, t)}{\partial t}$ , as all eigenvalues of the matrix are positive even for very large  $n$ . This is not necessarily the case for some of the other centerline equations (again, see appendix A) unless additional regularizations are added, which may affect the physical meaning of the equations. The possibility of resolving very fine scales along the length of the fiber is desirable especially when dealing with turbulent flows.

### 2.3 Spheroid model

The above slender body model is valid for arbitrary parameterizations of the centerline  $\mathbf{X}(s, t)$  and a wide choice of radius functions. However, to validate the model we will focus on a simple case where the centerline is a straight line and the radius function corresponds to an ellipsoid. In this case the torques have a known expression due to Jeffery [13] and the motion of such a particle in simple flows is well-known [4, 19] which makes this choice of geometry a perfect arena for model validation. We will now briefly review some theory related to spheroids immersed in viscous fluids.

An axisymmetric spheroid in the particle frame is given by

$$\frac{x^2}{a^2} + \frac{y^2}{a^2} + \frac{z^2}{b^2} = 1,$$

where  $a$  and  $b$  are the distinct semi-axis lengths. The particle shape is characterized by the dimensionless aspect ratio  $\lambda = b/a > 0$ , which distinguishes between spherical ( $\lambda = 1$ ), prolate ( $\lambda > 1$ ) and oblate ( $\lambda < 1$ ) particles (the latter two shapes are also called as rods and disks). In the case of a slender prolate spheroid, we take  $a = \epsilon$ . The axisymmetric moment of inertia tensor for a spheroid in the body frame is

$$\mathbf{J} = ma^2 \text{diag} \left( \frac{(1 + \lambda^2)}{5}, \frac{(1 + \lambda^2)}{5}, \frac{2}{5} \right),$$

where  $m = \frac{4}{3}\pi\lambda a^3\rho_p$  is the particle mass and  $\rho_p$  is the particle density. Jeffery [13] calculated the torque  $\mathbf{N}$  of an ellipsoid in creeping Stokes flow, which in the above axisymmetric case reads

$$\begin{aligned} N_x &= \frac{16\pi\lambda\mu a^3}{3(\beta_0 + \lambda^2\gamma_0)} \left[ (1 - \lambda^2)S_{yz} + (1 + \lambda^2)(\Omega_x - \omega_x) \right], \\ N_y &= \frac{16\pi\lambda\mu a^3}{3(\alpha_0 + \lambda^2\gamma_0)} \left[ (\lambda^2 - 1)S_{zx} + (1 + \lambda^2)(\Omega_y - \omega_y) \right], \\ N_z &= \frac{32\pi\lambda\mu a^3}{3(\alpha_0 + \beta_0)} (\Omega_z - \omega_z), \end{aligned} \tag{5}$$

where  $S_{ij} = \frac{1}{2} \left( \frac{\partial u_i}{\partial x_j} + \frac{\partial u_j}{\partial x_i} \right)$  is the fluid shear tensor and  $\boldsymbol{\Omega} = \frac{1}{2} \nabla \times \mathbf{u}$  is the fluid rotation, both taking constant values in shear flow. The values  $\alpha_0$ ,  $\beta_0$  and  $\gamma_0$  are  $\lambda$ -dependent parameters that were calculated in [9].

There are a number of distinctions to make between this model and the slender body model. First, Jeffery assumes that the particle is small enough that the fluid Jacobian  $\nabla \mathbf{u}$  is constant across the volume of the spheroid. In shear flow,  $\nabla \mathbf{u}$  is constant everywhere, hence this assumption is true and the model validity is independent of the size of the particle. However, in more complex flows such as turbulence, the Jeffery model is only valid for  $a, b \ll \eta$  for Kolmogorov length  $\eta$ . On the other hand, the slender model requires only that the maximal cross sectional radius  $\epsilon \ll \eta$  to be valid. Hence, the slender body model is valid for particles with lengths larger than  $\eta$  whilst satisfying the Stokes flow assumptions. Second, the Jeffery torque depends on the fluid velocity derivatives only, while the slender body model derives the torques from the velocity field along the centerline. Because of this, we cannot expect the models to coincide when the particle is aligned exactly in the shear plane (i.e., the plane where  $\mathbf{u} = \mathbf{0}$  but  $\frac{\partial u_j}{\partial x_i} \neq 0$ ).

### 3 Numerical experiments

This section presents numerical results for the slender body model and comparisons with other similar models. We begin with a validation of the slender body expression (4) by comparing the total force  $\mathbf{F}$  given by inverting (4) for a stationary slender body velocity with the exact expression for the Stokes drag on a particular object (when available) or with an expression valid asymptotically as  $\epsilon \rightarrow 0$ . We consider the slender prolate spheroid (section 3.2; exact expression given by Chwang and Wu [5]), the straight, uniform cylinder with hemispherical endpoints (section 3.2; asymptotic expression given by Keller and Rubinow [16]), and the slender torus (section 3.3; asymptotic expression given by Johnson and Wu [15]). In each case we expect  $\mathcal{O}(\epsilon \log \epsilon)$  agreement between the force  $\mathbf{F}$  computed using (4) and the exact or asymptotically accurate expressions; however, we find that this trend is clearly visible only in the closed loop setting. We then examine the rotational dynamics of a prolate spheroid in shear flow using expression (4) and compare it with the Jeffery model for ellipsoids [13]. We look at the dynamics of the two models for a range of aspect ratios and orientations and then explore the effect of the discretization parameter on the periodic Jeffery orbits. We finally compare the dynamics of thin rings to oblate spheroids for a range of fluid viscosities.

#### 3.1 Computational considerations

In many applications, one needs to simulate the dynamics of thousands or millions of particles; hence computational cost plays a role in determining the model choice. One thing to consider is that the slender body model involves inverting a  $3n \times 3n$  matrix at each time step, where  $n$  is the user-defined discretization parameter that arises from discretizing the integral in equation (4). On the other hand, the Jeffery model requires an accurate approximation of the fluid Jacobian at the location of the particle center of mass, while the slender body model only requires the fluid velocity values at the  $n$  locations on its centerline. When the fluid velocity is defined at discrete locations in space, such

as in direct numerical simulations of turbulent flows, the Jeffery model is faced with the problem of approximating the fluid Jacobian at the location of the particle center of mass, which is more costly than just interpolating the velocity field. In practice, however, one should use the Jeffery model when computing dynamics of small, thin ellipsoids when possible and the slender body model for more complicated shapes or longer particles. As the purpose of this article is focused on the theoretical and numerical validation of the slender body model, computational cost and numerical methods will be left for future work.

### 3.2 Free ended fibers in constant flow

We validate the free end formulation of (4) in the case of a slender body with straight centerline  $\mathbf{X}(s) = s\mathbf{e}_x$ ,  $s \in [-1/2, 1/2]$ , aligned with the  $x$ -axis. Here we will consider both the slender prolate spheroid with radius function  $r(s)$  as in (2) and a slender cylinder with hemispherical caps at the fiber endpoints. In both cases, we take the actual filament length to be  $2\sqrt{1/4 + \epsilon^2}$ , but distribute the force density  $\mathbf{f}(s)$  only along  $[-1/2, 1/2]$ . As in the closed loop setting, we use (4) to calculate the drag force  $\mathbf{F}$  on the slender body as it translates with unit speed, and compare this  $\mathbf{F}$  to either exact or asymptotically accurate expressions for the Stokes drag on a prolate spheroid or cylinder. In both cases we will use the unit normal vector  $\mathbf{e}_r(s) = \cos(2\pi s)\mathbf{e}_y + \sin(2\pi s)\mathbf{e}_z$ , which rotates once in the  $yz$ -plane perpendicular to  $\mathbf{X}(s) = s\mathbf{e}_x$  for  $s \in [-1/2, 1/2]$ . This normal vector is chosen because it represents a sort of average normal direction along the length of the filament.

In the free end setting, we also need to make sure that the computed force density  $\mathbf{f}(s)$  is decaying sufficiently rapidly at the fiber endpoints to ensure that the solution makes sense physically. The inclusion of the decaying radius function  $r(s)$  in the slender body velocity expression (4) ensures this decay by making the integral kernel very large near the fiber endpoints.

In the case of a prolate spheroid, we can actually compare the total force  $\mathbf{F}$  given by (4) to the analytical expression for Stokes drag on a spheroid calculated by Chwang and Wu [5] (see table 1). We consider the drag force on a slender prolate spheroid translating with unit speed in either the  $y$ -direction (perpendicular to the semi-major axis) or the  $x$ -direction (parallel to the semi-major axis). In all cases, the integral term of (4) is discretized using the trapezoidal rule with uniform discretization along the filament centerline. We use  $n = 2/\epsilon$  discretization points.

We also look at a plot of the computed force per unit length  $\mathbf{f}(s)$  along the filament (figure 2) to verify that the force density makes sense physically.

From figure 2, we can see that the force density  $\mathbf{f}(s)$  decays rapidly as  $s \rightarrow \pm 1/2$ , but does not vanish identically at  $|s| = 1/2$ . However, it should be noted that in [22], we are given the force density  $\mathbf{f}(s)$ ,  $s \in [-1/2, 1/2]$ , and use it to solve for the corresponding slender body velocity. In that case, the force must vanish identically at  $\pm 1/2$  to yield a unique velocity. Since in this case we are using the fiber velocity to solve for the force

$\epsilon$	$\mathbf{F} \cdot \mathbf{e}_y$ for $\mathbf{u} = \mathbf{e}_y$		$\mathbf{F} \cdot \mathbf{e}_x$ for $\mathbf{u} = \mathbf{e}_x$		$\epsilon  \log \epsilon $
	Expression (4)	Chwang-Wu	Expression (4)	Chwang-Wu	
0.01	-2.4498	-2.4618	-1.5245	-1.5302	0.0461
0.005	-2.1579	-2.1673	-1.3051	-1.3094	0.0265
0.0025	-1.9281	-1.9358	-1.1408	-1.1442	0.0150
0.00125	-1.7426	-1.7491	-1.0133	-1.0159	0.0084

Table 1: Comparison of the computed (via expression (4)) and exact (from Chwang and Wu [5]) Stokes drag force  $\mathbf{F}$  on a slender prolate spheroid of length  $2\sqrt{1/4 + \epsilon^2}$  with semi-major axis aligned with the  $x$ -axis. Columns 2 and 3 compare the  $y$ -component of  $\mathbf{F}$  for a spheroid translating with unit speed in the  $y$ -direction, while columns 4 and 5 compare the  $x$ -component of  $\mathbf{F}$  for translation in the  $x$ -direction. Note that for both directions, the force difference decreases with  $\epsilon$ , but not quite at the expected  $\epsilon \log \epsilon$  rate.

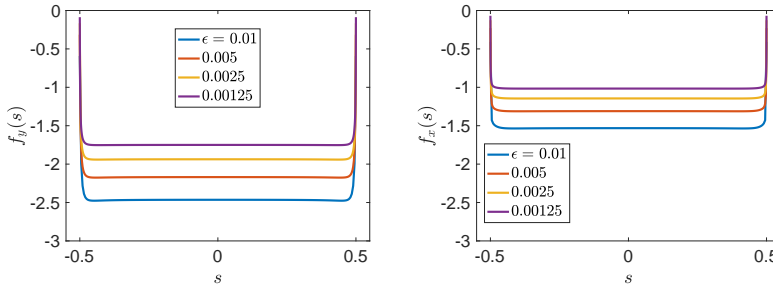


Figure 2: Force per unit length  $\mathbf{f}(s)$ ,  $s \in [-1/2, 1/2]$ , along the prolate spheroid with semi-major axis aligned with the  $x$ -axis. The left figure shows the  $y$ -component of the force density for the cylinder translating with unit speed in the  $y$ -direction, while the right figure shows the  $x$ -component of the force density for the cylinder translating in the  $x$ -direction. Note that in both flows the force density  $\mathbf{f}(s)$  decays to near zero at  $s = \pm 1/2$ , as expected.

density, it appears that what we are doing instead here is ignoring a certain (small) amount of force contribution from the very ends of the fiber (between  $1/2 \leq |s| \leq \sqrt{1/4 + \epsilon^2}$ ). Whether or not this is a good approximation is unclear – it is possible that the same force density could result from flows that differ slightly at the actual fiber endpoints. However, it appears that because  $\mathbf{f}(s)$  decays so rapidly at  $s = \pm 1/2$ , any force contribution beyond this would be negligible. This may indicate that sufficient decay in the slender body radius toward the endpoints of the fiber ensures that the endpoints (beyond  $|s| = 1/2$ ) are not contributing a significant amount to the total force and thus can be safely ignored.

To test the formulation (4) for a different choice of radius function  $r(s)$ , we next consider

the drag force on a straight cylinder with uniform radius everywhere along its length except for hemispherical caps at the fiber endpoints. In particular, we take the cylinder to be the same length as the prolate spheroid (actual fiber endpoints at  $s = \pm\sqrt{1/4 + \epsilon^2}$ ) with a radius that decays smoothly to zero at the endpoint via a hemispherical cap of radius  $\epsilon$  centered at  $d_\epsilon = \sqrt{1/4 + \epsilon^2} - \epsilon$ :

$$er(s) = \begin{cases} \epsilon, & -d_\epsilon \leq s \leq d_\epsilon \\ \sqrt{\epsilon^2 - (s + d_\epsilon)^2}, & s < -d_\epsilon \\ \sqrt{\epsilon^2 - (s - d_\epsilon)^2}, & s > d_\epsilon \end{cases}$$

$$d_\epsilon := \sqrt{1/4 + \epsilon^2} - \epsilon.$$

As in the case of the prolate spheroid, we distribute the force density  $\mathbf{f}(s)$  along the interval  $[-1/2, 1/2]$ . Using (4) to find  $\mathbf{F}$  in the same way as in the case of the prolate spheroid, we compare the resulting drag force with the asymptotic expression derived by Keller and Rubinow [16] in table 2.

$\epsilon$	$\mathbf{F} \cdot \mathbf{e}_y$ for $\mathbf{u} = \mathbf{e}_y$		$\mathbf{F} \cdot \mathbf{e}_x$ for $\mathbf{u} = \mathbf{e}_x$		$\epsilon  \log \epsilon $
	Eqn (4)	Keller-Rubinow	Eqn (4)	Keller-Rubinow	
0.01	-2.6433	-2.6401	-1.6864	-1.6712	0.0461
0.005	-2.3085	-2.3024	-1.4216	-1.4094	0.0265
0.0025	-2.0472	-2.0417	-1.2274	-1.2189	0.0150
0.00125	-1.8384	-1.8342	-1.0796	-1.0738	0.0084

Table 2: Comparison of the computed (via expression (4)) and asymptotic (from Keller and Rubinow [16]) Stokes drag force  $\mathbf{F}$  on a cylinder of length  $2\sqrt{1/4 + \epsilon^2}$  with hemispherical endpoints and with centerline along the  $x$ -axis. Columns 2 and 3 compare the  $y$ -component of  $\mathbf{F}$  for a cylinder translating with unit speed in the  $y$ -direction, while columns 4 and 5 compare the  $x$ -component of  $\mathbf{F}$  for translation in the  $x$ -direction. Here the expected  $\epsilon \log \epsilon$  scaling of the difference between forces is less apparent, particularly in the  $y$ -direction. This may be due to endpoint effects (see figure 3).

The computed drag force in table 2 agrees well with the asymptotic expression of Keller and Rubinow [16]; however, the computed force-per-unit-length  $\mathbf{f}(s)$  is not as physically reasonable at the fiber endpoints. According to [22], in the case of a cylinder with hemispherical caps, we actually want a faster rate of decay in the force near the fiber endpoints – in particular, we need  $\mathbf{f}(s)/(1/4 - s^2) \in C(-1/2, 1/2)$ . However, as shown in figure 3, flow about the cylinder results in wild oscillations in  $\mathbf{f}(s)$  near the fiber endpoints. Possibly this indicates that this method (and likely others based on slender body theory) are really designed to treat prolate spheroids with sufficient decay in radius near the fiber endpoints.

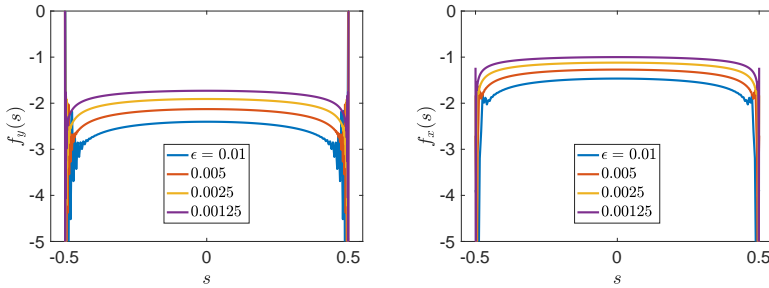


Figure 3: Force per unit length  $\mathbf{f}(s)$ ,  $s \in [-1/2, 1/2]$ , along the uniform cylinder with hemispherical caps at the endpoints and centerline aligned with the  $x$ -axis. The left figure shows the  $y$ -component of the force density for the cylinder translating with unit speed in the  $y$ -direction, while the right figure shows the  $x$ -component of the force density for the cylinder translating in the  $x$ -direction. Comparing with figure 2, it is clear that the shape of the radius function  $r(s)$  at the fiber endpoint has a large effect on  $\mathbf{f}(s)$ . In particular, despite the decay in  $\mathbf{f}(s)$  at the very endpoint of the fiber, the oscillations leading up to the endpoint brings the physical validity of this force density into question.

### 3.3 Closed loops in constant flow

To validate the slender body approximation (4) in the closed loop setting ( $\mathcal{I} = \mathbb{T}$ ), we compute the Stokes drag about a translating thin torus of length 1 with centerline in the  $xy$ -plane and axis of symmetry about the  $z$ -axis. We compare the computed drag force for various values of  $\epsilon$  to the asymptotic expression of Johnson and Wu [15] (see table 3). Note that for the thin filaments that we consider here, the Johnson and Wu expression for the drag force corresponds well with the semianalytic expression for a torus translating in the  $z$ -direction, derived by Majumdar and O'Neill [18] with corrections by Amarakoon, et al. [1]. The Majumdar-O'Neill expression, consisting of an infinite sum of Legendre functions, holds for general values of  $s_0$ , where  $s_0$  is defined to be the ratio of the outer radius of the torus (measured centerline to longitudinal axis) to the cross sectional radius. In [1], Amarakoon, et al. numerically verify the reported  $\mathcal{O}(s_0^{-2})$  accuracy of the Johnson-Wu expression. In our case, we are mainly concerned with the parameter region  $s_0 = 1/(2\pi\epsilon) > 10$ , so the Johnson-Wu expression agrees with the exact expression for Stokes drag in the  $z$ -direction to at least two digits.

Since the torus centerline  $\mathbf{X}(s)$  is planar, we choose the normal vector  $\cos(2\pi s)\mathbf{e}_x + \sin(2\pi s)\mathbf{e}_y$  to also lie in the  $xy$ -plane. The integral term in (4) is discretized using the trapezoidal rule, and the number of discretization points  $n$  along the fiber centerline is taken to be  $n = 2/\epsilon$ . Given zero background flow and uniform unit speed in the  $z$ -direction (columns 2 and 3, table 3) and  $y$ -direction (columns 4 and 5, table 3), the discretized operator (4) is inverted to find the force per unit length  $\mathbf{f}(s)$ , which is then



summed over  $s$  to find the drag force  $\mathbf{F}$ . We plot the calculated  $\mathbf{f}(s)$  in figure 4 to verify that the computed force density makes physical sense. For all computations, we take the viscosity  $\mu = 1$ .

$\epsilon$	$\mathbf{F} \cdot \mathbf{e}_z$ for $\mathbf{u} = \mathbf{e}_z$		$\mathbf{F} \cdot \mathbf{e}_y$ for $\mathbf{u} = \mathbf{e}_y$		$\epsilon  \log \epsilon $
	Eqn (4)	Johnson-Wu	Eqn (4)	Johnson-Wu	
0.01	-2.4093	-2.3503	-1.8740	-1.8292	0.0461
0.005	-2.1076	-2.0806	-1.6309	-1.6103	0.0265
0.0025	-1.8788	-1.8664	-1.4484	-1.4389	0.0150
0.00125	-1.6979	-1.6922	-1.3051	-1.3007	0.0084

Table 3: We consider a translating slender torus of length 1 with centerline lying in the  $xy$ -plane, and compare the resulting Stokes drag force given by the slender body model (expression (4)) to the asymptotic expression calculated by Johnson and Wu [15]. Columns 2 and 3 compare the  $z$ -component of the drag force for a slender torus translating with speed 1 in the  $z$ -direction (“broadwise translation”), while columns 4 and 5 show the  $y$ -component of the drag for translation in the  $y$ -direction (“translation perpendicular to the longitudinal axis”). Here we can see an approximate  $\epsilon \log \epsilon$  scaling in the difference between the two expressions.

Our method agrees quite well with the asymptotic expression of Johnson and Wu – as expected, table 3 shows roughly an  $\mathcal{O}(\epsilon \log \epsilon)$  difference between the slender body approximation to the drag force and the asymptotic expression. This is encouraging since both (4) and the Johnson-Wu asymptotics are based on the Stokeslet/doublet expression (3). We have chosen these particular values of  $\epsilon$  so that our method can also be compared with the regularized Stokeslet method of Cortez and Nicholas [7].

### 3.4 Free ended fibers in shear flow

In this section we calculate the angular momentum of a prolate spheroid with aspect ratio  $\lambda = 1/\epsilon$  in the shear flow field  $\mathbf{u}(z) = (z, 0, 0)^T$ . The torques are derived using both slender body theory (equation (4)) and the Jeffery model (equation (5)) for comparison. Figure 5a shows how the torque of the ellipsoid varies as a function of its orientation. Here,  $\theta_2$  is the second Euler angle and  $\theta_2 = [-\pi/2, \pi/2]$  corresponds to a full revolution about the  $y$ -axis. We see that the torques agree at  $\theta_2 = \pm\pi/2$  and the discrepancy between the two models increases as the orientation approaches alignment in the shear plane; in particular, the torque in the slender body model goes to zero but the Jeffery torque remains bounded away from zero. Since the fluid velocity is exactly zero along the particle centerline, the slender body model does not yield a torque on the particle. On the other hand, in the Jeffery model, the spheroid is aware of the non-zero fluid velocity gradient, and hence experiences a non-zero torque at this orientation.

Figure 5b shows the difference between the  $y$ -component of the torques due to Jeffery

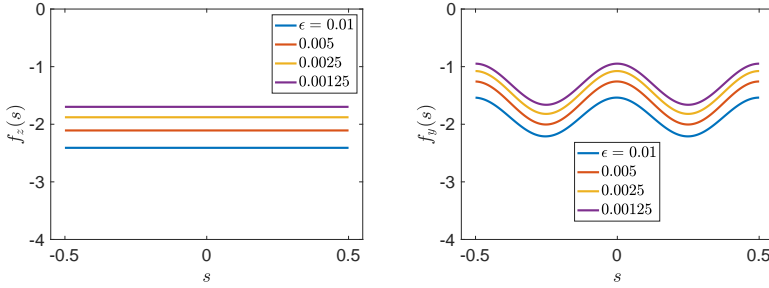


Figure 4: Force per unit length  $\mathbf{f}(s)$ ,  $s \in \mathbb{T}$ , along the slender torus with centerline in the  $xy$ -plane. The left figure shows the  $z$ -component  $\mathbf{f}(s) \cdot \mathbf{e}_z$  for a slender body translating with unit speed in the  $z$ -direction, while the right picture shows the  $y$  component  $\mathbf{f}(s) \cdot \mathbf{e}_y$  for translation with unit speed in the  $y$ -direction.

and slender body theory as a function of  $\epsilon$  for different values of  $n$ . The particles are oriented with  $\theta_2 = \pi/2$ , perpendicular to the shear plane. We see roughly  $\mathcal{O}(\epsilon \log(\epsilon))$  convergence for the five largest values of  $\epsilon$ . For smaller values of  $\epsilon$ , the model converges at a slower rate. This is similar to the observed convergence in the force values (table 1), which are calculated for  $\epsilon \leq 10^{-2}$ . In addition, the two models show better agreement as the discretization parameter  $n$  is increased.

Figure 6 shows the the  $y$ -component from equation (1) of the torques due to slender body theory and Jeffery. The ODE for angular momentum is solved using one of MATLAB's built in functions such as `ode15s`. The particles are aligned as before with initial conditions  $\mathbf{m}_0 = (0, 0.1, 0)^T$  and Euler angles  $(0, \pi/2, 0)^T$ ; hence the only non-zero component of the angular momentum is  $m_y$ . We observe that for a relatively low aspect ratio (i.e., figure 6a) the models do not agree so well, however  $\lambda = 5$  is not considered to be in the “slender” regime and we therefore do not expect good agreement here. As  $\lambda$  increases, the dynamics become almost indistinguishable.

We now turn our attention to figure 7, which displays how the choice of the discretization parameter  $n$  affects the solution quality. Figure 7a shows  $m_y$  for the slender body model for different numbers of discretization points  $n$  and figure 7b shows its 40 highest Fourier modes. The main observation here is that the model becomes more accurate as  $n$  increases. In particular, if  $n$  is chosen to be too low (here, too low corresponds to roughly less than  $1/(2\epsilon)$ ) then the model does not resolve the low frequency modes, which can be seen by the spike at  $k = 16$  in figure 7b, where only the  $n = 50$  and 100 lines are able to reasonably capture this mode correctly.

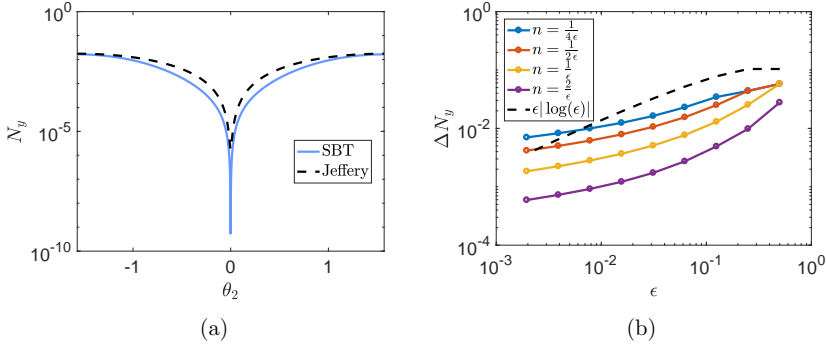


Figure 5: (a) The  $y$ -component of the torque for a prolate spheroid with  $\lambda = 100$  for different orientations in shear flow. The values  $\theta_2 = 0, \pm\pi/2$  correspond to alignment parallel and perpendicular to the shear plane, respectively. (b) The difference  $\Delta N_y$  between the  $y$ -component of the torques due to Jeffery and slender body theory for a prolate spheroid of aspect ratio  $\lambda = 1/\epsilon$  aligned in the  $z$ -direction in shear flow.

### 3.5 Closed loops and oblate spheroids in shear flow

In this section we compare the rotational dynamics of a thin torus modeled by slender body theory to the rotational dynamics of an oblate disk of similar shape and mass. This comparison differs from the prolate spheroid comparisons in that here the particle shapes are different and we do not expect the two solutions to coincide. The slender torus experiences a force only along its centerline, whilst the oblate spheroid experiences a force all across its surface. In addition, the moment of inertia tensor for a torus of inner radius  $2\epsilon$  and of outer radius  $a$  (measured from the center of mass to the centerline) is given by

$$J_T = m_T \text{diag} \left( \frac{4a^2 + 5\epsilon^2}{8}, \frac{4a^2 + 5\epsilon^2}{8}, \frac{4a^2 + 3\epsilon^2}{4} \right).$$

Setting the mass of the torus to  $m_T = 2m_p/5$ , where  $m_p$  is the mass of the spheroid, we have the relation  $J - J_T = \mathcal{O}(\epsilon^2)$  for an oblate spheroid with semi minor axis length  $b = \epsilon$ . Due to the particle shape, the oblate spheroid experiences a much stronger torque; hence for the torques to be of the same magnitude, a viscosity of  $\mu_T = 200\mu$  is chosen for the torus. The particles are placed at rest in the shear flow with the initial Euler angles  $(0.01, 0.01, 0.01)$ . We do this for two reasons: the first being that the Euler angles  $(0, 0, 0)$  correspond to a neutrally stable orbit where the ellipsoid exhibits a tumbling motion forever. The second reason is that these angles correspond to exact alignment in the  $xy$  plane, where the slender model will not experience a force since the fluid velocity is exactly zero.

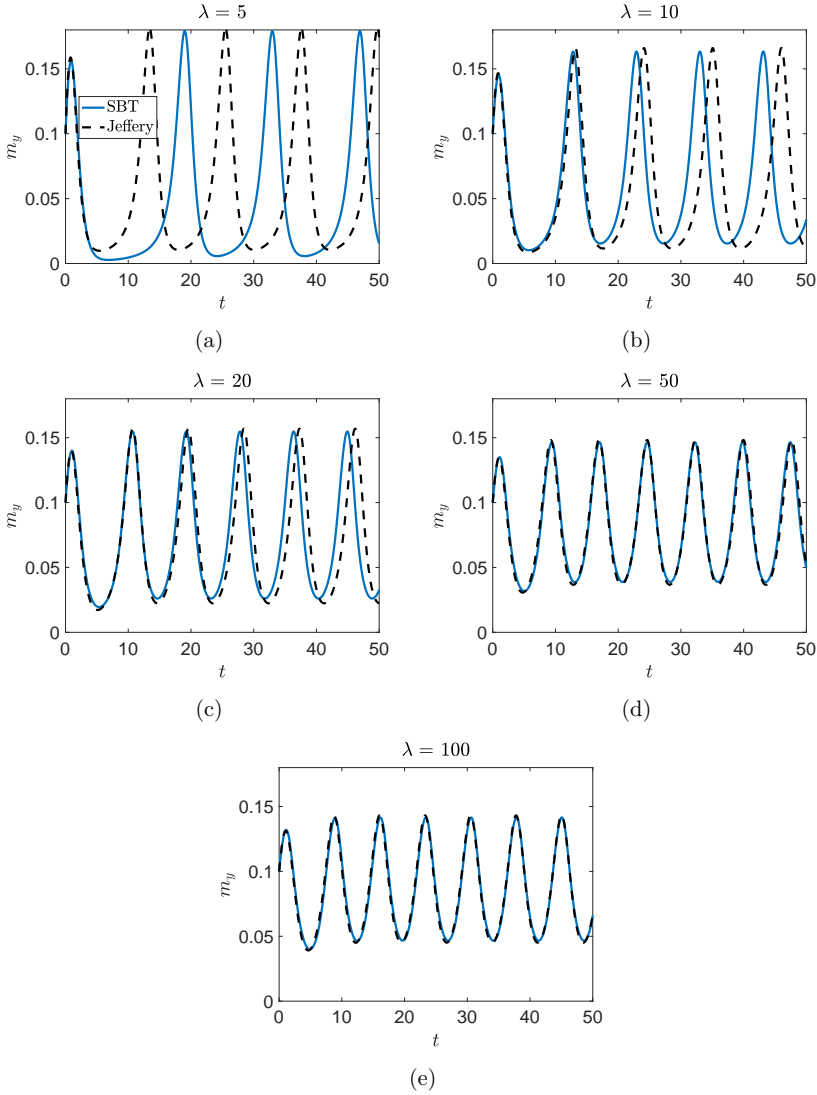


Figure 6: The  $y$ -component of the angular momentum of a particle in shear flow calculated from slender body theory (blue) and Jeffery (black, dashed). The aspect ratio takes different values in the range  $\lambda \in [10, 100]$ . The simulation parameters are  $\mu = 0.06$ ,  $n = \frac{2}{\epsilon}$

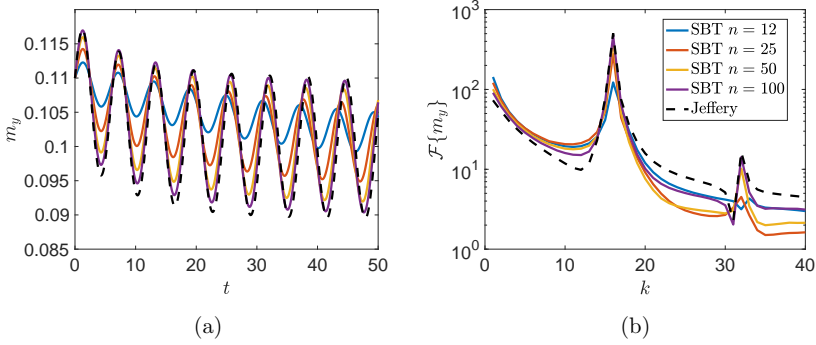


Figure 7: The  $y$ -component of the angular momentum of a particle in shear flow (a) and the first 40 Fourier modes (b). The colored lines are calculated from slender body theory with discretization parameter varying in the range  $n \in [12, 100]$  and the dashed line is due to Jeffery. The simulation parameters are  $\mu = 0.01$  and  $\lambda = 50$  and  $\mathbf{m}_0 = (0, 0.11, 0)^T$ .

Challabotla et al. [4] conduct a similar experiment with oblate spheroids in shear flow and observe two phases of rotation: (1) an unstable wobbling phase of length proportional to the particle inertia, and (2) a stable rolling phase, where the spheroid aligns and rolls perfectly in the shear plane. Figure 8 shows  $\mathbf{m}(t)$  for the thin ring with  $\epsilon = 1/100$  and oblate spheroid with  $\lambda = 1/100$  for three different values of  $\mu$  (and the corresponding values of  $\mu_T$ ). For the spheroid model, we observe the temporary initial wobbling phase followed by the stable rolling phase where the particle rotates in the shear plane with a constant  $m_z$  component. In addition, as the relative particle inertia increases (that is, as the  $\mu$  decreases), the wobbling phase is prolonged. These two observations are in agreement with the results in [4]. If we turn our attention to the thin ring, we observe some similarities: there is an initial wobbling phase followed by a somewhat different rolling phase. In the rolling phase, the particle's symmetry axis (the  $z$ -axis in the particle frame) precesses about the  $y$ -axis in the inertial frame. This is seen as oscillations in the  $m_x$  and  $m_y$  components about a mean zero value, which in turn affects the  $m_z$  component. A possible explanation for this precession is the fact that the slender ring does not experience a torque in the  $x$  or  $y$  directions (i.e., a restoring torque) when the axis of symmetry aligns perfectly with the  $y$ -axis in the inertial frame, since the gradient of the fluid velocity is not used in the calculation of the slender body torque. Hence the ring is susceptible to wobbling/precession at this orientation. This is in contrast with the spheroid, which experiences a non-zero torque in shear flow because of the positive fluid velocity gradient, regardless of the particle orientation. These discrepancies may not appear in more complex 3D flows and geometries.

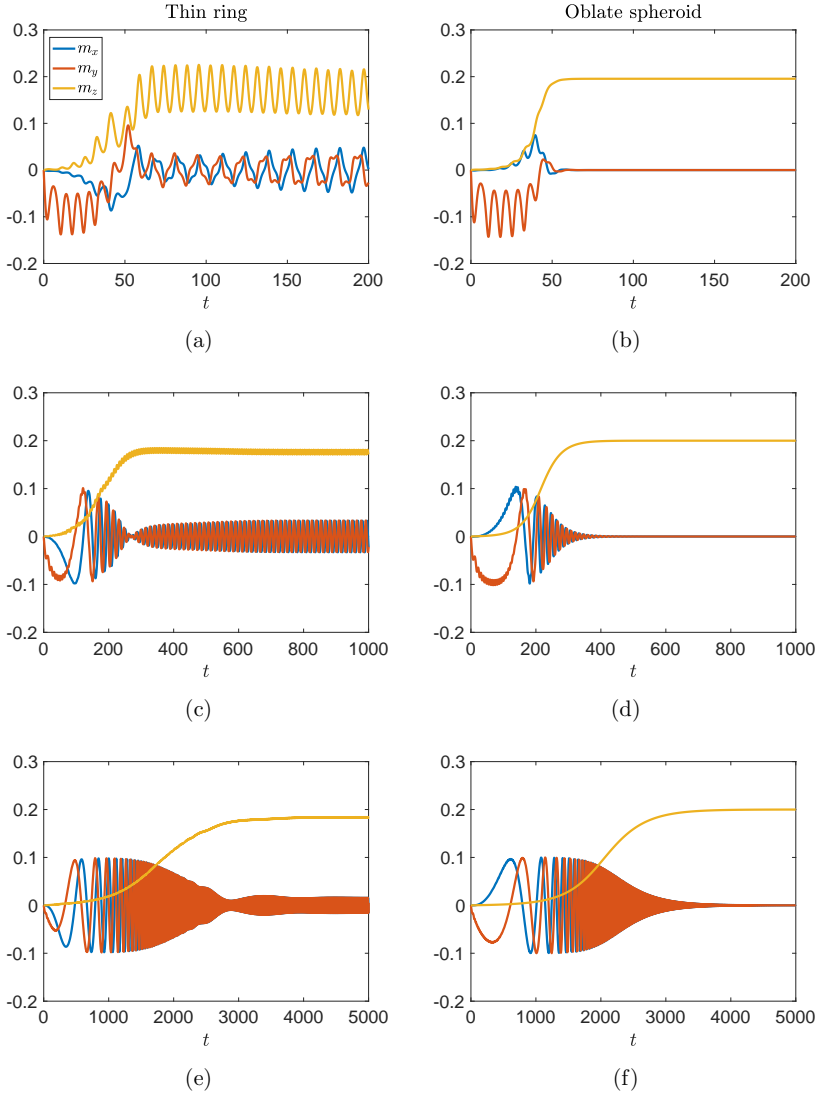


Figure 8: The angular momentum components of a thin ring (left column) and an oblate spheroid (right column) for  $\mu_0 = 0.01, 0.001$  and  $0.0001$  (from top to bottom). The particle parameters are  $\epsilon = \frac{1}{100}$ ,  $\lambda = \frac{1}{100}$ ,  $\mu_T = 200\mu$ ,  $m_T = \frac{2}{5}m$ ,  $m = 1$ ,  $a = 1$ ,  $n = \frac{1}{2\epsilon}$

## 4 Conclusion

In this paper we consider a model for thin, rigid fibers in viscous flows based on slender body theory. We investigate using the slender body approximation for the fluid field away from the fiber centerline as an approximation for the motion of the fiber itself by evaluating the expression on a curve along the slender body surface. Numerically, this yields a matrix equation for the force density along the length of the fiber that appears to be suitable for inversion even for very fine discretization of the fiber centerline.

For simple geometries and simple flows, we compare the slender body model to exact or asymptotically accurate expressions for the total force and torque acting on the particle. For the thin prolate spheroid, we compare the Stokes drag force predicted by slender body theory to the exact expression of Chwang and Wu [5]; for the cylinder, we compare with the asymptotic expression of Keller and Rubinow [16]; and for the thin torus, we compare with the asymptotic force expression of Johnson and Wu [15]. In the case of the prolate spheroid and the thin torus, we find essentially  $\mathcal{O}(\epsilon \log \epsilon)$  agreement between our model and the exact or asymptotically accurate force values (tables 1 and 3), which is the accuracy predicted by rigorous error analyses [21, 22].

We also compared the torques on a thin prolate spheroid in shear flow for which the exact torques are given by Jeffery [13]. In the case of a thin torus, we qualitatively compared the dynamics of the torus with the Jeffery torques on an oblate spheroid of similar size. For the prolate spheroid, we found good agreement between our model and the Jeffery model, especially as the aspect ratio of the particle increases. In particular, in the slender body model, the dynamics appear to be better resolved for finer discretization of the filament (large  $n$ ). For the thin torus, we observe somewhat similar results to those of Challabotla [4] for oblate spheroids; namely, we observe an initial “wobbling” phase followed by a steady “rolling” phase. The main difference is that in the rolling phase, the thin torus precesses about the directions perpendicular to the shear plane, while the spheroid maintains a constant angular momentum. This may be due to the fact that the slender model does not explicitly experience torque through the gradient, but only the values of the fluid velocity at the location of the centerline.

In the future, we aim to use this model to simulate elongated particles to determine the length scale at which the Jeffery model for prolate spheroids begins to lose validity in turbulent flows. We also aim to study the aggregation properties of many slender particles with more complicated shapes in turbulence (for example, helices or arbitrary closed loops). On the theoretical side, we would also like to obtain a more complete characterization of solvability conditions for the centerline equation. This would involve a spectral analysis of the equation (4) as well as the slender body PDE of [21, 22].

## A Other limiting slender body velocity expressions

Here we provide a brief overview of other methods used to obtain an expression for the motion of the fiber centerline  $\frac{\partial \mathbf{X}(s,t)}{\partial t}$ .

One such method is that of Lighthill [17] in which, away from  $s = s'$ , we simply plug  $\mathbf{x} = \mathbf{X}(s)$  into the integral expression (3) (note that the doublet has negligible effect away from  $s = s'$ ). Near  $s = s'$ , under the assumption that the centerline is essentially straight and the force density is approximately constant within this small region, the expression (3) can be evaluated exactly to obtain

$$8\pi\mu(\mathbf{u}^L(s, t) - \mathbf{u}_0(\mathbf{X}(s, t), t)) = 2(\mathbf{I} - \mathbf{e}_s \mathbf{e}_s^T) \mathbf{f}(s, t) + \int_{|\mathbf{R}_0| > \delta} \left( \frac{\mathbf{I}}{|\mathbf{R}_0|} + \frac{\mathbf{R}_0 \mathbf{R}_0^T}{|\mathbf{R}_0|^3} \right) \mathbf{f}(s', t) ds';$$

$$\mathbf{R}_0(s, s', t) = \mathbf{X}(s, t) - \mathbf{X}(s', t), \quad \delta = \epsilon r(s) \sqrt{\epsilon}/2.$$

Here  $\mathbf{u}^L(s, t)$  approximates  $\frac{\partial \mathbf{X}(s, t)}{\partial t}$ , the actual motion of the fiber centerline, and  $\mathbf{u}_0(\mathbf{X}(s, t), t)$  is the fluid flow at the spatial point  $\mathbf{x} = \mathbf{X}(s, t)$  in the absence of the fiber.

Another popular method is that of Keller and Rubinow [16] in which the expression (3) is evaluated on the *actual* slender body surface (i.e. at a distance  $\epsilon r(s)$  from  $\mathbf{X}(s, t)$ ) and the method of matched asymptotics is used to obtain an expression for  $\epsilon = 0$ . In the far field (away from  $s = s'$ ), (3) is simply Taylor expanded about  $\epsilon = 0$ . In the near field (near  $s = s'$ ), the expression (3) is rewritten in terms of the rescaled variable  $\xi = (s - s')/\epsilon$  and then expanded about  $\epsilon = 0$ . The far- and near-field expressions are then matched to create a centerline velocity expression that includes a local operator and a singular finite-part non-local operator:

$$8\pi\mu(\mathbf{u}^{\text{KR}}(s, t) - \mathbf{u}_0(\mathbf{X}(s, t), t)) = -\mathbf{\Lambda}[\mathbf{f}](s, t) - \mathbf{K}[\mathbf{f}](s, t).$$

In the free end setting, the operators  $\mathbf{\Lambda}$  and  $\mathbf{K}$  are given by

$$\mathbf{\Lambda}[\mathbf{f}](s, t) := [(\mathbf{I} - 3\mathbf{e}_s \mathbf{e}_s^T) + (\mathbf{I} + \mathbf{e}_s \mathbf{e}_s^T)L(s)] \mathbf{f}(s, t)$$

$$\mathbf{K}[\mathbf{f}](s, t) := \int_{-1/2}^{1/2} \left[ \left( \frac{\mathbf{I}}{|\mathbf{R}_0|} + \frac{\mathbf{R}_0 \mathbf{R}_0^T}{|\mathbf{R}_0|^3} \right) \mathbf{f}(s', t) - \frac{\mathbf{I} + \mathbf{e}_s(s) \mathbf{e}_s(s)^T}{|s - s'|} \mathbf{f}(s, t) \right] ds',$$

where  $L(s) = \log \left( \frac{2(1/4 - s^2) + 2\sqrt{(1/4 - s^2)^2 + 4\epsilon^2 r^2(s)}}{\epsilon^2 r^2(s)} \right)$ . Note that we define  $L$  in this way to avoid singularities at the fiber endpoints; thus this  $L$  differs slightly from the expression given by [11] or the expression in [27].

In the closed loop setting,  $\mathbf{\Lambda}$  and  $\mathbf{K}$  are given by

$$\mathbf{\Lambda}[\mathbf{f}](s, t) := [(\mathbf{I} - 3\mathbf{e}_s \mathbf{e}_s^T) - 2(\mathbf{I} + \mathbf{e}_s \mathbf{e}_s^T) \log(\pi\epsilon/4)] \mathbf{f}(s, t)$$

$$\mathbf{K}[\mathbf{f}](s, t) := \int_{\mathbb{T}} \left[ \left( \frac{\mathbf{I}}{|\mathbf{R}_0|} + \frac{\mathbf{R}_0 \mathbf{R}_0^T}{|\mathbf{R}_0|^3} \right) \mathbf{f}(s', t) - \frac{\mathbf{I} + \mathbf{e}_s(s) \mathbf{e}_s(s)^T}{|\sin(\pi(s - s'))/\pi|} \mathbf{f}(s, t) \right] ds'.$$

However, a spectral analysis of the Keller-Rubinow operator  $-(\mathbf{\Lambda} + \mathbf{K})$  in the case of simple fiber geometries (see Götz [11] for the straight centerline and Shelley and Ueda [24] for the circular centerline) shows that the Keller-Rubinow expression is not suitable



for inversion. In particular, the operator  $-(\mathbf{\Lambda} + \mathbf{K})$  has a vanishing or nearly vanishing eigenvalue at some wavenumber  $k \sim 1/\epsilon$ . This high wavenumber instability limits the level to which the fiber can be discretized for numerics. It seems likely that more complicated centerline geometries also lead to a similar conclusion. Therefore in order to use the Keller-Rubinow expression for numerical simulations, the kernel of the operator  $\mathbf{K}$  must be regularized. For example, in [24, 27], the denominators in the kernel of  $\mathbf{K}$  are replaced by  $\sqrt{|\mathbf{R}_0|^2 + \delta^2}$  and  $\sqrt{\sin^2(\pi(s - s'))/\pi^2 + \delta^2}$ , where  $\delta = \delta(\epsilon)$  is chosen according to the fiber radius to maintain the same asymptotic accuracy as the Keller-Rubinow expression. This regularization, however, lacks a physical justification and clear connection to the expression (3).

Another common technique for describing the motion of the fiber centerline is to instead use the method of regularized Stokeslets (see [3, 6, 7]) to obtain an alternate version of (3). In this method, the Stokeslet is approximated by the (smooth) solution to

$$-\mu\Delta\mathbf{u} + \nabla p = \mathbf{f}\phi_\delta(\mathbf{x}), \quad \text{div } \mathbf{u} = 0$$

where  $\phi_\delta$  is a smooth, radially symmetric function with  $\int_{\mathbb{R}^3} \phi_\delta = 1$ . The parameter  $\delta$  determines the spread of  $\phi_\delta$  and, in the case of slender body theory, is usually chosen such that  $\delta \sim \epsilon$ . The slender body approximation is then constructed as in (3), but now the resulting expression is not singular at  $\mathbf{x} = \mathbf{X}(s)$ , and the velocity of the slender body itself may be approximated by simply evaluating the regularized expression along the fiber centerline. The method of regularized Stokeslets can be used to construct regularized versions of the Lighthill and Keller-Rubinow expressions [7]. However, from the outset, the method of regularized Stokeslets approximates a slightly different problem from (3), and it is not entirely clear that these solutions should be close for any  $\delta$ . The choice of regularization parameter  $\delta$  greatly affects the resulting dynamics; however, a systematic justification for this parameter choice is lacking.

## References

- [1] A. Amarakoon, R. Hussey, B. J. Good, and E. G. Grimsal. Drag measurements for axisymmetric motion of a torus at low Reynolds number. *Phys. Fluids*, 25(9):1495–1501, 1982.
- [2] G. Batchelor. Slender-body theory for particles of arbitrary cross-section in Stokes flow. *J. Fluid Mech.*, 44(3):419–440, 1970.
- [3] E. L. Bouzarth and M. L. Minion. Modeling slender bodies with the method of regularized Stokeslets. *J. Comput. Phys.*, 230(10):3929–3947, 2011.
- [4] N. R. Challabotla, C. Nilsen, and H. I. Andersson. On rotational dynamics of inertial disks in creeping shear flow. *Phys. Lett. A*, 379(3):157–162, 2015.

- [5] A. T. Chwang and T. Y.-T. Wu. Hydromechanics of low-Reynolds-number flow. Part 2: Singularity method for Stokes flows. *J. Fluid Mech.*, 67(4):787–815, 1975.
- [6] R. Cortez, L. Fauci, and A. Medovikov. The method of regularized Stokeslets in three dimensions: analysis, validation, and application to helical swimming. *Phys. Fluids*, 17(3):031504, 2005.
- [7] R. Cortez and M. Nicholas. Slender body theory for Stokes flows with regularized forces. *Commun. Appl. Math. Comput. Sci.*, 7(1):33–62, 2012.
- [8] R. Cox. The motion of long slender bodies in a viscous fluid part 1. general theory. *J. Fluid Mech.*, 44(4):791–810, 1970.
- [9] I. Gallily and A.-H. Cohen. On the orderly nature of the motion of nonspherical aerosol particles. ii. inertial collision between a spherical large droplet and an axially symmetrical elongated particle. *J. Colloid Interface Sci.*, 68(2):338–356, 1979.
- [10] H. Goldstein, C. Poole, and J. Saffko. Classical mechanics, 2002.
- [11] T. Götz. *Interactions of fibers and flow: asymptotics, theory and numerics*. Doctoral dissertation, University of Kaiserslautern, 2000.
- [12] G. Hancock. The self-propulsion of microscopic organisms through liquids. *Proc. R. Soc. Lond. A*, 217(1128):96–121, 1953.
- [13] G. B. Jeffery. The motion of ellipsoidal particles immersed in a viscous fluid. *Proc. R. Soc. Lond. A*, 102(715):161–179, 1922.
- [14] R. E. Johnson. An improved slender-body theory for Stokes flow. *J. Fluid Mech.*, 99(02):411–431, 1980.
- [15] R. E. Johnson and T. Y. Wu. Hydromechanics of low-Reynolds-number flow. Part 5: Motion of a slender torus. *J. Fluid Mech.*, 95(2):263–277, 1979.
- [16] J. B. Keller and S. I. Rubinow. Slender-body theory for slow viscous flow. *J. Fluid Mech.*, 75(4):705–714, 1976.
- [17] J. Lighthill. Flagellar hydrodynamics. *SIAM review*, 18(2):161–230, 1976.
- [18] S. Majumdar and M. O’Neill. On axisymmetric Stokes flow past a torus. *Z. Angew. Math. Phys.*, 28(4):541–550, 1977.
- [19] W. Mao and A. Alexeev. Motion of spheroid particles in shear flow with inertia. *J. Fluid Mech.*, 749:145–166, 2014.

- [20] J. Martin, A. Lusher, R. C. Thompson, and A. Morley. The deposition and accumulation of microplastics in marine sediments and bottom water from the Irish continental shelf. *Sci. Rep.*, 7(1):10772, 2017.
- [21] Y. Mori, L. Ohm, and D. Spirn. Theoretical justification and error analysis for slender body theory. *Comm. Pure Appl. Math.*, to appear, 2018.
- [22] Y. Mori, L. Ohm, and D. Spirn. Theoretical justification and error analysis for slender body theory with free ends. *arXiv preprint arXiv:1901.11456*, 2019.
- [23] P. Mortensen, H. Andersson, J. Gillissen, and B. Boersma. Dynamics of prolate ellipsoidal particles in a turbulent channel flow. *Phys. Fluids*, 20(9):093302, 2008.
- [24] M. J. Shelley and T. Ueda. The Stokesian hydrodynamics of flexing, stretching filaments. *Phys. D*, 146(1):221–245, 2000.
- [25] B. Tapley, E. Celledoni, B. Owren, and H. I. Andersson. A novel approach to rigid spheroid models in viscous flows using operator splitting methods. *Numer. Algorithms*, pages 1–19, 2019.
- [26] B. K. Tapley. Computing cost-effective particle trajectories in numerically calculated incompressible fluids using geometric methods. *arXiv preprint arXiv:1901.05236*, 2019.
- [27] A.-K. Tornberg and M. J. Shelley. Simulating the dynamics and interactions of flexible fibers in Stokes flows. *J. Comput. Phys.*, 196(1):8–40, 2004.
- [28] G. A. Voth and A. Soldati. Anisotropic particles in turbulence. *Annu. Rev. Fluid Mech.*, 49:249–276, 2017.
- [29] H. Zhang, G. Ahmadi, F.-G. Fan, and J. B. McLaughlin. Ellipsoidal particles transport and deposition in turbulent channel flows. *Int. J. Multiph. Flow*, 27(6):971–1009, 2001.
- [30] L. Zhao, N. R. Challabotla, H. I. Andersson, and E. A. Variano. Rotation of non-spherical particles in turbulent channel flow. *Phys. Rev. Lett.*, 115(24):244501, 2015.



## HIGH PERFORMANCE PHASE-RESOLVED WAVE MODELLING FOR IRREGULAR COASTAL TOPOGRAPHY

W. WANG<sup>1</sup>, C. PAKOZDI<sup>2</sup>, A. KAMATH<sup>2</sup> AND H. BIHS<sup>2</sup>

<sup>1</sup>Department of Civil and Environmental Engineering  
Norwegian University of Science and Technology  
Trondheim 7491, Norway  
e-mail: weizhi.wang@ntnu.no, web page: <https://reef3d.com/>

<sup>2</sup> Department of Civil and Environmental Engineering  
Norwegian University of Science and Technology  
Trondheim 7491, Norway

**Key words:** Large-scale, Fully nonlinear potential flow, Irregular topography

**Abstract.** The Norwegian coast presents complex bathymetry due to the deep and wide fjords. The complexity includes significant water depth variation, deep water condition and irregular coastlines. Despite that phase-averaged spectral wave models are still widely used in coastal engineering, phase-resolved models are needed to represent more wave transformation phenomena such as diffraction and to provide time domain information. Computational fluid dynamics (CFD) wave models are seen to be able to provide accurate phase-resolving simulations for a wide variety of wave hydrodynamic phenomena. However, coastal wave propagation is typically a large-scale phenomenon and CFD is too computationally demanding for such simulations. Many numerical models based on shallow water wave theories are more computationally efficient, but the usage of such models are limited by the deep water conditions at the Norwegian fjords. Potential flow models have been proven to be effective for large-scale long duration sea state simulation, however, the inclusion of irregular solid boundaries has been a challenging task. In this paper, the authors present an efficient phase-resolving fully nonlinear potential flow model with efficient and flexible boundary treatments to meet the challenge of large-scale wave modelling over complex bathymetry. The model is developed as part of the high-performance open-source hydrodynamics program REEF3D. The high-order discretisation schemes and parallel computation support in REEF3D are directly inherited by the new potential flow model. The complex bathymetry is efficiently represented using the bottom-following  $\sigma$ -coordinate system. The coastlines are detected based on the bed elevation and water depth. The model is validated with wave propagation over a submerged bar in 2D. Then a large-scale 3D simulation over the natural topography at Sulafjord is presented.

## 1 INTRODUCTION

As part of the National Transport Plan (NTP), the coastal highway project E39 aims to build a continuous ferry-free road connection between Kristiansand and Trondheim along the west coast of Norway. The route covers around 1100 km with seven major fjord crossings [10]. With the fjords connected by bridges, the traveling time between Kristiansand and Trondheim is estimated to be reduced by half. However, the broad and deep fjords challenge the traditional long-span bridge design and therefore floating bridges are proposed for several fjord crossings. Consequently, the knowledge of wave behaviours inside the fjords is more critical. A computationally efficient numerical wave model will contribute to the safe and cost-efficient bridge designs and adaptive engineering solutions for future scenarios in a changing climate.

The commonly used coastal wave models are in general within three categories, the spectral wave model, the shallower wave model and the potential flow model. The third-generation spectral wave model SWAN [6] is an efficient wave model solving the energy action balance equations for the wave field. However, it only provides phase-averaged solution in frequency domain and fails where strong diffraction takes place [23, 22]. Two dimensional phase-resolving wave models based on shallow water assumptions, such as the various Boussineq-type models [15, 18], are seen to be effective tools for the wave simulation at shallow water condition with mild changes of bathymetry. However, Norwegian coasts usually have deepwater condition inside the fjords. For example, the wave length of a typical swell at the entrance of Sulafjord is estimated to be about 450 m, while the deepest water depth also reaches 450 m, creating a typical deepwater wave scenario. With such water condition, the shallow water models cannot be applied at a typical Norwegian coast. With the goal of simulation large-scale wave propagation, turbulence and viscosity are not as significant as they are for local phenomena such as breaking wave and wave-structure interactions. In this case, wave models based on potential flow theory proves to be an ideal alternative since they are usually computationally efficient and the application is not limited by wave depth. The high-order spectrum (HOS) model such as HOS-NWT [8] and HOS-Ocean [9] and the fully nonlinear potential flow model such as OceanWave3D [11] are the representative models of the kind. However, the Fast Fourier Transform (FFT) based HOS models are not flexible enough for significant water depth changes and the curvilinear grid used in OceanWave3D demands extra efforts for the grid generation at complex coastlines. An efficient boundary treatment algorithm and an effective grid generation method are needed to enable a potential flow solver for efficient wave modelling at the Norwegian coastal water.

In this presented manuscript, the authors propose a new fully-nonlinear potential flow (FNPF) model that provides both computational efficiency and effective treatments for the complex coastal boundaries. The proposed FNPF model solves the Laplace equation

on a  $\sigma$ -grid with a finite difference method. The  $\sigma$ -grid follows the bottom topography as well as the free surface elevation, offering a robust and flexible solution for varying bathymetry. The irregular coastal topography is represented with an effective coastline algorithm based on the local water depth and seabed elevation. Relaxation zones are arranged along the coastlines so that the reflection properties at the coastlines can be customised based on site-specific scenarios. The combination of the  $\sigma$ -grid and the wetting-drying scheme allows for effective grid generation for complex coastal topographies. The model is developed as part of the open-source wave hydrostatic model REEF3D. The code uses high-order discretisation schemes in space and time and provides fully parallel computation using Message Passing Interface (MPI). The code has been widely used for various hydrodynamic studies, for example, wave interactions with surface piercing cylinders [7, 14], extreme wave generation [4], free falling objects into water [13], local scour around a pipeline [1] and new developments of a non-hydrostatic Navier-Stokes solver [3]. The proposed potential flow model REEF3D::FNPF inherits the high-order schemes and parallel computation capacity from the REEF3D framework. In comparison to the CFD solvers, the presented model is much more computationally efficient and ideal for large-scale time domain analyses of wave propagation in the fjords. The flexibility and efficiency of the model are described in detail by [5].

## 2 NUMERICAL MODEL

### 2.1 Governing equations

The governing equation for the proposed fully nonlinear potential flow model is the Laplace equation:

$$\frac{\partial^2 \Phi}{\partial x^2} + \frac{\partial^2 \Phi}{\partial y^2} + \frac{\partial^2 \Phi}{\partial z^2} = 0. \quad (1)$$

Boundary conditions at the free surface and the bottom are required in order to solve the governing equation for the velocity potential  $\Phi$ . At the free surface, the fluid particles remain at the surface at all times and the pressure in the fluid is equal to the atmospheric pressure. These conditions form the kinematic and dynamic boundary conditions at the free surface respectively:

$$\frac{\partial \eta}{\partial t} = -\frac{\partial \eta}{\partial x} \frac{\partial \tilde{\Phi}}{\partial x} - \frac{\partial \eta}{\partial y} \frac{\partial \tilde{\Phi}}{\partial y} + \tilde{w} \left( 1 + \left( \frac{\partial \eta}{\partial x} \right)^2 + \left( \frac{\partial \eta}{\partial y} \right)^2 \right), \quad (2)$$

$$\frac{\partial \tilde{\Phi}}{\partial t} = -\frac{1}{2} \left( \left( \frac{\partial \tilde{\Phi}}{\partial x} \right)^2 + \left( \frac{\partial \tilde{\Phi}}{\partial y} \right)^2 - \tilde{w}^2 \left( 1 + \left( \frac{\partial \eta}{\partial x} \right)^2 + \left( \frac{\partial \eta}{\partial y} \right)^2 \right) \right) - g\eta. \quad (3)$$

where  $\eta$  is the free surface elevation,  $\tilde{\Phi} = \Phi(\mathbf{x}, \eta, t)$  is the velocity potential at the free surface,  $\mathbf{x} = (x, y)$  represents the location at the horizontal plane and  $\tilde{w}$  is the vertical velocity at the free surface.

At the bottom, the vertical water velocity perpendicular to the boundary is zero as the fluid particle cannot penetrate the solid boundary. This gives the bottom boundary condition:

$$\frac{\partial \Phi}{\partial z} + \frac{\partial h}{\partial x} \frac{\partial \Phi}{\partial x} + \frac{\partial h}{\partial y} \frac{\partial \Phi}{\partial y} = 0, \quad z = -h. \quad (4)$$

where  $h = h(\mathbf{x})$  is the water depth measured from the still water level to the seabed.

The Laplace equation, together with the boundary conditions are solved with a finite difference method on a  $\sigma$ -grid. The  $\sigma$ -grid follows the water depth changes and therefore is very adaptive to irregular boundaries. A Cartesian grid is transformed to a  $\sigma$ -coordinate based on the following formulation:

$$\sigma = \frac{z + h(\mathbf{x})}{\eta(\mathbf{x}, t) + h(\mathbf{x})}. \quad (5)$$

Once the velocity potential  $\Phi$  is obtained in the  $\sigma$ -coordinate system, the velocities can then be calculated:

$$u(\mathbf{x}, z) = \frac{\partial \Phi(\mathbf{x}, z)}{\partial x} = \frac{\partial \Phi(\mathbf{x}, \sigma)}{\partial x} + \frac{\partial \sigma}{\partial x} \frac{\partial \Phi(\mathbf{x}, \sigma)}{\partial \sigma}, \quad (6)$$

$$v(\mathbf{x}, z) = \frac{\partial \Phi(\mathbf{x}, z)}{\partial y} = \frac{\partial \Phi(\mathbf{x}, \sigma)}{\partial y} + \frac{\partial \sigma}{\partial y} \frac{\partial \Phi(\mathbf{x}, \sigma)}{\partial \sigma}, \quad (7)$$

$$w(\mathbf{x}, z) = \frac{\partial \Phi(\mathbf{x}, z)}{\partial z} = \frac{\partial \sigma}{\partial z} \frac{\partial \Phi(\mathbf{x}, \sigma)}{\partial \sigma}. \quad (8)$$

The irregular coastlines are detected based on local bed elevation and water depth. In comparison to the curvilinear approach, the method is straightforward and there is no demand for complex grid generation in the horizontal plane. In order to customise the reflection property of the coastlines, relaxation zones are applied along the solid boundary. In this way, the model offers the flexibility to represent different types of coastlines.

The model offers different wave generation algorithms. In this study, a Neumann boundary condition is used for wave generation at the inlet condition, where the velocity potential at the boundary is calculated using the desired analytical horizontal velocity:

$$\varphi_{i-1} = -u(\mathbf{x}, z, t) \Delta x + \varphi_i. \quad (9)$$



where  $u(\mathbf{x}, z, t)$  is the analytical horizontal velocity.

At the numerical beach, a relaxation method [16] is used to reduce the wave properties to hydrostatic values following the relaxation function proposed by [16]:

$$\Gamma(\tilde{x}) = 1 - \frac{e^{(\tilde{x}^{3.5})} - 1}{e - 1} \text{ for } \tilde{x} \in [0; 1]. \quad (10)$$

where  $\tilde{x}$  is a dimensionless length scaled to the length of the relaxation zone.

The Laplace equation is discretised using second-order central differences . It is then solved using a parallelised geometric multi-grid preconditioned conjugated gradient solver provided by Hypr [24]. High-order schemes are used for spatial and temporal discretisation. The convection terms at the free-surface boundary conditions are discretised with the 5-order Hamilton-Jacobi version of the weighted essentially non-oscillatory (WENO) scheme [12]. For the time treatment, a third-order TVD Runge-Kutta scheme [20] is used. Adaptive time stepping is used by controlling a constant CFL number. The model supports parallel computation following the domain decomposition strategy. Ghost cells are used to exchange information between adjacent domains. These ghost cells are updated with the values from the neighbouring processors via Message Passing Interface (MPI).

The model is able to generate different types of regular and irregular waves. In this study, a multi-directional irregular wave field is generated at Sulafjord. The JON-SWAP spectrum suggested by DNV-GL and the Pierson-Neumann-James (PNJ) directional spreading function [19] are used to form the directional spectrum. The formulations for the two spectra are shown in Eqn. 11 and Eqn. 14:

$$S(\omega) = \frac{5}{16} H_s^2 \omega_p^4 \omega_i^{-5} \exp\left(-\frac{5}{4} \left(\frac{\omega_i}{\omega_p}\right)^{-4}\right) \gamma^{\exp\left(\frac{-(\omega - \omega_p)^2}{2\sigma^2 \omega_p^2}\right)} A_\gamma. \quad (11)$$

$$A_\gamma = 1 - 0.287 \ln(\gamma). \quad (12)$$

$$\sigma = \begin{cases} 0.07 & \text{if } \omega \leq \omega_p \\ 0.09 & \text{if } \omega \geq \omega_p \end{cases} \quad (13)$$

where  $H_s$  is the significant wave height,  $\omega_p$  is the peak angular frequency,  $N$  is the number of wave components, peak enhancement factor  $\gamma$  is typically chosen to be 3.3.

$$G(\beta_j) = \begin{cases} \frac{2}{\pi} \cos^n(\beta_j - \bar{\beta}) & , \text{ if } |\beta_j| < \frac{\pi}{2} \\ 0 & , \text{ else.} \end{cases} \quad (14)$$

where  $\bar{\beta}$  is the principal direction and  $\beta_j$  is the direction of each incident wave component measured counterclockwise from the principal direction. The shape parameter  $n$  determines the strength of the directional spreading. In the current study  $n = 20$  is used to represent a narrow spreading sea state.

Breaking waves are detected following certain breaking wave criteria. In deep water, wave breaking criterion associated with wave steepness is used:

$$\frac{\partial \eta}{\partial x} \geq \beta \quad (15)$$

In shallow water domain, the depth-induced wave breaking is detected following this criterion:

$$\frac{\partial \eta}{\partial t} \geq \alpha \sqrt{gh}. \quad (16)$$

### 3 Numerical results

#### 3.1 Wave propagation over a submerged bar

At first, the proposed model is validated with wave propagation over a submerged bar [2]. The 2D numerical wave tank is 35 m long, the water depth at the input boundary is 0.4 m. A Neumann boundary condition is arranged at the inlet boundary to generate waves. A numerical beach of two wavelengths 8.73 m is located at the outlet. The submerged bar begins at  $x = 6$  m and elevates following a slope of 1 : 20 until the top platform at  $x = 12$  m, with a height of 0.3 m. The top platform remains 2 m before it starts a downwards slope of 1 : 10 and reaches the bottom at  $x = 17$  m. Nine wave gauges are located at  $x = 4.0$  m, 10.5 m, 12.5 m, 13.5 m, 14.5 m, 15.7 m, 17.3 m, 19.0 m and 21.0 m. The incident wave height is  $H = 0.02$  m and the wavelength is  $L = 3.73$  m. The configurations of the numerical wave tank are shown in Fig. 1.

The simulation time is 35 s, the CFL number is kept at 1.0 and 10  $\sigma$ -grid is used in the vertical direction. The grid convergence study in the horizontal direction is shown in Fig. 2, where 170 grid per wavelength is able to reach grid convergence and capture the high-frequency wave components. With the chosen grid resolution, 16000 grids are used in total. The time series at the nine wave gauges are shown in Fig. 3. It is seen that the wave elevations in the numerical wave tank agree with the experimental measurements at all the wave gauges during the entire wave transformation process. The wave shoaling effect with increasing wave heights is clearly observed at the windwards side of the submerged bar. The wave then decomposes into several higher frequency components at the lee side of the submerged bar. Those high-frequency short waves are also well represented in the numerical wave tank. In comparison, a CFD simulation requires 1322000 grids to resolve the high-frequency wave components. With 4 cores on a Mac Book Pro, the

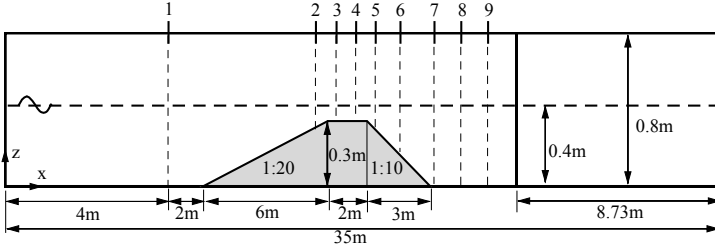


Figure 1: Numerical wave tank setup of the wave propagation over a submerged bar. The locations of the wave elevation gauges are marked with short vertical line segments from 1 to 9. The grey-shaded object is the submerged bar. A wave generation zone of 3.73 m and a numerical beach of 7.46 m are located at the left end and right end of the tank respectively.

FNPF simulation takes 138 s, while the CFD simulation takes about 17 hours using 12 cores on a Mac Pro.

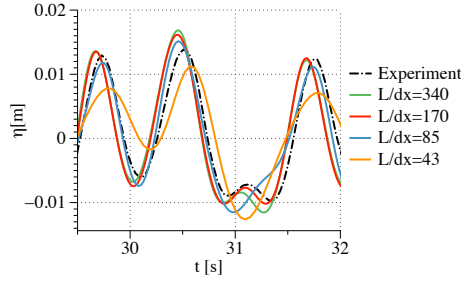


Figure 2: Grid convergence study at wave gauge 8.

### 3.2 Wave propagation over natural bathymetry near Norwegian coast

With the capacity of modelling wave propagation over varying bathymetry and high computational efficiency, the model is used to simulate large-scale wave propagation over natural topography in Sulafjord. The bathymetry data is obtained from the Norwegian Mapping Authority Kartverket. Fig. 4 shows the geographical domain of Sulafjord and the proposed options of the fjord-crossing and the crossing locations [21]. The chosen simulated area is shown as a black box in Fig. 4. The most dangerous wave direction for the fjord is shown as a red arrow in Fig. 4 [17]. In this paper, narrow spreading multi-directional irregular waves are simulated with the principal direction aligned with the

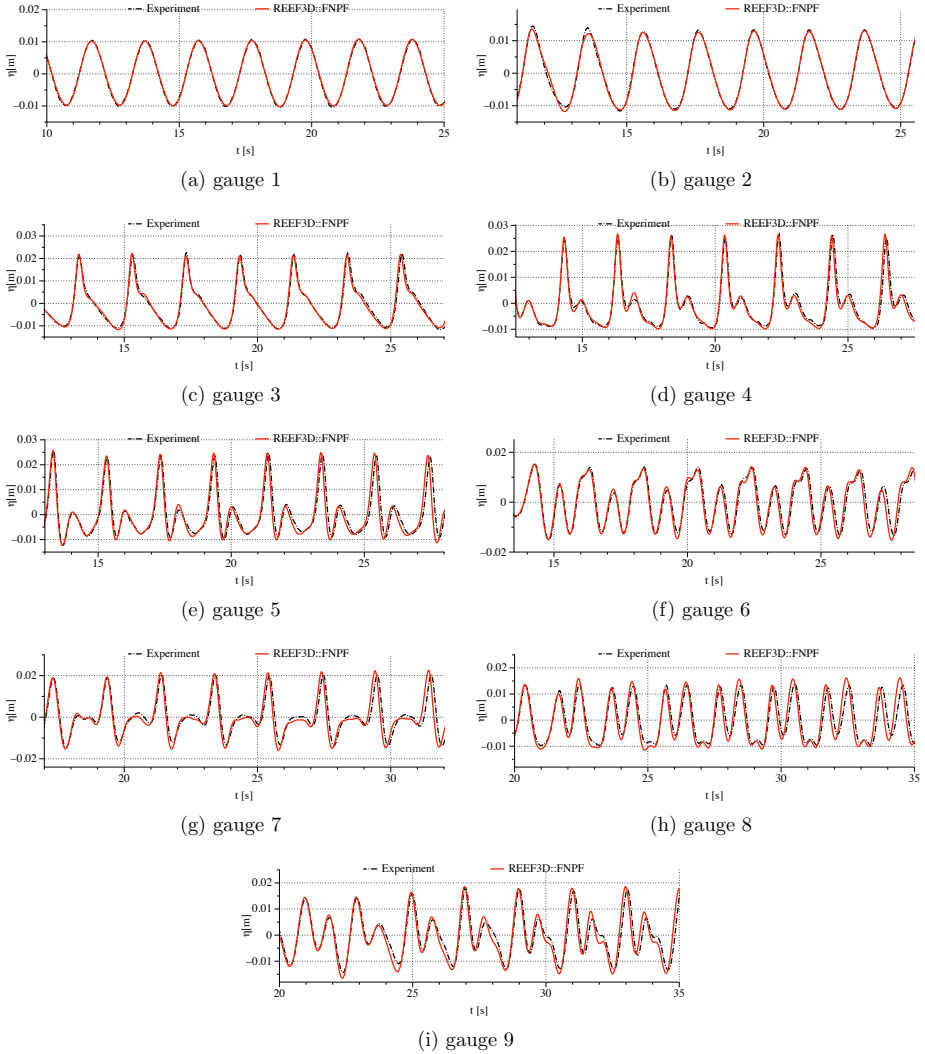


Figure 3: Surface elevations of the wave transformation over a submerged bar. (a)-(i) time series of the surface elevations at different wave gauges with 170 grids in one wave length and  $CFL = 1.0$ .

most dangerous wave direction. Therefore, the chosen domain is rotated in the numerical wave tank (NWT) so that the inlet boundary is perpendicular to the most dangerous wave direction. The resulting NWT has a Cartesian coordinate system with the x-axis ranging from 0 to 10000 m and y-axis ranging from 0 to 9000 m. The ongoing field measurements are conducted at three locations D, A and B, as shown in Fig.4. The coordinates of the three wave gauges in UTM 33 coordinate system and in the coordinate system of the numerical wave tank are listed in Table 1.

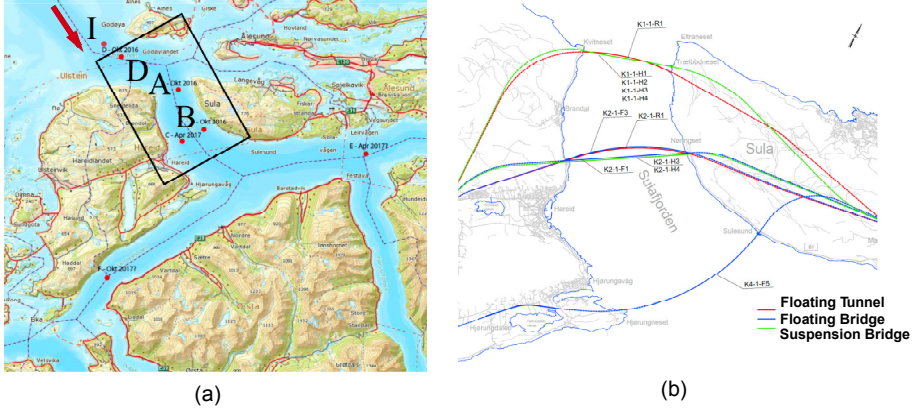


Figure 4: Illustration of the coastal area at Sulafjord, (a) locations of the wave gauges in Sulafjord and the simulated domain shown as the black box. The red arrow indicates the most dangerous wave direction for the fjord [17], (b) proposed fjord crossing options

Table 1: The wave height probes at Sulafjord

Probe denotation	x (UTM)	y (UTM)	x (NWT)	y (NWT)
I	31600.00	6957000.00	-	-
D	33109.42	6956082.14	81.5	2050.7
A	38596.05	6953729.83	5155.4	5195.8
B	40026.88	6950883.83	8307.4	4735.5

The simulated input wave has a significant wave height 2.67 m and a peak period 16.86 s. The dimension of the numerical tank is 10000 m long and 9000 m wide and the maximum water depth is 457 m. The wave generation boundary is shown as a black box

and the numerical beaches are shown as yellow boxes in Fig. 5. A grid size of 20 m is used in the simulation ensuring 20 to 40 grids per wave length for the wave components in the irregular wave field. 10 vertical grids are used, resulting in 2.475 million grids in total, and the CFL is kept 1.0 during the simulation.

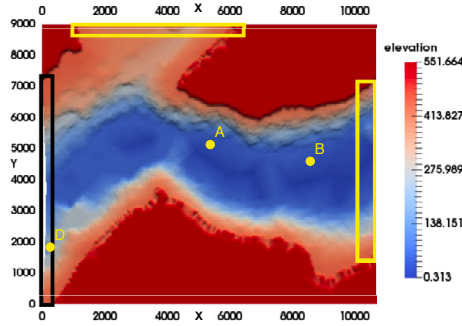


Figure 5: Bathymetry and numerical tank setup of the Sulafjord simulation. The black box is the wave generation boundary, the yellow boxes are the numerical beaches.

A 11500 s simulation is performed with 64 processors on the supercomputer Vilje, ensuring 3-hour time series at all three wave gauges. The computation time is 6.3 hours, only twice the length of the simulated time. The model demonstrates a high computational efficiency and a relatively low demand for computational infrastructure, making it appealing for industrial applications. The horizontal velocity field in the simulation is shown in Figure. 6:

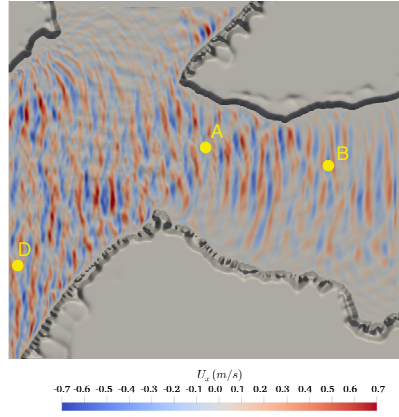


Figure 6: Horizontal velocities in the wave field in the Sulafjord simulation.

It is seen that the multi-directional irregular wave field is well represented and the wave diffraction and refraction phenomena can be clearly observed near the coastlines. With the complex wave transformation and wave-wave interaction, the statistical properties inside the fjord vary from location to location. To demonstrate this spatial variation, the simulated wave height  $H_s$ , peak period  $T_p$  and wave steepness  $\epsilon$  calculated using  $H_s$  and  $T_p$  at the three wave gauges D, A and B are normalised by the input wave parameters and compared in Figure. 7. Since D is located near the wave generation boundary, the wave properties are close to the input wave. However, the waves are higher, shorter and steeper at location A with the simulated sea state, indicating a more severe wave condition. The phenomenon is assumed to be a result of a combination of the shoaling process and wave reflection at location A. Further into the fjord towards location B, the wave condition becomes milder again in comparison to location A. Generally, the wave condition is possible to become more severe at some regions inside the fjord in comparison to the input waves at the entrance of the fjord. This is a phenomenon worth of attention in the bridge design. However, in order to systematically study the wave behaviour inside the fjord, more sea states need to be tested and the measured waves on site will provide more realistic input wave condition.

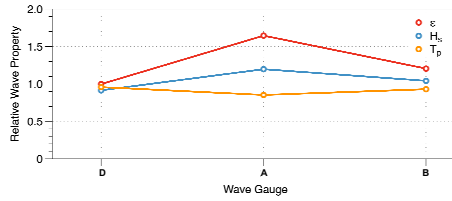


Figure 7: Variations of the normalised significant wave height  $H_s$ , peak period  $T_p$  and wave steepness  $\epsilon$  at the three wave gauges in the Sulafjord simulation. The horizontal dashed line indicate the input wave properties.

#### 4 CONCLUSIONS

A fully nonlinear potential flow model REEF3D::FNPF is described in the paper to provide an efficient tool for the numerical simulation of wave propagation with complex bathymetry and coastline in a large-scale domain. The model is validated against experimental data of wave propagation over a submerged bar. The shoaling and wave decomposition process are well represented and the time series at the designated wave gauges agree with the experimental measurements. The numerical model is then used to simulate waves in Sulafjord with complex bathymetry and coastline. A 3-hour simulation with 2.475 million grids is finished within 6.3 hours using 64 cores on the supercomputer Vilje. It marks a significant computational efficiency improvement and enables long duration wave simulation at large-scale domain. The complex wave transformation inside the fjord is well represented. The comparison of the wave conditions at three locations inside fjord shows that some locations might experience more severe wave condition than the incoming waves due to the local wave transformation and interaction. Further investigations of inhomogeneity and cross-spectrum analyses can be performed with a specifically arranged wave gauge array following the same methodology presented in the paper. The computational efficiency enables more systematic studies and full-scale validations against the wave measurements in the future.

#### Acknowledgement

This study has been carried out under the E39 fjord crossing project (No. 304624) and the authors are grateful to the grants provided by the Norwegian Public Roads Administration. This study was supported in part with computational resources at the Norwegian University of Science and Technology (NTNU) provided by The Norwegian Metacenter for Computational Sciences (NOTUR, <http://www.notur.no>) under project no. NN2620K, <http://www.notur.no>.



## REFERENCES

- [1] AHMAD, N., BIHS, H., MYRHAUG, D., KAMATH, A., AND IVIND A. ARNTSEN. Numerical modelling of pipeline scour under the combined action of waves and current with free-surface capturing. *Coastal Engineering* 148 (2019), 19 – 35.
- [2] BEJI, S., AND BATTJES, J. A. Experimental investigation of wave propagation over a bar. *Coastal Engineering* 19 (1993), 151–162.
- [3] BIHS, H., KAMATH, A., AGGARWAL, A., AND PAKOZDI, C. Efficient Wave Modeling using Nonhydrostatic Pressure Distribution and Free Surface Tracking on Fixed Grids. *Journal of Offshore Mechanics and Arctic Engineering* 141, 4 (apr 2019), 41805–41806.
- [4] BIHS, H., KAMATH, A., ALAGAN CHELLA, M., AND ARNTSEN, Ø. A. Extreme Wave Generation, Breaking, and Impact Simulations Using Wave Packets in REEF3D. *Journal of Offshore Mechanics and Arctic Engineering* 141, 4 (jan 2019), 41802–41807.
- [5] BIHS, H., WANG, W., MARTIN, T., AND KAMATH, A. REEF3D::FNPF - A Flexible Fully Nonlinear Potential Flow Solver. In *Proceeding of 38th International Conference on Ocean, Offshore Arctic Engineering* (2019 in press).
- [6] BOOIJ, N., RIS, R. C., AND HOLTHUIJSEN, L. H. A third-generation wave model for coastal regions, 1. model description and validation. *Journal of Geophysical Research* 104 (1999), 7649–7666.
- [7] CHELLA, M. A., BIHS, H., AND MYRHAUG, D. Wave impact pressure and kinematics due to breaking wave impingement on a monopile. *Journal of Fluids and Structures* 86 (2019), 94 – 123.
- [8] DUCROZET, G., BONNEFOY, F., LE TOUZÉ, D., AND FERRANT, P. A modified High-Order Spectral method for wavemaker modeling in a numerical wave tank. *European Journal of Mechanics - B/Fluids* 34 (July 2012), <http://dx.doi.org/10.1016/j.euromechflu.2012.01.017>.
- [9] DUCROZET, G., BONNEFOY, F., LE TOUZÉ, D., AND FERRANT, P. HOS-ocean: Open-source solver for nonlinear waves in open ocean based on High-Order Spectral method. *Computer Physics Communications* 203 (June 2016), 245–254.
- [10] ELLEVSET, O. Project overview coastal highway route E39. [www.vegvesen.no/attach ment/300340/binary/527486](http://www.vegvesen.no/attach%20ment/300340/binary/527486), January.
- [11] ENGSIG-KARUP, A., AND BINGHAM, H. Boundary-fitted solutions for 3d nonlinear water wave-structure interaction. In *IWWWFB24* (2009), p. 20.

- [12] JIANG, G. S., AND SHU, C. W. Efficient implementation of weighted ENO schemes. *Journal of Computational Physics* 126 (1996), 202–228.
- [13] KAMATH, A., BIHS, H., AND ARNTSEN, Ø. A. Study of Water Impact and Entry of a Free Falling Wedge Using Computational Fluid Dynamics Simulations. *Journal of Offshore Mechanics and Arctic Engineering* 139, 3 (mar 2017), 31802–31806.
- [14] KAMATH, A., CHELLA, M. A., BIHS, H., AND IVIND A. ARNTSEN. Evaluating wave forces on groups of three and nine cylinders using a 3d numerical wave tank. *Engineering Applications of Computational Fluid Mechanics* 9, 1 (2015), 343–354.
- [15] MADSEN, P. A., MURRAY, R., AND SØRENSEN, O. R. A new form of the Boussinesq equations with improved linear dispersion characteristics. *Coastal Engineering* 15 (1991), 371–388.
- [16] MAYER, S., GARAPON, A., AND SØRENSEN, L. S. A fractional step method for unsteady free surface flow with applications to non-linear wave dynamics. *International Journal for Numerical Methods in Fluids* 28 (1998), 293–315.
- [17] NORGESKART. Sulafjord. <http://www.norgeskart.no/?ga=1.148519543.1531380854.14846589939/26136/6963625/-land/+sjo>.
- [18] NWOGU, O. Alternative form of Boussinesq equations for nearshore wave propagation. *Journal of Waterways, Port, Coastal, and Ocean Engineering* 119, 6 (1993), 618–638.
- [19] PIERSON, W. J., NEUMANN, G., AND JAMES, R. W. Practical methods for observing and forecasting ocean waves by means of wave spectra and statistics.
- [20] SHU, C. W., AND OSHER, S. Efficient implementation of essentially non-oscillatory shock capturing schemes. *Journal of Computational Physics* 77 (1988), 439–471.
- [21] STATENSVEGVESEN. Illustrasjonskart E39 sulafjorden. <https://www.vegvesen.no/Euro+paveg/e39sulafjorden>, 2015.
- [22] SWAN. User manual swan cycle iii version 41.10a. Tech. rep., Delft University of Technology, 2017.
- [23] THOMAS, T. J., AND DWARAKISH, G. Numerical wave modelling a review. *Aquatic Procedia* 4 (2015), 443 – 448.
- [24] VAN DER VORST, H. BiCGStab: A fast and smoothly converging variant of Bi-CG for the solution of nonsymmetric linear systems. *SIAM Journal of Scientific Computing* 13 (1992), 631–644.

## NUMERICAL INVESTIGATION OF SCOUR BENEATH A SUBMARINE PIGGYBACK PIPELINE

Guang Yin<sup>1</sup>, Muk Chen Ong<sup>1</sup>

<sup>1</sup>Department of Mechanical and Structural Engineering and Materials Science  
University of Stavanger, 4036 Stavanger, Norway  
e-mail: guang.yin@uis.no, muk.c.ong@uis.no

**Key words:** scour, piggyback pipelines, SedFoam

**Abstract.** *In the present study, an open-source multi-dimensional Eulerian two-phase flow solver, SedFoam (based on OpenFOAM) is used to investigate the scour process beneath piggyback pipelines near the seabed. In the present model, the fluid Reynolds stress is solved using a two-phase  $k$ - $\epsilon$  model and the particle stress are modeled by kinetic theory for granular flow. The influences of different gap ratios between the small and large pipelines of the piggyback on the scour depth, sediment profiles as well as the surrounding flow field are studied.*

### 1 INTRODUCTION

Over the last decades, scour beneath a piggyback pipeline has been studied extensively by both experiments and numerical simulations. A piggyback pipeline consists of one large pipeline and a small one which is rigidly installed above the large one. It is found (Zhao & Cheng 2008; Zhao et al., 2015; Zhang et al., 2016 and 2017) that the scour depth beneath the piggyback is larger compared with that beneath a single pipeline. Furthermore, the scour depth increases with decreasing gap ratio between the two pipelines (Zhao & Cheng 2008). Two kinds of numerical methods have been devoted to the investigations of the sediment transport around the seabed. One of them is the single-phase model (Hoffmans & Pilarczyk 1995; Liu & Garcia 2008). In this model, semi-empirical formulations are used to resolve the bed-load transport rate and suspended-load flux boundary condition. Recently, the two-phase model has been developed to resolve more

complex physical phenomena in the process of sediment transport (Hsu & Liu 2004; Dong & Zhang 2002; Lee et al., 2016; Rusche 2003; Weller 2002). In the two-phase model, both the fluid phase and particle phase are assumed to be continuums governed by mass and momentum conservation equations. In the present study, an open-source multi-dimensional Eulerian two-phase solver, SedFoam, based on OpenFOAM (Cheng et al., 2017; Chauchat et al., 2017) is used to investigate the local scour beneath a piggyback pipeline. Two-dimensional (2D) simulations are carried out. The  $k-\varepsilon$  model is used to resolve the turbulence stress and the kinetic theory is adopted to model the particle stress. The paper is organized as follows. Section 2 gives a brief introduction on the model in the present study. The results of the scour beneath the piggyback pipelines with different gap ratios between the large pipeline and the small pipeline are presented in Section 3. Finally, the conclusion is made in Section 4.

## 2 MATHEMATICAL FORMULATION

In the two-phase flow model (Cheng et al., 2017), the continuum assumption is applied for both particle and fluid phases. The mass conservation equations for the two phases are

$$\frac{\partial(1-\phi)}{\partial t} + \frac{\partial(1-\phi)u_i^f}{\partial x_i} = 0 \quad (1)$$

$$\frac{\partial\phi}{\partial t} + \frac{\partial\phi u_i^s}{\partial x_i} = 0 \quad (2)$$

where  $\phi$  denotes the sediment volumetric concentration,  $u_i^f$  are the mean fluid velocities.  $u_i^s$  are the mean sediment velocities.  $x_i$  are the Cartesian coordinates and  $i=1,2$  are horizontal, vertical directions, respectively. The momentum equations for the two phases are

$$\frac{\partial\rho^f(1-\phi)u_i^f}{\partial t} + \frac{\partial\rho^f(1-\phi)u_i^f u_j^f}{\partial x_j} = -\frac{\partial(1-\phi)p^f}{\partial x_i} + \frac{\partial\tau_{ij}^f}{\partial x_j} + \rho^f(1-\phi)g\delta_{i2} + M_i^{fs} \quad (3)$$

$$\frac{\partial\rho^s\phi u_i^s}{\partial t} + \frac{\partial\rho^s\phi u_i^s u_j^s}{\partial x_j} = -\frac{\partial\phi p^f}{\partial x_i} - \frac{\partial p^s}{\partial x_i} + \frac{\partial\tau_{ij}^s}{\partial x_j} + \rho^s\phi g\delta_{i2} + M_i^{sf} \quad (4)$$

where  $\rho^f$  and  $\rho^s$  are the densities of the fluid and sediment respectively.  $g = 9.8\text{m/s}^2$

is the gravitational acceleration.  $p^f$  is the fluid pressure and  $\tau_{ij}^f$  is the fluid stress, which is expressed by

$$\tau_{ij}^f = R_{ij}^{ft} + R_{ij}^{fv} \quad (5)$$

The fluid stress comprises of two parts. One of them is the viscous stress

$$R_{ij}^{fv} = \rho^f (1 - \phi) \nu^f \left( \frac{\partial u_i^f}{\partial x_j} + \frac{\partial u_j^f}{\partial x_i} - \frac{2}{3} \frac{\partial u_k^f}{\partial x_k} \delta_{ij} \right) \quad (6)$$

( $\nu^f$  is the fluid kinematic viscosity) and the other is the turbulent Reynolds stress

$$R_{ij}^{ft} = \rho^f (1 - \phi) \left[ \nu^{ft} \left( \frac{\partial u_i^f}{\partial x_j} + \frac{\partial u_j^f}{\partial x_i} - \frac{2}{3} \frac{\partial u_k^f}{\partial x_k} \delta_{ij} \right) - \frac{2}{3} k^f \delta_{ij} \right] \quad (7)$$

( $\nu^{ft}$  is the eddy viscosity and  $k^f$  is the turbulent kinetic energy) which requires further closure by the turbulence model. In the present study, the  $k - \varepsilon$  model is used, and the eddy viscosity is obtained as

$$\nu^{ft} = C_\mu \frac{(k^f)^2}{\varepsilon^f} \quad (8)$$

with the empirical parameter  $C_\mu = 0.09$ .

The fluid turbulent kinetic energy and the turbulent dissipation are obtained through their transport equations. Only the equation of fluid turbulent kinetic energy is presented here as

$$\begin{aligned} \frac{\partial k^f}{\partial t} + u_j^f \frac{\partial k^f}{\partial x_j} = & - \frac{R_{ij}^{ft}}{\rho^f} \frac{\partial u_i^f}{\partial x_j} + \frac{\partial}{\partial x_j} \left[ \left( \nu^f + \frac{\nu^{ft}}{\sigma_k} \right) \frac{\partial k^f}{\partial x_j} \right] - \varepsilon^f - \frac{2\beta(1-\alpha)\phi k^f}{\rho^f(1-\phi)} \\ & - \frac{1}{(1-\phi)} \frac{\nu^{ft}}{\sigma_\varepsilon} \frac{\partial \phi}{\partial x_j} (s-1) g \delta_{j2} \end{aligned} \quad (9)$$

Two additional terms appear in (9) compared with that of single-phase flows. The fourth term in the right hand denotes drag dissipation and the last term represents density stratification effects. The drag parameter  $\beta$  is associated with the sediment concentration as

$$\beta = \begin{cases} \frac{150\phi\nu^f\rho^f}{(1-\phi)d^2} + \frac{1.75\rho^f|\mathbf{u}^f - \mathbf{u}^s|}{d}, \phi \geq 0.2 \\ \frac{0.75C_d\rho^f|\mathbf{u}^f - \mathbf{u}^s|(1-\phi)^{-1.65}}{d}, \phi < 0.2 \end{cases} \quad (10)$$

where  $d$  denotes the sediment diameter and the drag coefficient  $C_d$  is defined as

$$C_d = \begin{cases} \frac{24(1+0.15Re_p^{0.678})}{Re_p}, Re_p \leq 1000 \\ 0.44, Re_p > 1000 \end{cases} \quad (11)$$

In the formula,  $Re_p = (1-\phi)|\mathbf{u}^f - \mathbf{u}^s|d/\nu^f$  is the particle Reynolds number. The transport equation of the fluid turbulence dissipation  $\varepsilon^f$  can be derived by analogy in a similar way to the  $k^f$  equation.

The particle stress  $\tau_{ij}^s$  and the particle pressure  $p^s$  both consist of a collisional part and a frictional part

$$p^s = p^{sc} + p^{sf} \quad (12)$$

$$\tau_{ij}^s = \tau_{ij}^{sc} + \tau_{ij}^{sf} \quad (13)$$

For the collisional part, the kinetic theory of granular flow (Lun & Savage 1987) is employed where the collisional normal stress  $p^{sc}$  and the collisional shear stress  $\tau_{ij}^{sc}$  are associated with the granular temperature  $\Theta$  as

$$p^{sc} = \rho^s\phi[1+2(1+e)\phi g_{s0}]\Theta \quad (14)$$

$$\tau_{ij}^{sc} = \mu^{sc} \left[ \frac{\partial u_i^s}{\partial x_j} + \frac{\partial u_j^s}{\partial x_i} \right] + \left( \lambda - \frac{2}{3}\mu^{sc} \right) \frac{\partial u_k^s}{\partial x_k} \delta_{ij} \quad (15)$$

where

$$\mu^{sc} = \rho^s d \sqrt{\Theta} \left[ \frac{4\phi^2 g_{s0}(1+e)}{5\sqrt{\pi}} + \frac{\sqrt{\pi} g_{s0}(1+e)(3e-1)\phi^2}{15(3-e)} + \frac{\sqrt{\pi}\phi}{6(3-e)} \right] \quad (16)$$

$$\lambda = \frac{4}{3} \phi^2 \rho^s d g_{s0} (1+e) \sqrt{\frac{\Theta}{\pi}} \quad (17)$$

The granular temperature  $\Theta$ , which quantify the intensity of the particle velocity fluctuation, is obtained through a balance equation. This can be seen in Cheng et al. (2017) and is not presented in detailed here.

The frictional normal stress  $p^{sc}$  due to the enduring contact when the sediment concentration is above a certain threshold value is determined by

$$p^{sf} = \begin{cases} 0, \phi < \phi_f \\ F \frac{(\phi - \phi_f)^m}{(\phi_{\max} - \phi)^n}, \phi \geq \phi_f \end{cases} \quad (18)$$

where  $\phi_f = 0.57$ ,  $\phi_{\max} = 0.635$  and the empirical parameters are  $F = 0.05$ ,  $m = 3$ ,  $n = 5$ .

The frictional shear stress is given by

$$\tau_{ij}^{sf} = \mu^{sf} \left[ \frac{\partial u_i^s}{\partial x_j} + \frac{\partial u_j^s}{\partial x_i} \right] - \frac{2}{3} \mu^{sf} \frac{\partial u_k^s}{\partial x_k} \delta_{ij} \quad (19)$$

where  $\mu^{sf}$  is the frictional viscosity calculated by

$$\mu^{sf} = \frac{\sqrt{2} p^{sf} \sin(\theta_f)}{2 \sqrt{S_{ij}^s S_{ij}^s}} \quad (20)$$

In the expression,  $S_{ij}^s$  is the sediment shear rate and  $\theta_f$  is the angle of repose, which is

set to be the value of  $32^\circ$  for the sediment in the present study.

Finally, the interphase momentum transfer is given by

$$M_i^{fs} = -M_i^{sf} = -\phi \beta (u_i^f - u_i^s) + \beta \frac{v^f}{\sigma_c} \frac{\partial \phi}{\partial x_i} + p^f \frac{\partial (1-\phi)}{\partial x_i} \quad (21)$$

The first two terms are associated with the drag force through the drag parameter  $\beta$ .

The first term is the mean drag force resulted from the mean velocity difference between the two phases and the second term is the fluid suspension term. The third term is the interphase pressure correlation term.

The boundary conditions for the numerical simulations are set as follows

- No-slip boundary condition is applied for the fluid and the particle velocities on the surface of the two pipelines and the bottom boundary, which is assumed to be far enough below the fluid-sediment interface. The sediment concentration is set as zero gradient on the surface of pipelines and the rigid bed. Wall-function boundary conditions are imposed on the surface of pipelines for  $k^f$  and  $\varepsilon^f$ .
- At the top boundary, the velocities of the two phases as well as the sediment concentration are assumed to be zero gradient.
- At the inlet, a one-dimensional (1D) simulation is carried out to obtain the profiles of the velocities  $u_i^f, u_i^s$ , the sediment concentration  $\phi$  and  $k^f, \varepsilon^f$  for the 2D simulations. Zero gradient boundary condition is applied for the pressure.
- At the outlet, zero gradient boundary condition is used for the velocities of the two phases where the flow goes out of the domain. The velocities of the two phases are set to be the mean velocity value where the flow goes inside the domain. The sediment concentration  $\phi$  is set as zero gradient and the hydrostatic pressure

$p^f = \rho^f g y$  is imposed for the pressure.

Figure 1 shows the computational domain of the present simulation with a piggyback pipeline configuration. The diameter of the large pipeline is  $D$  and the diameter of the small pipeline is  $0.2D$ . The mean grain size diameter is  $d_{50} = 3.6 \times 10^{-4} \text{ m}$ . The density of the sediment is  $\rho^s = 2.6 \times 10^3 \text{ kg/m}^3$ . The density of the fluid is  $\rho^f = 1.0 \times 10^3 \text{ kg/m}^3$ . The Shields parameter  $\theta = \tau_\infty / [g(\rho^s - \rho^f)d_{50}]$ , obtained from the 1D simulation at the inlet is  $\theta = 0.3285$  close to the undisturbed Shields parameter of  $\theta = 0.33$  in Lee et al. (2016). The computational domain is  $45D$  long and  $h + 1.5D$  height ( $h = 0.23 \text{ m}$ , the same height as Lee et al., 2016). The distance between the center of the large pipeline and the inlet is  $15D$  and the distance between the center of the large pipeline and the outlet is  $30D$ . The initial sediment layer is set to be  $1.5D$  high. The effects of gap ratio between the two pipelines are studied. Simulations are carried out for the gap ratios of  $G/D = 0.25, 0.0625, 0$ .



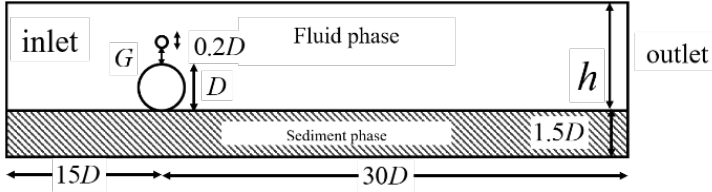


Figure 1. Computational domain

### 3 RESULTS AND DISCUSSION

Figure 2 shows time histories of the scour depth with different  $G/D$ . For the three gap ratios considered in the present study, the scour depth increases with decreasing  $G/D$ , and the scour depths of piggyback pipelines are larger than that of the single pipeline, which is  $0.8 \sim 1D$ .

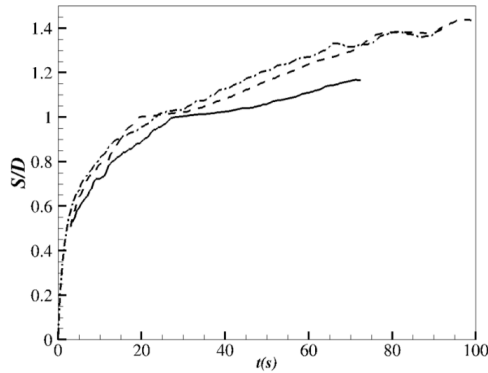
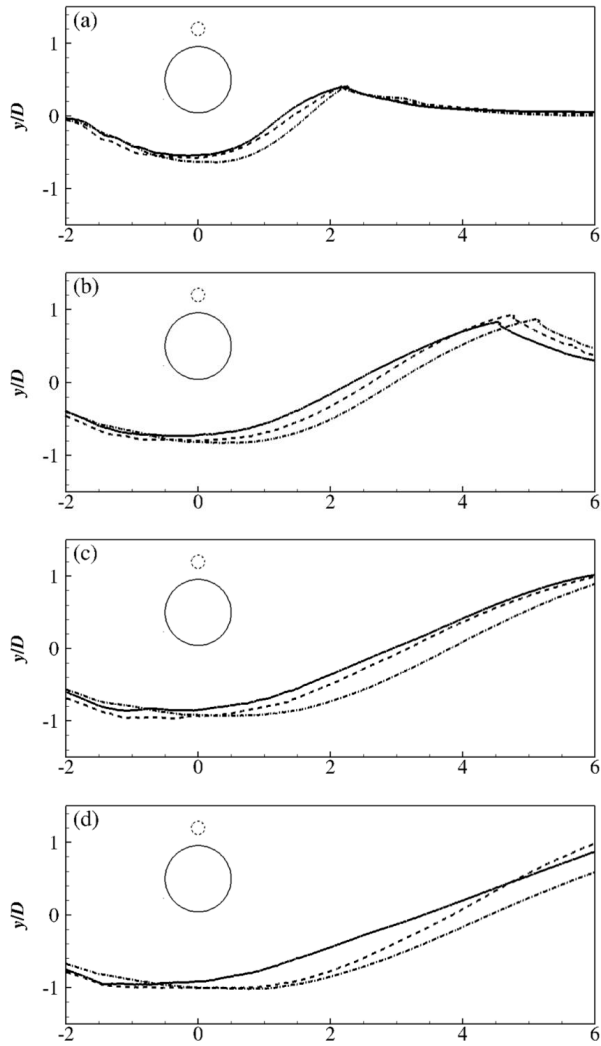


Figure 2. Time histories of the scour depth. Solid:  $G/D = 0.25$ ; Dash:  $G/D = 0.0625$ ; Dash-dotted:  $G/D = 0$

Figure 3 shows sediment profiles, which are denoted by  $\phi = 0.5$ , of the piggyback pipelines at five time steps of  $t = 4s, 11s, 18s, 25s, 30s$ . It is obvious that the difference between the sediment profiles in the front of the pipelines is small while behind the pipelines, there is large difference in the sediment profiles between different cases. Furthermore, the sand dune behind the pipelines for  $G/D = 0$  moves faster than other

cases.



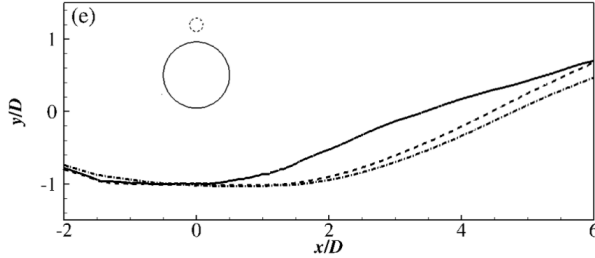


Figure 3. Sediment bed profiles at five time instants (a)  $t = 4s$  (b)  $t = 11s$  (c)  $t = 18s$  (d)  $t = 25s$  (e)  $t = 30s$ . Solid:  $G/D = 0.25$ ; Dash:  $G/D = 0.0625$ ; Dash-dotted:  $G/D = 0$  (the dashed small pipeline is located with  $G/D = 0.25$  is shown as an example)

Figure 4 presents the horizontal velocity contours and the streamlines of the fluid phase at  $t = 25s$ . Four high-speed regions are observed in the flow fields. The first one is observed above the sand dune behind the piggyback pipelines, which moves the sand dune behind the pipelines downstream. There is a large recirculation behind the sand dune that washes away the sediment from the sand dune (Lee et al., 2016). The second one is formed above the small pipelines and the third one is formed in the gaps between the two pipelines. The high-speed region above the small pipelines becomes weaker with decreasing  $G/D$ . The fourth high-speed region is formed below the large pipeline and is getting stronger with decreasing  $G/D$ , indicating that the sediment transport in the scour hole is getting more active. It is also shown that weak flow exists within the sediment bed because the present two-phase model can capture the motions of water within the sediment. At the same time step, for large gap ratio of  $G/D = 0.25$ , the two recirculation zones behind the two pipelines are weakly connected. When the small pipeline is getting closer to the large one, the high-speed jet-like flow through the gap is becoming stronger and the wake zone behind the large pipeline tends to be suppressed by that behind the small pipeline. Finally, when  $G/D = 0$ , the two wake zones almost merge together and two large recirculation motions are formed, which is similar to those behind a single pipeline.

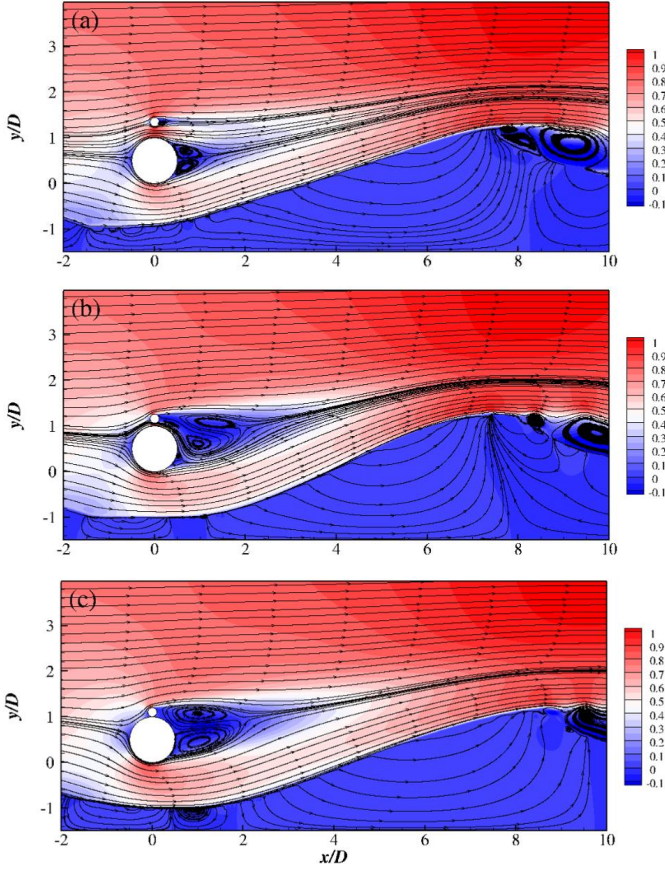


Figure 4. Fluid phase flow streamlines and the horizontal velocity contours of the fluid phase at  $t = 25s$ : (a)  $G/D = 0.25$ ; (b)  $G/D = 0.0625$ ; (c)  $G/D = 0$ .

Further comparison is made for the turbulent kinetic energy of the fluid phase at  $t = 25s$ , as shown in Figure 5. High level of turbulent motions is formed in front of the piggyback pipelines. For the large gap ratio  $G/D = 0.25$ , there is strong turbulent kinetic energy around the gap between the two pipelines. When the gap ratio becomes smaller, high level of turbulent kinetic energy tends to move to the fringe of the wake zone behind the piggyback pipelines and the turbulent kinetic energy is getting stronger in the scour

hole, which induces stronger sediment transport beneath the piggyback pipelines and causes deeper scour depth as shown in Figure 2.

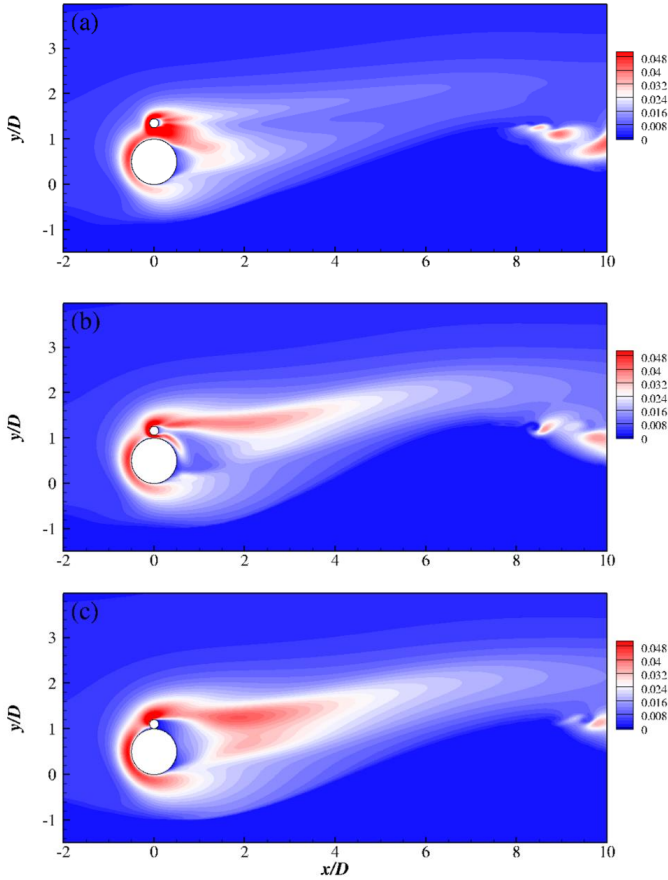


Figure 5. Fluid phase turbulent kinetic energy at  $t = 25s$  : (a)  $G/D = 0.25$  ; (b)  $G/D = 0.0625$ ; (c)  $G/D = 0$

#### 4 CONCLUSIONS

The present study presents the application of the two-phase solver, SedFoam on the scour process below piggyback pipelines with different gap ratios between the two pipelines. 2D simulations are carried out combined with the  $k-\varepsilon$  turbulence model and

the kinetic theory of the granular flow. The main conclusions can be outlined as follows:

- The piggyback configurations in the present study increase the scour depth compared with that of a single pipeline. The scour depth increases with decreasing  $G/D$  and the piggyback pipeline with  $G/D=0$  causes the largest scour depth.
- With decreasing  $G/D$ , the wake zone of the large pipeline tends to be suppressed by the wake zone of the small pipeline. For  $G/D=0$ , the wake zone appears to be similar to that behind a single pipeline but with the larger diameter  $1.2D$ .
- Strong turbulent kinetic energy is observed in front of the piggyback pipelines. With decreasing  $G/D$ , high turbulent energy becomes distributed in the fringe of the wake zone and there is stronger turbulent kinetic energy beneath the piggyback pipeline, which causes active sediment transport and larger scour depth.

## ACKNOWLEDGMENTS

This study was supported in part with computational resources provided by the Norwegian Metacenter for Computational Science (NOTUR), under Project No: NN9372K.

## REFERENCES

- [1] Chauchat, J., Cheng, Z., Nagel, T., Bonamy, C., & Hsu, T. J. 2017. SedFoam-2.0: a 3-D two-phase flow numerical model for sediment transport. *Geoscientific Model Development*, 10(12).
- [2] Cheng, Z., Hsu, T. J., & Calantoni, J. 2017. SedFoam: A multi-dimensional Eulerian two-phase model for sediment transport and its application to momentary bed failure. *Coastal Engineering*, 119, 32-50.
- [3] Dong, P., & Zhang, K. 2002. Intense near-bed sediment motions in waves and currents. *Coastal Engineering*, 45(2), 75-87.
- [4] Hoffmans, G. J., & Pilarczyk, K. W. 1995. Local scour downstream of hydraulic structures. *Journal of Hydraulic Engineering*, 121(4), 326-340.
- [5] Hsu, T. J., & Liu, P. L. F. 2004. Toward modeling turbulent suspension of sand in the nearshore. *Journal of Geophysical Research: Oceans*, 109(C6).
- [6] Lee, C. H., Low, Y. M., & Chiew, Y. M. 2016. Multi-dimensional rheology-based two-phase model for sediment transport and applications to sheet flow and pipeline scour. *Physics of Fluids*, 28(5), 053305.
- [7] Liu, X., & García, M. H. 2008. Three-dimensional numerical model with free water surface and mesh deformation for local sediment scour. *Journal of Waterway, Port, Coastal, and Ocean Engineering*, 134(4), 203-217.

- [8] Lun, C. K. K., & Savage, S. B. 1987. A simple kinetic theory for granular flow of rough, inelastic, spherical particles. *J. Appl. Mech*, 54(1), 47-53.
- [9] Rusche, H. 2003. Computational fluid dynamics of dispersed two-phase flows at high phase fractions (Doctoral dissertation, Imperial College London (University of London)).
- [10] Zhang, Q., Draper, S., Cheng, L., & An, H. 2016. Time Scale of Local Scour around Pipelines in Current, Waves, and Combined Waves and Current. *Journal of Hydraulic Engineering*, 143(4), 04016093.
- [11] Zhang, Q., Draper, S., Cheng, L., Zhao, M., & An, H. 2017. Experimental study of local scour beneath two tandem pipelines in steady current. *Coastal Engineering Journal*, 59(01), 1750002.
- [12] Zhao, E., Shi, B., Qu, K., Dong, W., & Zhang, J. 2018. Experimental and Numerical Investigation of Local Scour Around Submarine Piggyback Pipeline Under Steady Current. *Journal of Ocean University of China*, 17(2), 244-256.
- [13] Zhao, M., Vaidya, S., Zhang, Q., & Cheng, L. 2015. Local scour around two pipelines in tandem in steady current. *Coastal Engineering*, 98, 1-15.
- [14] Zhao, M., & Cheng, L. 2008. Numerical modeling of local scour below a piggyback pipeline in currents. *Journal of Hydraulic Engineering*, 134(10), 1452-1463.





# A POWER LAW OF PARTICLE ENSTROPY IN A TURBULENT CHANNEL FLOW AT A MEDIUM REYNOLDS NUMBER

YUCHENG JIE<sup>1</sup>, HELGE I. ANDERSSON<sup>2</sup> AND LIHAO ZHAO<sup>1,\*</sup>

<sup>1</sup>AML, Department of Engineering Mechanics  
Tsinghua University  
Beijing 100084, China  
\*e-mail: zhaolihao@tsinghua.edu.cn

<sup>2</sup> Department of Energy and Process Engineering  
Norwegian University of Science and Technology  
Trondheim 7491, Norway  
e-mail: helge.i.andersson@ntnu.no

**Key words:** Particle-laden flows; turbulent channel flows; direct numerical simulation; spheroidal particles

**Abstract.** High Reynolds number particle-laden turbulence simulations are deficient in earlier studies, especially for non-spherical particles, contrary to the extensiveness of these flows in reality. A turbulent channel flow laden with spheroidal particles is explored in present study at a relatively higher Reynolds number comparing to most turbulent channel flow simulations with non-spherical particles. The flow is obtained by *Direct numerical simulation* (DNS), together with a one-way coupled *Lagrangian particle tracking* (LPT) method to capture the motion of point-like particles. A power law of particle enstrophy versus wall-normal location is discovered away from the wall, a region that does not exist in low Reynolds number simulations. This indicates that many underlying phenomena of particle-laden flows remain to be explored in turbulent channel flows at high Reynolds numbers. The power law is prominent and arises from a similar power law of fluid enstrophy while scarcely related to the shape and inertia of particles.

## 1 Introduction

Particle-laden flows are universal in both natural phenomena and daily lives of human beings. For example, pollen or sand suspended in the lower atmosphere, plankton in oceanic flows and fibers in paper-making pulp are all particles, usually of irregular shapes, in fluid flows [1, 2, 3]. The Reynolds numbers involved in these problems are usually quite high. For instance, friction Reynolds number of a turbulent flow in a desert can

easily reach a magnitude of  $10^6$  or even larger [2]. Therefore, it is of great significance to perform numerical simulations of turbulent flows suspended with particles at high enough Reynolds number. While the Reynolds numbers of turbulent flow simulations are unfortunately limited due to computer capacity. Thanks to the rapid development of computer performance in recent decades, the Reynolds number and computational domain of simulations increase enormously [4, 5].

Figure 1 shows the development of DNS of turbulent channel flows and those with particles through comparing their friction Reynolds numbers  $Re_\tau$  versus time. The first DNS of turbulent channel flow was performed by Kim et al. in 1987 [6]. Then the Reynolds number booms in recent years owing to rapid development of computer hardware. In 1989, McLaughlin first performed a DNS of a turbulent channel flow suspended with spherical particles [7] while the first DNS of turbulent channel with non-spherical particles was accomplished by Zhang et al. in 2001, more than a decade later [8]. On the other hand, the friction Reynolds number of turbulent channel flow has reached  $Re_\tau \approx 5200$  in 2015 by Lee & Moser [5]. As for particle-laden turbulent channel flow, Bernardini [9] performed simulations up to  $Re_\tau = 1000$ , including spheres with Stokes numbers in the range  $St = 1 - 1000$ , in order to study the Reynolds number scaling of concentration profiles and deposition for spherical particles. Most recently, Ouchene et al. [10] carried out a simulation at  $Re_\tau = 1440$  with prolate spheroidal particles and investigated acceleration statistics. As shown in Figure 1, it takes nearly ten more years for  $Re_\tau$  of turbulent channel flows with particles to reach the same magnitude as those without particles.

However, most simulations of non-spherical particle-laden channel flows were confined to relatively low Reynolds numbers about 200, including studies of tracers [11], inertial prolate particles [12, 13] and oblate ones [14]. Therefore, a vast potential of growth exists for simulations of non-spherical particle-laden turbulent flows, where significant phenomena and mechanisms of particle-laden flows may hide.

Since there are rare simulations of turbulent channel flows suspended with non-spherical particles, a DNS of turbulent channel flow at  $Re_\tau = 600$  with non-spherical particles was performed in the present study. In the present investigation, a simple sort of non-spherical particle, spheroidal particle, is adopted. We aim to explore rotational behavior of spheroidal particles in the region away from the walls, which is not present in low Reynolds number turbulence, instead of regions in the vicinity of the walls.

## 2 Methods

The turbulent channel flow is obtained through DNS, together with a Lagrangian particle tracking method to track each individual particle. In the present simulation, the size of particle is smaller than Kolmogorov scale, the smallest scale in turbulent flows. In addition, the mass fraction of particle in the channel flow is also small enough so that a one-way coupling method could be employed, namely the interaction between particles and the reacting force from particle to the fluid are neglected. To describe the movement of spheroidal particles, two sets of reference frames are distinguished, the *inertial frame*

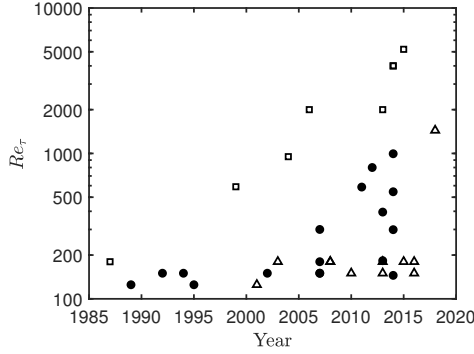


Figure 1: Friction Reynolds numbers of DNS versus time. Open squares: turbulent channel flows; solid circles: turbulent channel flows with spherical particles; open triangles: turbulent channel flows with non-spherical particles. (The figure is original and the data points are collected from more than thirty publications.)

$x_i = \{x_1, x_2, x_3\} = \{x, y, z\}$  and the *particle frame*  $x'_i = \{x'_1, x'_2, x'_3\} = \{x', y', z'\}$ . The origin of the particle frame is fixed at the particle mass center and the coordinate axis  $z'$  is aligned with the symmetry axis of the spheroid.

## 2.1 Eulerian fluid phase

The fluid is incompressible Newtonian fluid, with density  $\rho$  and kinematic viscosity  $\nu$ . The Navier-Stokes equations:

$$\frac{\partial u_i}{\partial x_i} = 0 \quad (1)$$

$$\frac{\partial u_i}{\partial t} + u_j \frac{\partial u_i}{\partial x_j} = -\frac{1}{\rho} \frac{\partial p}{\partial x_i} + \nu \frac{\partial^2 u_i}{\partial x_j \partial x_j} \quad (2)$$

are solved in conjunction with periodic boundary conditions in the streamwise ( $x$ ) and spanwise ( $y$ ) direction and no-slip boundary condition at both walls in the wall-normal ( $z$ ) direction. A second-order finite-difference scheme is used in the wall-normal direction while in the streamwise and spanwise direction, a pseudo-spectral method is employed. Moreover, a second-order Adams-Bashforth scheme is adopted for time evolution. The DNS solver was adopted in several previous studies. [15, 12, 14, 16]

Hereinafter,  $x_i$  denotes coordinates of the inertial reference frame in three different directions,  $p$  stands for pressure and  $u_i$  represents instantaneous velocity. Since only one-way coupling of particle-laden flow is considered, there is no reacting force of particles on fluid. In addition, the gravity force is neglected. Based on half-channel height  $h$  and friction velocity  $u_\tau$ , the friction Reynolds number of this turbulent channel flow is defined as  $Re_\tau = u_\tau h / \nu = 600$ . Viscous scales, such as viscous length scale  $\delta_\nu = \nu / u_\tau$  and time

$Re_\tau$	$L_x \times L_y \times L_z$	$N_z$	$\Delta x^+$	$\Delta y^+$	$\Delta z_c^+$	$\Delta z_1^+$
590 [17]	$2\pi h \times \pi h \times 2h$	257	9.7	4.8	7.2	0.044
550 [5]	$8\pi h \times 3\pi h \times 2h$	384	8.9	5.0	4.5	0.003
600	$6h \times 3h \times 2h$	384	9.375	4.6875	5.2876	0.143

Table 1: Simulation parameters of the present study ( $Re_\tau = 600$ ) and the previous studies at similar Reynolds numbers [17, 5].

	$\lambda < 1$	$\lambda = 1$	$\lambda > 1$
$K'_{xx} = K'_{yy}$	$\frac{32\pi a(1-\lambda^2)^{3/2}}{(3-2\lambda^2)(\pi-C)-2\lambda(1-\lambda^2)^{1/2}}$	$6\pi a$	$\frac{16\pi a\sqrt{(\lambda^2-1)^3}}{(2\lambda^2-3)\ln\left(\lambda+\sqrt{(\lambda^2-1)}\right)+\lambda\sqrt{(\lambda^2-1)}}$
$K'_{zz}$	$\frac{16\pi a(1-\lambda^2)^{3/2}}{(1-2\lambda^2)(\pi-C)+2\lambda(1-\lambda^2)^{1/2}}$	$6\pi a$	$\frac{8\pi a\sqrt{(\lambda^2-1)^3}}{(2\lambda^2-1)\ln\left(\lambda+\sqrt{(\lambda^2-1)}\right)-\lambda\sqrt{(\lambda^2-1)}}$
$C$	$2\tan^{-1}\left(\lambda(1-\lambda^2)^{-1/2}\right)$		

Table 2: Analytical expressions for resistance tensor components

scale  $\tau_\nu = \nu/u_\tau^2$ , are adopted to normalize physical variables, denoted by a superscript + after normalization. The size of the channel is  $6h \times 3h \times 2h$  in the streamwise, spanwise and wall-normal direction, respectively.  $384^3$  grid points are used and grid spacings are uniform in the streamwise and the spanwise direction, namely  $\Delta x^+ = 9.375$  and  $\Delta y^+ = 4.6875$  respectively. Grids in the wall-normal direction are refined in the vicinity of the walls so the spacings vary from  $\Delta z_1^+ = 0.143$  to  $\Delta z_c^+ = 5.2876$ . The time step of the present DNS is  $\Delta t^+ = 0.018$ .

To compare the grid resolution between the present simulation and the previous studies at similar Reynolds numbers [17, 5], Table 1 is provided to show the parameters of the three simulations. The grid spacing in the streamwise and the spanwise directions are approximately the same. The grid spacing  $\Delta z_c^+$  in the channel center is fine enough as shown in the table. The near-wall grid spacing in the wall-normal direction  $\Delta z_1^+$  in the present study is larger than those in the previous studies, while statistics of fluid flow are not affected. The mean streamwise velocity and the root-mean-squares of vorticity fluctuations are shown in Figure 2(a) and (b), respectively. The triangles represent results from Moser et al. [17], while the circles stand for those from Lee & Moser [5]. The circles, the triangles and the corresponding line, denoting results in the present study, are coincident, showing that the profiles of mean streamwise velocity and rms of vorticity fluctuations are almost the same. This suggests that the resolution of the present simulation is fine enough to obtain reliable flow field.

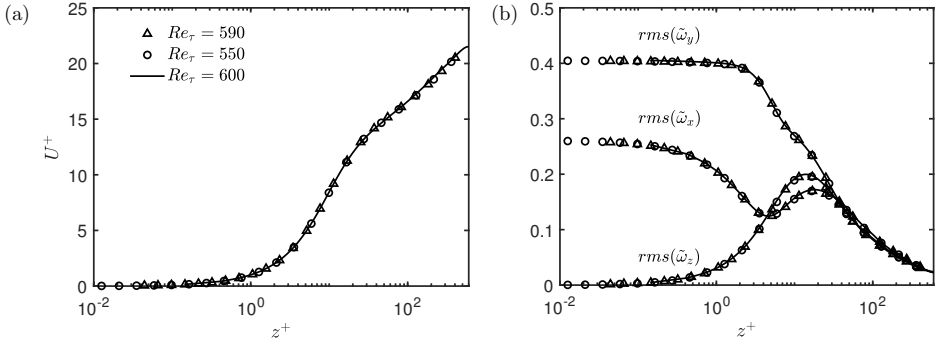


Figure 2: (a) Mean streamwise velocity versus wall-normal distance; (b) Root-mean-squares of vorticity fluctuations versus wall-normal distance.

	$\lambda < 1$	$\lambda = 1$	$\lambda > 1$
$\alpha_0 = \beta_0$	$\frac{-\lambda}{2(1-\lambda^2)^{3/2}} \left( C - \pi + 2\lambda(1-\lambda^2)^{1/2} \right)$	$\frac{2}{3}$	$\frac{\lambda^2}{\lambda^2-1} + \frac{\lambda}{2\sqrt{(\lambda^2-1)^3}} K$
$\gamma_0$	$\frac{1}{(1-\lambda^2)^{3/2}} \left( \lambda C - \lambda\pi + 2(1-\lambda^2)^{1/2} \right)$	$\frac{2}{3}$	$-\frac{2}{\lambda^2-1} - \frac{\lambda}{\sqrt{(\lambda^2-1)^3}} K$
$K$	$\ln \left( \frac{\lambda - \sqrt{(\lambda^2-1)}}{\lambda + \sqrt{(\lambda^2-1)}} \right)$		

Table 3: Analytical expressions for shape factors

## 2.2 Lagrangian particle phase

A Lagrangian tracking method was utilized to simulate the translation of particles. And the torque acting on spheroidal particles is considered to compute rotation of particles. First of all, the shape of a spheroid is described by an aspect ratio  $\lambda = c/a$ , where  $c$  is the distance from center to pole along the symmetry axis and  $a$  is the equatorial radius of the spheroid. Therefore,  $\lambda > 1$  stands for prolate particles while  $\lambda < 1$  denotes oblate ones. An orthogonal transformation matrix  $A_{ij}$  is adopted, which describes linear transformation between the two reference frames  $x_i = A_{ij}x'_j$ . Hereinafter, the superscript  $'$  denotes variables in the particle frame. In present study, since the particle Reynolds number is small ( $Re_p = |v - u|a/\nu \ll 1$ ), only the Stokes force is considered. The

translation and rotation of a particle is governed by:

$$m \frac{dv_i}{dt} = F_i = \pi \mu a K_{ij} (u_j - v_j) \quad (3)$$

$$I'_{ij} \frac{d\omega'_j}{dt} + \varepsilon_{ijk} \omega'_j I'_{kl} \omega'_l = N'_i \quad (4)$$

$$m = \frac{4}{3} \pi a^3 \lambda \rho_p. \quad (5)$$

In equations (3) and (4),  $v_i$  represents particle velocity while  $\omega'_i$  stands for angular velocity of spheroids in the particle frame.  $m$  is the mass of a single particle ( $\rho_p$  is the density of particles) and  $I'_{ij}$  is its moment of inertia. The resistance tensor  $K_{ij}$  in the inertial frame can be obtained by equation (6), where  $K'_{ij}$  denotes the resistance tensor in the particle frame [18]:

$$K_{ij} = A_{ik}^T K'_{kl} A_{lj}. \quad (6)$$

The analytical expressions for the resistance tensor components are listed in Table 2.

The torque  $N'_i$  in equation (4) was first derived by Jeffery [19] for an ellipsoidal particle in creeping flow. It is related to the shape of the spheroid, fluid strain rate tensor  $S'_{ij}$  and rotation vector of fluid  $\Omega'_i$  in the particle frame:

$$N'_x = \frac{16\pi\mu a^3\lambda}{3(\beta_0 + \lambda^2\gamma_0)} [(1 - \lambda^2) S'_{yz} + (1 + \lambda^2) (\Omega'_x - \omega'_x)] \quad (7)$$

$$N'_y = \frac{16\pi\mu a^3\lambda}{3(\alpha_0 + \lambda^2\gamma_0)} [(\lambda^2 - 1) S'_{xz} + (1 + \lambda^2) (\Omega'_y - \omega'_y)] \quad (8)$$

$$N'_z = \frac{32\pi\mu a^3\lambda}{3(\alpha_0 + \beta_0)} (\Omega'_z - \omega'_z). \quad (9)$$

The shape parameters  $\alpha_0, \beta_0, \gamma_0$  are functions of aspect ratio (see Table 3)

To evaluate the influence of inertia, a Stokes number is defined based on the particle response time  $\tau_p$  and fluid viscous time scale  $\tau_\nu$ . As derived by Shapiro and Goldenberg [20] and Challabotla et al. [14], expressions for particle response time of prolate and oblate spheroids are:

$$\tau_{p,prolate} = \frac{2}{9} \frac{\rho_p a^2 \lambda \ln(\lambda + \sqrt{\lambda^2 - 1})}{\rho \nu \sqrt{\lambda^2 - 1}} \quad (10)$$

$$\tau_{p,oblate} = \frac{2}{9} \frac{\rho_p a^2 \left[ \pi - 2 \tan^{-1} \left( \lambda (1 - \lambda^2)^{-1/2} \right) \right]}{\rho \nu 2(1 - \lambda^2)^{1/2}}. \quad (11)$$

Both the translation and rotation equations of particles are solved by using an explicit second-order Adams-Bashforth scheme. The fluid flow variables at the particle position

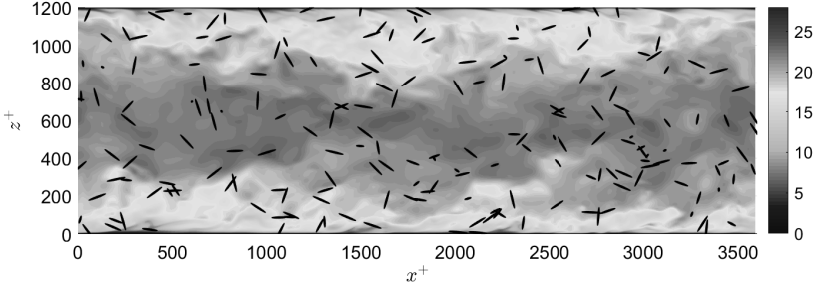


Figure 3: Orientations of non-spherical particles ( $\lambda = 10, St = 1$ ) in a streamwise-wall-normal plane. Size of particle is enlarged for visualization purpose.

were obtained by using a quadratic interpolation scheme. Fifteen sorts of spheroidal particles are inserted into the fully developed flow. The number of particles is  $N_p = 6 \times 10^5$  for each sort, which is sufficiently large enough to make statistics smooth. Aspect ratios and Stokes numbers are  $\lambda = 10, 3, 1.001, 0.33, 0.1$  and  $St = 1, 5, 30$ , respectively. The time-window for statistics of particles ranges from  $t^+ = 2610$  to  $t^+ = 3492$ . Although particles are drifting towards the walls due to turbophoresis, the orientation and rotation statistics are unaffected during the sampling period.

### 3 Results

In the first place, the orientations of spheroidal particles suspended in the channel flows are shown in Figure 3. The background color represents the magnitude of fluid streamwise velocity while the black ellipsoids stand for particles, orienting towards different directions, as reflected by the projection of the spheroid into the  $(x, z)$ -plane. Orientation and rotation of particles are greatly influenced by the wall, or shear in the vicinity of wall, according to previous investigations [21, 12, 14, 22, 16]. But there are rare studies which concentrate on behaviors of particles away from the wall in a turbulent channel flow. Bernardini [9] have studied the Reynolds number scaling of spherical particles concentration profiles and deposition at  $Re_\tau$  up to 1000. In the present research, we concentrate on the behaviors of spheroidal particles away from the walls, mainly the rotational motion of particles.

The degree of particle's rotation is described by the magnitude of particle enstrophy, which is defined as  $\langle \tilde{\omega}_i^+ \tilde{\omega}_i^+ \rangle = \langle \tilde{\omega}_x^+ \tilde{\omega}_x^+ + \tilde{\omega}_y^+ \tilde{\omega}_y^+ + \tilde{\omega}_z^+ \tilde{\omega}_z^+ \rangle$ . The tilde sign  $\tilde{\cdot}$  denotes fluctuation of a physical variable hereafter. Enstrophy of three sorts of *spherical* particles with different Stokes numbers is calculated and shown in Figure 4. The Stokes numbers of particles are 1, 5, 30, which have a quite small influence on the curves of particle enstrophy. However, all these curves seem to be linear from about  $z^+ = 100$  to  $z^+ = 400$  in the double-logarithmic coordinates, which reveals that a power law of

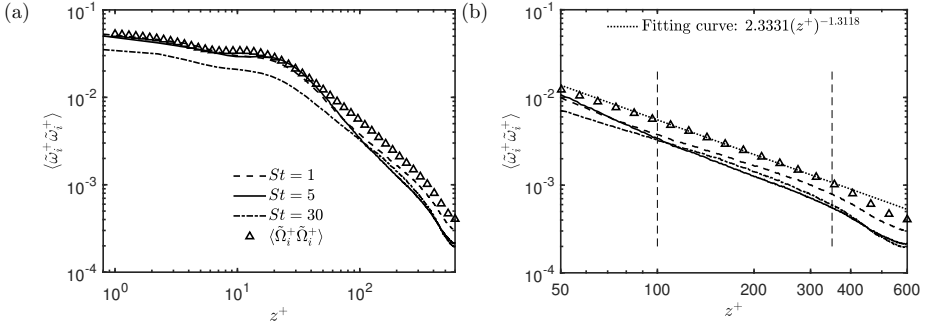


Figure 4: (a) and (b) Mean enstrophy of spherical particles with  $St = 1, 5, 30$  and a quarter of fluid enstrophy ( $\langle \tilde{\Omega}_i^+ \tilde{\Omega}_i^+ \rangle$ ) versus wall-normal location  $z^+$ . The dotted fitting curve of  $\langle \tilde{\Omega}_i^+ \tilde{\Omega}_i^+ \rangle$  in (b) indicating the power law of enstrophy.

enstrophy versus  $z^+$  exists. The size of these particles are all smaller than the Kolmogorov scale and the rotational motion of small-scale fluid eddies have a great influence on rotation motion of particles. Therefore, the power law of particle enstrophy could arise from similar property of fluid. The power law is assumed to be related to fluid vorticity enstrophy, which is displayed in Figure 4. The fluid enstrophy is defined as  $\langle (2\tilde{\Omega}_i^+)(2\tilde{\Omega}_i^+) \rangle = 4\langle \tilde{\Omega}_i^+ \tilde{\Omega}_i^+ \rangle = 4(\langle \tilde{\Omega}_x^+ \tilde{\Omega}_x^+ \rangle + \langle \tilde{\Omega}_y^+ \tilde{\Omega}_y^+ \rangle + \langle \tilde{\Omega}_z^+ \tilde{\Omega}_z^+ \rangle)$ , where  $\Omega_i^+$  stands for rotation vector of fluid, namely one half of the corresponding fluid vorticity. A similar power law of fluid enstrophy is present as expected (see Figure 4). In addition, the dotted line is obtained by linear fitting of fluid enstrophy at a range of  $z^+ = 100 \sim 350$ . The exponent of the power law is about  $-1.3118$  and the correlation coefficient between fluid enstrophy and wall-normal location is  $-0.9997$ , quite approaching to unity, where the minus sign represents negative correlation. Hence, it is reasonable that the power law of fluid enstrophy gives rise to the power law of particle enstrophy.

In addition, the effect of particle shape is considered. Enstrophy of different *spheroidal* particles are presented in Figure 5. There is only a little discrepancy between enstrophy of different spheroids with the same Stokes number. And the discrepancy is near zero when wall-normal location  $z^+ > 100$ . (Note the double-logarithmic plot.) It indicates that the aspect ratio has negligible effects on particle enstrophy away from the wall. Moreover, there is also a prominent power law of particle enstrophy versus wall-normal location. Therefore, we can concluded that the power law of particle enstrophy exists for all aspect ratios and Stokes numbers involved. It is assumed that the power law of enstrophy versus  $z^+$  obeys  $\langle \tilde{\omega}_i^+ \tilde{\omega}_i^+ \rangle \sim (z^+)^k$ , namely,  $\ln \langle \tilde{\omega}_i^+ \tilde{\omega}_i^+ \rangle \sim k \ln z^+$ , where  $k$  is the exponent. The power law is most prominent between about  $z^+ = 100$  till  $z^+ = 350$ , the two vertical dashed lines in the figures. Hence, the range of wall-normal location



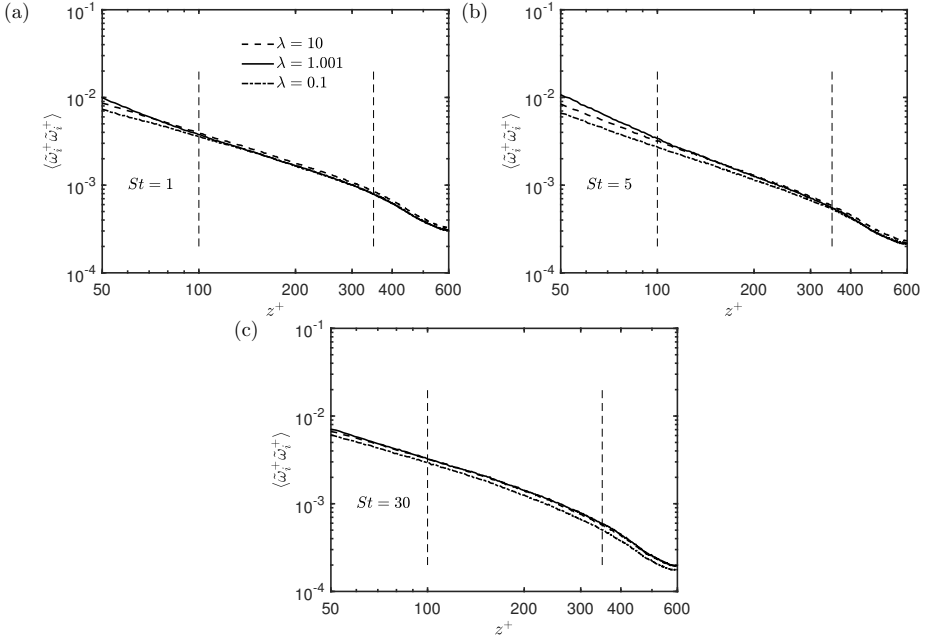


Figure 5: Enstrophy of spheroidal particles. (a)  $St = 1$ ; (b)  $St = 5$ ; (c)  $St = 30$ .

from  $z^+ = 100$  to  $z^+ = 350$  is chosen to further analyze the exponent of the power law. The fitted exponents  $k$  for each sort of particle are calculated and displayed in Figure 6(a), while the correlation coefficients between enstrophy and wall-normal location are presented in Figure 6(b), where the minus sign represents negative correlation. Correlation coefficients in Figure 6(b) are quite approximate to unity, revealing a strong correlation. As indicated by Figure 6(a), the exponents approximate about  $-1.3$ , quite similar to that of fluid enstrophy ( $-1.3118$ ). This supports that the power law of fluid enstrophy directly induces the power law of particle enstrophy. Both Figure 6(a) and 6(b) suggest that inertia have a greater influence on the power law than aspect ratio of particles. It is conjectured that the power law would extend to a larger range of wall-normal locations if the Reynolds number increases.

We assume that the rotation of particles in this region ( $z^+ = 100 \sim 350$ ) is more similar to that in the center of the channel than that in the vicinity of the walls. It is revealed by Zhao et al. [16] that the total particle enstrophy varies slightly versus aspect ratio  $\lambda$  in the channel-center. However, the preference for either spinning or tumbling is strongly shape-dependent. The enstrophy decreases when particle inertia increases, suggesting that the preferential orientation of inertial spheroidal particles changes with

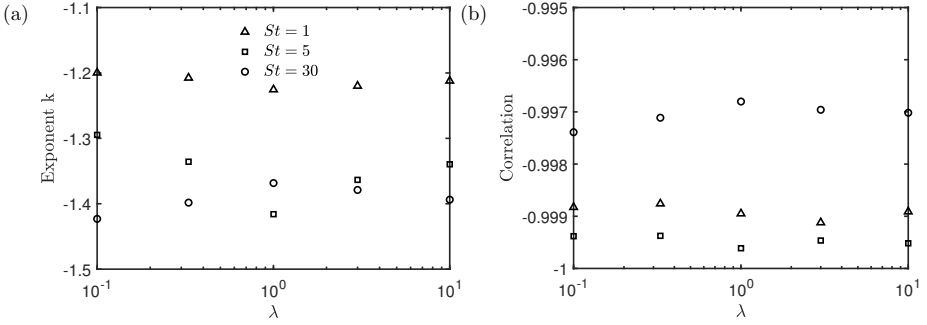


Figure 6: (a) Power law exponent  $k$ ; (b) The correlation coefficients between the particle enstrophy and the wall-normal distance  $z^+$  (the minus sign represents negative correlation).

Stokes number. Different Stokes number results in different preferential orientation versus fluid vorticity, as a consequence, affecting rotation rate of particles. Therefore, the Stokes number effect is dominant comparing to aspect ratio effect in Figure 6.

#### 4 Conclusions

A particle-laden turbulent channel flow at a relatively high Reynolds number  $Re_\tau = 600$  was simulated by DNS coupled with Lagrangian point particle methods, using a one-way coupling approach. Fifteen types of spheroidal particles are examined, including three Stokes numbers  $St = 1, 5, 30$  and five aspect ratios  $\lambda = 10, 3, 1.001, 0.33, 0.1$ . It is revealed in Figure 1 that most particle-laden channel flow simulations are confined to relatively low Reynolds numbers, especially those with non-spherical particles (about  $Re_\tau < 200$ ). Instead of concentrating on particle behaviors in the vicinity of wall, we focus on motion of particles away from the walls. The enstrophy of inertial spheroidal particles is calculated and presented in Figure 4 and 5, where a power law of enstrophy versus wall-normal location emerges at about  $z^+ = 100 \sim 350$ . Aspect ratios and Stokes numbers have minor influences on the power law and the exponents are about  $-1.3$ . Correlation coefficients are quite close to unity, indicating that the power law is outstanding in the actual region. A similar power law of fluid enstrophy is present and results in the power law of particle enstrophy, since shape and inertia only show slight influences on particle enstrophy in this region.

Many undiscovered phenomena and mechanisms of spheroidal particles may arise when the Reynolds number is high enough. For instance, large scale coherent structures in high Reynolds number turbulence could affect the translation and rotation of particles, which remains to be further explored. These investigations make an increasing request for high Reynolds number particle-laden turbulence simulations.

## Acknowledgements

The work was supported by the Natural Science Foundation of China (grant Nos. 11702158, 91752205 and 11490551) and the Research Council of Norway. The Research Council of Norway provided a scholarship to the author Yucheng Jie. The authors acknowledge the computational resources through grant No. NN2694K (Program for Supercomputing).

## REFERENCES

- [1] Sabban, L. and van Hout, R. Measurements of pollen grain dispersal in still air and stationary, near homogeneous, isotropic turbulence *J. Aerosol Sci.* (2011) **42**:867–882.
- [2] Wang, G. and Zheng, X. Very large scale motions in the atmospheric surface layer: a field investigation *J. Fluid Mech.* (2016) **802**:464–489.
- [3] Lundell, F., Söderberg, L.D. and Alfredsson, P.H. Fluid mechanics of papermaking *Annu. Rev. Fluid Mech.* (2011) **43**:195–217.
- [4] Smits, A.J., McKeon, B.J. and Marusic, I. High-Reynolds number wall turbulence *Annu. Rev. Fluid Mech.* (2011) **43**:353–375.
- [5] Lee, M. and Moser, R.D. Direct numerical simulation of turbulent channel flow up to  $Re_\tau \approx 5200$  *J. Fluid Mech.* (2015) **774**:395–415.
- [6] Kim, J., Moin, P. and Moser, R. Turbulence statistics in fully developed channel flow at low Reynolds number *J. Fluid Mech.* (1987) **177**:133–166.
- [7] McLaughlin, J.B. Aerosol particle deposition in numerically simulated channel flow *Phys. Fluids A-Fluid* (1989) **1**:1211–1224.
- [8] Zhang, H., Ahmadi, G., Fan, F.G. and McLaughlin, J.B. Ellipsoidal particles transport and deposition in turbulent channel flows *Int. J. Multiphase Flow* (2001) **27**:971–1009.
- [9] Bernardini, M. Reynolds number scaling of inertial particle statistics in turbulent channel flows *J. Fluid Mech.* (2014) **758**:R1.
- [10] Ouchene, R., Polanco, J.I., Vinkovic, I. and Simoëns, S. Acceleration statistics of prolate spheroidal particles in turbulent channel flow *J. Turbul.* (2018) **19**:827–848.
- [11] Challabotla, N.R., Zhao, L. and Andersson, H.I. Shape effects on dynamics of inertia-free spheroids in wall turbulence *Phys. Fluids* (2015) **27**:061703.

- [12] Mortensen, P.H., Andersson, H.I., Gillissen, J.J.J. and Boersma, B.J. Dynamics of prolate ellipsoidal particles in a turbulent channel flow *Phys. Fluids* (2008) **20**:093302.
- [13] Zhao, L., Marchioli, C. and Andersson, H.I. Slip velocity of rigid fibers in turbulent channel flow *Phys. Fluids* (2014) **26**:063302.
- [14] Challabotla, N.R., Zhao, L. and Andersson, H.I. Orientation and rotation of inertial disk particles in wall turbulence *J. Fluid Mech.* (2015) **766**:R2.
- [15] Gillissen, J.J.J., Boersma, B.J., Mortensen, P.H. and Andersson, H.I. On the performance of the moment approximation for the numerical computation of fiber stress in turbulent channel flow *Phys. Fluids* (2007) **19**:035102.
- [16] Zhao, L., Challabotla, N.R., Andersson, H.I. and Variano, E.A. Rotation of non-spherical particles in turbulent channel flow *Phys. Rev. Lett.* (2015) **115**:244501.
- [17] Moser, R.D., Kim, J. and Mansour, N.N. Direct numerical simulation of turbulent channel flow up to  $Re_\tau = 590$  *Phys. Fluids* (1999) **11**:943–945.
- [18] Brenner, H. The Stokes resistance of an arbitrary particle *Chem. Eng. Sci.* (1963) **18**:1–25.
- [19] Jeffery, G.B. The motion of ellipsoidal particles immersed in a viscous fluid *Proc. R. Soc. Lond. A* (1922) **102**:161–179.
- [20] Shapiro, M. and Goldenberg, M. Deposition of glass fiber particles from turbulent air flow in a pipe *J. Aerosol Sci.* (1993) **24**:65–87.
- [21] Mortensen, P.H., Andersson, H.I., Gillissen, J.J.J. and Boersma, B.J. On the orientation of ellipsoidal particles in a turbulent shear flow *Int. J. Multiphase Flow* (2008) **34**:678–683.
- [22] Challabotla, N.R., Zhao, L. and Andersson, H.I. Orientation and rotation dynamics of triaxial ellipsoidal tracers in wall turbulence *Phys. Fluids* (2016) **28**:123304.

## ON SIMULATION OF PARTICLE-LADEN WAKE FLOW

ZHAOYU SHI<sup>1</sup>, FENGJIAN JIANG<sup>2,3</sup>, HELGE I. ANDERSSON<sup>1</sup> AND HÅKON STRANDENES<sup>4</sup>

<sup>1</sup>Department of Energy and Process Engineering, Norwegian University of Science and Technology (NTNU)

Campus Gløshaugen, 7491 Trondheim, Norway

e-mail: helge.i.andersson@ntnu.no, zhaoyu.shi@ntnu.no

Web pages: <https://www.ntnu.edu/employees/helge.i.andersson>

<https://www.researchgate.net/profile/Shi.Zhaoyu>

<sup>2</sup> Department of Marine Technology, NTNU

Campus Tyholt, 7491 Trondheim, Norway

e-mail: fengjian.jiang@ntnu.no

<sup>3</sup> Department of Ships and Ocean Structure, SINTEF Ocean

Marinteknisk senter Tyholt, 7052 Trondheim, Norway

e-mail: Fengjian.Jiang@sintef.no

Web page: <https://www.sintef.no/en/all-employees/employee/?empId=7875>

<sup>4</sup> Kreuzinger und Manhart Turbulenz GmbH

Kirchenstraße 34, 81675 Munich, Germany

e-mail: h.stranden@km-turbulenz.no

Web page: <http://www.km-turbulenz.de/index.php>

**Key words:** numerical simulation, particle concentration, wake flow

**Abstract.** To preliminarily investigate the inertial particle distribution in the unsteady flow around a circular cylinder, we perform three-dimensional numerical simulations of particle-laden cylinder wake flow at  $Re_D = 100$ , defined based on cylinder diameter and uniform incoming flow velocity. A one-way coupling approach is utilized in the dilute suspensions. A strong correlation between local vortex structures and particle concentration is observed. Particle concentration presents different patterns at different Stokes numbers. Particles at very small Stokes numbers are distributed uniformly across the whole vortex cores. Particles at intermediate Stokes numbers aggregate mainly on the outer borders of vortex core regions and leave the vortex core a void region. The particles at large Stokes numbers are swept less away from the high vorticity region and even form a passage through the outer range of vorticity in the near wake. It is also observed that the detached particle bow shock appears when  $Sk$  is 3 and above. Moreover, some heavy particles are trapped inside the vortex cores close to the downstream border while particles align smoothly along the upstream border.

## 1 INTRODUCTION

The transportation and concentration of inertial particles in laminar and turbulent flows play an important role in many engineering and natural situations, i.e. sediments in rivers and scour around offshore wind-turbine foundations etc. Unlike tracer particles, inertial particles follow their own dynamics resulting from the interaction with local vortex structures, known as *preferential concentration*. Previous numerical work in different particle-laden flows has been well-established by using direct numerical simulation (DNS) for homogeneous isotropic turbulence [1] [2] and channel flows [3]. Many statistical measures, such as particle distribution PDF, correlation dimension [4] and Voronoï diagrams [5] etc., are employed to investigate the relationship between particle concentration and local flow structures. However, there is still a lack of research on particle-laden wake flow although pioneering work has been done for plane wake [4] and cylinder wakes [6] [7]. Most numerical and experimental results provided visualization results of particle distribution from light to heavy particles in wakes and showed a clear inertia-dependency of concentration. Some mechanisms have been proposed to account for particle concentration, such as centrifugal mechanism and the sweep-stick property for zero-acceleration points in the flow [1]. The underlying mechanism, unfortunately, is still not fully understood, especially not for the wake flow due to the lack of quantitative analysis.

The particle concentration pattern not only depends on particle inertia, but also vortex structures in the wake. The vortex shedding at different Reynolds numbers is comprehensively described in Williamson's review [8]. Considering the computational cost of tracking millions of particles, most previous direct numerical simulations stayed at low Reynolds numbers. In order to introduce turbulence in the particle-laden cylinder wake flow, the Reynolds-Averaged-Navier-Stokes (RANS) method is commonly utilized to study the particle concentration at high Reynolds numbers [9]. However, the significant streamwise vortices in a turbulent wake flow are wiped out in steady RANS, while unsteady RANS is still unable to properly account for turbulent fluctuations which makes the transient solution doubtful.

We aim at investigating particle concentration by DNS at higher Reynolds number. The particle library implemented in MGLET has been validated in homogeneous isotropic turbulence by Gobert [10] [11]. We consider two-dimensional unsteady laminar flow around a straight circular cylinder at  $Re_D = 100$  in this paper as a preliminary study. The computational details of the flow configuration is given in section 2. The visualization results of particle distributions at different Stokes numbers are given in section 3. Finally, we conclude the observed concentration patterns in section 4.

## 2 COMPUTATIONAL DETAILS

### 2.1 Flow configuration

We set a straight circular cylinder with diameter  $D$  and length  $5.12D$  in an incompressible flow of a Newtonian fluid. The flow configuration is illustrated in figure 1, which

is a box with lengths of  $L_x$ ,  $L_y$  and  $L_z$ . We define the streamwise direction as x-direction, crossflow direction as y-direction and spanwise direction as z-direction. The Reynolds number  $Re_D = U_0 D / \nu$  is given by the free-stream velocity  $U_0$  and the cylinder diameter  $D$  ( $\nu$  is kinematic viscosity of the incompressible fluid). Other quantities in our simulation are all measured by  $U_0$  and  $D$ .

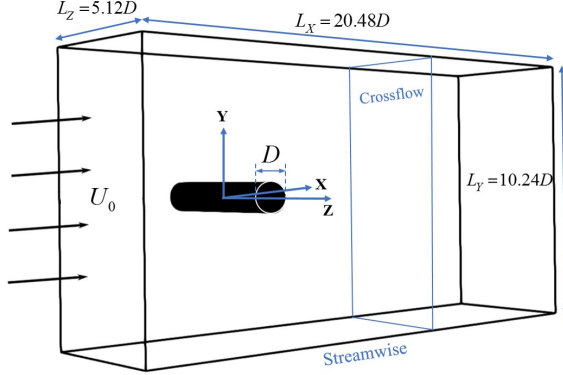


**Figure 1:** Three-dimensional computational domain for the flow around a straight circular cylinder. Note that the domain is not to scale.

As a preliminary test of inertial particle dispersion in the cylinder wake flow, we only choose a relatively short domain to avoid unnecessary computational cost. Figure 2 perceptually shows the domain size in our case compared with an experimental visualization from Zdravkovich [12], both at  $Re_D = 100$ . The lower plot in figure 2 is a snapshot of the vorticity field in spanwise direction in a fully developed flow obtained from our simulation. As depicted in figure 2, the computational domain only approximately includes three pairs of vortices in the near wake region. The flow around a circular cylinder at  $Re_D = 100$  is often taken as a benchmark to validate a CFD solver, in which the wake flow stays two-dimensional but unsteady [8]. The boundary conditions used in the simulations are summarised below:

- Inlet: uniform free stream,  $u_i = (U_0, 0, 0)$ .
- Outlet: Neumann boundary conditions for the velocity components ( $\partial u / \partial x = \partial v / \partial x = \partial w / \partial x = 0$ ) and zero pressure ( $p = 0$ ).
- Two vertical sides normal to Z-direction: periodic condition.
- Two horizontal sides normal to Y-direction: free-slip boundary condition, i.e.  $v = 0$  and  $\partial u / \partial y = \partial w / \partial y = 0$ .

- The surface of the cylinder is treated as a no-slip and impermeable wall.

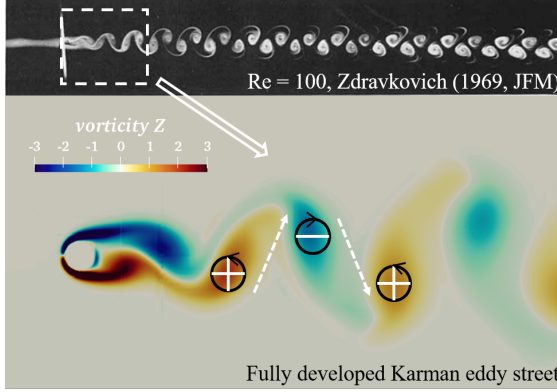


**Figure 2:** Sketch of the comparison of the domain sizes at  $Re_D = 100$  between an experiment by Zdravkovich [12] and the simulation in this paper.

## 2.2 Numerical methods

In order to directly solve the incompressible three-dimensional transient flow around a cylinder, we utilize a second-order finite volume method to discretize the Navier-Stokes equation

$$\frac{\partial u_i}{\partial x_i} = 0, \quad (1)$$

$$\underbrace{\frac{\partial u_i}{\partial t}}_{\text{time change rate}} + \underbrace{u_j \frac{\partial u_i}{\partial x_j}}_{\text{convection}} = \underbrace{-\frac{1}{\rho_f} \frac{\partial p}{\partial x_i}}_{\text{pressure force}} + \underbrace{\nu \frac{\partial^2 u_i}{\partial x_j \partial x_j}}_{\text{viscous diffusion}} \quad (2)$$

The simulations are performed by the well-verified DNS/LES solver MGLET [13]. Fluid velocity and pressure information are stored in discretized 3D staggered equidistant Cartesian grids [14]. In equation (2), the viscous diffusion term is approximated by a central-difference scheme, and eq(2) is time advanced by an explicit low-storage third-order Runge-Kutta scheme. Meanwhile, a Poisson equation is iteratively solved by the combination of successive-over-relaxation (SOR) and Stone's strongly implicit procedure (SIP), and also is corrected to fulfill mass conservation equation. In order to handle the boundary condition of particle-wall interaction, the cut-cell finite-volume approach is implemented in MGLET to extract the normal vector, which is crucial when particles impinge the wall.



The cuboid Cartesian cells are intersected by the curved wall, and the cell shape is exactly computed from the intersection. This results in the formation of the finite volume with polyhedron shape. This process is enforced by employing the direct-forcing Immersed Boundary Method (IBM). A Ghost-cell methodology of IBM is enforced in the standard MGLET [15], while a cut-cell IBM approach implemented as a new feature in MGLET, for the first time, is applied in this study [16].

When the flow is statistically periodic, particles are seeded from the inlet boundary with uniform velocity  $U_0$  and distributed randomly into the flow field. Considering the heavy computation of resolving the flow around finite-size particles, point-particles are the most commonly used model to track particles in an Euler-Lagrangian framework. The particles are assumed to be small, spherical and inertial ( $\rho_p/\rho_f = 1000$ ,  $\rho_p$ ,  $\rho_f$  are the particle and the surrounding fluid density). We also assume particle suspension here is dilute with volume fraction below  $10^{-6}$ , so that particle collisions rarely occur, and particles are one-way coupled to the statistically periodic wake flow. The Maxey-Riley equation which describes the particle motion reduces to eq(3) with only Stokes drag force acting on particles:

$$\frac{du_{p,i}}{dt} = \frac{C_D Re_p}{24\tau_p} (u_{f@p,i} - u_{p,i}) \quad (3)$$

where  $u_{p,i}$  is particle velocity component updated by an adaptive fourth-order Rosenbrock-Wanner scheme with third-order error estimator,  $u_{@p,i}(t) = u(t, x_{p,i}(t))$  is the fluid velocity component seen by the particle at position  $x_{p,i}$  obtained by linear interpolation. An explicit Euler scheme is used to update particle position.  $\tau_p = \frac{\rho_p d^2}{18\rho_f \nu}$  is particle relaxation time ( $d$  is particle diameter), and we define Stokes number  $Sk = \tau_p/\tau_f$  as a non-dimensional parameter to measure the particle inertia ( $\tau_f = D/U_0$ ). The Stokes drag coefficient  $C_D$  is a function of particle Reynolds number  $Re_p = d \|\mathbf{u}_p - \mathbf{u}_{f@p}\|/\nu$ , and we use a piecewise model to include five different  $Re_p$ -dependent Stokes drags referenced from Clift et al [17]:

$$C_D = \begin{cases} 3/16 + 24/Re_p & Re_p < 0.01, \\ 24/Re_p(1 + 0.15Re_p^{0.687}) + 0.42/(1 + 4.25 \times 10^4 Re_p^{-1.16}) & Re_p < 3 \times 10^5, \\ 29.78 - 5.3 \times \log_{10} Re_p & 3.5 \times 10^5 < Re_p < 4 \times 10^5, \\ 0.1 \log_{10} Re_p - 0.49 & 4 \times 10^5 < Re_p < 10^6, \\ 0.19 - 8 \times 10^4/Re_p & 10^6 < Re_p. \end{cases} \quad (4)$$

We set particles into three groups by Stokes number  $Sk$  ranging from light to heavy ones, and each group includes three different  $Sk$  cases with the corresponding  $Sk$  shown in table 1. The total number of particles in each group is around 410000. Particles in one grid are assigned to one CPU to proceed the parallelization. For the simplicity of the

problem, the interaction between a particle and the cylinder wall is taken as fully elastic bouncing.

**Table 1:** Particle conditions of simulation runs.

Group	Light			Medium			Heavy		
$Sk$	5.6e-5	1.7e-3	5.6e-3	0.1	0.55	1.0	3.0	6.5	10.0
Npart	413685			411755			419009		

### 2.3 Computational mesh

The computational domain is discretized by a multi-level structured Cartesian mesh, where the grids are constructed by cubic boxes with different grid spacings in an unstructured arrangement. Figure 3 gives an impression of four-level grids, where  $N \times N \times N$  cells are uniformly filled in each grid box, regardless of the grid size. The region close to the cylinder needs the finest grid, and we define the minimum grid spacing as spatial resolution. The grid size increases by a factor of 2, i.e. the size of level-4 grid in figure 3 is  $0.02D$  while  $0.16D$  for level-1 grid.

In order to examine the sufficiency of the mesh for case  $Re_D = 100$ , we generate two additional meshes(case 2 and 3). Table 2 provides the details of the time-averaged drag-coefficient  $C_D$ , the root-mean-square of the lift force coefficient  $C_{L-rms}$  and the spanwise force  $C_Z$  calculated from all three cases. The difference of these quantities between all cases is very modest while the Strouhal numbers  $St = fD/U_0$  are slightly higher than the reference value 0.16, which could be caused by insufficient time windows. We also note that  $C_D$  and  $C_{L-rms}$  are higher than the commonly recognized approximate numbers 1.3 and 0.22 respectively. This is known to arise from the lack of crossflow domain size in our simulations. To ensure the accuracy of the interpolation to obtain particle velocity and a physical vorticity field, we prefer the finer mesh with 2.09million cells. Figure 4 presents three normalized forces around the cylinder including drag coefficient  $C_D$ , lift coefficient  $C_L$  and spanwise force coefficient  $C_Z$ . The regular waves of  $C_D$  and  $C_L$  indicate a fully developed unsteady laminar flow. Since the cylinder is almost independent of the spanwise force with  $C_Z$  being  $10^{-6}$ , the flow can be trusted as two dimensional flow. The Strouhal number in case 1 can be approximately obtained as 0.176 from the average of 34 time periods of the lift coefficient.

## 3 PARTICLE CONCENTRATION

The occurrence of a Kármán vortex-street is the typical characteristic of flow around a circular cylinder in the laminar vortex shedding regime  $49 < Re_D < 194$  [8], as figures 5 and 6 present. These large-scale vortical structures in the wake have a significant effect on

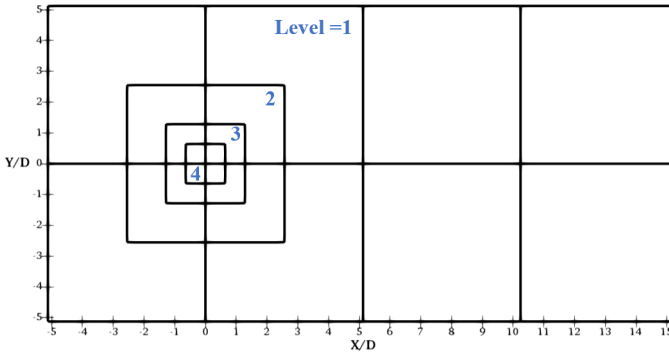


**Figure 3:** Sketch of the multigrids (4-level shown here). A slice of the multi-level grid box distribution in the (X,Y)- plane is shown. Each square represents a 3D grid box and contains the amount of  $N \times N \times N$  grid cells. Grid resolution increases as the square size gets smaller.

**Table 2:** Grid independence study for  $Re_D = 100$ . Ngrid and Ncell represent the total number of grid boxes and cells, respectively.

Case	Resolution	$C_D$	$C_{L-rms}$	$C_Z$	$St$	Ngrid	Ncell
1	0.02D	1.932	0.483	-1.527e-6	0.176	64	2.09million
2	0.04D	1.965	0.507	-1.327e-6	0.177	32	1.05million
3	0.08D	2.061	0.542	8.509e-13	0.178	16	0.52million

the dispersion of inertial particle, known as preferentially concentration. Here we observe the particle distribution at various Stokes number  $Sk$  from 0.0056 to 10. Since the flow is two-dimensional at  $Re_D = 100$ , we only present the particle distribution and vorticity in an (X,Y)-plane.

For the very low- $Sk$  particles shown in figure 5(a), they can be regarded as tracers following the flow evolution and thus uniformly scattered in the flow field. No accumulation is visually identifiable. In figure 5(b), however, periodic void regions appear in the vortex cores for both positive and negative vorticity. The particles are swept away from vortex cores indicating a slight effect of inertia. The void regions become larger with the shedding vortex growing along the streamwise direction, as marked in figure 5(b) with white curves.

Figure 6 presents instantaneous snapshots of particle distribution for medium and heavy particles. In the left panels, we observe the inertial particles of  $Sk=0.55$  and 1 also cannot follow the fluid as particles of  $Sk=0.1$ , and continue to run away from the vortex

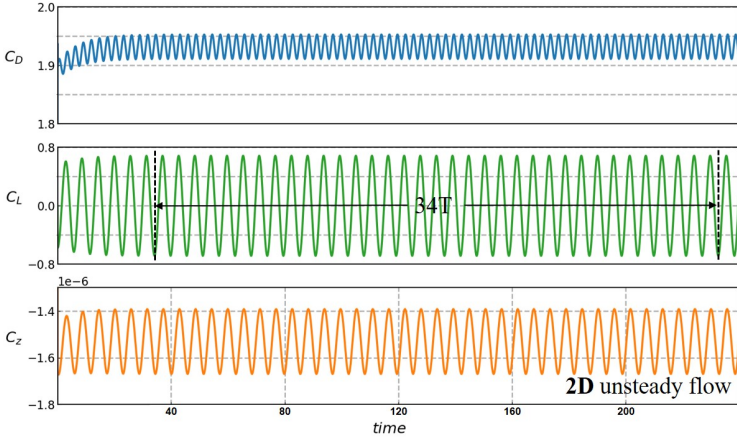


**Figure 4:** The drag coefficient  $C_D$ , lift coefficient  $C_L$  and normalized force  $C_Z$  in spanwise direction at  $Re_D = 100$ . Case 1 with spatial resolution 0.02D.

cores due to the centrifugal force. The edges of these void regions reach closer to the outer range of vorticity braids as particle inertia plays a more significant role in the distribution pattern. As we can compare in figure 6(a)~(c), the void regions are getting wider and longer as  $Sk$  increases. However, figures 6(d) ~ (f) show quite opposite patterns when  $Sk$  continues increasing from 3 to 10, in which the length of void regions is decreasing. It is observed that particles get less and less driven to the outer border, and the heavy particles behave more like bullets. They tend to pass through the vortex center and form a connected passage in the near wake instead of the individual void regions shown in figure 6(a)~(c).

Comparing the particle distribution at  $Sk=1.0$  and 10 in figure 7(a), we observe that the particles accumulate along the upstream border which makes the border smooth. In contrast, a small portion of particles stay inside the vortex core near the downstream, and more particles are trapped inside the vortex core as  $Sk$  increases. The velocity of the particles located upstream is slightly smaller than the ones at downstream shown in figure 7(b). The observations in figure 5 and 6 indicate a strong  $Sk$ -dependency of particle concentration in the wake flow. Similar pattern of the particle distribution can also be found in Tang's experiments and DNS results in plane wake [4], and the numerical simulation work for cylinder wakes in [6] [7] at higher  $Re$  numbers with three-dimensional effect. The most interesting phenomenon for heavy particles is that a detached particle bow shock is clearly observed in front of the cylinder with a distance due to the fully elastic collision model. The shock angle is getting wider as  $Sk$  increases, and the shock wave is hardly influenced by the wake as  $Sk=6.5$  and 10.

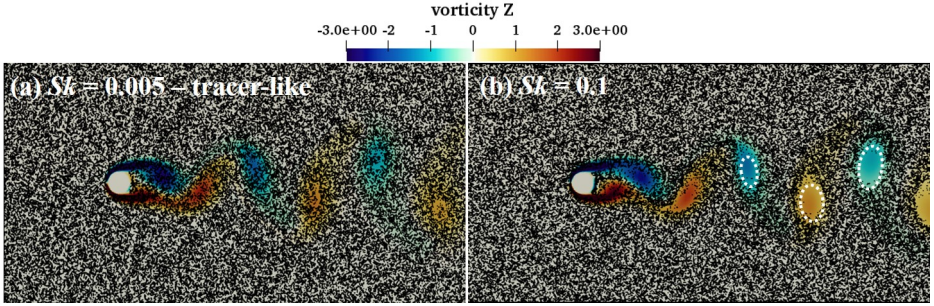


**Figure 5:** Instantaneous snapshots of particle distribution and Z-direction vorticity in the light particle simulations: (a)  $Sk=0.005$  and (b)  $Sk=0.1$ .

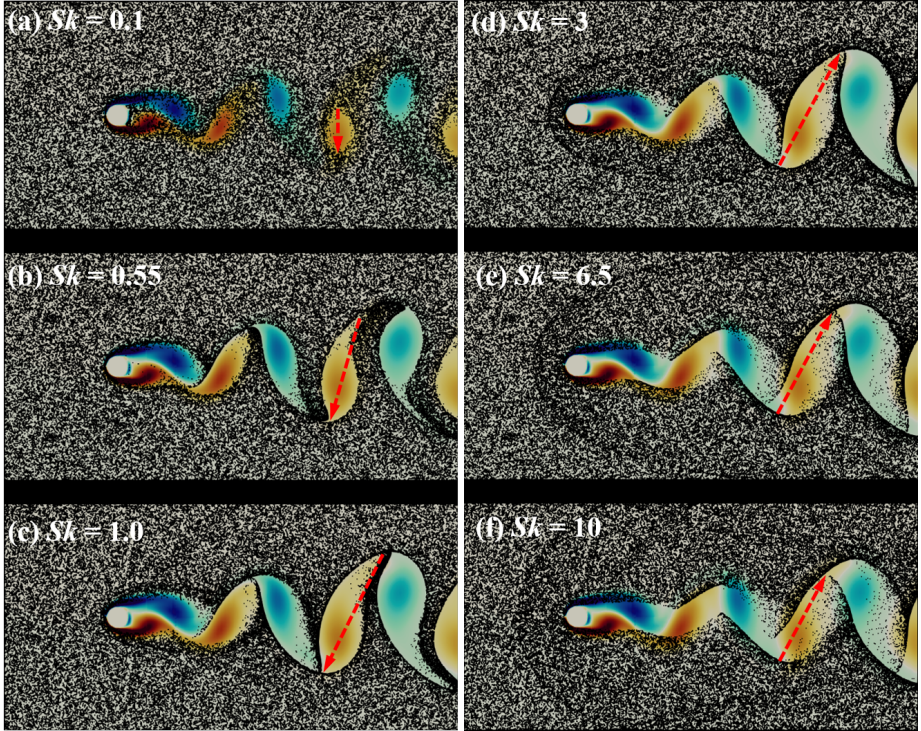


**Figure 6:** Instantaneous snapshots of particle distribution and Z-direction vorticity at different  $Sk$ . The left panel corresponds to the medium particles: (a)~(c)  $Sk=0.1, 0.55, 1.0$  and the right panel corresponds to the heavy particles: (b)~(f)  $Sk=3.0, 6.5, 10$ .



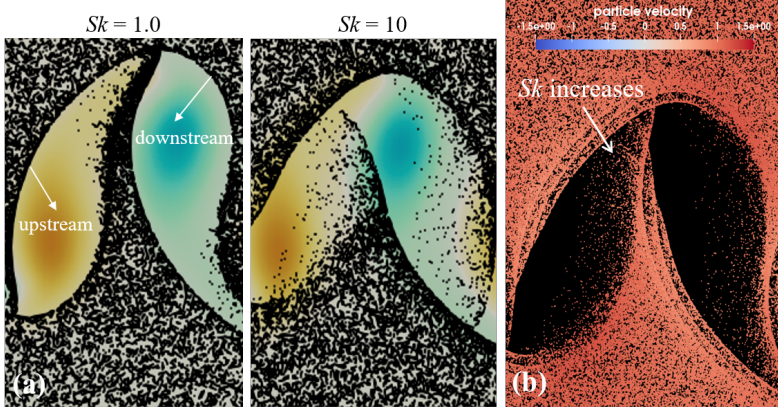


**Figure 7:** (a) Comparison of the instantaneous particle distribution in the same vortex pair at  $Sk=1.0$  and  $10$ . (b) Superimposed particle velocity distribution at  $Sk=3, 6.5, 10$  in the 1 vortex pair.

#### 4 CONCLUSIONS

In this preliminary study, we performed numerical simulation for particle-laden flow around a circular cylinder at  $Re_D = 100$ . We aim at studying the inertial particle distribution at different Stokes numbers  $Sk$  ranging from  $0.0056$  to  $10$ . The Lagrangian method was used to track the trajectories of point particles with one-way coupling.

It is found that the particle distribution presents various patterns between light, intermediate and heavy particles. The particle concentration is strongly correlated to the vortex structure. The particles at extremely small Stokes numbers completely follow the fluid motion and disperse across the vortex cores without preferential concentration. The particles at intermediate Stokes numbers show different degrees of preferential concentration at  $Sk=0.1, 0.55, 1$ . The common tendency is that particles concentrate on the outer boundaries of vortices due to the centrifugal force, and thus separate void zones appear. The empty regions expand larger as Stokes number increases but remain below  $1$ . For the heavy particles, the void regions appear as a passage especially at  $Sk=10$ , which indicates that bullet-like particles get across the outer boundaries of vorticity and maintain their own motions. Also we find that particles would flow back towards the vortex core region but still pass smoothly around the front edge. Based on all simulation results, we clearly can see an inertial effect on the pattern of particle concentration.

## 5 ACKNOWLEDGEMENTS

The use of the Norwegian HPC **Fram** was granted by the Norwegian Research Council under project nn2649k and nn9191k. The work is financially supported by *NTNU Energy* for a research fellowship.

## REFERENCES

- [1] Monchaux, R., Bourgoïn, M., Cartellier, A. Analyzing preferential concentration and clustering of inertial particles in turbulence. *Int. J. Multiphase Flow* (2012) **40**:1-18
- [2] Ireland, P. J., Bragg, A. D., Collins, L.R. The effect of Reynolds number on inertial particle dynamics in isotropic turbulence. Part 1. Simulations without gravitational effects. *J. Fluid Mech.* (2016) **796**:617-658
- [3] Zhao, L. H., Challabotla, N. R., Andersson, H.I., Variano, E.A. Rotation of non-spherical particles in turbulent channel flow. *Phys. Rev. Lett.* (2015) **115**:244501
- [4] Tang, L., Wen, F., Yang, Y., Crowe, C. T., Chung, J. N., Troutt, T. R. Self-organizing particle dispersion mechanism in a plane wake. *Phys. Fluids* (1992) **4**:2244-2251
- [5] Garca-Villalba, M., Kidanemariam, A. G., Uhlmann, M. DNS of vertical plane channel flow with finite-size particles: Voronoi analysis, acceleration statistics and particle-conditioned averaging. *Int. J. Multiphase Flow* (2012) **46**:54-74
- [6] Kun, L., Fan, J. R., Li, W.C., Cen, K. F. Transient, three-dimensional simulation of particle dispersion in flows around a circular cylinder ( $Re = 140-260$ ) *Fuel* (2009) **88**:1294-1301
- [7] Yao, J., Zhao, Y. L. , Hu, G. L., Fan, J. R., Cen, K. F. Numerical simulation of particle dispersion in the wake of a circular cylinder. *Aerosol Science and Technology* (2009) **43**:174-187
- [8] Williamson, C. H. K. Vortex dynamics in the cylinder wake. *Annu. Rev. Fluid. Mech.* (1996) **28**:477-539
- [9] Ong, M. C., Holmedal, L. E., Myrhaug, D. Numerical simulation of suspended particles around a circular cylinder close to a plane wall in the upper-transition flow regime. *Coastal Engineering* (2012) **61**:1-7
- [10] Gobert, C., Analytical assessment of models for large eddy simulation of particle laden flow. *J. Turbul* (2010) **11**
- [11] Gobert, C., Large Eddy Simulation of Particle-Laden Flow (Doctoral dissertation). Technical University of Munich, Munich, German (2009).

- [12] Zdravkovich, M. Smoke observations of the formation of a Kármán vortex street. *J. Fluid Mech.* (1969) **37**(3):491-496.
- [13] Manhart, M., Friedrich, R. DNS of a turbulent boundary layer with separation. *Int. J. Heat Fluid Flow* (2002) **23**:572-781.
- [14] Manhart, M. A zonal grid algorithm for DNS of turbulent boundary layers. *Comput. Fluids* (2004) **33**:435-461.
- [15] Peller, N., Duc, A. L., Tremblay, F., Manhart, M. High-order stable interpolations for immersed boundary methods. *Int. J. Numer. Meth. Fluids* (2006) **52**:1175-1193.
- [16] Mittal, R., Iaccarino G. Immersed boundary methods. *Annu. Rev. Fluid. Mech.* (2005) **37**:239-261.
- [17] Clift, R., Grace, J. R., Weber, M. E. Bubbles, Drops and Particles. *Academic Press*. New York (1978)
- [18] Eaton, J.K., Fessler, J.R. Preferential concentration of particles by turbulence. *Int. J. Multiphase Flow* (1994) **20**:169-209



## Authors Index

Andersson, Helge I. ....	81, 197,	Jayaram, Rohith .....	197
.....	343, 395, 407	Jiang, Fengjian .....	81, 407
Anker, Jan Christian .....	51	Jie, Yucheng .....	395
Aursand, Mads .....	61	Kamath, A. ....	101, 367
Bacca, Mattia .....	25	Kristensen, Tor E. ....	115
Bihs, H. ....	101, 367	Kristoffersen, Frederik .....	211
Bruland, Oddbjørn .....	265	Kumar, Mukesh .....	237
Brvik, Tore .....	149	Kvamsdal, Trond .....	237, 323
Celledoni, Elena .....	343	Kvarving, Arne M. ....	237
Dahl Aguilera, Hans Martin .....	27	Lamballais, E. ....	1
Evje, Steinar .....	139	Liu, Shengnan .....	311
Fossan, Ingar .....	165	Liu, Xuyan .....	249
Fossum, Hannibal E. ....	115	McMeeking, Robert M. ....	25
Gillissen, Jurriaan J.J. ....	197	Moraru, Adina .....	265
Granum, Henrik .....	149	Morin, David .....	149
Holmas, Tore .....	165	Müller, Bernhard .....	211
Holzapfel, Gerhard A. ....	249	Ohm, Laurel .....	343
Hopperstad, Odd Sture .....	149	Okstad, Knut M. ....	237
Janocha, Marek Jan .....	181	Omang, Marianne G. ....	285

Ong, Muk Chen .....	181, 311, 381	Tian, Cai .....	81
Osnes, Andreas N. ....	115, 285	Urheim, Stig .....	27
Pakozdi, C. ....	101, 367	Vartdal, Magnus .....	285
Perkis, Andrew .....	265	Vicente Cruz, R. ....	1
Pettersen, Bjørnar .....	81	Wang, W. ....	101, 367
Prot, Victorien .....	27	Yin, Guang .....	381
Prot, Victorien E. ....	249	Zhao, Lihao .....	197, 395
Qu, Sen .....	311		
Rasheed, Adil .....	323		
Reif , Bjørn A. P. ....	285		
Rüther, Nils .....	265		
Saleh, Omar A. ....	25		
Shi, Zhaoyu .....	407		
Skallerud, Bjørn .....	27, 61		
Skallerud, Bjørn H. ....	249		
Strandenes, Hakon .....	407		
Tabib, Mandar V. ....	323		
Tapley, Benjamin K. ....	343		
Teigen Giljarhus, Knut Erik .....	139		